JAERI-Conf
2004-005

INDC(JPN)-192/U

JP0450472

PROCEEDINGS OF THE 2003 SYMPOSIUM ON NUCLEAR DATA
NOVEMBER 27-28, 2003, JAERI, TOKAI, JAPAN

April 2004

(Eds.) Takaaki OHSAWA* and Tokio FUKAHORI

日本原子力研究所
Japan Atomic Energy Research Institute

本レポートは、日本原子力研究所が不定期に公刊している研究報告書です。
入手の問合わせは、日本原子力研究所研究情報部研究情報課（〒319-1195 茨城県那珂郡東海村）あて、お申し越し下さい。なお、このほかに財団法人原子力弘済会資料センター（〒319-1195 茨城県那珂郡東海村日本原子力研究所内）で複写による実費頒布を行っております。

This report is issued irregularly.
Inquiries about availability of the reports should be addressed to Research Information Division, Department of Intellectual Resources, Japan Atomic Energy Research Institute, Tokai-mura, Naka-gun, Ibaraki-ken 〒319-1195, Japan.

編集兼発行　日本原子力研究所

JAERI－Conf 2004－005

Proceedings of the 2003 Symposium on Nuclear Data
November 27-28, 2003, JAERI, Tokai, Japan

(Eds.) Takaaki OHSAWA* and Tokio FUKAHORI

Japanese Nuclear Data Committee
Tokai Research Establishment
Japan Atomic Energy Research Institute
Tokai-mura, Naka-gun, Ibaraki-ken

(Received February 6, 2004)

The 2003 Symposium on Nuclear Data was held at Tokai Research Establishment, Japan Atomic Energy Research Institute (JAERI), on 27th and 28th of November 2003. Japanese Nuclear Data Committee and Nuclear Data Center, JAERI organized this symposium. In the oral sessions, presented were 18 papers on topics of ADS development and nuclear data for transmutation, nuclear data needs for next generation reactors and future JENDL plan, frontier of nuclear physics studies and nuclear data measurements, advanced science study and nuclear data, nuclear data needs and activities in Asian region, future of nuclear data study and other subjects. In the poster session, presented were 26 papers concerning experiments, evaluations, benchmark tests and so on. Those presented papers are compiled in the proceedings.

Keywords: Nuclear Data, Symposium, Proceedings, Nuclear Reaction, JENDL, Experiment, Evaluation, Benchmark Test, Cross Section, ADS, Next Generation reactors.

*Kinki University

2003年核データ研究会報文集
2003年11月27日～28日，東海研究所，東海村

日本原子力研究所東海研究所
シグマ研究委員会
（編）大澤　孝明*・深堀　智生

（2004年2月6日受理）

2003年核データ研究会が、2003年11月27日と28日の両日、日本原子力研究所東海研究所において開催された。この研究会は、日本原子力研究所のシグマ研究委員会と核データセンターが主催して開いたものである。口頭発表では、ADS開発と核種変換のための核データ、次世代炉等への核データニーズと次期JENDL構想、核物理研究及び核データ測定の最前線、物理研究の最先端と核データ、アジア地域の核データニーズ及び活動、わが国の核データ研究の今後、その他のトピックスについての18件の報告があった。ポスター発表では、26件の発表があり、それらは、核データの測定、評価や評価済核データのベンチマークテスト等に関するものであった。本報文集は、それらの論文をまとめたものである。

東海研究所：〒319-1195 茨城県那珂郡東海村白方白根2-4
* 近畿大学

Program Committee

Takaaki OHSAWA(Chairman)	Kinki University
Tokio FUKAHORI	Japan Atomic Energy Research Institute
Hideo HARADA	Japan Nuclear Cycle Development Institute
Osamu IWAMOTO	Japan Atomic Energy Research Institute
Hideki MATSUMOTO	Mitsubishi Heavy Industries, Ltd.
Tsuneo NAKAGAWA	Japan Atomic Energy Research Institute
Hiroyuki OIGAWA	Japan Atomic Energy Research Institute
Keisuke OKUMURA	Japan Atomic Energy Research Institute
Yukinobu WATANABE	Kyushu University

プログラム委員会

大澤　孝明（委員長）	近畿大学
深堀　智生	日本原子力研究所
原田　秀郎	核燃料サイクル開発機構
岩本　修	日本原子力研究所
松本　英樹	三菱重工業（株）
中川　庸雄	日本原子力研究所
大井川　宏之	日本原子力研究所
奥村　啓介	日本原子力研究所
渡辺　幸信	九州大学

This is a blank page.

Contents

目　次

This is a blank page.

1. Introduction

The 2003 symposium on nuclear data was held at Tokai Research Establishment, Japan Atomic Energy Research Institute (JAERI), on 27th and 28th of November 2003, with about 120 participants. Japanese Nuclear Data Committee and Nuclear Data Center, JAERI organized the symposium.

The program of the symposium is listed below. In the oral sessions, presented were 18 papers on topics of release of ADS development and nuclear data for transmutation, nuclear data needs for next generation reactors and future JENDL plan, frontier of nuclear physics studies and nuclear data measurements, advanced science study and nuclear data, nuclear data needs and activities in Again region, future of nuclear data study and other subjects. In the poster session, presented were 26 papers concerning experiments, evaluations, benchmark tests and so on. Those presented papers are compiled in the proceedings.

Program of Symposium on Nuclear Data 2003

Nov. 27 (Thu.)

9:30-9:40

1. Opening Address A. Hasegawa (JAERI)

9:40-10:30

2. ADS Development and Nuclear Data for Transmutation (1)

Chairperson: H. Takano (JAERI)

2.1 Present Status of Minor Actinide Nuclear Data [25+5] T. Nakagawa (JAERI)

2.2 Present Status of Fission Yield Data [15+5] J. Katakura (JAERI)

10:30-12:00

3. ADS Development and Nuclear Data for Transmutation (2)

Chairperson: H. Oigawa (JAERI)

3.1 Estimation for Effect of JENDL-3.3 on Neutronics Characteristics of ADS [25+5]

K. Tsujimoto (JAERI)

3.2 Current Status of Spallation Product Data [25+5] V. Artisyuk (TIT)

3.3 Particle and Heavy Ion Transport Code System; PHITS [25+5]

K. Niita (RIST)

12:00-13:00 Lunch

13:00-14:30

4. Poster Session (Odd Numbers)

14:30-16:30

5. Nuclear Data Needs for Next Generation Reactors and Future JENDL Plan

Chairperson: H. Matsumoto (MHI)

5.1 Analysis of RMWR (Reduced-Moderation Water Reactor) Mockup Experiments in FCA using JENDL-3.2 and JENDL-3.3 [25+5] S. Okajima (JAERI)

5.2 Target accuracy of MA nuclear data and progress in validation by post irradiation experiments with the fast reactor "JOYO" [25+5] S. Ohki (JNC)

5.3 Nuclear Data for Emergency Preparedness of Nuclear Power Plants - Evaluation of Radioactivity Inventory in PWR by Using JENDL-3.3 - [25+5] Y. Yoshida (INSS)

5.4 Next Version of JENDL General Purpose File [25+5] K. Shibata (JAERI)

16:30-16:45 Coffee Break

16:45-17:45

6. Frontier of Nuclear Physics Studies and Nuclear Data Measurements

Chairperson: Y. Watanabe (Kyushu U.)

6.1 Fission Modes and Mass Distribution in Heavy Actinide Region Studied with Multi-dimensional Langevin Equation [25+5] T. Ichikawa (JAERI)

6.2 Measurement of Neutron-production Double-differential Cross Sections for Continuous Neutron-incidence Reaction up to 100 MeV [25+5] S. Kunieda (Kyushu U.)

18:00-20:30 Reception (Akogi-ga-Ura Club)

Nov. 28 (Fri.)

9:30-10:30

7. Advanced Science Study and Nuclear Data

Chairperson: K. Oyamatsu (Aichi Shukutoku U.)

7.1 Cosmo-nuclear Physics Studied by Neutrons [25+5] Y. Nagai (RCNP)

7.2 Astrophysics and Photoreaction Data [25+5] H. Utsunomiya (Konan U.)

10:30-10:45 Coffee Break

10:45-11:45

8. Nuclear Data Needs and Activities in Again Region

Chairperson: A. Hasegawa (JAERI)

8.1 Neutron- and Proton-induced Nuclear Data Evaluation of Thorium, Uranium and Curium Isotopes for Energies up to 250 MeV [25+5] Y.-O. Lee (KAERI)

8.2 Status Report and Measurements of Total Cross Sections at Pohang Neutron Facility [25+5] G. Kim (Kyungpook National Univ.)

12:00-13:00 Lunch

13:00-14:30

9. Poster Session (Even Numbers)

14:30-15:45

10. Future of Nuclear Data Study - 40th Anniversary of JNDC –

Chairperson: M. Igashira (TIT)

10.1 Forty Years Experience on Nuclear Data Evaluation [20+5]

T. Murata (Aitel)

10.2 JENDL Reactor Constant and its Application [20+5]

A. Zukeran (Hitachi)

10.3 What JNDC should be in the Future? [20+5] T. Yoshida (Musashi Inst. Tech.)

15:45-16:00

11. Poster Award and Closing Address T. Ohsawa (Kinki U.)

Poster Session

Nov. 27 (Thu.) 13:00-14:30 Odd Numbers

Nov. 28 (Fri.) 13:00-14:30 Even Numbers

P.1 Measurement of Double Differential Cross Sections of Secondary Heavy Particles Induced by Tens of MeV Particles M. Hagiwara (Tohoku U.)

P.2 Measurements of Differential Thick Target Yield for Fe, Cu(p,xn) Reactions at 35 and 50 MeV T. Itoga (Tohoku U.)

P.3 Measurements of Deuteron-Induced Activation Cross Sections for Aluminum, Copper

This is a blank page.

2. Papers Presented at Oral Sessions

This is a blank page.

2.1 Present Status of Minor Actinide Nuclear Data

Tsuneo NAKAGAWA
Nuclear Data Center, Japan Atomic Energy Research Institute
Tokai-mura, Naka-gun, Ibaraki-ken 319-1195
e-mail: nakagawa@ndc.tokai.jaeri.go.jp

Present status of neutron-induced fission and capture cross sections of Np to Cm isotopes was investigated. It is emphasized in this talk that new experimental data are needed in order to improve the current evaluated nuclear data libraries.

1. Introduction

Nuclear data of minor actinides (MA) are important for estimation of amount of MA in reactors, and for study of transmutation technology of MA. From the benchmark tests [1] with post irradiation experiments indicated that the current evaluated data of JENDL-3.3, ENDF/B-VI and JEFF-3.0 could not predict well the amounts of MA in the reactors, in particular for Am and Cm isotopes. A report [2] from a group studying ADS (Accelerator Driven System) for transmutation of MA showed large discrepancies among k-eff values calculated from JENDL-3.3, ENDF/B-VI and JEF-2.2. In order to improve the current evaluated data, we have to know well the present status of MA data.

In the present paper, the status of thermal cross sections and the cross sections above 1 keV are summarized mainly for Np, Am and Cm isotopes. The data of number of neutrons per fission are also shown.

2. Thermal cross sections

The most serious problem of thermal neutron cross sections is the ^{241}Am capture cross section. Several experimental data exit for this cross section. However their recent experimental data are larger than the thermal cross sections recommended in the current evaluated data libraries. Table 1 shows the comparison of recent experimental data with the evaluated data. JENDL-3.3 gives the largest cross section of 640 barns, while it is smaller than the experiments.

The total cross section of ^{241}Am was measured before 1976. Those experimental data are well reproduced by the current evaluated data. The total cross section at 0.0253 eV is about 650 barns at the largest. The evaluation for JENDL-3.3 was based on mainly the total cross sections reported in 1970's, and gave the large thermal cross section of 654 barns. However the recent experimental data for the capture cross section are larger than this total cross section.

Katoh et al. [3] reported the thermal capture cross section of ^{237}Np recently. Their data of 141.7±5.4 barns is smaller than the evaluated data (162 b of JENDL-3.3, and 181 b of ENDF/B-VI and JEFF-3.0) and experimental data of Kobayashi et al. [4] (158±3 b) and Weston et al. [5] (180±6 b).

Table 2 shows the measurements reported after 1990 for the thermal cross sections, resonance integrals and resolved resonance parameters. It is noticeable that the measurements for Cm isotopes are quite scarce, and those for other isotopes are not many enough too. In order to improve the evaluated data below the resonance region, we strongly need new experimental data for the MA.

Table 3 gives very rough status of the data in the thermal energy region. "○" means that many experimental data exit and the evaluated data are in good agreement with them, "△" that not enough because of discrepancies among experimental data themselves and evaluated data, and "×" that no experimental data are available, therefore the reliability of the evaluated data is quite low. For many isotopes, the current experimental data are not enough and too old.

3. Lead Slowing Down Spectrometer

Cross-section measurements with lead slowing down spectrometers have been performed using KULS at Kyoto University and RINS at Rensselaer Polytechnic Institute. These experimental facilities have very strong neutron intensities. Therefore average cross sections can be measured with very good statistical accuracies. Those data can be used to test the resonance parameters given in the evaluated data libraries.

Figure 1 shows the ^{243}Am fission cross sections as an example. It is seen that the data of JEFF-3.0 are too small, and the ENDF/B-VI has a little problem above 10 eV. From the comparison of JENDL-3.3 and those experimental data, discrepancies have been found for ^{237}Np fission, ^{237}Np capture, ^{244}Cm fission and ^{246}Cm fission cross sections [6].

4. Isomeric Ratio of ^{241}Am neutron capture cross section

The isomeric ratio (IR) of ^{241}Am neutron capture is one of important nuclear data for estimation of nuclear production above ^{242}Am. Experimental data exist in the thermal region, which are about 0.9. However no good experimental data are available in the higher energy region.

The data of JENDL-3.3 was calculated with the statistical model, and normalized to the upper limit of error bar of the data measured by Wisshak et al. [7] at 29 keV. However it has been pointed out that the IR to ^{242g}Am given in JENDL-3.3 is too small above the thermal region. Kawano et al. [8] evaluated this quantity recently on the basis of the statistical model calculation and integral data measured at Los Alamos, and obtained larger values than JENDL-3.3.

Figure 2 shows IR to the ground state of ^{242}Am. The data of 0.84 at 300 keV is an integral data measured by Dovbenko et al. [9] using BR-5 reactor. The data of Kawano et al. gives IR of about 0.85 in a typical fast reactor spectrum [10]. The data of Kawano et al. are the most reliable at the present among the current evaluated data.

5. Cross Sections above 1 keV

Fission cross sections above 1 keV have relatively many experimental data. Figure 3 shows the fission cross section of ^{241}Am. The experimental data reported after 1980 in the figure are consistent with each other and the data of JENDL-3.3 are in good agreement with them.

The fission cross section of ^{243}Am are shown in Fig. 4. The experimental data are separated into two groups in the MeV region. The reason of these discrepancies is not clear. JENDL-3.3 follows the data in the lower group.

The data of ^{242}Cm are illustrated in Fig. 5. The data of ENDF/B-VI is largely underestimated. JENDL-3.3 and JEFF-3.0 reproduce well experimental data.

In the case of ^{243}Cm fission cross section, the experimental data are discrepant with each other as shown in Fig. 6. JENDL-3.3 is based on the most recent data of Fursov et al. [11]

In Figures 7 and 8, examples of capture cross sections are given. The ^{241}Am capture cross section in Fig. 7 has experimental data up to several hundred keV. At the higher energies, evaluated data are largely discrepant. For the ^{243}Cm capture cross section, no experimental data are available in the energy range above 1 keV. We therefore cannot confirm the reliability of the current evaluated data.

Table 4 shows the statistics of recent measurements of fission and capture cross sections reported after 1990. The fission cross sections have been often reported. On the contrary no data have been reported for the capture cross sections after 1990. The present status of the cross sections is summarized in Table 5. The situation of the fission cross section is better than the capture cross section whose experimental data are too old or not available.

6. Number of Neutrons per Fission

An example of the total number of neutrons per fission (ν) is given in Fig. 9 where shown are the evaluated data of ν-total and experimental data of ν-prompt or ν-total for ^{241}Am. The evaluated data are discrepant from each other. JENDL-3.3 adopted a fitting curve reported by Khokhlov et al. [12] However their measured data points stored in EXFOR are not reproduced with the fitting curve as

shown in the figure. Since these data points inconsistent with Ref. [12] were not available at the time of evaluation, JENDL-3.3 dose not reproduce them.

In the case of ^{243}Cm in Fig. 10, the experimental data exist only at the thermal energy. The evaluated data reproduce those experimental data, while the energy dependences are different. For many nuclides the situation is the similar to ^{243}Cm.

7. Conclusions

It was found that the current experimental data are not enough to deduce the accurate evaluated data for MA. New measurements are strongly expected for the ^{241}Am thermal cross sections, capture cross sections above the resolved resonance region for Cm isotopes, and so on.

References

[1] Okumura K.: to be published in JAERI-Research report edited by Research Committee on Reactor Physics.
[2] Tujimoto K. et al.: *INDC(NDS)*-428, p.187 (2001).
[3] Katoh T. et al.: J. *Nucl. Sci. Technol.*, **40**, 559 (2003).
[4] Kobayashi K. et al.: *J. Nucl. Sci. Technol.*, **31**, 1239 (1994).
[5] Weston L.W. and Todd J.H.: *Nucl. Sci. Eng.*, **79**, 184 (1981).
[6] Nakagawa T. and Iwamoto O.: *JAERI-Data/Code* 2002-025 (2003).
[7] Wisshak K. et al.: *Nucl. Sci. Eng.*, **81**, 396 (1982).
[8] Kawano T. et al.: *LA-UR*-03-4354 (2003).
[9] Dovbenko A.G. et al.: *LA-TR*-71-74 (1971).
[10] Okumura K.: private communication (2003).
[11] Fursov B.I. et al. : 1997 Trieste, Vol. 1, p.488 (1997).
[12] Khokhlov Yu.A. et al. : 1994 Gatlinburg, Vol. 1, p.272 (1994).
[13] Mughabghab S.F.: *Neutron Cross Sections*, Vol.1, Part B., Academic Press. Inc. (1984).
[14] Shinohara N. et al.: *J. Nucl. Sci. Technol.*, **34**, 613 (1997).
[15] Fioni G. et al.: *Nucl. Phys.*, **A693**, 546 (2001).
[16] Maidana N.L. et al.: *Radiochim. Acta*, **89**, 419 (2001).

Table 1 ^{241}Am thermal capture cross sections

Reference	cross section (barns)
Mughabghab [13]	587±12
Shinohara et al. [14]	854±58
Fioni et al. [15]	696±48
Maidana et al.[16]	(660)*
JENDL-3.3	640
ENDF/B-VI	619
JEFF-3.3	616

* Maidana et al. [16] reported the cross section to ^{242}Am ground state (602±9 barns). The total capture was estimated by assuming the isomeric ratio of 0.91.

Table 2 Thermal cross sections, resonance integrals and resonance parameters reported after 1990

Nuclide	thermal cross section	Res. Integ.	Res. Parms.
Np236	σf(96)	RIf(96)	Res(96)
Np237	σc(94,03)	RIc(94,99,03)	Res(94)
Np238	σc(03), σf(95,96,97)	RIf(95)	Res(96)
Pu236	σf(90)	RIf(90)	Res(90)
Pu238	σf(90)	RIf(90)	
Am241	σc(97,01,01), σf(96)	RIc(97,01)	
Am242g	σc(01)		
Am242m	σf(01)		
Am243	σc(98), σf(99)		
Cm247	σf(94)	RIf(94)	Res(94)

Table 3 Present status of thermal cross sections

Nuclide	fission	capture	comments
Np237	△[1]	△[2]	1) not agree with KULS, 2) large discrepancies
Pu238	△	△[1]	1) old experiments.
Pu242	×	○	
Am241	○	△[1]	1) large discrepancies
Am242m	△[1]	×	1) large discrepancies
Am243	△[1]	△[2]	1) large discrepancies, 2) old experiments
Cm242	×	△[1]	1) old experiments (absorption)
Cm243	△	△	old experiments
Cm244	△	△	old experiments
Cm245	○	△	old experiments
Cm246	△	△	old experiments

Table 4 Fission and capture cross sections reported after 1990

Np236	σf(96,97)	Am242m	σf(91,97,97)
Np237	σf(many)	Am243	σf(99,99)
Np238	σf(96)	Cm243	σf(90,91,97)
Pu236	σf(90,97)	Cm244	σf(91,97)
Pu238	σf(97)	Cm245	σf(91,91,97,97)
Pu242	σf(98)	Cm246	σf(91,97,97)
Pu244	σf(98)	Cm247	σf(91,91,94,97,97)
Am241	σf(99)	Cm248	σf(97)

Table 5 Present status of fission and capture cross sections

Nuclide	fission	capture	comments
Np237	△[1]	△[2]	1) discrepancies: E<100keV. 2) not enough: E> 100keV
Pu238	△[1]	△[2]	1) discrepancies. 2) old exp, no data: E>100keV
Pu242	○[1]	△[2]	1) no exp.: E<100keV. 2) no exp.: E>100keV
Am241	○	△[1]	1) no experiments: E>100keV
Am242m	△[1]	×	1) large discrepancies
Am243	△[1]	△	1) large discrepancies
Cm242	△[1]	×	1) no experiments in the MeV region
Cm243	△[1]	×	1) no experiments: E<100keV
Cm244	△[1]	×[2]	1) discrepancies. 2) no exp.: E>10 keV
Cm245	○	×	
Cm246	○	×	

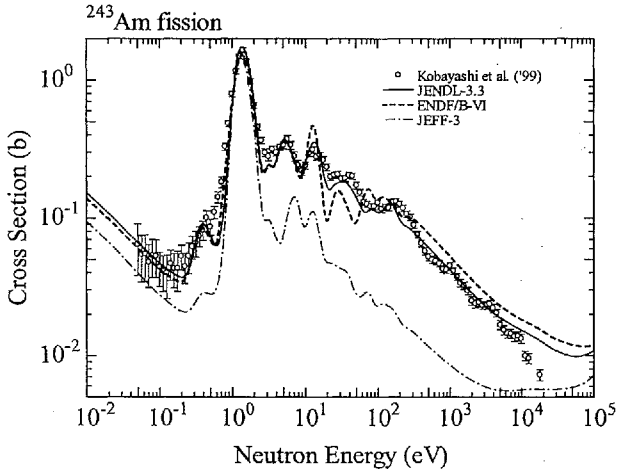

Fig. 1 ^{243}Am fission cross section measured At KULS

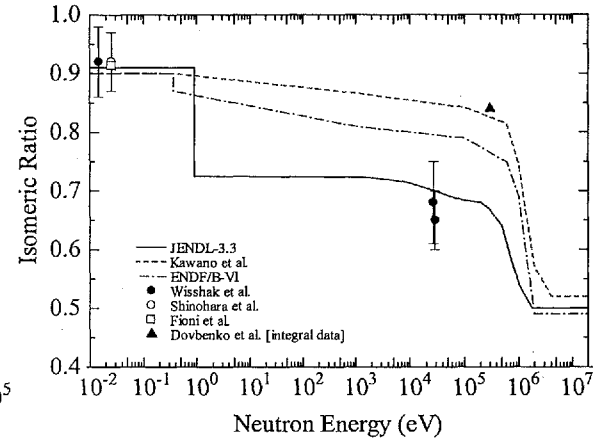

Fig.2 Isomeric ratio ^{241}Am neutron capture

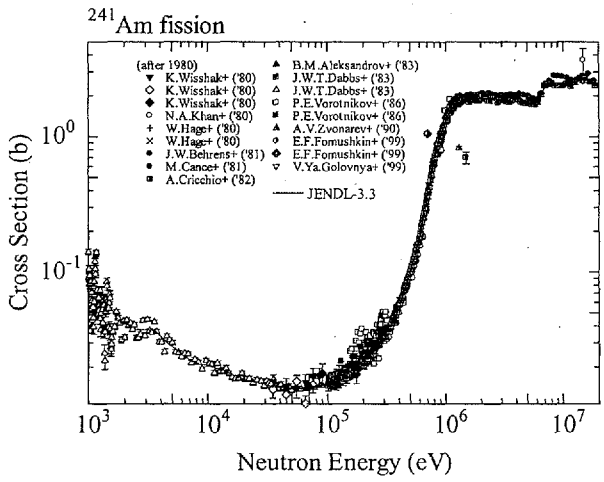

Fig.3 ^{241}Am fission cross section

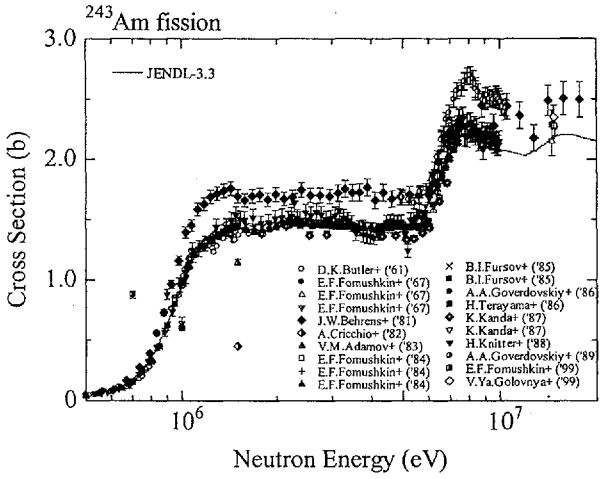

Fig.4 ^{243}Am fission cross section

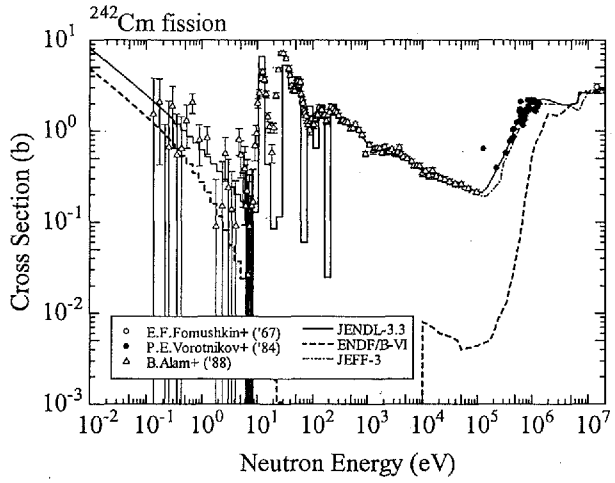

Fig. 5 ^{242}Cm fission cross section

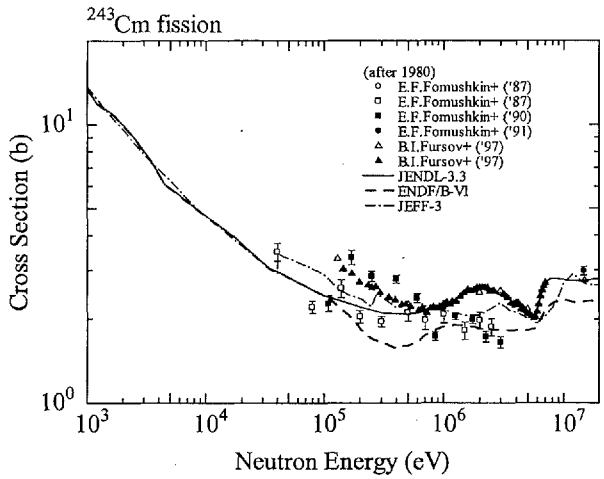

Fig. 6 ^{243}Cm fission cross section

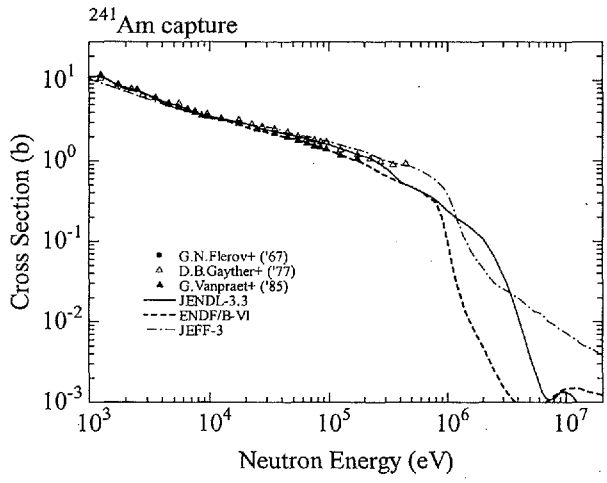

Fig. 7 ^{241}Am neutron capture cross section

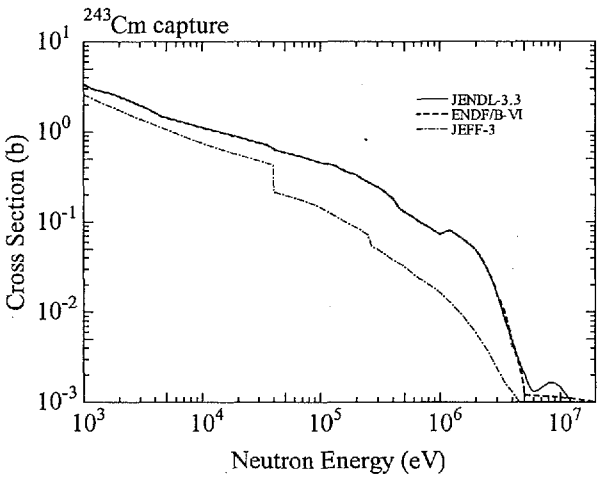

Fig. 8 ^{243}Cm neutron capture cross section

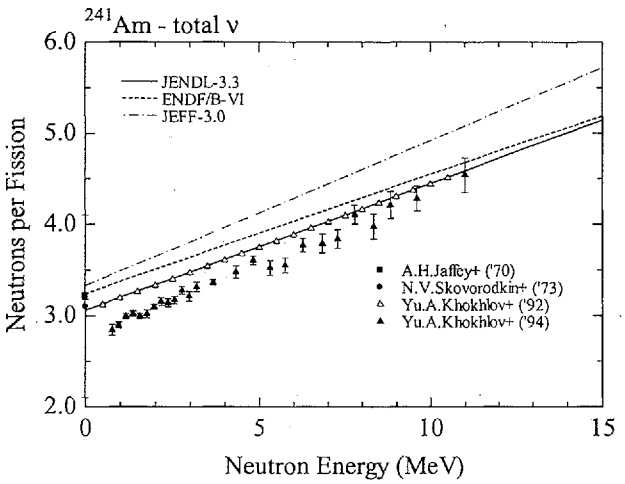

Fig. 9 ^{241}Am neutrons per fission

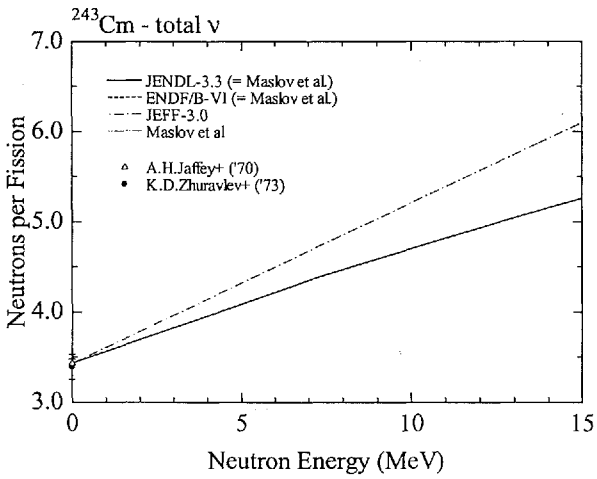

Fig. 10 ^{243}Cm neutrons per fission

2.2 Present Status of Fission Yield Data

Jun-ichi KATAKURA
Nuclear Data Center
Japan Atomic Energy Research Institute
Tokai-mura, Naka-gun, Ibaraki-ken, 319-1195
e-mail : katakura@ndc.tokai.jaeri.go.jp

Fission yield data of minor actinides are needed for transmutation of nuclear waste by an ADS system. The yield data, however, are not enough for the application. The present status of the yield data is presented in this report.

1 Introduction

In the study of transmutation systems of minor actinides using accelerator driven system (ADS), fission yields data are needed for the calculation of neutron economy, reactor kinetics, decay heat and inventory. The yields needed for the application are those by high energy neutron- or proton-induced fission. The high energy means here that exceeds the range of traditional reactor application. In the reactor application neutrons are produced by fission and the maximum energy is below 20 MeV. In an ADS system, however, the primary neutrons are produced by spallation reaction by protons of energy of a few GeV. The energy of the spallation neutrons exceeds much higher than 20 MeV. Then the fission yields as a function of incident energy above 20 MeV are needed for such ADS application.

In this report the present status of fission yields data are described. First the situation of evaluated nuclear data file is described. After that the status of systematics and nuclear model for high energy fission is presented.

2 Status of Evaluated Nuclear Data File

There are several evaluated fission yield data, ENDF/B, JENDL, JEFF and so on. The number of types of fission yield data is 60 for ENDF/B-VI [1] which has the most plentiful data. The JENDL-3.3 file [2] has 20 types of fission yield and the JEF-2.2 file [3] has 39 types. The number of fissile nuclides is 38 for ENDF/B-VI, 11 for JENDL-3.3 and 21 for JEF-2.2 respectively. As an example the data in the ENDF/B-VI file are listed in Table 1. The data included in the file are designated as circle symbol.

Table 1 Fission yield data in ENDF/B-VI

Nuclides	Energy			
	Thermal	Fission	High Energy	Spontaneous
^{227}Th	○			
^{229}Th	○			
^{232}Th		○	○	
^{231}Pa		○		
^{232}U	○			
^{233}U	○	○	○	
^{234}U		○	○	
^{235}U	○	○	○	
^{236}U		○	○	
^{237}U		○		
^{238}U		○	○	○
^{237}Np	○	○	○	
^{238}Np		○		

continued on next page

Nuclides	Energy			
	Thermal	Fission	High Energy	Spontaneous
^{238}Pu		○		
^{239}Pu	○	○	○	
^{240}Pu	○	○	○	
^{241}Pu	○	○		
^{242}Pu	○	○	○	
^{241}Am	○	○	○	
^{242m}Am	○			
^{243}Am		○		
^{242}Cm		○		
^{243}Cm	○	○		
^{244}Cm		○		○
^{245}Cm	○			
^{246}Cm		○		○
^{248}Cm		○		○
^{249}Cf	○			
^{250}Cf				○
^{251}Cf	○			
^{252}Cf				○
^{253}Es				○
^{254}Es	○			
^{254}Fm				○
^{255}Fm	○			
^{256}Fm				○

As seen in this table, the yield data are categorized as thermal, fission, high energy and spontaneous fission. The therms of "thermal", "fission" and "high energy" mean that the energy of neutrons which cause fission. The high energy means 14.7 MeV for traditional application. These categories are common even for other evaluated data. The fission yield data by neutrons of much higher energy than 14.7 MeV are needed for the field of innovative nuclear technology like ADS to reduce high level nuclear waste. These data, however, are not included in the evaluated nuclear data files available now.

For the ADS application it is reported that the yield data of the minor actinides from ^{237}Np through ^{245}Cm are needed for the incident energy up to 150 MeV[4]. The nuclides listed in table 1 cover the needed nuclides but the energy is not enough for the application. Then systematics or nuclear models are needed to be developed to estimate the fission yield of high energy fission.

IAEA organized in 1997 a Coordinated Research Program (CRP) entitled "Fission Product Yield Data Required for Transmutation of Minor Actinide Nuclear Waste" to develop fission yield systematics or nuclear models as a tool for an evaluation of energy dependent fission yields up to 150 MeV. As the scope of the CRP covers the ADS application, the benchmark tests proposed in the IAEA CRP are briefly described in the next section.

3 IAEA Benchmark Test

The purpose of the CRP is to develop systematics or nuclear model which is applicable to transmutation of nuclear waste. During the term of the CRP some systematics and model calculations had been presented by the participants. The CRP was first planned to be 4 years term. At the planned last meeting, benchmark calculations using the systematics and theoretical models presented in the CRP were proposed and the CRP was extended for one year to accomplish the proposed benchmark calculations. In the benchmark calculations, two kinds of comparisons were performed. One is the comparison with experimental mass distribution which is called Type A comparison. The other is the comparison among the calculations using the proposed systematics and theoretical models. The second type comparison is called Type B. The proposed benchmark calculations are listed in Table 2.

As the Type B comparisons are performed among calculations only, it is a good demonstration of the present status of the fission yield prediction.

Table 2 Benchmark Calculation

Type A		Type B	
Nuclide	Energy (MeV)	Nuclide	Energy (MeV)
^{233}U	Thermal, 1.0	^{237}Np	13, 28, 50, 100, 160
^{237}Np	Thermal, 5.0+5.5, 16.5	^{241}Am	13, 28, 50, 100, 160
^{245}Cm	Thermal	^{245}Cm	13, 28, 50, 100, 160
^{238}U	1.6, 5.5, 8, 10, 14-15, 21		
	13, 28, 50, 100, 160		
	E_p= 20, 50		
^{239}Pu	0.17, 7.9, 14-15		
^{242}Pu	15.1		

The comparisons were performed for the mass distributions of post- and pre-neutron emissions. As the systematics we proposed [5] is that can calculate only the mass distribution of post-neutron emission, the comparisons of the mass distribution of post-neutron emission are shown.

As examples of Type A comparisons, some of the mass distributions of low energy fission, intermediate energy and high energy fission are shown here. These comparisons are those presented at the CRP meeting in 2002. The result of the comparison of the low energy fission is shown in Fig. 1.

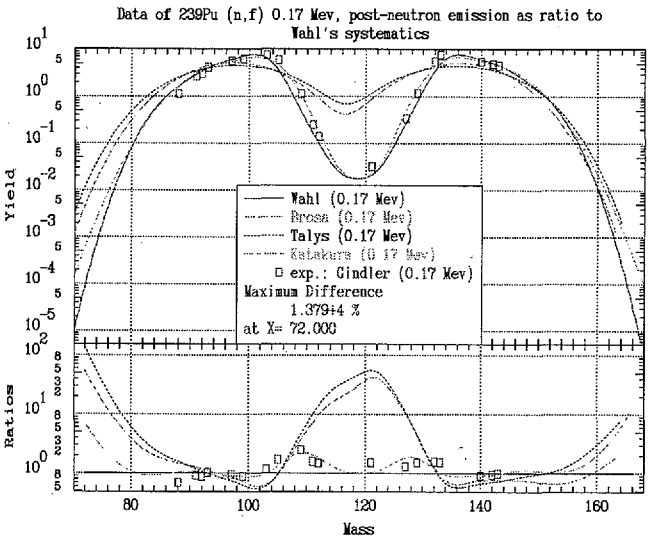

Fig. 1 Mass distribution of ^{239}Pu fission by 0.17 MeV neutrons

The lines in the figure are the mass distributions calculated by participants using systematics or theoretical models. The upper part shows the mass distributions and the lower part the ratios to Wahl's systematics. Two calculations by systematics designated as Wahl and Katakura seem to be consistent with the measured data designated by square. The calculations by theoretical model designated as Brosa and Talys show large deviation at the valley part of the distribution. Figure 2 shows the comparison of the mass distribution of ^{238}U fission by 160 MeV neutrons. The energy of 160 MeV is close to the limit in the CRP scope.

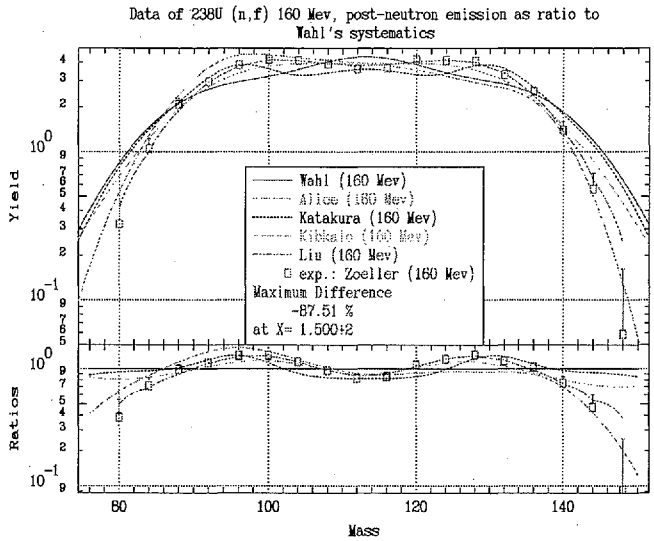

Fig. 2 Mass distribution of ^{238}U fission by 160 MeV neutrons

As seen in these figures the deviation among the calculations of high energy fission seems to be less than that of low energy fission but the descrepancy still remain at valley and the wing part.

As other examples, the comparisons of intermediate energy fission are shown in Figs. 3 and 4.

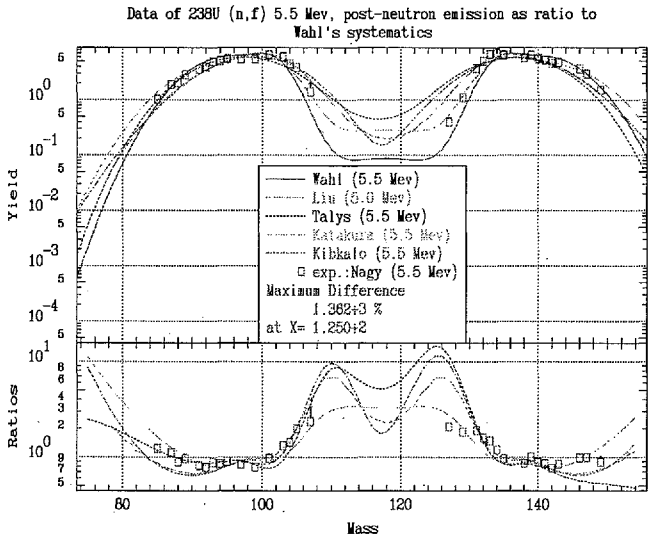

Fig. 3 Mass distribution of ^{238}U fission by 5.5 MeV neutrons

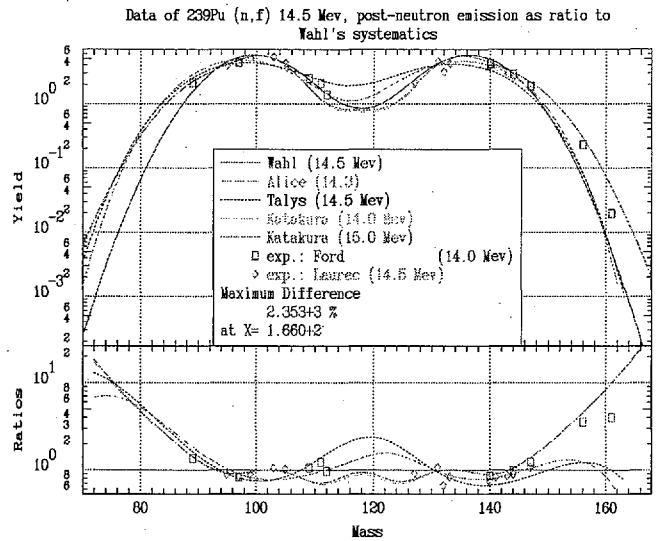

Fig. 4 Mass distribution of ^{239}Pu fission by 14.5 MeV neutrons

These comparisons show the degree of the reproduction of the systematics or nuclear models used. The reproduction of the proposed systematics and nuclear models seems to be still not enough.

For Type B comparisons, the mass distributions of ^{237}Np, ^{241}Am and ^{244}Cm by 13 MeV and 160 MeV are shown in Figs. 5, 6 and 7. The left-hand side in these figure shows the mass distribution by 13 MeV neutrons and the left-hand side the mass distribution by 160 MeV.

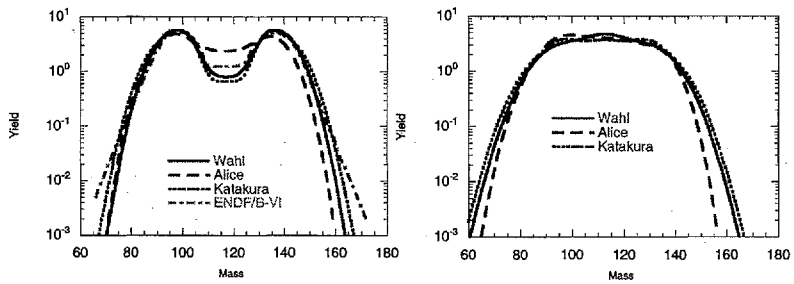

Fig. 5 Mass distributions of ^{237}Np fission by 13 and 160 MeV neutrons

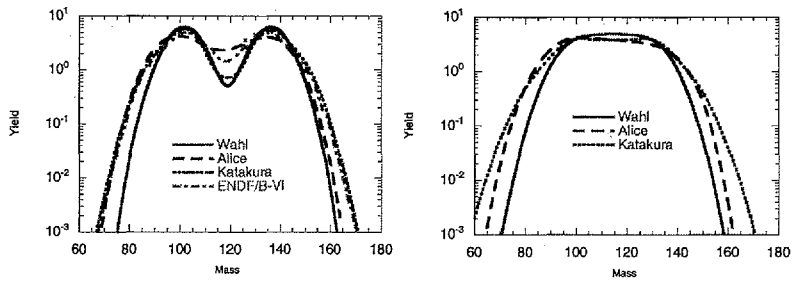

Fig. 6 Mass distributions of ^{241}Am fission by 13 and 160 MeV neutrons

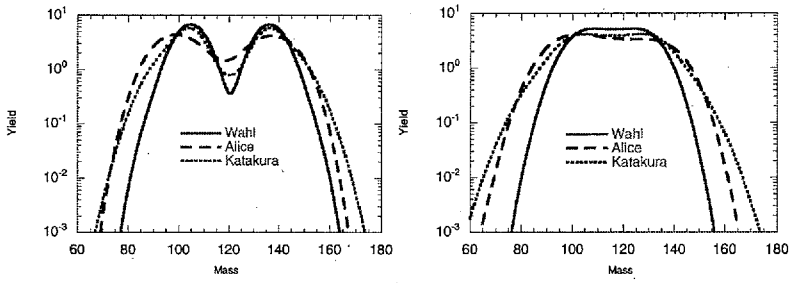

Fig. 7 Mass distributions of ^{244}Cm fission by 13 and 160 MeV neutrons

In these figures, the evaluated data of ENDF are also shown for ^{237}Np and ^{241}Am fission by 13 MeV neutrons. In the ENDF file, mass distributions by "high energy" neutrons are given for ^{237}Np and ^{241}Am. As the term of "high energy" means 14.7 MeV in the ENDF file which is close to 13 MeV, those data are shown for comparison. As there are no experimental data comparable for these yield, these comparisons only show the difference among different types of systematics and theoretical models. We can not say which one is good or bad. These figures show just the present status of fission yield prediction. In order to develop more reliable systematics or theoretical model, more data of minor actinides by high energy fission are strongly required.

4 Summary

The status of fission yield data was presented in this report. The evaluated data of fission yield are restricted in the region of traditional nuclear energy application. For the application to ADS system, fission yield data by higher energy neutrons than 100 MeV are needed. For such high energy fission, the present systematics or theoretical models are not alway give reliable estimation. In the technological application, it is important to know the accuracy of the estimated values. In order to have reliable accuracy, measured data of minor actinides in high energy region are indispensable. Although the measurement using minor actines seems to be difficult, it would be a challenging task for experimentalists interested in ADS or advance nuclear energy systems.

References

[1] Cross Section Evaluation Working Group, *ENDF/B-VI Summary Documentation*, BNL-NCS-17541 (ENDF-201) (1991), edited by P. F. Rose, National Nuclear Data Center, Brookhaven National Laboratory, Upton, NY, USA.

[2] K. Shibata, et al., J. Nucl. Sci. Technol., 39, 1125 (2002).

[3] C. Nordborg, M. Salvatores, *Status of the JEF Evaluated Data Library*, Nuclear Data for Science and Technology, edited by J. K. Dickens (American Nuclear Society, LaGrange, IL, 1994).

[4] 'Overview of Physics Aspects of Different Transmutation Concepts', report NEA/NSC/DOC(94)11 (1994).

[5] J. KATAKURA, *A Systematics of Fission Product Mass Yields with 5 Gaussian Functions*, JAERI-Research 2003-004 (2003).

2.3 Estimation for Effect of JENDL-3.3 on Neutronics Characteristics of Accelerator-Driven System

Kasufumi TSUJIMOTO, Toshinobu SASA, Hiroyuki OIGAWA, and Hideki TAKANO
Center for Proton Accelerator Facilities, Japan Atomic Energy Research Institute
Tokai-mura, Naka-gun, Ibaraki-ken 319-1195
e-mail : ktsuji@omega.tokai.jaeri.go.jp

The latest version of Japanese Evaluated Nuclear Data Library (JENDL-3.3) was released in last year. Primary purpose of this study was to estimate an effect of a revision of nuclear data library on neutronics characteristics of accelerator-driven subcritical system (ADS). The burnup calculations using both JENDL-3.3 and JENDL-3.2 were performed for JAERI proposed ADS. The detailed contribution of each nuclide and reaction on the difference of the calculation results, such as effective multiplication factor and burnup swing, were investigated. Moreover, to validate the nuclear data of actinides, the burnup analysis for the actinides samples irradiated at the Dounreay Prototype Fast Reactor were carried out.

1. Introduction

The Japanese long-term program called OMEGA has started in 1988 for research and development of new technologies for partitioning and transmutation of minor actinides (MA) and fission products. Under the OMEGA Program, for a dedicated transmutation system, the Japan Atomic Energy Research Institute (JAERI) has been proceeding with the research and development on accelerator-driven subcritical system ADS[1].

The ADS is a hybrid system that consists of a proton accelerator, a spallation target and a subcritical core. The proton beam current required to keep predefined power level is directly related to the effective multiplication factor (k_{eff}) of system. Therefore, calculational accuracies of k_{eff} and burnup change of k_{eff} are very important in neutronics design of ADS. In the latest version of Japanese Evaluated Nuclear Data Library, JENDL-3.3, nuclear data for many MA nuclides were revised from previous version, JENDL-3.2. In this study, the effect of a revision of nuclear data library on neutronics characteristics of ADS, especially k_{eff} and burnup swing, were investigated.

2. Effect of Nuclear Data on Nuclear Characteristics of ADS

The latest version of Japanese Evaluated Nuclear Data Library (JENDL-3.3) was released in last year. Primary purpose of this study was to estimate an effect of a revision of nuclear data library affects on neutronics characteristics of accelerator-driven subcritical system (ADS). The calculated neutronics characteristics were effective multiplication factor (k_{eff}) and burnup swing. The burnup calculations using both JENDL-3.3 and JENDL-3.2 were performed.

The calculated core was a lead-bismuth cooled ADS proposed by JAERI[2] for a dedicated transmutation system of MA. For the fuel, mixture of mono-nitride of MA (60%) and plutonium (40%) recovered from high-level waste from power reactor were used with inert matrix. In this study, two types fuel with different isotopic composition of MA were assumed. Case-1 and Case-2 corresponded to MA from spent fuel of UO_2 and MOX fuel PWR, respectively[3]. The isotopic compositions of MA for both cases are indicated in Table1. The burnup calculations were performed using revised ATRAS code system[4] under conditions of initial k_{eff} of 0.95 (results by

JENDL-3.2), core thermal power of 800MWth, and proton beam energy of 1.5GeV. Bunrup period was 600 effective full power days. After each burnup cycle, all fuel were removed from the core and recycled for next burnup cycle after cooling time. In the refabrication process, the fission products were removed and only MA of equal mass to the burnup fuel was added to the recycled fuel.

Time evolutions of k_{eff} during five burnup cycle are showed in Fig.1. In Case-1, difference between results using JENDL-3.3 and JENDL-3.2 for k_{eff} at initial state and the burnup swing is small. On the other hand, in Case-2, k_{eff} at initial state by JENDL-3.3 is about 2% smaller than that by JENDL-3.2, and difference of burnup swing is significant. To survey the reason of discrepancy between the results using JENDL-3.3 and JENDL-3.2, contribution of each nuclide for difference of k_{eff} at beginning and end of first cycle were calculated. The results are shown in Table 2. From Table 2, in Case-1, it is obvious that contributions of ^{237}Np and ^{241}Am are dominant and compensate each other, though k_{eff} values shows good agreement. In Case-2, contribution of ^{241}Am is emphasized since an amount of ^{237}Np is very small in MA. For ^{237}Np, ^{241}Am, and ^{243}Am which are main nuclides in MA, contribution of each reaction on difference of k_{eff} at BOC of first cycle are presented in Table 3. The results showed that the effects of capture reaction and $\nu\Sigma_f$ are dominant.

For ^{237}Np and ^{241}Am, sensitivity analysis were carried out using SAGEP code[5] to investigate more detailed information which is depend on neutron energy. The sensitivity coefficients, difference of cross section between JENDL-3.3 and JENDL-3.2, and the energy breakdown of reactivity change are shown in Fig.2. The sensitivity coefficients of fission cross section and ν-value have peak values about 1MeV because the threshold fission cross section, while that of capture cross section are large from 10keV to 1MeV. From energy breakdown of reactivity change of ^{237}Np and ^{241}Am, differences of cross section above 10 keV are dominant for the difference of k_{eff}. Moreover, the contribution of ν-values overcome the effect of fission cross sections, since ν-values changed about 3% for both ^{237}Np and ^{241}Am. The results showed that the effect of a revision of nuclear library on neutronics characteristics of ADS is significant.

3. Validation of Nuclear Data using Integral Experiment

For evaluation and improvement of nuclear data, not only differential experiments but also integrated experiments are indispensable. Actinide samples which were irradiated in the Dounreay Prototype Fast Reactor (PFR) are precious experimental data for MA[6,7]. The samples were milligram quantities of actinide oxides of 21 different isotopes from thorium to curium. The results of chemical analyses and comparison with calculational results by JENDL-3.3 and JENDL-3.2 are shown in Fig.3. In Fig.3, fission per initial metal atom (FIMA) for samples and difference between beginning and ending of chemical analyses for main isotopes in samples are presented for some typical samples. The calculations were done by ORIGEN-2 code[8].

The results showed that differences between C/E values using JENDL-3.3 and JENDL-3.2 are small for FIMA. On the other hand, for difference during irradiation for main isotopes, the C/E values for ^{235}U and ^{241}Am by JENDL3.3 are improved, though the result of ^{237}Np shows underestimation. Large disagreement for ^{238}Pu sample does not change. Therefore, from the burnup analysis for actinide samples irradiated at PFR, further improvement is needed for nuclear data of MA while JENDL-3.3 shows relatively good result.

4. Conclusion

The effect of the revision of nuclear data in JENDL-3.3 on neutronics characteristics of ADS, such as k_{eff} and burnup swing, was investigated. The results showed that the effect of the revision was significant. The contribution of the capture cross section and the ν-value of ^{237}Np and ^{241}Am were especially large. Moreover, for the validation of nuclear data, the burnup calculations for the actinide samples irradiated at PFR were performed. For ^{235}U and ^{241}Am, the calculation results by

JENDL-3.3 are improved though the result of ^{237}Np shows underestimation. For MA nuclides, further improvement of nuclear data is needed.

References

[1] Mukaiyama T., Takizuka T., Mizumoto M., Ikeda Y., Ogawa T., Hasegawa A., Takada H., and H. Takano H. : " Review of research and development of Accelerator-driven System in Japan for transmutation of long-lived nuclides," *Prog. Nucl. Energy*, ADS special edition, **38**, No. 1-2, p.107, (2001).

[2] Tsujimoto K., Sasa T., Nishihara K., Takizuka T., and Takano H.,:" Accelerator-Driven System for Transmutation of High-level Waste," *Prog. Nucl. Energy*, **37**, No. 1-4, p. 339, (2000).

[3] " Accelerator-driven Systems (ADS) and Fast Reactors (FR) in Advanced Nucler Fuel Cycles : A Comparative Study," Nuclear Energy Agency, Organization for Economic Cooperation and Development (2002).

[4] Tsujimoto K., Sasa T., Nishihara K., Oigawa H. and Takano H.,:" Neutronics Design for Lead-Bismuth Cooled Accelerator-Driven System for Transmutation of Minor Actinide", *J. Nucl. Sci. Technol.*, **41**(1) (2004) (to be published)

[5] Hara A., Takeda T., and Kikuchi Y.:" SAGEP: Two-Dimensional Sensitivity Analysis Code Based on Generalized Perturbation Theory" , JAERI-M-84-27 (in Japanese).

[6] Shinohara N., Kohno N., Nakahara Y., Tsujimoto K., Sakurai T., Mukaiyama T., and Raman S.:" Validation of Minor Actinide Cross Sections by Studying Samples Irradiated for 492 Days at the Dounreay Prototype Fast Reactor — I : Radiochemical Analysis" , *Nucl. Sci. Eng.*, 144, 115 (2003).

[7] Tsujimoto K., Kohno N., Shinohara N., Sakurai T., Nakahara Y., Mukaiyama T., Raman S.:" Validation of Minor Actinide Cross Sections by Studying Samples Irradiated for 492 Days at the Dounreay Prototype Fast Reactor — II : Burnup Calculations," *Nucl. Sci. Eng.* , 144, 129 (2003).

[8] A. G. Croff,: "ORIGEN2: A Versatile Computer Code for Calculating the Nuclide Compositions and Characteristics of Nuclear Materials," *Nuclear Technology*, **62**, 335 (1983).

Table 1 Plutonium and MA compositions resulting from reprocessing of UO_2(Case-1) and MOX(Case-2) fuel from PWR (nuclide atom%)

	Case-1	Case-2
^{238}Pu	2.7	4.1
^{239}Pu	55.3	41.9
^{240}Pu	23.9	30.5
^{241}Pu	9.5	10.6
^{242}Pu	7.1	11.3
^{241}Am	1.5	1.7
Total	100	100
^{237}Np	46.4	4.4
^{241}Am	37.1	58.3
^{243}Am	12.7	26.1
^{244}Cm	3.8	11.3
Total	100	100

Table 2 Contribution of each actinide nuclides for difference of k_{eff} by JENDL-3.3 and JENDL-3.2 at BOC and EOC of first cycle (%Δk/k)

Nuclides	Case-1		Case-2	
	BOC	EOC	BOC	EOC
^{237}Np	-0.908	-0.717	-0.091	-0.075
^{238}Pu	0.051	0.403	0.084	0.035
^{239}Pu	0.016	0.072	0.010	-0.038
^{240}Pu	-0.078	-0.117	-0.105	-0.146
^{241}Pu	-0.010	0.099	-0.014	0.117
^{242}Pu	-0.011	-0.026	-0.019	-0.040
^{241}Am	1.304	0.980	2.140	1.640
^{242m}Am	—	-0.218	—	-0.302
^{243}Am	0.120	0.088	0.249	0.198
^{242}Cm	—	-0.074	—	-0.099
^{243}Cm	—	-0.011	—	-0.009
^{244}Cm	0.010	-0.011	0.030	-0.004
^{245}Cm	—	-0.061	—	-0.115

Table 3 Contribution of each reaction of ^{237}Np, ^{241}Am, and ^{243}Am for difference of k_{eff} by JENDL-3.3 and JENDL-3.2 at BOC of first cycle (%Δk/k)

Case-1

	Total	Σ_c	Σ_f	$\nu\Sigma_f$	Σ_s
^{237}Np	-0.908	-0.573	0.040	-0.395	0.030
^{241}Am	1.304	0.639	0.009	0.544	0.112
^{243}Am	0.120	0.131	0.004	-0.012	-0.004

Case-2

	Total	Σ_c	Σ_f	$\nu\Sigma_f$	Σ_s
^{237}Np	-0.091	-0.055	0.004	-0.041	0.002
^{241}Am	1.640	1.014	0.016	0.939	0.174
^{243}Am	0.198	0.275	0.008	-0.027	-0.010

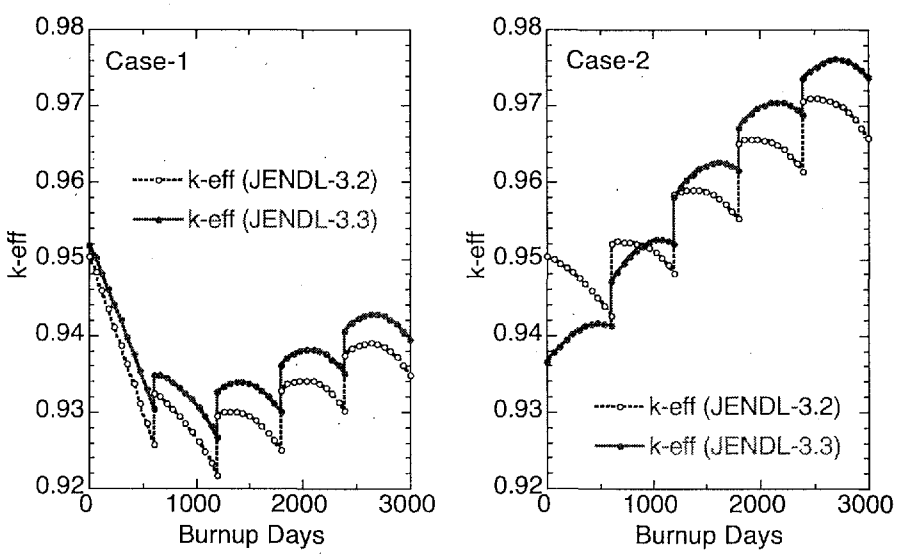

Fig.1 Time evolutions of k_{eff} during five burnup cycle

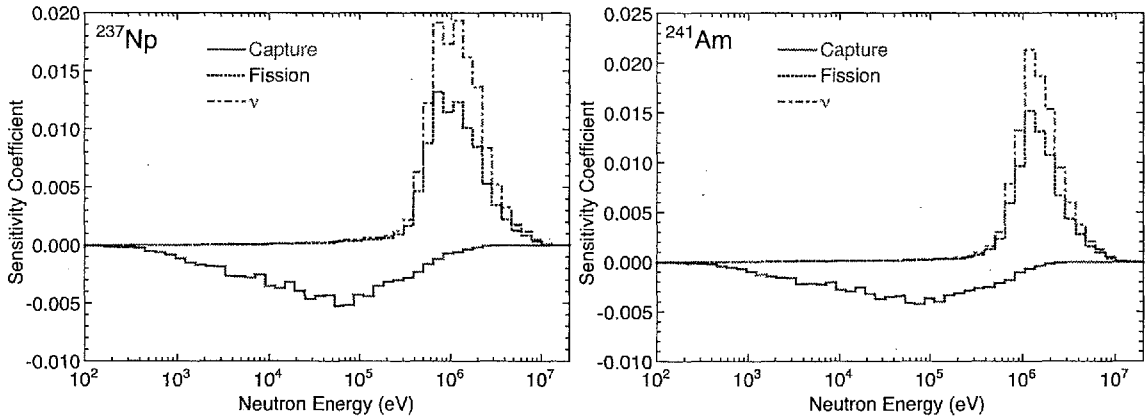

(a) Sensitivity coefficients for k_{eff}

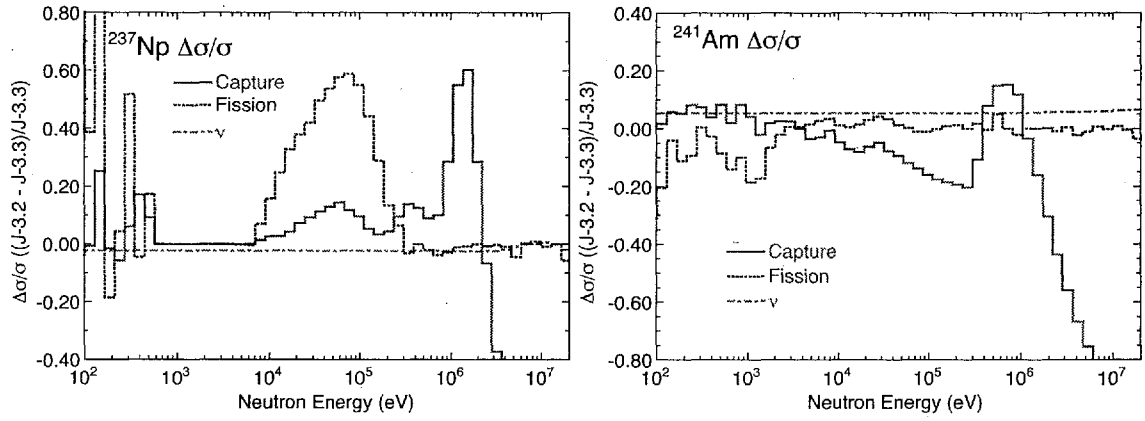

(b) Difference of cross section between JENDL-3.3 and JENDL-3.2

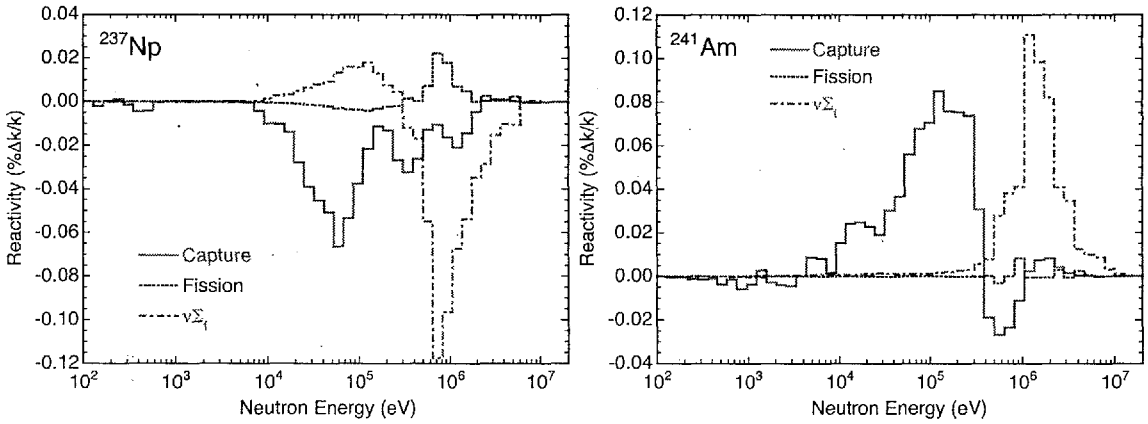

(c) Energy break down of reactivity change

Fig.2 Sensitivity coefficient for keff, difference of cross section between JENDL-3.3 and JENDL-3.2, and energy break down of reactivity change for ^{237}Np and ^{241}Am

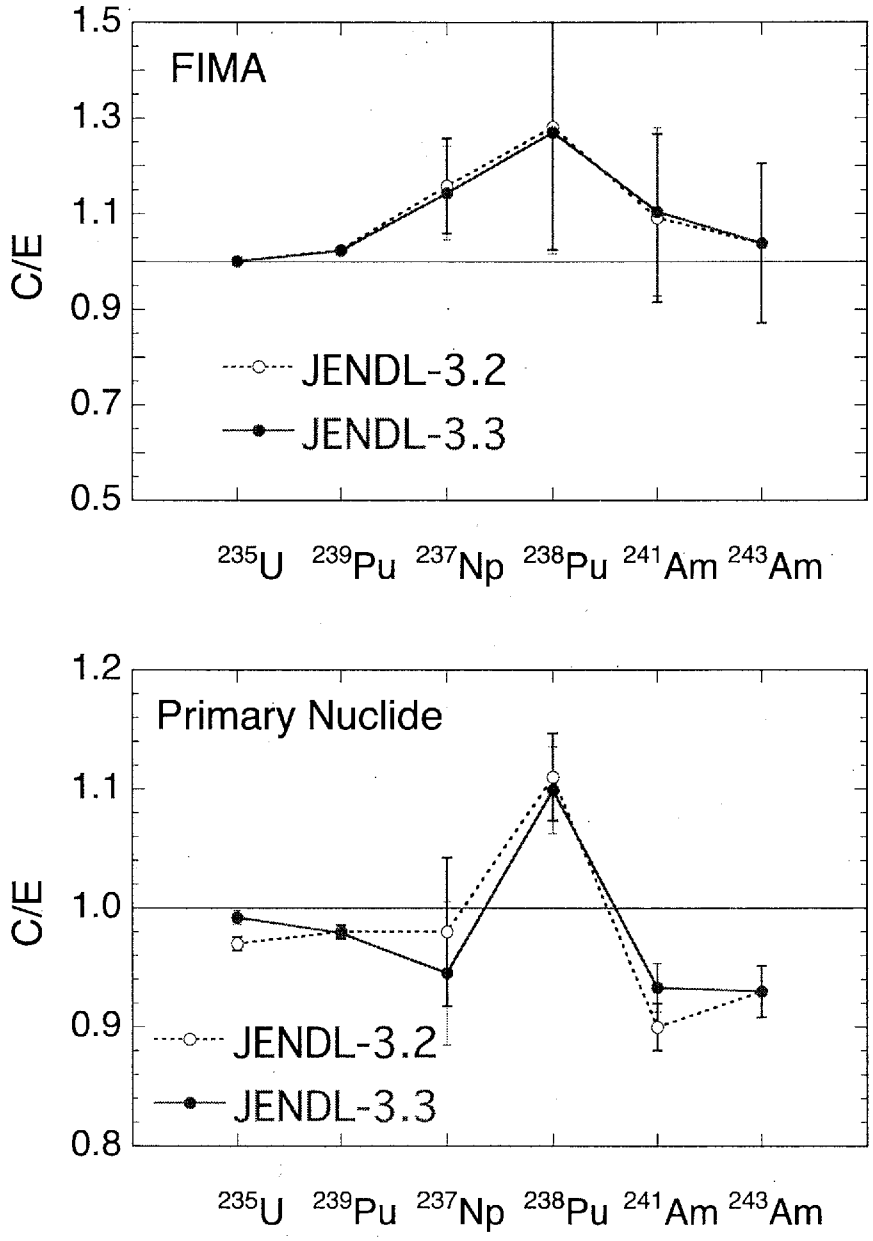

Fig.3 C/E values by JENDL-3.3 and JENDL-3.2 for some actinide samples irradiated at PFR

2.4 Current Status of Spallation Product Data: Nuclear Engineering View-Point

V.Artisyuk, M.Saito, T.Sawada

Research Laboratory for Nuclear Reactors, Tokyo Institute of Technology
2-12-1 O-okayama, Meguro-ku, Tokyo 152-8550, Japan
TEL: +81-3-5734-3074; FAX: +81-3-5734-2959
e-mail: artisyuk@nr.titech.ac.jp

Abstract

Proton induced isotopic transformation in spallation targets of accelerator-driven systems (ADS) is becoming a key factor in selecting the reference target material&design options. The present paper gives an outlook of the current status of data on spallation products from the view-point of nuclear engineering stressing the isotopes whose accumulation would significantly effect the target performance.

1. INTRODUCTION

The maturing of the accelerator technology toward practical implementation in the form of accelerator-driven systems gave rise to the specific concern about isotope transformation in neutron producing targets. Associated terminology sometimes looks confusing. The term "spallation" that in nuclear physics is generally reserved for identification of specific nuclear reaction with emission of secondary nucleons, by engineering community is taken in a complex like "spallation neutron source" or "spallation target" to identify the vital design element responsible for neutron generation induced by accelerated ions. Strictly speaking, in this element pure spallation reaction might be accompanied by reactions like, for example, high energy fission and multi-fragmentation having a different mechanism from classical spallation. In addition to that, if the target is large enough, the secondary nucleons emitted through spallation will be moderated and trigger the nuclear reactions through mechanism of compound nucleus, like capture reaction.

Leaving the terminological issue to the field of nuclear physics, by "spallation products" (SP) in this paper we mean those nuclides accumulated in neutron producing target which are different from initial target material. Nowadays, at the edge of ADS implementation, it seems to be instructive to compare the current status of SP-data with that of fission products (FP) at the edge of implementation of critical nuclear reactors. In his classical monograph on physics of nuclear kinetics, G. Keepin pointed out that measurement of about 120 FP resulted in a reasonably accurate picture of mass and charge distribution for major fuels [1]. Available data on FP yields in neutron induced fission is usually tabulated for thermal, 1 MeV and 14 MeV of incident neutron energies and this covers all the spheres of fission technology application. The situation with SP is much more complicated. Though the list of materials for spallation target of ADS is limited to several heavy elements (Sn, Ta, W, Hg, Pb, Bi, Th, U), the energy of incident protons considered in ADS ranges from hundred MeV to several GeV. In this energy interval nuclides with mass number characteristic to FP form only the subset of long list of SP ranging from light fragments like tritons and helium to isotopes closed to initial target materials. Because of high price and complexity of the experiments with accelerator, experimental data base on SP yields is rather limited. Before the burst of interest to ADS from technological community (that happened about two decades ago) the high energy experiments were almost entirely focused on specific aspects of nuclear physics, like problem-oriented cross-section systematics. As for the engineering community, in early ADS projects, it was sufficient to know spatial distribution of neutron and heat generation to estimate target design characteristics and this was well supported

by simulation with computer codes based on existing models validated on some integral experiments. This stage of research was comprehensively reviewed in Ref.2.

Further maturing of ADS development put forward the necessity of detailed knowledge of nuclear processes to estimate the dose impact for personnel, material damage, target cooling time and decommissioning scenarios. These challenges were considered in Ref.3 which made an attempt to prioritize the needed experiments. In brief, the high priority list of isotopes and reactions was elaborated with the upper energy assumed at 200 MeV. Above this energy the high-energy transport codes are recognized to reveal sufficient predictive power. In the list of isotopes four nuclides belonging to the class of target materials ^{184}W, ^{208}Pb, ^{232}Th, ^{238}U were nominated [3].

Currently, for technological reasons liquid metal spallation targets keep the leading positions among candidates for ADS, lead and lead-bismuth eutectic being of the highest priority. Recent progress and history of studies on residual nuclides in lead irradiated by protons are summarized and reviewed in Ref.4. It is worth to refer briefly the activity of three experimental groups which keep nowadays the leadership in experimenting on spallation products' yields and the number of reactions inherent to analysis of lead targets. Given in Ref.4 are the results of experiments on 127 residual nuclides from lead for proton energies between 64.8 and 2.6 GeV identified in ZSR (Hannover) by gamma spectrometry [4]. For fixed proton energy of 1 GeV, production cross-sections of more than 400 nuclides were measured with direct gamma spectrometry at ITEP (Moscow) [5]. By the inverse kinematic method realized in GSI (Darmstadt) with magnetic fragment separation about 900 nuclides from 1 GeV/A ^{208}Pb+p reaction were identified [6]. As one can see the list of SP depends on experimental technique and this list anyway exceeds the list of fission products recognized as essential for reactor kinetic. Obviously such a long list of nuclides illustrates the skills of experimental groups and definitely might help to improve the theoretical models responsible for simulation of high-energy nuclear reactions. However the question about significance of SP accumulation is still open and this paper attempts in identification of particular group of SP that might effect on ADS performance. This is done on the basis of lead target which is treated as the number one candidate for ADS designing.

2. GLANCE AT MASS DISTRIBUTION

Figure 1 gives a typical illustration of SP yields obtained with computer code CASCADE (original Russian code developed especially for the high-energy simulation in Joint Institute of Nuclear Research (Dubna) and modified in Obninsk Institute of Nuclear Power Engineering (Obninsk) [7]. The reference energy is 1.6 GeV which is the highest one among ADS projects. Figure 2 incorporates the experimental data obtained by leading experimental groups with reference energy of 1 GeV [5]. As one can see from Fig.1 typical SP distribution curve reveals three classes of spallation products. One is represented by sharp peak in the region of light nuclides (isotopes of hydrogen and helium). The second one comprises intermediate nuclides with mass numbers characteristic to fission products of nuclear reactors. The third is formed near the mass number of initial target nuclei. The gap between the last two peaks for heavy nuclides (W, Pb, U) is filled by either products of high-energy fissions (descending heavy fragment tail) or residuals from evaporation stage following spallation reaction (sometimes they refer to this as "deep spallation"). Non-uniqueness of nuclear mechanism responsible for this region leads to significant uncertainties as it is shown in Fig.2 that gives an order-of-magnitude difference in experimental data. Simulation with help of theoretical models gives even more pronounced difference. Figure 3 reflects this fact by showing production cross-sections for ytterbium, neodymium and lead isotopes (incorporated data was taken partly from Ref.10 and added with results obtained with CASCADE [7] and MCNPX [11] codes. As it is seen for the case of lead isotopes, the closer residual nuclide to initial target material, the better agreement among the theoretical results and experimental data is observed. Ytterbium and neodymium

isotopes are representative of the residuals close to the valley between two peaks and theoretical modeling in this region definitely needs to be improved.

The detailed comparison of the models is out of the scope of the present report, though significance of the nuclides of this region is stressed in the next section.

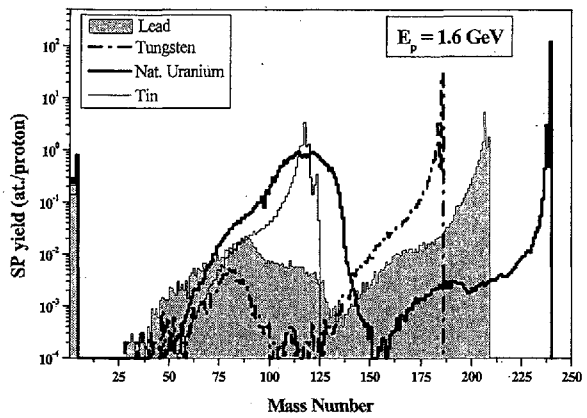

Fig.1 Mass distribution of spallation products in various targets irradiated by 1.6 GeV protons (calculated by CASCADE [7]) [8]

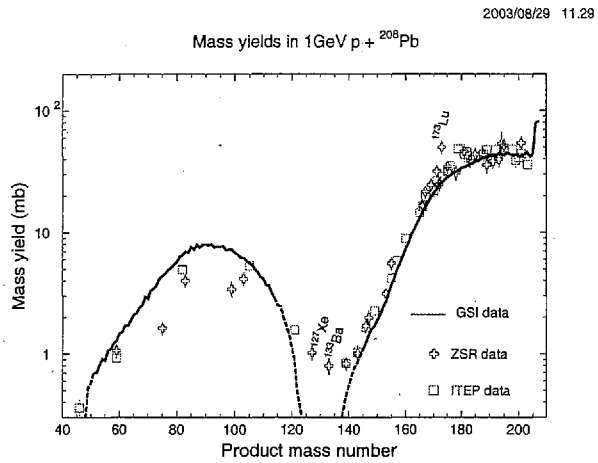

Fig.2 Mass distribution of spallation products from ^{208}Pb irradiated by 1 GeV protons (comparison of various experimental data [9])

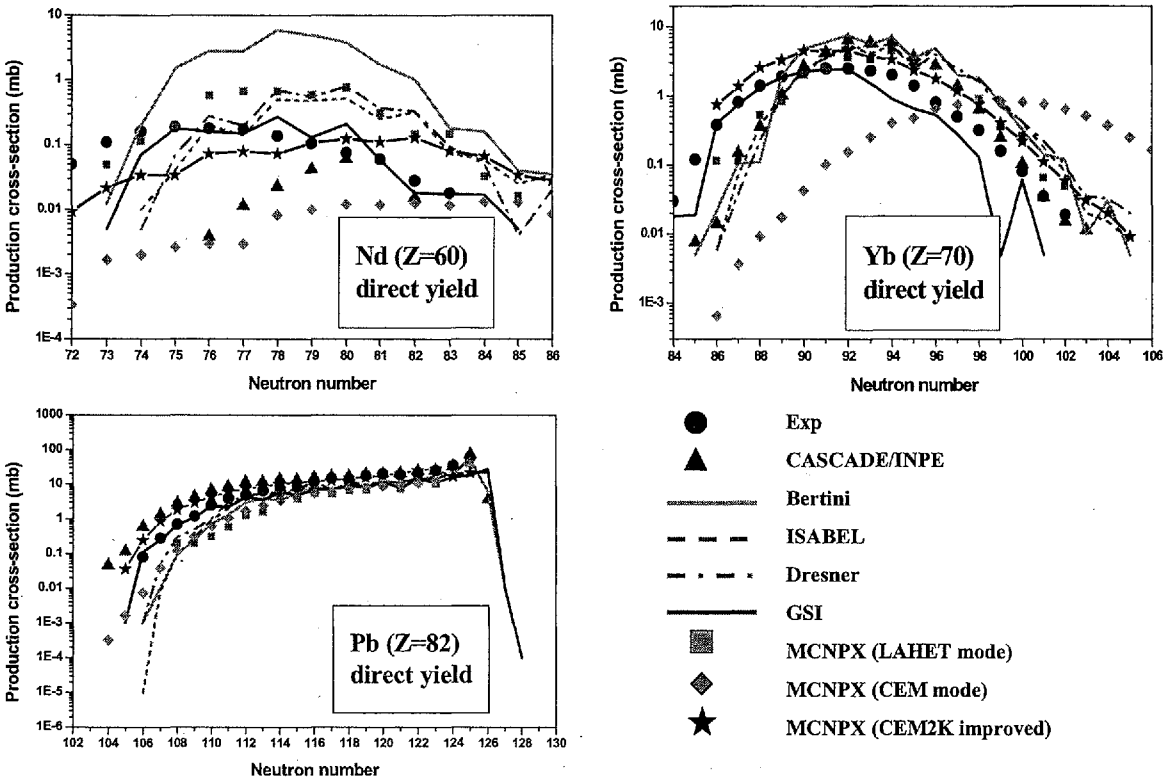

Fig.3 Independent yields of lead, ytterbium and neodymium isotopes in 1 GeV/A ^{208}Pb+p reaction obtained with various models and compared with experimental data reported in Ref.10

3. CHALLENGE OF SPALLATION PRODUCTS

So far the experimental studies on SP accumulation were oriented to validation of general predictive power of theoretical models and associated computer codes. In view of complexity of the processes involved it seems to be difficult to provide reasonable accuracy for all the range of mass numbers and, for this reason, it is instructive to select the nuclides of importance and concentrate the efforts on improving the accuracy in this particular area. Several criteria from technology side might be put forward. Among them radiation damage, corrosion and radiological issues are of the highest importance. Liquid metal targets give the possibility to reduce significantly the problem of radiation damage, (for example swelling due to accumulation of gaseous SP is avoided) and this fact stimulated interest to lead and lead-bismuth eutectic. Corrosion issues of SP accumulation have not been studied yet. The main focus was one the analysis of their radioactivity. Frequently targets are compared with respect to accumulation of polonium which is volatile and toxic (^{210}Po undergoes alpha decay with $T_{1/2}$ =138 days). Accumulation of ^{210}Po goes mainly by neutron capture in ^{209}Bi, thus giving the possibility of one-step production reaction in the Pb-Bi eutectic, and, at least two-step reaction in pure lead starting from neutron capture in double-magic nucleus of ^{208}Pb. Polonium was an important argument and continuous issue of contention in the debate of advantages and disadvantages of lead and lead-bismuth targets.

Several target design options were developed exclusively to response polonium challenge. Thus, polonium free operation was considered as the main point in favor of solid tungsten [12] and liquid tin [13] spallation targets. Lead-tin alloy (38.1Pb-61.9Sn) was proposed as a target material with no "serious polonium or toxic daughters' accumulation" [14]. Opposite to aforementioned accentuation of polonium, in Russia there is an opinion that itsactivity is not a big problem and could not be a criterion in making the choice between lead and lead-bismuth, at least. The main reason, as they say, is that "the main contribution to long-lived activity ($T_{1/2}$ > 100 days) for both target materials is caused not by ^{210}Po, but by various isotopes of Bi, Te, Hg, and Au accumulated due to (p,xn) and (n,xn) reactions in high-energy part of proton and neutron spectra" [15]. For example, specific activity of mercury isotopes exceeds that of polonium by factor of 35, at proton energy and current of 800 MeV and 1–30 mA, correspondingly, and they single out the long-lived ^{194}Hg (520 yr) nuclide rather than polonium [16]. Whatever elaborated analysis of induced activity could be performed it would offer no more than pure nuclear physics and is insufficient to judge on how much adverse effect this brings to the human environment. Along with relatively high specific activity, implicitly included in the polonium concern is its alpha decay mode and volatile physical form whose combination brings polonium inhalation toxicity to an extreme. All this should emphasize the importance of toxicity units for characterization of induced activity. With respect to spallation products such a characterization was done by the authors of the present paper in Ref.17,18 that reveals the importance of rare earths. Among them there several alpha emitters (see Fig.4), four of them being with half-lives less than that of uranium $^{146}_{62}$***Sm*** ($T_{1/2}$=1×10^{8}yr), $^{148}_{64}$***Gd*** ($T_{1/2}$=74.6yr), $^{150}_{64}$***Gd*** ($T_{1/2}$=1.8×10^{6}yr) and $^{154}_{66}$***Dy*** ($T_{1/2}$=3×10^{6}yr). For incident proton energy of about 1 GeV, their location in mass distribution is in the problematic interval identified in the previous section. Figure 5 gives 90% fraction of the overall generated toxicity (which is just a translation of the cumulative yield (measured in atoms per proton) into toxicity units (ALI per proton)) for some representative reactions. For broad interval of proton energy these values are determined by only three nuclides: ^{113m}Cd ($T_{1/2}$=14.1 yr) for tin, ^{194}Hg($T_{1/2}$=520 yr) contributing generated toxicity of lead at low energies, and ^{148}Gd($T_{1/2}$=74.6 yr), which is significant for both tungsten and lead. Judging from Fig.5, overall generated toxicity (with exception of tin) is increased with energy increase and, what important, this growth is largely due to ^{148}Gd which is the RE isotope. Important to note, that tungsten advocated for his polonium-free advantage reveals the highest toxicity exclusively due to alpha activity of rare earths. Coming back to Fig.1 one can conclude that their

accumulation in W target is more pronounced than in Pb (or Pb-Bi) because mass number of initial nuclides is closer to this problematic region.

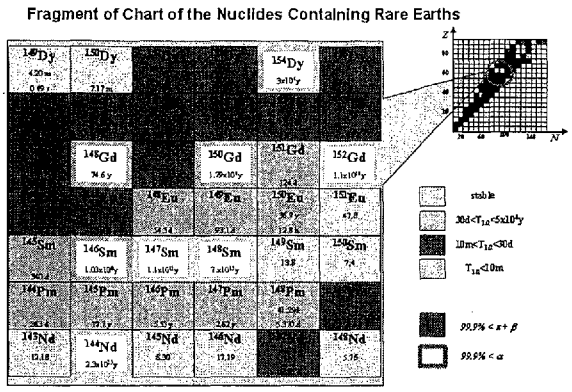

Fig.4 Fragment of Chart of Nuclides with alpha-emitting Rare Earths

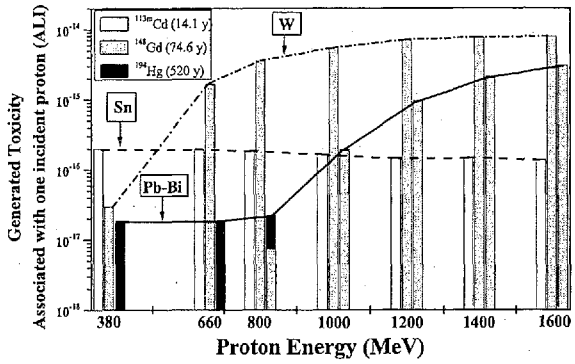

Fig.5 Toxicity from singular interaction of proton with one nucleus in Pb-Bi, W, and Sn targets as a function of proton energy [17]

Figure 6, a,b comprise the dynamics of ^{210}Po and important SP accumulation in large bare Pb-Bi target expressed in units of activity (Bq) and toxicity (ALI). Polonium reaches its equilibrium state within 1 year – operation time common for nuclear facilities between two successive shutdowns for maintenance. Other nuclides presented by Fig.6 require several decades. Since their half-lives longer than for ^{210}Po, their decay within maintenance periods is not essential, so, one can reasonably expect that all the selected nuclides reach equilibrium within the ADS lifetime. It is seen that for the reference beam parameters ^{210}Po equilibrium activity is inferior only to tritium (Fig. 6,a). Nevertheless, tritium hazard generally is not stressed in SP analysis. Implicitly, it warns that activity is a crude measure in hazard characterization. Figure 6,b underlines the significance of alpha emitting rare earths exemplified by ^{148}Gd ($T_{1/2}$=74.6 yr) whose equilibrium toxicity is almost by one order of magnitude higher than that of ^{210}Po. What important is that their toxicities become equal rather soon just after 3.5 years of operation. The essential result is that neither activity nor ^{210}Po is a criterion to select material for target of ADS. Rather than these, the toxicity of alpha emitting rare earths must be carefully looked at. Recently, similar conclusion was reported by Los Alamos group . They found that despite of low activity level of ^{148}Gd it encompasses almost two thirds of the total dose burden in the LANSCE facilities based on present yield estimates [19].

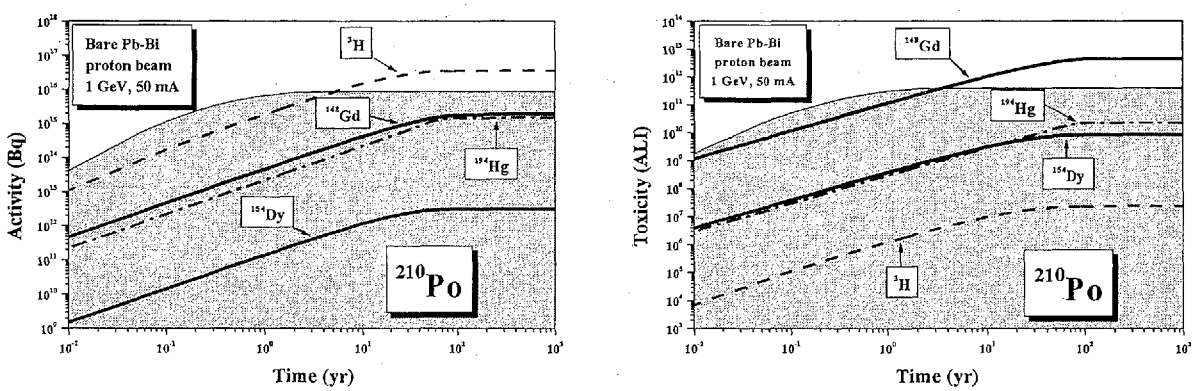

Fig.6 Time dependent activity (Bq) and toxicity (ALI) of selected isotopes in Pb-Bi target irradiated with 1 GeV protons (beam current 50 mA)

Rare earths are known also for their large capture cross-sections and they are broadly used in reactors as burnable poisons. The effect of their accumulation on neutronics and reactivity coefficients in ADS is knot touched yet. That is subject of our future research.

3. CONCLUSIONS

The focus of this paper is on accumulation of spallation products from the view point of their effect on target performance. Rare earths spallation products were identified as the most problematic in terms of toxicity. Review of experiments on their accumulation showed the big discrepancy in available data. Theoretical evaluations do not agree well either. Thus improvement of data on rare earths production in spallation target is important for further successful ADS development.

References

[1] Keepin G.: "Physics of Nuclear Kinetics", Adison-Wesley Publ.Co. Inc. (1965)
[2] Vasilkov R.: "Free Neutron Production with Hydrogen Ion Accelerators for Nuclear Fuel Cycle Needs", *Muon Catalyzed Fusion*, 7, 245 (1992)
[3] Koning A., et al: Nuclear Data for Accelerator Driven Systems: Nuclear Models, Experiments and data Libraries, *Nucl. Instr. Meth.*, A414, 49 (1998)
[4] Gloris M., et al: "Proto-Induced Production of Residual Radionuclides in Lead at Intermediate Energies", *Nucl. Instr. Meth.*, A464, 593 (2001)
[5] Titarenko Yu., et al: "Nuclide Production in ^{197}Au , ^{208}Pb, and ^{nat}U Irradiated with 0.8-1 GeV Protons: Comparison with other Experiments and with Theoretical Predictions ", Workshop on Nuclear Data for the Transmutation of Nuclear Waste, September 1-5, 2003, GSI, Darmstadt, Germany (2003)
[6] Enqvist T., et al: "Isotopic Yields and Kinetic Energies of Primary Residues in 1 A GeV ^{208}Pb+p Reactions", *Nucl. Phys. A686,* 481 (2001)
[7] Barashenkov V. et al: "Computer Software Package "CASCADE/INPE", *Atomnaya Energiya*, 87, 283 (1999)
[8] Saito M, Artisyuk V, Stankovsky A.:Radiological Hazard of Long-Lived Spallation Products", IAEA Workshop on Advanced Nuclear Reactor and Fuel Cycle Concepts, USA, ANL, Nov.28.-Dec.1 (2000).
[9] Titarenko Yu., et al: "Nuclear Physics Research to Validate ADS. Review of the Works Carried out by ITEP Laboratory 344", Materials of Russian-Japanese ADS Seminar, 19December, 2003, ITEP, Moscow, Russia
[10]Wlazlo W., et al.: "Isotope Production in 1×A GeV ^{208}Pb on Proton Reaction", Proc. 3-rd Int. Conf. On Accelerator-Driven Transmutation Technology and Applications (ADTTA'99), Prague, Czech Republic, 7-11 June (1999)
[11] Waters L., "MCNPX User's Manual", Rev 0, LA-UR 99-6058, LANL, Nov. 14 (1999).
[12] Takizuka T., et al: "JAERI Accelerator-Driven System Project", Status Report on Accelerator Driven Systems: Energy Generation and Transmutation of Nuclear Waste, IAEA-TECDOC-985, p.87 (1997)
[13] Khorosanov G., et al: "Lead and Tin Targets for Reducing Polonium Waste", Proc. 3-rd Int. Conf. On Accelerator-Driven Transmutation Technology and Applications (ADTTA'99), Prague, Czech Republic, 7-11 June (1999)
[14]Park J., wt al.:, "Review of Liquid Metal Corrosion Issues for Potential Containment Materials for Liquid Lead and Lead-Bismuth Eutectic Spallation Targets as a Neutron Source", Nucl. Eng. Des., 196, 315 (2000)
[15] Shvedov O., et al.: "ADS Program in Russia", In the Status Report on Accelerator Driven Systems: Energy Generation and Transmutation of Nuclear Waste, IAEA-TECDOC-985, p.313, (1997)
[16]Yefimov E., et al.: "Problems of Molten Lead-Bismuth Target Development for Accelerator-Driven Systems", Proc. 3-rd Int. Conf. On Accelerator-Driven Transmutation Technology and Applications (ADTTA'99), Prague, Czech Republic, 7-11 June (1999)
[17] Saito M, et al.: " Radiological Hazards of Spallation Products in Accelerator-Driven System", *Nuclear Science and Engineering*, 142, 22 (2002)
[18] Artisyuk V., et al.: "Radiological Hazard of Long-Lived Spallation Products in Accelerator-Driven System", *Progress in Nuclear Energy*, 40, 637 (2002)
[19] Corzine K., et al.: " 148Gd Production Cross Section Measurements for Accelerator Target Facilities", ANS meeting, Washington DC, November 17-21, 2002

2.5 Particle and Heavy Ion Transport Code System; PHITS

Koji Niita

RIST (Research Organization for Information Science & Technology)
Tokai-mura, Naka-gun, Ibaraki-ken 319-1106, Japan

Intermediate and high energy nuclear data are strongly required in design study of many facilities such as accelerator-driven systems, intense pulse spallation neutron sources, and also in medical and space technology. There is, however, few evaluated nuclear data of intermediate and high energy nuclear reactions. Therefore, we have to use some models or systematics for the cross sections, which are essential ingredients of high energy particle and heavy ion transport code to estimate neutron yield, heat deposition and many other quantities of the transport phenomena in materials

We have developed general purpose particle and heavy ion transport Monte Carlo code system, PHITS (Particle and Heavy Ion Transport code System) [1], based on the NMTC/JAM code [2] by the collaboration of Tohoku University, JAERI and RIST. The PHITS has three important ingredients which enable us to calculate (1) high energy nuclear reactions up to 200 GeV, (2) heavy ion collision and its transport in material, (3) low energy neutron transport based on the evaluated nuclear data.

In the PHITS, the cross sections of high energy nuclear reactions are obtained by JAM model [3]. JAM (Jet AA Microscopic Transport Model) [3] is a hadronic cascade model, which explicitly treats all established hadronic states including resonances and all hadron-hadron cross sections parametrized based on the resonance model and string model by fitting the available experimental data.

The PHITS can describe the transport of heavy ions and their collisions by making use of JQMD [4] and SPAR code. The JQMD (JAERI Quantum Molecular Dynamics) [4] is a simulation code for nucleus nucleus collisions based on the molecular dynamics. The SPAR code is widely used to calculate the stopping powers and ranges for charged particles and heavy ions.

The PHITS has included some part of MCNP4C code, by which the transport of low energy neutron, photon and electron based on the evaluated nuclear data can be described. Furthermore, the high energy nuclear data like LA150 and JENDL high energy file can be also used by the PHITS.

[1] H. Iwase, et al.: J. Nucl. Sci. Technol. **39** (2002) 1142
[2] K. Niita, et al.: Nucl. Instr. and Meth. **B184** (2001) 406
[3] Y. Nara, et al.: Phys, Rev. **C61**, 024901 (2001)
[4] K. Niita, et al.: Phys, Rev. **C52**, 2620 (1995)

2.6 Analysis of RMWR (Reduced-Moderation Water Reactor) Mockup Experiments in FCA using JENDL-3.2 and JENDL-3.3

M. Andoh, M. Fukushima, T. Yamane and S. Okajima
Research Group for Reactor Physics, Department of Nuclear Energy System,
Japan Atomic Energy Research Institute
Tokai-mura, Naka-gun, Ibaraki-ken 319-1112
E-mail: andoh@fca001.tokai.jaeri.go.jp

Abstracts

The critical experiments have been carried out at the FCA to estimate the accuracy of prediction of the core characteristics in the design study of RMWR. A part of the experiments was analyzed by two different conventional deterministic methods: the SRAC code system and a standard calculation code system for a fast reactor, and a probabilistic method, MVP. The C/E values were compared between the JENDL-3.2 and JENDL-3.3 libraries. The calculation overestimates the criticality. The C/E values of the central fission rate ratios become larger in the order, F49/F25, F37/F25, F28/F25. For C28/F25 the calculation agrees with the measured one within twice of the experimental error. For the moderator void effect the calculation underestimates the measurement. When the C/E values are compared between JENDL-3.2 and JENDL-3.3, there is no large C/E discrepancy between JENDL-3.2 and JENDL-3.3 except for the criticality. For the criticality JENDL-3.3 gives larger C/E value than JENDL-3.2.

1. Introduction

To estimate the accuracy of prediction of core characteristics in the design study of RMWR[1)], a program of critical experiments was planned at the fast critical facility, FCA. This program consisted of two phases; the first phase critical experiments in the mock-up core composed of uranium fuel plates and the second ones in the mock-up core composed of a combination of uranium and plutonium fuel plates to simulate MOX fuel. The principal aim of the first phase experiments is to study the basic characteristics of the RMWR core and that of the second phase is focused on the nuclear characteristics of the MOX fueled core. The first phase experiments were carried out between 2001 and 2002. The second phase ones are under way

These experiments have been analyzed by using JENDL-3.2[2)] and JENDL-3.3[3)] libraries and their results have been compared.

2. Brief Description of Mockup cores

The FCA-RMWR mockup core is a coupled system of a central test zone and a driver zone. The test zone is represented by a close to rectangular prism with about 38 cm in square base and 61 cm in height, as shown in Fig. 1. It is surrounded by the enriched U driver zone and two blanket zones; an inner blanket zone of 30cm in thickness containing a significant amount of depleted uranium oxide and sodium, and an outer blanket zone of 15cm in thickness containing only depleted uranium metal. The test zone is composed of a combination of uranium/plutonium fuel plates and moderator material (foamy polystyrene) plates to simulate the neutron energy spectrum of RMWR (Fig. 2). The principal cell averaged parameters of the test zone are shown in Table 1. The cell averaged fissile enrichment of the test zone is 15 atom % of ^{235}U and the hydrogen to nuclear fuel atomic number ratio (H/Fuel) is systematically changed from 0.1 to 0.8.

The measurements were made for criticality (keff value), central fission rate ratios, moderator void reactivity worth, central sample reactivity worth and ^{238}U Doppler effect.

3. Calculation method

The nuclear reactions in the RMWR core are dominantly occurred in the intermediate neutron energy range. Two different conventional deterministic methods, therefore, were used to analyze the experiments; the SRAC code system and a standard calculation code system for a fast reactor (FR code system). The cell averaged effective cross sections for each cell were obtained by the collision probability calculation with a one-dimensional infinite slab model and the group constant set generated from the JENDL-3.2 or JENDL-3.3 libraries. The effective cross sections in the resonance energy range were calculated by the table-look-up method of resonance shielding factors based on the narrow resonance approximation. The criticality and the forward and adjoint fluxes were calculated by the three-dimensional transport calculation code THREEDANT with P0-S8 approximation. The infinite dilution cross section of fission reaction for the detector was used in the central fission rate calculation while the cell averaged effective capture cross section was used in the central capture rate calculation,

In order to minimize the uncertainties of core geometrical modeling and data processing for the multi group cross sections generation, a probabilistic calculation system, a continuous-energy Monte Carlo code MVP, was also used to analyze the criticality (keff value) and the central fission rate ratios. In this analysis, the numbers of neutron histories were 2 millions and 5 millions for the criticality and the central reaction rate ratios with considering the geometrical model of the detector, respectively.

4. Comparison between Calculation and Experiment

The comparison between calculated (C) and experimental (E) results, C/E value, is shown in Table 2 to 4.

Criticality

The calculation overestimates the criticality. In the deterministic methods, the anisotropic effect of neutron leakage, caused by the plate-type fuels and materials, cannot be considered. If the effect is considered, the calculated value will become about 1~2% smaller. When the results are compared between JENDL-3.2 and JENDL-3.3, JENDL-3.3 gives larger C/E values than JENDL-3.2.

Central reaction rate ratio

The C/E values of the central fission rate ratios become larger in the order, $^{239}Pu/^{235}U$ (F49/F25), $^{237}Np/^{235}U$ (F37/F25), $^{238}U/^{235}U$ (F28/F25). From these results, the calculation code systems have a tendency to give a harder neutron spectrum. There is no significant difference in the C/E values between the SRAC and FR systems except for the F49/F25 in the XXI-1D core. The MVP calculation with JENDL-3.3 gives large underestimation for the F49/F25 in the XXII-1 (65V) core. We need further investigation in the analysis of it. For the ratio of ^{238}U capture to ^{235}U fission rates (C28/F25), the MVP calculation agrees with the measured data within twice of the experimental error. When the C/E values of the C23/F25 are compared between JENDL-3.2 and JENDL-3.3, there is no large difference between them.

Reactivity Worth Measurement

As the moderator void effect, the reactivity worth caused by the void fraction change of polystyrene plates from 65% to 95% in the central cell of the test zone were measured. The calculation underestimates the measured value by 10% and more. The C/E values obtained by JENDL-3.2 agree with those by JENDL-3.3.

As the ^{238}U Doppler effect, the Doppler reactivity worth of the UO_2 sample due to sample temperature change from room temperature to 800°C was measured. The calculation with using JENDL-3.2 and JENDL-3.3 agrees with the experiment within twice of measurement error.

In the analysis of Pu sample reactivity worth, the SRAC system shows the C/E dependency on Pu contents. When the C/E values are compared between JENDL-3.2 and JENDL-3.3, there is no large discrepancy.

5. Summary

The critical experiments at the FCA have been carried out to estimate the accuracy of prediction of core characteristics in the design study of RMWR. The first phase experiments, of which the purpose is to study the basic characteristics of the RMWR core, were finished. The second phase experiments, which are focused on the nuclear characteristics of the MOX fueled core, are under way. The analyses were carried out by two different conventional deterministic methods, the SRAC code system and a standard calculation code system for a fast reactor (FR code system), and a probabilistic method, MVP. The C/E values were compared between the JENDL-3.2 and JENDL-3.3 libraries.

In the analysis of the criticality, the calculation overestimated the measurement and

JENDL-3.3 gives larger C/E values than JENDL-3.2. For the central reaction rate ratio, the C/E values become larger in the order, F49/F25, F37/F25, F28/F25. On the other hand, the calculation agreed with the measured C28/F25 within twice of the experimental error. When the C/E values were compared between JENDL-3.2 and JENDL-3.3, there was no large difference between them except for the MVP calculation for the F49/F25 in the XXII-1 (65V) core. In the analysis of the reactivity worth measurement, the calculation showed the underestimation in the moderator void effect and the C/E dependency in the Pu sample worth. However, there was no large C/E discrepancy between JENDL-3.2 and JENDL-3.3.

The further detail analyses will be carried out to solve the problems, such as the underestimation in the moderator void effect and the C/E dependency in the Pu sample reactivity worth after completing the experiments in the other cores with different moderator voidage fraction.

References

1) S. Uchikawa : "Status and Future Program of Research and Development on Reduced-moderation Water Reactors", in Summary of the 6th Workshop on the Reduced-moderation Water Reactor, JAERI-Conf 2003-020 (2003).
2) T. Nakagawa, *et al.* : *J. Nucl. Sci. and Technol.*, **32**, 1259 (1995).
3) S. Shibata, *et al.*: *ibid.*, **39**, 1125 (2002).

Table 1 Cell averaged parameters of the test zone in FCA RMWR mockup cores

Core name	1st phase	2nd phase			RMWR
	XXI-1 D2	XXII-1(45V)	XXII-1(65V)	XXII-1(95V)	
Enrichment (%)	15.2	15.8	15.8	15.8	10
Vm/Vf *	1.7	0.6	0.6	0.6	0.18
Void fraction (%)	80	45	65	95	68
H/Fuel **	0.50	0.81	0.52	0.091	

* Volume fraction of moderator to fuel plates in a cell

** Atomic number ratio between Hydrogen and Fuel materials in a cell

Table 2 Ratio of calculated to measured criticality (keff value)

Core name	SRAC		FR		MVP	
	J-3.2	J-3.3	J-3.2	J-3.3	J-3.2	J-3.3
XXI-1 D2	1. 0196 ±0.02%	-	1. 0155 ±0.02%	-	1. 0036 ±0.04%	-
XXII-1 (65V)	1. 0057 ±0.04%	1. 0071 ±0.04%	1. 0003 ±0.04%	1. 0013 ±0.04%	1. 0099 ±0.05%	1. 0107 ±0.04%

Table 3 Comparison of central reaction rate ratios between calculation and experiment

Reaction	Core name	SRAC		FR		MVP	
		J-3.2	J-3.3	J-3.2	J-3.3	J-3.2	J-3.3
F28/F25	XXI-1 D2	1.10	-	1.10	-	1.00±6%	-
	XXII-1 (65V)	1.18	1.17	1.18	1.17	1.20±8%	1.15±10%
F37/F25	XXI-1 D2	1.06	-	1.03	-	0.92±5%	-
	XXII-1 (65V)	1.06	1.07	1.07	1.07	1.08±7%	1.02±8%
F49/F25	XXI-1 D2	0.84	-	0.99	-	0.89±12%	-
	XXII-1 (65V)	0.99	0.99	1.00	1.00	0.92±11%	0.83±11%
C28/F25	XXII-1 (65V)	1.03	1.04	1.13	1.13	1.01±2%	1.05±2%

* Measurement error : F28/F25 ±6%, F37/F25 ±5%, F49/F25 ±4%, C28/F25 ±2%

Table 4 Comparison of reactivity worth between calculation and experiment

Item		Core name	SRAC		FR	
			J-3.2	J-3.3	J-3.2	J-3.3
Moderator void effect *		XXII-1 (65V)	0.84	0.85	0.87	0.87
U-238 Doppler effect ** (Sample: UO_2)		XXI-1 D2	(1.07) †	-	1.09	-
		XXII-1 (65V)	(0.83) †	(0.84) †	1.00	1.01
Pu sample ***	Pu (92)	XXII-1 (65V)	0.92	0.92	0.95	0.95
	Pu (81)	XXII-1 (65V)	1.02	0.96	1.10	1.05
	Pu (75)	XXII-1 (65V)	1.17	1.15	0.92	0.90

* Reactivity worth due to moderator void fraction change from 65% to 95% in the central cell of the test region.

** Doppler sample reactivity worth due to sample temperature change from room temperature to 800 °C.

*** Pu (92) : 239/240/241/242=91.7/8.0/0.2/0.1, Pu (81) : 239/240/241/242=80.3/18.6/0.7/0.4, Pu (75) : 239/240/241/242=73.0/23.1/1.7/2.2.

† Calculation was carried out by the diffusion code (CITATION) with 2-dimensional model.

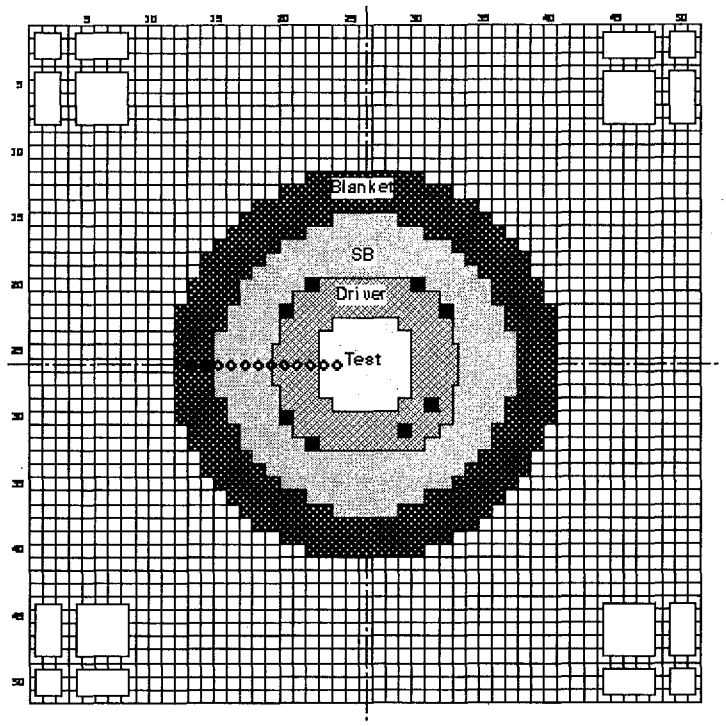

Fig. 1 Cross-section view of the first phase FCA-RMWR core

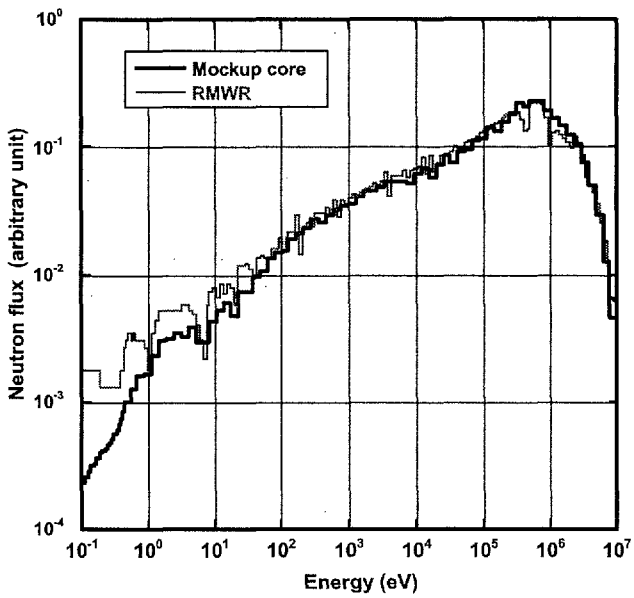

Fig. 2 Calculated neutron energy spectra

2.7 Target accuracy of MA nuclear data and progress in validation by post irradiation experiments with the fast reactor "JOYO"

Shigeo OHKI, Kenji YOKOYAMA, Kazuyuki NUMATA*, and Tomoyuki JIN*
Oarai Engineering Center, Japan Nuclear Cycle Development Institute
4002, Narita-cho, Oarai-machi, Higashi-Ibaraki-gun, Ibaraki 311-1393
**NESI Incorporation*
1-9-12, Kita-Ueno, Taito-ku, Tokyo, 110-0014
Corresponding e-mail: ohki@oec.jnc.go.jp

This paper presents a discussion about the target accuracy of MA nuclear data for fast reactor cycle system development, as well as the validation work on those nuclear data by PIE analyses. The PIE analyses are in progress on fuels and MA samples (^{237}Np, ^{241}Am, ^{243}Am, ^{244}Cm) irradiated at the experimental fast reactor "JOYO". The analysis result on the first examined MA sample suggested the necessity of re-evaluation of the isomeric ratio for ^{241}Am capture reaction both in ENDF/B-VI and in JENDL-3.3. The above result contributes to the uncertainty-reduction both of burnup reactivity loss and of gamma energy release from fuel assemblies.

1. Introduction

Japan Nuclear Cycle Development Institute is developing a commercialized fast reactor cycle system that involves the recycling of minor actinide (MA) nuclides. To develop a burnup calculation method and to validate MA nuclear data, we have launched isotopic composition analyses of post irradiation examination (PIE) results. The irradiations were performed at the experimental fast reactor "JOYO".

MA recycling in fast reactors brings about the reduction of burnup reactivity loss, the increase of sodium void reactivity, and the increase of decay heat and neutron emission from fuel assemblies. Before getting into the PIE analyses, nuclear-data-induced uncertainties for above-mentioned quantities were evaluated tentatively as described in **Section 2**. We discussed the relation between target accuracy of those quantities and that of MA nuclear data. Then, the influential MA nuclear data having a priority in validation work were selected.

PIE analyses are in progress on (1) JOYO MK-I core fuel, (2) JOYO MK-II driver fuel, and (3) MA samples (^{237}Np, ^{241}Am, ^{243}Am, ^{244}Cm) irradiated at JOYO MK-II core. The former two analyses are dedicated to the development of a burnup calculation method, as well as to the validation of capture cross-sections for major heavy metal nuclides (^{238}U, ^{239}Pu, ^{240}Pu, etc.). The third one is expected to be applied directly to the validation of MA nuclear data. The present status of those PIE analyses is reported in **Section 3**.

2. Target accuracy of MA nuclear data

In this section, we try to estimate how much the uncertainty of MA nuclear data influences on reactor core parameters and fuel-cycle-related quantities. The contributions from MA nuclear data uncertainty were compared with the target accuracy assumed for each quantity. Then we discussed the necessity of MA nuclear data improvement and its target accuracy. A demonstration-type sodium-cooled FBR core concept[1] was employed as a reference. The reactor thermal power is 1600 MW_{th}. The operation cycle length is 375 EFPD. Fuel exchange is performed by 3 dispersed batches. The average fuel burnup is 85700 MWd/t. Fuel type is mixed oxide, and the plutonium enrichment is about 19 weight % of heavy metal. MA extracted from LWR spent fuel (denoted as LWR-MA hereafter) was assumed to be mixed to the active core fuel homogeneously. The MA contents were $^{237}Np/^{241}Am/^{243}Am/^{244}Cm$ = 49/30/16/5 (weight %), and its amount in heavy metal was set to 2.7 weight %.

Nuclear-data-induced uncertainty was evaluated by the following formula:

$$Standard\ deviation = \sqrt{\mathbf{GMG}^T}.$$

The **G** and **M** stand for a vector of cross-section sensitivity coefficients and a cross-section covariance matrix, respectively. They are expanded in the space of nuclide, reaction, and energy group number. Sensitivity coefficients were calculated by using the SAGEP code[2]. For covariance matrix, the JENDL-3.2 covariance file[3] was used for major nuclides. Since covariance for MA nuclides was not available, variance of MA nuclear data was tentatively deduced from discrepancies among the following major nuclear data libraries: JENDL-3.3[4], ENDF/B-VI release 5[5], and JEF-2.2[6]. Note that there is no confidence that the discrepancy among those libraries is equivalent to actual uncertainty.

First, fuel-cycle-related quantities such as decay heat, neutron emission, and gamma energy release from a fuel assembly loaded in the central core region are discussed. We restricted our investigation to cross section uncertainty concerning the prediction of burnt amount of heavy metal sources, and did not consider the errors associated with decay constants, Q-values, neutron and gamma yields, and so on. The time point of evaluation was set to 4 years after the discharge. The results are summarized in **Table 1**. For decay heat and neutron emission, ^{243}Am capture and ^{244}Cm capture reactions were found to be the main contributors. They were related to the net generation of important source nuclide ^{244}Cm. For gamma energy release, both

Table 1 Nuclide and reaction-wise contribution to the uncertainty for fuel-cycle-related quantities (1σ, %)

(600MWe-FBR, LWR-MA 2.7% added, 4-year-cooled)

Source Nuclide	Contributed Nuclide and Reaction	Decay heat	Neutron emission	Gamma energy release
^{238}Pu	^{238}Pu Capture	1.2		
	^{241}Am Isomeric Ratio	1.2		
^{241}Am	^{241}Am Capture			1.4
^{242m}Am	^{241}Am Isomeric Ratio			4.7
^{243}Cm	^{241}Am Capture			1.5
	^{242}Cm Capture			6.9
	^{243}Cm Capture			1.0
	^{243}Cm Fission			1.7
	^{241}Am Isomeric Ratio			2.3
^{244}Cm	^{243}Am Capture	2.4	4.5	
	^{244}Cm Capture	2.3	4.4	
(cf.) Target accuracy (tentative value)		5～10	5～10	5～10

* Contributions of MA were deduced from the discrepancy of nuclear data libraries.
** Contributions less than 1.0% are not indicated.

isomeric ratio of ^{241}Am capture reaction and ^{242}Cm capture reaction gave relatively large contributions, around 5% or more. If we assume the target accuracy is 5–10%, then the cross-sections of above contributed reactions turn out to have necessity of improvement.

As important reactor core parameters for recycling MA, we investigated effective multiplication factor (k_{eff}), sodium void reactivity, and burnup reactivity loss. The nuclear-data-induced uncertainty for those quantities is listed in **Table 2** together with the target accuracy. For k_{eff} and sodium void reactivity, the contributions from MA nuclear data were relatively small compared with other data such as ^{238}U inelastic scattering, ^{239}Pu fission, ^{239}Pu fission spectrum, and ^{238}U delayed neutron yield (ν_d). Meanwhile, we found a certain amount of contributions from both ^{241}Am capture and its isomeric ratio to the burnup reactivity loss. These are related to the generation of the efficient fissile material ^{242m}Am. It is also necessary to improve capture cross-sections of major heavy metal nuclides (^{238}U, ^{239}Pu, ^{240}Pu) for the burnup reactivity loss.

As a result, the following MA nuclear data were selected to have a higher priority for improving the accuracy: ^{241}Am capture, ^{241}Am isomeric ratio, ^{243}Am capture, ^{242}Cm capture, and ^{244}Cm capture. We also found that the present discrepancies of MA nuclear data had relatively small impacts on fast reactor cycle systems as long as MA abundance in fuel is less than a few percent of heavy metal. However, since there is no confidence that the discrepancy among libraries is equivalent to the actual uncertainty, necessity for measurement and validation works still exists. Preparation of covariance files for MA nuclear data is also required for a practical uncertainty evaluation in the future.

Table 2 Nuclide and reaction-wise contribution to the uncertainty for reactor core parameters (1σ, %)

(600MWe-FBR, LWR-MA 2.7% added)

Contributed Nuclide and Reaction	k_{eff} (BOC)	Sodium void reactivity (BOC)	Burnup reactivity loss
^{238}U Capture	0.24	0.8	3.6
^{238}U Inelastic Scattering	0.47	2.0	
^{239}Pu Capture	0.12		2.2
^{239}Pu ν_p	0.12	0.7	
^{239}Pu Fission	0.47	2.6	1.5
^{240}Pu Capture	0.10	0.5	2.1
^{241}Pu Capture	0.10		1.3
^{241}Pu Fission	0.10	0.5	1.0
^{241}Am Capture			1.3
^{241}Am Isomeric Ratio	-	-	1.9
^{242m}Am Fission			0.6
^{242}Cm Fission			0.5
^{244}Cm Capture			0.5
Lumped FP (^{239}Pu) Capture			1.4
Lumped FP (^{241}Pu) Capture			0.6
^{23}Na Capture		0.8	
^{23}Na Elastic Scattering		1.1	
^{23}Na Inelastic Scattering		1.7	
^{23}Na μ-average		0.6	
Fe Capture	0.10	0.7	
Fe Elastic Scattering		1.0	
Fe Inelastic Scattering	0.28	0.7	
^{239}Pu Fission Spectrum	0.40		
^{238}U ν_d	-	1.9	1.9
^{239}Pu ν_d	-	1.2	1.2
^{241}Pu ν_d	-	0.7	0.7
Others	0.28	1.4	1.0
Total (root of sum of squares)	0.94	5.2	6.5
(cf.) Target accuracy (tentative value)	0.3	10	5

* Contributions of MA were deduced from the discrepancy of nuclear data libraries.
** Contributions less than 0.05% (1.0%) are not indicated for k_{eff} (for sodium void reactivity and burnup reactivity loss).

3. Progress in PIE analyses

(1) JOYO MK-I core fuel

So far, most of the analyses for JOYO MK-I core fuel have been completed. The ^{235}U enrichment (^{235}U/U) of the fuel was about 23 weight %, and the plutonium enrichment (Pu/(U+PU)) was about 18 weight %. We analyzed about 70 specimens up to 5% of burnup. The neutron flux history was calculated by 3-dimmensional whole core diffusion calculation taking into account the fuel exchange pattern through 11 operation cycles. The effective cross-sections were prepared from the fast reactor group constant set JFS-3-J3.2R based on JENDL-3.2[7]. Nuclide depletion calculation aiming at each PIE specimen was performed by the ORIGEN2 code with the neutron flux history and spectrum obtained by the preceding whole core calculation. The C/E values for main nuclides (^{235}U, ^{239}Pu, ^{241}Pu) didn't show any significant inconsistency. However, large dispersions were observed in C/E values for minority isotopes such as ^{238}Pu, ^{240}Pu, and ^{242}Pu. Those dispersions possibly came from measurement. Such a discrepancy was reduced in the latest MK-II driver fuel PIE data, for which refined experimental technique had been applied. We carry on finding out the cause of larger discrepancy of the MK-I C/E values, while proceed to the MK-II driver fuel analyses.

(2) MA sample irradiation

We have just started the PIE analysis of the MA samples (^{237}Np, ^{241}Am, ^{243}Am, ^{244}Cm) irradiated at JOYO MK-II core. Twenty-five MA samples were loaded at the two irradiation positions in the 3rd and the 5th assembly row (see **Fig. 1**). The irradiation was performed for 200-250 EFPD during the period of 1994 to 1999. PIE of the first sample (one of the ^{243}Am samples) was finished in October, 2003. The preliminary analysis result on the ^{243}Am sample is presented in the rest of this paper. The sample was loaded in the 3rd row, and the axial position was +350 mm upper from the core midplane (core height was 55 cm). That is, the sample was loaded in upper reflector region, and it was adjacent to control rod absorber. We suspected that the calculation modeling error could be large.

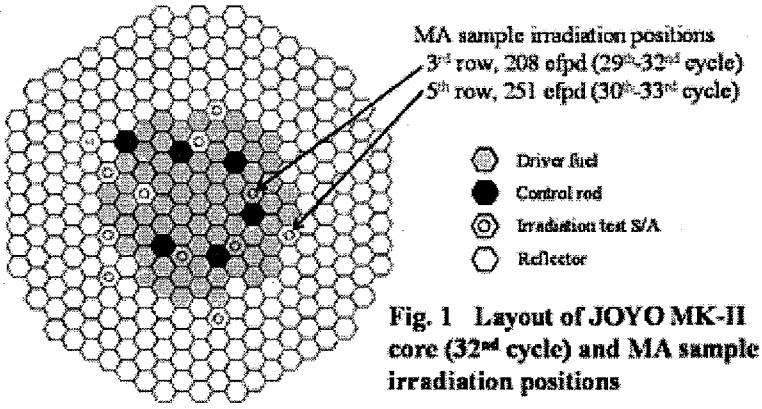

Fig. 1 Layout of JOYO MK-II core (32nd cycle) and MA sample irradiation positions

The ^{243}Am sample was initially composed of 12.2% of ^{241}Am and 87.8% of ^{243}Am. We focused on the generation of ^{242m}Am from ^{241}Am, as well as that of ^{244}Cm from ^{243}Am. Main purpose of the former transmutation process was to validate the isomeric ratio (IR) of ^{241}Am capture reaction. There exist only two IR evaluations with following large discrepancy: about 0.8 (ground/(ground + meta)) given from ENDF/B-VI under fast reactor spectrum, while about 0.7 from JENDL-3.3. This discrepancy influenced strongly on the generation amount of ^{242m}Am.

Preliminary calculation method is illustrated in **Fig. 2**. Burnup calculation of MA sample was carried out by the use of the ORIGEN2 code. The power history during MA irradiation was referred to the data from JOYO core management code system[8]. The absolute flux level and neutron spectrum were obtained by 70-group 3-dimmensional whole core static calculation, where the transport and mesh

effects were corrected. The effective cross section of control rod was prepared by the reaction rate ratio preservation (RRRP) method[9]. Infinitely-diluted cross-sections for MA nuclides were obtained from major nuclear data libraries (JENDL-3.2, JENDL-3.3, ENDF/B-VI release 5, and JEF-2.2), which were condensed into 1-group to be used in ORIEGN2 calculation.

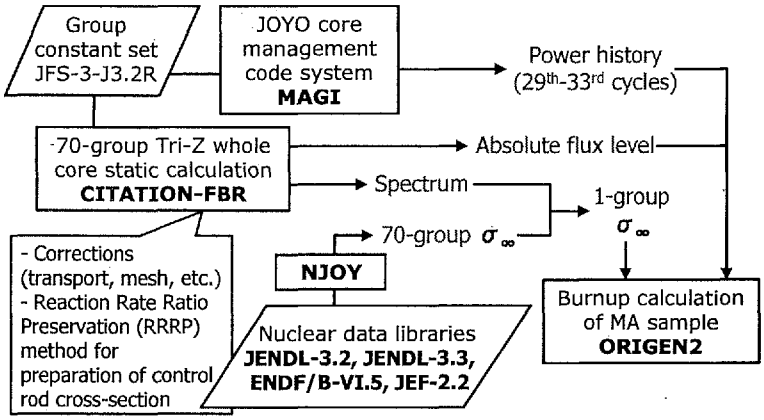

Fig. 2 Preliminary calculation method for the MA samples

The result of the preliminary calculation was summarized in **Table 3**. Assuming IR = 0.8 and using JENDL-3.2, we obtained the preliminary C/E value of 1.30 for the abundance ratio of ^{242m}Am/^{241}Am. In the case of IR = 0.85, the C/E value reduced to 1.00. To use other nuclear data libraries (IR was set to 0.85) changed the C/E value no more than 6%. The experimental error was about 2% via mass spectroscopy, which was small enough. The above results implied the possibility that the IR of ^{241}Am capture reaction lies around 0.85. This is consistent with the independent PIE results with PFR[10] and PHENIX[11]. Necessity of re-evaluation of the IR both in ENDF/B-VI and in JENDL-3.3 is suggested.

For the abundance ratio of ^{244}Cm/^{243}Am, the present calculations were systematically underestimated by 10-20%. We have met the difficulty in measuring the ratio of Cm/Am, in which relatively large experimental error (about 10%) arose from alpha spectroscopy. We now try to improve the measurement accuracy by means of the isotope dilution analysis.

Finally, calculation modeling dependency for the ^{243}Am sample was investigated. The heterogeneity effect of the sample-loaded assembly and the self-shielding effect of sample nuclides were found to be small. However, by the reason that the sample was loaded in reflector region with adjacent to control rod absorber, there was 5% of transport effect on neutron flux level, and the 3-4% of changes in one-group capture cross-sections for ^{241}Am and ^{243}Am took place from ambiguity of control rod modeling in the RRRP calculation. Significant uncertainty from nuclear data of structure material could also be anticipated. So, we had better concentrate on the other samples loaded in core region in future detailed analysis. Anyway, single result we have just obtained is never enough. We carry on the

Table 3 Comparison of C/E values for the isotopic abundance ratio of irradiated MA samples

	PFR [Ref.10]	JOYO (preliminary result on the ^{243}Am sample)					PHENIX [Ref.11]
Nuclear data library	JENDL-3.2	JENDL-3.2	JENDL-3.2	JENDL-3.3	ENDF/B-VI.5	JEF-2.2	JEF-2.2
^{241}Am Isomeric ratio	0.80	0.80	0.85	0.85	0.85	0.85	0.85
^{242m}Am / ^{241}Am	1.29	1.30	1.00	1.02	0.94	1.03	1.03
^{244}Cm / ^{243}Am	0.95	0.84	0.84	0.84	0.83	0.88	0.96

analyses for the remaining samples, increase the number of results, and apply detailed calculation modeling. The error estimation for both experiment and calculation will work out for practical utilization of the analysis results.

4. Summary

To develop a commercialized fast reactor cycle system involving the recycling of MA nuclides, we have launched the isotopic composition analyses of PIE results for fuels and MA samples (^{237}Np, ^{241}Am, ^{243}Am, ^{244}Cm) irradiated at the experimental fast reactor "JOYO". For reducing the uncertainty of burnup reactivity loss, as well as neutron emission and gamma energy release from fuel assemblies, the following MA nuclear data are selected to have a higher priority in accuracy-improvement: ^{241}Am capture, ^{241}Am isomeric ratio, ^{243}Am capture, ^{242}Cm capture, and ^{244}Cm capture. The analysis result on the first examined MA sample (one of ^{243}Am samples) implies the possibility that the ^{241}Am isomeric ratio lies around 0.85, which suggests the necessity of re-evaluation of the data both in ENDF/B-VI and in JENDL-3.3. We carry on the analyses for the remaining samples, increase the number of results, and apply detailed calculation modeling in order to sophisticate the interpretation of analysis results.

References

[1] H. Hayashi, *et al.*, *Progress Report of the Design Study on a Large Scale Reactor – Design Study on a 600MWe Class Plant –*, PNC TN9410 92-137 (1992), [in Japanese].

[2] T. Takeda and T. Umano, "Burnup Sensitivity Analysis in a Fast Breeder Reactor – Part I: Sensitivity Calculation Method with Generalized Perturbation Theory", *Nucl. Sci. Eng.*, **91**, 1 (1985).

[3] K. Shibata, *et al.*, "JENDL-3.2 Covariance File", *J. Nucl. Sci. Technol.*, **Suppl. 2**, 40 (2002).

[4] K. Shibata, *et al.*, "Japanese Evaluated Nuclear Data Library Version 3 Revision-3: JENDL-3.3", *J. Nucl. Sci. Technol.*, **39**, 1125 (2002).

[5] Cross Section Evaluation Working Group, *ENDF/B-VI Summary Documentation*, BNL-NCS-17541 (ENDF-201) (1991).

[6] OECD/NEA (Ed.), *The JEF-2.2 Nuclear Data Library*, JEFF Report 17 (2000).

[7] T. Nakagawa, *et al.*, "Japanese Evaluated Nuclear Data Library Version 3 Revision-2: JENDL-3.2", *J. Nucl. Sci. Technol.*, **32**, 1259 (1995).

[8] Y. Ohkawachi, *et al.*, *JOYO MK-II Core Characteristics Database – Update to JFS-3-J3.2R –*, JNC TN9400 2003-029 (2003), [in Japanese].

[9] K. Sugino and T. Iwai, *Advances in Methods of Commercial FBR Core Characteristics Analyses – Investigations of a Treatment of the Double-heterogeneity and a Method to Calculate Homogenized Control Rod Cross Sections –*, PNC TN9410 98-067 (1998), [in Japanese].

[10] K. Tsujimoto, *et al.*, "Validation of Minor Actinide Cross Sections by Studying Samples Irradiated for 492 Days at the Dounreay Prototype Fast Reactor – II: Burnup Calculations", *Nucl. Sci. Eng.*, **144**, 129 (2003).

[11] R. Soule and E. Fort, "Contribution to the Validation of JEF2 Actinide Nuclear Data: Analysis of Fuel and Sample Irradiation Experiments in PHENIX", *Proc. Int. Conf. on Future Nuclear Systems, Global '97*, Yokohama, Japan, Oct. 5-10, 1997, p.1332 (1997).

2.8 Nuclear Data for Emergency Preparedness of Nuclear Power Plants －Evaluation of Radioactivity Inventory in PWR using JENDL 3.3－

Yoshitaka Yoshida, Itsuro Kimura
Institute of Nuclear Technology, Institute of Nuclear Safety System Inc. (INSS)
Sata 64, Mihama-cho, Mikata-gun, Fukui-ken, 919-1205 Japan
E-mail: yoshida@inss.co.jp, kimura@inss.co.jp

The radioactivity inventories in PWR cores, one with UO_2 fuels and the other with 1/4 mixed oxide fuels, which focused on emergency preparedness of nuclear power plants were calculated by ORIGEN2.2 code using the newest nuclear data in Japan, namely JENDL3.3 (neutron cross sections), JENDL FP decay data file 2000 (decay data) and JNDC second version (fission yields). It is seen that these results agree with those for seven cases in which rather older nuclear data and ORIGEN2.1 code have been used. However, in details, these results exceed those by conventional method using ORIGEN2.1 code with its built-in nuclear data from a few % to 7%. It is found that this difference is mainly caused by neutron cross sections, fission yields and calculation codes.

1. Introduction

The purpose of emergency preparedness of nuclear power plants is to protect the public and the employees from radiation exposure and radioactive materials in a severe accident. Therefore, it is necessary to evaluate the accumulation of the radioactivity inventory in a reactor core and the diffusion of radioactive materials to the containment vessel in the accident as precisely as possible. And then, it is required to evaluate their leakage from the containment vessel and their movement to the concerned points inside and outside of the plant accurately. At present, conventional methods using codes such as ORIGEN2.1[(1),(2)] with nuclear data, namely neutron cross sections, decay data and fission yields, which are built-in the code are still often utilized for safety analysis without strict review. Old conventional methods using rather older code and nuclear data are not always inferior to newer ones, but it is advisable to adopt the newest code and nuclear data in which most of the contents are deeply and strictly examined and their uncertainties are also evaluated.

In this work, the radioactivity inventories in PWR cores, one with UO_2 fuels and the other with 1/4 mixed oxide (MOX) and 3/4 UO_2 fuels, have been calculated by a newer burnup code, ORIGEN2.2[(3)], using the newest nuclear data, namely JENDL3.3[(4)] (neutron cross sections), JENDL FP decay data file 2000[(5)] (decay data : it is referred to as JNDC 2000), and JNDC second version[(6)] (fission yields : it is referred as JNDC V2). The results are compared with those for 7 cases in which rather older nuclear data and ORIGEN2.1 have been used. Thereafter, these new radioactivity inventory data are adopted into the database in our employees dose prediction system[(7)] for emergency preparedness of nuclear power plants.

Table 1 Evaluated reactor cores and burnup conditions

	UO_2 Core	MOX Core
Core Composition	UO_2 (7×17 Fuels)	1/4MOX (7×17 Fuels)
Number of Fuel Assemblies	193	157 (UO_2:117) (MOX:40)
Maximum Burn up	55GWd/t	48GWd/t
Burn up Cycle	3 Batches	3 Batches
Average Burn up	36.7GWd/t	30.6GWd/t
Power Ratio	37.6 MW/t	36.7 MW/t

2. Calculated Reactor Cores and Calculation Method

Two cores of PWRs (4 loop plant with UO_2 fuels and 3 loop plant with 1/4 MOX fuels and 3/4 UO_2 fuels) were chosen for evaluation. The conditions of these two cores and fuel burnup are tabulated in Table 1. The burnup calculation was carried out by either ORIGEN2.2 or ORIGEN2.1 to obtain radioactivity inventories and the decay of radioactive nuclides after reactor shutdown was also calculated. We calculated the radioactivity inventories of the UO_2 and MOX cores for 8 cases of the combinations as shown in Table 2. In this table the case 0 is regarded as the basic case in this work. The case 7 is the conventional method which is often used for safety analysis in Japan. The data sets used in the burnup calculation are shown as corresponding

neutron cross section libraries in Table 3. Although, the radioactivity inventories were calculated during the burnup and longer time after shutdown, only those at the shutdown and 2, 12 and 24 hours after it are compared and discussed in this work. For the use of emergency preparedness, total amounts of radioactivity, total noble gases (0.5 MeV conversion value) and total iodines (^{131}I equivalent thyroid conversion value of a child) are considered. In order to find the sensitivity of different nuclear data and code to the basic case, we calculated the difference factor DF defined as follows,

$$DF = \frac{(C_0 - C_i)}{C_i}$$

where C_0 and C_i are the radioactivity inventories obtained for the basic case and for the case i, respectively. The object of the comparison and its purpose are tabulated in Table 4.

Table 2 Combinations of nuclear data, namely neutron cross sections, decay data and fission yields, and calculation code

Case	Radio-activity Inventory	Nuclear Cross Sections	Decay Data	Fission Yields	Calculation Code
0 (Base)	C_0	JENDL 3.3	JNDC2000	JNDC V2	ORIGEN2.2
1	C_1	JENDL 3.2	JNDC2000	JNDC V2	ORIGEN2.2
2	C_2	Built-in ORIGEN	JNDC2000	Built-in ORIGEN	ORIGEN2.2
3	C_3	JENDL 3.3	JNDC V2	JNDC V2	ORIGEN2.2
4	C_4	JENDL 3.3	Built-in ORIGEN	JNDC V2	ORIGEN2.2
5	C_5	JENDL 3.3	JNDC2000	JNDC V2	ORIGEN2.1
6	C_6	JENDL 3.2	JNDC V2	JNDC V2	ORIGEN2.1
7	C_7	Built-in ORIGEN	Built-in ORIGEN	Built-in ORIGEN	ORIGEN2.1

Table 3 Data sets used in burnup calculation

Nuclear Cross Section Library	UO_2 Core	MOX Core	
		UO_2 Fuel	MOX Fuel
JENDL3.3	PWR47J33	PWR41J33	PWRM0205J33
JENDL3.2	PWR47J32	PWR41J32	PWRM0205J32
Built-in ORIGEN	PWR-U50	PWR-U50	PWR-PUPU

Table 4 Object and purpose of comparison and difference factor

Case Number	Object of Comparison		Difference Factor	Purpose
S1	JENDL 3.3(JNDC V2)	JENDL 3.2(JNDC V2)	$(C0-C1)/C0$	Sensitivity to Nuclear Cross Section and Fission Yields
S2	JENDL 3.3(JNDC V2)	Built-in ORIGEN	$(C0-C2)/C0$	
S3	JNDC 2000	JNDC V2	$(C0-C3)/C0$	Sensitivity to Decay Data
S4	JNDC 2000	Built-in ORIGEN	$(C0-C4)/C0$	
S5	ORIGEN2.2	ORIGEN 2.1	$(C0-C5)/C0$	Sensitivity to Calculation Code
S6	Newest Version	Previous Version	$(C0-C6)/C0$	Sensitivity to Nuclear Data and Code
S7	Newest Version	Conventional Calculation	$(C0-C7)/C0$	

Table 5 Calculated results of total amount, noble gases and iodines

Case	Object of Comparison	Type of Core	Difference Factor (%)											
			Total Amount				Noble Gases				Iodines			
			0 hr	2 hr	12 hr	24 hr	0 hr	2 hr	12 hr	24 hr	0 hr	2 hr	12 hr	24 hr
S1	JENDL 3.3 vs. JENDL3.2	UO_2	0.17%	0.21%	0.25%	0.26%	-0.08%	-0.13%	-0.04%	0.02%	0.10%	0.10%	0.10%	0.10%
		MOX	0.17%	0.22%	0.25%	0.26%	-0.09%	-0.22%	-0.18%	-0.08%	0.11%	0.11%	0.12%	0.12%
S2	JENDL 3.3 vs. Built-in ORIGEN	UO_2	1.55%	1.34%	1.32%	1.28%	2.24%	0.31%	2.93%	2.78%	0.25%	0.30%	0.34%	0.41%
		MOX	1.70%	1.58%	1.61%	1.58%	2.17%	0.96%	3.42%	3.11%	0.38%	0.43%	0.47%	0.54%
S3	JNDC 2000 vs. JNDC V2	UO_2	0.19%	0.48%	0.32%	0.17%	-0.01%	-0.26%	-0.33%	0.21%	0.00%	0.01%	0.01%	0.00%
		MOX	0.18%	0.44%	0.29%	0.16%	-0.01%	-0.25%	-0.26%	0.24%	0.00%	0.00%	0.01%	0.00%
S4	JNDC 2000 vs. Built-in ORIGEN	UO_2	0.23%	0.85%	0.70%	0.56%	-0.20%	1.18%	0.48%	0.01%	-0.02%	0.03%	0.11%	0.18%
		MOX	0.18%	0.83%	0.70%	0.57%	-0.20%	1.21%	0.52%	0.05%	-0.04%	0.00%	0.07%	0.15%
S5	ORIGEN2.2 vs. ORIGEN2.1	UO_2	1.51%	1.33%	1.22%	1.19%	2.48%	2.50%	1.99%	1.83%	1.73%	1.73%	1.71%	1.70%
		MOX	2.50%	2.33%	2.23%	2.20%	2.70%	2.93%	3.36%	3.42%	3.49%	3.49%	3.52%	3.55%
S6	Newest Version vs. Previous Version	UO_2	1.68%	1.81%	1.58%	1.42%	2.31%	2.05%	1.57%	1.99%	1.73%	1.74%	1.73%	1.71%
		MOX	2.77%	2.94%	2.72%	2.57%	2.51%	2.35%	2.82%	3.48%	3.50%	3.51%	3.55%	3.57%
S7	Newest Version vs. Conventional Calculation	UO_2	2.89%	3.21%	2.99%	2.80%	3.23%	2.77%	4.90%	4.29%	1.78%	1.87%	2.01%	2.17%
		MOX	4.06%	4.44%	4.28%	4.09%	4.15%	4.52%	6.85%	6.15%	3.31%	3.40%	3.55%	3.73%

3. Results and Discussion

The calculation results of the difference factors of the total amounts of radioactivity inventories, noble gases and iodines for both cores at the reactor shutdown and after 2, 12 and 24 hours after it are tabulated in Table 5. As a whole, the radioactivity inventories agree with each other within 7% of the difference factor. Sensitivities of each factor of the nuclear data and of the calculation code to the difference factor are shown in Figs. 1~9 with some discussion below.

(1) Neutron cross sections and fission yields

The difference factor of 3 quantities by JENDL3.3 and JENDL3.2 in Table 5 are less than 0.3%, however those by JENDL3.3 and built-in ORIGEN are much larger. The largest difference factors appear for noble gases at 12 and 24 hours after the reactor shutdown, namely 2.93% and 2.78% for 12 and 24 hours for the UO_2 core. This tendency is slightly enhanced for the MOX core. The breakdown of noble gases is shown in Fig. 1, in which large contribution of ^{135}Xe is observed at 12 and 24 hours for both cases. Therefore, the large difference factors of noble gases seen in Table 5 are mainly due to the ^{135}Xe buildup. The neutron fluxes for the cases of 1, 4 and 5 are shown in Fig. 2. As seen in this figure, since the neutron fluxes obtained with built-in ORIGEN are smaller than those calculated with JENDLs (3.3 and 3.2) and with JNDC V2, noble gases, mainly ^{135}Xe, for the former are less than those for the latter.

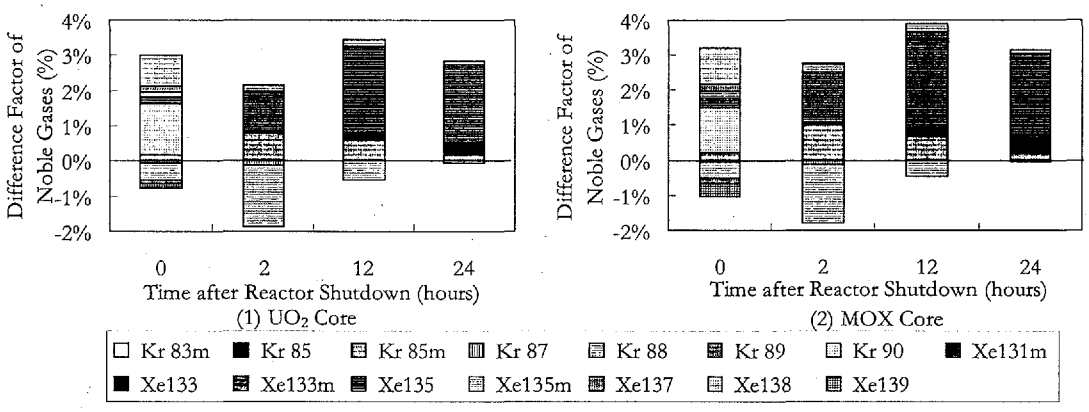

Fig. 1 Breakdown of difference factors between JENDL3.3 and built-in ORIGEN for noble gases.

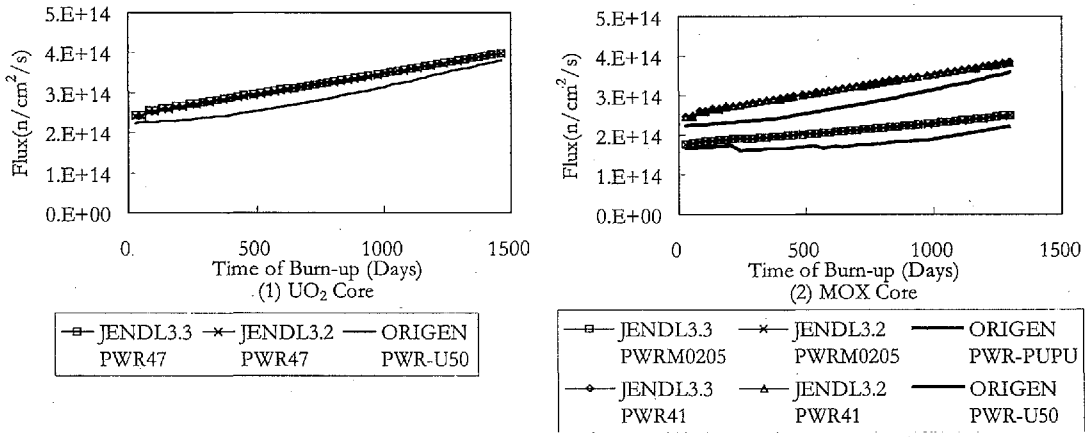

Fig. 2 Neutron flux with burnup obtained with different neutron cross section data.

(2) Decay data

The difference factors of 3 quantities with different decay data (JNDC 2000, JNDC V2 and built-in ORIGEN) are small in general, but those of noble gases for 2 hours with JNDC 2000 and built-in ORIGEN are slightly large as about 1%. The breakdown of noble gases in these cases are shown in Fig. 3. The quantities of ^{88}Kr at 2 hours and those of ^{135m}Xe at 2 and 12 hours calculated with built-in ORIGEN are less than those with JNDC 2000. Therefore, these nuclides would increase the difference factors of noble gases.

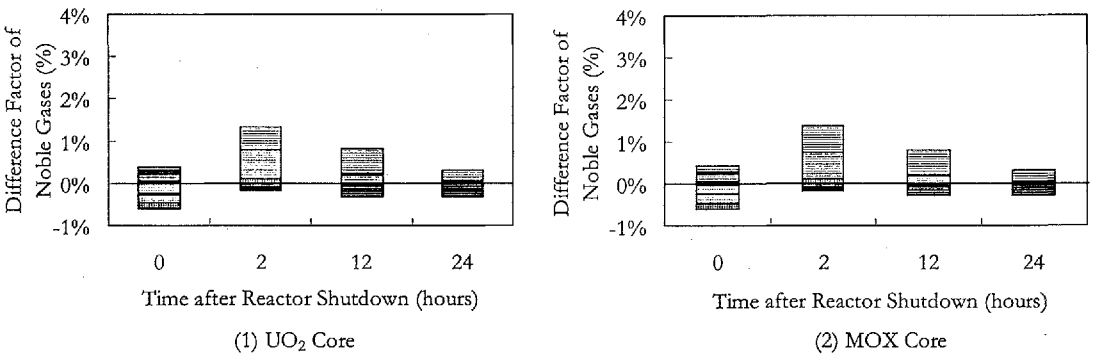

Fig. 3 Breakdown of difference factor between JNDC 2000 and built-in ORIGEN for noble gases. The patterns are as same as those in Fig. 1.

(3) Calculation code

All of the difference factors of 3 quantities between the two calculation codes, ORIGEN2.1 and ORIGEN2.2, show considerably large as from 1.2% to 3.6%. The difference factors for the MOX core are much larger than those for the UO_2 core. The breakdowns of noble gases and iodines are shown in Fig. 4 and Fig. 5, respectively. The quantities of ^{88}Kr, ^{133}Xe, ^{135}Xe, ^{131}I and ^{133}I calculated by ORIGEN2.1 are less than those by ORIGEN2.2. Therefore, these nuclides would increase the difference factors of 3 quantities between the two codes. The noticeably large difference factors for the MOX core are probably caused by defective algorithm calculating total fission rate of the minor actinoides in ORIGEN2.1, which is given in the release note of ORIGEN2.2[1].

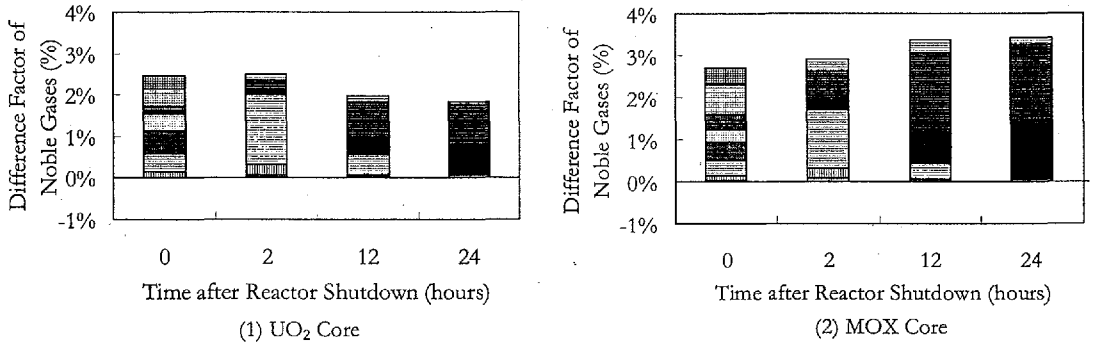

Fig. 4 Breakdown of difference factor between ORIGEN 2.2 and ORIGEN 2.1 for noble gases. The patterns are as same as those in Fig. 1.

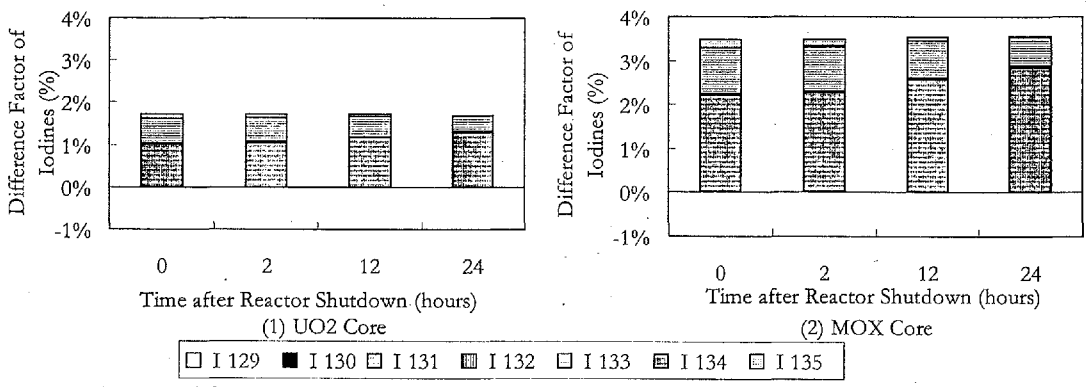

Fig. 5 Breakdown of difference factors between ORIGEN2.2 and ORIGEN2.1 for iodines.

(4) Combination of nuclear data and codes

All of the 3 quantities calculated by the previous version, namely ORIGEN2.1 with JENDL3.2 and JNDC V2, are smaller than those by the new ones, *i.e.* the basic case. This tendency for the MOX core is about

twice of the UO_2 core. The breakdowns of noble gases and iodines are shown in Fig. 6 and Fig. 7, respectively. The quantities of ^{88}Kr, ^{133}Xe and ^{135}Xe calculated by the previous version are about 2% for the UO_2 core and about 3% for the MOX core less than those by the new one. The quantities of ^{131}I and ^{133}I obtained by the previous version are also about 2% for the UO_2 core and about 3.5% for the MOX core less than those by the new one. Since the results of comparison of neutron cross section and decay data show less difference factors, the above differences are mainly due to the calculation codes, ORIGEN2.1 and ORIGEN2.2.

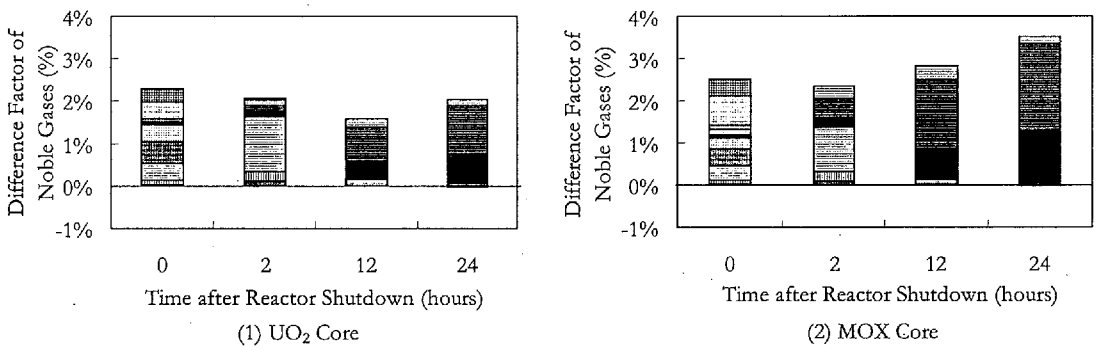

Fig. 6 Breakdown of difference factors between newest version and previous one for noble gases. The patterns are as same as those in Fig. 1.

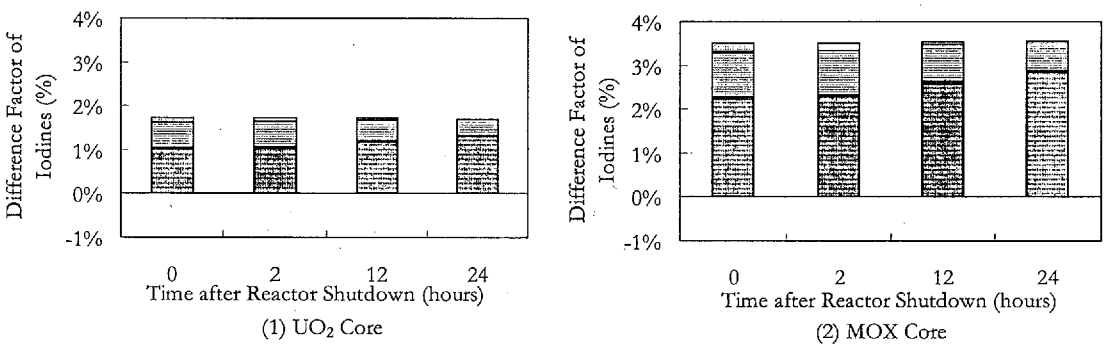

Fig. 7 Breakdown of difference factors between newest version (basic case) and previous one for iodines. The patterns are as same as those in Fig. 5.

All of the 3 quantities obtained by the conventional method are considerably smaller than those for the basic case. This tendency is even enhanced for the MOX core. The breakdown of noble gases is shown in Fig. 8. The maximum difference factors for the sum of the ^{133}Xe and ^{135}Xe by the conventional method are about 4% and 6% for the UO_2 core and the MOX core, respectively. The breakdown of iodines are depicted in Fig. 9. The difference factors for sum of ^{131}I and ^{133}I by the conventional method are about 2% and about 3.5% for the UO_2 core and the MOX core, respectively.

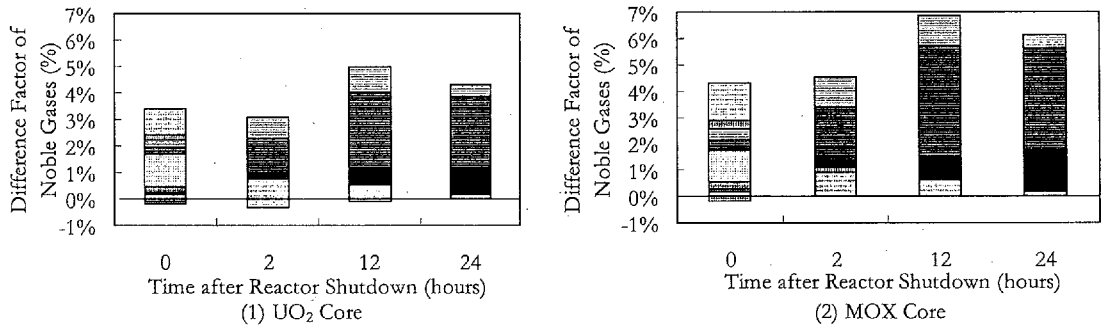

Fig. 8 Breakdown of difference factors between newest version (basic case) and conventional method for noble gases. The patterns are as same as those in Fig.1.

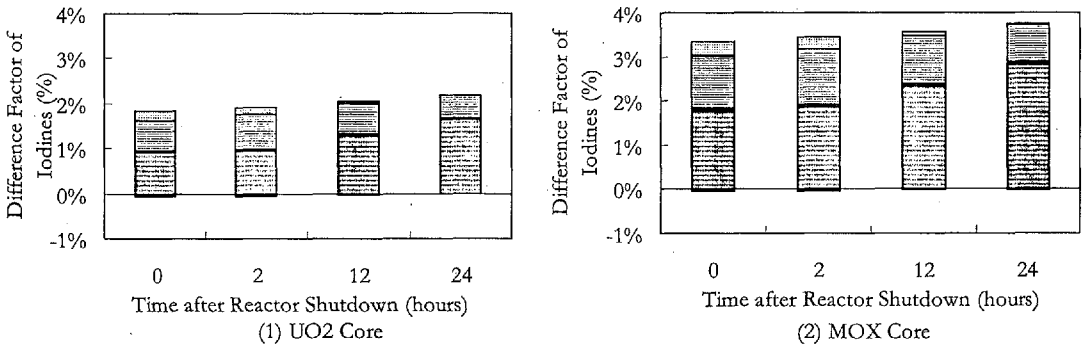

Fig. 9 Breakdown of difference factors between newest version (basic case) and conventional method for iodines. The patterns are as same as those in Fig. 5.

Since the difference factors for different decay data show little values, the difference factors between the conventional method and the basic case are mainly composed of the difference of the neutron cross sections and fission yields between the case 2 and the basic case and the difference of the calculation codes.

4. Conclusions

As a part of the works to construct a prediction system for emergency preparedness of nuclear power plants, the radioactivity inventories in PWR cores, one with UO_2 fuels and the other with 1/4 MOX and 3/4 UO_2 fuels, were calculated by ORIGEN2.2 with the newest nuclear data in Japan (the basic case), and the results were compared with those by the conventional method using ORIGEN2.1 with the built-in nuclear data, and with those for other 6 cases. As a whole, radioactivity inventories agree with each other within 7% of the difference factor. In details, the followings have been pointed out:

(1) Concerning the neutron cross sections, the difference factors by JENDL3.3 and JENDL3.2[8] are small, however those of noble gases at 12 and 24 hours after reactor shutdown between JENDL3.3 and built-in ORIGEN are close to 3% for the UO_2 core, and a little more for the MOX core. This is mainly due to higher buildup of ^{135}Xe which is caused by higher neutron fluxes by JENDL3.3 than those by built-in ORIGEN.

(2) Between 2 calculation codes, ORIGEN2.2 and ORIGEN2.1, there are considerably large difference factors. This tendency is much larger for the MOX core than that for UO_2 core. This difference is considered to be caused by defective algorithm calculating total fission rate of the minor actinoides in ORIGEN2.1.

(3) All of the 3 quantities, *i.e.* total amount, noble gases and iodines, obtained by the conventional method are considerably smaller than those for the basic case. This difference is furthermore enhanced for the MOX core. It is found that this difference is mainly caused by neutron cross sections, fission yields and calculation codes.

Since most of the newest nuclear data have been thoroughly evaluated with the newest experimental data and theoretical models, it is recommended to use them not only for the emergency preparedness of nuclear power plants, but also for their safety analysis in general.

As future subjects, we are planning to investigate the causes of the differences in more details, to make the comparison of the inventories of the major actinoides (U and Pu) and the minor actinoides (Np, Am and Cm), and to make the comparison of the decay heats all together.

References:

(1) A. G. Coff : *Users Manual for the ORIGEN2 Computer Code*, ORNL/TM-7175, (1980).

(2) S. B. Ludwig : *ORIGEN2 Version2.1 Release Notes*, CCC-371/ALLCP/02, (1991).

(3) S. B. Ludwig, A. G. Coff : *Revision to ORIGEN2 Version 2.2*, CCC-371/ORIGEN2.2, (2002).

(4) K. Shibata, T. Kawano, T. Nakagawa, et al.: "Japanese Evaluated Nuclear Data Library Version3 Revision-3 : JENDL3.3", *J. Nucl. Sci. Technol.* 39 [115], (2002).

(5) J. Katakura, T. Yoshida, K. Oyamatsu, et al. : *JENDL FP Decay Data File 2000*, JAERI-1343, (2001)

(6) K. Tasaka, J. Katakura, H. Ihara, et al. : *JNDC Nuclear Data Library of Fisson Products – Second Version*, JAERI-1320, (1990).

(7) Y. Yoshida, T. Irie, T. Kohriyama, et al. : "Design Study on Dose Evaluation Method for Employees at Severe Accident", *Journal of Nucl. Sci. and Technol. (in Japanese)*, 1 [2], pp.191-201, (2001).

(8) T. Nakagawa : "JENDL-3 Revision 2", *Proceedings of the 1993 Symposium on Nuclear Data*, November 18-19 1993, Tokai, Japan, JAERI-M 94-019, (1994).

2.9 Next Version of JENDL General Purpose File

Keiichi SHIBATA
Nuclear Data Center
Japan Atomic Energy Research Institute
Tokai-mura, Naka-gun, Ibaraki-ken 319-1195
e-mail: shibata@ndc.tokai.jaeri.go.jp

The latest version JENDL General Purpose File, JENDL-3.3, was released in 2002. JENDL-3.3 is regarded as one of the major libraries in the world for its quality and size. The next version has been discussed at an *ad hoc* committee in the Japanese Nuclear Data Committee.

1. Introduction

JENDL-3.3[1)] was released in May 2002. It is the latest version of JENDL-3 series which have been developed since 1980s. The Steering Committee in the Japanese Nuclear Data Committee (JNDC) set up an *ad hoc* committee, which is referred to as the Committee on Next JENDL, in order to discuss the next version of JENDL General Purpose File. The Committee on Next JENDL consisted of evaluators, experimentalists, and users. It was agreed in the Committee that we should develop JENDL-4 with a giant leap from JENDL-3.3 instead of performing minor modifications.

We discussed the demands for JENDL-4 by inviting many specialists for various applications. Considered were the technologies for light water and fast breeder reactors, the development of accelerator-driven systems (ADS), shielding, criticality safety, fusion neutronics, radiation damage, neutron therapy, the production of radioactive material for medical use, and astrophysics. As a result, the Committee recognized strong needs for JENDL-4.

This report deals with the purposes, rough specifications, key subjects and issues for JENDL-4.

2. Demands for JENDL-4

The demands for JENDL-4 were collected by interviewing with the specialists for various applications.

LWR and FBR technologies

- More accurate minor actinide and FP data are required.
- FP yield data should be re-examined.
- Evaluation of spontaneous fission neutron spectra is required.
- Gamma-ray production data are needed for all nuclei.
- More covariances are needed.

Development of ADS

- More accurate minor actinide data are required.
- FP yield data should be re-examined.

Criticality Safety

- More accurate minor actinide and FP data are required.
- Gamma-ray production data are needed.

Radiation Damage Study

- ^{59}Ni data should be evaluated, since its contribution is significant but there exist no data in JENDL-3.3.
- Charged-particle and PKA spectra, and KERMA factors are requisite for a radiation damage study.

High Energy Accelerator Shielding

- All the data are covered by the JENDL High Energy Files, which are being developed.

Fusion Neutronics

- The problems with JENDL-3.3 should be resolved by comparing with benchmark experiments at FNS and OKTAVIAN.
- Charged-particle spectra are required for light nuclei.
- Covariances are needed for further analyses.
- The data for IFMIF are required. These data will be produced as activities on JENDL High Energy Files.
- Light charged-particle (p, d, t, ^{3}He, ^{4}He) induced-reaction data are required. The demand might be covered by a special purpose file instead of JENDL-4.

Boron Neutron Capture Therapy

- Data are required for neutron sources such as Li(p,n) and Ta(p,n), for moderator materials such as Li, F, Al, for tissue-equivalent materials such as H, C, N, O, and for ^{10}B(n, α) reaction. These data will be prepared by JENDL High Energy Files, which are being developed.

Other Demands

In the beginning of FY2002, the demands for Next JENDL were collected by internet. The items, which are not overlapped with the ones mentioned above, are given as follows:

- Nuclear model codes should be developed in Japan to accumulate evaluation expertise.

- International cooperation should be promoted because of man power shortage in Japan.
- Inner-shell electron ionization data should be evaluated for medical use. Unfortunately, it is impossible to achieve this task by considering the present framework of JNDC.
- The information on JENDL should be extended to various fields other than nuclear energy applications.

3. Purposes of JENDL-4

The Committee agreed that JENDL-4 should be developed for researches on innovative reactors such as a reduced-moderation water reactor and an ADS, high burn-up and the use of MOX fuels for LWR, criticality safety with burn-up credit, medical use and astrophysics. JENDL-4 should be regarded as a system including reactor constants. Quality assurance of JENDL-4 is important so that it can be used as a standard nuclear data library in Japan.

4. Specifications of JENDL-4

4.1 Incident particles

Up to JENDL-3.3, the incident particles are limited to neutrons. JENDL-4 will include charged-particle and photon induced reaction data as well as spontaneous fission data in addition to neutron-induced reaction data.

4.2 Maximum incident energies

The range from 10^{-5} eV to 20 MeV is mandatory. However, the maximum energy can be extended to a larger value than 20 MeV depending on data needs.

4.3 Nuclides to be considered

We discussed how many nuclides should be included in JENDL-4. Some people stated that more than a thousand nuclides would be required for burn-up calculations. We reached a conclusion that there are no needs to increase the number of nuclides drastically. There is a possibility that the nuclides required for burn-up calculations might be prepared by the Working Group on Evaluation of Astrophysics Data in JNDC.

So far, the data contained in JENDL have been evaluated by ourselves. For example, JENDL-3.3 does not contain ^{197}Au data, since the data were not evaluated in JNDC. However, from the viewpoints of users, a library should contain all data required for applications. In JENDL-4, we may take the whole data on particular nuclides from other libraries, if the data are necessary.

4.4 Data format

We are going to adopt the ENDF-7 format[2)], which will be determined later. Requirements for format change should be given to CSEWG.

5. Key Subjects

5.1 Incident particles and maximum energy

JENDL-4 will include neutron, charged-particle, and photon induced reaction data as well as spontaneous fission spectral data. Limited is the number of nuclides for charged-particle-, photon-induced reaction data and spontaneous fission.

5.2 Problems with JENDL-3.3

It is necessary to solve problems with JENDL-3.3 by considering benchmark analyses and users' experiences.

5.3 Minor actinide and FP data

The importance of minor actinide data is increasing due to high burn-up, use of MOX fuels and ADS. Therefore, the accuracy of minor actinide data should be improved.

FP data should be also improved because of criticality safety with burn-up credit and of the development of innovative reactors.

5.4 Covariances

Covariance data are required to evaluate uncertainties in design calculations using nuclear data. JENDL-3.3 contains covariances for 20 nuclides. However, the quantity is not enough, and further evaluation is necessary.

5.5 FP yields and fission neutron spectra

FP yields should be re-examined. Neutron spectra emitted from neutron-induced and spontaneous fission should be evaluated.

5.6 Gamma-ray production data

Secondary gamma-ray production data should be added when re-evaluation is performed.

5.7 Charged-particle and recoil nucleus spectra

Evaluation of charged-particle and recoil nucleus (PKA) spectra is essential for a research on radiation damage.

5.8 Data consistency

We have to pay attention to consistency of data such as energy balance of spectra.

5.9 Data to be added

JENDL-4 should include ^{59}Ni and ^{197}Au data required by users.

6. Development of JENDL-4

6.1 General remark

The JAERI Nuclear Data Center should take the initiative to carry out evaluation, compilation and benchmarking and to produce reactor constants in cooperation with JNDC. Each working group in JNDC will work on an allocated task for JENDL-4. The Steering Committee in JNDC is responsible for providing each working group with good

circumstances so that it could achieve the mission efficiently.

6.2 Role of each group

JAERI Nuclear Data Center

- Coordination of the whole JENDL-4 project
- In charge of minor actinide data evaluations
- To develop tools for covariances and provide them for evaluators
- In charge of important nuclides such as structural materials and major actinides
- In charge of ^{59}Ni and ^{197}Au data

Evaluation and Calculation Support System WG

- To make a guideline of evaluations, which leads to a textbook
- To consider the use of standards in JENDL
- To develop evaluation tools and provide them for evaluators

FP Nuclide Evaluation WG

- To evaluate FP data
- Covariances for capture cross sections
- Gamma-ray production data

FP Yield Data Evaluation WG

- To evaluate FP yield data and fission neutron spectra
- Consideration of uncertainties in FP yield data

High Energy Nuclear Data Evaluation WG

- To decide on for which nuclide the maximum incident energy should be extended, and to provide the data
- To provide PKA data and proton- and photon-induced reaction data for JENDL-4

Reactor Integral Test, Shielding Integral Test and Evaluation of Nuclide Generation WGs

- Selection of benchmark problems
- To make criteria for data validation
- To carry out benchmark analyses and to feed the results back to evaluators
- To construct databases of input and output of benchmark calculations together with experimental data

Standard Group Constant WG

- To generate standard group constants based on JENDL-4 by considering needs

JENDL Compilation Group

- To compile evaluations and carry out checking
- To make review kits and set up a review system in JNDC. The critical review is necessary for quality assurance.

Steering Committee

- To make arrangements for JENDL-4 evaluations

- Strong link with AESJ Nuclear Data and Reactor Physics Divisions
- To cooperate with AESJ Standard Committee and to make JENDL-4 a standard nuclear data library in Japan

7. Some Issues

7.1 Resonance analysis

The resolved resonance parameters for most of important nuclides contained in JENDL-3.3 were taken from the analyses by the ORNL group using SAMMY code[3]. Such a situation is not preferable by considering the fact that the resonance parameters are most important nuclear data for energy applications. We should have Japanese specialists who can deal with resonance analyses in universities or in research organizations. As the first step, people are encouraged to attend a SAMMY workshop which holds periodically.

7.2 Nuclear model codes

We frequently use nuclear model codes made in foreign countries. However, it is recognized that our own nuclear model codes should be developed in order to improve the reliability of evaluations and to reflect the recent knowledge on nuclear physics.

7.3 Thermal scattering law data

Unfortunately, JENDL does not have thermal scattering law data. This matter should be discussed in JNDC.

7.4 Processing codes

The evaluated data are usually processed for nuclear energy applications. We have to keep a man power to develop and maintain the processing codes.

8. International Cooperation

It is forty years since JNDC was founded. The number of evaluators is steadily decreasing without replacements. To supplement the present situation, we should join international evaluation activities such as NEANSC/WPEC and IAEA/CRP. We should also keep a good relation with KAERI, CEA, and LANL in which nuclear data evaluations are actively performed. We may have some common data in JENDL, ENDF and JEFF. However, we have no intention to make a world-wide unified library at present.

9. Quality Assurance

It is necessary to raise the reliability of JENDL-4 better than that of JENDL-3.3. Thus, we need to make criteria for quality assurance. Extensive benchmark analyses should be performed for various applications before the release of JENDL-4. A database will be produced so that users could refer the input and output of benchmark calculations together with experimental data. For users' convenience, we should make reactor constants based on

JENDL-4 for typical applications such as transport and burn-up calculations. It is believed that these activities make JENDL-4 a standard nuclear data library in Japan.

10. Conclusions

The *ad hoc* Committee on Next JENDL discussed about JENDL-4 and made recommendations and proposals for JENDL-4. On the 22nd of December 2003, the Steering Committee in JNDC decided to start the JENDL-4 project proposed by the present report. We should go forward although there exist some difficulties such as man power shortage.

Acknowledgments

The author would like to thank the members of the *ad hoc* Committee on Next JENDL for preparing the present report. He also acknowledges all the members of JNDC for discussing the next version of JENDL.

References

1) K. Shibata, T. Kawano, T. Nakagawa, O. Iwamoto, J. Katakura, T. Fukahori, S. Chiba, A. Hasegawa, T. Murata, H. Matsunobu, T. Ohsawa, Y. Nakajima, T. Yoshida, A. Zukeran, M. Kawai, M. Baba, M. Ishikawa, T. Asami, T. Watanabe, Y. Watanabe, M. Igashira, N. Yamamura, H. Kitazawa, N. Yamano and H. Takano: "Japanese Evaluated Nuclear Data Library Version 3 Revision-3: JENDL-3.3", *J. Nucl. Sci. Technol.*, **39**, 1125 (2002).
2) Cross Section Evaluation Working Group: To be published, National Nuclear Data Center, Brookhaven National Laboratory.
3) N.M. Larson: "Updated Users' Guide for SAMMY: Multilevel R-Matrix Fits to Neutron Data Using Bayes' Equation," ORTL/TM-9179/R4 (1998).

JP0450482

JAERI−Conf 2004−005

2.10 Fission Modes and Mass Distribution in Heavy Actinide Region Studied with Multi-Dimensional Langevin Equation

Takatoshi ICHIKAWA
Advanced Science Research Center, Japan Atomic Energy Research Institute
Tokai-mura, Naka-gun, Ibaraki 319-1195, Japan
e-mail: takichi@popsvr.tokai.jaeri.go.jp

Tomomasa ASANO, Takahiro WADA, Masahisa OHTA
Department of Physics, Konan University
Okamoto 8-9-1, Kobe 658-8501, Japan

We evaluate the mass-energy distribution with the 3-dimensinal Langevin equation in the potential energy surface including the shell correction. From the analysis of our results, we expect the existence of several modes in the fission of ^{270}Sg. We show that the dynamical effect plays an important role with respect to the components of the asymmetric mode with low-TKE.

I. Introduction

In the fission of low excited actinides and transactinides, mass and total kinetic energy (TKE) distributions consisting of some components were observed. These experimental results exhibit the presence of different deformation paths, which is well reviewed in several articles [1,2]. The aim of this study is the reproduction of the mass and TKE distribution and the investigation of the dynamical fission paths obtained by the numerical calculation.

For example, the measurement of the mass-energy distribution of the fission fragments of ^{270}Sg was performed by Itkis *et al.* [3]. It was observed that in the low energy fission, the mass-asymmetric components with low-TKE appear, whereas this component vanishes in the case of the high excitation energy. It appears that in the low energy fission, the shell effect has a very important role.

The problem of fission modes has been studied theoretically as well [4,5]. The multi-dimensional energy surface was calculated with Strutinsky's shell correction method and the search for the saddle points and the valley paths leading to fission in the multi-dimensional energy surface was performed. These static methods reproduce the fission paths expected from the experimental result. However, this is insufficient for the evaluation of the mass and TKE distribution.

Therefore, we propose a dynamical approach by solving the multi-dimensional Langevin equation numerically on the energy surface including the shell correction. In the high excitation energy where the shell effect vanishes, the fission process has been studied on the basis of the fluctuation-dissipation dynamics and the Langevin equation has been succeed in describing this dynamics. By including the shell correction energy to the potential

energy surface, we apply this method to the fission of the low excitation energy.

In this paper, we show the mass distribution of fission fragments of ^{270}Sg at the excitation energy E*=28 MeV by solving the three-dimensional Langevin equation. The origin of the mass-asymmetric component with low-TKE is investigated in terms of the fission paths obtained by numerical calculation. The influence of the potential energy on the dynamics is also discussed.

II. Framework

The shape of nucleus is described by the two-center parameterization. Z_0 denotes the distance between the harmonic oscillators in the unit of the radius of the spherical compound nuclei $\left(R_0 = r_0 \left(A_1 + A_2\right)^{1/3}\right)$, δ denotes the deformation of the fragments with the constraint that both fragments have same deformation ($\delta_1 = \delta_2$) and α the mass asymmetry parameter ($\alpha = \left(A_1 - A_2\right) / \left(A_1 + A_2\right)$), where A_1 and A_2 are the mass number of the fragments. The liquid drop energy, the surface energy and the coulomb energy are also calculated with this parameterization.

We describe the fission process by the following equation, called as the Langevin equation,

$$\begin{aligned} \frac{dq_i}{dt} &= \left(m^{-1}\right)_{ij} p_j, \\ \frac{dp_i}{dt} &= -\frac{\partial V}{\partial q_i} - \frac{1}{2}\frac{\partial}{\partial q_i}\left(m^{-1}\right)_{jk} p_j p_k - \gamma_{ij}\left(m^{-1}\right)_{jk} p_k + g_{ij} R_j(t), \end{aligned} \tag{1}$$

where the suffix stands for Z_0, δ or α. Summation over repeated indices is implied. $V(q)$ is the potential energy taken account of shell effect, $m_{ij}(q)$ and $\gamma_{ij}(q)$ are the shape dependent collective inertia and dissipation tensors, respectively. We assume the random forces as the white noise type of which the normalized random force $R(t)$ is to satisfy $\langle R(t)\rangle$=0, $\langle R_i(t_1) R_j(t_2)\rangle = 2\delta_{ij}\delta(t_1 - t_2)$. The strength of random force g_{ij} is calculated from $\gamma_{ij} T = g_{ik} g_{kj}$ that is given by the fluctuation-dissipative theorem. T denotes the temperature of the compound nucleus that is defined as $E^* = aT^2$ with the excitation energy E^* of a compound nucleus and the level density parameter a of Töke and Swiatecki [6]. The inertia tensor is calculated using the hydrodynamical model with Werner-Wheeler approximation [7] for the velocity field, and wall-and-window one-body dissipation [8] is adopted for the dissipation tensor.

The shell correction energy of the two-center shell model is calculated with the code TWOCTR [9, 10]. The shell correction energy depends on the temperature of the nucleus. The temperature dependent factor of the shell correction energy is assumed as $\exp\left(-E^*/E_d\right)$, where E_d is the shell damping energy that is taken to be 20 MeV [11].

III. Numerical Results and Discussion

We study the fission of the compound nucleus of ^{270}Sg in the case of the excitation energy E*=28 MeV and the origin of the mass-asymmetric fission modes from the analysis of dynamical fission paths obtained by the numerical solution of the 3-dimensional

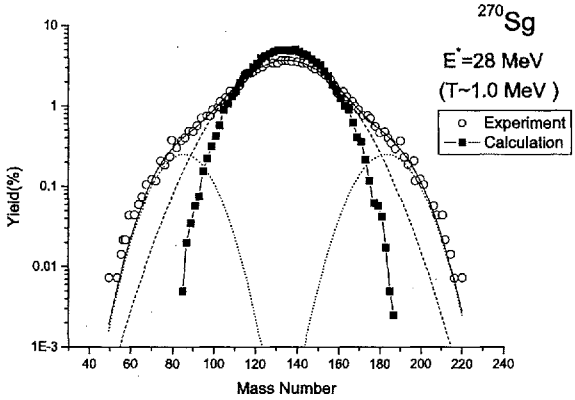

Figure 1: Mass distribution of the fission fragments of ^{270}Sg. The open circle and solid square denote the experimental and the numerical results, respectively.

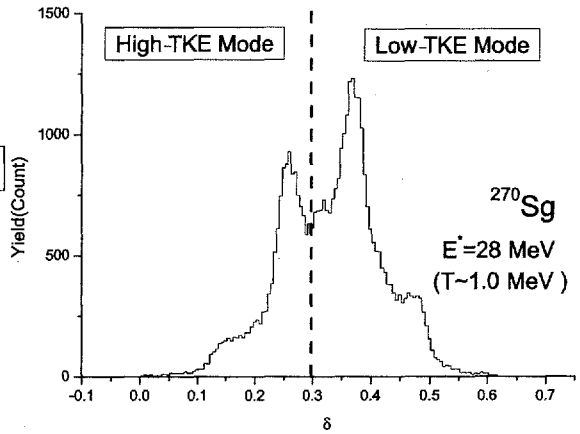

Figure 2: Deformation distribution of the fission fragments at scission configuration.

Langevin equation.

Figure 1 shows the mass distribution of the fission fragments as a function of the mass number of the fission fragments. The open circle and the solid square denote the experimental result and our numerical one, respectively. We obtain the mass distribution with the single peak, whereas it is seen that the experimental mass distribution consists of some Gaussian-components. In our result, the fission fragments with the large mass asymmetry are underestimated. In the experiment [3], the quasi-fission component was not separated in terms of the measurement of the angular distribution of fission fragments. We expect that this underestimation of our results comes from the mixture of the quasi-fission component in the experimental data.

In order to evaluate the quasi-fission component in the experimental data, we perform three-Gaussian fitting for the mass distribution of the experimental result. The mass-symmetric component is denoted by the dashed line and the mass-asymmetric components are denoted by the dotted lines in Figure 1. From the analysis of the TKE distribution, the mass-asymmetric component has the low TKE and differs from the characteristic of the fission mode in the region of the actinide nucleus. It is expected that this asymmetric component comes from the quasi-fission. In this paper, we focus on the distribution coming from the fission of the compound nucleus corresponding to the dashed line in Figure 1 and the investigation is restricted to fission modes with mass number around 80-190.

Figure 2 shows the deformation distribution of the fission fragment at the scission configuration. It seems that the mass distribution of our results consists of the single component, whereas two peaks is clearly seen at δ=0.25 and 0.36 in the deformation distribution. From the calculation in the liquid-drop energy surface without the shell

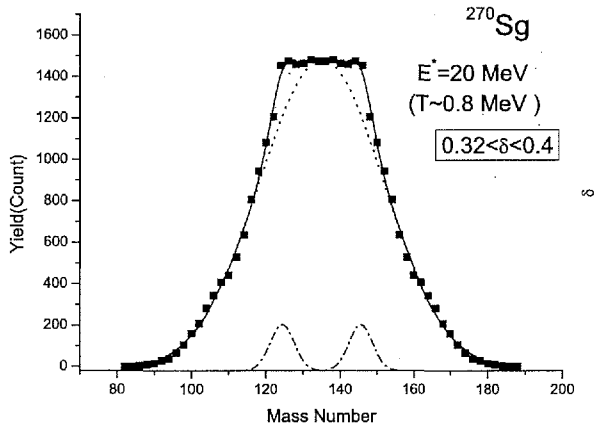

Figure 3: Mass distribution of the fission fragments with the deformation $0.32<\delta<0.4$.

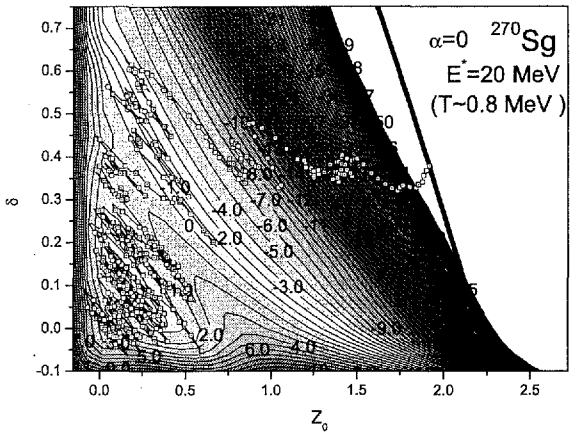

Figure 4: Landscape of the potential energy of ^{270}Sg projected to Z_0-δ plane at α=0.0 with the sample trajectory.

correction, it seems that the peak at δ=0.36 corresponds to the liquid-drop like mode. It is expected that the peak at δ=0.26 appears due to the shell effect. The mass distribution of the events with the deformation $\delta<0.3$ has a very sharp single peak and the average of the TKE value is high compared with the liquid-drop like fission. This is because of the contribution of the components with the peak at δ=0.26 affected by the shell effect.

On the other hand, the mass distribution of the events with $\delta>0.3$ is the liquid drop like one. However, the mass-asymmetric component appears in the liquid-drop like distribution. In order to see the shell effect clearly, we perform the calculation at the excitation energy E*=20 MeV. This corresponds to the increase of the shell correction energy by 50%. Figure 3 shows the mass distribution of the events with $0.32<\delta<0.4$ in the case of E*=20 MeV. We obtain the mass distribution having the flat top. In order to estimate the mixture of the components, we perform three-Gaussian fitting for this mass distribution. The solid line denotes the result of the fitting with three-Gaussian. The dotted line denotes the main Gaussian component used in the fitting. The peak of the dotted line is at 135, *i.e.* this is the mass symmetric division and is the liquid-drop like component. The peaks of the mass-asymmetric components denoted by the dash-dotted lines are at 144 and 125. We expect that this mass-asymmetric component corresponds to the standard II mode proposed by Itkis *et al.* [3]. In the following, we discuss this mass-asymmetric component that appears in the liquid-drop like distribution.

We consider the origin of this mass-asymmetric component. Although the dynamical motion is calculated in the three-dimensional parameter space, it is instructive to look at the potential surface projected onto two-dimensional spaces like Z_0-α and Z_0-δ. We show the time evolution of the deformation of the sample trajectory in this mode. Figure 4 shows the sample trajectory in the mass-asymmetric component with low-TKE and the potential energy landscape projected to the Z_0-δ plane at α=0. The solid line with the

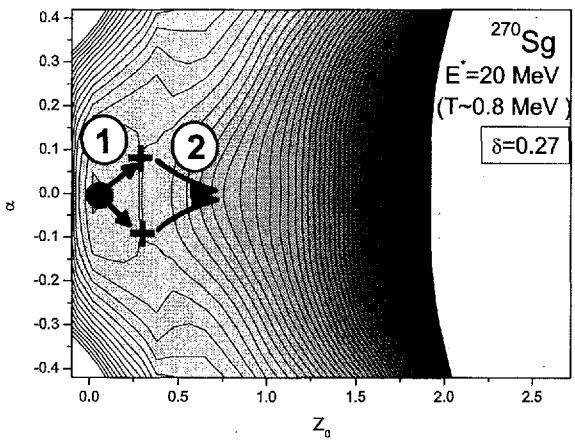

Figure 5: Landscape of the potential energy of ^{270}Sg projected to Z_0-α plane at δ=0.27.

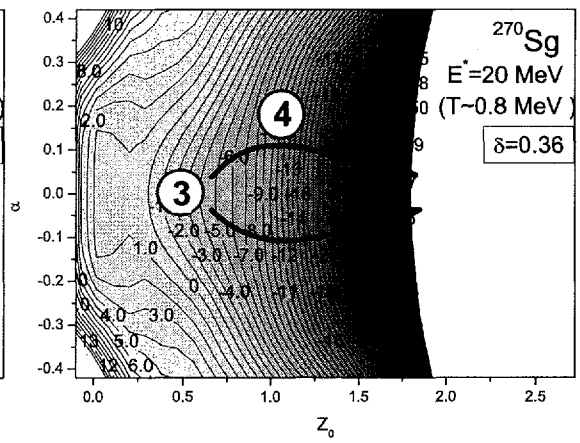

Figure 6: Landscape of the potential energy of ^{270}Sg projected to Z_0-α plane at δ=0.36.

squares denotes the sample trajectory of the mass-asymmetric exit channel at δ=0.36 that corresponds to the one of peaks of the distribution shown in Figure 2.

At first, the Brownian particle remains around the ground state. Receiving the random force from the heat bath, the Brownian particle goes through the first saddle point around at δ=0.27. The deformation δ increases with Z_0 until δ=0.65. After it passes through Z_0=0.5, δ decrease to 0.36. Finally, the Brownian particle goes to the scission line with random-walking.

Figure 5 shows the potential projected to the Z_0-α at δ=0.27 that corresponds to the saddle point deformation in the Z_0-δ plane of Figure 4. Figure 6 shows the potential projected to Z_0-α at δ=0.36 that corresponds to the maximum of the distribution in Figure 4. In the Z_0-α plane, the saddle point is around at Z_0=0.25 and α=$\pm$0.1. First, in Figure 5, when the fissile nucleus goes from the ground state to the saddle point according to the potential surface, the mass asymmetry α increases (the arrow 1). After passing through the saddle point (the cross), the fissile nucleus goes toward scission and Z_0 and δ increase. At the same time, α decreases following the potential slope as shown by the arrow 2 in Figure 5. As is seen from the sample trajectory in Figure 4, after passing through the saddle point, the deformation δ increases from 0.25 to 0.65 with large fluctuation while the increase of Z_0 is relatively small(around the number 3 in Fig. 6). With the increase of δ, the bump due to the shell effect becomes prominent at Z_0 =0.75 and α=0 in Figure 5. Since the Brownian particle keeps away from this bump, the mass asymmetry α increases again (the arrow 4) and the fissile nucleus goes to the asymmetric direction. This is how the asymmetry of fission fragments is determined.

It should be noted that the potential around Z_0=1.2$\sim$2.0 is very flat in α direction in the present system. In addition, the mass asymmetry α at the scission point differs from the one at the saddle point. Therefore, it is inappropriate to determine the mass

asymmetry α by the potential valley; the dynamics after the saddle point plays a very important role for the determination of the mass asymmetry at scission. The mass asymmetry distribution cannot be evaluated only from the position of the saddle point such as the discussion with the static calculation. Thus, we conclude that the dynamical calculation is very important for the understanding of the mass distribution and the fission paths.

Acknowledgements

The authors would like to express his gratitude to Dr. Yuichiro Nagame for his helpful suggestions. The authors wish to thank Prof. Hiromichi Nakahara (Tokyo Metropolitan University) for his valuable advises from the early stage of this study. We wish to thank Dr. Shuhei Yamaji (The Institute of Physical and Chemical Research) for his valuable advises and discussions.

References

[1] *"Fifty Years Research in Nuclear Fission"*, Nucl. Phys. **A502**, (1989).

[2] P. Armbruster, Rep. Prog. Phys. **62**, 465 (1999).

[3] M. G. Itkis *et al.*, Phys. Rev. C **59**, 3172 (1999).

[4] V. V. Pashkevich, Nucl. Phys. **A477**, 1 (1988).

[5] P. Möller, R. Nix, and W. J. Swiatecki, Nucl. Phys. **A469**, 1 (1987).

[6] J. Tōke and W. J. Światecki, Nucl. Phys. **A372**, 141 (1981).

[7] H. J. Krappe, J. R. Nix, and A. J. Sierk, Phys. Rev. C **20**, 992 (1979).

[8] J. R. Nix and A. J. Sierk, Phys. Rev. C **15**, 2072 (1977).

[9] S. Suekane, A. Iwamoto, S. Yamaji, and K. Harada, JAERI-memo. 5948 (1974).

[10] A. Iwamoto, S. Yamaji, S. Suekane, and K. Harada, Prog. Theor. Phys. **55**, 115 (1976).

[11] A. V. Ignatyuk, G. N. Smirenkin, and A. S. Tishin, Sov. J. Nucl. Phys. **21**, 255 (1975).

JP0450483

JAERI－Conf 2004－005

2.11 Measurement of Neutron-Production Double-Differential Cross Sections for Continuous Neutron-Incidence Reaction up to 100 MeV

Satoshi KUNIEDA[1*], Takehito WATANABE[1], Nobuhiro SHIGYO[1], Kenji ISHIBASHI[1], Daiki SATOH[2], Yosuke IWAMOTO[3], Takashi NAKAMURA[4] and Robert C. Haight[5],

[1]*Department of Applied Quantum Physics and Nuclear Engineering, Kyushu University*
[2]*Japan Atomic Energy Research Institute*
[3]*High Energy Accelerator Research Organization*
[4]*Cyclotron and Radioisotope Center, Tohoku University*
[5]*LANSCE-3, Los Alamos National Laboratory*

The inclusive measurements of neutron-incident neutron-production double-differential cross sections in intermediate energy range is now being carried out. Spallation neutrons are used as incident particles. As a part of this, the experiment was performed by using of NE213 liquid organic scintillators to detect outgoing-neutrons. Incident-neutron energy was determined by time-of-flight technique, and outgoing-neutron energy spectrum was derived by unfolding light-output spectrum of NE213 with response functions calculated by SCINFUL-R. Preliminary cross sections were obtained up to about 100 MeV, and were compared with calclations by the GNASH code. It will be hoped to get pure measurements by using of measured response functions for our detectors used in this study.

I. Introduction

Nuclear reaction data especially for neutrons and protons are required in the intermediate energy region for programs of accelerator driven transmutation system, radiotherapy, and space development. Because it is difficult to get many measurements in this energy region, model calculations have been playing the major role. For example, calculation codes such as the GNASH[1)] based on the exciton and Hauser-Feshbach statistical model, NMTC/JAM[2)] based on the intranuclear-cascade-evaporation model, and the JQMD[3)] based on the quantum-molecular-dynamics had developed to get cross sections. Several measurements of double-differential cross sections (DDX) for proton-incident neutron-production have been reported in the wide intermediate energy region,[4–11)] and have been used to get reliabilities of model calculation, and/or to improve the models themselves. On the other hand, neutron-incident DDX measurements are very scarce in the intermediate energy region (Only a few of measurements[12, 13)] had reported for neutron-production DDXs above about 20 MeV). It is difficult to get reliabilities on the model calculations for neutron-incidence.

The purpose of this study is to measure neutron-production DDXs for neutron-incidence in the wide intermediate energy range by using of spallation neutrons as incident particles. Liquid organic scintillators were used to detect outgoing-neutrons, and the fission chamber was used to know the number of incident-neutrons. Incident-neutron energy was determined by the time-of-flight (TOF) between the neutron source and neutron detectors. Outgoing-neutron energy spectrum was obtained by unfolding charge-integration spectrum with calculated response functions of the detector. Preliminary results were compared with the model calculations by the GNASH code.

II. Experiment

1. Neutron source and neutron beam line

The experiment was performed at the 4FP15L beam line of WNR facility[14)] in Los Alamos Neutron Science Center (LANSCE). The schematic view of the neutron source and the neutron beam line used in this study is shown in **Fig. 1**. Intense white neutrons covering up to about 750 MeV were provided from the Target-4 area where spallation reactions were triggered on the thick tungsten target by the part of the high-current (about 2 μA) 800 MeV proton beam from linear accelerator. This neutron beam line was 15° angled to the direction of the proton beam incidence, and was about 90 m long. To decrease the number of low-energy (up to several tens

* Corresponding author, Tel. +81-92-642-3765, Fax. +81-92-642-3769, E-mail: kuni@meteor.nucl.kyushu-u.ac.jp

MeV) neutrons from the Target-4 area, a polyethylene block of 101.6 mm thick was placed upstream on the beam line. Neutron flux was introduced into the the detector room through iron collimators of 35.7 mm in diametor that defined the beam size.

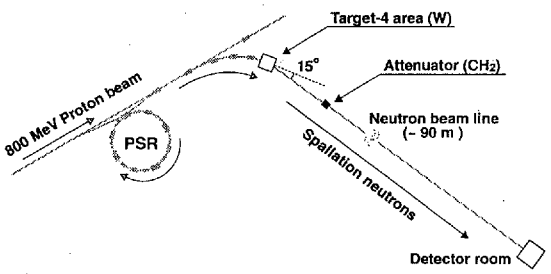

Fig. 1 Schematic view of the neutron source and the 4FP15L neutron beam line at WNR facility in LANSCE.

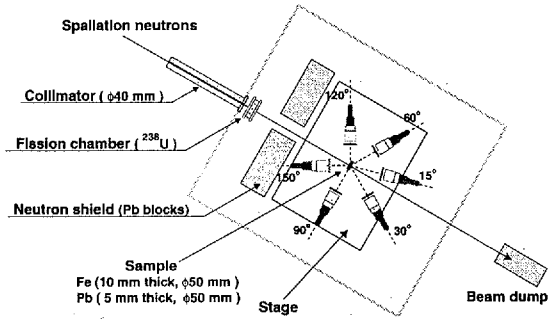

Fig. 2 Schematic view of the experimental setup.

2. Experimental setup

The layout of the experimental arrangement is shown in **Fig. 2**. Cylindrical NE213 liquid organic scintillators were arranged at 15°, 30°, 60°, 90°, 120°, and 150° to detect outgoing-neutrons. The size of all these detectors were 127 mm thick and 127 mm in diameter, and were optically connected with photomultipliers. The average distance between the sample and detectors was about 0.7 m. NE102A plastic scintillators of 10 mm thick were also set in front of all NE213 detectors to reject charged-particle events. To obtain the number of incident netrons, the fission ionization detector[15] was set right behind the collimator. Iron (10 mm and 40 mm thick) and lead (5 mm thick) were selected as samples. All of these samples were of natural compositions.

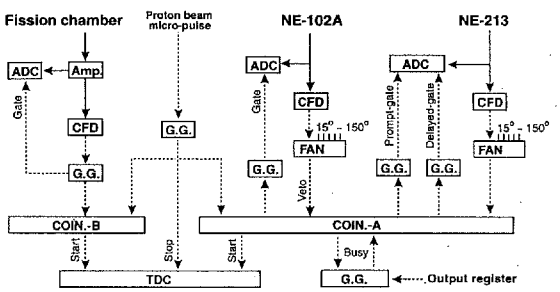

Fig. 3 Schematic draw of the electical circuit for online data aquisitions.

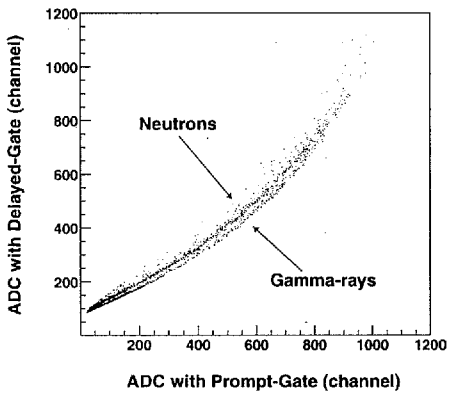

Fig. 4 Example scatter plot for charge-integrations with the prompt-gate and the delayed-gate for NE-213.

The schematic block diagram of electrical circuit for online data acquisitions is shown in **Fig. 3**. Analog signals from all detectors were branched into two. One of these was converted into logic signal by the constant-fractional-discriminator (CFD) for each detector, and was sent to the coincidence module (COIN.). Proton beam micro-pulses were delayed about 2.8 μ sec., and their width was adjusted by the gate-generator (G.G.) to be able to accept conincidences with logic signals of detectors within the micro-pulse spacing. The proton beam micro-pulse spacing was about 1.8 μ seconds. The lower energy limit of the neutron energy that could be accepted at COIN.-A and COIN.-B was about 10 MeV. To eliminate most of charged particle events, logic signals from the NE102A were used as veto signals at COIN.-A. Coincidence signals were issued from either COIN.-A or COIN.-B, and were sent to the time-to-digital converter (TDC) as the start signal for TOF measurement. On the one hand, micro-pulses of proton beam (delayed about 2 μ seconds; this time interval corresponded to the maximum

range of TDC module used in this experiment) were used as the stop signal. Charge-integrations of analog signals were also recorded by using of charge-sensitive analog-to-digital converters (ADCs) for all neutron detectors after coincidences were caused. For signals from photomultipliers of NE213s, two kind of charge-integrations were recorded to discriminate neutrons and gamma-ray events using the two gate integration method.[16] As shown in **Fig. 4**, neutron and gamma-ray events are separated successfully.

3. Calibration

Charge-integration spectra were calibrated for all neutron detectos to get corresponding electron-equivalent light-output. The γ-ray compton-edges of ^{60}Co and Pu-Be sources were used with the semi-empirical formula of Dietze et al.[17] for low-energy parts. For the calibrations of higher-energy neutrons, spallation neutrons (collimators of 1 mm in diametor was used to identify the one neutron event) were induced directly into all NE213s as shown in **Fig. 5**. Neutron energies were identified by TOF, and were possible to be converted into light-unit by the empirical equation by Cecil et al.[18] Maximum channels of ADC spectra were used as corresponding charge-integration values. The relationship between charge-integrations and electron-equivalent light-output for NE213 is shown in **Fig. 6**. This example is for the detector used at 15°.

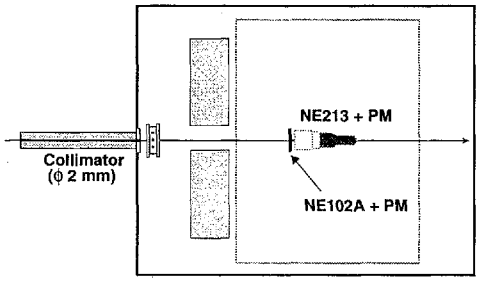

Fig. 5 Setup for the calibration of NE213 by using of spallation neutrons.

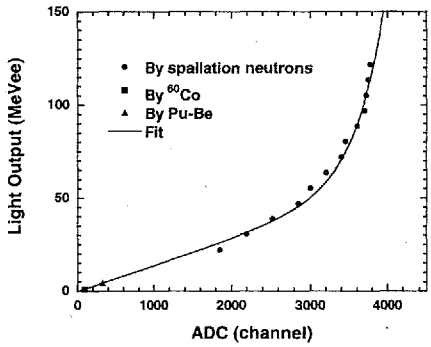

Fig. 6 Relationship between charge-integrations and electron-equivalent light-output for NE213.

III. Analysis

1. Determination of incident neutron energy

Because raw data obtained in the online measurement were of whole events for overall incident energy range that were allowed in this data acquisition system, the incident-neutron energy was required to be identified for all outgoing-neutron evrents to get DDX. In this study, incident neutron energies were determined by the TOF technique, on the assumption that the total TOF between the Target-4 and the neutron detector was exhausted only by the incident-neutron. Because the flight path between the Target-4 and the sample (Time-B) was quite long enough to ignore the distance between the sample and all neutron detectors (Time-A), this assumption was acceptable. Time-A and Time-B were estimated, and are compared in **Fig. 7**. For example of 100 MeV neutron incidence, the ratio of time-A on time-B was not more than 3.5 % above about outgoing neutron energy of 5 MeV that correspond the lower energy limit of the n-γ discrimination.

A typical TOF spectrum are shown in **Fig. 8**. The sharp peak seen in this graph is flash gamma-ray events from the Target-4, and were used as the time fiducial to get TOFs of incident-neutron events. Outgoing neutron events that were triggerd by incident-neutrons of the energy range above about 10 MeV were obtained in this measurement.

2. Getting the number of incident neutrons

To normalize the outgoing-neutron spectrum, the number of incident neutrons must be known, and was possible to be gotten by the equation

$$N(E) = \frac{n_f(E)}{\sigma_f(E) \times \epsilon_{det} \times \rho_f} \tag{1}$$

where, $N(E)$, $n_f(E)$, and $\sigma_f(E)$ are the desired number of incident neutrons, the number of fission events detected by fission chamber, and the fission cross sections of ^{238}U for corresponding neutron energy E respectively. ϵ_{det}

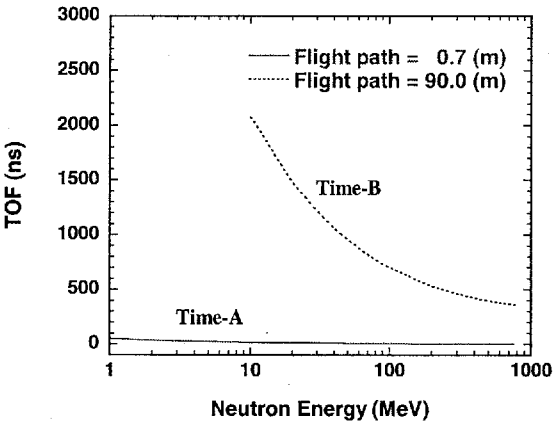

Fig. 7 Estimations of Time-A and Time-B.

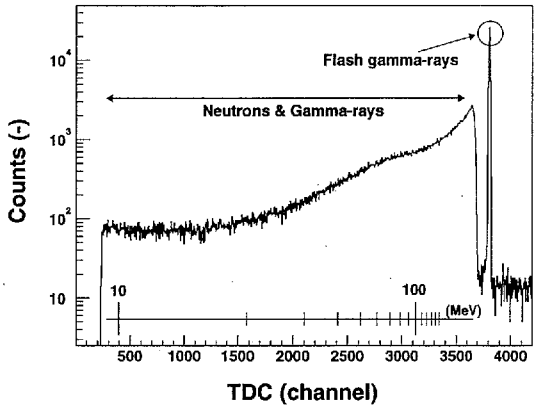

Fig. 8 Typical TOF spectrum between the Target-4 and NE213.

is the detection efficiency of the fission chamber, and ρ_f is the arial density of the number of atoms of fissionable material deposited on the foil in the chamber (see ref[15]). $n_f(E)$ was also determined by TOF. Measured fission cross sections[19,20] were used as $\sigma_f(E)$.

3. Outgoing neutron energy spectra

Electron-equivalent light-unit spectrum was obtained from the charge-integration spectrum of NE213 based on calibration analysis. The example light-output spectra that were normalized by the number of incident-neutrons and were subtracted background (sample-out) spectra are shown in **Fig. 9** at 90 - 110 MeV neutron-incidence for the iron target.

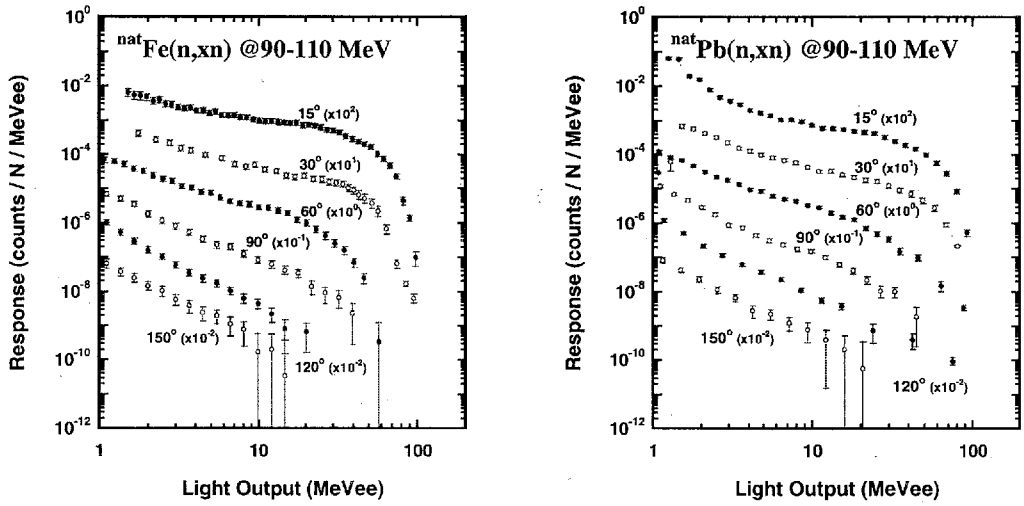

Fig. 9 Example light-output spectra of NE213 at 90 - 110 MeV neutron-incidence for the iron sample.

Outgoing-neutron energy spectra were determined by unfolding measured light-output spectra with response functions of NE213. The FERDO[21] unfolding code was used to get optimal neutron energy spectrum. The SCINFUL-R[22] calculations, that were adjusted to reproduce measurements[23] by light attenuation and reduction factors, were used as response matrix elements for all neutron detectors. Examples of response functions are shown in **Fig. 10**.

Gaussian shape window functions that determined energy resolutions of outgoing-neutron energy spectrum were assumed to be 10 $\sim$ 80 %, and the lowest light-output thresold levels were fixed around 2 MeVee in the unfolding process. Because neutron detectors were not large enough to differentiate neutron energy above 120

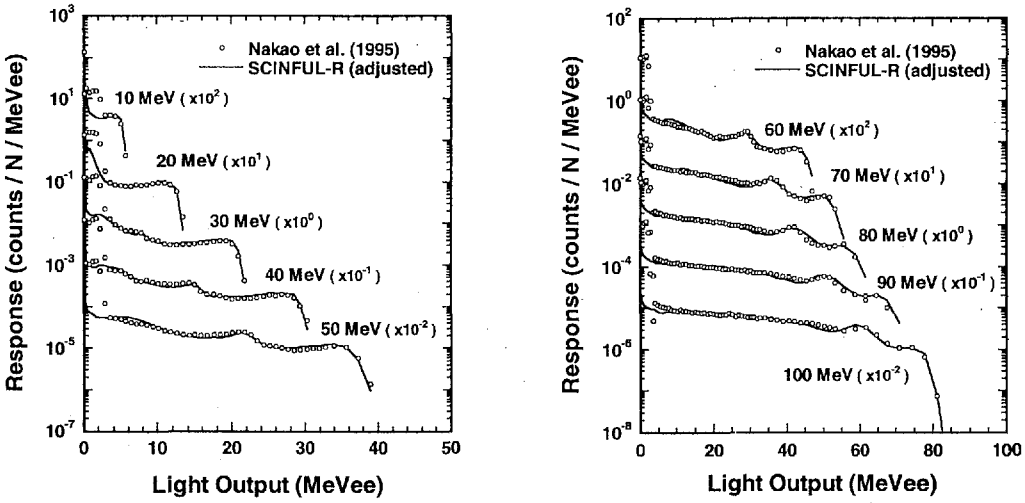

Fig. 10 Example neutron response functions of NE213 for 10 - 100 MeV used in this unfolding process.

MeV in respect to charge-integration of NE213, data analysis was performed up to around this energy. Obtained double-differential cross sections were shown in **Fig. 11** at 90 - 110 MeV neutron-incidence for the iron sample and the lead sample with calculations by the GNASH code. DDX can be calculated basing on the Kalbach and Mann's systematics[24] with the exciton pre-equilibrium model and the Hauser-Feshbach statistical evaporation model in this code.

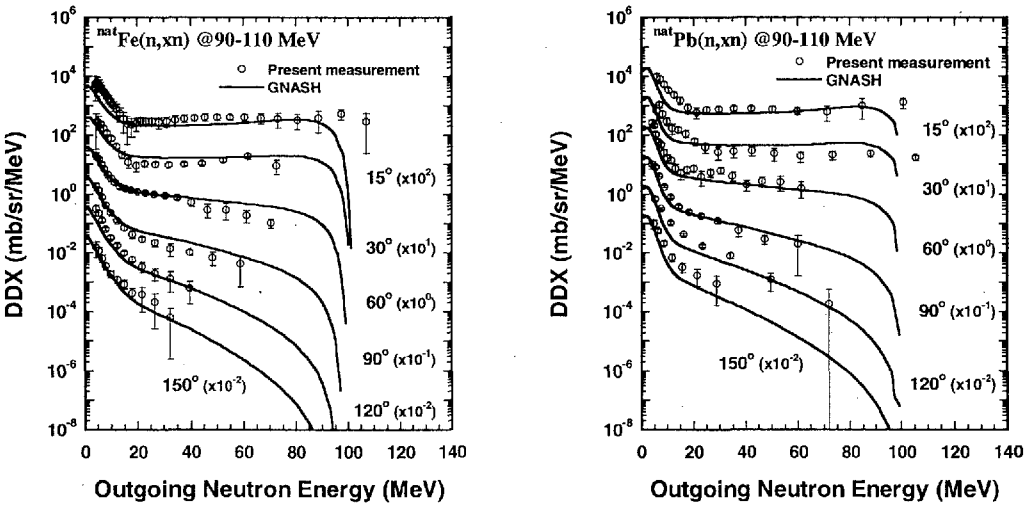

Fig. 11 Preliminaly DDX for iron and lead sample with calculations at 90 - 110 MeV.

It must be known that these approach and results are preliminary, because calculational response functions were used in this analysis. Neutron detectors usually have thier own chracters due to the depletion of the NE213 and the transmission efficiency of the light signal to the photomultiplier, and a slight difference of response functions are tend to affect the final neutron energy spectrum. Response functions for neutron detectors used in this measurement should be used in the unfolding process radically.

IV. Summary

Double-differential cross sections were measured for (n,xn) by using of spallation neutrons as incident-particles. Incident-neutron energy was determined by TOF between the neutron source and neutron detectors. Preliminary DDXs were obtained up to about 100 MeV by unfolding charge-integration spectrum of NE213 with calculational response functions, and were compared with calculations by the GNASH code.

Recently, response functions have been measured for all NE213s used in the present measurement by using of spallation neutrons, and the analysis is now being proceeded. It will be hoped to get pure measurements by using of measured response functions in the unfolding process.

References

1) P. G. Young, E. D. Arthur, and M. B. Chadwick, LA-6947 (1977) ; LAUR-88-382 (1988).
2) K. Niita, H. Takada, S. Meigo, and Y. Ikeda, *J. Nucl. Instrum. Methods Phys. Res.*, **B184**, 406 (2001).
3) K. Niita, S. Chiba, T. Maruyama, H. Takada, T. Fukahori, Y. Nakahara, A. Iwamoto, *J. Phys. Rev.* **C52**, 2620 (1995).
4) B. E. Bonner, J. E. Simmons, C. R. Newsom, P. J. Riley, G. Glass, J. C. Hiebert, Mahavir Jain*, and L. C. Northcliffe, *J. Phys. Rev.* **C18**, 1418 (1978).
5) S. Cierjacks, Y. Hino, F. Raupp, L. Buth, D. Filges, P. Cloth, and T. W. Armstrong, *J. Phys. Rev.* **C36**, 1976 (1987).
6) M. M. Meier, D. A. Clark, C. A. Goulding, J. B. MaClelland, C. E. Moss, and W. B. Amian, *J. Nucl. Sci. Eng.*, **102**, 310 (1989).
7) W. Scobel, M. Trabandt, M. Blann, B. A. Pohl, B. A. Remington, R. C. Byrd, C. C. Foster, R. Bonetti, C. Chiesa, S. M. Grimes, *J. Phys. Rev.* **C41**, 2010 (1990).
8) S. Stamer, W. Scobel, W. B. Amian, R. C. Byrd, R. C. Haight, J. L. Ullmann, R. W. Bauer, M. Blann, B. A. Pohl, J. Bisplinghoff, R. Bonetti, *J. Phys. Rev.* **C47**, 1647 (1993).
9) W. B. Amian, R. C. Byrd, D. A. Clark, C. A. Goulding, M. M. Meier, G. L. Morgan, and C. E. Moss, *J. Nucl. Sci. Eng.*, **115**, 1 (1993).
10) T. Nakamoto, K. Ishibashi, N. Matsufuji, N. Shigyo, K. Maehata, S. Meigo, H. Takada, S. Chiba, M. Numajiri, T. Nakamura, Y. Watanabe, *J. Nucl. Sci. Technol.*, **32**, 827 (1995).
11) S. Leray, F. Borne, S. Crespin, J. Frehaut, X. Ledoux, E. Martinez, Y. Patin, E. Petibon, P. Pras, A. Boudard, R. Legrain, Y. Terrien, F. Brochard, D. Drake, J. C. Duchazeaubeneix, J. M. Durand, S. I. Meigo, G. Milleret, D. M. Whittal, W. Wlazlo, D. Durand, C. Le Brun, F. R. Lecolley, J. F. Lecolley, F. Lefebvres, M. Louvel, C. Varignon, F. Hanappe, S. Menard, L. Stuttge, J. Thun, *J. Phys. Rev.* **C65**, 044621 (2002).
12) A. Marcinkowski, R. W. Finlay, G. Randers-Pehrson, C. E. Brient, R. Kurup, S. Mellema, A. Meigooni, R. Tailor, *J. Nucl. Phys.*, **A402**, 220 (1983).
13) E. L. Hjort, F. P. Brady, J. R. Drummond, B. McEachern, J. H. Osborne, J. L. Romero, D. S. Sorenson, and H. H. K. Tang, *J. Phy. Rev.*, **C53**, 237 (1996).
14) P. W. Lisowski, C. D. Bowman, G. J. Russell, and S. A. Wender, *J. Nucl. Sci. Eng.*, **106**, 208 (1990).
15) S. A. Wender, S. Balestrini, A. Brown, R. C. Haight, C. M. Laymon, T. M. Lee, P. W. Lisowski, W. MacCorkle, R. O. Nelson, W. Parker, and N. W. Hill, *J. Nucl. Instrum. Methods Phys. Res.*, **A336**, 226 (1993).
16) M. Moszynsky, et al., *J. Nucl. Instrum. Methods.*, **A343**, 563 (1994).
17) G. Dietze, H. Klein, *J. Nucl. Instrum. Methods.*, **193**, 549 (1982).
18) R. A. Cecil, B. D. Anderson, and R. Madey, *J. Nucl. Instrum. Methods.*, **161**, 439 (1979).
19) P. Staples, P. W. Lisowski, and N. W. Hill, Presented in APS/AAPT Conference, Washington, April 18-12, 1995; *Bull. Am. Phys. Soc.*, **40**, 962 (1995).
20) V. I. Goldanskiy, V. S. Penkina, and E. Z. Tarumov, *ZETP (Sov. J. of Experimental and Theoretical Physics)*, **29**, 778 (1955).
21) B. W. Rust, D. T. Ingersoll, and W. R. Burrus, "A user's manual for the FERDO and FERD unfolding codes", Oak Ridge National Laboratory ORNL/TM-8720, (1983).
22) S. Meigo, *J. Nucl. Instrum. Methods Phys. Res.*, **A401**, 365 (1997).
23) N. Nakao, T. Nakamura, M. Baba, Y. Uwamino, N. Nakanishi, H. Nakashima, S. Tanaka, *J. Nucl. Instrum. Methods Phys. Res.*, **A362**, 454 (1995).
24) C. Kalbach, *J. Phys. Rev.* **C37**, 2350 (1988).

JP0450484

2.12 Nuclear Astrophysics Probed by kev Neutrons

Y. NAGAI
Research Center for Nuclear Physics, Osaka Univ. Ibaraki, Osaka 567-0047, Japan
E-mail:nagai@rcnp.osaka-u.ac.jp

Abstract:

Various elements observed in Galaxies can be used as relics to trace the history of the Galaxy after the Big Bang. Light elements up to 7Li were produced during the primordial nucleosynthesis in the early universe and the rest of the observed elements were synthesized in stars through various nuclear reaction processes. By studying the physics conditions of these processes when these light and heavier elements were synthesized, one could construct models about the evolution of stars and stellar nucleosynthesis to be used to trace the history. In this paper we discuss keV neutron induced reactions of a nucleus to construct the models.

1. Introduction

The history of the universe after the Big Bang has been an interesting subject to be studied. It can be traced by referring various elements observed in the universe and in Galaxy as relics. In order to trace the history, therefore, it is necessary to construct models of the evolution of these elements. It is well known that light elements up to 7Li would have been synthesized during the primordial nucleosynthesis [1] and elements heavier than Fe were produced by slow- and rapid-neutron capture processes in stars [2]. In these processes keV neutron induced reaction of a nucleus plays crucial roles, since the reaction cross-section determines the production yield of these elements, which is necessary to construct the models.

Concerning the light elements a standard Big Bang model predicts the nucleosynthesis up to 7Li in the early universe, and the observed abundance of the light elements are claimed to be in good agreement with the calculated value by standard Big Bang models [3]. A decade ago, however, inhomogeneous Big Bang models have been proposed as alternative models of the standard big bang models [4]. According to the models, an intermediate mass nucleus up to A≈30 could have been produced in neutron rich regions mainly via neutron capture reactions [5]. The prediction differs from that of the standard models, and therefore a possible discrimination between these two models would provide us crucial information about the physics conditions in the early universe. In order to estimate the production yield of the intermediate mass nuclei in the framework of the inhomogeneous models it is certainly important to measure the neutron capture cross section of the light nuclei at astrophysical relevant energy. A possible comparison of the estimated yield with observation can discriminate a certain inhomogeneous model from others.

Concerning the elements heavier than Fe we have reasonable models of the nucleosynthesis in evolved stars such as the sun [6]. However, we do not have proper models for the nucleosynthesis of heavy elements

in less-evolved metal-deficient stars [7]. Currently a lot of efforts are being made to observe the heavy elements abundance in these less-evolved stars to construct the models of stellar evolution and nucleosynthesis [8]. The observed abundance is considered to carry important information on the nucleosynthetic processes in the earlier Galactic stellar generations. Concerning the s-process nucleosynthesis in these metal-deficient stars, light nuclei abundant in the stars would act as a strong neutron poison to influence the production yield of the heavy elements [7]. How these light elements strongly act as a neutron poison depends on the cross section of the neutron capture reaction of these elements. Concerning the r-process nucleosynthesis the astrophysical site remains as an open question. It has been claimed as one of the possible site to be in nascent neutron star winds [9], in which light nuclei would also act as a possible neutron poison.

Both in the primordial- and stellar-nucleosyntheses a neutron induced reaction of light nuclei plays an important role for the construction of the models of the stellar evolution and nucleosynthesis in the Galaxy. While, the study of the neutron induced reaction of light nuclei is also quite important for nuclear physics. Since the main part of the gamma-ray transition amplitude after the keV neutron capture reaction of few-body system is usually either forbidden or hindered, one can learn the roles of non-nucleonic degrees of freedom in the reaction, which has been an important subject for many years [10]. In addition, since the level density of light nuclei is low, one can observe a discrete γ-ray emitted promptly from a neutron capturing state feeding to a low-lying state of a final nucleus [11]. The γ-ray carries unique information of electromagnetic property, and therefore one can learn the mechanism of the keV neutron capture reaction. The information is quite important to estimate the neutron capture reaction cross section of an unstable nucleus at stellar energy for calculating the production yield for primordial intermediate mass nuclei and r-process nuclei.

2. Experimental method

keV neutron capture reaction cross section of a nucleus has been measured by either an activation or a prompt γ-ray detection method. In the latter method a prompt discrete γ-ray emitted from a neutron capturing state feeding to a low-lying state of a final nucleus is measured. Since a discrete γ-ray characterizes a final nucleus, one can identify a true signal from the neutron capture reaction of a target nucleus free from background and determine a small capture cross section of a light nucleus unambiguously. The discrete γ-ray carries a unique electromagnetic property such as E1, M1 and E2 etc. Therefore its observation gives us unique information of initial and final states of a final nucleus, which connects the γ-ray. Through the information one can learn the neutron capture reaction mechanism and nuclear structure of the final nucleus. It could happen that such nuclear physics information is quite unique and can be hardly obtained by other experimental approaches. Our experimental method to use the prompt γ-ray detection method is described briefly [12]. Pulsed keV neutrons are produced by the $^{7}Li(p,n)^{7}Be$ reaction using pulsed protons provided from the 3MV Pelletron Accelerator of the Research Laboratory for Nuclear Reactors at the Tokyo Institute of Technology. Discrete prompt γ-rays from a capturing sample are

detected by an anti-Compton NaI(Tl) γ-ray spectrometer [13]. The spectrometer is placed at 125.3° with respect to the proton beam direction to obtain an angle-integrated γ-ray intensity for the dipole transition. A gold sample has been used for normalization of the cross section, since the capture cross section of gold is well known.

Since the (n,p) and/or (n,α) reaction of a light nucleus also plays important roles in stellar nucleosynthesis, we have developed a gas scintillation drift chamber (GSDC) to detect low energy charged particles with a large solid angle of 4 π and high efficiency of 100 % [14]. Here, it should be noted that both the reaction cross section and energy of emitted charged particles induced by low energy neutrons are low. The high sensitivity of the GSDC for detecting low-energy charged particles emitted from the keV neutron-induced reaction of a nucleus has been shown for the measurement of the $^{14}N(n,p)^{14}C$ reaction cross section [15].

3. Results and discussions

The cross-section of the neutron-capture reaction of various light nuclei has been successfully measured by detecting their discrete γ-rays at several neutron energies between 10 and 550 keV with an uncertainty of 5~10 %. What we have learned through the studies are as follows. First, we have for the first time observed a non-resonant direct p-wave capture reaction process at astrophysical relevant energy of a few 10 keV [11]. Because of the new process in the reaction the cross section we obtained is significantly larger than the value estimated assuming a 1/v law and using the thermal neutron capture cross section. The present result has a big astrophysical impact. It indicates clearly that light nuclei act as a strong neutron poison in the nucleosynthesis of heavy elements especially in less evolved metal deficient stars [16] and in addition in estimating the production yield of various nuclei in many astrophysical sites one must take into account the new process so far ignored. Second, we could clearly clarify the important role of the meson exchange currents in the keV neutron capture reaction of few-body system [17]. Third, the physics reason why the non-resonant direct p-wave capture reaction process becomes important even in the keV energy region is clarified as the unique nature of the neutron capturing nucleus with a $1^+/2$ ($s_{1/2}$) state and with relatively low neutron binding energy [18]. Hence the keV incident neutrons can be captured directly by a target nucleus transferring an orbital angular momentum of 1 to the final nucleus.

4. Future Prospect

Elemental abundance observed in less-evolved ultra metal deficient stars provides us crucial information to construct the models to trace the history of the Galaxy. Among various elements, heavier elements than iron carry important information of the generation of stars, in which the elements were synthesized by the slow- and rapid-neutron capture process of a nucleus. Since many important and interesting problems of the neutron induced reaction of a nucleus remain to construct the solid models of stellar evolution and nucleosynthesis, it would be extremely important to extend such studies using intense spallation neutrons provided such as by J-PARC. Here, one can use rare-abundant samples and even long-lived radioisotopes.

References

[1] G.Gamow: Phys.Rev. 70, 527 (1946), P.J.E.Peebles: Astrophys. J., 146, 542 (1966), R.V.Wagoner, W.A.Fowler and F.Hoyle: Astrophys. J., 148, 3 (1967)

[2] E.Burbidge, G.Burbidge, W.A.Fowler and F.Hoyle: Rev. Mod. Phys. 29, 547 (1957), R.Gallino et al.: Astrophys. J. 334, L45 (1988)

[3] A.M.Boesgaard and G.Steigman: Annu.Rev.Astron. Astrophys. 23, 319 (1985)

[4] J. H. Applegate, C. J. Hogan and R. J. Scherrer: Phys. Rev. D35, 1151 (1987)

[5] R. A. Malaney and W.A.Fowler: Astrophys. J., 333, 14 (1988)

[6] D. D. Clayton: Principles of Stellar Evolution and Nucleosynthesis (The University of Chicago Express, Chicago and London, 1983)

[7] N. Prantzos, M. Hashimoto and K.Nomoto: Astronomy & Astrophysics, 234, 211 (1990)

[8] C.Sneden et al.: Astrophys. J. 467, 819 (1996)

[9] S.E.Woosleys and R.D. Hoffman: Astrophys. J. 395, 202 (1992)

[10] J.Carlson and R.Schiavilla et al.: Rev. Mod. Phys. 70, 743 (1998) and references therein.

[11] Y.Nagai et al., Astrophys. J. 372, 683 (1991), T.Ohsaki et al.: Astrophys. J. 422, 912 (1994), M.Igashira et al.: Astrophys. J. 441, L89 (1995), T.Kikuchi T. et al.: Phys. Rev. C 57, 2724 (1998)

[12] M.Igashira et al.: Nucl. Instr. Meth. A 245, 432 (1986), Y.Nagai et al., Astrophys. J. 372, 683 (1991)

[13] T.Ohsaki et al.: Nucl. Instr. Meth. A 425, 302 (1999)

[14] T.Shima et al.: Nucl. Instr. Meth. A 356, 347 (1995)

[15] T.Kii et al.: Phys. Rev. C59, 3397 (1999)

[16] M.Rayet and M.Hashimoto: Astronomy and Astrophysics. 354, 740 (2000)

[17] Y.Nagai et al.: Phys. Rev. C56, 3173 (1997)

[18] Y. K. Ho, H.Kitazawa and M.Igashira: Phys. Rev. C44, 148 (1991), A.Mengoni, T.Otsuka and M.Ishihara: Phys. Rev. C52, R2334 (1995)

JP0450485

JAERI－Conf 2004－005

2.13 Astrophysics and Photoreaction Data

H. Utsunomiya
Department of Physics, Konan University
8-9-1 Okamoto, Higashinada, Kobe 658-8501, Japan
e-mail: hiro@konan-u.ac.jp

The present status of photoreaction studies at AIST and the prospect of the future at SPring-8 are presented. The Konan University and the Université Libre de Bruxelles launch a 5-year project, starting in 2004, of constructing an extended NACRE compilation in which photonuclear reactions will be included.

1. Introduction

There are three major real-photon sources that have been used in nuclear physics: radioactive isotopes, bremsstrahlung, and positron annihilation in flight [1,2]. Recently, a new generation of γ-ray sources has emerged at synchrotron radiation facilities that are devoted to material science. The idea of producing γ rays in the laboratory by interactions between laser photons and relativistic electrons was born in 1963 [3,4]. The idea was first put into reality for practical purposes at Frascati in 1980's [5]. However, its use for astronuclear physics had been ignored until recently.

Photonuclear data of astrophysical relevance concern (γ,γ), (γ,n), (γ,p), and (γ,α) reactions near particle thresholds without/with Coulomb barrier effects in exit channels. As shown in the literature [6], photoneutron reaction rates are determined by the product of a Planck spectrum of black-body radiation and photoneutron cross sections. As a result, (γ,n) cross sections just above thresholds are of astrophysical significance. Although a nuclear physics database for electric giant dipole resonance was constructed after major contributions from the Lawrence Livermore National Laboratory and Saclay [7], the data near thresholds lack sufficient accuracy for astrophysical use. Coulomb barrier effects make (γ,p), and (γ,α) reactions difficult to measure and (γ,γ) cross sections below particle thresholds should never be forgotten for photoreactions on nuclei with thermally equilibrated excited states [8].

2. The present status at AIST

Real photon beams in the MeV region have been developed at the National Institute of

Advanced Industrial Science and Technology (AIST) in *head-on* collisions of laser photons with relativistic electrons stored in the accumulator ring TERAS [9]. The laser Compton scattering (LCS) plays a role of *photon accelerator*, producing quasi-monochromatic γ beams in the energy range of 1 - 40 MeV. They are bremsstrahlung-free unlike the positron annihilation in flight, and 100% linearly (circularly) polarized. Because of the monochromaticy, the AIST-LCS beam is best suited to excitation function measurements of photoreaction cross sections with enriched target materials. In addition, photo-activation of natural foils by the AIST-LCS beam can be done for nuclei whose isotopic abundance is sufficiently large.

The AIST-LCS γ-beam with a rather limited intensity (10^{4-5} photons/sec) was so far used to measure cross sections of ^{9}Be(γ,n)$\alpha\alpha$ for supernovae nucleosynthesis [10,11], ^{181}Ta(γ,n)^{180}Ta [12] for the p-process nucleosynthesis, and D(γ,n)p [13] for big bang nucleosynthesis. The latest photoneutron cross section measurements include ^{186}W, ^{187}Re, and ^{188}Os for the s-process nucleosynthesis and cosmochronometry, and ^{93}Nb and ^{139}La for the p-process nucleosynthesis. Measurements for many more nuclei will follow over the next 5 years.

Large differences were found in electromagnetic quantities (B(E1)$\downarrow$ and Γ_{γ}(M1)) for ^{9}Be between the present real-photon measurement and the electron scattering (virtual-photon) measurement. The present experimental data are analyzed with the help of a microscopic model of the ^{9}Be nucleus [14-16]. The reaction rate of $\alpha\alpha$(n,γ)^{9}Be was evaluated from the photoneutron cross section [11] and compared with those of the CF88 [17] and the NACRE [18] compilations. A factor of two difference was found with respect to CF88 over the temperature range T = (0.1 - 10) $\times$ 10^{9} K, while reasonable agreement with NACRE was obtained, putting aside details in the treatment of individual states in ^{9}Be.

Figure 1 shows photonuclear data for ^{181}Ta [12]. Their interpretation has necessitated a microscopic understanding of threshold behavior of photoneutron cross sections, showing the advantage of a QRPA calculation over a conventional Lorentzian- or hybrid-model analysis. From these nuclear data, it appears that ^{180}Ta, the nature's rarest isotope and the only naturally occurring isomer, can be a p-process nuclide. Nuclear challenges remain in order to reliably evaluate the ^{180}Ta p-process yield from various stellar locations reviewed in [8]. They include ^{180}Ta photo-destruction rate and ^{181}Ta photo-neutron branching to the ^{180}Ta. These would help constraining reaction models.

Figure 2 shows photonuclear data for deuterium [13]. The filled circles are from this work. The photodisintegration data for deuterium were converted to cross sections of the p(n,γ)D capture reaction. A least-squares fit to the present cross section combined with the existing capture data [19,20] was obtained. It has to be pointed out that the capture cross section was evaluated only theoretically for more than 30 years since the compilation [21]. Furthermore, details of the latest evaluation by Hale compiled in ENDF/B-VI [22] can no

longer be traced. The present work has provided an experimental confirmation of the theoretical evaluation, offering the foundation for recent discussions of the baryon density based on observations of primeval deuterium-to-hydrogen ratios in metal-poor hydrogen clouds at high redshifts toward quasars [23-25]. One may be entering a new era of Big-Bang nucleosynthesis through an independent confirmation of the baryon density by the observation of temperature anisotropies of the cosmic microwave background (CMB) radiation by the Wilkinson Microwave Anisotropy Probe (WMAP) satellite [26].

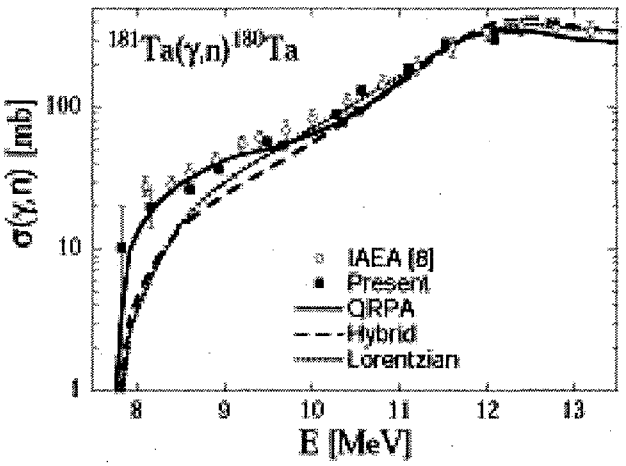

Figure 1. Photodisintegration cross sections for ^{181}Ta(γ,n)^{180}Ta.

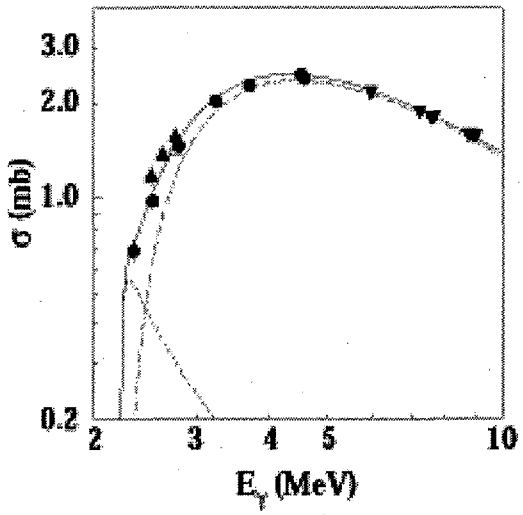

Figure 2. Photodisintegration cross sections for D(γ,n)p.

3. The future prospect at AIST

Currently two γ-sources are under development at the 8 GeV Super-Photon ring (SPring-8) in Japan: one γ-source is based on inverse Compton scattering of far-infrared laser photons with $\lambda = 118.8$ μm from 8-GeV electrons, the other one being a high-energy radiation from a 10 tesla superconducting wiggler (SCW) [27]. The former is rather white with maximum energy ~ 10 MeV, while the latter is characterized by exponential tails extending to several MeV. It is expected that their intensities are 10^{7-8} photons/sec/MeV near neutron thresholds, ~ 8 MeV.

Figure 3 shows energy spectra of the SCW radiations calculated following the prescription of [28,29]. It is remarkable that the exponential tails of the radiation are equivalent to temperatures of a few to several billions of Kelvin (T_9). In other words, the SCW radiation *mimics* the Planck spectrum of black-body radiation generated in particular during supernova explosions. In a promising astrophysical site for the p-process, the O/Ne layers of massive stars during their pre-supernova phase [30-32] or during their explosions as

type-II supernovae [33,34,31,32], temperatures of the blackbody radiation lie in the T_9 = 1.7 - 3.3 range. These temperatures can be accessed by the SCW at lower magnetic fields. The intensity of the high-energy tail of the SCW radiation strongly depends on the magnetic field. Under this condition, the SCW radiation can be used to directly determine photonuclear reaction rates by the activation technique without manipulations such as superposition of several Bremsstrahlung spectra with different end-point energies [35].

Experimentally, the higher the intensity the more feasible the measurement. The intensity at the maximum 10 Tesla field is indeed attractive. The threshold behavior of the photoneutron cross section can be parametrized by

$$\sigma(E) = \sigma_0 \, [(E_\gamma - S_n)/S_n]^p,$$

where E_γ is the γ-ray energy and S_n is the neutron separation energy. When a neutron with an orbital angular momentum l is emitted in a photodisintegration, p is given by $l + 1/2$. Generally different values of l contribute, depending on the spin and the parity of the residual nucleus in the photodisintegration. This is in interesting contrast with the fact that s-wave neutrons are preferentially captured at low energies. σ_0 and p are parameters to be determined experimentally. Based on Eq.(1), a few measurements of the photoreaction rate with the SCW radiation at the highest available magnetic fields enable us to determine these experimental parameters. This method is most promising in the p-process study, opening up a variety of applications. We have a long list (not presented here) of photoreactions to be studied by the photoactivation technique.

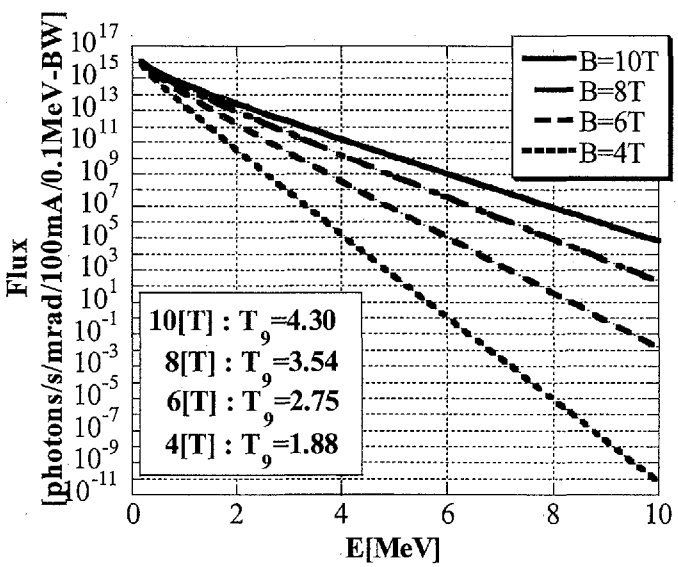

Figure 3. Synchrotron radiation from a 10 Tesla superconducting wiggler at SPring-8 (calculations).

The highest priority would be placed on the photo-destruction of ^{180}Ta among the long list, ^{180}Ta[0.012%](γ,n)^{179}Ta[$T_{1/2}$=1.82 y]. Preparing enriched ^{180}Ta material for photonuclear reactions is out of question. This reaction can be studied by photoactivation of natural tantalum foils with a high-intensity γ-source at SPring-8 (see [36] for details). On the other hand, a higher luminosity of the order of 10^{11} photons/sec is awaited by another p-process nuclide ^{138}La[0.09%] whose photo-destruction leads to ^{137}La[$T_{1/2}$=6 $\times$ 10^4 y].

4. Konan-Brussels Database

Since the first compilation by W.A. Fowler *et al.* in 1967 [21], the astrophysics community benefited from a series of the CalTech compilations [21,37-39,17]. It was nearly 10 years after the last one that a new compilation NACRE [18], a partial update of the CalTech compilation, was constructed.

The Konan University and the Université Libre de Bruxelles are launching a 5-year project, starting in April 2004, of constructing an extended NACRE compilation based on a comprehensive convention between the two universities. In the first place this may be a *public service* to the international astrophysics and very low-energy nuclear physics communities. In addition, we intend to stimulate experimental, observational, and theoretical developments in astrophysics.

We are at the start of an unexplored field of photonuclear reaction studies with new g sources available at synchrotron radiation facilities. In addition to reactions induced by neutrons and charged particles, the Konan-ULB database will also include information on photonuclear reactions. To be most successful and continuously updated, our compilation and evaluation effort has clearly to benefit from the input from the international nuclear astrophysics community.

Acknowledgements

This work was supported in part by the Japan Private School Promotion Foundation and by the Japan Society for the Promotion of Science.

References

[1] R.L. Bramblett, J.T. Cladwell, G.F. Auchampaugh, and S.C. Fultz, Phys. Rev. **129**, 2723 (1963).
[2] R. Bergère, H. Beil, and A. Veyssière, Nucl. Phys. **A121**, 463 (1968).
[3] R.H. Milburn, Phys. Rev. Lett. **10**, 75 (1963).
[4] F.R. Arutyunian and V.A. Tumanian, Phys. Lett. **4**, 176 (1963).
[5] L. Federici *et al.*, Nuovo Cimento **59 B**, 247 (1963).
[6] P. Mohr, K. Vogt, M. Babilon, J. Enders, T. Hartmann, C. Hutter, T. Rauscher, S. Volz, and A. Zilges, Phys. Lett. **B488**, 127 (2000).
[7] S.S. Dietrich and B.L. Berman, At. Data Nucl. Data Tables **38**, 199 (1988).
[8] M. Arnould and S. Goriely, Phys. Rep. **384**, 1 (2003).

[9] H. Ohgaki, S. Sugiyama, T. Yamazaki, T. Mikado, M. Chiwaki, K. Yamada, R. Suzuki, T. Noguchi, and T. Tomimasu, IEEE Trans. Nucl. Sci. **38**, 386 (1991).
[10] H. Utsunomiya, Y. Yonezawa, H. Akimune, T. Yamagata, M. Ohta, M. Fujishiro, H. Toyokawa, and H. Ohgaki, Phys. Rev. **C63**, 018801 (2001).
[11] K. Sumiyoshi, H. Utsunomiya, S. Goko, and T. Kajino, Nucl. Phys. **A709**, 467 (2002).
[12] H. Utsunomiya, H. Akimune, S. Goko, M. Ohta, H. Ueda, T. Yamagata, K. Yamasaki, H. Ohgaki, H. Toyokawa, Y.-W. Lui, T. Hayakawa, T. Shizuma, E. Khan, and S. Goriely, Phys. Rev. **C67**, 015807 (2003).
[13] K.Y. Hara, H. Utsunomiya, S. Goko, H. Akimune, T. Yamagata, M. Ohta, H. Toyokawa, K. Kudo, A. Uritani, Y. Shibata, Y.-W. Lui, and H. Ohgaki, Phys. Rev. **D68**, 072001 (2003).
[14] P. Descouvemont, Eur. Phys. J. **A12**, 413 (2000).
[15] N. Itagaki and K. Hagino, Phys. Rev. **C66**, 057301 (2002).
[16] K. Arai, P. Descouvemont, D. Baye, and W.N. Catford, Phys. Rev. **C68**, 014310 (2003).
[17] G.R. Caughlan and W.A. Fowler, At. Data Nucl. Data Tables **40**, 283 (1988).
[18] C. Angulo *et al.,* Nucl. Phys. **A656**, 3 (1999).
[19] T.S. Suzuki *et al.*, Astrophys. J. **439**, L59 (1995).
[20] Y. Nagai *et al.*, Phys. Rev. **C56**, 3173 (1997).
[21] W.A. Fowler, G.R. Caughlan, and B.A. Zimmerman, Ann. Rev. Astr. Ap. **5**, 525 (1967).
[22] G.M. Hale, D.C. Dodder, E.R. Siciliano, and W.B. Wilson, Los Alamos National Laboratory, ENDF/B-VI evaluation, Mat #125, Rev. 1, 1991.
[23] C.B. Netterfeld *et al.*, Astrophys. J. **571**, 604 (2002).
[24] D. Stompor *et al.*, Astrophys. J. **561**, L7 (2001).
[25] C. Pryke *et al.*, Astrophys. J. **568**, 46 (2002).
[26] D.N. Spergel *et al.*, Astrphys. J. Suppl. **148**, 175S (2003).
[27] A. Ando *et al.*, J. Synchrotron Rad. **3**, 201 (1996); ibid. **5**, 360 (1998).
[28] J.D.Jackson, *Classical Electrodynamics*, (Wisley, 2nd ed.), Section 14.6.
[29] K-J. Kim, AIP Conference Proceedings, **184**, 565 (1989).
[30] M. Arnould, Astron. Astrophys. **46**, 117 (1976).
[31] M. Rayet, M. Arnould, M. Hashimoto, N. Prantzos, and K. Nomoto, Astron. Astrophys. **298**, 517 (1995).
[32] T. Rauscher, A. Heger, R.D. Hoffman, and S.E. Woosley, Astrophys. J. **576**, 323 (2002).
[33] S.E. Woosley and W.M. Howard, Astrophys. J. Suppl. **36**, 285 (1978).
[34] M. Arnould, M. Rayet, and M. Hashimoto, in *Unstable Nuclei in Astrophysics*, edited by S. Kubono and T. Kajino (World Scientific, Singapore, 1992), p. 23.
[35] K. Vogt, P. Mohr, M. Babilon, J. Enders, T. Hartmann, C. Hutter, T. Rauscher, S. Volz, and A. Zilges, Phys. Rev. **C63**, 055802 (2001).
[36] S. Goko, in the proceedings of Tours Symposium 2003, Tours France, August 26 - 29, 2003 (to be published).
[37] W.A. Fowler, G.R. Caughlan, B.A. Zimmerman, Annu. Rev. Astron. Astrophys. **13**, 69 (1975).
[38] M.J. Harris, W.A. Fowler, G.R. Caughlan, B.A. Zimmerman, Annu. Rev. Astron. Astrophys. **21**, 165 (1983).
[39] G.R. Caughlan, W.A. Fowler, M.J. Harris, B.A. Zimmerman, At. Data Nucl. Data Table **32**, 197 (1985).

2.14 Neutron- and Proton-Induced Nuclear Data Evaluation of Thorium, Uranium and Curium isotopes for Energies up to 250 MeV

Young-Ouk Lee and Jonghwa Chang

Korea Atomic Energy Research Institute, Korea
P.O. Box 105 Yusong, Taejon 305-600, Korea
e-mail: yolee@kaeri.re.kr

Tokio Fukahori, and A. Yu. Konobeyev
Japan Atomic Energy Research Institute

The evaluation of neutron- and proton nuclear data for thorium-232, U-233,234,236, and Cm-243,244,245,246 isotopes have been performed at energies up to 250 MeV. Neutron data was evaluated at energies from 20 MeV to 250 MeV, and combined with the JENDL-3.3 data at 20 MeV, while proton data was obtained for energies from 1 to 250 MeV. Nuclear model parameters are largely based on the IAEA-RIPL recommendation, and adjusted to better reproduce the available measurements. The coupled channel optical model was applied to calculate the total, reaction, elastic, and direct inelastic cross sections, and to obtain the transmission coefficients. Decay of excited nuclei was described with the Hauser-Feshbach and exciton models using the GNASH code to simultaneously handle neutron, proton, deuteron, triton, helium-3, α, γ emissions and fissions. Special attention was paid on the fission cross sections for energies where experimental data are scant, using appropriate systematics and fittings. Particles and γ emission spectra after fission were calculated based on the the statistical approach of Fong, and adjusted to the experimental data using the ALICE-ASH code.

1. Introduction

Within the frame work of the JENDL high energy library, the evaluation of neutron- and proton nuclear data for thorium-232, U-233,234,236, and Cm-243,244,245,246 isotopes have been performed at energies up to 250 MeV. Neutron data was evaluated at energies from 20 MeV to 250 MeV, and combined with the JENDL-3.3 data at 20 MeV, while proton data was obtained for energies from 1 to 250 MeV.

2. Models and Codes

Nuclear model parameters are largely based on the IAEA-RIPL recommendation, and adjusted to better reproduce the available measurements. The coupled channel optical model was applied to calculate the total, reaction, elastic, and direct inelastic cross sections, and to obtain the transmission coefficients. Decay of excited nuclei was described with the Hauser-Feshbach and exciton models using the GNASH code to simultaneously handle neutron, proton, deuteron, triton, helium-3, α, γ emissions and fissions. Special attention was paid on the neutron fission cross sections to achieve continuity and

consistency with the existing JENDL-3.3 evaluation using theoretical and experimental fission barriers, and fittings. Primary pre-equilibrium emission spectra of helium-3 and α-particles were calculated with the coalescence pick-up model using the ALICE/ASH code, and fed into the GNASH calculation. Particles and γ emission spectra after fission were calculated based on the the statistical approach of Fong, and adjusted to the experimental data using the ALICE-ASH code. The original frame of the procedure is based on the ECIS-GNASH code system for the evaluation of non-fissionable spherical nuclei for energies up to 150 MeV. With some modifications and expansions, JAERI Nuclear Data Center has been using it for the evaluation of JENDL High Energy File for energies up to 250 MeV. Meanwhile, for the intermediate energy evaluation of actinide nuclei, a major change was made onto it to handle the rotational coupled-channel optical model and fission. The new code system for the actinide evaluation consists of three main nuclear model codes such as the ECIS [1], GNASH [2], ALICE-ASH [3] and ALICE95Y [3] with pre-/post processors and auxiliary tools supporting them.

The ECIS code performs the coupled-channel optical model calculation to provide total, reaction, elastic, and direct inelastic cross sections, and elastic and inelastic scattering angular distributions. It is also used to produce the transmission coefficients for neutron, proton, deuteron, triton, helium-3, and alpha particles. Usually input files for various cases are prepared by PREG_ROTW with appropriate optical models. The GNASH code performs Hauser-Feshbach and exciton model calculation to handle n, p, d, t, he-3, α, and γ emission as well as fission. Original version was modified to handle 8 decay modes simultaneously including γ and fission for energies up to 250 MeV of incident neutron and proton on nuclei as heavy as up to Cm-247. The ALICE-ASH code provides precompound spectra via the hybrid and GDH models, and fission cross sections via the Bohr-Wheeler approach. The ALICE95Y code, combined with the ALICE-ASH, performs post-fission emission and fission yield calculations using statistical approach of Fong with the adjustment to experimental data.

3. Results and Comparisons

In this article, only the neutron total, proton non-elastic, and fission cross sections are presented in Figs. 1, 2, 3 and 4 compared with available measurements. More details of evaluated results and discussions will be available in [4]. As seen in Fig. 1, present evaluation of neutron total cross sections are consistent with the existing JENDL-3.3 evaluation at the neutron energy of 20 MeV. Figure 2 shows neutron-induced fission cross sections, which are continuous with the existing JENDL-3.3 evaluation except the U-234 case, and consistent with the measurements. The proton non-elastic cross sections are in Fig. 3, where the comparisons were made only for Th-232 and U–233 with the measurements. Figure 4 presents proton-induced fission cross sections, where Th-233 and U-233,234,246 cases are compared with the available measurements showing good agreements, while only theoretical results are presented for the case of Curium isotopes.

Acknowledgments

This work was performed between February and May, 2003, during the stay of one

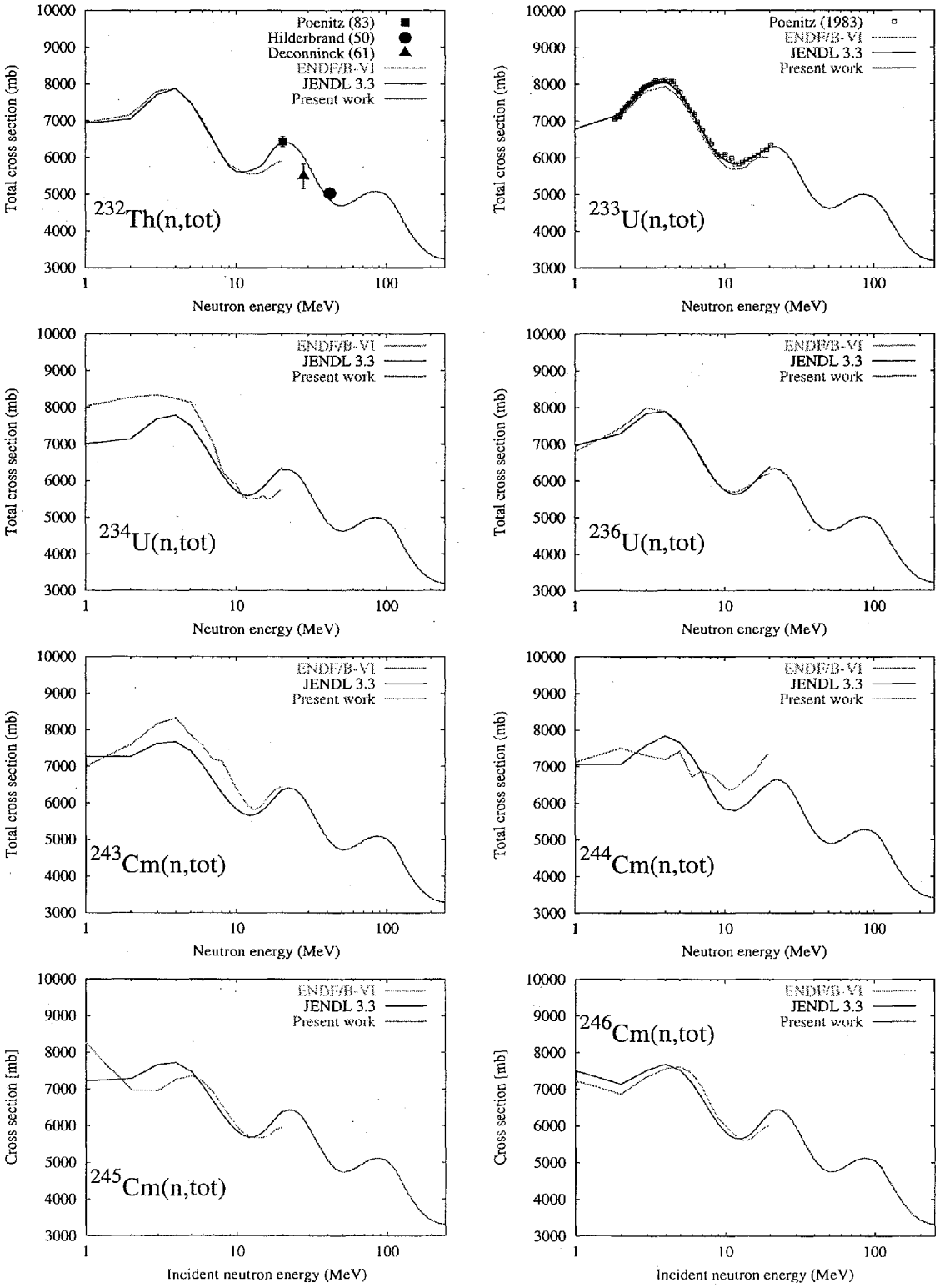

Figure 1: Evaluated neutron total cross sections for minor actinides

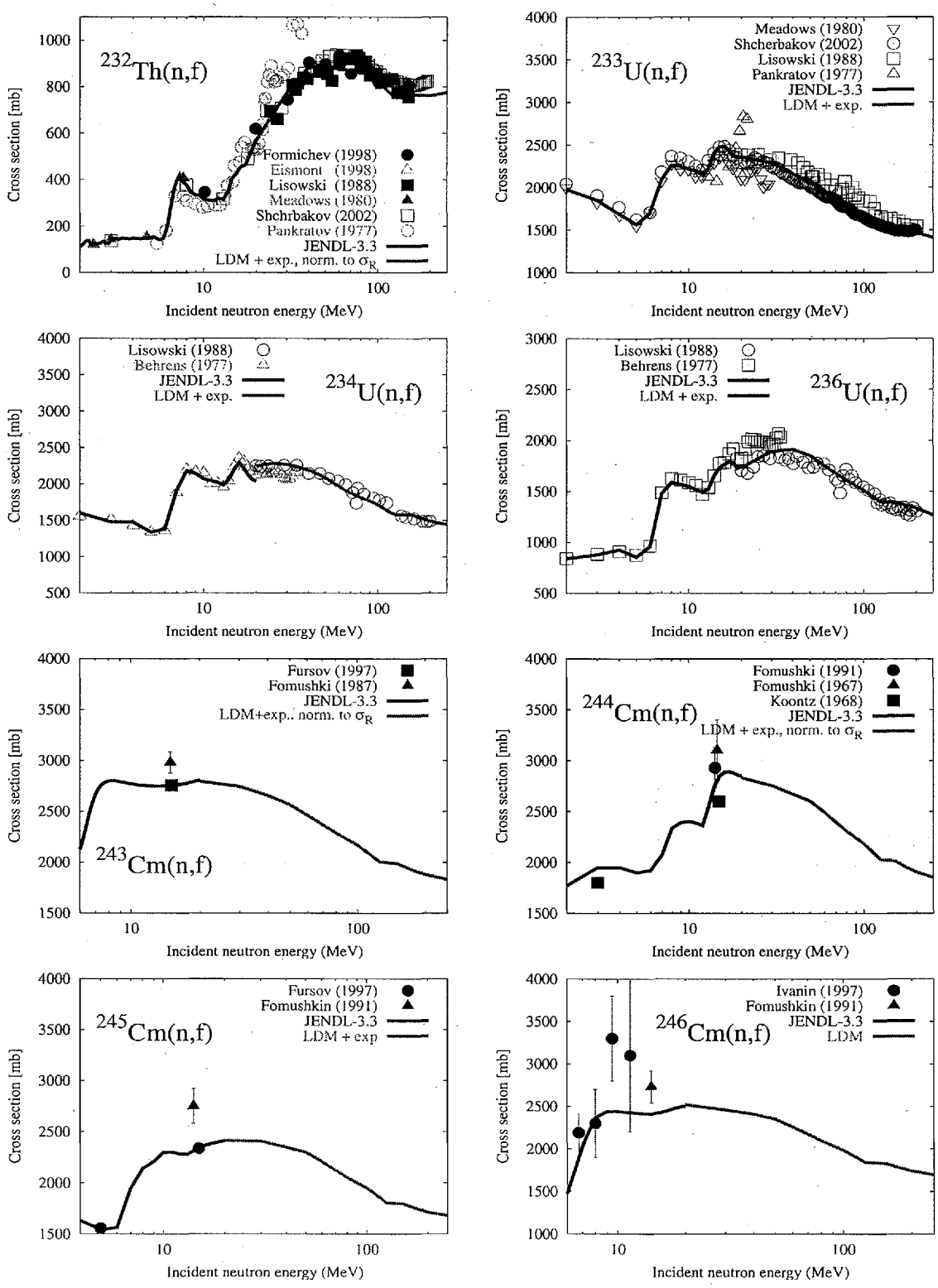

Figure 2: Evaluated neutron fission cross sections for minor actinides

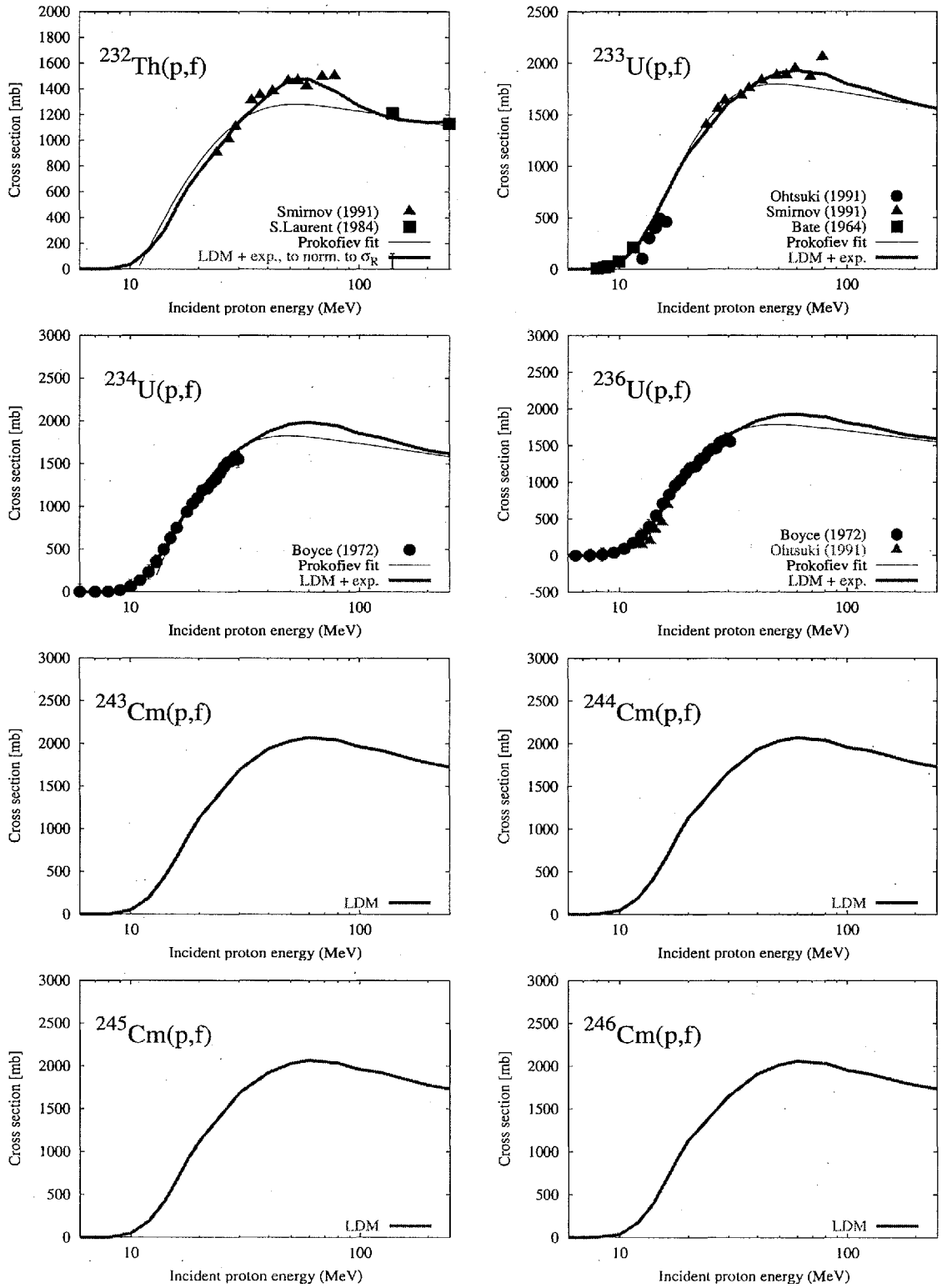

Figure 3: Evaluated proton fission cross sections for minor actinides

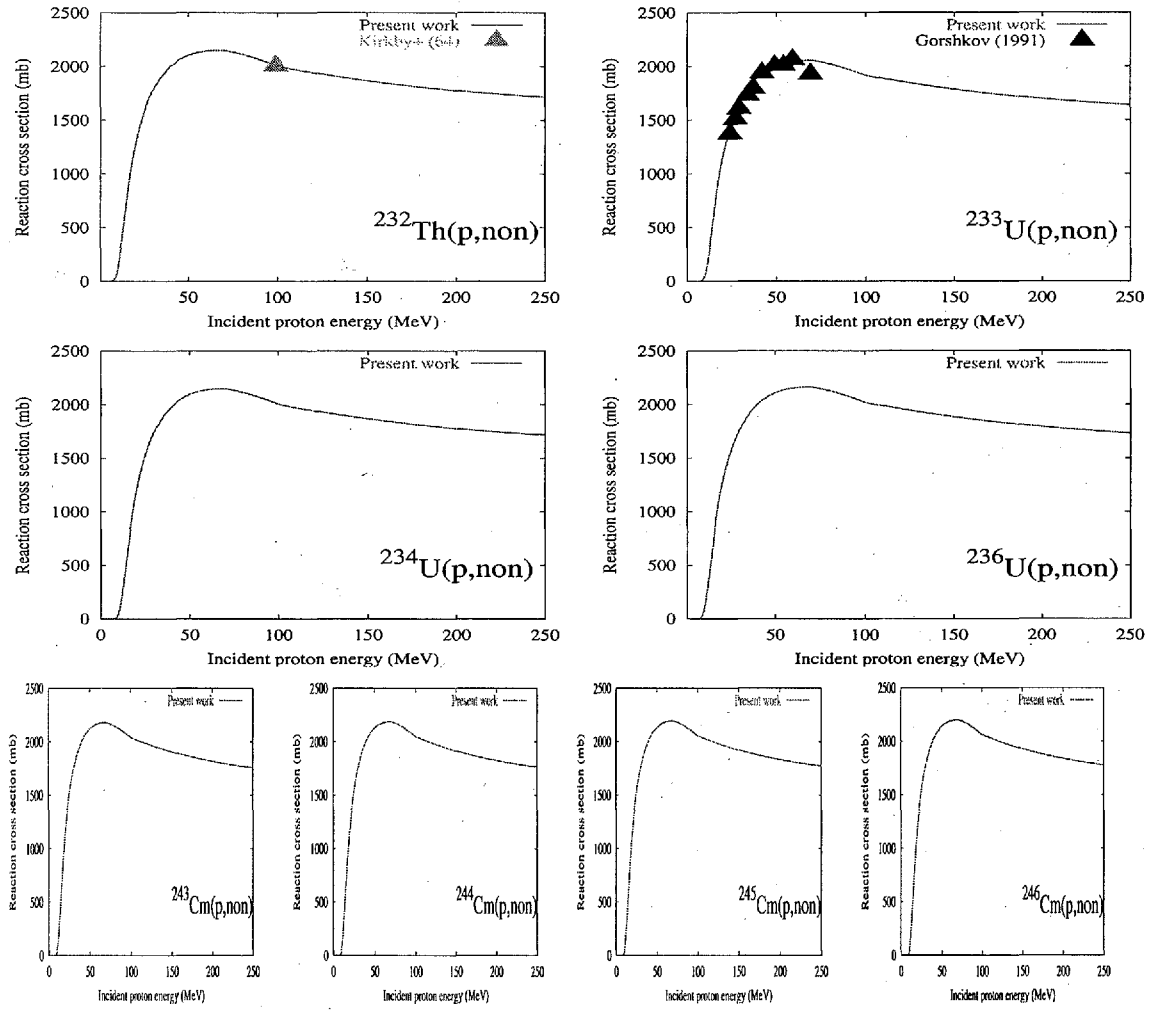

Figure 4: Evaluated proton non-elastic cross sections for minor actinides

of the authors(Y.-O. Lee) at JAERI under the Foreign Scientists Invitation System of JAERI.

– References –

[1] Raynal, J.: *Notes on ECIS94*. Tech. Rep. CEA-N-2772, Commisariat á l'Energie Atomique (CEA), Saclay, France (1994).

[2] Young, P. G., *et al.*: In A. Gandini, G. Reffo, eds., *Proc. of the IAEA Workshop on Nuclear Reaction Data and Nuclear Reactors - Physics, Design, and Safety*, 227–404, Singapore (1996). Trieste, Italy, April 15 - May 17, 1996, World Scientific Publishing, Ltd.

[3] Konobeyev, A. Y., *et al.*: *Code ALICE/ASH for calculation of excitation functions, energy and angular distributions of emitted particles in nuclear reactions*. Tech. Rep. INPE, Obninsk, February (1997).

[4] Lee, Y., *et al.*: *J. of Nucl. Sci. and Tech.* (to be submitted).

2.15 Status Report and Measurement of Total Cross-sections at the Pohang Neutron Facility

G. N. Kim,* A. K. M. M. H. Meaze, H. Ahmed, and D. Son
Institute of High Energy Physics, Kyungpook National University, 1370 Sankyuk-Dong, Puk-Gu, Daegu 702-701, Korea

Y. S. Lee, H. S. Kang, M. H. Cho, I. S. Ko, and W. Namkung
Pohang Accelerator Laboratory, Pohang University of Science and Technology, San 31 Hyoja–Dong, Nam–Gu, Pohang 790 – 784, Korea

K. J. Yoo, Y. A. Kim and J. Chang
Korea Atomic Energy Research Institute, 150 Deokjin-dong, Yuseong-gu ,Daejeon, Korea

We report the status of the Pohang Neutron Facility which consists of an electron linear accelerator, a water-cooled Ta target, and an 11-m time-of-flight path. It has been equipped with a four-position sample changer controlled remotely by a CAMAC data acquisition system, which allows simultaneous accumulation of the neutron time of flight spectra from 4 different detectors. It can be possible to measure the neutron total cross-sections in the neutron energy range from 0.1 eV to 100 eV by using the neutron time of flight method. A ^{6}LiZnS(Ag) glass scintillator was used as a neutron detector. The neutron flight path from the water-cooled Ta target to the neutron detector was 10.81±0.02 m. The background level was determined by using notch-filters of Co, In, Ta, and Cd sheets. In order to reduce the gamma rays from Bremsstrahlung and those from neutron capture, we employed a neutron-gamma separation system based on their different pulse shapes. The present measurements are in general agreement with the evaluated data in ENDF/B-VI. The resonance parameters were extracted from the transmission data from the SAMMY fitting and compared with the previous ones.

I. INTRODUCTION

Pulsed neutrons based on an electron accelerator (linac) are a powerful tool to measure the energy dependence of cross-sections with high resolution by using time of flight (TOF). The Pohang Neutron Facility (PNF) was proposed in 1997 [1] and constructed at the Pohang Accelerator Laboratory on December 1998 [2]. It consists of a 100-MeV electron linac, water-cooled Ta neutron producing target, and an 11-m-long evacuated flight vertical tube leading to the detector location. The electron linac consists of a thermionic RF-gun, an alpha magnet, four quadrupole magnets, two SLAC-type accelerating sections, a quadrupole triplet, and a beam-analyzing magnet. A 2-m long drift space is added between the first and the second accelerating section to insert an energy compensation magnet or a beam transport magnet for other research. The overall length of the linac is about 15 m. As a photoneutron target, it is necessary to use heavy mass materials in order to produce intense neutrons by way of bremsstrahlung under high-power electron beams. We have chosen a tantalum as the target material, which has advantages of high density (16.6 g/cm^3), high melting point (3,017°C), and high resistant against the corrosion by cooling water. Since we have to utilize the space and infrastructures at PAL, an 11 m long TOF path and a detector room were constructed vertically to the electron linac. The

* E-mail: gnkim@knu.ac.kr, Tel.: +82-53-950-6328

TOF tubes were made by stainless steel with two different diameters of 15 and 20 cm. The neutron beam line was equipped with a four–position sample changer which can allow the simultaneous total cross-section measurement for four different samples. The sample changer is controlled remotely by a special CAMAC module, which is part of a CAMAC data acquisition system in which great advances have resulted from simultaneous accumulation of the neutron TOF spectra from four different detectors. The facility details of PNF are described elsewhere [3].

We report the measured total cross-sections of natural Dy, Ag, Ti, and W in the neutron energy range from 0.1 eV to 100 eV by using the neutron TOF method at the PNF. The measured result was compared with the evaluated data in ENDF/B-VI. The resonance parameters for Dy and Ag were also reported and the results were compared with the previous ones.

II. EXPERIMENTAL ARRANGEMENT

The experimental arrangement for the transmission measurements is shown in Fig. 1 (a). The target is located in the position where the electron beam hits its center. To reduce the gamma-flash generated by the electron burst in the target, this one was placed 55 mm away from the center of the neutron guide. The target was composed of ten Ta plates with a diameter of 4.9 cm and an effective thickness of 7.4 cm [4]. There was a 0.15-cm water gap between Ta plates in order to cool the target effectively. The housing of the target was made of titanium. This target was set at the center of a cylindrical water moderator contained in an aluminum cylinder with a thickness of 0.5 cm, a diameter of 30 cm, and a height of 30 cm. The water level in the moderator was 3 cm above the target surface, which was decided based on a measurement of the thermal neutron flux [5]. The measurement was also compared with the Monte Carlo N-Particle (MCNP) transport code [6].

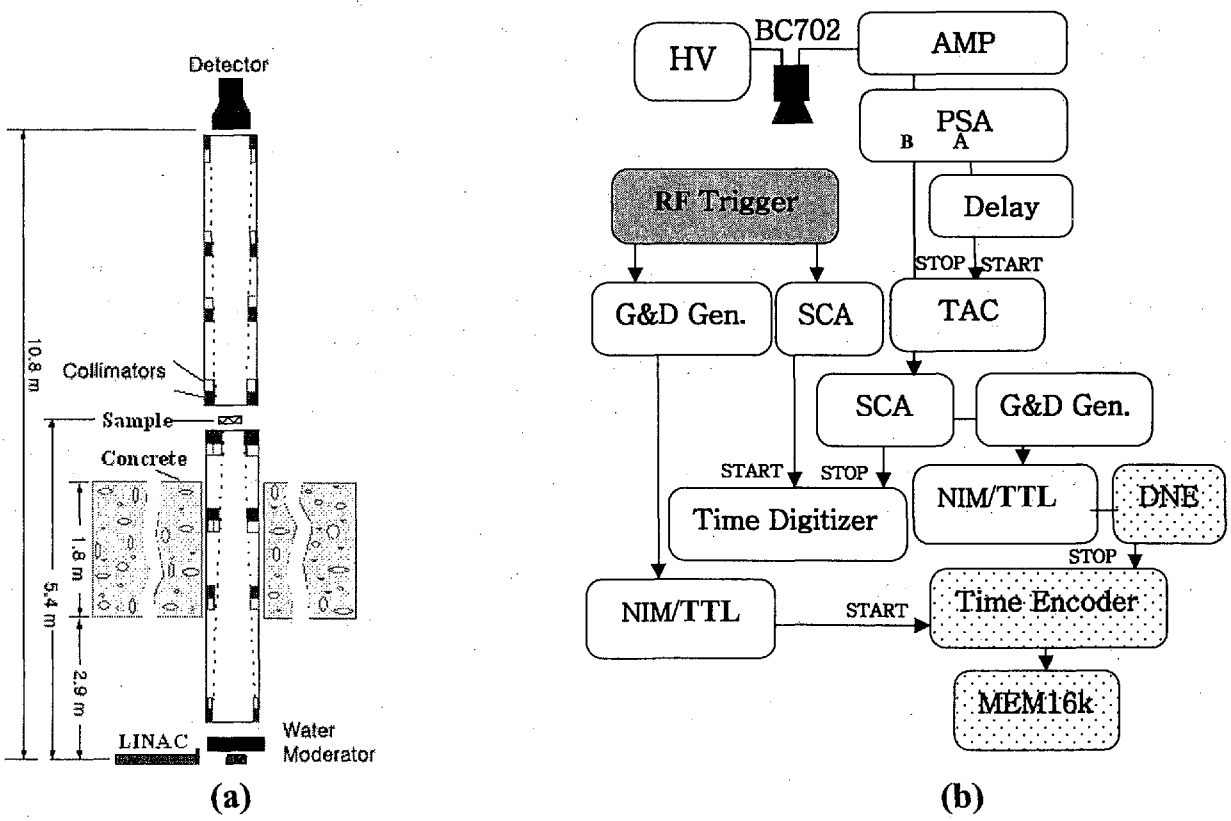

Fig.1. (a) Experimental setup and (b) data acquisition system for the transmission measurements.

The neutron guide tubes were constructed of stainless steel with two different diameters, 15 cm and 20 cm, and were placed perpendicularly to the electron beam. The neutron collimation system was mainly composed of H_3BO_3, Pb and Fe collimators, which were symmetrically tapered from a 10-cm diameter at the beginning, to a 5-cm diameter in the middle position where the sample changer was located, to an 8-cm diameter at the end of guide tube where the neutron detector was placed. There was 1.8-m-thick concrete between the target and the detector room.

The sample changer consists of a disc with 4 holes; each hole is 8 cm in diameter, which matches the hole of the collimator in the neutron beam line. The sample changer, which is controlled remotely by the CAMAC module, has two important goals: Firstly, it allows data taking from up to 4 different samples simultaneously. Secondly, the exposition time for each sample may be selected individually and be precisely controlled by electronics. The last point allows systematic errors owing time variations in the neutron beam intensity to be avoided. The distance between centers of two opposite holes is 31 cm. The holders allow solid samples, as well as liquid or powder ones, to be fixed in special cassettes. The pressurized cover with a rubber O–ring prevents penetration of dust and moisture into the device. There are three windows in the sample changer: two for control and management and the other for samples downloading. All of them are transparent and pressurized. The beam transmission windows – one in the fixed disk of the sample changer, another in a top of cover (see Fig.2), are covered with aluminum foil and pressurized. The movement of the mobile disk with samples is performed by an electric motor with a built-in reduction gearbox. The time of movement between two neighboring positions is 10 sec. The mobile disk moves only in one direction, like a revolver. This decreases the backlash in fixing the sample position. Besides, a combination of an electrical and a rigid spring system allows the sample position to be fixed to better then 1 mm. Photographs of the sample changer are shown in Fig. 2.

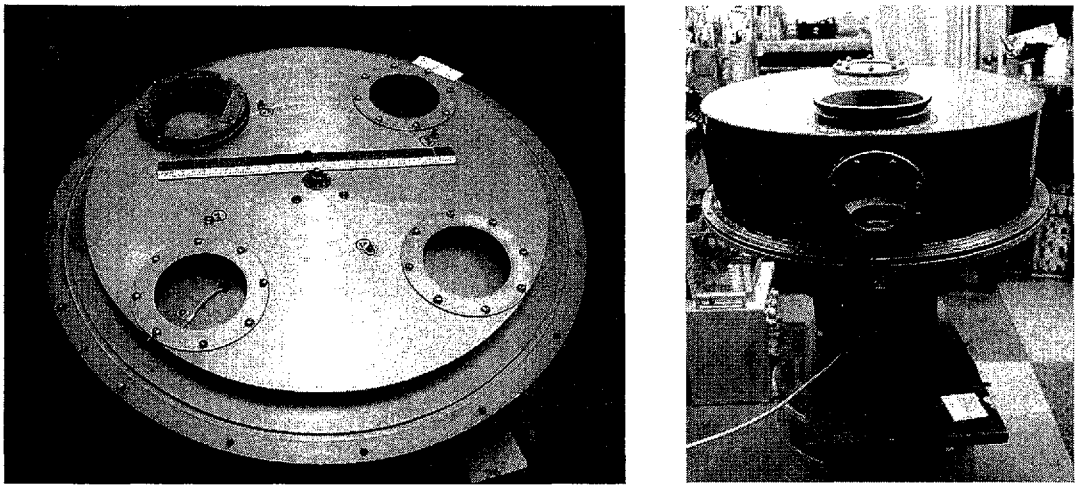

(a) **(b)**

Fig. 2. (a) Inside part of the sample changer without a cover, and (b) outside view of the sample changer with a cover which is in its permanent location on the PNF upright neutron beam line.

The physical parameters of the samples used in the total cross-section measurements are given in Table 1. A set of notch filters of Co, Ta, and Cd plates with thickness of 0.5 mm, 0.2 mm, and 0.5 mm, respectively, was also used for the background measurement and the energy calibration. The transmission samples were placed at the midpoint of the flight path and were cycled into the neutron beam by using the automatic sample changer with four sample positions.

The neutron detector was located at a distance of 10.81 m from the photo-neutron target. A ^{6}Li-ZnS(Ag) scintillator BC702 from Bicron (Newbury, Ohio) with a diameter of 127 mm and a thickness of 15.9 mm mounted on an EMI-93090 photomultiplier was used as a detector for the neutron TOF

spectrum measurement. This scintillator consists of a matrix of a lithium compound enriched to 95% ^{6}Li dispersed in a fine ZnS(Ag) phosphor powder. The detection process employs the nuclear reaction ^{6}Li $(n,\alpha)^3$H in which the resulting α - particle and ^{3}H produce scintillations upon interacting with the ZnS(Ag).

Table 1. Physical parameters of the samples used in the experiment.

Sample	Purity (%)	Size (cm^2)	Thickness (mm)	Weight (g)
Ag	99.98	10×10	0.5	53.04
Dy	99.9	10×10	0.5	37.95
W	99.98	10×10	0.2	19.30
Ti	99.9	10×10	0.5	4.50

III. DATA TAKING AND ANALYSIS

Figure 1 (b) shows the configuration of the data acquisition system used in our measurement. Two different data acquisition systems were used for the neutron TOF spectra measurements: one for the NIM-based system and the other for the CAMAC-based system. The main purpose of the NIM-based system was neutron-gamma separation and the parallel accumulation of the neutron TOF spectra if necessary.

The dynode signal from a BC702 scintillator was connected through an ORTEC-571 amplifier (AMP) to an ORTEC-552 pulse-shape analyzer (PSA) for use in neutron-gamma separation. A fast NIM signal from the "A" output of the PSA was delayed by 60 ns and used as the start signal for an ORTEC-567 time-to-amplitude converter (TAC). The "B" output signal from the PSA was used as the stop signal for the TAC. One of TAC outputs was connected to an ORTEC-550A single channel analyzer (SCA), and the other output signal was fed to a multi-channel pulse-height analyzer (MCA) for neutron-gamma separation. The output signal of the SCA was used as stop signals for a 150-MHz Turbo MCS (Time Digitizer) and for a time encoder of the CAMAC-based system for the neutron TOF spectra measurement. The output of the SCA was sent to an ORTEC-416A gate and delay generator (G&D Gen.) and a TTL/NIM module in order to form the proper signal for the CAMAC system. This output signal was connected to a time encoder through a detector number encoder (DNE). The DNE allowed data taking from up to 4 detectors simultaneously. The time encoder had 4096 channels and a minimal dwell time of 0.5 μs. MEM16k is a memory of 16k capacity and collected the TOF spectra during the measurement.

The 10-Hz RF trigger signal for the modulator of the electron linac was connected to a G&D Gen.; one of output signals was used as the start signal for both the time digitizer and the time encoder, and the other output was sent to the counter through a TTL/NIM converter. The remote control signal from the TTL/NIM was used as the start pulse for the time digitizer for parallel data accumulation. In distinction with the direct use of the start pulse from the RF trigger for the time digitizer, this scheme temporarily interrupts the start pulse sequence while the sample changer moves. The counter has 4 independent inputs, as well as the relevant displays for data and control signals. It is used to accumulate the monitor counts for each position of the sample changer and to control the duration of sample exposure.

The CAMAC part is controlled by PC software via an interface card and crate controller (not shown in Fig. 1 (b)). The program sets and controls the following parameters:

- the numbers and quantity of actual detectors used in the measurement;
- the actual number of TOF channels and dwell time for each detector (may be different);
- the duration of the exposition for each sample as the number of starts from the linac.

It also sets the number of full turnovers of the SC and provides a data record from the MEM16K to the relevant files for future processing. Parallel data acquisition with both the Turbo-MCS system and the

CAMAC system may be used if one desires to optimize the dwell time for different regions of the TOF spectra. For example, the CAMAC time encoder dwell time may be set to 0.5 μs to get good energy resolution in the high-energy part of the TOF spectra while the simultaneous setting for the Turbo-MSC might be 1.5 μs to approach, say, 1 meV in the low-energy region of the TOF spectra. A command file written in special script language synchronizes the CAMAC and the Turbo-MCS.

In order to adjust the neutron-gamma separation circuit used in this experiment, we used two radiation sources, ^{137}Cs and ^{252}Cf. Cesium emits gamma radiation at 662 keV, and californium emits neutrons along with gamma radiation of 100 and 160 keV. The MCA pulse-height spectra of γ rays from ^{137}Cs, neutrons and γ rays from ^{252}Cf, and noise from the neutron detector are shown in Fig. 3. We can see a shape difference between the neutron and the gamma-ray pulse-height spectra. In order to discriminate the gamma-ray and the noise contribution from the neutron TOF spectra, we set the lower-level discriminator (LLD) threshold voltage of the SCA to 1.12 V in the integral operation mode. The threshold voltage of the SCA was determined as the value at which the output signal of the SCA in the oscilloscope was almost zero when increasing the LLD value from the minimum voltage. The corresponding LLD value of 1.12 V is indicated as a line in Fig. 3 (a).

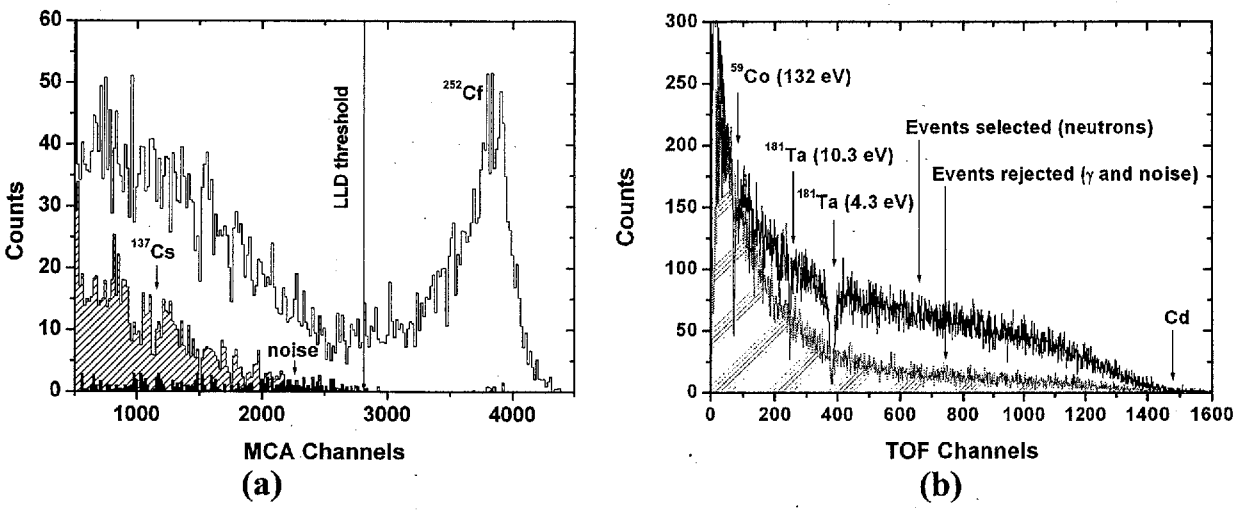

Fig. 3. (a) Pulse height spectra of γ rays from ^{137}Cs, neutrons and γ rays from ^{252}Cf, and noise from the neutron detector, (b) Neutron TOF spectra for events selected and rejected by the LLD setting value.

The effectiveness of this LLD value was tested with the neutron TOF spectra obtained by using notch-filters of Co, Ta and Cd, as shown in Fig. 3 (b). The upper solid curve was obtained with events selected by the LLD setting value, and the lower doted curve was obtained with events rejected by the LLD setting value. Figure 3 (b) demonstrates that the neutron-gamma separation circuit could discriminate gamma-rays from neutrons effectively.

We could estimate the background level by using resonance energies of the neutron TOF spectra of notch-filters of Co, In and Cd as shown in Fig. 4. The

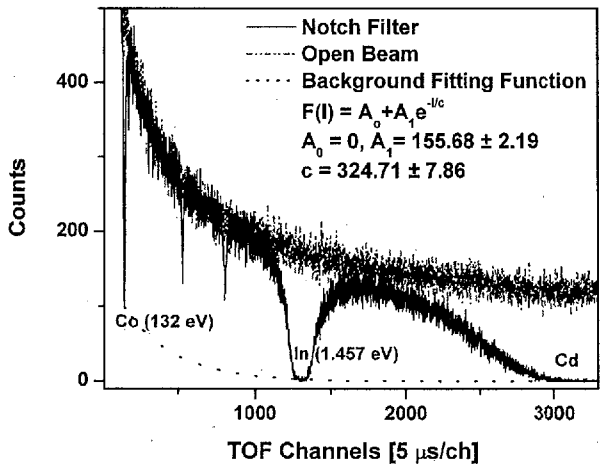

Fig. 4. Background level determination with Co, In, and Cd samples. The background fitting function was determined by using the black resonance energy of the notch filters.

magnitude of the background level was interpolated between the black resonances by using the fitting function $F(I) = A_0 + A_1 e^{-I/c}$, where A_0, A_1, and c are constants and I is the channel number of the time digitizer.

The measurements were performed with two samples simultaneously. The two other positions of the sample changer were empty to collect the neutron TOF spectra without a sample (open beam). The positions of the samples were chosen in the following sequence: sample 1 – empty – sample 2 – empty. The exposition times for both sample 1 and sample 2 were 15 minutes (9000 pulses of PNF linac); for each empty position, it was 7.5 minutes. Thus, the durations for the samples were the same as those for the total open beam measurements. The interleaving sequence of free positions of the sample changer was chosen to minimize the influence of slow and/or/ small variation of the neutron beam intensity. If the beam intensity variations or its drift was fast and/or large, then these partial measurements were excluded from the total statistics. The total data taking times for Ag, Dy, W, and Ti were 65, 16, 48, and 43 hours, respectively, with the same times for the open beams.

The net neutron TOF spectra for the sample-in and the open beam for W and Dy as for an example are shown in Fig. 5, together with the estimated background level which is indicated by dash line. The neutron energy E in eV corresponding to each channel I in the TOF spectrum is derived from the relation $E = \{72.3 \times L/(I - I_0) \times W\}^2$, where L is the neutron flight path in meters, W is the channel width in microseconds, and I_0 is the channel of TOF=0 when the neutron burst was produced. In this experiment, we found I_0 to be equal to 5 channels.

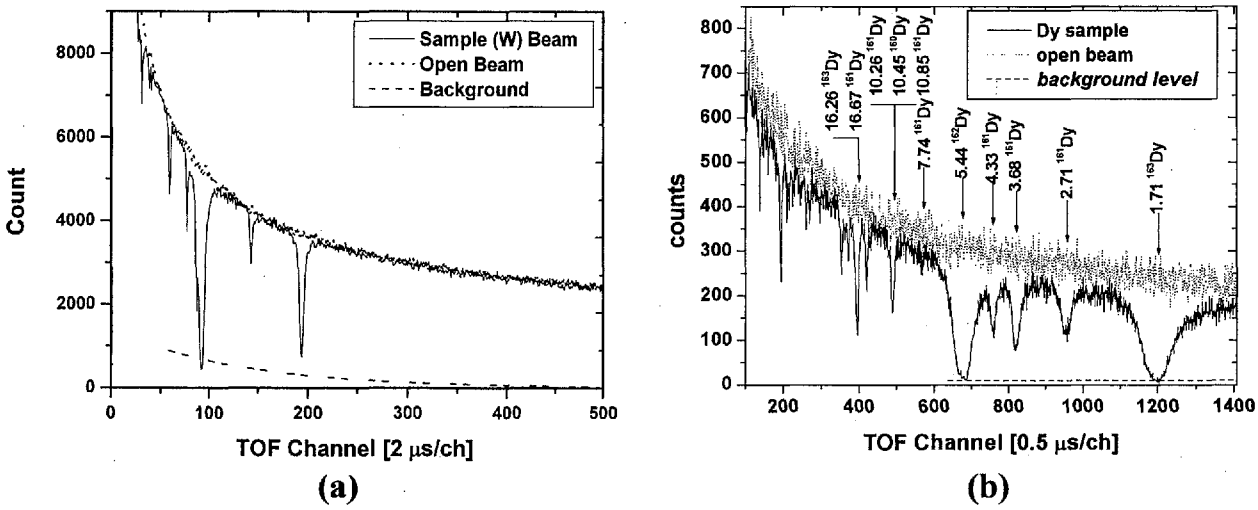

Fig. 5. Neutron TOF spectra for the sample in and out for (a) W and (b) Dy samples, together with the background level indicated as a dotted line.

The neutron total cross-section is determined by measuring the transmission of neutrons through the sample. The transmission rate of neutrons at the i-th group energy E_i is defined as the fraction of incident neutrons passing through the sample compared to that in the open beam. Thus, the neutron total cross-section is related to the neutron transmission rate $T(E_i)$ as follows:

$$\sigma(E_i) = -\frac{1}{\sum_j N_j} \ln T(E_i), \tag{1}$$

$$T(E_i) = \frac{[I(E_i) - IB(E_i)]/M_I}{[O(E_i) - OB(E_i)]/M_O}, \tag{2}$$

where N_j is the atomic density per cm^2 of the j-th isotope in the sample. $I(E_i)$ and $O(E_i)$ are the foreground counts for the sample in and out, $IB(E_i)$ and $OB(E_i)$ are the background counts for sample in and out, and M_I and M_O are monitor counts for the sample-in and the open beam, respectively. In this measurement, we assumed the monitor counts to be equal during the measurement.

IV. RESULTS AND DISCUSSION

The total cross-sections of natural W, Ti, Dy, and Ag were obtained in the energy range from 0.1 eV to 100 eV by using the neutron TOF method as shown in Fig. 6. We only considered the statistical errors for the present measurements because the other sources of uncertainties, which include the detection efficiencies, the geometric factor for the sample, and the other systematic errors, are negligible.

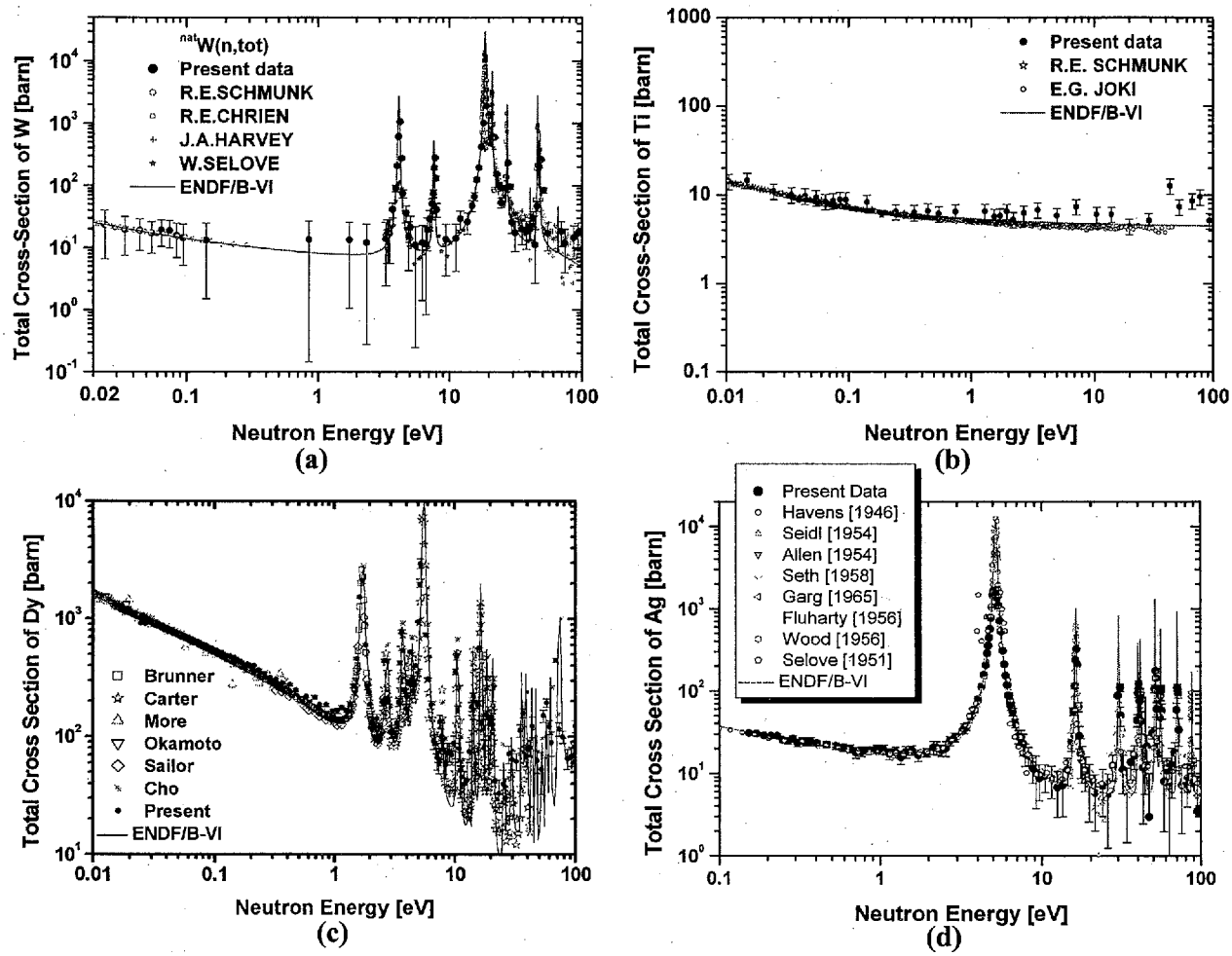

Fig. 6. Measured total cross sections for (a) W, (b) Ti, (c) Dy, and (d) Ag samples, respectively.

The present measurement for the neutron total cross-sections of natural W is compared with other data measured by Schmunk *et al.* [7], Chrien and Zimmerman [8], Harvey *et al.*[9], and Selove [10] and with the evaluated data in ENDF/B-VI [11] as shown in Fig. 6 (a). Figure 6 (b) shows the neutron total cross-sections for natural Ti compared with the other data measured by Schmunk *et al.* [7] and Joki [12] and with the evaluated data in ENDF/B-VI [11]. The neutron total cross-sections of Dy as shown in Fig. 6 (c) is compared with other data measured by Moore [13], Okamoto [14], Sailor *et al.* [15], Brunner et al. [16], Knorr et al. [17], Carter [18], and Cho et al. [19] and the evaluated data in ENDF/B-VI [11]. The present measurements for the neutron total cross sections of Ag is compared with other data measured

by other groups [20] and the evaluated data in ENDF/B-VI [11] as shown in Fig. 6 (d). The present measurements without any corrections are generally in good agreement with other data and the evaluated one in the energy range between 0.1 eV and 100 eV.

There are many resonance peaks in the neutron total cross sections for Dy and Ag. In order to get the resonance parameters of each resonance peak, we fit the transmission data with the SAMMY code [21]. This code uses the Reich-Moore approximation [22] in the application of the R-matrix formalism. An implementation of Bayes' theorem is used to fit the requested resonance parameters to the data. For the Doppler broadening and resolution analysis, the MULTI method [23] is applied: the free gas model is applied to the Doppler broadening and the convolution of Gaussian and exponential function to the resolution. Resolution function $R(E,E')$ used in this calculation is the convolution of Gaussian and exponential function and its mathematical expression is as follows:

$$R_{GE}(E,E') = \frac{1}{\Delta_E \Delta_G \sqrt{\pi}} \int_{E-\Delta E_S}^{\infty} dE^0 \exp\left\{-\frac{\left(E^0 - (E - \Delta E_S)\right)}{\Delta_E}\right\} \exp\left\{-\frac{\left(E' - E^0\right)^2}{\Delta_G^2}\right\}, \tag{3}$$

where the width of Gaussian resolution function Δ_G is given by

$$\Delta_G = E[aE + b]^{1/2}, \tag{4}$$

and the width of exponential resolution function Δ_E is given by

$$\Delta_E = cE^{3/2}. \tag{5}$$

The energy shift ΔE_S, which is automatically determined in the SAMMY, is introduced in order to locate the maximum of the broadening function at $E' = E$. The constant values of a, b, and c are 1.3645×10^{-6} eV^{-1}, 9.1281×10^{-6}, and 6.3969×10^{-4} eV$^{-1/2}$, respectively.

The resonance parameters for the Dy and Ag isotopes have been obtained from the SAMMY fitting and listed in listed in Table 2 and 3, respectively, where they are compared with the existing data [24],[25] listed in the brackets. The quantity J and l is the spin of a particular resonance. The resonance energy of each state is generally in good agreement with the existing data.

Table 2. Resonance parameters for the Dy isotopes.

Dy Isotope	J	E (eV)		$g\Gamma_n$ (meV)	Γ_γ (meV)
163	2	Present	1.7093 ± 0.0007	0.9344 ± 0.0105	91.574 ± 0.827
		Mughabghab	(1.713 ± 0.004)	(0.85 ± 0.05)	(102.6 ± 0.8)
160	1/2	Present	1.8871 ± 0.0321	0.1394 ± 0.0135	124.97 ± 12.32
		Mughabghab	(1.88)	(0.20)	(105.80)
161	3	Present	2.6979 ± 0.0028	0.3929 ± 0.0122	130.12 ± 6.632
		Mughabghab	(2.71 ± 0.02)	(0.328 ± 0.015)	(119 ± 10)
161	2	Present	3.6618 ± 0.0025	0.9524 ± 0.0243	139.14 ± 6.087
		Mughabghab	(3.68 ± 0.03)	(0.89 ± 0.04)	(124 ± 15)
161	2	Present	4.2810 ± 0.0041	0.6677 ± 0.0273	130.25 ± 8.702
		Mughabghab	(4.33 ± 0.02)	(0.575 ± 0.065)	(80 ± 3)
162	1/2	Present	5.3697 ± 0.0022	14.492 ± 0.4007	262.08 ± 11.08
		Mughabghab	(5.44 ± 0.02)	(21 ± 1.5)	(148 ± 15)
163	2	Present	5.8377 ± 0.0775	0.0198 ± 0.0014	108.07 ±10.81
		Mughabghab	(5.81)	(0.0135)	(108.60)
161	3	Present	7.6632 ± 0.0195	0.4284 ± 0.0340	158.01 ± 14.46
		Mughabghab	(7.74)	(0.30)	(107.00)

Table 3. Resonance parameters for Ag isotopes.

Ag Isotope	J	l	E(eV)		Γ_γ (meV)	$g\Gamma_n$ (meV)
107	1	0	Present	-11.142	108.06	14.613
			Landolt-Boernstein	(-11.1)	(141.50)	(24.587)
107	0	0	Present	16.423±0.004	363.54±10.64	1.886±0.028
			Landolt-Boernstein	(16.3)	(134)	(2.917)
107	1	1	Present	18.899±0.140	100.00±10.00	0.000105±0.000011
			Landolt-Boernstein	(18.9)	(100)	(0.000105)
107	1	1	Present	20.323±0.147	99.99±10.00	0.00012±0.00001
			Landolt-Boernstein	(20.3)	(100)	(0.00012)
107	1	1	Present	35.826±0.233	99.997±10.00	0.000286±0.000029
			Landolt-Boernstein	(35.84)	(100)	(0.000285)
107	1	0	Present	41.726±0.0264	163.78±15.68	1.891±0.095
			Landolt-Boernstein	(41.57)	(137)	(4.5)
107	1	1	Present	42.751±0.276	100.00±10.00	0.003511±0.000351
			Landolt-Boernstein	(42.81)	(100)	(0.003495)
107	0	0	Present	45.264±0.118	150.12±14.94	0.462±0.0423
			Landolt-Boernstein	(44.9)	(147)	(0.3)
107	1	0	Present	51.756±0.018	314.97±24.32	7.286±0.219
			Landolt-Boernstein	(51.56)	(133)	(23.4)
107	1	1	Present	64.197±0.428	99.970±9.997	0.01951±0.001950
			Landolt-Boernstein	(64.24)	(100)	(0.018975)
107	2	1	Present	64.565±0.431	99.997±10.00	0.02631±0.000263
			Landolt-Boernstein	(64.74)	(100)	(0.0026)
107	1	1	Present	72.667±0.494	99.981±9.998	0.02722±0.00272
			Landolt-Boernstein	(73.21)	(100)	(0.027)
107	1	0	Present	82.827±0.598	139.07±13.91	0.01403±0.001403
			Landolt-Boernstein	(82.600)	(139.07)	(0.0014)
109	1	0	Present	5.186±0.001	(345.27±3.608)	4.4633±0.00032193
			Landolt-Boernstein	(5.145)	(143)	(9.6495)
109	1	0	Present	30.674±0.011	432.99±24.17	3.3719 ±0.0851
			Landolt-Boernstein	(30.6)	(130)	(6.33)
109	1	1	Present	32.694±0.214	100.09±10.01	0.0068938±0.000690
			Landolt-Boernstein	(32.7)	(100)	(0.0069975)
109	1	0	Present	40.492±0.020	231.62±19.89	2.7860±0.1113
			Landolt-Boernstein	(40.3)	(131)	(3.24)
109	0	0	Present	56.048±0.0318	171.55±16.32	4.8898±0.22453
			Landolt-Boernstein	(55.8)	(139)	(11.623)
109	1	0	Present	71.260±0.038	138.85±13.44	9.725±0.469
			Landolt-Boernstein	(71.)	(120)	(26.019)
109	1	0	Present	88.474±0.336	130.81±13.07	1.6569±0.15893
			Landolt-Boernstein	(87.7)	(130)	(4.70)

The measured total cross-section of Dy in the neutron energy range from 0.025 to 8 eV was compared with the SAMMY fitting results as shown in Fig. 7 (a). The SAMMY prediction of total cross-section and the present data are in good agreement with each other with $\chi^2/N=1.04$. In Fig. 7 (b), the measured total cross section of natural Ag in the neutron energy range from 1 eV to 65 eV was compared with the SAMMY fitting results. The SAMMY prediction of total cross section and the present data are in good agreement with each other with $\chi^2/N=1.41$.

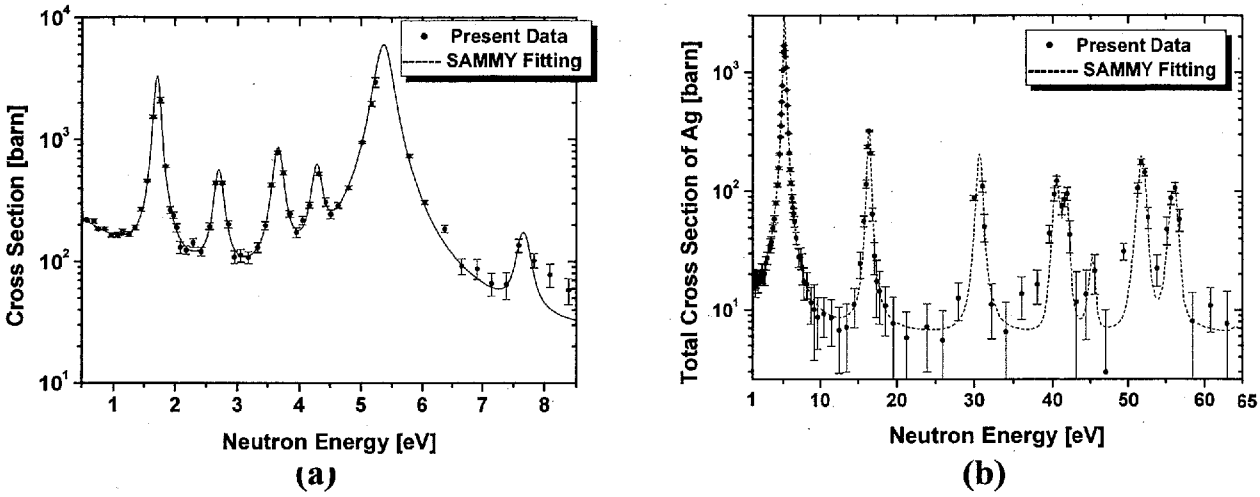

Fig. 7. Comparison of the measured total cross sections of (a) Dy and (b) Ag with the predicted ones from the SAMMY fitting.

V. CONCLUSION

The Pohang Neutron Facility was constructed as a pulsed neutron facility based on an electron linac for producing nuclear data in Korea. It consists of an electron linac, a water cooled Ta target, and an 11-m long TOF path.

The neutron total cross-section of natural W, Ti, Dy and Ag have been measured in the neutron energy region from 0.025 eV to 100 eV by using a ^{6}Li-ZnS(Ag) scintillator and the neutron TOF method. The present results are in good agreement with the evaluated data in ENDF/B-VI and the previous measurements. The resonance parameters of Dy and Ag isotopes have been determined by fitting the transmission data and their results are also in agreement with the previous ones.

ACKNOWLEDGMENTS

The authors would like to express their sincere thanks to the staff of the Pohang Accelerator Laboratory for the excellent electron linac operation and their strong support. This work is partly supported through the Long-term Nuclear R&D program of the Korea Atomic Energy Research Institute and through the Science Research Center (SRC) program of the Institute of High Energy Physics, Kyungpook National University.

REFERENCES

[1] G. N. Kim, J. Y. Choi, M. H. Cho, I. S. Ko, W. Namkung, and J. H. Jang, in *Proceedings International Conference on Nuclear Data for Science and Technology*, edited by G. Reffo, A. Ventura and C. Grandi (Trieste, Italy, May 19-24, 1997), p. 556.

[2] H. S. Kang, J. Y. Choi, Y. J. Park, S. H. Kim, G. N. Kim, M. H. Cho, I. S. Ko, and W. Namkung, in *Proceedings of First Asian Particle Accelerator Conference*, edited by Y. H. Chin, M. Kihara, H. Kobayashi, N. Akasaka, K. Nigorikawa, and M. Tobiyama (Tsukuba, Japan, Mar. 23-27, 1998), p. 743.
[3] G. N. Kim, Y. S. Lee, V. Skoy, V. Kovalchuk, M. H. Cho, I. S. Ko, W. Namkung, D. W. Lee, H. D. Kim, S. K. Ko, S. H. Park, D. S. Kim, T. I. Ro, and Y. G. Min, J. Korean Phys. Soc. **38**, 14 (2001).
[4] W. Y. Baek, G. N. Kim, M. H. Cho, I. S. Ko, and W. Namkung, in Proceedings of Workshop on Nuclear Data Production and Evaluation, edited by J. Chang and G. N. Kim (Pohang, Korea, Aug. 7-8, 1998).
[5] G. N. Kim, V. Kovalchuk, Y. S. Lee, V. Skoy, M. H. Cho, I. S. Ko, W. Namkung, D. W. Lee, H. D. Kim, S. K. Ko, S. H. Park, D. S. Kim, T. I. Ro, and Y. G. Min, Nucl. Instr. Meth. **A 485**, 458 (2002).
[6] MCNP, A general Monte Carlo N-Particle transport code system, Version 4B, Los Alamos National Laboratory, LA-12625-M, (1997).
[7] R. E. Schmunk, P. D. Randolf, and R. M. Brugger, J. Nucl. Sci. Eng. **7**, 193 (1960).
[8] R. E. Chrien, and R. L. Zimmerman, Bull. Am. Phy. Soc., **3**, 19 (1958).
[9] J. A. Harvey, G. G. Slaughter, and R. C. Block, Bulletin of American Physical Society, **3**, 177 (1958).
[10] W. Selove, Phys. Rev. **84**, 864 (1951).
[11] R. F. Ross, ENDF-201, ENDF/B-VI Summary Documentation, BNL-NCS-17541, 4th Ed. (ENDF/B-VI), Brookhaven National Laboratory (1991).
[12] E. G. Joki, J. E. Evans, and R. R. Smith, J. Nucl. Sci. Eng. **11**, 298 (1961).
[13] W. M. Moor, Bulletin of American Physical Society, **6**, 70, (1961).
[14] K. Okamoto, JAERI Report, JAERI-1069 (1964).
[15] V. L. Sailor, H. H. Landon, and H. L. Jr. Foote, Phys. Rev. **96**, 1014 (1954).
[16] J. Brunner and F. Widder, Report EIR-123 (1967).
[17] K. Knorr and W. Schmatz, Atomk-ernenergie **16** (9), 49 (1970).
[18] R. S. Carter, Exfor Data File 11897 (1983).
[19] H. J. Cho, K. Kobayashi, S. Yamamoto, Y. Fujita, Y. S. Lee, G. N. Kim, I. S. Ko, M. H. Cho, W. Namkung, S. K. Ko, Annals of Nuclear Energy, **27**, 1259 (2000).
[20] W. W. Havens, Jr. and J. Rainwater, Phys. Rev. **70**, 154 (1946); W. Selove, Phys. Rev. **84**, 869 (1951); F. G. P. Seidi, D. J. Hugges, H. Palevsky, J. S. Levin, W. Y. Kato, and N. G. Sjostrand, Phys. Rev. **95**, 476 (1954); R. G. Allen, T. E. Stephenson, C. P. Stanford, and S. Bernstein, Phys. Rev. **96**, 1297 (1954); R. G. Fluharty, F. B. Simpson, and O. D. Simpson, Phys. Rev. **103**, 1778 (1956); R. E. Wood, Phys. Rev. **104**, 1425 (1956); K. K. Seth, D. J. Hughes, R. L. Zimmerman, and R. C. Garth, Phys. Rev. **110**, 692 (1958); J. B. Garg, J. Rainwater, and W. W. Havens, Jr., Phys. Rev. **137**, B547 (1965).
[21] N. M. Larson, RSICC Peripheral Shielding Routine Collection SAMMY-M2a: A Code System for Multilevel R-Matrix Fits to Neutron Data Using Bayes' Equations, PSR-158, SAMMY-M2a, Oak Ridge National Laboratory (1999) (unpublished).
[22] C. W. Reich and M. S. Moore, Phys. Rev. **111**, 929 (1958).
[23] F. A. George, "MULTI, A FORTRAN Code for Least-Square Shape Fitting of Neutron Cross-Section Data Using the Reich-Moore Multilevel Formalism," LA-5473-MS, Los Alamos Scientific Laboratory (1974).
[24] S. F. Mughabghab "Neutron Cross-sections," Vol.1, (Academic Press, NY, 1984).
[25] Landbolt-Boernstein/New Series: Numerical Data and Functional Relationships in Science and Technology, Group I: Elementary Particles, Nuclei and Atoms, Volume 16: Low Energy Neutron Physics, Subvolume B: Tables of Neutron Resonance Parameters, (Ed. by H. Schopper, Springer, Feb. 1998), pp. 197.

2.16 Forty Years Experience on Nuclear Data Evaluation (Personal View)

Toru Murata
AITEL corp.; 4-1 Ukishima-cho, Kawasaki-ku, Kawasaki, Japan
murat@green.ocn.ne.jp

Japanese Nuclear Data Committee (JNDC) was organized in 1963. Since then many activities have been made successfully by JNDC. The results of the activities were summarized in chronological table and some remarks based on the forty years experience in evaluation work were described.

1. Evaluation Activities

During the last forty years, JNDC has prepared and released several versions of general purpose neutron nuclear data file JENDL and special purpose data files such as FP decay heat data file, neutron dosimetry, neutron activation, (α,n) reactions and so on. And now JNDC is preparing high energy nuclear data files of neutron and proton incident reactions and photo-reaction data file. Several dozens of researchers, as the JNDC members, attended to the development of evaluation methods, evaluation work, verification of the evaluated data and compilation of the data files, almost as a side job.

Chronological table of these works is shown in Table 1. In the third column of the table, names of main software for the nuclear data evaluation developed or prepared in JNDC are given. These codes were utilized productively to evaluate the nuclear data files shown in the fourth column of the table. Besides these codes, experimental data supplied by several domestic universities and national organizations are great help for JENDL evaluation. These experimental data are

DDX by /Osaka Univ./ Tohoku Univ.
Fission Cross Section by /Tohoku Univ./ Kyoto Univ.
(n,γ) Cross Section by /Tokyo Inst. of Tech./Kyoto Univ./ JNC/ JAERI
Charged Particle Production by /Tohoku Univ./ JAERI,
Charged Particle Reaction by Kyushu Univ.
Resonance Parameter by JAERI
Activation Cross Section by /JAERI/ Nagoya Univ.
FP Decay Heat by Univ. of Tokyo
KERMA Factor by JAERI

2. Some remarks on evaluation work

In the course of evaluation work, some interesting problems are recognized personally in nuclear physics aspects and evaluation support aspect. But, at present, these problems are not solved and left untouched because of lack of ability and spare time. Some of them are described below;

Nuclear physics aspect:

- Resonance analysis,

An approximated R-matrix theory was applied successfully to analyze total cross section of

neutrons incident on ^{14}Nand ^{16}O[2]. The theory also applied to analyze the (α, n) reaction of light nuclides[3]. In the analysis, total width, incident channel width and outgoing channel width are given as parameters besides other resonance parameters. Principally, total width is not a parameter, but determined by sum of all outgoing channels. So, all experimental data of outgoing channels are required for the analysis. For almost cases, it is not practical to acquire all open channel data. Some approximation should be made to obtain partial width for channels of which experimental data are not available.

• Deformed optical potential and single particle states.

Next stage evaluation is planned for fission product nuclides and minor actinides. For these nuclides, optical model potentials will be resurveyed. Structure of reaction cross section is reflected by single particle shell states of the optical model real part potential. As an example, neutron single particle states are surveyed for ^{90}Zr+n. The results are shown in Fig.1. Similar survey will be effective to determine deformed potential depth and deformation. For deformed potential, is there correspondence with Nilsson orbits?

• More elaborate gamma-ray transition model.

Gamma-ray transition probability called Weisskopf units is used frequently in calculation of capture cross section, gamma-ray energy spectrum and so on. However, it is well known that Weisskopf units are differing from experimental transition probability by some order of magnitudes. Empirical distributions of the difference were studied by Wilkinson[5] in 1956. Since then many good experimental data have been accumulated. New study of the empirical distributions would contribute to the development of more elaborate model. If the development of elaborate model will not be attained, new empirical distributions will be integrated in calculation codes of capture cross section and so on.

• Photoreaction sum rule

Though there are plentiful experimental data for photo-neutron production, experimental data of photo-absorption cross section are scarce. With resonance parameters obtained by analysis of photo-neutron cross section, photo-absorption cross section can be calculated assuming photon widths. Photon widths are estimated to reproduce integral of photo-absorption cross section. Integral of photo-absorption cross section are known to be proportional to N*Z/A. Preliminary result is shown in Fig.2. More careful study on the relationship should be made.

• Fission cross section analysis.

JNDC has not yet cross section calculation code including fission process with double humped fission barrier.

• Calculation of number of fission neutron (ν_p and ν_d).

For high energy file and photo-reaction file, ν_p and ν_d should be estimated in the incident energy region over 20 MeV. Is there simple model or systematics to estimate the quantities?

Evaluation work aspect:

• Automatic reading of experimental data shown in figures

For neutron incident data, EXFOR file includes almost experimental data as numerical data. But for charged particle incident data, in many cases, we must read the values in a figure.

• Dialogue type easy system to make ENDF format files.

ENDF format is complicated and to make the file, we must consult with the manual and it is very time consuming and tedious labor.

• More effective and rapid accomplishment of evaluation work.

To attain this problem, some system, management and/or tools should be studied.

Table 1 Chronological Table of JNDC (an abbreviation of table of ref. 1)

Year	JNDC	Codes for Eval.	Evaluation
1963	organized by JAERI and AESJ*	ELIESE	
1965	1st seminar on ND		
1966	1st JNDC News		1st eval.(σ_{total} of C+n)
1968	ND Lab.		
1969	Sub-Com.on ND, and Reactor Const.		
1970			JENDL eval. started
1972			28FPND
1973	Sub-Com.on N.Fuel Cycle	CASTHY,SPLINT	JENDL-1planned
1974		(DWUCK4)	JENDL-0
1976	ND center		1st Chart of Nuclides, Benchmark test of JENDL-1
1977	Mass Chain eval.took part	(GNASH)	JENDL-1 released(72nuclides), JENDL-2 planned
1978	1st Nuclear Data symposium	NDES	
1979			JENDL-3 planned
1981		ASREP	FP decay data file 1
1982		CLUSTR, Simul.CS.eval.code	JENDL-2 released(89nuclides)
1984			100FPND
1985	JENDL-2 awarded by AESJ(special prize)		
1987		PEGASUS	(α ,n) data eval.started
1986	Special Purpose File Promotion Report		
1988	Mito Int.Conf. on Nuclear Data	(ECIS88),SINCROS	FP decay data file 2
1989		(GMA)	JENDL-3 released(171nuclides)
1990			JENDL-3.1(324)
1991	Standardization of FP decay data awarded by AESJ		Dosimetry file, Gas prod.file released
1993	High Energy File WG	ALICE-F	
1994			JENDL-3.2released(340nuclides)
1995	ND Center home page		
1996			Activation file96
1997		KALMAN	
1999			Fusion File99
2000		SOC,DSD	FP decay data File 2000
2001	Tsukuba Int.Conf. on Nuclear Data	QMD/JAM	
2002			JENDL-3.3released(337nuclides)
2003			(α ,n) data file released, Photo-react.,HE File in preparation.

* AESJ: Atomic Energy Society of Japan

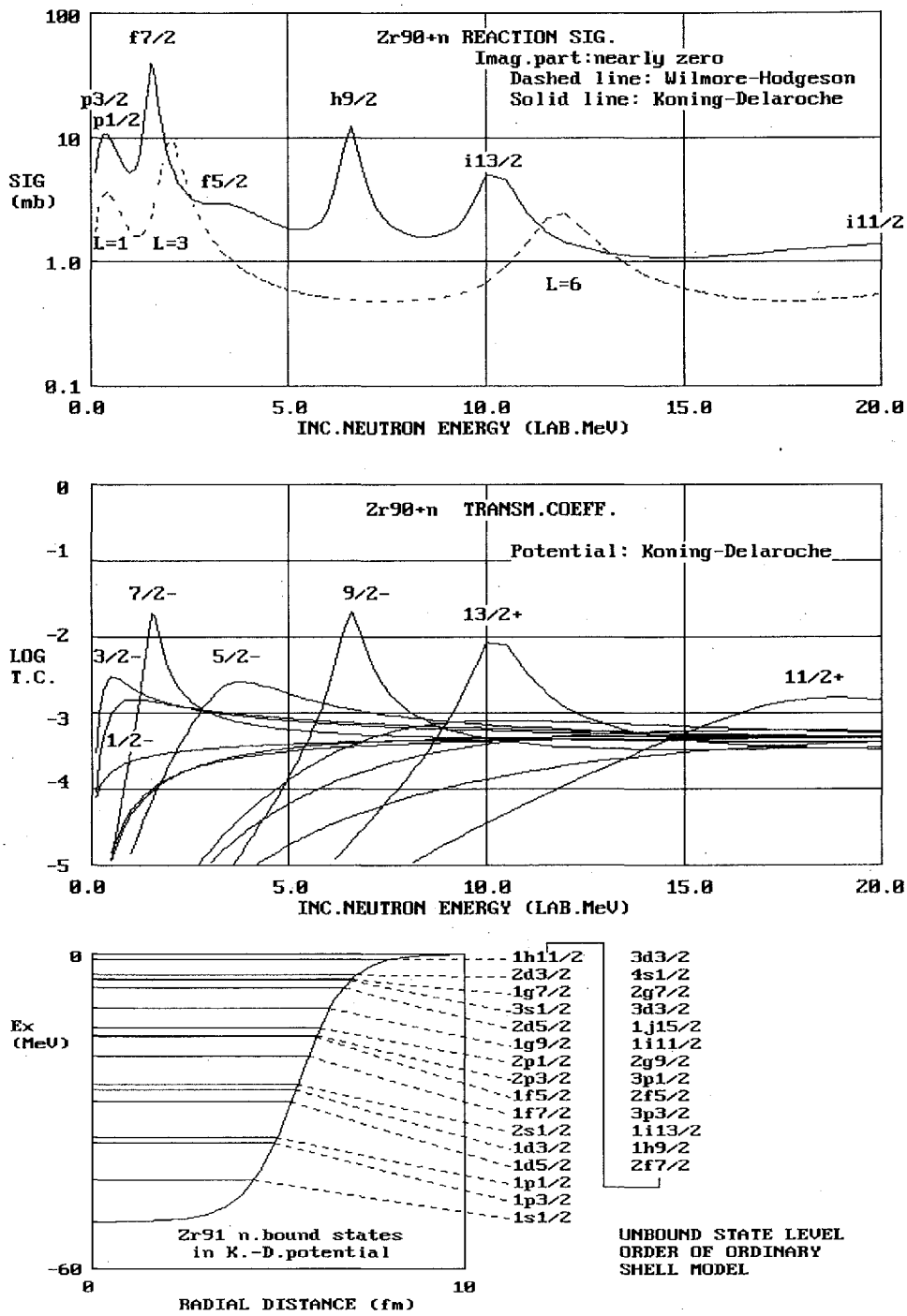

Fig.1 Top: Compound nucleus formation cross section calculated with Koning-Delaroche[4] and Wilmore-Hodgson (no $\ell \cdot s$ term) potential for imaginary potential nearly zero.
Middle: Transmission coefficients for Koning-Delaroche potential for determination of shell model states of peaks in the top figure.
Bottom: Shell model states of bound states in Koning-Delaroche potential and unbound ordinary shell model states with ℓ^2 term. Some correspondences are recognized with the states in the top figure.

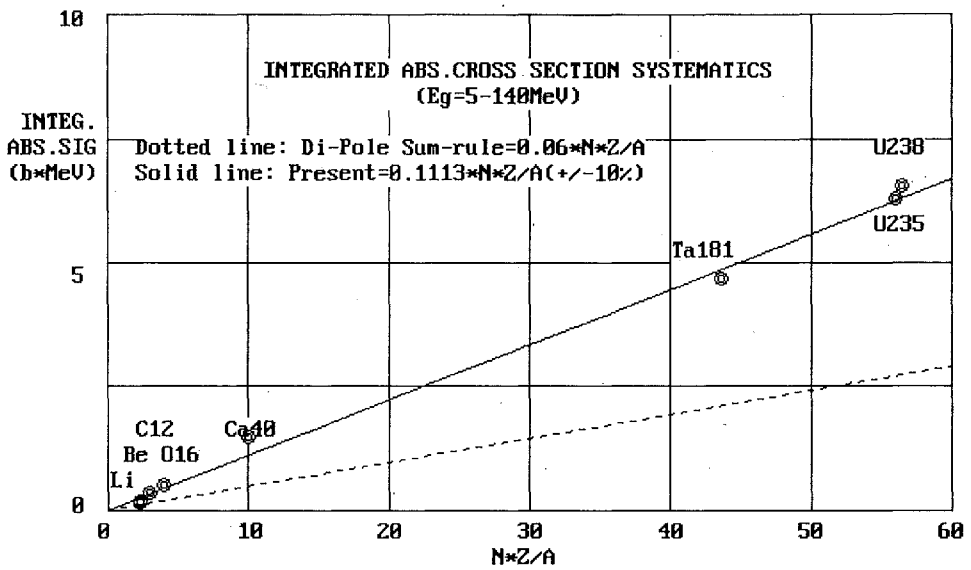

Fig.2 Integrated photo-absorption cross section systematics, In abscissa N, Z and A are neutron, proton and mass number of target nucleus, respectively.

Acknowledgements

Thanks are due to Dr. T. Nakagawa (JAERI) for helpful discussion and preparation of related material.

References

1) Nakagawa, T. : Kaku Data News No.74,21(2003) (in Japanese)
2) Murata, T. : Proc. Int. Conf. Nuclear Data for Sci. and Tech., Mito, 1988, p.557
3) Murata, T., Shibata, K. : Proc. Int. Conf. Nuclear Data for Sci. and Tech., Tsukuba, 2001. p.76
4) Koning, A. J., Delaroche, J.P. : Nucl. Phys., A713, 231 (2003)
5) Wilkinson, D. H.: Phil. Mag. [8] 1,127 (1956), summarized in "Nuclear Spectroscopy" edited by F.Ajzenberg-Selove, part B, p.852

JP0450489

JAERI－Conf 2004－005

2.17 JENDL Reactor Constant and its Application

::::::: The 40th Anniversary of Japan Nuclear Data Committee :::::::

Atsushi ZUKERAN

Power & Industrial System R&D Laboratory, Hitachi, Ltd.,
7-2-1 Omika, Hitachi 319-1221, Japan
e-mail: atsushi_zukeran@pis.hitachi.co.jp

Abstract

The status of reactor constants about 27 years ago is briefly reviewed from the criticality predictions and nuclear data processing codes. In the second section, status of current users of JENDL-3.3 and/or JENDL-3.2 is consulted with the 2003 Fall Meeting of Atomic Energy Society of Japan. In the third section, the reliabilities of JENDL-3.3 and -3.2 are reviewed mainly from the application to light water reactor (LWR) mockup experiments; MISTRAL and BASALA made on EOLE critical facility of Cadarache Laboratory in France, since an extensive evaluation for nuclear data applicability to LWR have been scarcely performed in relative to for FBR. The results of international benchmark cores and criticality safety analyses are briefly reviewed. In the concluding remarks, overall applicability is shown as a summary with respect to all reactor parameters obtained in the LWR mockup experiment and some remarks are noted.

I. A Glance of the History of Reactor Constants

The activity of the 40 years of JNDC should be faithfully celebrated and highly appreciated, and I would say "Congratulations!, so long time for nuclear data". In this period, some files in the world ended and some new ones like CENDL were born. Our JENDL is a highly qualified and big file compared to ENDF/B and JEFF. The contents of these files have been significantly enriched, and currently the energy range is extending so as to dealing with the neutronics of ADS and the other application is for astrophysics.

On the other side, reliability of reactor constants is increasing together with the brushing up of the evaluated nuclear data files. Following two examples show a typical status of reactor constants used for nuclear performance parameters about 30 years ago.

(a): International Intercomparison

International intercomparison of LLMFBR nuclear characteristics[1)] had been conducted by ANL. Sixteen participants, as shown below, had calculated overall nuclear performance parameters of large sodium cooled fast breeder reactor by using their own libraries. The results were intercompared and discussed at ANL(Chicago) (1978).

USA(ANL)[ENDF/B-VI], USA(HEDL)[ENDF/B-VI], Belgium[KEDAK-2], France[CARNAVAL-III,IV], Italy[ENDF/B-IV], Switzerland[ENDF/B-III,-VI], Japan[JENDL,JAERI-FAST-2,GJAERI-FAST-2(25)], Germany[KEDAK-3,KFKINR], Sweden[ENDF/B-III], England(UKAEA)[FGL-5], USSR[BNAB-70]

where Country[data set], and the mean k_{eff}-value, $\overline{k}_{eff}$, and its standard deviation was

$\overline{k}_{eff} = 1.00000 \pm 0.01292$,
with the maximum $(k_{eff} - \overline{k}_{eff}) = 0.151\%$ and minimum $(k_{eff} - \overline{k}_{eff}) = -2.458\%$.

The standard deviation of ±0.01292 is seemed to be about twice of current deviation even if similar comparison was taken place at present.

(b): MOZART Project

The first LLMFBR Mockup experiment in JAPAN, namely MOZART(**M**onju **Z**ebra **A**ssembly **R**eactor **T**est)[2] project had been performed in ZEBRA critical assembly of Winfrith (UK). The MOZART experiment analyses were made by six domestic participants with their libraries; JAERI[JAERI-FAST], Hitachi[HIM-2], Toshiba[NNS-2], Mitsubishi[MICS-V/2], Fuji[FX-2] and Sumitomo[SEAI]. The JAERI-Fast set was based on their own evaluated nuclear data, but the other five domestic libraries were so-called modified Abagyan Set since at that time the text book for this library was available in JAPAN and it had been modified taking into account ENDF/B-I with ETOX nuclear processing code. The final recommended k_{eff} was

k_{eff} (C/E) $= 0.9973 \pm 0.0033$ for MZA Core (approximately spherical core),
k_{eff} (C/E) $= 0.9972 \pm 0.0034$ for MZB Core (cylindrical core for MONJU physics mockup).

These C/E-values are significantly close to unity within about ±0.3% which are better than those of current benchmark test and experiment analyses mentioned later. For the MOZART case, consistency between mockup and calculated cores was deeply investigated and twelve corrections were applied.

Comparing the (a)'s k_{eff}-values with the current results shown by Figs. 1 and 3, the reliability of k_{eff} prediction has been improved with time. The trend approaching forward unity, however, seems not to be monotonous, and some fluctuation in the process of updating version is found.

II. JENDL-3.3 Users

1. Users in the 2003 Fall Meeting of the Atomic Energy Society of JAPAN

The users in the reactor physics session of the 2003 Fall Meeting[3] were consulted and the following statistic was obtained as

Table 1 JENDL-3.3 and/or JENDL-3.2 Users

Nuclear Data	Presentations	Fraction (%)	Note
JENDL-3.3 and -3.2	4	29	Mainly MISTRAL, BASALA and BFS analyses.
JENDL-3.2	9	64	PIE data analysis included, see summary.
ENDF/B-VI	1	1	BWR core simulation: 3 group kinetics model.

where SRAC and/or MVP libraries are used except ENDF/B-VI case. JENDL-3.3 reactor constants are not yet widely used since SRAC and MVP libraries have been recently released.

2. Users in FBR project

JNC provides multi-group cross section library based on JENDL-3.3 and -3.2 for FBR Project. They say the 900-group constant is available ,where hyperfine group effect is taken into account by bi-mixture slowing down code PEACO. Besides, they have a unified cross section set ADJ200R based on the cross section adjustment.

Therefore, as long as FBR project, only one reactor constant set given by JNC is commonly used. The newest version of JENDL-3.3 will be cited for their future library although the current adjustment was applied for JENDL-3.2.

3. Users in LWR project

No standard or common used reactor constant, at present, is available for LWR reactor, but as shown in section III.2 SRAC and MVP with their cross section libraries have been commonly used like

a standard library in many universities and organizations such as NUPEC (Nuclear Power Engineering Corporation). Analyses of LWR mockup experiments MISTRAL and BASALA[4,5] of Section III are typical examples for SRAC and MVP.

Individual cross section library used for BWR, PWR core designs and fuel management seems to be produced from JENDL-3.3 or -3.2 file but detailed information isn't opened.

III. Applicability of JENDL Reactor Constants

1. Benchmark Test

Criticality benchmark test for well known fourteen cores were made by Takano et al,[6] where continuous energy Mote Carlo code MVP with JENDL-3.3 nuclear data was used. Resultant k_{eff}'s are shown in Fig.1.

The calculated to experiment ratio (C/E) and their standard deviation is approximately

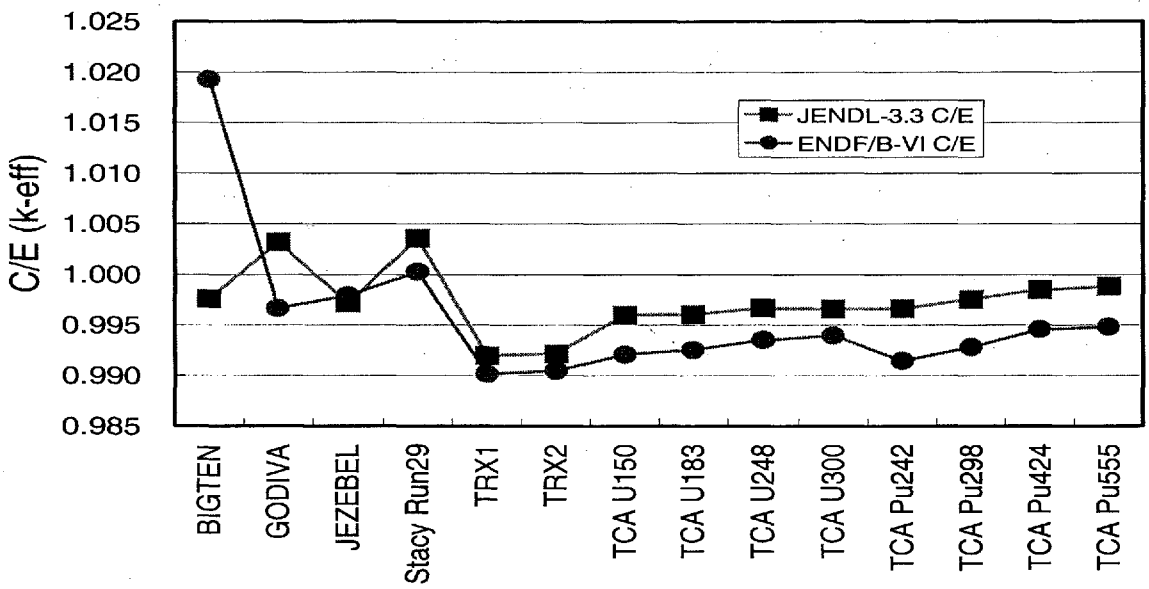

Fig. 1 The C/E values for thermal cores calculated with JENDL-3.3 and ENDF/B-VI.5

$$k_{eff} \quad C/E - value \simeq 1.000 \pm 0.005$$

where the TRX-1 and -2 cores are excluded since their k_{eff}'s may be improved by more careful treatment of ^{238}U cross sections by taking into account hyperfine group effect. Therefore, the current reliability of JENDL-3.3 for criticality may be within ±0.005.

2. MISTRAL and BASALA MOX Physics Mock-up Experiment

(1) Core Specifications in MISTRAL and BASALA MOX Physics Mock-up Experiments

Some mockup experiments focusing on the fast reactor such as MONJU had been carried out for overall core performance parameters so far. For light water reactors, however, such mockup experiment had never been extensively performed, although well known benchmark cores like those used by H. Takano et al[6] as well as experiments for a few parameters in TCA or FCA of JAERI are available

Recently, MOX core physics mock-up experiments MISTRAL and BASALA[4,5] had been doned in the EOLE Light Water Critical Facility at Cadarache Lab. of CEA, France, where overall nuclear performance parameters as shown in Table 2 are measured. For instance, reactivity worth of a cruciform

BWR control blade shown in Fig.2 as well as effective delayed neutron fraction β_{eff} were obtained.

The analyses have been made by NUPEC with four organizations, and serious evaluation of the applicability of nuclear data and codes to LWRs fueled with partial or full MOX has been made. The detailed C/E-values of overall nuclear performance parameters are shown in detail in references 4) and 5), and thus the results are shortly summarized in Table 3 where results of criticality safety[7] and PIE data analysis[3] are shown together.

Table 2 Nuclear Performance Parameters measured in MISTRAL and BASALA Cores[4,5]

Item	MISTRAL Core				BASALA Core	
	Core 1	Core 2	Core 3	Core 4	Core 1	Core 2
Core Specification	UO2 -Homo.	MOX -Homo.	MOX -Homo.	PWR Mockup	BWR Mockup	BWR Mockup
Water to Heavy Metal(H/HM)	5.1	5.2	6.2	5.8	5.0	9.0
Water to Fuel Vol.frac.	1.8	1.8	2.1	2.0	1.7	3.1
Fuel pitch(cm)	1.32	1.32	1.39	1.32	1.13	1.35
Enrichment (to Total Pu)	UO2 3.7%	MOX 7.0%, etc.	MOX 7.0%	MOX 7.0%	MOX 7%, etc.	MOX 7%, etc.
(1): Critical Mass	○	○	○	○	○	○
(2): Boron Concentration	○	○	○	○	—	—
(3): Buckling	○	○	○	—	—	—
(4): Spectrum Index	○	○	○	—	—	—
Power Distribution						
(5): Radial	○	○	○	○	○	○
(6): Axial	○	○	○	○	○	○
(7): Isothermal Temp. Coeff.	○	○	○	—	—	○
Reactivity Worth						
(8): Boron	○	○	○	○	—	○
(9): Absorvers	○ (4 Types)	○ (4 Types)	○ (2 Types)	—	—	—
(10): Burnable Poison	—	—	—	—	○	○
(11): Cluster Control Rod	—	—	—	○	—	—
(12): Criciform Control Blade	—	—	—	—	—	○
(13): Two Dimensional Void	—	—	○	—	○	—
(14): Water Hole	○	○	—	—	—	—
(15): Water Rod	—	—	—	—	○	—
(16): β_{eff}	○	○	—	—	—	—

○ : Measurement was performed.

(2) Analyses of MISTRAL and BASALA Experiments

Nuclear data used for analyses are mainly JENDL-3.2 and -3.3, and partially ENDF/B-VI and JEF-2.2. The application of JENDL-3.3 is also limited to k_{eff} and spectrum index since the release of the JENDL-3.3 cross section libraries was on the way of experiment analyses.

Core and/or cell calculation codes are SRAC diffusion (CITATION) and transport (TWOTRAN) routines, and continuous energy Monte Carlo code MVP was also used as shown in Table 3. Thermal cut-off energy of 1.82 eV is optimized so as to take into account ^{240}Pu resonance and effective energy range of up-scattering.

Geometrical calculation models for MVP were as built as experiment. For analysis by SRAC, two dimensional XY geometry for a quarter of core is basically used when the 1/4 symmetry exits, while the two dimensional XY geometry for full core was employed for non-1/4 symmetry core. Then, experimental axial buckling was applied to Z-axes, and sixteen group cross section set was prepared by group collapsing from PEACO hyperfine group cross sections. For integral boron worth, three dimensional XYZ geometery for a quater of core was adopted.

Table 3 Nuclear Data and Reactor Constant

a)	Nuclear Data: JENDL-3.2 and Partially JENDL-3.3
b)	Group Constant SRAC 107 group set ⟸ Spectrum Index(5X5Rods) 16 group set condensed from PEACO hyperfine group cross sections and neutron spectra ⟸ Single Ros Cell: Fuel+Clad+Overclad+Moderator Thermal cut-off=1.82 eV
c)	Cell Calculation SRAC 107 group set Pij-method
d)	Core Calculation SRAC-CITATION -TWOTRAN MVP: History: $10000 \times 1000 = 10^7$, Criticality: $\frac{\Delta k}{k} = 0.02\%$, Power Distribution: $\frac{\Delta P}{P} = 1\%$

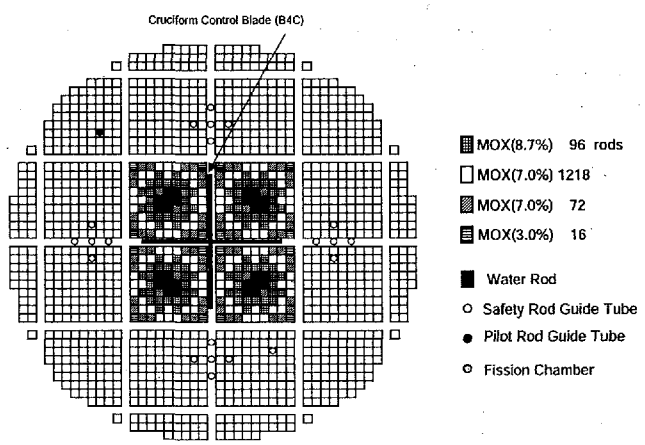

Fig. 2 BASALA Core 2 with Cruciform Control Blade for BWR

(3) Results of MISTRAL Experiment, BASALA Experiment, Criticality Safety and PIE Data Analyses

The results of experiment analyses are shown in references 4) and 5) in detail, and a short summary is shown in Table 4 where discrepancies in unit of experimental error are shown. Only k_{eff} trends are shown in Fig. 3 for individual critical core and five nuclear data files.

As shown in Fig. 3, the k_{eff}-values for MOX cores are increasing with core from about 1.0032 of MISTRAL Core 4 (UO2-REF) to 1.0074 of BASALA Core 1, although k_{eff} for UO_2 core is around unity. The increment of k_{eff} is expected that the transmutation effect from ^{241}Pu with half-life = 14.290 y to ^{241}Am. This effect has been already corrected for Fig. 3. The effect, however, could not flatten the k_{eff} trend. Further study has been continued and thus the reason of increment will be made soon clear.

In order to interpret above increasing trend, the transmutation effect to the neutron balance is intuitively formulated and the following expression can be obtained

$$\frac{\delta keff}{keff} = \left\{ \frac{\nu\sigma_f^{Am241} - \nu\sigma_f^{Pu241}}{\nu\sigma_f^{Pu241}} \cdot \frac{<\nu\Sigma_f\phi>^{Pu241}}{<\nu\Sigma_f\phi>} - \frac{\sigma_a^{Am241} - \sigma_a^{Pu241}}{\sigma_a^{Pu241}} \cdot \frac{<\Sigma_a\phi>^{Pu241}}{<\Sigma_a\phi>} \right\} \times \{1 - exp(-\lambda^{Pu241}t)\}; \quad (1)$$

where λ^{Pu241} means ^{241}Pu decay constant for half-live=14.290 y, $<\nu\Sigma_f\phi>$= Total neutron production reaction rate and $<\nu\Sigma_f\phi>^{Pu241}$= ^{241}Pu neutron production reaction rate. Eq.(1) means that the changes of effective neutron production and absorption cross sections take place between ^{241}Am and ^{241}Pu, and their effect to k_{eff} is given by the multiplications of fractional isotopic reaction rates, and the second term with the decay constant of ^{241}Pu is increasing function, similar trend to Fig. 3, with respect to time t in the range from 0(EPICURE MH1.2) to about 7(BASALA Core1) years. In the MISTRAL and BASALA experimental analyses, direct k-difference method was used instead of this simple expression.

The k_{eff} for criticality safety is shown in Table 4, k_{eff} = 1.0007 ± 0.0011 for 39 LEU-SOL-THERM Benchmark Configuration and , k_{eff} = 0.9980 ± 0.0019 for 24 LEU-COMP-THERM Benchmark Configuration, respectively, i.e. the criticality is fairly well predicted within ±0.2%.

As mentioned previously, JENDL3.3 had been used only for the k_{eff}'s for all cores and the spectrum indexes of the MISTRAL cores because of the release time of SRAC and MVP libraries. For the spectrum index, the fission reaction rate ratio of U-238 to U235, denoted by F28/F25, is about 28% underestimation (= 0.72 ± 1.8%) and similarly for those of Pu240 to Pu239 (F40/F49) is about 11% underestimated (= 0.89 ± 2.8%) beyond the experimental errors, In general such a threshold reaction is generally difficult to enter into an agreement with the experimental data because it is significantly affected by the higher energy flux, while the other non-threshold reaction are predicted within experimental errors.

As summarized in Table 4, the other nuclear performance parameters are well predicted by JENDL-3.3 or -3.2 nuclear data. Typical example is the reactivity worth of cruciform B_4C control blade for BWR whose (C/E-1)-value is within experimental error (6%), and also the effective delayed neutron fraction is fairly well predicted.

The analysis of PIE data for a BWR core in FUKUSHIMA site gives well agreement of atomic

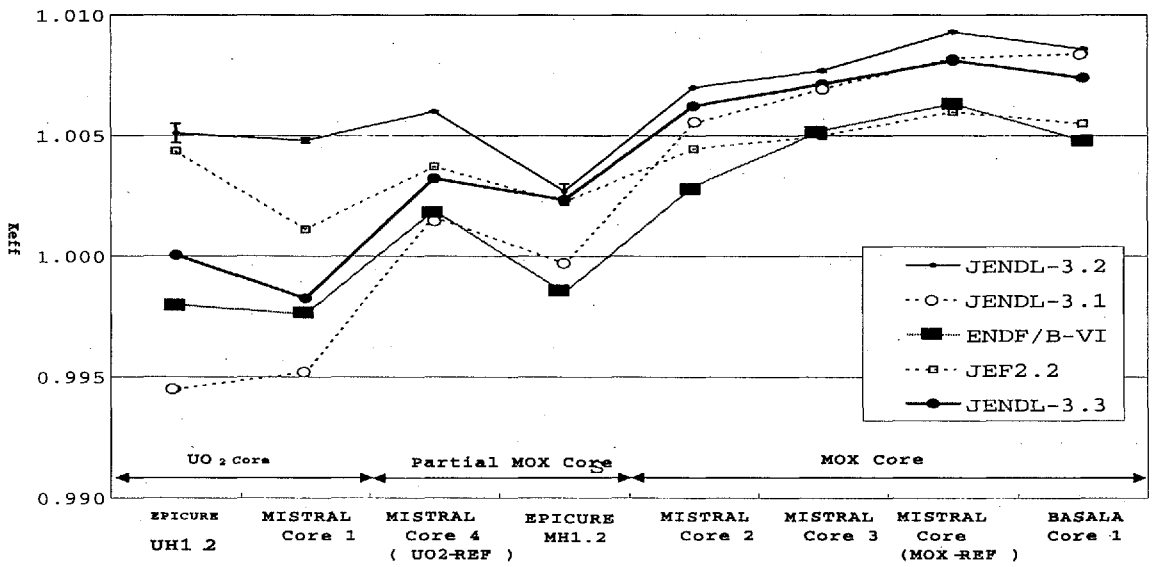

Fig. 3 Criticalities of EPICURE, MISTRAL and BASALA Cores

number densities with the experimental data except ^{241}Am.

Table 4 Summary of Benchmark Test, MISTRAL, BASALA, Criticality Safety and IPE Data Analysis

No.	Quantity	Reliability
(1)	Criticality	—(J3.3) Takano Benchmark Test: K_{eff} C/E$\simeq 1.0000 \pm 0.005^{*)}$ —(J3.3) MISTRAL and BASALA: K_{eff} C/E$\simeq 1.0000^{+0.0081^{*)}}_{-0.0017}$,where the lowest and highest dicrepancies are shown as errors. —(J3.3) Criticality Safety: $K_{eff} = 1.0007 \pm 0.0011$ for 39 LEU-SOL-THERM, $K_{eff} = 0.9980 \pm 0.0019$ for 24 LEU-COMP-THERM
(2)	Boron Concentration	Integral Worth $\lvert C/E - 1\rvert \leq$Exp. error$\simeq$ 5.3% except Core 4 with 10% overestimation
(3)	Spectrum Index	—(J3.3) $\lvert C/E - 1\rvert \leq$Exp. error (2.4 $\sim$ 7.6%), except F28/F25= 0.72 $\pm$ 1.8$^{\dagger)}$% (Exp.Error=10%) and F40/F49= 0.89 $\pm$ 2.8% (Exp.Error=5.9%), $^{\dagger)}$:MVP statistical error
(4)	Conversion Factor	—(J3.2) $\lvert C/E - 1\rvert \leq$Exp. error (1.4 $\sim$ 3.0%)
(5)	==== Power Distribution ====	
(5.1)	Radial	—(J3.2) $\lvert C/E - 1\rvert \leq$Exp. error $\simeq$ 1.5%
(5.2)	Axial	—(J3.2) $\lvert C/E - 1\rvert \leq$Exp. error $\simeq$ 1.5%
(6)	Isothermal Temperature Co-efficient	—(J3.2) $\lvert C/E - 1\rvert \leq 2\times$ Exp. error (gaussed from figure)
(7)	==== Worth ==========	
(7.1)	Absorvers	—(J3.2) $\lvert C/E - 1\rvert \leq$Exp. error $\simeq$ 6.8 $\sim$ 13%, except UO_2-Gd_2O_3 C/E= 1.13 $\pm$ 8.2% in MISTRAL Core 3
(7.2)	PWR Cluster Control Rod	—(J3.2) $\lvert C/E - 1\rvert \leq$Exp. error $\simeq$ 6%
(7.3)	BWR Cruciform Control Blade	—(J3.2) $\lvert C/E - 1\rvert \leq$Exp. error $\simeq$ 6%
(7.4)	Void	—(J3.2) $\lvert C/E - 1\rvert \leq 2\times$ Exp. error $\simeq$ 12%
(7.5)	Water Hole	—(J3.2) $\lvert C/E - 1\rvert \leq 2\times$ Exp. error $\simeq$ 14%
(8)	β_{eff}	—(J3.2) $\lvert C/E - 1\rvert \leq 2\times$ Exp. error $\simeq$ 3.2%
(9)	Analyses of PIE data$^{\sharp)}$	Isotopic Weight $(C/E) \pm 1\sigma(standard\,deviation)$ ^{234}U=1.05 $\pm$ 0.04, ^{235}U=1.04 $\pm$ 0.03, ^{236}U=0.94 $\pm$ 0.01, ^{238}U=1.00 $\pm$ 0.00, ^{238}Pu=0.94 $\pm$ 0.09, ^{239}Pu=0.99 $\pm$ 0.04, ^{240}Pu=0.99 $\pm$ 0.02, ^{241}Pu=0.96 $\pm$ 0.04, ^{242}Pu=0.92 $\pm$ 0.03, ^{241}Am=1.04 $\pm$ 0.24, well agreement, but larger calculational error for ^{241}Am because of missing power history effect to burn up process.

$^{\sharp)}$:Presentations by M. Sasagawa, T. Yamamoto, M. Sugawara and M. Yamamoto as D41 of the 2003 Fall Meeting of the Atomic Energy Society of Japan.

Remarks

[1]: Further analysis by using JENDL-3.3 library: JENDL-3.3 reactor constants not yet fully used.

[2]: Except k_{eff} and spectrum index, JENDL-3.2 and/or -3.3 fairy well predict reactor parameters, as shown in the summary Table 4. The overestimation of K_{eff} with the time as shown in Fig. 3 should be further studied. The k_{eff} deviation from JENDL-3.2 to -3.3 mainly comes from the ^{235}U's less neutron production rate by amount of -0.5%, ^{238}U more by +0.25, and ^{239}Pu more +0.12%, while ^{240}Pu less absorption rate by -0.25% and ^{241}Am more by +0.25% which are in cancellation each other.

[3]: The k_{eff}-value is jumping up and down depending on the revision of JENDL and its monotonous improvement cannot be expected. That may imply a limitation of k_{eff} prediction accuracy of about 0.5%. The k_{eff} is most important and basic quantity, and it is a result of the best balance of reaction rates among overall contributions from many constituent isotopes. Consequently, it is very sensitive to small perturbation destroying the balance. Therefore, in order to keep the best balance, equally and highly graded nuclear data of all isotopes are unavoidable. In the same sense, resonance parameters of fuel isotopes are key quantities to be continuously and carefully evaluated. Therefore, sensitivity approach should be adopted even for nuclear data evaluation as well as the cross section adjustment. If current C/E-value is a limitation of approaching from nuclear data side, the cross section adjustment method will be effective in order to guarantee practical accuracy.

[4]: Cell and/or core calculation code: As shown in Section II.1, general purpose neutronics calculational code SRAC and Monte Carlo code MVP are widely used by many users like standard codes. No problem has been found so far. Therefore, these codes and their cross section libraries can be nominated as the standard cross section libraries in Japan, since a study of standardization has been made by the Standard Cross Section Working Group of JNDC.

ACKNOWLEDGMENTS

The author is grateful to Dr. T. Yamamoto of JNES (Japan Nuclear Engineering and Safety Organization) and Dr. M. Sasagawa of NUPEC (Nuclear Power Engineering Corporation) for their kind suggestion with respect to the documents of MISTRAL and BASALA project, and also Dr. K. Ishii of Hitachi for his helpful discussions.

References

1) L.G.LeSage, R.D. McKnight, D.C. Wade, K.E. Freese, and P.J. Collins, "Proceedings of the NEACRP/IAEA Specialist Meeting on the INTERNATIONA COMPARISON CALCULATION OF A LARGE SODIUM-COOLED FAST BREEDER REACTOR," *ANL-80-78/NEA-CRP-L-243,* 1 (1978).
2) Atsushi ZUKERAN, Teruji INOUE, Takeo SUZUKI and Kanau KAWASHIMA, "Mockup Critical Experiments for Prototype Fast Breeder Reactor MONJU", *Review, Trans. At. Energy Soc. Japan,* Vol.18,No.11 pp.672～684, (1976).
3) Presentations from D31 to D48 in the Reactor Physics and Deign Session of the 2003 Fall Meeting of the Atomic Energy Society of Japan, Japan Atomic Energy Society, (2003).
4) Kazuya ISHII、Masahiro TATSUMI,Taro KAN、Yoshihira ANDOU、Toru YAMAMOTO、Yutaka IWATA, Takuya UMANO、Ryoji KANDA、"Analysis of MOX Core Physics Experiment MISTRAL", Technical Report, Trans. At. Energy Soc. Japan, Vol.2,No.1, pp.39≃ 54, (203).
5) Nuclear Power Engeering Corporation(NUPEC), "Research Report for Nuclear Reactor Cores efficiently using Plutonium Fuel" (in Japanese,"*Plutonium Yuukou Riyou Roshinn Gijyutu Chousa ni kannsuru Chousahoukokusyo*"), (2003).
6) Hideki TAKANO, Tsuneo NAKAGAWA and Kunio KANEKO, "Nuclear Data News", *No.72, P.12 (2002).*
7) A.C. Kahler, "Mote Carlo Eigenvalue Calculations with ENDF/B-VI.8,JEFF-3.0 and JENDL-3.3 Cross Sections for Selection of International Criticality Safety Benchmark Evaluation Project, Handbook Benchmarks", Nucl. Sci. Eng., **145**, pp. 213～ 224 (2003).

JP0450490

JAERI－Conf 2004－005

2.18 What JNDC should be in the Future?

Tadashi Yoshida

Musashi Institute of Technology, Tamazutsumi 1-28-1, Setagaya-ku, Tokyo 158-8557, Japan
e-mail: yos@ph.ns.musashi-tech.ac.jp

It is well recognized that Japanese Nuclear Data Committee, or Sigma Committee, contributed greatly to establish the solid basis of the Japanese nuclear science and technology. In 2002, JNDC completed JENDL-3.3 in close cooperation with the Nuclear Data Center of JEARI and is now ready to go on the JENDL-4 project. The ground on which the JNDC stands, however, have gradually been changed and the now the two research-and-development organizations, JAERI and JNC, are going to be united into one organization. In these backgrounds what JNDC should be in the future beyond these several years of big change must be defined. In order to discuss this issue a new Ad Hoc Committee was established and was asked to report on the future vision of JNDC. As an interim report, several plans and the main points of discussion in the Ad Hoc Committee is presented.

1. Introduction

The Japanese Nuclear Data Committee (JNDC) was established in 1963 and it has been playing a key role in developing the evaluated nuclear data libraries ranging from JENDL-1 to JENDL-3.3. Not only these libraries but various Special Purpose Files such as FP Decay Data File, Activation Cross Section File, High Energy File and so on, and a lot of related publications in addition, are the fruits of the close and excellent collaboration between JNDC and the Nuclear Data Center (NDC) of the Japan Atomic Energy Research Institute (JAERI). These libraries and files constitute a versatile and user-friendly data basis for nuclear science and technology. The committee also conducted long-term consecutive works such as compilation and evaluation of the nuclear structure and decay data for Nuclear Data Sheets. In this way the activities of JNDC made a huge contribution to the peaceful use of the nuclear energy in this country. Now at the beginning of the 21st century, advanced utilization of light water reactors and accomplishment of the nuclear fuel-cycle are being elaborated and there exist a further challenge for the innovative fission reactors deployable after 2030 when the reactors currently in operation start to fulfill their lifetimes. Technologies expected to realize these goals require more reliable and versatile nuclear data and this is why the activity of JNDC must still be continued toward the future.

2. Current Situation of JNDC

The committee, JNDC, which is known domestically as the *Sigma Committee*, has been working almost on the voluntary basis with partial but persistent financial support from JAERI. JNDC has rather a complex organization. On the one hand, it is one of the Special Committees of Atomic Energy Society of Japan (JNDC/AESJ), and one of the Research Committees of JAERI (JNDC/JAERI) on the other hand. In the course of years of its activity this duality worked favorably making the collaboration among the private, the academic and the governmental sectors very effective and smooth. With the help of this kind of the structural merits as well as the zeal of the participants JNDC has long been active and productive. It is, however, recognized that JNDC is now turning a corner after the four decades of its successful history. The most influential factor is the unification of JAERI and JNC (Japan Nuclear Cycle development Institute) anticipated in two years. It is still an

open question what part the JNDC/JAERI will take in the regime of the new organization. It is easy to see that this issue affects the fundamental ground of the JNDC activity. The recent change in the way of governmental funding to scientific activities is the second important concern we must think about. The funding is becoming more project-oriented and competition-based. This trend makes it difficult for the basic and long-term activity like production and the evaluation of nuclear data to be persistently funded. The third concern is the aging of the members of the Sigma committee.

On the other hand, Ad Hoc Committee on Next Generation JENDL chaired by K. Shibata reported on July 2003 that the next generation General Purpose Library, JENDL-4, must be produced and that JENDL-4 should possess higher quality than ever for the wider range of users from nuclear technology to medial and physical science. In the report[1] to the Head of NDC they give specifications of JENDL-4 in a detailed way. To achieve this goal, they describe, JNDC should optimize its organization flexible enough to cope with the difficulties brought about by the recent circumstances surrounding the nuclear science field.

3. Discussion on the Future of JNDC

As described in the preceding section, the ground on which the Japanese nuclear data community stands has gradually been changed and now the two research-and-development organizations, JAERI and JNC, are going to be united into one organization. JNDC, if it has to be active and productive still in the future, has to cope flexibly with this new situation. In this context, a new Ad Hoc Committee was established this year to discuss the future vision of JNDC. It was required to report the conclusion to the Head of NDC/JAERI by the end of fiscal year 2003. The members of the Ad Hoc Committee on the Future of JNDC are as follows: M. Igashira (TIT), K. Ikeda (MHI), T. Iwasaki (Tohoku), O. Iwamoto (NDC/JAERI), K. Oyamatsu (Aichi-Shukutoku), K. Shibata (NDC), H. Harada (JNC), N. Yamano (Sumitomo), T. Yoshida (chair, Musashi Tech) and Y. Watanabe (Kyushu).

The Committee met twice (July 16 and Oct. 17, 2003) in Tokyo. Through the discussion, the essentiality of JENDL-4 for the nuclear science and technology in the future was a consensus among almost all the participants in accordance with the final report[1] of the Ad Hoc Committee on Next Generation JENDL. Some people argued in favor of the continuation of the current dual JNDC/AESJ-and-JNDC/JAERI structure and others pointed out the difficulties in sustaining it in the coming years of restructuring of JEARI and JNC. It was also argued that, in order to keep the high-standard activity, JNDC/AESJ could possibly play an essential role in the transitional years of the restructuring. In this case the working groups belong to JNDC/AESJ, one of the Special Committees of the Atomic Energy Society, and they work with the funding from NDC and/or other bodies like MEXT or industry. Works must be organized in a project-oriented way to be funded and the problem is that this is not always suitable for the basic work like nuclear data evaluation.

4. Concluding Remarks

In this country there is a very long and fertile history of nuclear physics research. Nuclear technology for peaceful uses has made a big progress since its infancy in 1950's and now one-thirds of the electricity is produced by nuclear plants in this country. Nuclear data (and only this) fully connects these two different but mutually conjugate scientific fields. This point must be stressed and then we can understand that the discipline of nuclear data is essential as one of the fundamentals of subatomic science and that the activity of JNDC should not be terminated. The Ad Hoc Committee is now finalizing the report on the electric mail basis.

[1] K. Shibata et al.: private communication (2003)

3. Papers Presented at Poster Sessions

This is a blank page.

3.1 Measurement of double differential cross sections for fragment-production induced by tens of MeV particles.

M. Hagiwara, M. Baba, T. Oishi,
Cyclotron and Radioisotope Center, Tohoku University
E-mail: *hagi@cyric.tohoku.ac.jp*
T. Sanami
High Energy Accelerator Research Organization (KEK)
H. Nakashima, S. Tanaka
Japan Atomic Energy Research Institute
M. Takada
National Institute of Radiological Sciences

Measurements of differential fragment production cross sections for proton- and neutron-induced reaction are described. Double-differential fragment production cross section for 70 MeV protons and the yields for 65 MeV neutrons were obtained with a specially designed Bragg curve spectrometer (BCS). An experiment is also described for proton-induced reactions employing the E-TOF method to obtain complementary and more detailed information than neutron-induced reactions.

1. INTRODUCTION

Fragments which are secondary particles heavier than alpha-particle, cause a large local ionization. It is a serious problem for a semiconductor device and human in space environment. Therefore, the data for fragments production, in particular, the energy and angular doubly differential cross-section data (DDX) are required for dosimetry and evaluation of radiation effects in devices or instruments, such as single event upset (SEU) by cosmic rays. Up to now, however, experimental data of the fragment production are very scarce due to experimental difficulties of the detection. Thus, almost all past experimental data were obtained by the activation method that did not provide energy and angle information. Furthermore, theoretical calculation treating fragment production is very few. Therefore, it is important to accumulate reliable experimental DDX data for fragment production.

For fragment detection, we adopted 1) a Bragg curve spectrometer (BCS) providing various information with a single counter and 2) an energy-time of fight (E-TOF) method having the capability of mass identification in almost whole energy region for fragment. For 1), BCS was designed with special care to apply to a neutron beam, in addition to a charged particle beam and resulted in success to obtain light fragments by proton- and neutron-induced reactions. BCS proved very promising for fragments detection in neutron-induced reaction, while there are still some problems that should be solved. For 2), we have fabricated a chamber for measurements and started measurements.

This paper describes energy-angular fragment production measurements in neutron- and proton-induced reactions and experimental plan of extension to proton-induced reactions employing the energy and TOF method (E-TOF) method.

2. BRAGG CURVE SPECTROMETER (BCS)

2.1 Principle of BCS

Figure 1 shows a schematic diagram of BCS. It is a cylindrical gridded ionization chamber (GIC). The distance between the cathode and the grid is 27 cm, the grid and the anode is 0.5 cm. Wire radius and spacing of

the grid are 0.1mm and 1mm, respectively. Thus, the grid inefficiency is 2.6 %. Ring electrodes are arranged in 3 cm steps to achieve a homogeneous electric field. The chamber is filled with an Ar + 10%CH_4 gas at a pressure of 2.7×10^4 Pa (200 Torr). As shown in fig 2, if fragments enter the detector along the axis through a thin film window and ionize the gas in BCS, ionized electrons drift to the anode by the electric field keeping a shape of Bragg curve. The time distribution of the anode signal corresponds to the reversal of the ionization distribution (Bragg curve) by the fragment. Therefore the fast part of anode signal is proportional to the Bragg peak value that is in proportion to the atomic number (Z) of the fragment. The integration of the whole anode signal represents the total charge that is proportional to the fragment energy. Therefore, BCS can provide information on the energy and the atomic number of fragments using only the anode signal.

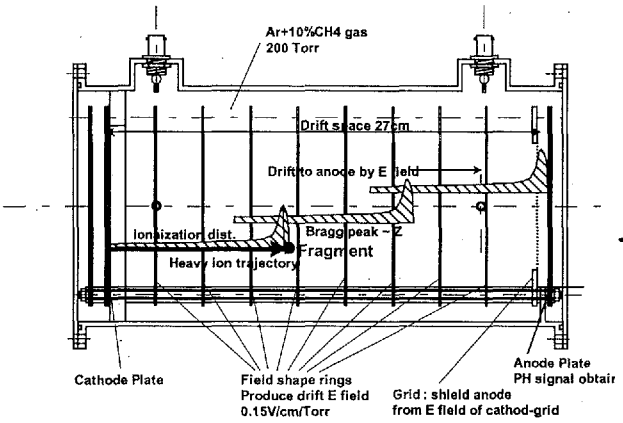

Fig.1 Schematic diagram of the Bragg curve spectrometer

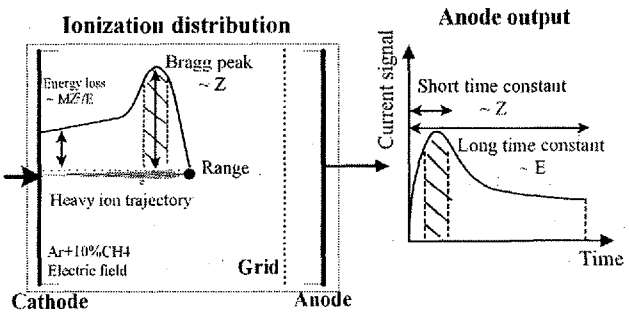

Fig. 2 Detection scheme of BCS method

To apply BCS to neutron-induced reactions, we put samples inside the chamber to decrease the energy loss of fragment and enlarge the detection solid angle. In this case, however, the following difficulties arise:

1) increase of backgrounds due to neutron irradiation of the chamber body and detection gas, and

2) distortion of anode signal due to angular spread of fragments.

To solve 1) we adopt tight neutron collimation, high-Z element electrodes having small fragment production rate, and an additional shield electrode. The shield electrode is installed in front of the chamber with the same potential as the cathode, to reject signals by charged particles from chamber wall in front of the cathode plate.

The problem 2) will be solved by using the above geometrical arrangement and employing the cathode signal which has dependence on the angle relative to the BCS axis [4, 5].

3. APPLICATION OF BCS TO PROTON-INDUCED REACTION

Figure 3 shows the experimental setup used in the case of proton-induced reaction at the cyclotron laboratory of National Institute of Radiological Science. The fragments emitted to 30 degree direction were measured. The proton energy was 70 MeV. Proton beam current was ~10 nA. For samples, foils of carbon 100 μm thick, and silicon 500 μm thick, aluminum 2 μm thick, and polypropylene 4 μm thick were employed.

Figure 4 shows the electronics block diagram used in a series of experiments. In this circuit, the energy signal and the Bragg peak signal were obtained from the anode signal by processing with a long time constant (6 μsec) and a short time constant (0.25 or 0.5 μsec), respectively. To reduce background events and dead time of ADC, only coincidental data between anode and cathode were accumulated by using 4F1V and GG (See fig. 4). The coincidence time is set to 6 μsec that is equivalent to the maximum traveling time of electrons from the cathode to grid. They are collected as a two-dimensioned data by KODAQ (Kakuken Online Data Acquisition System) [6] with CAMAC system.

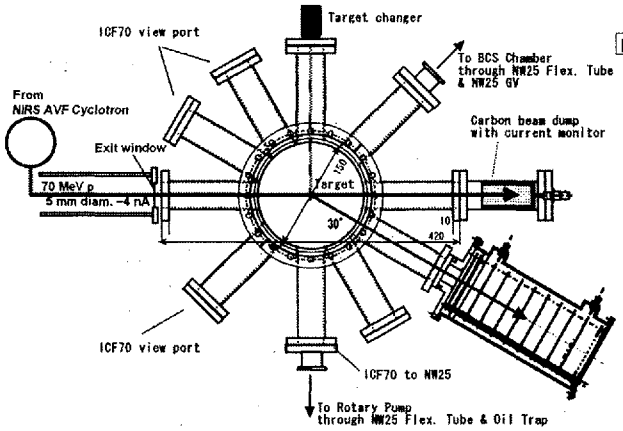

Fig. 3 The block diagram of electronics circuit

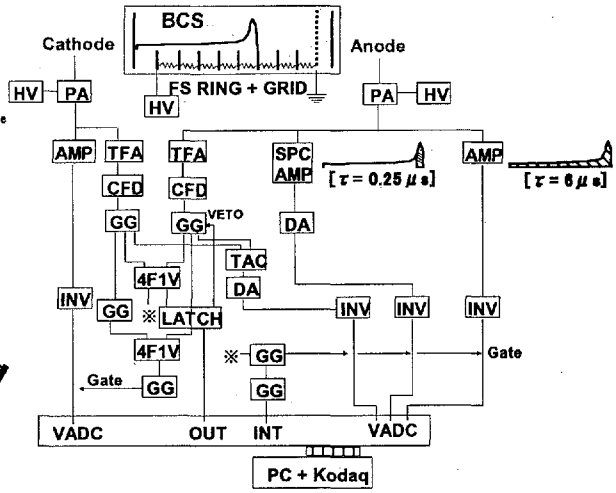

Fig. 4 The block diagram of electronics circuit

Figure 5 shows the measured two-dimensional spectrum on the energy *vs.* Bragg peak. Excellent separation of each fragment and S/N ratio are confirmed in the energy region where particles are separated as shown in fig.6. In this case, fragments lighter than carbon are produced mainly and heavier products are very few. The turning blows at maximum energy point in fig. 5 are caused by the fragments that have ranges longer than the cathode-grid distance. It is meaningful to extend the measurable energy range by developing a correction method for this effect. Energy calibration was performed by replacing a sample with ^{241}Am α source. The DDX for lithium, beryllium and boron from carbon obtained by polypropylene sample are shown in figs. 7-9. As observed in fig.7, the present results agree with the data by C. T. Roche [8] et al. in shape.

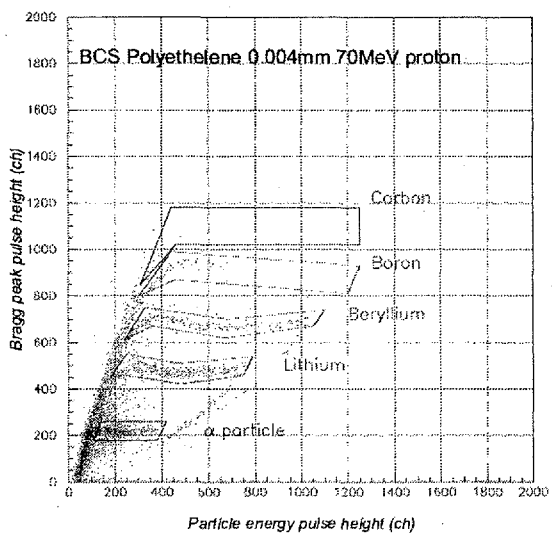

Fig. 5 the energy *vs* Bragg peak two-dimensional spectra for polypropylene 4 μm sample

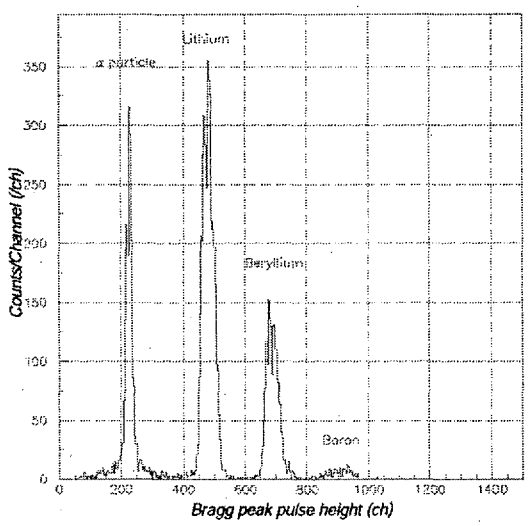

Fig. 6 the histogram of Bragg peak over separation limits for polypropylene 4 μm sample

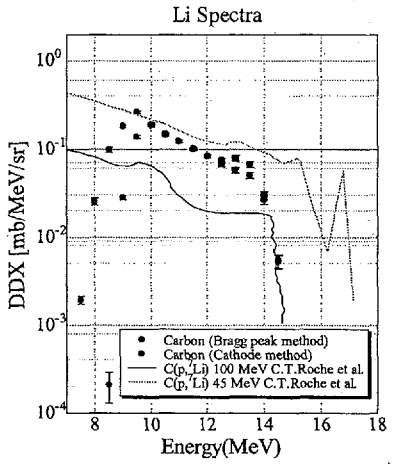

Fig. 7 Lithium spectra

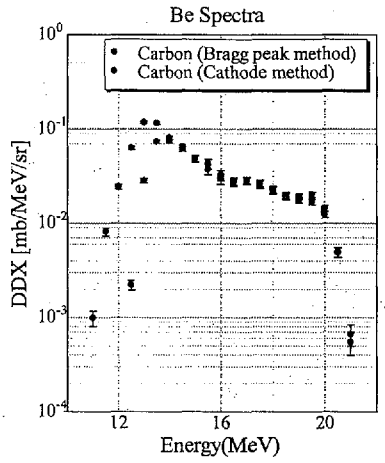

Fig. 8 Beryllium spectra

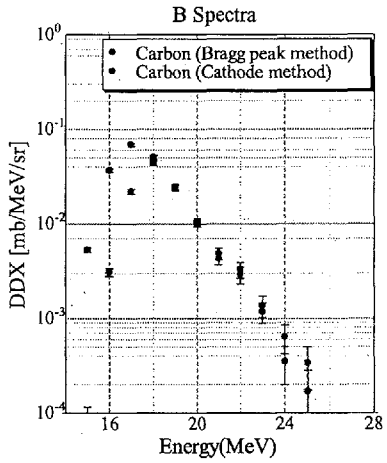

Fig. 9 Boron spectra

4. APPLICATION OF BCS TO NEUTRON-INDUCED REACTION

4.1Experimental setup

An experiment for neutron-induced reaction was performed using the ^{7}Li(p,n) neutron source at TIARA, JAERI, Takasaki site. To measure fragments from carbon, samples of carbon 100 μm thick, 200 μm thick, and nickel 100 μm thick, aluminum 6 μm thick were employed. Each sample set on the cathode plate inside was irradiated directly by neutrons collimated by a ~3 m long neutron collimator, and ~60 cm long additional collimator to avoid neutrons hitting the BCS structure. The proton energy was 70 MeV and the neutron peak energy was ~65 MeV [7]. Proton beam current was ~1 μA. Nickel and thin aluminum samples were used to evaluate the backgrounds originated from BCS gas and entrance window, respectively. This application might be the first trial to neutron-induced reaction in the world.

4.2 Result

Figure 10 shows the two-dimensional spectrum on the energy *vs.* Bragg peak for neutron-induced reaction on a 200 μm-thick carbon sample. The spectrum was obtained by only ~4 hour irradiation. The electronics circuit is the same as fig. 5. Fragments heavier than α particle are separated distinctly as shown in fig. 11, though the separation of Bragg peak was not better compared with proton-induced reaction. Hydrogen isotopes are eliminated by the electronics because of small energy loss in the chamber.

The energy spectra for each sample are shown in figs. 12-14. As observed in these figures the results of two carbon samples are in fair agreement. It will be due to the fact that the range of fragments in carbon (~several μm) is much shorter than sample thickness. These samples are too thick compared with fragment ranges but the spectra obtained were close to that from a thin sample. The yields for the nickel sample are lowest for all fragments because of smaller cross-sections for fragment emission than carbon and aluminum. The data for the thin aluminum sample are similar as the nickel case in magnitude and suggest that the data for nickel and aluminum are close to backgrounds. The lower limit of the spectrum (α particle: 2 MeV, carbon: 8 MeV) is governed by the particle identification limit of BCS and the upper limit by the range of the particle in the gas (α particle: 7.5 MeV, carbon: 38 MeV). We are considering to extend the dynamic range by treating the overlap at lower energy and blow in high energy end. For the purpose, improvement of BCS for more tight geometry and sample-changing mechanism, and also application of digital signal processing using a high speed digital oscilloscope are now in progress.

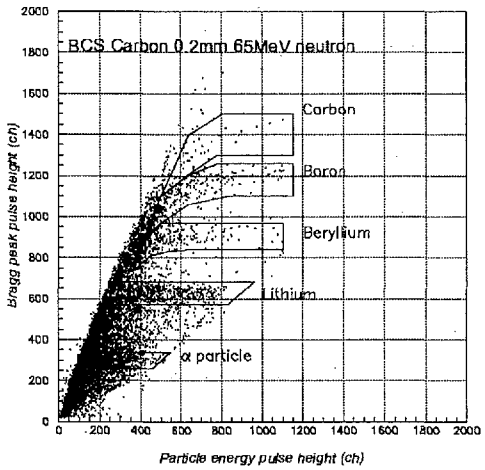

Fig. 10 the energy *vs* Bragg peak two-dimensional spectra for carbon 200 μm sample

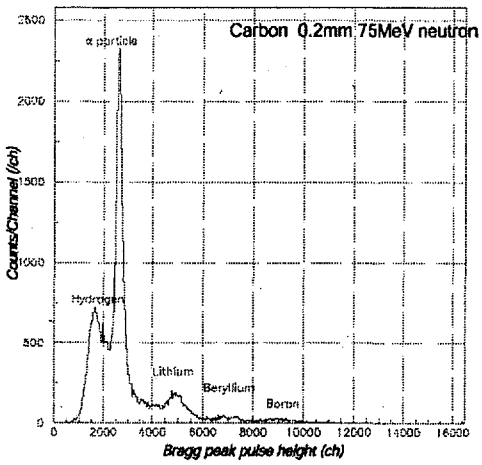

Fig. 11 the histogram of Bragg peak over separation limits for carbon 200 μm sample

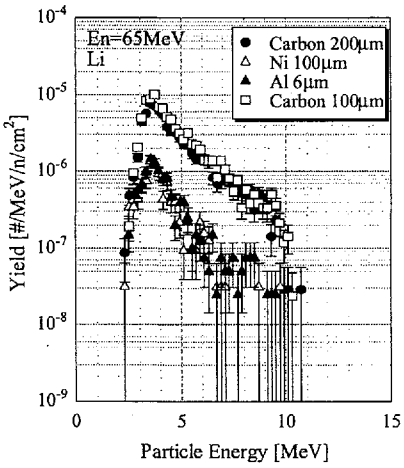

Fig. 12 Lithium spectra

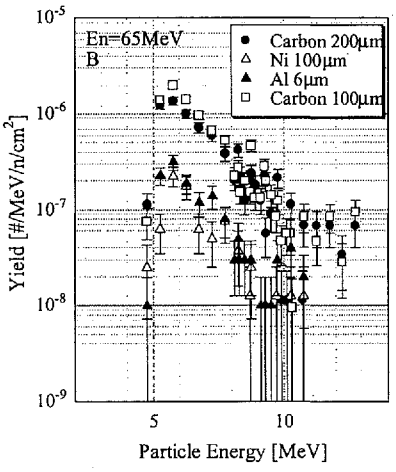

Fig. 13 Beryllium spectra

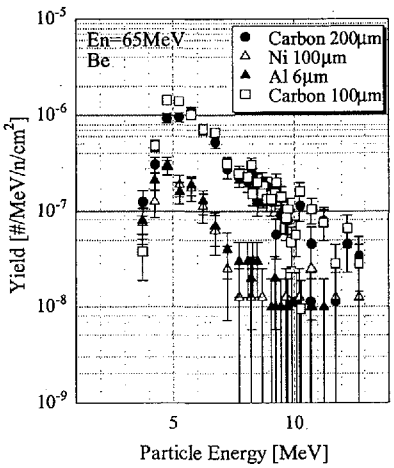

Fig. 14 Boron spectra

5. Fragment production experiment for proton-induced reactions with E-TOF method

In the case of neutron induced reaction, there are several difficulties such as 1)low counting rate, high backgrounds due to neutron bombardment of BCS body, and 3) non-monoenergetic neutron source and so on. We are now planning to do fragment measurement for proton-induced reactions using a energy-TOF method which is used in heavy ion detection. In this method, the energy and TOF of the fragment is measured and mass and atomic number are derived by combing the energy, TOF and energy loss information. Therefore, the dynamic range of fragment energy will be higher than in BCS, and much higher counting rate will be obtained. These data will be useful to complement neutron-induced data. Furthermore, the fragment production data for proton induced reaction are important and useful for analysis of soft errors around accelerators and in space. For the reason, we fabricated a chamber for proton-induced fragment measurement and are stating experiments. The schematic view of the chamber is shown in Fig.15.

For a start detector of TOF, we will employ a MCP (micro-channel plate) coupled with a thin Al film which has good time resolution and low energy loss for fragments. For a stop detector (E detector), MCP and SSD

which has good energy resolution will be adopted. The scattering chamber was designed to enable simultaneous measurements of BCS and E-TOF. The combination of these methods will be powerful for the measurement of fragments induced by charged particles.

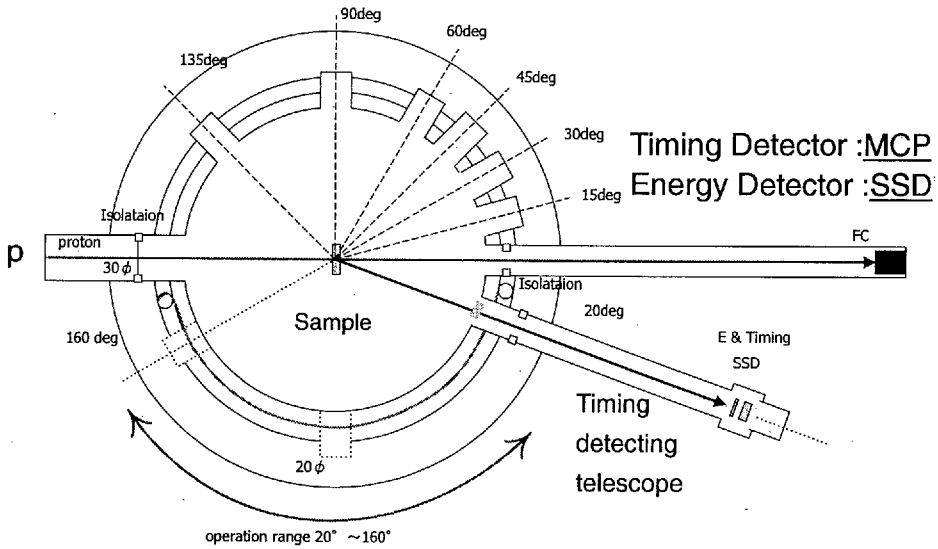

Fig.15 Schematic view of vacuum chamber for E-TOF measurement

6. SUMMARY

We developed a BCS detector and applied to proton- and neutron-induced reactions aiming at measurement of fragment production cross section. Through the experiments, BCS proved to be applicable to neutron-induced reaction. We intend to improve the measuring method with the refinement of data treatment as follows employing new data acquisition method:

1) evaluation and decrease of backgrounds,
2) extension of the dynamic range, and
3) correction for the effects of emission angle.

We are also preparing fragment production measurement for proton-induced reactions using the energy-TOF technique to extend energy range and improve data quality.

ACKNOWLEDGEMENT

The authors express their thanks to the operation crew of the NIRS cyclotron and TIARA cyclotron for their cooperation.

REFERENCES

(1) C.R.Gruhn, et al. *Nucl. Instrum. Methods*, **196** (1982) 33.
(2) N.J.Shenhav and H.Stelzer, *Nucl.Instrm.Meth.* **228** (1985) 359
(3) O.Bunemann, et al., *Can. J. Res.* **A27** (1949) 373
(4) N.Ito, M.Baba, et al., *Nucl.Instrum.Meth.* **A337** (1994) 474
(5) T.Sanami, et al. *Nucl. Instrum. Meth.* **A440** (2000) 403.
(6) K.Omata et al., INS-Rep-884, Institute for Nuclear Study, University of Tokyo, 1991
(7) M.Baba et al. *Nucl. Instrum. Meth.* **A428** (1999) 454
(8) C.T.Roche et al. Phys. Rev. C **14** (1976) 410

3.2 Measurements of Differential Thick Target Neutron Yield for Fe, Cu(p,xn) reactions at 35 and 50 MeV

Toshiro ITOGA, Masayuki HAGIWARA, Naoki KAWATA, Naoya HIRABAYASHI, Takeshi YAMAUCHI, Takuji OISHI, Mamoru BABA

Cyclotron and Radioisotope Center (CYRIC), Tohoku University, Aoba, Aramaki, Aoba-ku, Sendai, Miyagi 980-8579, Japan

e-mail : itogat@cyric.tohoku.ac.jp

Abstract

Differential thick target neutron yields (TTY) for ^{nat}Fe, ^{nat}Cu(p,xn) reactions were measured at 35 and 50 MeV at several laboratory angles between 0- and 110-deg using the time-of-flight method with the Tohoku Univ. AVF cyclotron and a beam-swinger system. We determined neutron energy spectra from ~0.4 MeV to the highest secondary neutron energy. The experimental results were compared with the LA150 data library.

1 Introduction

By the development of accelerator technology, high intensity and high energy accelerators are now available. Uses of the accelerators are expanding to material studies, medical treatment, radiobiology studies and environmental science as well as nuclear physics. Now some accelerators with high energy and intensity are under construction or in plan e.g., Japan Proton Accelerator Research Complex (J-PARC, which is promoted by the corporation of JAERI and KEK), Spallation Neutron Source (SNS, United States), and European Spallation Source (ESS). For the design of accelerator shielding and the accelerator-based neutron sources, differential thick target neutron yields (TTY) data are required. Data are required to be obtained with high energy resolution over a wide energy and angle range. However, such nuclear data files are not good enough in quality for high energy accelerators, and experimental data covering wide range of secondary neutron energies are very few.

In the present experiments, we obtained the TTY data for the ^{nat}Fe, ^{nat}Cu(p,xn) reaction at 35 and 50 MeV. These elements are very popular element for beam-lines and beam-dumps in accelerators. Therefore, it is important to know secondary neutron spectra from these elements bombarded by accelerated charged particles. The experiment was carried out as a part of the series of TTY measurements using a time-of-flight (TOF) technique at the Cyclotron and Radioisotope Center (CYRIC)[1], Tohoku University with the K=110 AVF cyclotron and the beam-swinger system.

2 Experiment

The experimental setup is shown in Fig.1. A proton beam accelerated by the AVF cyclotron was transported to the target room No.5 of CYRIC equipped with a beam-swinger system and a neutron TOF channel [2]. The beam swinger system changes the incident angle of the beam onto the target from

0-deg to 110-deg and enables to measure angular distributions with a fixed detector setup. The targets of Fe and Cu were plate of natural elements. Their sizes are shown in table 1. The target chamber was shielded with a 2.5 m thick concrete wall having a beam channel for collimeters which enable to measure neutrons under a low background environment. Emitted neutrons were detected by a NE213 liquid scintillation detector, 14 cm-diam × 10 cm-thick or 5 cm-diam × 5 cm-thick equipped with a pulse-shape-discriminator (PSD). The larger and smaller detectors were placed around ~11 m and ~3.5 m from the target, respectively. The shorter flight path was adopted to measure the low energy part (~0.4-3 MeV) of the neutron spectrum by low pulse-height bias (~0.4 MeV). The TOF, PSD and pulse-height data were collected event by event as three parameter list data for off-line analysis [3].

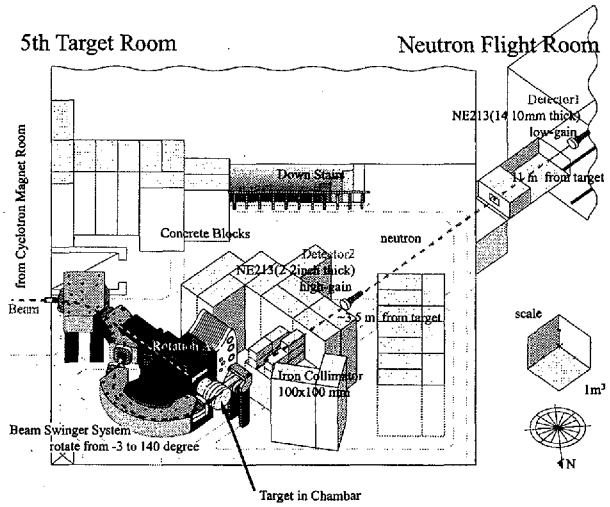

Fig 1: 5th target room and TOF room

3 Experimental procedure

The pulse width of proton beam was generally less than 1 ns in FWHM, and the beam current on the target was around 5 ~ 10 nA. The beam current was digitized and recorded by a scaler for normalization of the neutron TOF spectrum. The TOF data were obtained at five laboratory angles (0, 30, 60, 90, 110).

Table 1: Present measurements and target size

Proton energy [MeV]	Target	Angle [deg.]	Stopping range [mm]	Thickness [mm]
35	Fe	0, 30, 60, 90,110	2.26	3
	Cu		2.11	
50	Fe	0, 30, 60, 90,110	4.24	5
	Cu		3.93	

4 Data analysis

Neutron TOF spectra gated by the PSD signal and the lower pulse-height bias were converted into energy spectra. The efficiency *vs.* energy curves of the detectors were obtained by the calculation with a SCINFUL-R, whichi is revised version of the Monte Carlo code SCINFUL [4] and was verified to be accurate within ± 5 % up to 80 MeV [5]. The spectra were normalized by the integrated beam current.

5 Results and discussion

5.1 Experimental data

Figures 2 and 3 show the present results of differential thick taget neutron yield from the ^{nat}Fe, ^{nat}Cu(p,xn) reactions at 35 and 50 MeV. The data have not been corrected yet for the effect of neutron attenuation in the target and air. As shown, both spectra show almost similar feature with no marked structures. The neutron spectra show pronounced increase in lowest energy region because of evaporation neutrons and the yields are larger than light nulide like ^{nat}C and ^{nat}Al. The angular dependence of the spectra becomes stronger with increasing neutron energy.

In Fig.4, the present results are compared with the data by Nakamura et al., at E_p=52 MeV obtained by the unfolding technique [9]. The data by Nakamura et al. are limited in energy range but in fair agreement with the present one in the overlapping energy region.

5.2 Comparison with LA150

In the following, experimental data are compared with the TTY data derived from LA150. The TTY predicted by LA150 [6][7] was derived by using the following equation [8].

$$\frac{d^2Y(E_0)}{d\Omega} = N\int_0^T \frac{d^2\sigma\left(E_0 - \int_0^t \left(\frac{dE}{dt}\right) dt\right)}{dEd\Omega} \times e^{-N\sigma_{nonel}\left(E_0 - \int_0^t \left(\frac{dE}{dt}\right)dt\right)t} dt \qquad (n \cdot MeV^{-1} \cdot sr^{-1} \cdot projectile^{-1}),$$

where, E_0 is incident particle energy [MeV], N is density of target nulide [#/cm^3], T is thickness of the target [cm], σ_{nonel} is nonelastic cross section [cm^2], dE/dt is stopping power of incident particles [MeV/cm].

Figures 5 and 6 show comparison of the present results with the LA150 data library. Both data for ^{nat}Fe and ^{nat}Cu show marked disagreements with LA150 in higher energy region. Such disagreement with LA150 was observed also in the case of heavy nuclide as tungsten and tantalum [10].

In the future, we are planning to correct for the effect of the attenuation of neutron in the taget and air, and also do measurements for thin target to clarify the difference.

References

[1] Cyric web page. http://www.cyric.tohoku.ac.jp.

[2] K. Kumagai Y. Kikuchi T. Uekusa T. Uemori H. Fujisawa N. Sugimoto K. Itoh M. Baba et al. A. Terakawa, H. Suzuki. New fast-neutron time-of-flight facilities at cyric. Nucl. Instr. and Meth., Vol. 491,pp. 419 - 425, 2002.

[3] M. Ibaraki et al. Nucl. Sci. Eng., Vol. 35, p. 843, 1998.

[4] J. K. Dickens. ORNL-6463. Oak Ridge National Laboratory, 1988.

[5] S. Meigo. Measurements of the responce function and the detection e.ciency of an NE213 scintillator for neutrons between 20 and 65 MeV. Nucl. Instr. and Meth. in Phys. Res. A, Vol. 401, pp. 365 - 378, 1997.

[6] M. B. Chadwick, P. G. Young, R. E. MacFarlane, P. Moller, G. M. Hale, R. C. Little, A. J. Koning, S. Chiba. LA150 Documentation of Cross Sections, Heating, and Damage: Part A (Incident Neutrons). LANL Accelerator Production of Tritium Program, 1999.

[7] M. B. Chadwick, P. G. Young, R. E. MacFarlane, P. Moller, G. M. Hale, R. C. Little, A. J. Koning, S. Chiba. LA150 Documentation of Cross Sections, Heating, and Damage: Part B (Incident Protons). LANL Accelerator Production of Tritium Program, 1999.

[8] Takashi Nakamura. Radiation Physics and Accelerator safety Engineering. Chijin Shokan, 2001.

[9] T. Nakamura, M. Yoshida, K. Shin. Spectral measurements of neutrons and photons from thick targets of C, Fe, Cu and Pb by 52 MeV protons. Nucl. Instr. And Meth., 151, pp. 493 - 503, 1978.

[10] T. Aoki et al., Nucl. Sci. Eng., in print

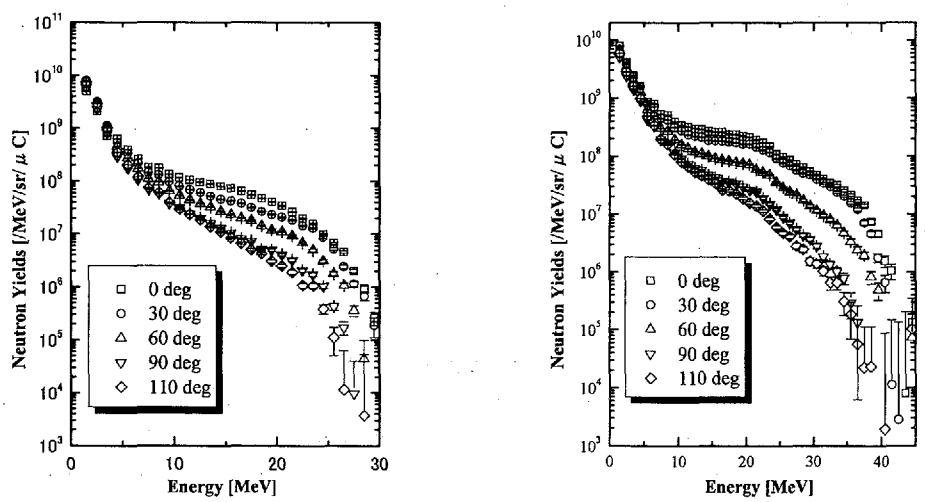

(a) E_p = 35 MeV (b) E_p = 50 MeV

Fig.2 : Experimental data for ^{nat}Fe(p,xn)

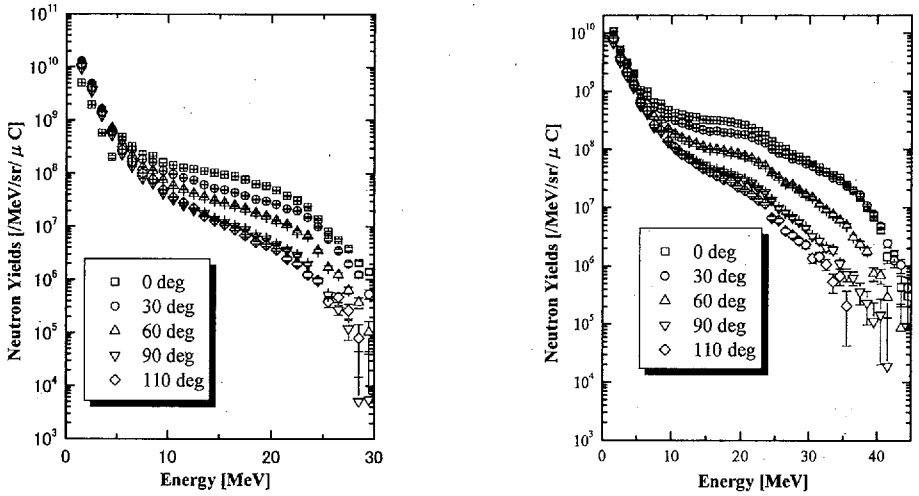

(a) E_p = 35 MeV (b) E_p = 50 MeV

Fig.3 : Experimental data for ^{nat}Cu(p,xn)

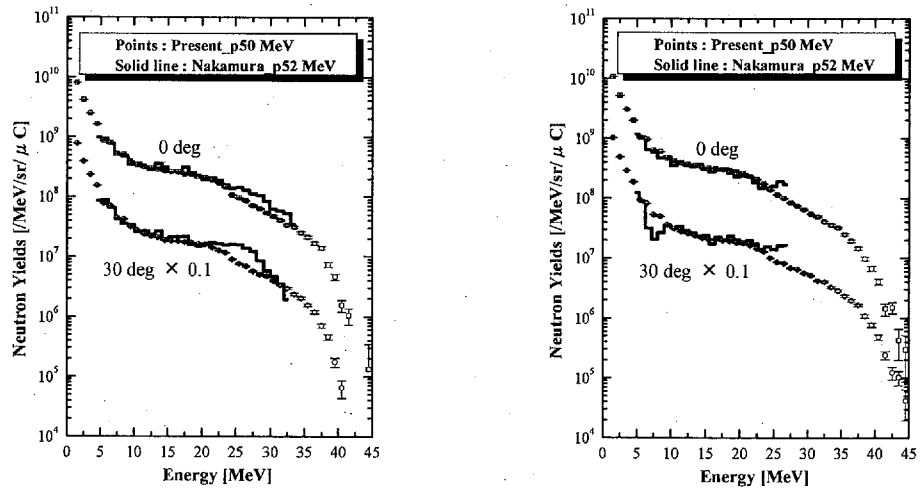

(a) Fe (b) Cu

Fig.4 : Comparison with Nakamura's data

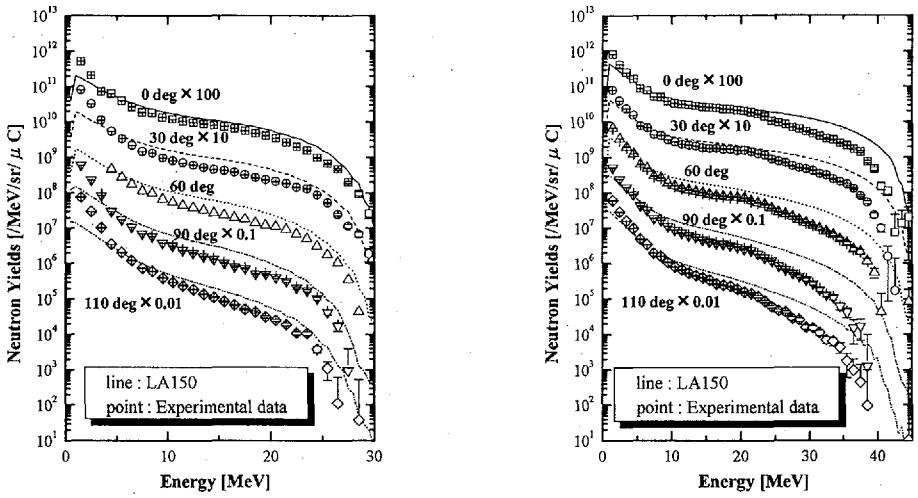

(a) E_p = 35 MeV　　(b) E_p = 50 MeV

Fig.5 : Compariosn with LA150 for ^{nat}Fe(p,xn)

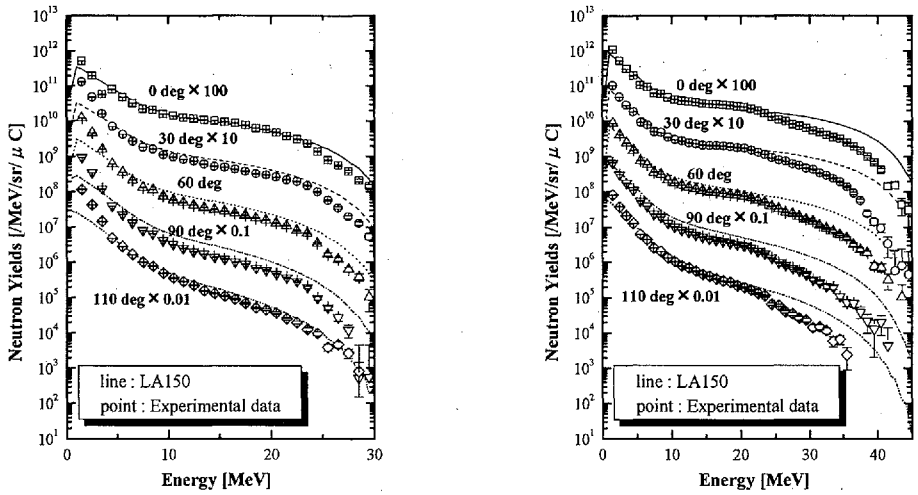

(a) E_p = 35 MeV　　(b) E_p = 50 MeV

Fig.6 : Compariosn with LA150 for ^{nat}Cu(p,xn)

3.3 Measurement of Deuteron-Induced Activation Cross-Sections for Aluminum, Copper and Tungsten in 22-34 MeV Region

Jun-ichi HORI[1†], Makoto NAKAO[1], Kentaro OCHIAI[1], Michinori YAMAUCHI[1], Noriko S. ISHIOKA[2], and Takeo NISHITANI[1]
[1]Department of Fusion Engineering Research, Japan Atomic Energy Research Institute
Tokai-mura, Naka-gun, Ibaraki-ken 319-1195, Japan
[2]Department of Ion-beam-applied Biology, Japan Atomic Energy Research Institute
Takasaki, Gunma 370-1192, Japan
e-mail: hori@rri.kyoto-u.ac.jp

Activation cross-sections for deuteron-induced reactions on aluminum, copper and tungsten were measured by using a stacked-foil technique at the AVF cyclotron in TIARA facility, JAERI. We irradiated three types of stacked-foil with 35 MeV deuteron beam and the activation cross sections for the $^{27}Al(d,x)^{27}Mg$, ^{24}Na, $^{nat}Cu(d,x)^{62,\ 63}Zn$, $^{61,\ 64}Cu$ and $^{nat}W(d,x)^{181-184,\ 186}Re$, ^{187}W reactions were obtained in 22-34 MeV region. The experimental cross sections were compared with other experimental ones and the data from ACSELAM library in the IRAC code system.

1. Introduction

International Fusion Materials Irradiation Facility (IFMIF) is an accelerator-based D-Li neutron source designed to produce an intense neutron field for testing fusion materials. The IFMIF is driven by two 40 MeV deuteron linear accelerators with 125 mA beam current. In the design of the IFMIF system, the long-term operation with a total facility availability of at least 70 % by hands-on maintenance is planned [1]. However, beam loss would activate the structure materials along the beam transport lines and make hands-on maintenance more difficult. Therefore, the accurate estimation of the activities produced in accelerator components and the selection of structure materials are important issues in order to determine the beam loss criteria for achieving the overall availability.

Aluminum is the main component of the beam tube and chamber. Copper is used in the cavity wall, electrodes and magnetic conductor. For beam slits and coating to protect the beam facing materials, high-Z elements are so useful that gold, tantalum and tungsten are candidate materials.

In this work, we focused on main twelve radioactive nuclei produced in Al, Cu and W by the irradiation with deuteron beam. Since those nuclei have half-lives longer than ten minutes, it would give effects on considering the cooling time for starting hands-on maintenance.

†Present address: Research Reactor Institute, Kyoto University, Kumatori-cho, Sennan-gun, Osaka 590-0494, Japan

2. Experimental Procedure and Data Processing

Activation cross sections were measured by using a stacked-foil technique. In order to cross-check the obtained cross sections, three different types of stack consisting of natural composition aluminum, copper and tungsten foils with chemical purity more than 99.95 % were prepared as shown in fig. 1. Every stack was wrapped in an aluminum foil of 10 μm in thickness. The thickness of the foil was 200 μm for Al, 25 μm for Cu and 20 μm for W. The stacks were irradiated with a 35 MeV deuteron beam at the AVF cyclotron in TIARA facility, JAERI. Each irradiation was performed with a 0.1 μA beam for 5 minutes. After suitable cooling time, the decayed gamma-rays emitted from the irradiated foils were measured by a calibrated Ge detector and the induced activities were obtained for the following nuclei as ^{27}Mg, ^{24}Na, ^{61,64}Cu. ^{62,63}Zn, $^{181-184}$, ^{186}Re, ^{187}W and ^{65}Zn.

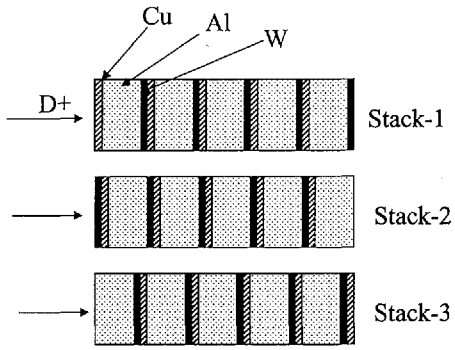

Fig. 1 Schematic view of the irradiated stacks

The energy degradation along the stack and the effective deuteron energy at the middle position of each foil were estimated by using the IRACM code[2]. The number of incident deuteron on each stack was determined from the ^{nat}Cu(d,x)^{65}Zn reaction cross section data reported by Takács *et al.*[3] and the observed ^{65}Zn activities. The elemental cross-sections were derived from the induced activities and the number of incident deuteron. The following errors were taken into account as well as statistical error (1-40 %) in the error estimation of the present results: the errors in the determination of continuous background for obtaining net counts of the decayed gamma-ray (1-30 %), the standard cross sections for the ^{nat}Cu(d,x)^{65}Zn reaction (12 %), the full energy efficiency of the Ge detector (3 %) and the foil thickness (1 %). Finally, the total uncertainty on cross section values was estimated as 13-50 %.

3. Results and Discussion

We have measured the elemental cross sections for producing the twelve radioactive nuclei and compared those with previous ones by other groups and the data from ACSELAM library calculated by using the ALICE-F code[4]. As the cross sections in ACSELAM library are given for each isotope target, we normalized the values to elemental cross sections by weighting with natural abundance in order to compare with the present results in figures.

3-1. Aluminum

The activities of three nuclei, ^{22}Na($T_{1/2}$=2.6y), ^{24}Na($T_{1/2}$=15.0h) and ^{27}Mg($T_{1/2}$=10m), are expected to be important from the viewpoint of hands-on maintenance. However, the ^{27}Al(d,αp2n)^{22}Na reaction has high threshold energy around 25 MeV and the ^{22}Na activity is very weak in 22-34 MeV region, so that the ^{22}Na production was not considered in this work.

The comparison of the present cross sections with other experimental ones and the data in ACSELAM library for producing ^{27}Mg and ^{24}Na are shown in figs. 2 and 3. For ^{27}Mg, there is only one experimental data reported by Wilson *et al.*[5] in low energy region. The present results are

larger than the data of ACSELAM by a factor of 1.3-2.0. Though the cross sections of the $^{27}Al(d,x)^{24}Na$ reaction were reported by many authors, the present results are in agreement with the data by Takács *et al.*[3], Martens *et al.*[6], and Michel *et al.*[7]. within experimental error. This work show that the data in ACSELAM for the $^{27}Al(d,x)^{22}Na$ reaction are about 1 order lower than the experimental ones.

3-2. Copper

Figures 4-7 show the present results for the $^{nat}Cu(d,x)^{61}Cu(T_{1/2}=3.33h)$, $^{64}Cu(T_{1/2}=12.7h)$, $^{62}Zn(T_{1/2}=9.19h)$ and $^{63}Zn(T_{1/2}=38m)$ reactions with other experimental ones and the data in ACSELAM library. In the energy region of 22-34 MeV, there exist only two experimental data reported by Bartell *et al.*[14] and Fulmer *et al.*[15] on those reactions. There are lots of differences between the two experimental data. In the case of ^{64}Cu, the present results are in agreement with their values within experimental error. For other nuclei, the present results support the shape of cross sections reported by Fulmer. However, their data become systematically higher than the present ones by a factor of 1.5-4.

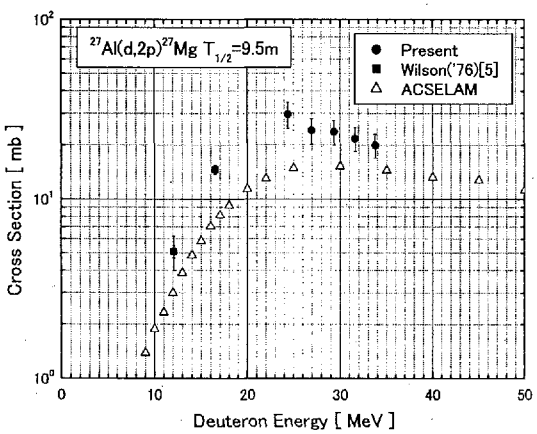

Fig. 2 Cross sections for the $^{27}Al(d,2p)^{27}Mg$ reaction

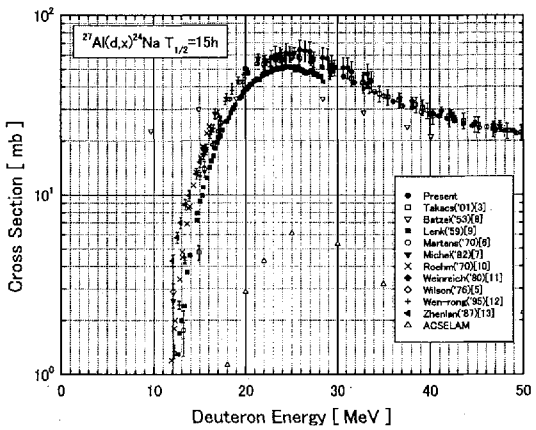

Fig. 3 Cross sections for the $^{27}Al(d,x)^{24}Na$ reaction

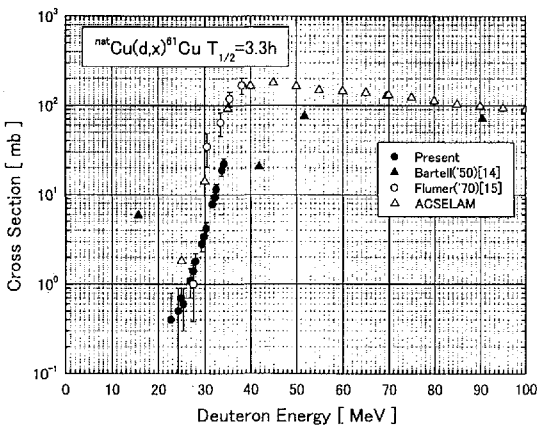

Fig. 4 Cross sections for the $^{nat}Cu(d,x)^{61}Cu$ reaction

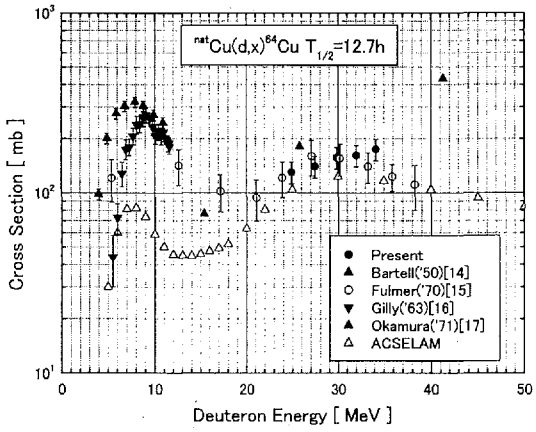

Fig. 5 Cross sections for the $^{nat}Cu(d,x)^{64}Cu$ reaction

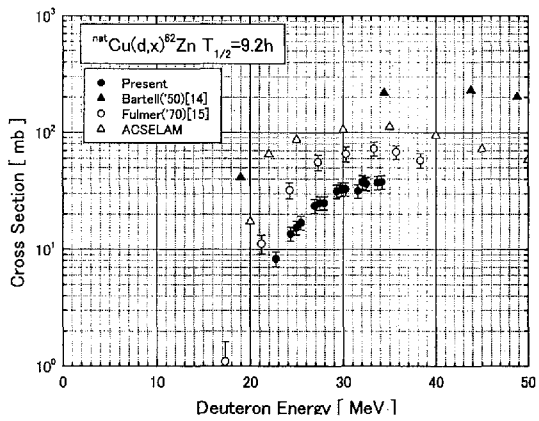

Fig. 6 Cross sections for the $^{nat}Cu(d,x)^{62}Zn$ reaction

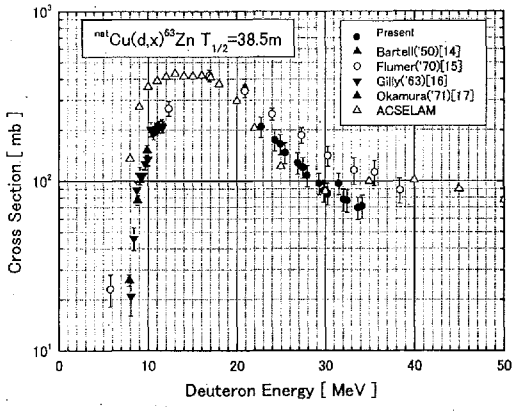

Fig. 7 Cross sections for the $^{nat}Cu(d,x)^{63}Zn$ reaction

The present results are in agreements with the data of ACSELAM except for the $^{nat}Cu(d,x)^{61}Cu$ and ^{62}Zn reactions. In the case of ^{64}Cu, large discrepancy between experimental and ACSELAM data was observed around 10 MeV as shown in fig. 5. It should be noted that the ^{64}Cu activity would be produced by not only $^{63}Cu(d,p)$ but also $^{63}Cu(n,\gamma)$ reaction. The latter reaction could be induced by secondary neutron, so that the experimental results would include the contribution.

3-3. Tungsten

Figures 8-13 show the present results for the $^{nat}W(d,x)^{181}Re(T_{1/2}=19.9h)$, $^{182g}Re(T_{1/2}=2.67d)$, $^{182m}Re(T_{1/2}=12.7h)$, $^{183}Re(T_{1/2}=70d)$, $^{184g}Re(T_{1/2}=38d)$, $^{184m}Re(T_{1/2}=169d)$, $^{186}Re(T_{1/2}=3.78d)$ and $^{187}W(T_{1/2}=23.72h)$ reactions with other experimental ones and the data in ACSELAM library.

In the energy region of 22-34 MeV, there are no experimental data. The present data are in fairly good agreement with the data in ACSELAM of ^{181}Re, $^{182m+g}Re$ and ^{183}Re. The valleys of cross section curves are also reproduced well in ACSELAM library. In the case of ^{186}Re, the present results show decreasing tendency above 24 MeV. For the $^{184m+g}Re$ and ^{187}W production reactions, this work shows that the bumps exist around 30 and 10 MeV, respectively. It should be noted that the ^{187}W could be produced by not only $^{186}W(d,p)$ but also $^{186}W(n,\gamma)$ reaction. The latter reaction is

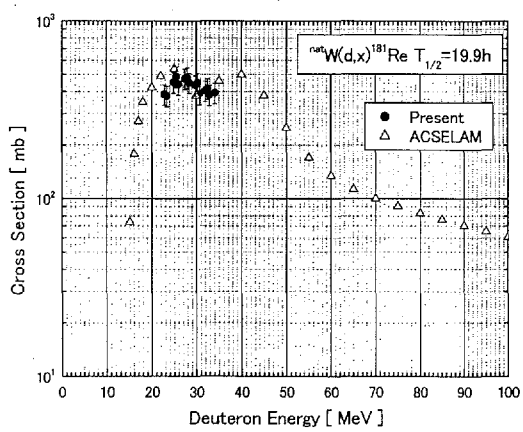

Fig. 8 Cross sections for the $^{nat}W(d,x)^{181}Re$ reaction

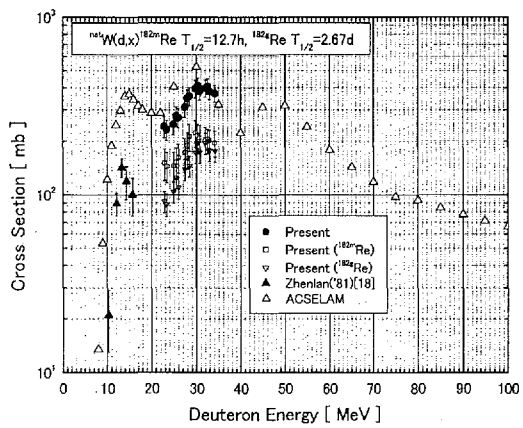

Fig. 9 Cross sections for the $^{nat}W(d,x)^{182}Re$ reaction

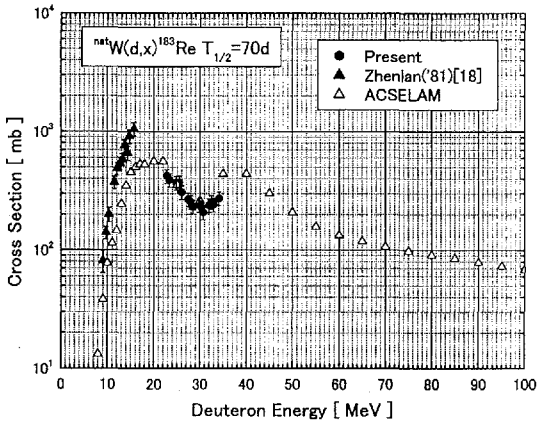

Fig. 10 Cross sections for the $^{nat}W(d,x)^{183}Re$ reaction

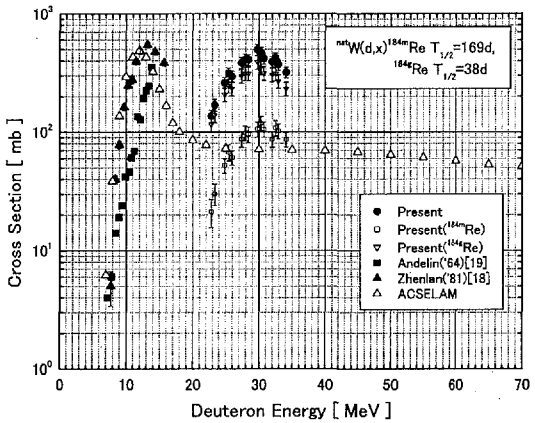

Fig. 11 Cross sections for the $^{nat}W(d,x)^{184}Re$ reaction

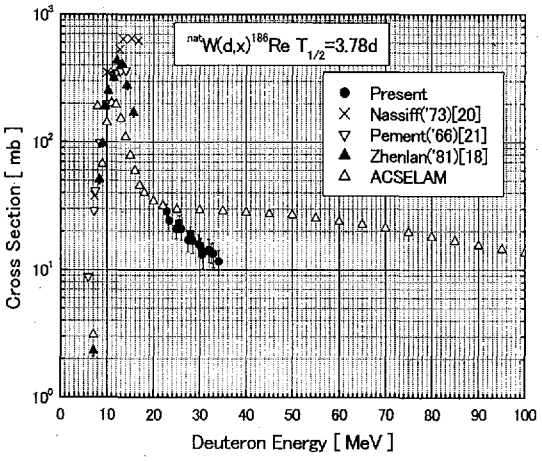

Fig. 12 Cross sections for the $^{nat}W(d,x)^{186}Re$ reaction

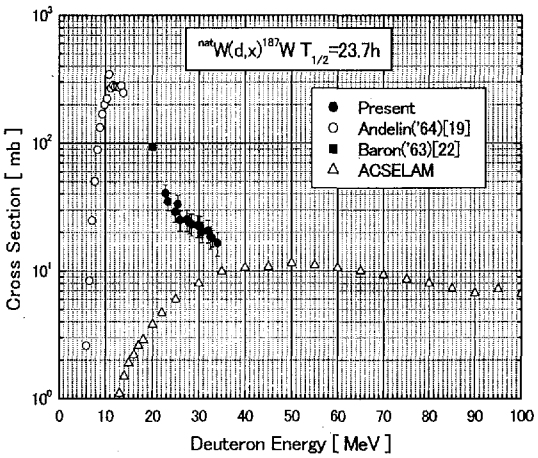

Fig. 13 Cross sections for the $^{nat}W(d,x)^{187}W$ reaction

induced by secondary low-energy neutron. The experimental results obtained by adopting an activation method include the component via the (n,γ) reaction. On the other hands, the values in ACSELAM were calculated for only (d,p) reaction. Previous experimental data by Andelin *et al.*[19] and Baron *et al.*[22] also show higher values than the data in ACSELAM about 1-2 order below 20 MeV.

Moreover, we have obtained the activation cross sections corresponding to producing the ground and meta-stable states for ^{182}Re and ^{184}Re as shown in figs. 9 and 11. The obtained branching ratios (σ_m/σ_g) were also shown in Fig. 14.

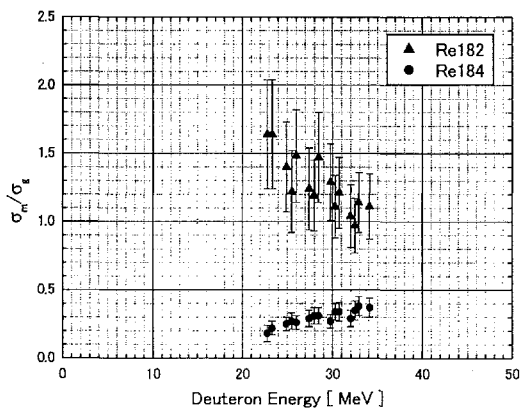

Fig. 14 The ratio of cross sections for producing the ground and meta-stable states of ^{182}Re and ^{184}Re

4. Conclusion

The activation cross-sections for the deuteron-induced reactions have been obtained for Al, Cu and W in 22-34 MeV region. Present results were compared with previous experimental ones and the values in ACSELAM library. For $^{nat}Al(d,x)^{24}Na$, it was pointed out that the values of ACSELAM are obviously lower than experimental ones by about 1 order. Present results show good agreements with ACSELAM library for the $^{nat}Cu(d,x)^{64}Cu$, ^{63}Zn and $^{nat}W(d,x)^{181-183}Re$ reactions. For the $^{27}Al(d,p)^{27}Mg$, $^{nat}Cu(d,x)^{61}Cu$, $^{62,63}Zn$, $^{nat}W(d,x)^{186}Re$ reactions, the discrepancy is shown between the present results and the data in ACSELAM by a factor of 1.3-4. This work showed that the bumps existed around 30 and 10 MeV for producing ^{184}Re and ^{187}W, respectively. Moreover, we obtained the ratio of cross sections for producing the ground and meta-stable states of ^{182}Re and ^{184}Re.

Acknowledgments

The authors would like to express their thanks to the AVF cyclotron staffs of TIARA facility in JAERI for operating the accelerator steadily.

References

[1] IFMIF International Team, "IFMIF-KEP; International Fusion Materials Irradiation Facility key element technology phase report," JAERI-Tech 2003-005 (2003).

[2] S. Tanaka, M. Fukuda, K. Nishimura, *et al.*, "IRACM: A Code System to Calculate Induced Radioactivity Produced by Ions and Neutrons," JAERI-Data/Code 97-019 (1997).

[3] S. Takács, *et al.*, *Nucl. Inst. Meth.*, **B 174**, 235-258 (2001).

[4] T. Fukahori; *Proc. of the Specialists' Meeting on High Energy Nuclear Data*, Tokai, October 3-4, 1991, JAERI-M 92-039. 114-122 (1992)

[5] R. L. Wilson, *et al.*, *J. Phys. Rev.*, **C13**, 976 (1976).

[6] U. Martens, G. W. Schweimer, *J. Zeitschrift für Physik*, **233**, 170 (1970).

[7] R. Michel, *et al.*, EXFOR No. A0158 (1982).

[8] R. Bartzel *et al.*, *Phys. Rev.*, **91**, 939 (1953).

[9] P. A. Lenk, *et al.*, *Phys. Rev.* **116**, 1229 (1959).

[10] H. F. Röehn, *et al.*, *J. Inorg. Nucl. Chem.* **31**, 3345 (1969).

[11] R. Weinreich, *et al.*, *J. Appl. Radiat. Isotopes*, 31, 223 (1980).

[12] Z. Wen-rong, *et al.*, *Chinese Nucl. Phys.*, **17**, 160 (1995).

[13] T. Zhenlan, *et al.*, *Chinese Nucl. Techniques*, **2**, 45 (1987).

[14] F. O. Bartell, *et al.*, *Phys. Rev.*, **80**, 1006 (1950).

[15] C. B. Fulmer, *et al.*, *Nucl. Phys.*, **A155**, 40 (1970).

[16] J. L. Gilly, *et al.*, *Phys Rev.*, **131**, 1727 (1963).

[17] H. Okamura, *et al.*, *Nucl. Phys.*, **A169**, 401 (1971).

[18] T. Zhenlan, *et al.*, *Chinese Nucl. Phys.*, 3, 242 (1981).

[19] R. L. Andelin, *et al.*, EXFOR C0722 (1964).

[20] S. J. Nassiff and H. Munzel, *Radiochim. Acta.*, **19**, 97 (1973).

[21] F. W. Pement and R. L. Wolke, *Nucl. Phys.*, **86**, 429 (1966).

[22] N. Baron, B. L. Cohen, *Phys. Rev.*, **129**, 2636 (1963).

3.4 Analysis of Continuum Spectra of (n, d) reactions with Direct Reaction Model

S.A. Sultana[1], Syafarudin[1], F. Aramaki[2], D. Maki[1], G. Wakabayashi[1], Y. Uozumi[1], N. Ikeda[1], M. Matoba[1], Y. Watanabe[3], H.M. Sen Gupta[4]
e-mail: sadia@nucl.kyushu-u.ac.jp

1. Department of Applied Quantum Physics and Nuclear Engineering, Kyushu University, Fukuoka, 812-8581
2. Kyushu Institute of Information Sciences, Dazaifu 818-0117
3. Department of Advanced Energy Engineering Science, Kyushu University, Kasuga, Fukuoka 816-8580
4. Department of Physics, University of Dhaka, Dhaka, Bangladesh

Abstract

Higher energy deuteron emission spectra in the continuum region in nucleon induced reactions, i.e. (p, d) and (n, d) reactions, are not reproduced well by the usual pre-equilibrium reaction model. It has been suggested that the one-step direct pick-up reaction model gives better predictions for the (p, d) reactions at incident energies of several tens MeV region. The present study aims to establish a method to analyze the continuum spectra of both the (p, d) and (n, d) reactions in the direct reaction scheme with global optical potentials. In this paper, we analyze the ^{58}Ni$(p, d)^{57}$Ni and ^{nat}Fe$(n, d)^{nat}$Mn reactions in ensemble by this model.

I. Introduction

There have been many works on one-nucleon transfer reactions. However, works on the (n, d) reaction have been yet scarce. As the (n, d) reaction data are not easy to be measured experimentally, it is desired to prepare a model which gives a reliable theoretical prediction, and to use it as a substitute of experimental results.

Some theoretical models have been proposed to study the continuum spectra excited by the (n, d)reactions [1–3], which can not reproduce well the experimental data [4].

For the (p, d) reaction continuum spectra, Syafarudin et al. [5] have given a procedure, which can reproduce well the spectra of the one-nucleon transfer reactions in higher emission energy region . The present work for the (n, d) reactions is an extension of the (p, d) reaction analyses . We have applied here the similar procedure to analyze the (n, d) reaction data with global optical potentials [6].

To predict the direct reaction continuum spectra of the (p, d) reaction, we adopted an approach suggested by Lewis [7]. According to this model, continuum spectra in the direct reaction scheme are given as a result of nuclear damping. From several studies on the direct reaction sheme, Matoba et al. reached eventually a decision to solve this critical problem [8, 9]. They assumed continuum spectra as an incoherent sum of all shell contribution and adopted an asymmetric Lorentzian form for the response function in the DWBA-based cross sections calculation and the experimental (p, d) double differential cross sections are predicted. In the present work the same method is applied for analysis of the (n, d) reactions to reproduce the double-differential cross-section. From this work, we can realize that this method is applicable not only for the (p, d) reactions, but also for the (n, d) reactions.

II. Experimental data

1. (p, d) reactions

The experiments were performed at the TIARA facility of JAERI. A proton beam of 68MeV from the AVF cyclotron was lead to the HB-1 beam line. Energy distributions of light ions emitted from the target were measured using a ΔE-E counter telescope, which consisted of two thin silicon ΔE-detectors and a CsI(Tl) E-detector with photo-diode readout. Details of the experimental procedure and the results have been reported in ref [10].

2. (n,d) reactions

The experiments were performed at the neutron source $^7Li\,(p,n)$ of the TIARA facility of JAERI. A spectrometer, which consisted of three counter telescopes mounted on a vacuum chamber to reduce the energy loss of secondary particles and charged particles in the air was used. Details of the experimental procedure and the results have been reported in ref [11].

III. Theoretical Analysis

In the present method, the theoretical calculations of the double differential cross-sections have been done by considering a direct reaction model as an incoherent sum of the direct reaction components, which are based on DWBA predictions and expressed as below:

$$\frac{d^2\sigma}{d\Omega dE} = 2.30\sum_{l,j}\left[\frac{C^2S_{l,j}(E)}{2j+1}\times\left(\frac{d\sigma}{d\Omega}\bigg|_{l,j}^{DW}(E)\right)\right] \tag{1}$$

where $d\sigma/d\sigma|_{l,j}^{DW}(E)$ is the cross-section calculated by a DWBA code DWUCK [12] and $C^2S_{l,j}(E)$, the spectroscopic factor expressed as-

$$C^2S_{l,j}(E) = \left(\sum C^2S_{l,j}\right)\times f_{l,j}(E) \tag{2}$$

where $\sum C^2S_{l,j}$ is the sum of the spectroscopic factors of all the predicted states and the distribution of strength function over the spectra is obtained by using an asymmetric Lorentzian function [8, 9, 13]

$$f_{l,j} = \frac{n_0}{2\pi}\frac{\Gamma(E)}{\left(|E-E_F|-E_{l,j}\right)^2+\Gamma^2(E)/4} \tag{3}$$

and

$$\int_0^\alpha f_{l,j}(E)dE = 1 \tag{4}$$

where n_0 is the renormalization constant and E_F is the Fermi energy. The Fermi energy can be calculated by using an empirical formula given in [14]. The sums of spectroscopic factors and the centroid energies $(E_{l,j})$ for $J = l \pm \frac{1}{2}$ shell orbits have been estimated by using BCS calculations. In these calculations, single particle energies required to calculate the centroid energy are calculated by the prescription of Bohr and Motelson [15]. Spreading width (Γ) is expressed by a function proposed by Brown and Rho [16] and by Mahaux and Sartor [13],as,

$$\Gamma(E) = \frac{\epsilon_0\left(E-E_F\right)^2}{\left(E-E_F\right)^2+E_0^2} + \frac{\epsilon_1\left(E-E_F\right)^2}{\left(E-E_F\right)^2+E_1^2} \tag{5}$$

where ϵ_0, ϵ_1, E_0 and E_1 are constants which express the effects of nuclear damping in the nucleus [8]. The estimated parameters [8] are

$$\begin{aligned} \epsilon_0 &= 19.4\,(\text{MeV}), \qquad E_0 = 18.4\,(\text{MeV}),\\ \epsilon_1 &= 1.40\,(\text{MeV}), \qquad E_1 = 1.60\,(\text{MeV}). \end{aligned} \tag{6}$$

The sum rule of the spectroscopic factors of nucleon orbits for $T \pm \frac{1}{2}$ isospin states is estimated with a simple shell model prescription [17]

$$\sum C^2S_{l,j} = \begin{cases} n_n(l,j) - \dfrac{n_p(l,j)}{2T+1} & \text{for} \quad T_< = T - \frac{1}{2} \\ \dfrac{n_p(l,j)}{2T+1} & \text{for} \quad T_> = T + \frac{1}{2} \end{cases} \tag{7}$$

where $n_{n(l,j)}$ and $n_{p(l,j)}$ are the numbers of neutrons and protons respectively for each (l,j) orbit and T is the isospin of the target nucleus.

Table 1
Optical model parameters used in the DWBA calculations.

^{58}Ni$(p,d)^{57}$Ni:

Particle	V (MeV)	r (fm)	a (fm)	r_c (fm)	W_v (MeV)	W_s (MeV)	r' (fm)	a' (fm)	V_{so} (MeV)	r_{so} (fm)	a_{so} (fm)
Proton	32.11	1.20	0.67	1.26	7.36	3.11	1.28	0.54	4.51	1.02	0.59
Deuteron	a	1.20	0.67	1.26	b	c	1.28	0.54	d	1.02	0.59
Neutron	e	1.25	0.65								

^{54}Fe$(n,d)^{53}$Mn:

Particle	V (MeV)	r (fm)	a (fm)	r_c (fm)	W_v (MeV)	W_s (MeV)	r' (fm)	a' (fm)	V_{so} (MeV)	r_{so} (fm)	a_{so} (fm)
Neutron	30.04	1.20	0.67		7.11	2.38	1.28	0.54	4.33	1.01	0.59
Deuteron	a	1.20	0.67	1.26	b	c	1.28	0.54	d	1.01	0.59
Proton	e	1.25	0.65	1.26							

^{56}Fe$(n,d)^{55}$Mn:

Particle	V (MeV)	r (fm)	a (fm)	r_c (fm)	W_v (MeV)	W_s (MeV)	r' (fm)	a' (fm)	V_{so} (MeV)	r_{so} (fm)	a_{so} (fm)
Neutron	29.65	1.20	0.67		7.11	2.30	1.28	0.54	4.34	1.02	0.59
Deuteron	a	1.20	0.67	1.26	b	c	1.28	0.54	d	1.02	0.59
Proton	e	1.25	0.65	1.26							

^{57}Fe$(n,d)^{56}$Mn:

Particle	V (MeV)	r (fm)	a (fm)	r_c (fm)	W_v (MeV)	W_s (MeV)	r' (fm)	a' (fm)	V_{so} (MeV)	r_{so} (fm)	a_{so} (fm)
Neutron	29.46	1.20	0.67		7.11	2.26	1.28	0.54	4.34	1.02	0.59
Deuteron	a	1.20	0.67	1.26	b	c	1.28	0.54	d	1.02	0.59
Proton	e	1.25	0.65	1.26							

^{58}Fe$(n,d)^{57}$Mn:

Particle	V (MeV)	r (fm)	a (fm)	r_c (fm)	W_v (MeV)	W_s (MeV)	r' (fm)	a' (fm)	V_{so} (MeV)	r_{so} (fm)	a_{so} (fm)
Neutron	29.28	1.20	0.67		7.11	2.22	1.28	0.54	4.34	1.02	0.59
Deuteron	a	1.20	0.67	1.26	b	c	1.28	0.54	d	1.02	0.59
Proton	e	1.25	0.65	1.26							

	Nonlocality parameters (fm)	Finite-range parameter (fm)	spin orbit term $\lambda = 25$
Proton	0.85	0.621	
Neutron	0.85	0.621	
deuteron	0.54		

[a] V = V(proton)+V(neutron), See ref. [6] for V(proton) and V(neutron).
[b] W_v = W_v (proton)+ W_v (neutron), See ref. [6] for W_v (proton) and W_v (neutron).
[c] W_s = W_s (proton)+ W_s (neutron), See ref. [6] for W_s (proton) and W_s (neutron).
[d] V_{so}= V_{so}(proton)+ V_{so} (neutron), See ref. [6] for V_{so} (proton) and V_{so} (neutron).
[e] Well depth adjusted to fit the separation energy.

This sum rule of each orbit is suitable for (p, d) reaction but for (n, d) reaction, we considered no contribution for $n_{n(l,j)}$ i.e. no contribution for IAS in the spectrum. So we applied 100% contribution for the spectra only for $n_{p(l,j)}$ and did some modification of the above sum rule equation i.e.

$$\sum C^2 S_{l,j} = \frac{n_{p(l,j)}}{2T+1} \tag{8}$$

IV. Results and Discussion

Experimental and theoretical double differential cross-sections, for the ^{58}Ni$(p, d)^{57}$Ni and the ^{nat}Fe$(n, d)^{nat}$Mn reactions at 68MeV and 75MeV, respectively are shown in fig 1. For natural Fe target, we consider isotopes (^{54}Fe, ^{56}Fe, ^{57}Fe and ^{58}Fe) with natural abundances and calculate their contributions to double-differential cross-sections. Table 1 shows the optical model parameters used in the DWBA calculations for the ^{58}Ni$(p, d)^{57}$Ni and ^{nat}Fe$(n, d)^{nat}$Mn reactions. In fig 1, thin solid curves represent the experimental spectra and thick one the theoretical. The calculated spectra of both the (p, d) and (n, d) reactions obtained from the same method of calculation are in good agreement with the experimental ones in the higher energy region . To compensate the experimental energy resolutions for the (p, d) and (n, d) reactions, a convolution integration was applied to the theoretical cross-section with experimental resolution.

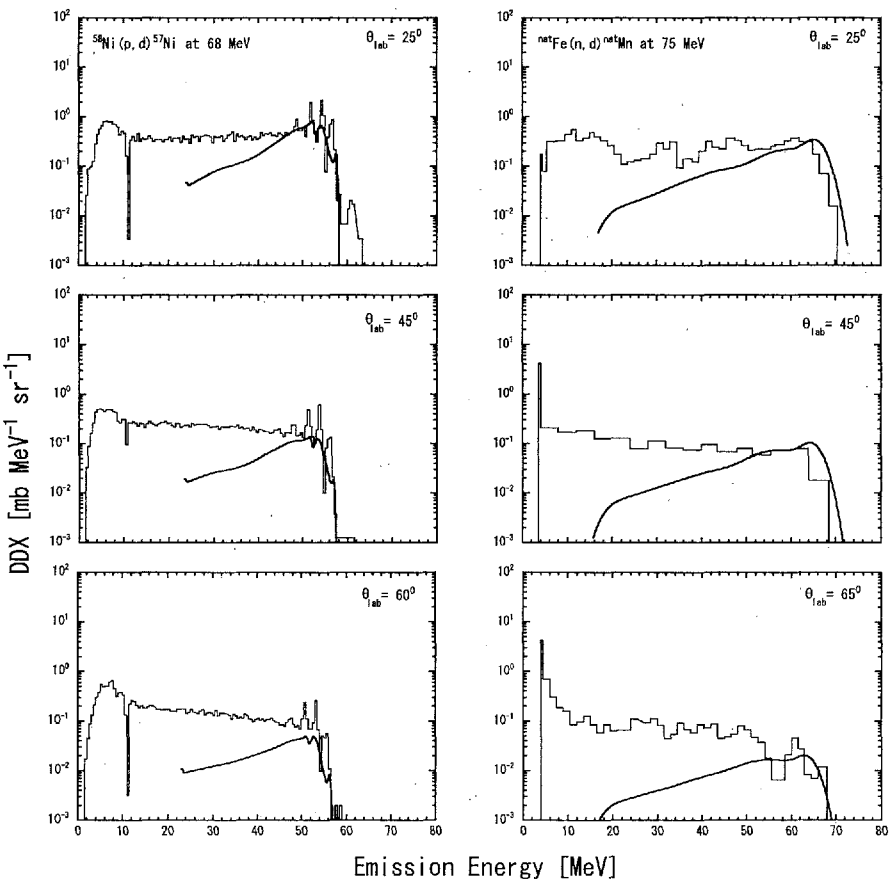

Fig. 1 ^{58}Ni(p, d) DDX data(left) and ^{nat}Fe(n, d) DDX data(right) at 68 MeV and 75 MeV respectively.The thin solid curves show the result of experimental data and the thick one the theoretical.

V. Conclusion

The ^{58}Ni$(p, d)^{57}$Ni and ^{nat}Fe$(n, d)^{nat}$Mn reactions data have been analyzed here with the same method of calculations.

The theoretical calculations can reproduce well experimental spectra of forward angles (25^0,45^0), at high outgoing energies. But for the spectra at backward angles (60^0 for ^{58}Ni and 65^0 for ^{nat}Fe), the calculated results are somewhat underestimated. It is thus possible that for the backward angles there may be some contribution from the pre-equilibrium reaction process.

As a whole, a fairly good overall agreement is found between the theoretical and experimental spectra in both the magnitude and shape of double-differential cross-section. So from all the above consideration we can conclude that this theoretical method is suitable not only for the (p, d) but also for (n, d) reactions. Further studies of the (p, d) and (n, d) reactions for the targets with atomic mass ranging 27-209 are now planned to make this theoretical procedure more global.

References

[1] P. G. Young, E. D. Arthur, and M. B. Chadwick, Los Alamos National Laboratory Report No. La - MS - 12343, 1992.
[2] H. Takada, J.Nucl. Sci. Technol. 33, 275 (1996).
[3] K. Niita, S. Chiba, T. Maruyama, Tomo. Maruyama, H. Takada, T. Fukahori, Y. Nakahara, A. Iwamoto, Phys. Rev., C52, 2620 (1995).
[4] I. Slypen, V. Corcalciuc, J. P. Meulders, Phys. Rev., C51, 1303 (1995).
[5] Syafarudin, F. Aramaki, G. Wakabayashi, Y. Uozumi, N. Ikeda, M. Matoba, K. Yamaguchi, T. Sakae, N. Koori and T. Maki, , J. Nucl. Sci. Technol., Suppl.2, Vol.1, P.377 (August 2002).
[6] A.J. Koning and J.P. Delaroche, Nucl. Phys., A713, 231 (2003).
[7] M. B. Lewis, Phys. Rev., C11, 145 (1975).
[8] M. Matoba, O. Iwamoto, Y. Uozumi, T. Sakae, N. Koori, H. Ohgaki, H. Kugimiya, H.Ijiri, T. Maki, and M. Nakano, Nucl. Phys., A581, 21 (1995).
[9] M. Matoba, K. Kurohmaru, O. Iwamoto, A. Nohtomi, Y. Uozumi, T. Sakae, N. Koori, H. Ohgaki, H. Ijiri, T. Maki, M. Nakano, and H. M. Sen Gupta, Phys.Rev., C53, 1792 (1996).
[10] M. Harada, Y. Watanabe, Y. Tanaka, Y. Matsuoka, K. Shin, S. Meigo, H. Takada, T.Sasa, O. Iwamoto, T. Fukahori, S. Chiba, and S. Tanaka, J. Nucl. Sci. Technol., Suppl.2, Vol.1, P.393 (August 2002).
[11] M. Baba, T. Sanami, Y. Nauchi, Y. Hirasawa, N. Hirakawa, H. Nakashima, S. Meigo,S. Tanaka, American Society for Testing and Materials, West Conshohocken, PA, P.447 (2001).
[12] P. D. Kunz, Code DWUCK, University of Colorado (Unpublished).
[13] C. Mahaux and R. Sartor, Nucl. Phys. A 493 (1989) 157; Adv. Nucl. Phys., 20, P.1 (1991).
[14] K. Hisamochi, O. Iwamoto, A. Kisanuki, S. Budihardjo, S. Widodo, A. Nohtomi, Y. Uozumi, T. Sakae, M. Matoba, M. Nakano, T. Maki, S. Matsuki, and N. Koori, Nucl.Phys., A564, 227 (1993).
[15] A. Bohr and B. R. Motelson, "Nuclear Structure" (W. A. Benjamin, INC., 1996, New York, Amsterdam) Vol. 1, Appendix 2D.
[16] G. E. Brown and M. Rho, Nucl. Phys., A372, 397 (1981).
[17] J. B. French and M. H. Macfarlane, Nucl. Phys., 26, 168 (1961).

3.5 Investigation of the proton-induced activation reactions on natural molybdenum.

M. S. Uddin, M. Hagiwara, F. Tarkanyi[1], F. Ditroi[1] and M.Baba
Cyclotron and Radioisotope Center, Tohoku University, Aramaki, Aoba-ku, Sendai 980-8578, Japan
[1]Institute of Nuclear Research of the Hungarian Academy of Sciences, Debrecen,H-4001, Hungary

Excitation functions of the proton-induced activation reactions on a natural molybdenum target were measured using the stacked foil activation technique in the energy range 22-67 MeV at the Tohoku Unuversity cyclotron laboratory. In addition the thick target integral yield was desired using the measured cross-section data.

1. Introduction

Molybdenum is important as an accelerator structural material and the measurement of cross-section data on this element is of interest to apply to the thin layer activation (TLA) technique to determine the rate of wear, corrosion and erosion processes of Mo. The ^{99m}Tc ($T_{1/2}$= 6.02 h) isotope is the single most important radioisotope for diagnostic nuclear medicine. The ^{99m}Tc labeled radio pharmaceuticals account for over 80 % of all diagnostic nuclear medicines used over the world and is provided through a ^{99}Mo→^{99m}Tc generator system.

In every day practice ^{99}Mo is produced by use of research reactors. There are two ways of ^{99}Mo production, i.e., the (n,γ) and (n, fission) nuclear reactions. Production of ^{99m}Tc and ^{99}Mo by charged particle bombardment is also possible. The most suitable reactions for the production of ^{99}Mo is ^{100}Mo(p,pn)^{99}Mo and ^{100}Mo(p,2p)^{99}Nb(15 s) → ^{99}Mo. For production of ^{99m}Tc the ^{100}Mo(p,2n)^{99m}Tc reaction is preferable.

Several authors have reported a variety of data of proton induced reactions on the molybdenum but most of these studies are limited to a maximum proton energy of 40 MeV. A few of them did measurement at higher energy, but large discrepancies are found among them [1,2]. Therefore, the data of isotope production from Mo target in medium proton energy are not sufficient yet. The present work was performed to give reliable excitation functions and thick target integral yields of Mo+p reactions in the energy range 22-67 MeV using the 90 MeV AVF Cyclotron at Cyclotron and Radioisotope Center (CYRIC) of Tohoku University.

The cross-sections were also calculated theoretically by using the Monte Carlo code, PHITS (Particle and Heavy Ion Transport code System) [3], which is a new version of NMTC/JAM code based on INC and GEM models, to compare with experimental values.

2. Experimental technique

The independent and "cumulative cross-sections" of the proton-induced reactions on molybdenum were measured as a function of proton energy in the range 22-67 MeV using the conventional stacked foil activation technique. Special care was taken in preparation of uniform targets with known thickness, in determination of the proton energy degradation and of the intensity of the bombarding beam along the target stack and in determination of the activities of the samples. High purity (> 99%) Mo foil (49.58 μm thick) of natural isotopic composition (^{92}Mo 14.8%; ^{94}Mo 9.3%; ^{95}Mo 15.9%; ^{96}Mo 16.7%; ^{97}Mo 9.6%; ^{98}Mo 24.1%; and ^{100}Mo 9.6%) was used as a target material for the irradiation. The stack was assembled from Mo, Cu and Al like as Cu–Al–Mo and 10 groups were set together in an aluminum holder for irradiation. The size of the target was about 1 cm ×1 cm which is sufficiently larger than the proton beam collimator diameter, 8 mm. The stacked samples were irradiated by a 70 MeV collimated proton beam (8 mm in diameter) of ~25 nA for 1 hr and 17 minutes using the AVF Cyclotron at CYRIC, Tohoku University. A proton beam accelerated by the AVF Cyclotron was transported to the target room. It was necessary to ensure that equal areas of the monitor and the target foils intercepted the beam. The irradiation geometry used guaranteed that practically the whole entering beam passed through every foil. Reactions induced on aluminum (102 μm thick) and copper (104.2 μm thick) foils were used to monitor the parameters of the bombarding beam. The complete excitation functions of the monitor reactions were measured simultaneously with the reactions induced on molybdenum to confirm the beam intensity and the energy, and also to check the relative behavior of the recommended data.

3. Data analysis

The activities of the radioactive products in the target and monitors were measured nondestructively using HPGe-detector gamma ray spectroscopy at 5 cm and 19 cm from the detector surface. The efficiency versus

energy curve of the detector was determined experimentally using the standard gamma-ray point sources with known strength, ^{152}Eu, ^{133}Ba, ^{241}Am, ^{60}Co and ^{137}Cs at both 5 cm and 19 cm from the endcap of the detector. The proton beam intensity was determined via the monitor reactions [4], ^{27}Al(p,x)^{22,24}Na and ^{nat}Cu(p,x)^{56}Co,^{62,65}Zn taken place at the top radioactive monitor foils of the stack considering that the monitor foils were irradiated simultaneously and measured at the same detector and in a comparable geometry as the Mo targets. The proton energy degradation along the stack was determined using the computer program SRIM-2002 [5].

The cross-sections were deduced for the production of ^{93m,99}Mo, ^{94,95,95m,96}Tc, ^{90,92m,95,96}Nb, ^{86,88,89}Zr and ^{86,87,88}Y in the proton energy range 22-67 MeV by using the well-known activation formula. The decay data for monitors and molybdenum were taken from ENSDF (1996) . The cross–section data of the monitors were taken from EXFOR [2003]. The thick target integral yields were determined by using the measured cross-sections and stopping power via integration from the respective threshold up to 67 MeV. The following errors were considered to derive total uncertainty on cross-section values: statistical error (0.3-5%), error in proton flux (5.8%) and the error in the energy dependence of efficiency calibration (~3%). The overall uncertainty of the cross-sections is around 10 %.

The activities of the140 keV, 776 keV and 765 keV gamma rays emitted from different radinuclides were also corrected by using the independent gamma rays of the corresponding radionuclides and the establishing decay curve.

The activity of 511 keV and 909.10 keV gamma lines were corrected for subtracting the background counts from total measuring counts. The data were corrected for the coincidence-summing effect caused by the coincidence detection of two or more gamma-rays.

We have observed good agreement between the measured results at short and long distances from the detector surface after the coincidence-summing correction. We have also obtained excellent agreement in the numerical values of proton fluxes determined individually using the monitor reactions after coincidence-summing correction

The proton flux determined was considered constant through the foil stacks to avoid the effects of the energy broadening and mean energy on the cross-section measurements. There is a very small loss in the number of protons and not possible to measure it practically.

4. Results and discussion

The measured excitation functions with other experiments and theoretical calculations are shown in Figs. 1-11. The thick target integral yields determined in the present work are given in Figs. 12-15. The obtained results are discussed in the following subsequent sections.

4.1. *Excitation functions of the proton-induced reactions on Mo*

4.1.1 *^{100}Mo(p,x)^{99}Mo and ^{nat}Mo(p,x)^{93m}Mo*

The measured excitation function of ^{99}Mo production is shown in Fig. 3. ^{99}Mo produced in directly or through the decay of the parent isotope ^{99}Nb (15 s) by proton activation on ^{100}Mo target isotope. To determine the production cross-section of ^{99}Mo, the isotopic aboundance of ^{100}Mo (9.6 %) was normalized to 100% enriched ^{100}Mo isotope. The hump at around 41 MeV in Fig.1 indicates two reaction channels leading to the production of ^{99}Mo are ^{100}Mo(p,pn)^{99}Mo (Q = –8.3 MeV) and ^{100}Mo(p,2p)^{99}Nb (15 s) → ^{99}Mo (Q = – 11.14 MeV). Takacs et al. [1] reported cross-section data up to 37 MeV and Levkovskij [6] reported up to 29 MeV for ^{99}Mo production on enriched ^{100}Mo isotope that are shown in Fig.1. Our measured values are consistent with Scholten et al.[7] at the two points, 22 and 35 MeV, but his results at other energies are scattered. Our measured values showed excellent agreement with Takacs et al. and Levkovskij in lower energy region and this fact confirms the reliability of our measured data at the energies above 37 MeV. Lagunas-solar et al.[8] reported numerical cross-section data shown in Fig.1 that are much lower than the recently published data in lower energy region.

The measured ^{93m}Mo production cross-section shown in Fig.2 increases almost linearly. Various reaction channels are opened at different stages depending on threshold energy in the overall investigated energy range contributed to the direct formation of ^{93m}Mo.

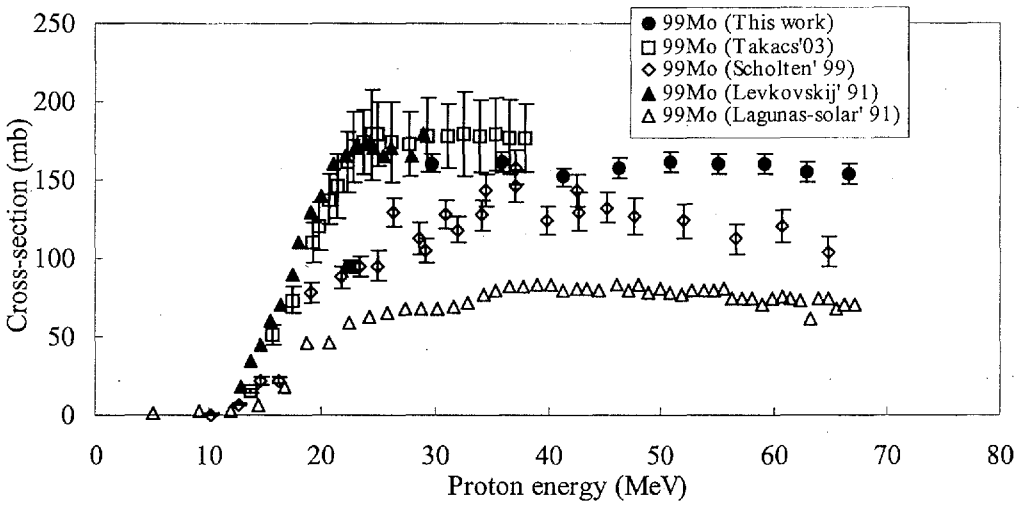

Fig.1 Excitation function of the $^{100}Mo(p,x)^{99}Mo$ reaction.

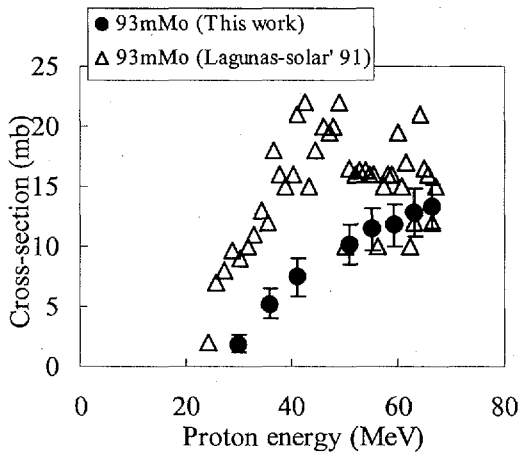

Fig.2 Excitation function of the $^{nat}Mo(p,x)^{93m}Mo$ reaction

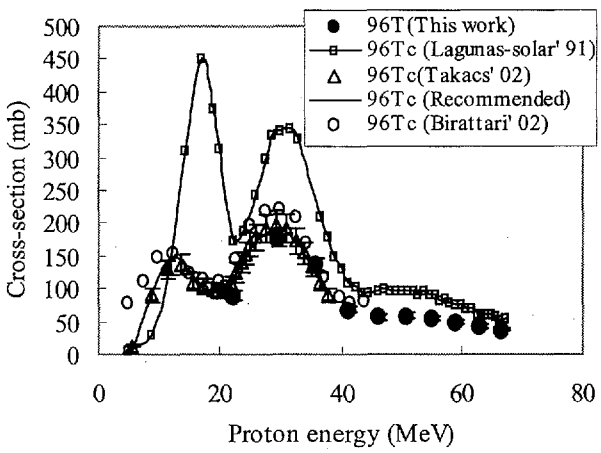

Fig.3 Excitation function of the $^{nat}Mo(p,x)^{96}Tc$ reaction.

4.1.2 $^{nat}Mo(p,x)^{96,95,95m,94}Tc$

To obtain high reliability, we measured excitation function of ^{96g}Tc production by using the intense independent gamma line, 812.5 keV. The measured excitation function of ^{96}Tc production shown in Fig. 5 is due to a sum of three single processes, $^{96}Mo(p,n)^{96}Tc$ (Q = – 3.75 MeV), $^{97}Mo(p,2n)^{96}Tc$ (Q = – 10.57 MeV) and $^{98}Mo(p,3n)^{96}Tc$ (Q = – 19.21 MeV). It is interesting to note that the recommended values and large number of recently published data for ^{96}Tc production are available only up to 38 MeV. Our measured values show very good agreement with the latest data reported by Takacs et al. and the recommended values shown in Fig.3 and that fact confirms the high reliability of the measured cross-section values of ^{96}Tc production in the whole investigated energy range of the present measurement. Only Lagunas-solar et al. reported ^{96}Tc production cross-sections in the energy range 5-67 MeV and it is so much higher than recommendation in lower energy region that it can not be believed and no explanation for such a high value was found in his work. Therefore our measured values may be considered as a first one from 40 MeV to 67 MeV.

Birattari et al.[9], Kormali et al. and Levkovskij indicate the reliability of the measured values of ^{94}Tc in lower energy region that are shown in Fig.4. Because of the short half-life and the existence of numerous reaction channels are available for ^{94}Tc production from a natural Mo target, this radionuclide was produced abundantly in the 22-67 MeV energy region studied in the present work. The measured excitation function of ^{95}Tc (20 h) radionuclide production via the numerous direct reaction channels and the IT decay of ^{95m}Tc (61 d) is compatible with Levkovskij (1991) and Birattari et al. (2002) both in shape and magnitudes. In the present work, the cross-sections for ^{95m}Tc production are also measured and shown in Fig. 5. In the cases of the investigated Tc-radionuclides productions, PHITS calculation does not provide cross-sections.

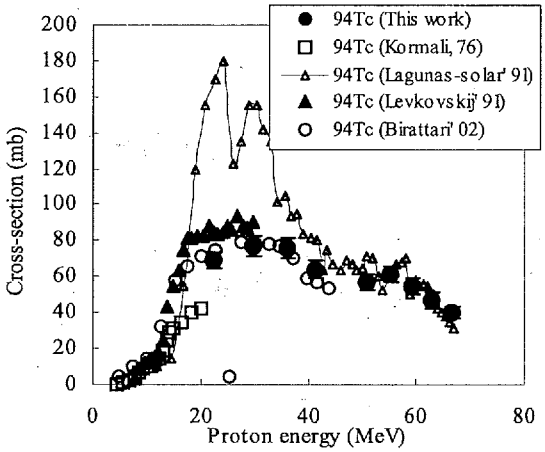

Fig.4 Excitation function of the $^{nat}Mo(p,x)^{94}Tc$ reaction.

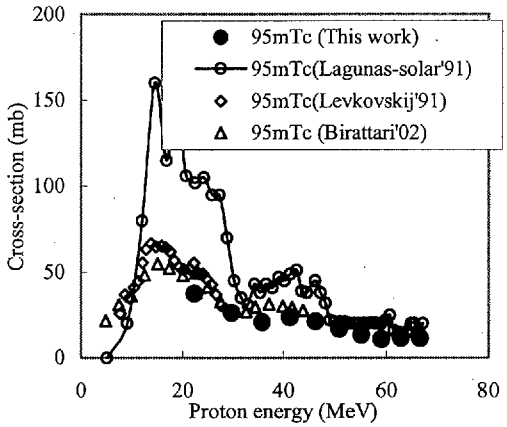

Fig.5 Excitation function of the $^{nat}Mo(p,x)^{95m}Tc$ reaction.

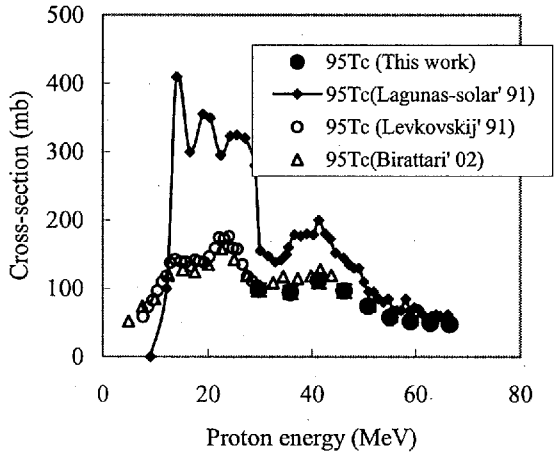

Fig.6 Excitation function of the $^{nat}Mo(p,x)^{95}Tc$ reaction

4.1.3 $^{nat}Mo(p,x)^{90,92m,95,96}Nb$

The production of Nb radioactivities must be considered as a potential sources of radionuclide contamination in the production of ^{99}Mo and /or ^{99m}Tc. The production cross-sections of Nb radionuclides in the investigated energy range are not reported yet anywhere. In the present work, ^{90}Nb, ^{92m}Nb, ^{95}Nb and ^{96}Nb radionuclides were identified as the reaction products and the obtained results are shown in Figs. 7 -9. The production of Nb radionuclides is most likely due to (p,α)-type reactions on Mo target, the Coulomb barrier in both the entrance and exit channels largely inhibits the probability of these reactions. In the case of ^{90}Nb, its production through the decay of the parent ^{90}Mo also contributed on the direct formation cross-sections from below 30 MeV as shown in Fig.7.

4.1.4 $^{nat}Mo(p,x)^{86,88,89}Zr$

Our measured excitation functions of Zr radionuclides along with the values of model calculation using the PHITS code are shown in Fig. 10. The theoretically calculated values of ^{89}Zr production are completely supporting the experimental values, both in shape and magnitudes. The PHITS calculation for ^{88}Zr radionuclide is also consistent with the measured excitation function. By considering the good agreement between the experiment and theoretical calculations, it could be mentioned that the productions of ^{89}Zr and ^{88}Zr radionuclides are most likely direct formations from Mo targets. The shape of excitation functions for ^{86}Zr is similar with model calculations.

4.1.5 $^{nat}Mo(p,x)^{86,87,88}Y$

The experimentally measured cross-sections for the productions of yttrium radionuclides from Mo target are not available in literature. The measured cross-sections are shown in Fig. 11 with the PHITS calculations. The measured excitation functions for all of the identified Y-radionuclides are larger than that of theoretical calculations using PHITS code. Because, all of the Y-radionuclides are produced through the decay of parent radionuclides, i.e., the experimental values are "commulative" while PHITS calculation shows the cross-section of direct reaction.

4.2. *Thick target integral yields as a function of proton energy*

Mo is an impotant material in nuclear technology. For different possible practical applications we have deduced the thick target integral yields by using the recently measured excitation functions and the available literature data at low energies, which was not covered by us. In most of the cases, the thick target integral yields are linearly rising with the increase of bombarding proton energy that are shown in Fig.12-15. It has been found from Fig. 15 that the contribution of the investigated energy range to the total integral yields (from threshold) is not very significance for ^{88}Y radionuclide.

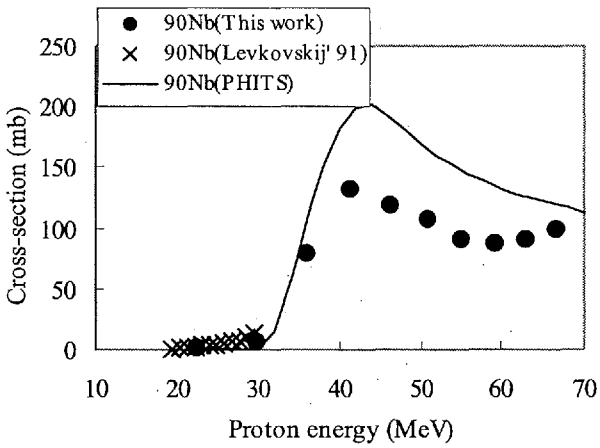

Fig.7 Excitation function of the $^{nat}Mo(p,x)^{90}Nb$ reaction.

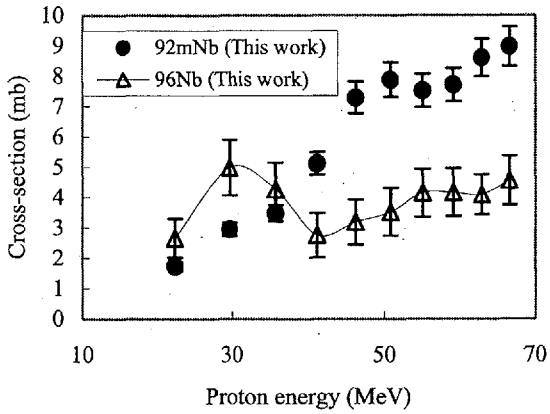

Fig.8 Excitation function of the $^{nat}Mo(p,x)^{92m,96}Nb$ reaction.

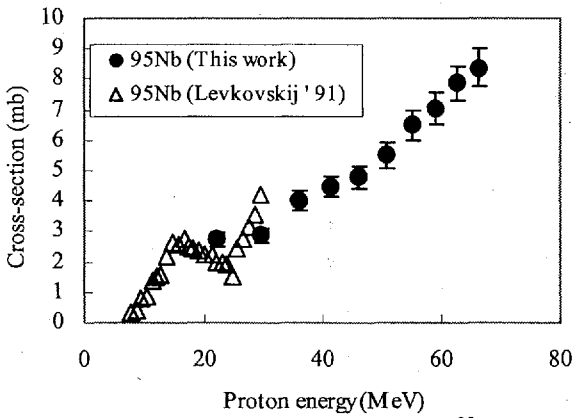

Fig.9 Excitation function of the $^{nat}Mo(p,x)^{95}Nb$ reaction.

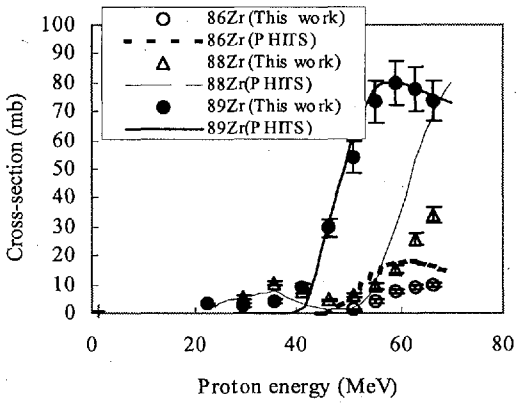

Fig.10 Excitation function of the $^{nat}Mo(p,x)^{86,88,89}Zr$ reaction.

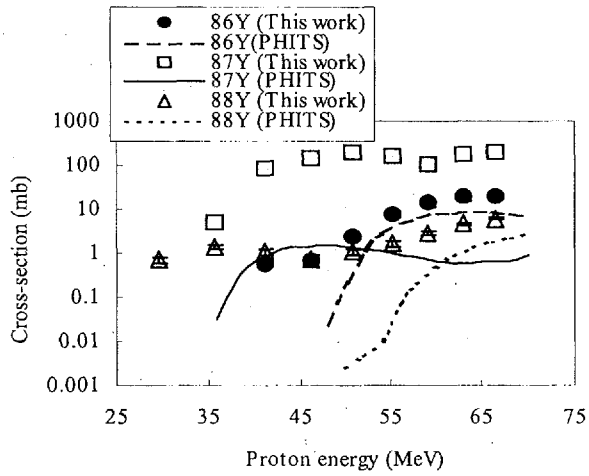

Fig.11 Excitation function of the $^{nat}Mo(p,x)^{86,87,88}Y$ reaction.

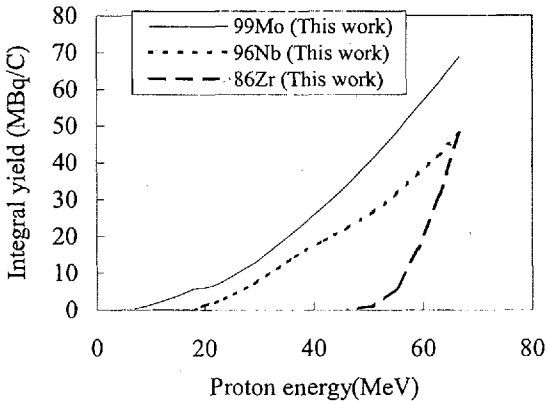

Fig. 12 Thick target integral yields for the production of ^{99}Mo, ^{96}Nb and ^{86}Zr radionuclides.

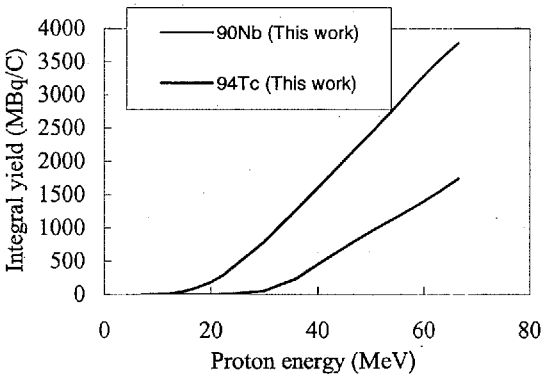

Fig. 13 Thick target integral yields for the production of ^{90}Nb, and ^{94}Tc radionuclides.

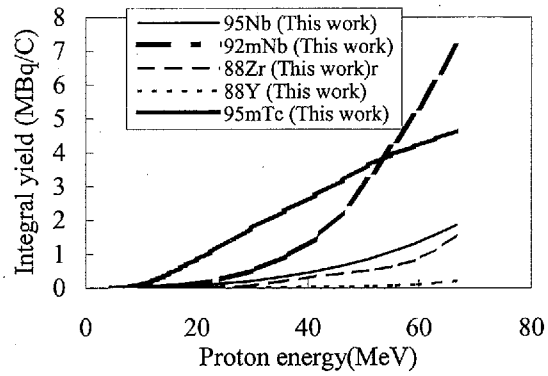

Fig. 14 Thick target integral yields for the production of ^{95}Nb, ^{92m}Nb, ^{88}Zr, ^{88}Y and ^{95m}Tc radionuclides.

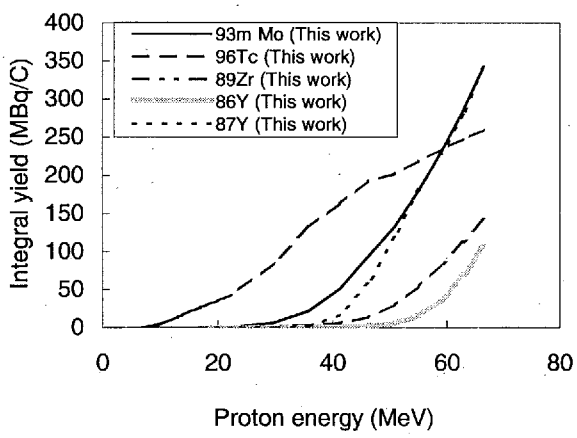

Fig. 15 Thick target integral yields for the production of ^{93m}Mo, ^{96}Tc, ^{89}Zr, ^{86}Y and ^{87}Y radionuclides.

5. Conclusion

We have measured the excitation functions for the production of the radionuclides with >4 h half lives through the proton-induced activation reactions on molybdenum in the energy range 22-67 MeV using the stacked foil technique. In the cases of Mo- and Tc-radionuclides, in view of the excellent consistency with the available literature and recommended data of lower energy region it may be considered our measured excitation functions as only one reliable above 38 MeV (upto 67 MeV). No cross-section data for Nb, Zr and Y radionuclides productions exist in our investigated energy range. The present experiment has given new data for all of the investigated proton-induced reactions on Mo in the energy range 22-67 MeV. In cases of the investigated Mo- and Tc-radionuclides and some of Nb-radionuclides, results were not obtained by PHITS due to its limitation.

From the new cross-sections, first integral yields are reported at higher energies (up to 67 MeV). We have to mention that in the investigated energy range no directly measured yield values exist .The cross-sections and integral yields obtained in the present work would be useful to upgrade theoretical codes, for estimation of the activity for future accelerator developments and other radiation safety problems, for thin layer activation technique and for checking the yield on enriched target for medical isotope production.

References

[1] i) Takacs S., Szucs Z., Tarkanyi F., Hermanne A. and Sonck M. :Radioanal. Nucl. Chem. 257(1), 195-210 (2003).
ii)Takacs S., Tarkanyi F., Sonck M. and Hermanne A. : Nucl. Inst. Method in Phy. Res. B !98, 183-196 (2002).
[2] Kormali S.M., Swindle D.L.and Schweikert E.A. : J. Radi.Chem. 31, 437 (1976).
[3] Iwase H., Niita K.and Nakamura T. : J. Nucl. Science and Technology. 39 (11), 1142-1151 (2002).
[4] Tarkanyi F., Takacs S., Gul K., Hermanne A., Mustafa M.G., Nortier M., Oblozinsky P., Qaim S.M., Scholten B., Shubin Y.N. and Youxiang, Z.: IAEA-TECDOC-1211, IAEA, Vienna, Chapter 4. Available from < www-nds.iaea.or.at/medical>, p.49 (2000).
[5] Ziegler J.F., Biersack J.P. and Littmark U. : Pergamon, New York (2002)
[6] Levkovskij V.N. : Inter-vesi. Moscow (1991).
[7] Scholten B., Lambrecht R.M., Cogneau M. and Vera Ruiz H.: J. Appl. Radiat. Isotopes. 51, 69 (1999).
[8] Lagunas-solar M.C., Kiefer P.M, Carvacho O.F., Lagunas C.A. and Cha Y.P.: J. Appl. Radiat. Isot. 42 (7), 643-657 (1991).
[9] Birattari C., Bonardi M., Gini L., Groppi F. and Menapace E. : J. Nucl. Scien. Tech., Suppl.2, 1302. August (2002)

JP0450496

JAERI－Conf 2004－005

3.6 PHOTODISINTEGRATION OF DEUTERIUM

K.Y. Hara*,
H. Utsunomiya, S. Goko, H. Akimune, T. Yamagata, and M. Ohta
Department of Physics, Konan University, Kobe 658-8501, Japan
H. Toyokawa, K. Kudo, A. Uritani, and Y. Shibata
National Institute of Advanced Industrial Science and Technology (AIST), 1-1-1 Umezono, Tsukuba, Ibaraki 305-8568, Japan
Y.-W. Lui
Cyclotron Institute, Texas A & M University, College Station, Texas 77843, USA
H. Ohgaki
Institute of Advanced Energy, Kyoto University, Gokanosho, Uji, Kyoto 611-0011, Japan

* *e-mail: kaoru@konan-u.ac.jp*

Abstract:
Photodisintegration cross sections were measured for deuterium with Laser Compton scattering γ beams at E_γ = 2.3 - 4.6 MeV. The present data made it possible to experimentally evaluate $R(E) = N_a\sigma v$ for the p(n,γ)D reaction with 6% uncertainty in the energy region relevant to big bang nucleosynthesis (BBN). The result confirms the past theoretical evaluation and the recent calculation based on the effective field theory. The reaction rate for the p(n,γ)D reaction is presented for the BBN in the precision era.

1. Introduction

Big bang nucleosynthesis (BBN), which is one of the cornerstones of big bang cosmology, has been developed based on the primeval abundances of four elements (D, ^{3}He, ^{4}He, ^{7}Li) [1-8]. BBN may be entering a precision era in view of the latest observations of deuterium abundances for quasar systems [9-12] and temperature anisotropies of the cosmic microwave background by WMAP [13]. In the precision era, the primeval abundance of deuterium is expected to play a role of a *cosmic baryometer* [14-17], because of its good sensitivity to baryon density.

Recently, a Monte Carlo method of directly incorporating nuclear inputs in the standard BBN calculations dramatically reduced uncertainties in the predicted abundances by as large as a factor of three [15, 18]. Among nuclear inputs for twelve key reactions in the standard BBN, however, only the one for p(n,γ)D is very scarce. Capture data for deuterium are available only at four energies relevant to the BBN [19, 20] though a large collection of photodisintegration data is available above 5 MeV [21-27]. In the energy region of the BBN, the cross section starts deviating from the $1/v$ law for the M1 capture and including the contribution from the E1 capture. The scarcity of data in this transitional energy region made a theoretical evaluation of the cross section mandatory. Although the theoretical cross section is available in the ENDF/B-VI data library [28], it is said that details of the evaluation are not possible to trace [15]. Very recently, revived attempts were made of evaluating the cross section within the framework of the effective field theory [29, 30].

Experimental cross sections for deuterium with sufficient accuracy are desired in the precision era. In this work, photodisintegration cross sections for deuterium were measured at 7 energies near threshold. We discuss the dependence of the p(n,γ)D reaction cross section on the energy relevant to the BBN in comparison with theoretical evaluations. We present the reaction rate of the p(n,γ)D reaction for BBN.

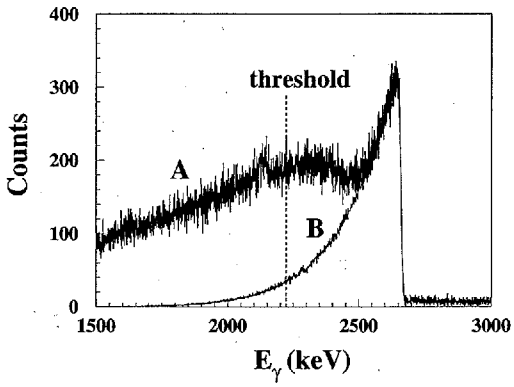

Figure 1: Response of a 120% Ge detector to the LCS γ rays (A) and an energy distribution of the LCS γ beam determined by a Monte Carlo analysis of the Ge response with the code EGS4 (B). A fractional γ flux above the threshold is responsible for the photodisintegration of deuterium.

2. Experimental method

The laser Compton scattering (LCS) γ beam has been developed at the National Institute of Advanced Industrial Science and Technology (AIST) [31, 32]. The LCS γ rays were produced in head-on collisions of Nd:YLF Q-switch laser photons with relativistic electrons in the accumulator ring TERAS. Quasi-monochromatic γ beams, which were collimated into a 2 mm spot in diameter with a 20 cm Pb block, were used to irradiate heavy water.

Energy spectra of the LCS γ rays were measured with a 120% Ge detector and analyzed with a Monte Carlo code EGS4 [33] to determine the tail profile of the LCS beam. An energy spectra of the LCS γ rays that best reproduced the Ge response (A) is shown (B) in Fig. 1. The fraction of LCS γ rays above 2.22 MeV was responsible for photodisintegration.

The total number of γ rays was determined from responses of a large volume (8 in. in diameter and 12 in. in thickness) NaI(Tl) detector to multi photons per pulse of the 1 kHz LCS beam and to single photons of the dc beam. The uncertainty in the total flux arose from nonlinearity in the response of our beam monitoring system to the pulsed multi photons. In view of the statistical analysis of pile-up spectra [34], we assigned 3% uncertainty to the γ flux.

The neutron detector consists of sixteen ^{3}He proportional counters (EURISYS MEASURES 96NH45) embedded in a polyethylene moderator. Eight counters were placed in a concentric ring at 7 cm from the beam axis; the other eight at 10 cm. The neutron detection efficiency was measured with a neutron source of ^{252}Cf whose uncertainty in the absolute neutron emission rate is 5%. The results for the ^{252}Cf source were well reproduced by Monte Calro simulations with the MCNP code [35]. The efficiencies for monoenergetic neutrons were calculated with the same code and were used in the data analysis.

3. Photodisintegration cross sections for deuterium

The present photodisintegration cross sections are shown in Fig. 2. The data analysis method and the numerical values of the cross sections are given in our recent paper [36, 37]. All the photonuclear data compiled in the IAEA document [38] are also shown in Fig. 2(a). In Fig. 2(b), the data of Bishop *et al.* [39], though not included in the IAEA compilation, are shown. The

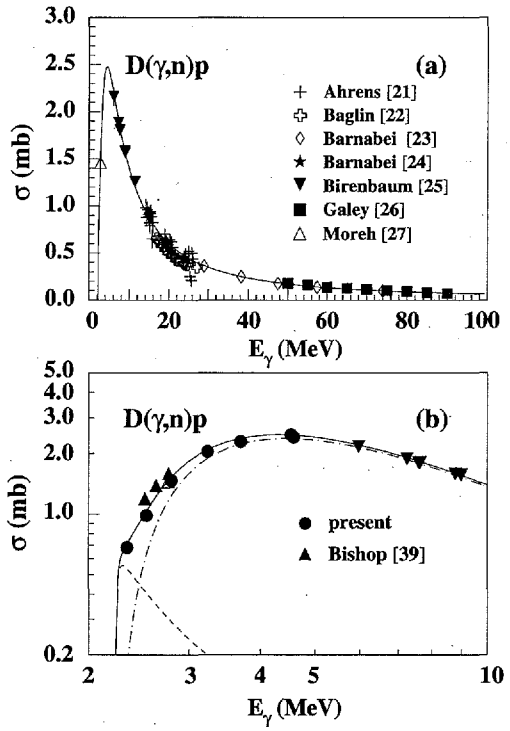

Figure 2: Photodisintegration cross sections for deuterium. The JENDL evaluations are shown by the dashed line for the M1 cross section, by the dot-dashed line for the E1 cross section, and by the solid line for the sum, respectively.

datum of Moreh *et al.* [27] is consistent with our data, whereas the data of Bishop *et al.* [39] are not. The solid line is the JENDL evaluation [40] which is the sum of the E1 (the dot-dashed line) and the M1 (the dashed line) cross sections. The JENDL evaluation is based on the M1 cross section of Segre [41] and the E1 cross section of the simplified Marshall-Guth model [42] below 10 MeV and that of Partovi above 10 MeV [43].

The systematic uncertainty of the cross section has three source: the neutron emission rate of the ^{252}Cf source (5%), the total flux of the LCS γ rays (3%), and the angular distribution of neutrons (2%). The overall systematic uncertainty is 6.2% after adding three sources in quadrature.

4. Evaluation of the reaction rate for the p(n,γ)D reaction

The present data were converted to capture cross sections with the detailed balance theorem. Figure 3 shows $R(E) = N_a \sigma v$ for the p(n,γ)D reaction as a function of the center of mass energy E, where N_a is the Avogadro's number, σ is the capture cross section, and v is the c.m. velocity. High-energy capture data [44-49] are also shown in the figure. A least squares fit was performed to the present data combined with the preceding data in the energy region up to 2 MeV. The preceding data included the latest thermal neutron capture datum [50], the capture data [19, 20], and the photodisintegration datum [27]. The data of Ref. [39] were not included in the fit. The same polynomial expansion formula as that [Eq. (19), m=5] in Ref. [7] was used. The thick solid

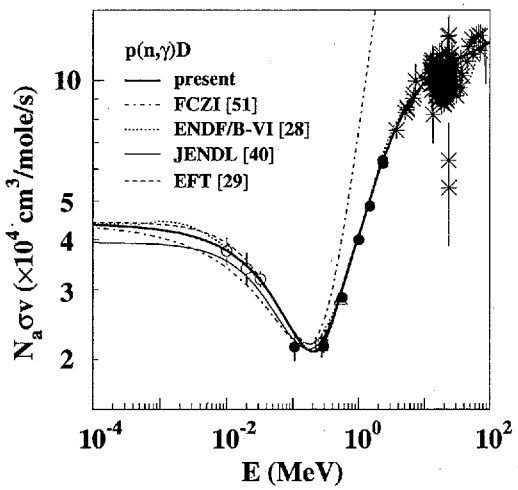

Figure 3: $R(E)=N_a\sigma v$ for the p(n,γ)D reaction as a function of the c.m. energy. Keys for the data are solid circles (present); open circles [19]; open square [20]; open triangle [27]. Only statistical uncertainties are shown for the present data. The high-energy data are from Refs. [44-49]. The dot-dashed line, the dotted line, the shin solid line, and the dashed line stand for the theoretical evaluations of FCZI [51], ENDF/B-VI [28], JENDL [40], and EFT [29], respectively. The solid line shows the present fit to the data connects to the JENDL evaluation at 1 MeV.

line shows the present fit to the data which is connected to the JENDL evaluation [40] at 1 MeV. The χ^2 value of the best fit was 0.61. The error involved in the fit was estimated to be 6%, which is dominated by the systematic uncertainty of the present measurement. For comparison, the theoretical evaluations of Fowler, Caughlan, and Zimmerman (FCZI) [51], ENDF/B-VI, and JENDL are shown by the dot-dashed line, the dotted line, and the thin solid line, respectively. In addition, the result of the effective field theory (EFT) calculation [29] is shown by the dashed line. The present $R(E)$ evaluation based on experimental data is consistent with the theoretical evaluations of the ENDF/B-VI and the EFT.

The reaction rate $N_a\langle\sigma v\rangle$, which is the thermal average of the present $R(E)$ function over the Maxwell-Boltzmann velocity distribution, was calculated in the temperature range $0.01<T_9<100$. The numerical intergration was made from 0.1 keV to 100 MeV. The resultant reaction rate is presented by the solid line in Fig. 4 in comparison with the past theoretical evaluation of FCZI (dot-dashed line) and ENDF/B-VI (dotted line).

5. Conclusions

Photodisintegration cross sections for deuterium were measured at 7 energies near threshold with the LCS γ beams at AIST. These cross sections resolve the scarcity of data relevant to BBN. The present data combined with the preceding data provide an experimantal fundation for the p(n,γ)D reaction cross section which has been evaluated only theoretically for more than three decades since the FCZI. The present $R(E)$ evaluated with 6% uncertainty confirms those theoretical evaluations made in the past and the recent EFT calculation. The reaction rate for the p(n,γ)D reaction is presented for the BBN in the precision era.

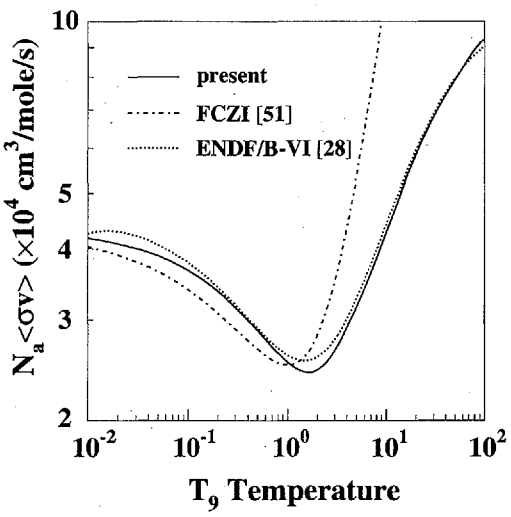

Figure 4: Reaction rate for the p(n,γ)D reaction. The solid line shows the present evaluation based on experimantal data. The theoretical evaluation of FCZI [51] and ENDF/B-VI [28] for the reaction rate were shown by the dotted line and the dashed line, respectively.

References

[1] P.J.E. Peebles, *Phys. Rev. Lett.* **16**, 410 (1966); *Astrophys. J.* **146**, 542 (1966).
[2] R.V. Wagoner, W.A. Fowler, and F. Hoyle, *Astrophys. J.* **148**, 3 (1967).
[3] H. Sato, *Prog. Theor. Phys.* **38**, 1083 (1967).
[4] H. Reeves, J. Audouze, W.A. Fowler, and D. Schramm, *Astrophys. J.* **179**, 909 (1973).
[5] L.M. Krauss and P. Romanelli, *Astrophys. J.* **358**, 47 (1990).
[6] T.P. Walker, G. Steigman, D.N. Schramm, K.A. Olive, and H.-S. Kang, *Astrophys. J.* **376**, 51 (1991).
[7] M.S. Smith, L.H. Kawano, and R.A. Malaney, *Astrophys. J. Suppl. Ser.* **85**, 219 (1993).
[8] C.J. Copi, D.N. Schramm, and M.S. Turner, *Science* **267**, 192 (1995).
[9] S. Burles and D. Tytler, *Astrophys. J.* **499**, 699 (1998).
[10] S. Burles and D. Tytler, *Astrophys. J.* **507**, 732 (1998).
[11] D. Kirkman, D. Tytler, S. Burles, D. Lubin, and J.M. O'Meara, *Astrophys. J.* **529**, 655 (2000).
[12] J.M. O'Meara, D. Tytler, D. Kirkman, N. Suzuki, and J.X. Provhaska, *Astrophys. J.* **552**, 718 (2001).
[13] D.N. Spergel *et al.*, Astrophys. J. Suppl. Ser. **148**, 175 (2003).
[14] D.N. Schramm and M.S. Turner, *Rev. Mod. Phys.* **70**, 303 (1998).
[15] K.M. Nollett and S. Burles, *Phys. Rev D* **61**, 123505 (2000).
[16] K.A. Olive, G. Steigman, and T.P. Walker, *Phys. Rep.* **333-334**, 389 (2000).
[17] S. Burles, K.M. Nollett, and M.S. Turner, *Astrophys. J. Lett.* **552**, L1 (2001).
[18] S. Burles, K.M. Nollett, J.W. Truran, and M.S. Turner, *Phys. Rev. Lett.* **82**, 4176 (1999).
[19] T.S. Suzuki *et al.*, *Astrophys. J. Lett.* **439**, L59 (1995).

[20] Y. Nagai *et al.*, *Phys. Rev. C* **56**, 3173 (1997).
[21] J. Ahrens *et al.*, *Phys. Lett.* **56***B*, 49 (1974).
[22] J.E.E. Baglin, R.W. Carr, E.J. Bentz, C.-P. Wu, *Nucl. Phys.* **A201**, 593 (1973).
[23] R. Bernabei *et al.*, *Phys. Rev. Lett.* **57**, 1542 (1986).
[24] R. Bernabei *et al.*, *Phys. Rev. C* **38**, 1990 (1988).
[25] Y. Birenbaum, S. Kahane, and R. Moreh, *Phys. Rev. C* **32**, 1825 (1985).
[26] J.A. Galey, *Phys. Rev.* **117**, 763 (1960).
[27] R. Moreh, T.J. Kennett, and W.V. Prestwich, *Phys. Rev. C* **39**, 1247 (1989).
[28] G.M. Hale, D.C. Dodder, E.R. Siciliano, and W.B. Wilson, Los Alamos National Laboratory, ENDF/B-VI evaluation, Mat No. 125, Rev. 1, 1991.
[29] J.-W. Chen amd M.J. Savage, *Phys. Rev. C* **60**, 065205 (1999).
[30] G. Rupak, *Nucl. Phys.* **A678**, 405 (2000).
[31] H. Ohgaki *et al.*, *IEEE Trans. Nucl. Sci.* **38**, 386 (1991).
[32] H. Ohgaki *et al.*, *Nucl. Instr. and Meth. A* **455**, 54 (2000).
[33] W.R. Nelson, H. Hirayama and W.O. Roger, "The EGS4 Code Systems" SLAC-Report No. 265, 1985.
[34] H. Toyokawa *et al.*, *IEEE Trans. Nucl. Sci.* **47**, 1954 (2000).
[35] J.F. Briesmeister, computer code MCNP, Version 4C (Los Alamos National Labratry, Los Alamos, 2000).
[36] H. Utsunomiya *et al.*, *Phys. Rev. C* **67**, 015807 (2003).
[37] K.Y. Hara *et al.*, *Phys. Rev. D* **68**, 072001 (2003).
[38] Photonuclear data for applications, "Cross Sections and Spectra", IAEA Report No. 1178, 2000.
[39] G.R. Bishop *et al.*, *Phys. Rev.* **80**, 211 (1950).
[40] T. Murata, Technical Report No. JAERI-M 94-019, 1994.
[41] E. Segre, *Nuclei and Particles* (Benjamin/Cummings, Mento Park, CA, 1977), p. 496.
[42] J.F. Marshall and E. Guth, *Phys. Rev.* **78**, 738 (1950).
[43] F. Partovi, *Ann. Phys.*(N.Y.) **27**, 79 (1964).
[44] M. Bosman *et al.*, *Phys. Lett. B* **82**, 212 (1979).
[45] T. Stiehler *et al.*, *Phys. Lett. B* **151**, 185 (1985).
[46] M. Cerineo, K. Ilakovac, I. Šlaus, and P. Tomaš, *Phys. Rev.* **124**, 1947 (1961).
[47] C. Dupont, P. Leleux, P. Lipnik, P. Macq, and A. Ninane, *Nucl. Phys.* **A445**, 13 (1985).
[48] P. Michel, K. Moeller, J. Moesner, and G. Schmidt, *J. Phys. G* **15**, 1025 (1989).
[49] P. Wauters *et al.*, *Few-Body Systems* **8**, 1 (1990).
[50] S.F. Mughbghab, M. Divadeenam, and N.E. Holden, *Neutron Cross Sections, Vol. 1, Neutron Resonance Parameters and Thermal Cross Sections, Part A*, Z = 1 - 60 (Academic, New York, 1981).
[51] W.A. Fowler, G.R. Caughlan, and B.A. Zimmerman, *Annu. Rev. Astron. Astrophys.* **5**, 525 (1967).

3.7 Reliability of prompt γ-ray intensities for the measurement of neutron capture cross sections.

Itaru Miyazaki[1], Toshiaki Shimizu[1], Michihiro Shibata[2], Akihiro Taniguchi[3], Kiyoshi Kawade[1], Hitoshi Sakane[4], Kazuyoshi Furutaka[4], Hideo Harada[4]

[1]*Department of Energy Engineering and Science, Nagoya University*

[2]*Radioisotope Research Center, Nagoya University*

[3]*Research Reactor Institute, Kyoto University*

[4]*Japan Nuclear Cycle Development Institute*

e-mail: i-miyazaki@ees.nagoya-u.ac.jp

We verified a new measuring method of cross sections for the thermal neutron capture detecting prompt γ-rays (the prompt-γ method). There was a tendency for measured cross section values by using the prompt-γ method to be smaller than those by using the activation method. The ratios, of measured cross section values by the prompt-γ method to those by used the activation method, are lower systematically from 1.0 ($\sigma_{prompt}=\sigma_{decay}$). It is considered the disagreement is caused by inaccuracy of the emission probabilities of prompt γ-rays. Because precision of emission probabilities is not enough, the new method cannot determine cross sections within 10%. It is necessary to measure precise emission probabilities of prompt γ-rays in (n, γ) reactions when we use the method.

1. Introduction

Cross sections for the neutron capture of long-lived fission products are needed for a nuclear transmutation technology. When we want to determine the cross sections, we utilize the activation method [1]. This method uses γ-rays following β-decay. If produced nuclei have too long half-lives or are stable, the utilization of the activation method is difficult or impossible. A measuring method by detecting prompt γ-rays (the prompt-γ method) is expected to solve this problem. The method doesn't depend on half-lives.

It is considered that the comparison of the prompt-γ method with the activation method, which has reliable actual results, can verify the new method. Therefore we measured the cross sections by using the prompt- γ method and the activation method. Then, these two measured cross section values were compared.

2. Experiment

Thermal neutron irradiations were carried out by the supermirror neutron guide tube (neutron flux 5×10^7 n/cm^2·s) at the Kyoto University Reactor [2]. Used detectors were 22, 38 and 90% HPGe detectors and a 90% GAMMA-X HPGe detector. The distance from a sample to the detector was 5 cm. Target nuclides were ^{23}Na, ^{27}Al, ^{51}V, ^{55}Mn, ^{64}Ni, ^{65}Cu, ^{141}Pr, ^{186}W and ^{197}Au. (Table 1) Measured reactions were selected by following five points; (1)Induced activities for the neutron capture have short half-lives enough to measure efficiently. (2)The emission probability of that γ-ray is large. (3)The cross section for the neutron capture is large, 0.2 to 1 b. (4)Abundance of the isotope of interest is large. Those points are important for an efficient measurement of cross section. (5)Lists of prompt γ-rays from the (n, γ) reactions are well known.

The schematic view of measuring processes was shown in Fig. 1. When the sample was irradiated, first γ-ray measurement was carried out simultaneously. The measurement was detecting prompt and β-decay γ-rays. Then, the irradiation stopped and the second measurement was carried out. The measurement was only detecting β-decay γ-rays. A box and plates made of a lithium fluoride (^{6}LiF) were used for shielding from neutrons. (Fig. 2) Because of those shields, the neutrons were activated surrounding materials including the detectors. A shutter made of a lithium fluoride stopped the irradiation. (Fig. 3) During no irradiation, leak of neutrons was smaller than 0.6%. (Fig. 4)

3. Results

For nine reactions, ratios of measured cross section values by the prompt-γ method to those by used the activation method were evaluated. The ratio is

$$Ratio = \frac{\sigma_{prompt}}{\sigma_{decay}} = \frac{Count_{prompt} / I_{prompt} \cdot \varepsilon_{prompt}}{Count_{decay} / I_{decay} \cdot \varepsilon_{decay}}$$

σ is measured values of cross sections. I is an emission probability. The emission probabilities are taken from ref. [3-8]. ε is efficiency of a γ-ray of interest. A subscript shows a measuring method. It is clearly seen that the ratios are lower systematically than 1.0 ($\sigma_{prompt}=\sigma_{decay}$) in Fig. 5. The ratios of ^{65}Cu and ^{186}W are -10% and –25% away from the others, respectively. Those of the other seven reactions were in agreement within 5%. Additionally, the ratios are scattered. It is considered the disagreement of the results is caused inaccuracy of the each emission probability of prompt γ-rays. Because their values are published for nuclear structure studies, it is thought that each value of them was not desired high accuracy.

4. Conclusion

We have concluded that the prompt-γ method cannot determine (n, γ) cross section within 10% because precise emission probabilities are not well known at present. Additionally, using more precise emission probabilities of γ-rays following β-decay, those of prompt γ-rays can be determined.

Using the prompt-γ method, we will determine the cross section of ^{104}Pd(n, γ) reaction which cannot be measured by using the activation method. We are going to construct the precise level scheme of ^{104}Pd(n, γ)^{105}Pd. We will gain the emission probabilities of the prompt γ-rays by balancing intensity of γ-rays at each level.

Acknowledgements

We would like to thank the operators at the Kyoto University Reactor for the neutron irradiation.

References

[1] K. Kawade, *et al.*, *Nuclear Instruments and Methods in Physics Research,* **A496** (2003) 183-197.

[2] T. Akiyoshi, *et al.*, *Journal of Nuclear Science Technology,* Vol. **29**, No. 10 (1992) 939-946.

[3] R.B. Firestone and V.S. Sirley, John Wiley & Sons, New York (1996).

[4] T.A.A. Tielens, *et al.*, *Nuclear Physics* **A403** (1983) 13-27

[5] H.H. Schmidt, *et al.*, *Physics Review* C Vol. **25**, No. 6 (1982) 2888-2901.

[6] S. Michaelsen, *et al.*, *Z. Physik A Hadrons and Nuclei* **338** (1991) 371-387.

[7] H. Miyahara, *et al.*, *Nuclear Instruments and Methods in Physics Research Sect.* A Vol. **324**, No. 1/2 (1993) 219-222.

[8] N. Marnada, *et al.*, *Journal of Nuclear Science and Technology,* Vol. **36**, No. 12 (1999) 1119-1124.

Table 1 List of reactions and samples

Reaction	Abundance	Chemical form	$T_{1/2}$	E_γ (Decay)	I_γ
$^{23}Na(n, \gamma)^{24}Na$	100	NaF	14.95h	1368.6	1
$^{27}Al(n, \gamma)^{28}Al$	100	Al	2.241min	1779.0	1
$^{51}V(n, \gamma)^{52}V$	99.8	V_2O_5	3.743min	1434.1	1
$^{55}Mn(n, \gamma)^{56}Mn$	100	Mn	2.578h	846.8	0.9887
$^{64}Ni(n, \gamma)^{65}Ni$	97.9(SI)	Ni	2.517h	1481.8	1
$^{65}Cu(n, \gamma)^{66}Cu$	99.6(SI)	CuO	5.088min	1039.3	1
$^{141}Pr(n, \gamma)^{142}Pr$	100	Pr_6O_{11}	19.12h	1575.9	0.037
$^{186}W(n, \gamma)^{187}W$	97.5(SI)	WO_3	23.72h	479.5	0.218
$^{197}Au(n, \gamma)^{198}Au$	100	Au	2.695d	411.8	0.9558

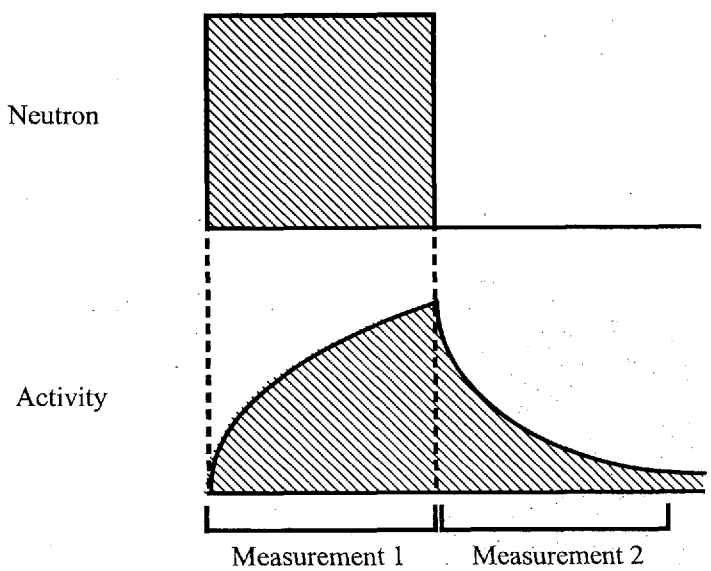

Fig. 1 The schematic view of the measuring process. "Measurement 1" was detecting prompt γ-rays including decay γ-rays. "Measurement 2" was detecting only decay γ-rays.

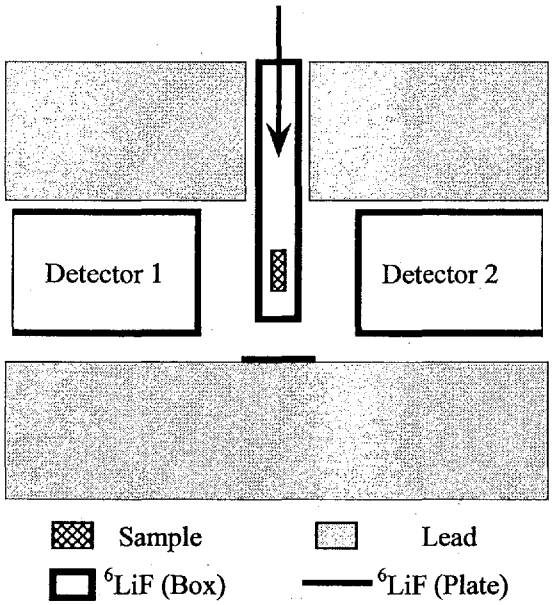

Fig. 2 The schematic view of the present experiment arrangement. The combination of "Detector 1" and "Detector 2" were 22% and 38% HPGe, or 90% HPGe and 90% GAMMA-X HPGe. Distance from sample to each detector was 5 cm.

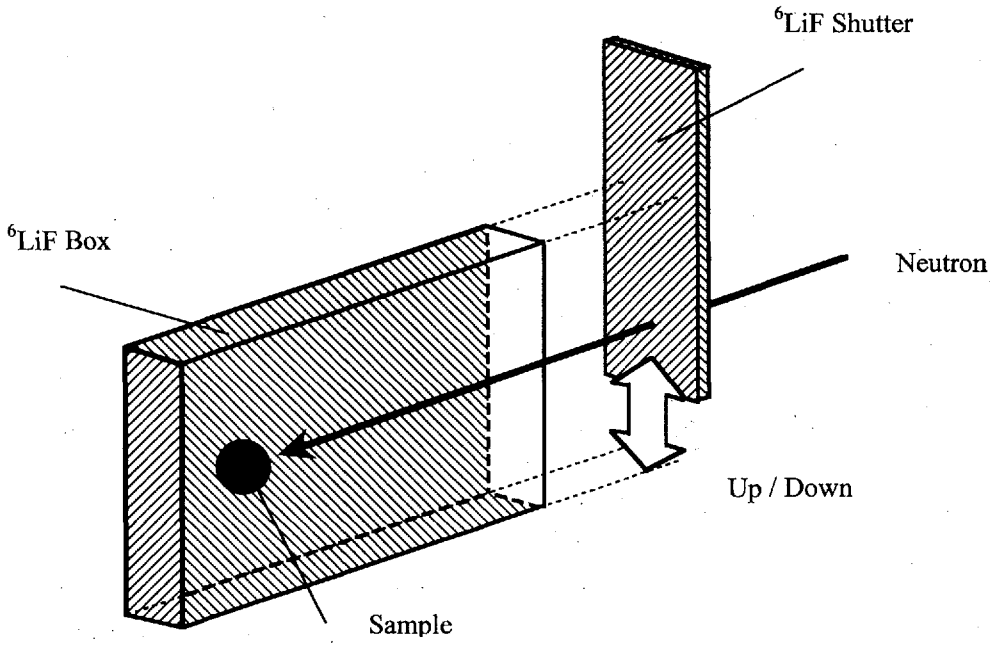

Fig. 3 The schematic view of the beam shutter and the target Box. The shutter moving down made the irradiation stop.

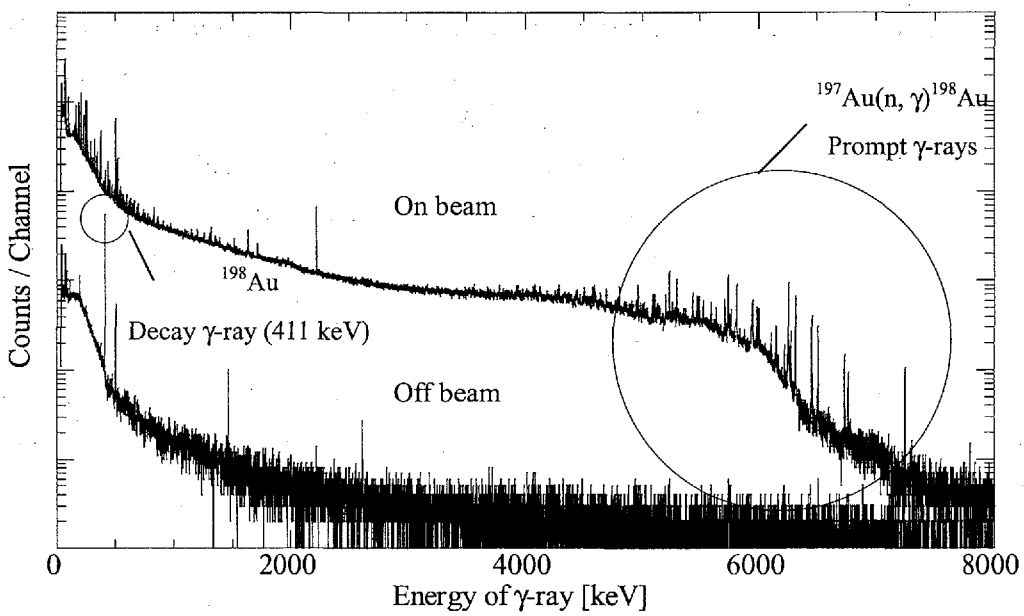

Fig. 4 Spectra for capture of thermal neutron in ^{197}Au. "On beam" and "Off beam" were switched by using a shutter made of ^{6}LiF. It is clearly seen that the γ-rays from the ^{197}Au(n, γ)^{198}Au reaction can be observed at "On beam" and cannot at "Off beam". It is considered that effects of the leaking neutrons are <0.6% at "Off beam".

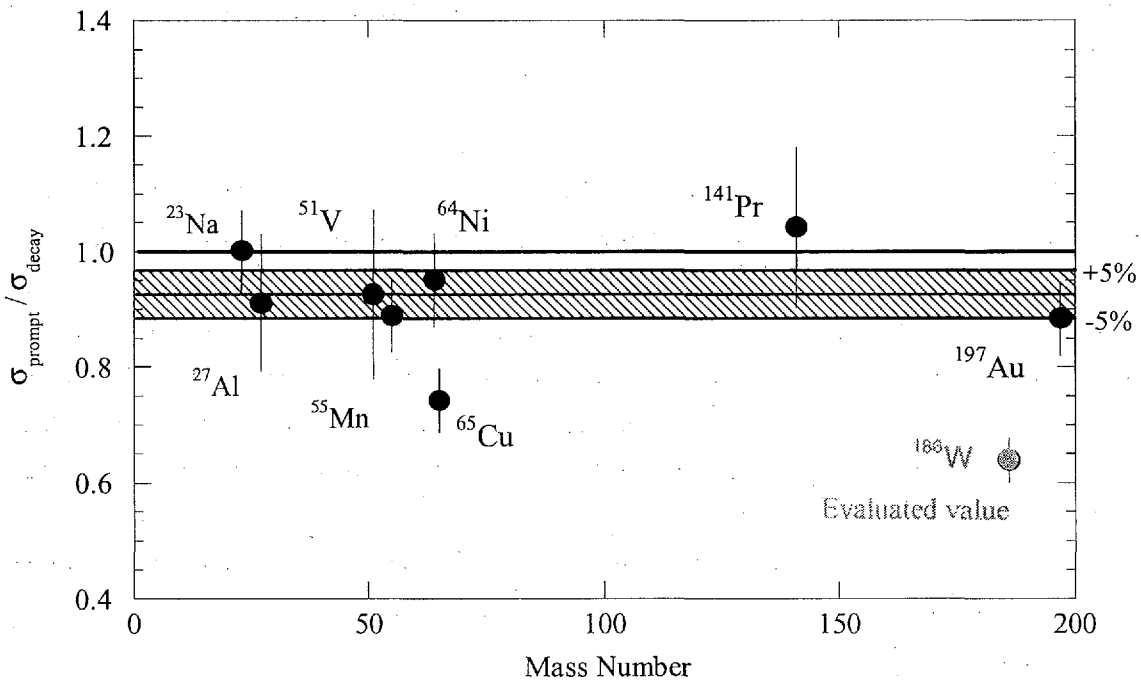

Fig. 5 The ratio of σ used prompt γ-rays to σ used β-decay γ-rays. Used detector was the 22% HPGe detector. It is clearly seen that the ratios are lower systematically than 1.0 ($\sigma_{prompt}=\sigma_{decay}$). The plot of ^{186}W are differentiated from the others because the values of emission probabilities of ^{186}W(n, γ)^{187}W is evaluated values.

3.8 Analysis of Low Energy Proton Capture Cross Section for Light Nuclei

Toru Murata and Satoshi Chiba*
AITEL corp.; 4-1 Ukishima-cho, Kawasaki-ku, Kawasaki, Japan
*JAERI; Tokai-mura, Naka-gun, Ibaraki-ken, Japan
murat@green.ocn.ne.jp, sachiba@popsvr.tokai.jaeri.go.jp

Proton capture cross sections of D, ^{6,7}Li, ^{9}Be, ^{10,11}B, ^{12}C, ^{14}N and ^{16}O in the incident energy region from 1 keV to 10 MeV were analyzed with direct reaction model for Deuteron and with resonance formula for other nuclides.

1. Introduction

For astrophysical estimation of stellar nucleosynthesis and hydrogen consumption in astrophysical environments, low energy proton capture cross sections for light nuclides are crucially important. In the present study, the experimental cross sections compiled in NACRE file[1] and other published data were analyzed for target nuclides; D, ^{6,7}Li, ^{9}Be, ^{10,11}B, ^{12}C, ^{14}N and ^{16}O in the incident proton energy region of 1keV to 10 MeV. The calculated cross sections will be used to calculate the astrophysical S factors and reaction rates.

2. Method

For Deuteron, analysis was made with the inverse reaction ^{3}He(γ,p)D analysis formula given by Gunn and Irving[2]. They give the cross section formula of the ^{3}T(γ,n)D reaction using a exponential type wave function. The formula was converted to the cross section of the ^{3}He(γ,p)D reaction by replacing the Q-value and Coulomb barrier penetration factors. For the barrier penetration factor calculation, orbital angular momentums of the emitted protons were assumed to be s-wave and p-wave and their mixing ratio was determined to reproduce the experimental cross section comparing with calculated inverse cross section.

For other nuclides, analyses were made with an approximated R-matrix resonance formula[3] given by

$$\sigma_{p\gamma}(E) = \frac{\pi}{k^2}\sum_{J\tau}\frac{(2J+1)}{2(2I+1)}\left|U_{J\tau}\right|^2 ,$$

with

$$U_{J\tau} = \frac{\sum_{\lambda} i\Gamma_{\lambda p}^{1/2}\Gamma_{\lambda\gamma}^{1/2}/(E_{\lambda}-E)}{1+\sum_{\lambda}(\Delta_{\lambda}-i\Gamma_{\lambda}/2)/(E_{\lambda}-E)} \quad \text{and} \quad \Gamma_{\lambda p} = 2P_{\ell}(E)\gamma_{\lambda}^{2},$$

where λ designates a resonance level and includes spin-parity J^{Π} and isospin τ, and other symbols are same as that of R-matrix theory by Lane and Thomas[4].

The initial resonance parameters were obtained from the compilation "Energy Levels of Light Nuclei"[5] and adjusted to reproduce experimental cross sections.

3. Results

Results of present analysis are shown in Fig.1 to Fig.9, comparing with experimental cross sections. Solid lines show the calculated cross section of the present analysis.

Figure 1 shows the $D(p,\gamma)^3He$ reaction cross section. Experimental data exist in the energy region of Ep(cm)=10keV to 22MeV.

Figure 2 shows the $^6Li(p,\gamma)^7Be$ reaction cross section analyzed with 2 resonances. Though resonance levels of gamma-ray emission were not cited in ref. 5), gamma-emission widths were assigned to two levels of low spin and large width, to reproduce experimental cross sections.

Figure 3 shows the $^7Li(p,\gamma)^8Be$ reaction cross section analyzed with 6 resonances. For the experimental data above Ep(lab)=1.5MeV, no experimental error was assigned in the original paper. Therefore 30% error was assumed to them presently.

Figure 4 shows the $^9Be(p,\gamma)^{10}B$ reaction cross section analyzed with 6 resonances including a negative resonance which corresponds to the excited state of ^{10}B; Ex=5.181MeV, $J^{\Pi}=1^+$. No experimental data were available in the energy region above Ep=2MeV, so, in this region, cross section was calculated using resonance parameters given in ref. 5) choosing appropriate spin-parity from candidates.

Figure 5 shows results of the $^{10}B(p,\gamma)^{11}C$ reaction analyzed with 6 resonances including a negative resonance which corresponds to the excited state of ^{11}C ; Ex=8.655MeV,$J^{\Pi}=7/2^-$. To reproduce the cross section in the energy region below Ep=1MeV, rather large nuclear radius parameter R_0 = 2.1 fm was adopted. In other cases, R_0 = 1.35 fm.

Figure 6 shows results of the $^{11}B(p,\gamma)^{12}C$ reaction analyzed with 12 resonances. In the energy region below Ep=0.3MeV, experimental data would exist, but not available presently, so, in this region, cross section was calculated using resonance parameters given in ref. 5).

Figure 7 shows results of the $^{12}C(p,\gamma)^{13}N$ reaction analyzed with 11 resonances. The experimental data in the energy region of Ep=1.5-3.0MeV are deduced from the differential cross sections of (p,γ_0) at 0° and 90° measured by Rolfs and Azuma[6]. And

the data of Ep>9MeV are (p,γ_0) cross section measured by Measday and Hasinoff[7], which almost agree with the (p,γ) activation cross section measured by Hill et al.[8]

Figure 8 shows results of the $^{14}N(p,\gamma)^{15}O$ reaction analyzed with 22 resonances. There are experimental data of the (p,γ_0) reaction in some energy regions above Ep=1MeV. Taking into account the structure of these data, cross sections were reproduced adjusting the resonance parameters given in ref. 5).

Figure 9 shows results of the $^{16}O(p,\gamma)^{17}F$ reaction analyzed with 8 resonances including a negative resonance which corresponds to the excited state of ^{17}F ; Ex=0.4956MeV,$J^{\pi}=1/2^{+}$.

4 . Conclusion

Low energy proton capture cross sections were reproduced well with simple formula for Deuteron, and with resonance formula for $^{6,7}Li$, ^{9}Be, $^{10,11}B$, ^{12}C, ^{14}N and ^{16}O. In some literatures[6),9)], smooth parts of cross section were explained to be caused by direct capture reaction, however, there are many cases which show interference with some resonances, and it was found that the smooth parts and the interferences were explained also by tails originated in some distant resonances of broad width, say giant resonance, and/or by negative resonances.

Thanks are due to Dr. T. Nakagawa (JAERI) for his kind preparation of related papers.

References

1) http://pntpm.ulb.ac.be/Nacre/barre_files.htm
2) Gunn, J.C. , Irving, J. Phil. Mag. 42(1951)1353
3) Murata, T. JAERI-Conf 98-003, p.215
4) Lane,A.M.,Thomas,R.G. Revs.Modern.Phys.30,257(1958)
5) Ajzenberg-Selove,F. Nucl.Physics A490(1988)1,; A=5-10,
Ajzenberg-Selove,F. Nucl.Physics A433(1985)1,; A=11-12,
Ajzenberg-Selove,F. Nucl.Physics A268(1976)1,; A=13-15,
Ajzenberg-Selove,F. Nucl.Physics A460(1986)1,; A=16-17
6) Rolfs,C., Azuma,R.E. Nucl.Physics A227(1974)291
7) Measday,D.F.,Hasinoff,D.L. can.J.Phys.51,1237(1973)
8) Hill,H.A.,Haase,E.L.,Knudsen,D.B. Phys.Rev.123,1301(1961)
9) Wiescher,M. et al. Phys.Rev.C28,1431(1093)
Evans,A.E.et al. Phys.Rev.149,863(1966)

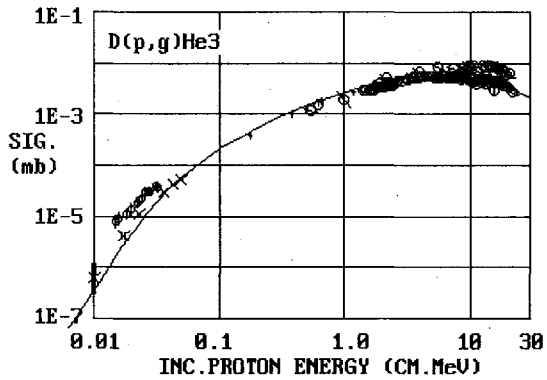

Fig.1 Proton capture cross section of D

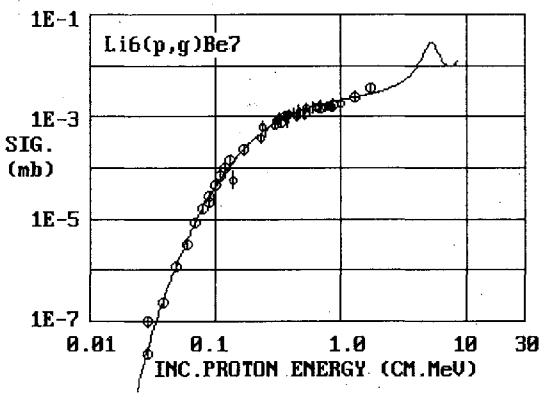

Fig.2 Proton capture cross section of ^{6}Li

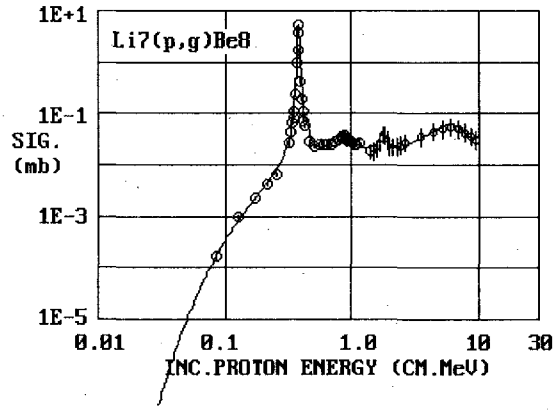

Fig.3 Proton capture cross section of ^{7}Li

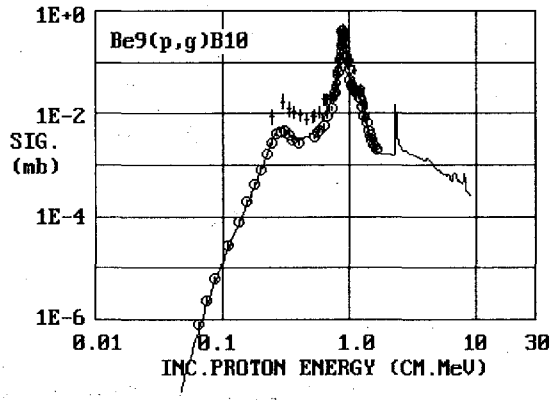

Fig.4 Proton capture cross section of ^{9}Be

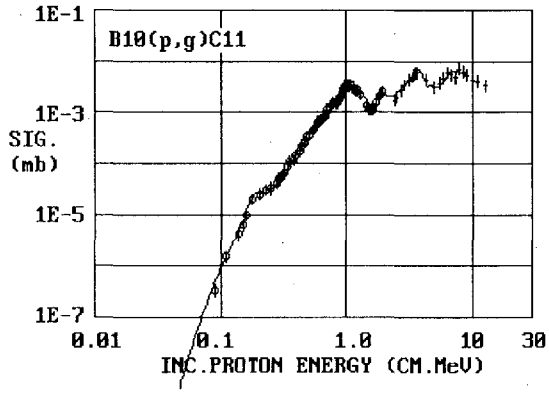

Fig.5 Proton capture cross section of ^{10}B

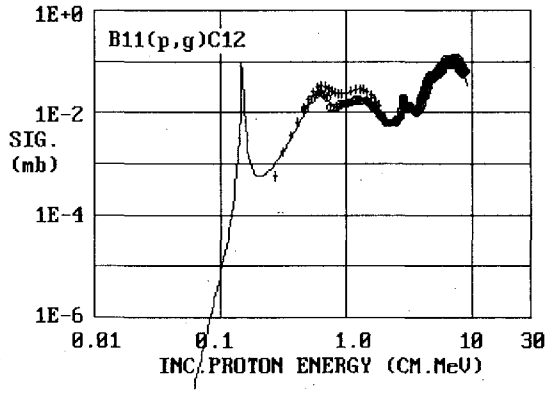

Fig.6 Proton capture cross section of ^{11}B

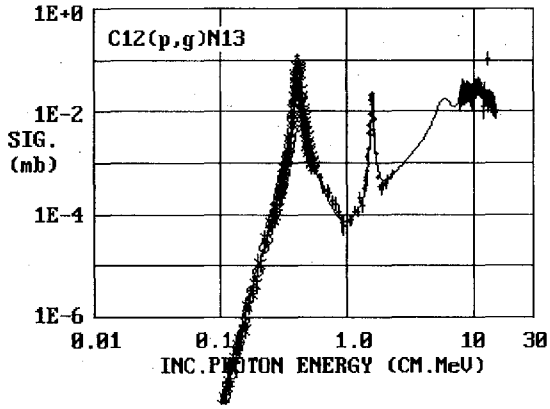

Fig.7 Proton capture cross section of ^{12}C

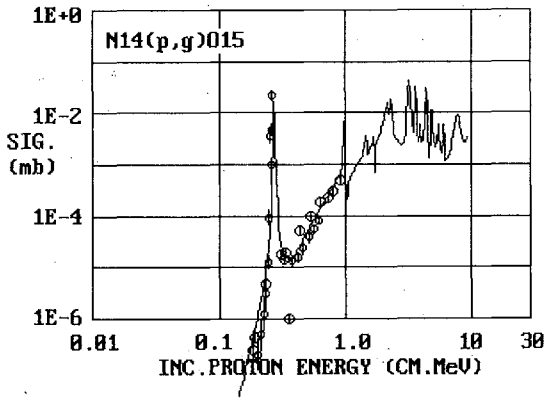

Fig.8 Proton capture cross section of ^{14}N

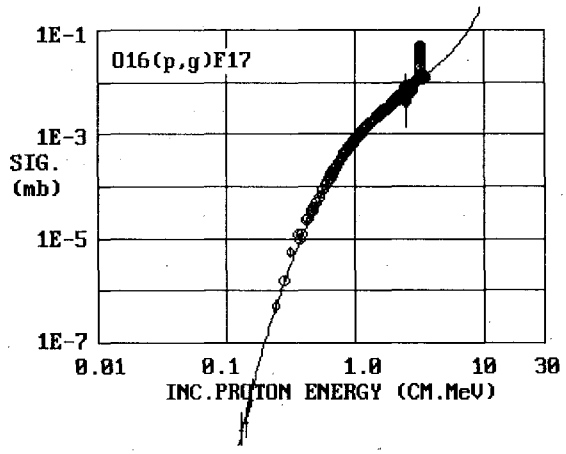

Fig.9 Proton capture cross section of ^{16}O

3.9 Measurements of the Effective Cross Section of the Th-233(n, γ)Th-234 Reaction Using the KUR Core

Hiroshi CHATANI
Research Reactor Institute, Kyoto University
Kumatori-cho, Sennan-gun, Osaka 590-0494, Japan
e-mail: chatani@rri.kyoto-u.ac.jp

Abstract

Approximately 100 mg of solid thorium (Ⅳ) nitrate tetrahydrate ($Th(NO_3)_4 \cdot 4H_2O$; thorium nitrate) was irradiated together with neutron fluence monitors of 0.1143%Au-Al and 0.483%Co-Al alloy foil, in the Kyoto University Reactor (KUR). The Th was chemically purified after irradiation and measured using high-purity germanium detectors (HPGes) including a low-energy photon spectrometer (LEPS), in order to obtain the gamma ray spectra of Th-234. On the other hand, the thermal neutron flux and epithermal index, i.e., the strength of the epithermal component relative to the density of neutrons including both thermal and epithermal neutrons, were determined by the Westcott convention using the multiple foil activation method in which the Au(n, γ)Au-198 and Co(n, γ)Co-60(g+m) reactions were used. The effective cross sections were determined for various epithermal indexes.

1. Introduction

In the thorium cycle, although the experimental value of the Th-233(n, γ)Th-234 reaction cross section is closely linked with the evaluation of the generation of U-233, only two reports on obtaining experimental values, including an unpublished paper, exist, as far as the author knows [1, 2]. Moreover, no one has ever used HPGe in the determination of the cross section. Therefore, in order to verify the widely used value of the cross section and to improve its accuracy, measurements of the effective cross section have been carried out.

2. Experimental

The experiments were performed three times using irradiation facilities of Hyd (Hydraulic conveyor: at the center of the core) and Slant (Slant exposure tube: outside the reflectors). In the case of using the Slant, experiments were repeated twice: Slant 1st and Slant 2nd. In this paper, unless otherwise noted, we describe the case of the experiment using Hyd, where the neutron flux is the most intense. Configurations and characteristics of the facilities have been presented in Ref. 3. Figure 1 shows the placement of the irradiation samples. Irradiation was applied at 5000 kW for 5 h. In order to wait for Th-233 and Th-231, produced by the reactions of Th-232(n, γ) and Th-232(n,2n), respectively, to decay out, chemical purification was performed more than 13 days after the irradiation. The flow diagram and details of the purification procedure are shown in Fig. 2 and in previous papers [4, 5, 6]. The final precipitate was cemented with glue; this was the Th sample. The recovery rate of Th-232 was roughly 50%.

The activity of Th-234 was determined from the area of the peak at 92.57 keV in the γ -ray spectra, which is a doublet of 92.35 and 92.78 keV with intensities (2.73±0.05) and (2.69±0.05)%, respectively [7] (see Fig. 3). The activity of Th-234 immediately after irradiation was (101,200 ± 2,500) Bq. Activities of Au-198 and Co-60 were also determined using the calibrated HPGes.

3. Determination of the effective cross section in the case of double neutron capture

The activity of Th-234 immediately after irradiation ($\lambda_3 N_3$) is determined by solving the differential equations (1) and (2), which represent the processes of the production and destruction of Th-233 and Th-234, respectively [8].

$$\frac{dN_2}{dt} = nv_0\hat{\sigma}_{12}N_1 - \lambda_2 N_2 \quad (1)$$

$$\frac{dN_3}{dt} = nv_0\hat{\sigma}_{23}N_2 - \lambda_3 N_3 \quad (2)$$

Here, N_1, N_2 and N_3 are the numbers of nuclides of Th-232, Th-233 and Th-234, respectively. $\hat{\sigma}_{12}$ and $\hat{\sigma}_{23}$ are the effective cross sections for the reactions of Th-232(n, γ)Th-233 and Th-233(n, γ)Th-234, respectively. λ_2 and λ_3 are the decay constants of Th-233 and Th-234, respectively. n is the density of neutrons including both thermal and epithermal neutrons. v_0 is 2200 m/s, and t is irradiation time. The solution is formulated as

$$\lambda_3 N_3 = \frac{\hat{\sigma}_{12}\hat{\sigma}_{23}(nv_0)^2 N_1}{\lambda_2(\lambda_2-\lambda_3)}\left[\lambda_2\left(1-e^{-\lambda_3 t}\right)-\lambda_3\left(1-e^{-\lambda_2 t}\right)\right] , \quad (3)$$

where t is 5 h. Therefore, $\hat{\sigma}_{23}$ can be calculated when the following is known: $\lambda_3 N_3$, $\hat{\sigma}_{12}$, amount of recovered Th-232 after the chemical purification (N_1) and Westcott conventionality thermal neutron flux (nv_0).

3. –1 Westcott conventionality thermal neutron flux determined using multiple foil activation method [9, 10]

This method of using the Au(n, γ)Au-198 and Co(n, γ)Co-60(g+m) reactions has been reported in detail in Ref. 3, therefore, in this section, the explanation is restricted to the essential points and the results.

nv_0 and epithermal neutron flux $nv_0 r\sqrt{T/T_0}$ are, respectively, equivalent to the intercept and slope of the linear equation

$$\frac{R}{\sigma_0\, gG_{th}} = nv_0 + nv_0\, r\sqrt{T/T_0}\,\frac{s_0 G_{epi}}{gG_{th}}, \quad (4)$$

where R is the reaction rate of the Au(n, γ) or Co(n, γ) reaction. G_{th} and G_{epi} are self-shielding factors within the foil for thermal and epithermal neutrons, respectively, and they are approximately unity, because Au and Co can be considered to be infinite dilution. $r\sqrt{T/T_0}$ is the epithermal index, T is neutron temperature and T_0 is 293.6 K. g and s_0 are measures of the departure of the cross-section law from the $1/v$ form in the thermal and epithermal regions, respectively. The former factor is the Westcott g-factor, which has been tabulated by Westcott [11] and Gryntakis and Kim [12]. If the cross section obeys the $1/v$ law, $g = 1$ and $s_0 = 0$. Furthermore, s_0 is defined by [13]

$$s_0 = \frac{1}{\sigma_0}\sqrt{\frac{4}{\pi}}\; I'_0, \quad (5)$$

where I'_0 is the reduced resonance integral which is obtained by subtracting the $1/v$-term from resonance integral I_0, which is given by $I'_0 = I_0 - 0.45\,\sigma_0$ when the cadmium cutoff energy E_{Cd} is 0.5 eV.

The same Eq. (4) with a common intercept and slope will be formed for the Au(n, γ)Au-198 and Co(n, γ)Co-60(g+m) reactions, if Au and Co are irradiated at the same time and at the same position. The nuclear data and parameters used are listed in Table 1. Figure 4 shows the plots of Eq. (4) and the results are shown in Table 2.

3. - 2 Effective cross section of the Th-232(n, γ)Th-233 reaction

The effective cross section is given by

$$\hat{\sigma}_{12} = \sigma_0\left(g + r\sqrt{T/T_0}\, s_0\right). \quad (6)$$

Accordingly, using the evaluated cross section and resonance integral of JENDL -3.2 [15], viz., $\sigma_0 = 7.4$ b and $I_0 = 84.4$ b, s_0 is defined to be 12.4. Therefore, $\hat{\sigma}_{12}$ can be calculated using $r\sqrt{T/T_0}$, which is never determined without experiment, as listed in Table 2, when g is assumed to be unity.

3. –3 Recovered amount of Th-232

The thorium contents in the Th samples were quantitatively analyzed using the activation method. Th samples for which the measurements of Th-234 and Pb-212 activities have been completed, were irradiated together with Th foil of known weights and 10 pieces of 5 mg Au foil in order to determine neutron fluences at the positions of the Th samples and Th foil, using the heavy-water neutron irradiation facility (D2O facility [16]), where uniform neutron flux is available to a certain extent. The targets were attached on a 15×7 cm piece of corrugated cardboard and then fastened onto the Bi layer of the D2O facility; irradiation was performed at 100 kW for 26 h. Relative neutron flux, i.e., relative reaction rates of the Au(n, γ)Au-198 reaction, on the cardboard is shown in Fig. 5. In the figure, -3, 0 and 3 cm on the abscissa are the positions of the Th samples, and -6 and 6 cm are those of the Th foil. The irregularity of the neutron flux was taken into account in the correction of induced activities of Pa-233 produced by the beta decay after the Th-232(n, γ) Th-233 reaction. Recovered amounts of Th-232 were 23.4, 19.7 and 43.7 mg in the cases of Hyd, Slant 1st and Slant 2nd, respectively.

4. Results and discussion

Results of the experiments are listed in Table 2. Johnston et al. [1] determined the effective cross section to be (1470 ± 100) b and the thermal neutron cross section to be 1450 b, and Hyde et al. [2] determined the effective cross section to be 1350 b (quoted from Ref. 1). The effective cross section varies mainly according to the epithermal index and effective cross section of the Th-232(n, γ)Th-233 reaction. Therefore, although, the comparison of the effective cross sections cannot be made unconditionally, our results are slightly smaller than those obtained by Johnston et al. [1] and Hyde et al. [2]. More irradiation experiments using Slant and Pn-2 (pneumatic tube No. 2) are being carried out.

Table 1 Nuclear data and parameters used in the determination of the neutron fluxes

Reactions	σ_0 (b) [a]	I_0 (b) [a]	g (at 40℃)	G_{th}	G_{epi}
Au(n, γ) Au-198	98.65±0.09	1550±28	1.005 [b]	0.999	0.996
Co(n, γ) Co-60(g+m)	37.18±0.06	74±2	1	1	1

a) Ref. [14]. b) Ref. [12]

Table 2 Results

Irradiation facilities:	Hyd	Slant (1st exp.)	Slant (2nd exp.)
nv_0 (n/s/cm^2)	(1.08±0.03)×10^{14}	(1.07±0.03)×10^{13}	(9.90±0.03)×10^{12}
$r\sqrt{T/T_0}$	0.0322 ± 0.0023	0.0129 ± 0.0009	0.0118 ± 0.0008
$\hat{\sigma}_{12}$ (b)	10.34 ± 0.21	8.59 ± 0.17	8.48 ± 0.17
$\hat{\sigma}_{23}$ (b)	1340 ± 90	1330 ± 90	1270 ± 90

Acknowledgement

We acknowledge Dr. S. Yamada, Associate Prof. (ret.) for his comprehensive assistance on the use of the LEPS, and Dr. Y. Sakurai for his suggestions and assistance on the use of the D2O facility.

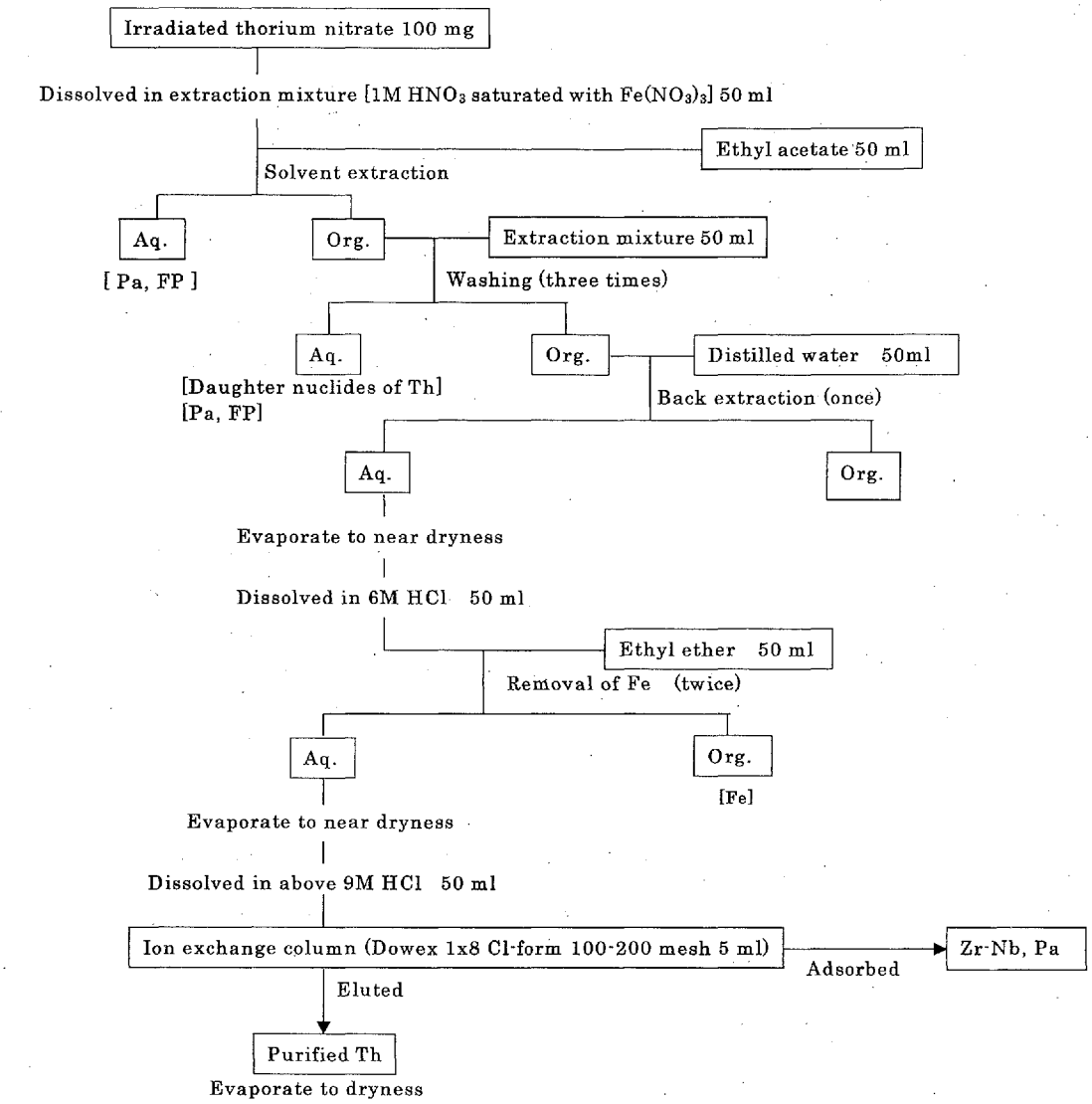

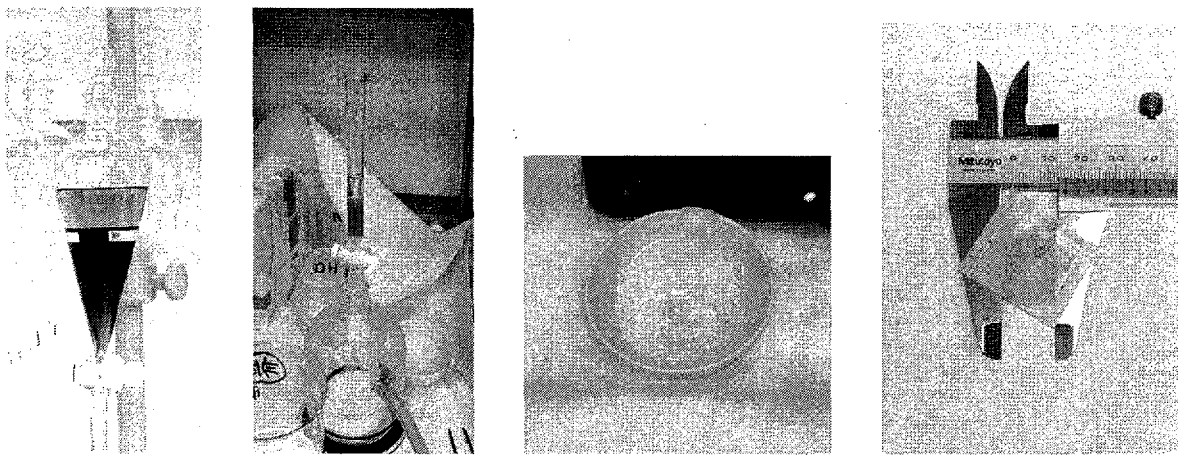

Solvent extraction　Ion exchange　Final precipitate (Purified Th)　Completion

Fig. 2 Flow diagram of the chemical purification and the photographs. It begins with the dissolution of the irradiated thorium nitrate into 1M nitric acid saturated with $Fe(NO_3)_3$ more than 13 days after irradiation.

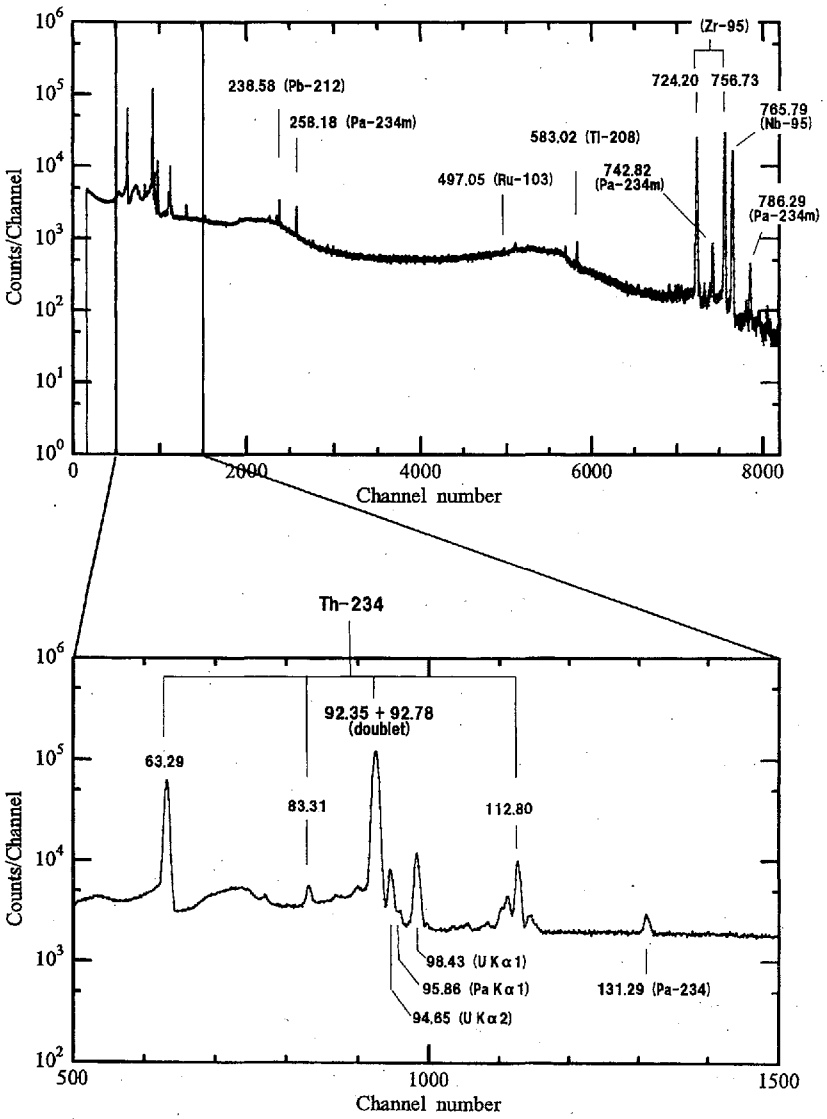

Fig. 3
Gamma-ray spectrum of the Th sample in the energy range from 20 to 820 keV (upper spectrum), obtained using a low-background high-resolution HPGe with a relative efficiency of 50%, at a S (Source) to D (Detector) distance of 10 cm. Accumulated for 52537 s. Waiting time after the chemical purification was 16 d. Numerical values are the energies of photons in keV. Lower spectrum is enlargement of the energy range from 50 to 150 keV. Activity of Th-234 was determined from the peak area of 92.57 keV (average of the two γ-ray energies of 92.35 and 92.78 keV). There is no appreciable interference caused by unwanted nuclides in the analysis of the 92.57 keV peak.

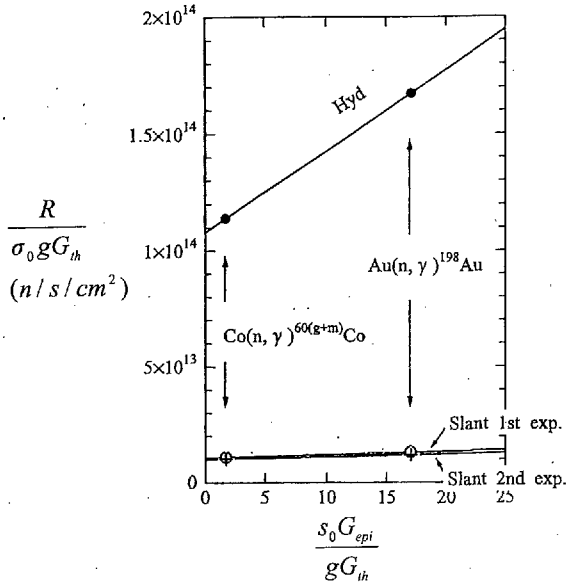

Fig. 4
Westcott conventionality thermal neutron fluxes nv_0 (intercepts) and epithermal neutron fluxes $nv_0 r\sqrt{T/T_0}$ (slopes) at the irradiation positions of thorium nitrate, determined from Eq. (4). The results are shown in Table 2.

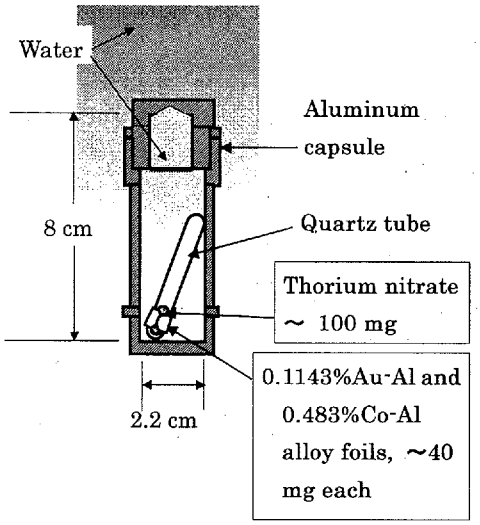

Fig. 1 Irradiation samples in an aluminum capsule of Hyd.

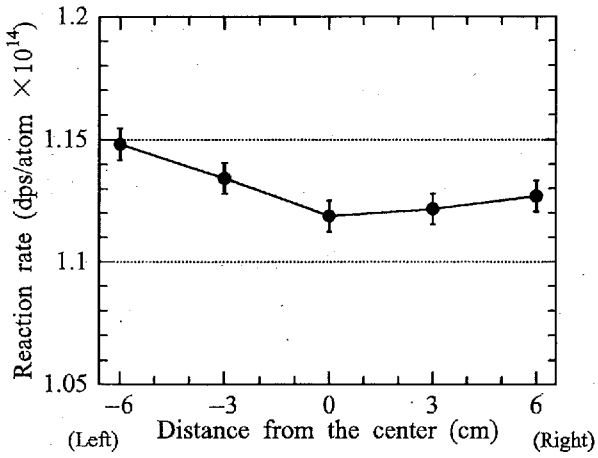

Fig. 5 Distribution of the reaction rates of the Au(n. γ)Au-198 reaction on the corrugated cardboard, which corresponds with that of neutron fluxes at the Th samples and Th foil positions.

References

[1] F. J. Johnston, J. Halperin and R. W. Stoughton, "The Thermal Neutron Absorption Cross-Section of ^{233}Th and the Resonance Integrals of ^{232}Th, ^{233}Th and ^{59}Co", J. Nucl. Energy, Part A: Reactor Science, **11**, 95 to 100 (1960).

[2] E. K. Hyde, R. J. Bruehlman and W. M. Manning, "The Neutron Capture Cross-Section of the 23 Minute Isotope, ^{233}Th", ANL-4165, (1948) Unpublished (Quoted from Ref. 1).

[3] H. Chatani, "Measurement of the Westcott Conventionality Thermal Neutron Flux and Suchlike at Irradiation Facilities of the KUR", JAERI-Conf 2003-06, 241-246 (June 2003): http://wwwndc.tokai.jaeri.go.jp/nds/proceedings/2002/chatani_h.pdf

[4] E. K. Hyde, "The Radiochemistry of Thorium", NAS-NS 3004 (Jan. 1960).

[5] K. Kobayashi, T. Hashimoto and I. Kimura, "Measurements of Average Cross Section for ^{232}Th(n,2n)^{231}Th Reaction to Neutrons with Fission-Type Reactor Spectrum and of Gamma-Ray Intensities of ^{231}Th", J. Nucl. Sci. Technol., **8**, 492-497 (1971).

[6] H. Chatani, "Measurement of Gamma-Ray Intensities of ^{231}Th Using Semiconductor Detectors", Nucl. Instrum. and Meth., **A 425**, 277-290 (1999).

[7] E. Browne and R. B. Firestone, "Table of Radioactive Isotopes", John Wiley & Sons, New York (1986).

[8] T. Sekine and H. Baba, "A Study of Reactor-Neutron-Induced Reactions: Double Neutron Capture Process and the Systematics of the (n,2n) Reaction", JAERI 1266 (1979).

[9] C. H. Westcott, W. H. Walker and T. K. Alexander, "Effective Cross Sections and Cadmium Ratios for the Neutron Spectra of Thermal Reactors", Proc. 2nd. Int. Conf. Peaceful Use of Atomic Energy, Geneva, New York, **16**, 70-76 (1958).

[10] H. Matsuoka and T. Sekine, "Reactor-Neutron Monitoring with Multiple Activation Detectors", JAERI-M 9552 (1981) (in Japanese).

[11] C. H. Westcott, "Effective Cross Section Values for Well-Moderated Thermal Reactor Spectra", AECL-1101 (1960).

[12] E. M. Gryntakis and J. I. Kim, "Absorption, Activation and Fission g(Tn)-Functions for Non 1/v-Nuclides", Radiochimica Acta, **22**, 128-147 (1975).

[13] W. H. Walker, C. H. Westcott and T. K. Alexander, "Measurement of Radiative Capture Resonance Integrals in a Thermal Reactor Spectrum, and the Thermal Cross Section of Pu-240", Can. J. Phys., **38**, 57-77 (1960).

[14] S. F. Mughabghab, M. Divadeenam and N. E. Holden, "Neutron Cross Sections", Vol. 1, Academic Press, New York (1981).

[15] T.Nakagawa, K.Shibata, S.Chiba, T.Fukahori, Y.Nakajima, Y.Kikuchi, T.Kawano, Y.Kanda, T.Ohsawa, H.Matsunobu, M.Kawai, A.Zukeran, T.Watanabe, S.Igarasi, K.Kosako and T.Asami: "Japanese Evaluated Nuclear Data Library Version 3 Revision-2: JENDL-3.2", J. Nucl. Sci. Technol., **32**, 1259-1271 (1995).

[16] Y. Sakurai and T. Kobayashi, "Characteristics of the KUR Heavy Water Neutron Irradiation Facility as a neutron irradiation field with variable energy spectra", Nucl. Instrum. and Meth., **A 453**, 569-596 (2000).

3.10 Half-life of ^{228}Pu and α decay of ^{228}Np

K. Nishio[1], H. Ikezoe[1], S. Mitsuoka[1], K. Satou[1], and C.J. Lin[1,2]

1. *Japan Atomic Energy Research Institute, Tokai-mura, Ibaraki 319-1195, Japan*
2. *China Institute of Atomic Energy, Beijing 102413, China*

Abstract

The neutron deficient nucleus ^{228}Pu was produced in the reaction of ^{34}S+^{198}Pt and the half-life was determined to be $1.1^{+2.0}_{-0.5}$ s. The half-life follows the Geiger-Nuttall curve for even-even Pu isotopes, which shows that α decay is the dominant decay mode. In this reaction, α decay of ^{228}Np was observed for the first time. The evaporation residue cross sections of ^{228}Pu($4n$), ^{228}Np($p3n$) and ^{225}U($\alpha 3n$) are reproduced by a statistical model calculation.

1 Introduction

Plutonium-228 was produced and identified for the first time by Andreyev *et al.*[1] in the fusion reaction of ^{24}Mg+^{208}Pb. However, they were not able to determine the half-life of ^{228}Pu. We produced ^{228}Pu in the fusion reaction ^{34}S+^{198}Pt[2] (compound nucleus ^{232}Pu) and the half-life was determined. For the actinide nuclei with proton number of Z=90−94 and neutron number of N=134−138, α-particle emission and electron capture (EC) are two competing decay modes, suggesting the dominant α-decay mode. For ^{228}Pu, a calculation suggests that the α-decay partial half-life, $T_{\alpha,1/2}$ =0.42 s [3], is two orders of magnitude shorter than that of EC-decay $T_{\mathrm{EC},1/2}$ =44 s [4].

In addition to ^{228}Pu, we have produced ^{228}Np in the same reaction and the α-decay was observed for the first time. The first production of ^{228}Np was made by Kuznetsov *et al.* [5], who determined the half-life of fission activity as 60 s in the reaction ^{22}Ne+^{209}Bi. The EC-delayed fission properties of ^{228}Np was studied by Kreek *et al.* [6] in detail. So far there is no report on the measurement of the α decay of ^{228}Np.

2 Experiment

The ^{34}S ions were accelerated to E_{beam}=170 and 172 MeV by the JAERI-tandem accelerator and irradiated a ^{198}Pt target. The target with thickness 390μg/cm^2 was made by sputtering an enriched ^{198}Pt material (98%) on a 1.2μm thick aluminum (Al) foil. The above bombarding energy corresponds to the center-of-mass energy ($E_{\mathrm{c.m.}}$) of 141 and 143 MeV, respectively, at the half-depth of the target layer.

The evaporation residues emitted in the beam direction were separated in flight from the primary beams by the JAERI-RMS [7]. The JAERI-RMS was set to transport fusion products with 16$^+$ charge state, which has the the probability of 0.18 in the charge state distribution. The total transport efficiency [8] for $4n$, $p3n$ and $\alpha 3n$ channels are determined

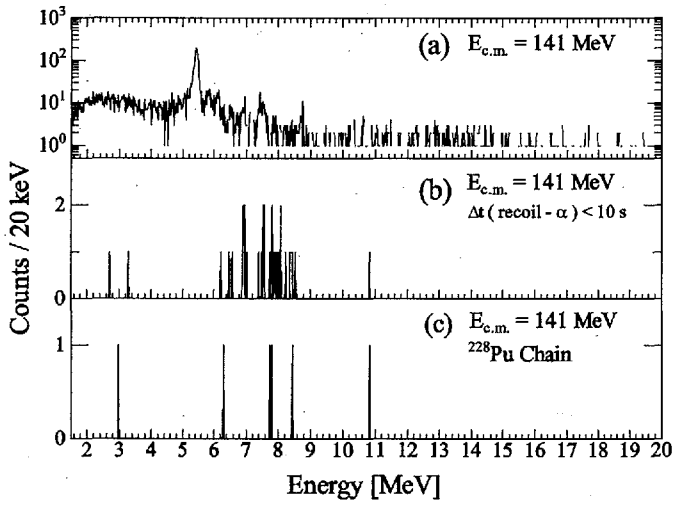

Figure 1: Energy spectra obtained from the PSD in the reaction of ^{34}S+^{198}Pt at $E_{c.m.}$ =141 MeV.

to be 0.086, 0.074, and 0.050, respectively. The ERs transported through the JAERI-RMS were implanted into a double-sided position-sensitive silicon detector (PSD; 73 × 55 mm^2) located in the focal plane. The identification of the nucleus is made by constructing an α-decay chain and finding the known α-particle energies (and also life-times) of descendants, whose decay position agrees with that of the recoil implantation. The position resolution were 0.15 mm and 0.26 mm in FWHM for X and Y, respectively. Typical energy resolution of the PSD was 75 keV (FWHM).

The α decay in the PSD is distinguished from the transported particle by determining that no time-of-flight (TOF) signal is present, and TOF is measured by two timing detectors separated by the distance of 30 cm and placed upstream the PSD. In the off-line data analysis, the ERs were separated from the scattered beam particles on the two dimensional spectrum of the TOF versus energy. This process considerably reduces the chance coincidence in finding a *recoil-α* correlation. Here, *recoil* means the event of the ER to hit the PSD.

3 Results and Discussions

Figure 1 shows the energy spectrum obtained from the PSD. The spectrum (a) shows the events which do not generate TOF signals and includes all events taken during a 41-hour run at the reaction energy of $E_{c.m.}$ =141 MeV. The large peak at 5.4 MeV is α-particles from the external α source (^{241}Am) which irradiated the silicon detector during the measurement. The broad 2−6 MeV spectrum is formed by scattered beam particles transported through the JAERI-RMS. As the detection efficiency of the timing detectors was not 100 %, such background particles are not fully rejected and appear in the spectrum (a). There are several α lines in Fig.1 (a) including α decays of ^{216}Th(7921keV,28ms), ^{215}Ac(7604,0.17s), ^{215}Th(7524:7395,1.2s), ^{212}Ra(6899,13s), ^{211}Ra(6.910,13s), ^{211}Fr(6534,3.1min), ^{207}Rn(6131, 9.3min) and ^{207}At(5758,1.8hr). These nuclei are produced, for the calibration purpose, by the reaction of the beam with ^{186}W nucleus contained in the ^{198}Pt target.

The correlation between the recoil implantation and the subsequent α-decays were searched for within the time interval Δt(*recoil*-α) of 10 s. We only selected chains in which the recoil implantation is followed by two or more α-decays. We obtained 18 chains and the corresponding α-particle energy spectrum is shown Fig.1(b). In this process, the condition was imposed that the *recoil* event generates the TOF and energy signal corresponding to the ERs on the two dimensional spectrum to reject chance events associated with the scattered particle.

Among the chains in Fig.1(b), we searched for one that is followed by a long-lived nuclues with the help of position agreement. The searching time is 120 min, long enough to observe the α decay of ^{212}Rn ($T_{1/2}$=23.9min [9]) as the descendant of ^{228}Pu. In this process, we found two decay chains, and the E_α-spectrum is shown in Fig.1(c). They are both attributed to the ^{228}Pu-chain based on their decay character as shown in Table.1. The half-life of ^{228}Pu was determined to be $1.1^{+2.0}_{-0.5}$ s. The obtained average α-particle energy of ^{228}Pu, 7772±35 keV, reasonably agrees with the data [1]. The present E_α and half-life are compared with the prediction of the Geiger-Nuttall law. In order to determine the α-decay Q-value, Q_α, for ^{228}Pu, we assumed that the detected α decay is from ground-state to ground-state transition, and the electron screening effect [10] is corrected for. The Q_α(7948±36 keV) and $T_{1/2}$ are plotted in Fig.2 together with the other data [9]. In this figure, the Geiger-Nuttall curves for elements Th, U, and Pu are drawn by using the expression and constants in [10]. Our data of ^{228}Pu follows the characteristics of Pu isotopes. This means that the ^{228}Pu decay is dominated by the α decay.

In order to find the α-decay of ^{228}Np with half-life of 61.4 s [6], the *recoil*-α chain was searched for in the time span of 10 s $\leq \Delta$t(*recoil*-α) $<$ 300 s. We set the condition that the recoil implantation is followed by two or more α-decays in this time region. Five chains starting from ^{228}Np are obtained at $E_{\rm c.m.}$ = 143 MeV, and the decay properties are listed in Table. 2. From the mass table of Audi and Wapstra [11], the α-decay Q value Q_α of ^{228}Np is obtained to be 7415 keV. This results in the α-decay energy of 7285 keV for the ground-state to ground-state α-decay of ^{228}Np. This is 100−220 keV larger than the experimental data. A possible reason is that the α decay predominantly produces the excited states of ^{224}Pa.

The obtained ER cross sections for ^{228}Pu, ^{228}Np and ^{225}U are shown in Fig. 3. The errors are in the margin of the statistical error. The data were compared to a statistical model calculation. For this purpose, the partial wave cross section for the fusion ^{34}S+^{198}Pt was calculated by using the CCDEF code [12], which was then inputted to the HIVAP code [13] to calculate the surviving probability and the ER cross section of the specific channel. In the CCDEF code, we took into account the couplings to inelastic channels of the projectile and target. For ^{34}S, deformation parameter (excitation energy) of the quadrupole and octupole vibrations are β_2=0.252 (2.13 MeV) [14] and β_3=0.330 (4.62 MeV) [15], respectively. β_3=0.05 (1.68 MeV) [15] was adopted for the octupole vibration of ^{198}Pt. We also took into account the static deformation of ^{198}Pt (β_2=−0.060 [16], β_4=−0.030 [17]). The calculated fusion cross section ($\sigma_{\rm fus}$) is shown on the upper section of Fig. 3 by the dashed curve. The dotted curve is the result of the one-dimensional barrier penetration model, which gives the barrier height of 141.1 MeV. The ER cross sections calculated by the HIVAP code are shown by the solid curve in each section of the figure. We have to adjust the factor $b_{\rm fac}$, by which the fission barrier height of the liquid-drop part [18] is multiplied to calculate the fission barrier, $B_{\rm f} = b_{\rm fac}B_{\rm LDM} - \delta W$, from 1.03 [19] to 1.00 so as to obtain reasonable agreement with the experimental data. The δW is the ground state shell energy

Table 1: Alpha-decay energy (in keV) and life-time (given in parenthesis) starting from the recoil implantation of ^{228}Pu ($4n$ channel). The literature value of kinetic energy of α particle and half-life (in square brackets) for ^{228}Pu [1] and the other nuclei [9] is shown in the first line. The time with symbol '<' represents the time interval relative to the preceding α decay. The signal with escaped event is indicated by '*esc*'. The signal of pile up, '*pil*', is caused by the α decays of a mother and a short-lived daughter indicated by '←'.

No.	^{228}Pu	^{224}U	^{220}Th	^{216}Ra	^{212}Rn
	7810	8466 [0.9ms]	8790 [9.7μs]	9349 [0.18μs]	6264 [23.9min]
II-1	7807 (0.35s)	–	10817_{pil} (<0.77ms)	←	6309 (34min)
II-2	7736 (2.76s)	8446 (3.2ms)	–	–	2960_{esc} (11min)

Table 2: Alpha-decay energy (in keV) and life-time starting from the recoil implantation of ^{228}Np ($p3n$ channel). The literature value for ^{228}Np [6] and the other nuclei [9] is shown in the first line. See the captions of Table 1 for the detailed explanation.

No.	^{228}Np	^{224}Pa	^{220}Ac	^{216}Fr	^{212}At
	– [61.4s]	$7488^{70\%}$ [0.79s]	$7855^{26\%}$ (26.4ms)	9005 [0.7μs]	$7679^{82\%}$,$7045^{0.45\%}$ [0.314s]
III-1	7183 (29s)	7529 (1.10s)	14048_{pil} (3.7ms)	←	3170_{esc} (0.070s)
III-2	7062 (128s)	7543 (0.20s)	7794 (58ms)	–	7687 (2.4ms)
III-3	7126 (196s)	7495 (0.56s)	13425_{pil} (21ms)	←	7012 (0.12s)
III-4	7177 (35s)	7521 (3.03s)	–	–	7658 (0.18s)
III-5	7065 (15s)	–	–	8969 (<3.39s)	–

correction.

The experimental ER cross section $1.7^{+2.2}_{-1.3}$ nb of the $4n$ channel at $E_{\rm c.m.}$ =141 MeV in the fusion reaction ^{34}S+^{198}Pt was close to 4±2 nb of the $4n$ channel of ^{24}Mg+^{208}Pb reaction at $E_{\rm c.m.}$ =118 MeV [1] which forms the same compound nucleus ^{232}Pu. For the ^{24}Mg+^{208}Pb reaction, we also calculated the cross sections of ^{228}Pu with the same procedure. In the CCDEF calculation, we used deformation parameters β_2=0.606 (1.37 MeV) [14] and β_3=0.250 (7.62 MeV) [15] to take into account the couplings to the excited states of ^{24}Mg. For the excitation of ^{208}Pb, parameters β_2=0.054 (4.09 MeV) [14] and β_3=0.110 (2.61 MeV) [15] are adopted. The calculated result is 6 nb at $E_{\rm c.m.}$=118 MeV, reproducing the experimental data in [1]. Since the excitation energy, $E_{\rm ex}$=43 MeV, of ^{34}S+^{198}Pt at $E_{\rm c.m.}$=141 MeV is close to $E_{\rm ex}$ =44 MeV of ^{24}Mg+^{208}Pb at $E_{\rm c.m.}$=118 MeV, the survival probability for both systems are nearly identical. The fusion cross section given by the CCDEF code is $\sigma_{\rm fus}$ = 69 mb of ^{34}S+^{198}Pt, which agrees with $\sigma_{\rm fus}$ = 184 mb of ^{24}Mg+^{208}Pb within factor of $\sim$ 3.

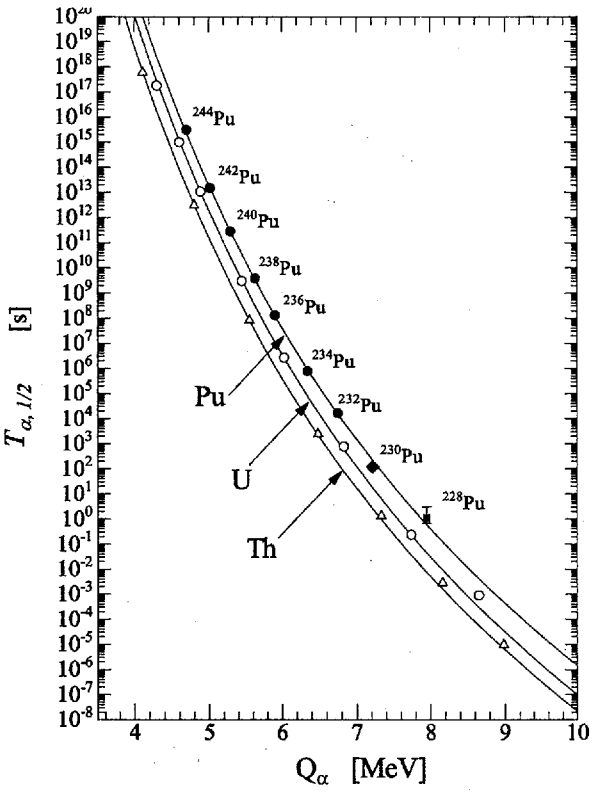

Figure 2: Alpha-decay energy and half-life for ^{228}Pu (solid square with error bar) is plotted on the map of $T_{\alpha,1/2}$ versus Q_α together with the other nuclei (solid circle=Pu, open circle=U, open triangle=Th [9]). The $T_{\alpha,1/2}$-value for ^{230}Pu [20] is shown by the solid diamond. Geiger-Nuttall curve for even-even Pu, U, and Th isotopes [10] are shown by the solid curves.

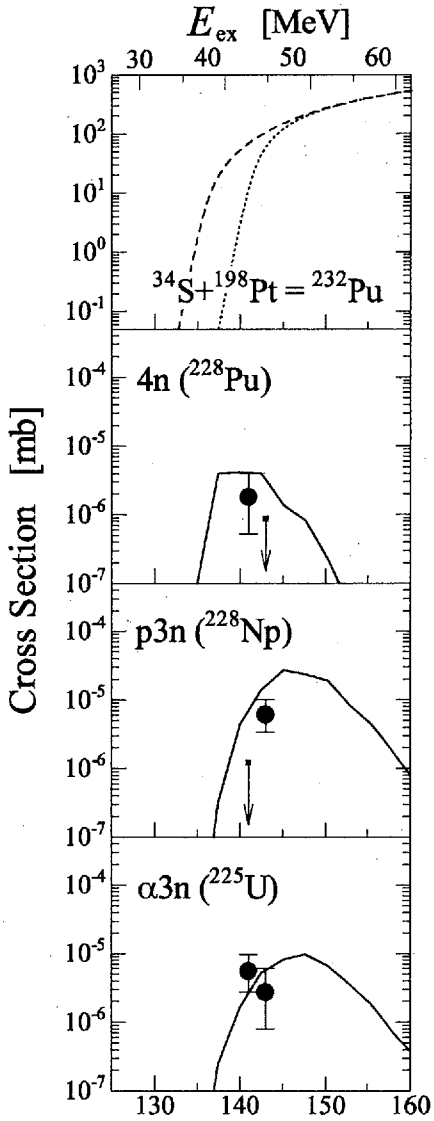

Figure 3: Evaporation residue cross sections for ^{228}Pu, ^{228}Np, and ^{225}U are shown together with the statistical model calculation (solid curve). The vertical bar with arrow shows the upper limit of the cross section. The fusion cross section calculated by the CCDEF code is shown by the dashed-curve, and the fusion cross section of the one-dimensional barrier penetration model is shown by the dotted-curve.

References

[1] A.N. Andreyev *et al.*, Z. Phys. A **347** (1994) 225.

[2] K. Nishio *et al.*, Phys. Rev. C **68** (2003) 064305.

[3] H. Koura, J. Nucl. and Radiochem. Sci., **3**, 201 (2002)

[4] T. Tachibana, M. Yamada, Proc. Inc. Conf. on exotic nuclei and atomic masses, Arles, 1995 (Editions Frontieres, Gif-sur-Yvette, 1995) p.763.

[5] V.I. Kuznetsov, N.K. Skobelev, and G.N. Flerov, Sov. J. Nucl. Phys. **4**, 202 (1967)

[6] S.A. Kreek *et al.*, Phys. Rev. C **50**, 2288 (1994)

[7] H. Ikezoe *et al.*, Nucl. Instrum. Meth. A **376**, 420 (1996)

[8] T. Kuzumaki *et al.*, Nucl. Instrum. Meth. A, **437**, 107 (1999)

[9] R.B. Firestone, Table of Isotopes, edited by V.S. Shirley (Wiley, New York, 1996)

[10] J.O. Rasmussen, 'Alpha, Beta, and Gamma-ray spectroscopy', Vol.1, North-Holland, Amsterdam (1966) pp.701

[11] G. Audi and A.H. Wapstra, Nucl. Phys. **A 595**, 409 (1995)

[12] J.O. Fernández Niello, C.H. Dasso and S. Landowne, Comput. Phys. Commun. **54**, 409 (1989)

[13] W. Reisdorf and M. Schädel, Z. Phys. A **343**, 47 (1992)

[14] S. Raman *et al.*, At. Data and Nucl. Data Tables **36**, 1 (1987)

[15] R. H. Spear, At. Data and Nucl. Data Tables, **42**, 55 (1989)

[16] P. Raghavan, At. Data and Nucl. Data Tables, **42**, 189 (1989)

[17] P. Möller, J.R. Nix, W.D. Myers and W.J. Swiatecki, At. Data and Nucl. Data Tables, **59**, 185 (1995)

[18] S. Cohen, F. Plasil and W.J. Swiatecki, Ann. Phys. **82**, 557 (1974)

[19] K. Nishio *et al.*, Phys. Rev. C, **62**, 014602 (2000), S. Mitsuoka *et al.*, Phys. Rev. C, **62**, 054603 (2000)

[20] P. Cagarda *et al.*, GSI Scientific Report 2001 (2002)

JP0450501

JAERI－Conf 2004－005

3.11 Impact of the Total Absorption Gamma-Ray Spectroscopy on FP Decay Heat Calculations

Tadashi YOSHIDA[1], Takahiro TACHIBANA[2], Jun-ichi KATAKURA[3]

[1]*Musashi Institute of Technology, Tamazutsumi 1-28-1, Setagaya-ku, Tokyo 158-8557, Japan*
e-mail: yos@ph.ns.musashi-tech.ac.jp
[2]*Senior High School of Waseda University, Kamishakujii 3-31-1, Nerima-ku, Tokyo 177-0044, Japan*
[3]*Nuclear Data Center, Japan Atomic Energy Research Institute Tokai-mura, Ibaraki 319-1195, Japan*

We calculated the average β- and γ-ray energies, E_β and E_γ, for 44 short-lived isotopes of Rb, Sr, Y, Cs, Ba, La, Ce, Pr, Nd, Pm, Sm and Eu from the data by Greenwood et al, who measured the β-feed in the decay of these nuclides using the total absorption γ-ray spectrometer. These E_β and E_γ were incorporated into the decay data files from JENDL, JEF2.2 and ENDF-B/VI, and the decay heats were calculated. The results were compared with the integral measurements by the University of Tokyo, ORNL and Lowell. In the case of JENDL, where the correction for the so-called Pandemonium effect is applied on the basis of the gross theory, the very good agreement is no longer maintained. The γ-ray component is overestimated in the cooling time range from 3 to 300 seconds, suggesting a kind of an over-correction as for the Pandemonium effect. We have to evaluate both the applicability of the TAGS results and the correction method itself in order to generate a more consistent data basis for decay heat summation calculations.

1. Introduction

Summation calculation is a powerful and versatile method, which is widely used to predict the various aggregate behaviors of fission products (FPs) including the FP decay heat. In doing summation calculation of the decay heat, attention has to be paid on the so-called *Pandemonium problem*[1],[2] or missing of the β-strengths in the high-energy region of the daughter nucleus in the published decay schemes of high Q-valued short-lived isotopes. Calculations based on the decay data suffering from this problem tend to underestimate the γ-ray component of the decay heat and to overestimate the β-ray component. In order to compensate these lost strengths, nuclear-model calculation based on the gross theory of β-decay[3] were performed and the calculated results were adopted in the JENDL FP Decay Data File 2000[4], the preceding version of which is known as the JNDC FP Decay Data Library[5]. The American libraries, ENDF/B-V and VI[6], adopt the same kind of correction to get rid of the Pandemonium problem. By virtue of this recipe the calculated decay heat became highly consistent with the measured one. There still remains, however, small but non-negligible discrepancy in the γ-ray component in the cooling-time range from 300 to 3000s[7]. In order to remedy this persistent disagreement, an European group (Algora and Tain as spokespersons) started the measurement of the β-feeding in the decay of some important FPs including the neutron-rich Tc isotopes[8] by using the total absorption γ-ray spectrometer (TAGS). At least in principle TAGS is free from the β-feed missing, which, for example, leads to the Pandemonium problem. In 1990s there had been an extensive program[9] in which the β-feeds in Rb, Sr, Y, Cs, Ba, La, Ce, Pr, Nd, Pm, Sm and Eu isotopes were measured by this technique.

2. Decay Heat and TAGS

A typical TAGS system consists of a large NaI(Tl) scintillation detector having a deep axial well with the radioactive source in it[8],[9]. In principle all of the γ-rays emitted in a cascade accompanied by the de-excitation of a certain level deposit their energy in the scintilltor giving the level energy to which the β-transition takes place. Therefore the TAGS gives the level energy as the pulse energy and

the β-feeding rate as the pulse height simultaneously. These are the basic information required to calculate the average β- and γ-ray energies per one β-decay of the parent nucleus. If the TAGS measurement is carried out ideally, the average β- and γ-ray energies (E_β and E_γ) obtained in this way are of the best quality and free from the Pandemonium problem. In reality, however, there exist several difficulties which might makes the TAGS away from the ideal. These are the photon loss, the β-particle contamination, the finite energy resolution and so on. Partly because of this, JENDL did not adopt TAGS data as the basis of the E_β and E_γ calculation. It is certain, however, that TAGS data are appropriate to yield the E_β and E_γ values in its intrinsic nature.

3. Calculation of the Average Energies

We calculated the average β- and γ-ray energies for 44 short-lived isotopes of Rb, Sr, Y, Cs, Ba, La, Ce, Pr, Nd, Pm, Sm and Eu from the TAGS data obtained by Greenwood et al.[9]. The average β-ray energy release per one β-decay E_β is calculated by using the β-feeding intensities I_β as,

$$E_\beta = \sum_i R(E_i)\cdot[f_\beta(-E_i)/f_0(-E_i)] \ , \tag{1}$$

with

$$R(E_i) = \frac{I_\beta(E_i)}{\sum_i I_\beta(E_i)} \ , \tag{2}$$

$$f_\beta(-E) = \int_1^{-E/mc^2+1} mc^2(E_0-1)pE_0(-E/mc^2+1-E_0)^2 F(Z_d, E_0)dE_0 \ , \tag{3}$$

where

$$f_0(-E) = \text{The integrated Fermi function.} \tag{4}$$

Here m is the electron rest mass, Z_d the proton number of the daughter nucleus of the β-decay, E_i the transition energy measured from the parent state to the i-th energy level in the daughter nucleus. The function F is the Fermi function. For simplicity, we adopted the integrated Fermi function f_0 of allowed transition for all transitions in the calculation. The average γ-ray energy release per one β-decay E_γ is also expressed as

$$E_\gamma = \sum_i R(E_i)\cdot(Q+E_i) \ , \tag{5}$$

The measured β-feeding intensities of 44 FP isotopes mentioned above are given in Ref.[9]. These FP nuclei have Q_β-values ranging from 1MeV to 6MeV. The values of E_{max}/Q_β are between 69% and 97%, where E_{max} is the maximum excitation energy in the daughter nucleus for which the β-feeding intensity is measured. We adopted these β-feeding intensities for the calculation of E_β and E_γ with the use of the above equations. However, sometimes only ambiguous data are given in the table of Ref. [9]. In such cases, we treated them in the following manner in the calculation;

(1) When only the maximum or minimum values are given, we adopted these values as the β-feeding intensities of the energy levels.

(2) When only total b-feedind intensity of more than two energy levels is given, we share out the total intensity equally among these energy levels.

The vales of E_β thus obtained are compared with those values adopted in JENDL FP Decay Data File[4]. We found that the newly calculated values are, on an average, 0.9 times smaller than those values in JENDL. As for the E_γ values, they are 1.3 times larger than the values in JENDL on an

average. The reason of the decrease of E_β and the increase of E_γ is that many new β-feeding intensities are found in the region of the high excitation-energy in the TAGS measurement. The vales of E_γ are affected more directly by these high excitation-energy strength than the values of E_β as can be seen in equations (1) and (5).

4. Decay Heat Calculations

The E_β and E_γ values calculated in Sect. 3 were incorporated into the decay data files from JENDL, JEF2.2[10] and ENDF/B-VI. JENDL and ENDF/B-VI are corrected for the Pandemonium effect and JEF2.2 is not. Using these original and modified libraries, the decay heats after a burst fission were calculated with the summation method and the results were compared with the integral measurement from the University of Tokyo[11], Oak Ridge National Laboratory[12] and University of Massachusetts Lowell[13]. In Figs. 1 and 2 the results for the γ-ray component of Pu-239 are displayed for the original and the TAGS modified libraries, respectively, along with the integral measurements. In the case of JEF2.2, where any theoretical correction is not made for the missing of the β-strengths, improvement is remarkable (dotted curves). This implies that the TAGS detects the high-energy β-strengths as is expected and that the E_β and E_γ values derived therefrom correctly reflects the contribution from the high-energy β-strengths. On the other hand, in the case of JENDL (solid curves), where the correction is applied on the basis of the gross theory, the very good agreement is no longer maintained. The γ-ray component is overestimated in the cooling time range from 3 to 300 seconds suggesting a kind of an over-correction. In this cooling time range, the dominant nuclides which increase the γ-ray component (and correspondingly decreases the β-ray component) from the JENDL original are Cs-141 and La-144 as is seen from Fig. 3, which shows the effect of the nuclide-wise replacement of JENDL E_γ by TAGS energy E_γ. These 11 isotopes shown in Fig. 3 are those which have relative contributions more than 0.5 % in the cooling time range less than 100s.

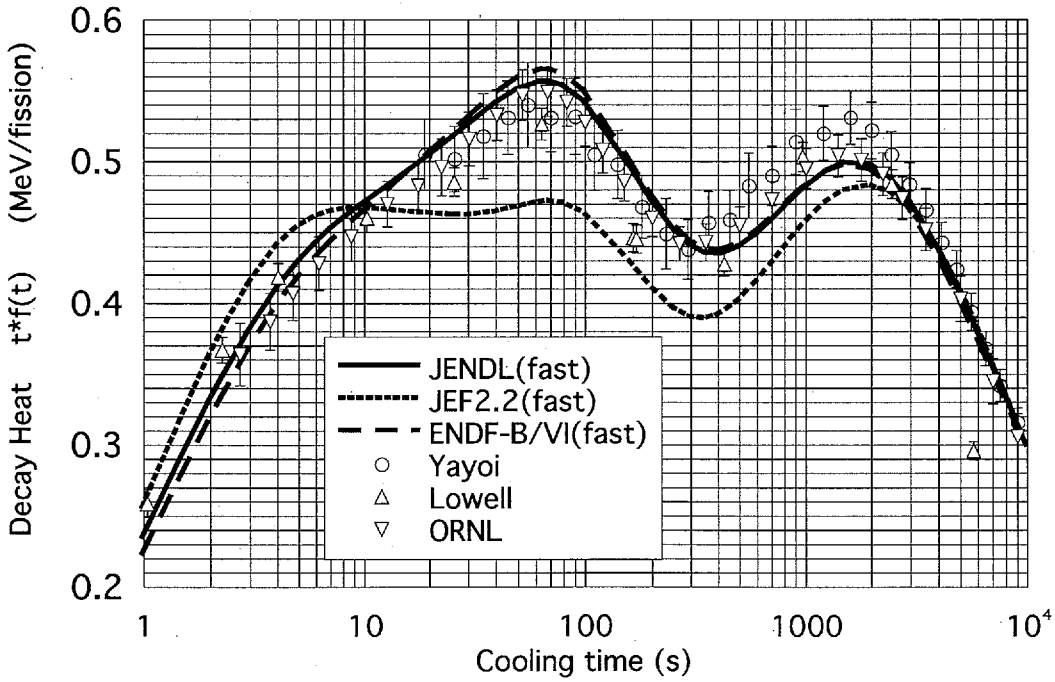

Fig. 1 Decay heat after a burst fission in Pu-239 before the TAGS correction (γ-ray component)

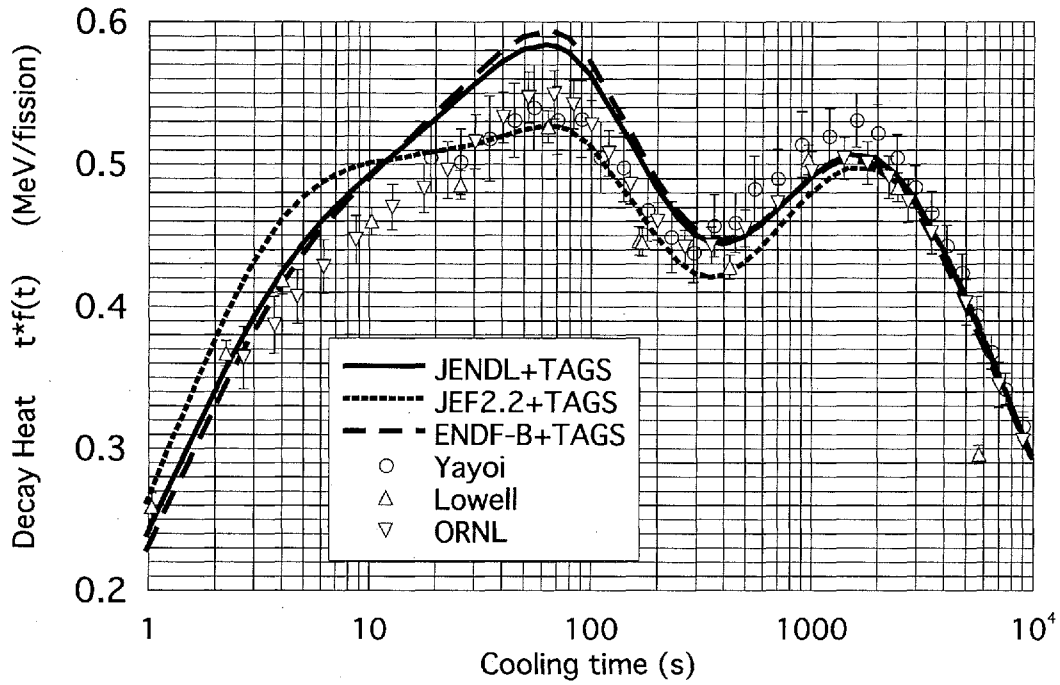

Fig. 2 Decay heat after a burst fission in Pu-239 after the TAGS correction (γ-ray component)

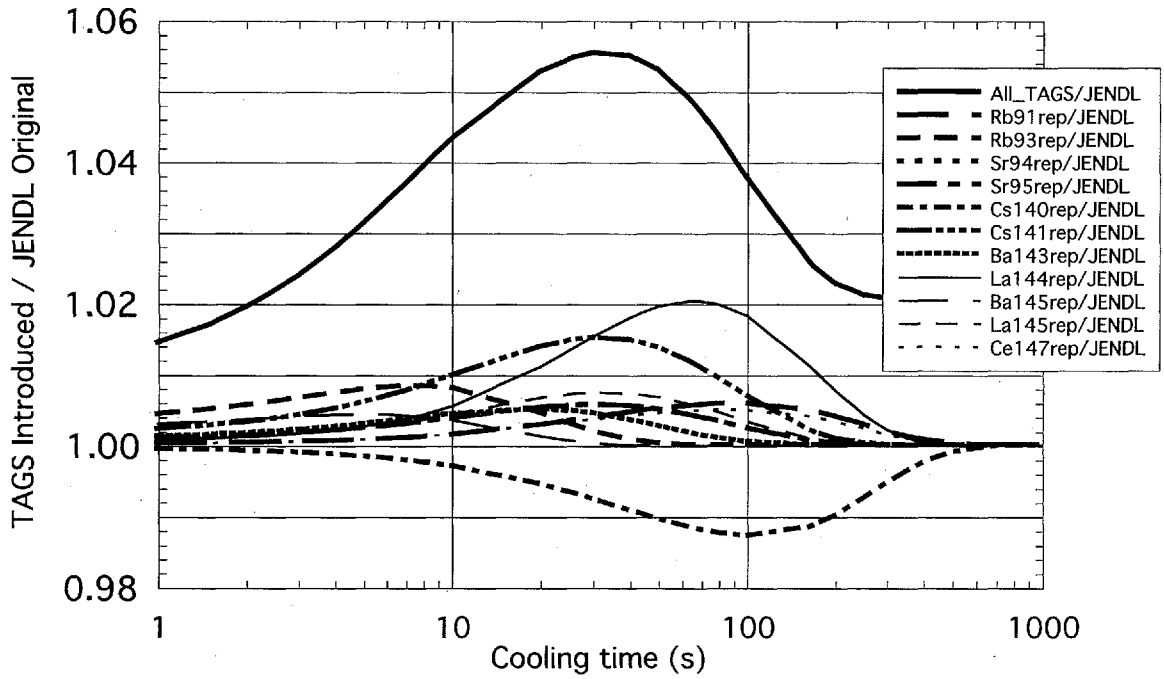

Fig. 3 Effect of introduction of TAGS energies into JENDL summation calculation (fast fission in Pu-239, γ-ray component)

5. Discussion

As can be seen in Fig. 2, the γ-ray component of the decay heats around 50s cooling for Pu-239 becomes overestimate by adopting the newly calculated E_γ values. These overestimations, which are probably found in other fissioning systems like U-235, Pu-241 and so on too, are mainly due to the increase of E_γ values of many nuclides such as shown in Fig. 3. As for La-144, one of the largest contributors, we should point out that (1.2 ± 0.1) % is given for the β-feed intensity to the ground state of Ce-144 in Ref.[9]. However, this value is very suspicious because this transition is the third-forbidden transition $(3^-) \rightarrow 0^+$. This reduces the reliability of their values for La-144. This value 1.2 ± 0.1 is not adopted in the latest Nuclear Data Sheets[14]. In this way we have to evaluate all of the TAGS data nuclide by nuclide before drawing a definite conclusion.

6. Concluding Remarks

The fact that the JENDL calculation is deteriorated by the introduction of the TAGS energies is an unexpected result. It is, however, still true that JENDL reproduces the short-cooling FP decay heat extremely well[4] for almost all the fissioning systems such as Th-232, U-233, U-235, U-238, Pu-239 and Pu-241, measured at Tokyo, Oak Ridge and Lowell. Taking into the account the recent progress in the TAGS measurements, we have to reconsider the correction method and to try to generate a consistent data basis for decay heat summation calculations.

References

[1] Hardy J.C., Carrez L. C., Jonson B., Hansen P.G.: Phys. Lett., **71B**, 307 (1977)
[2] Yoshida T, Nakasima R.: *J. Nucl. Sci. Technol.*, **18**, 393 (1981)
[3] Takahashi K., Yamada M., Kondoh T.; *Atom. Data and Nucl. Data Tables*, **12**, 101 (1973) and the references therein
[4] Katakura J., Yoshida T., Oyamatsu K., Tachibana T., JENDL FP Decay Data File 2000, JAERI 1343 (2001)
[5] Tasaka K., et al.: JNDC Nuclear Data Library of Fission Products -second Version-, JAERI-1320 (1990)
[6] Katakura J., England T.R.: Augmentation of ENDF/B Fission Product Gamma-Ray Spectra by calculated Spectra, LA-12125-MS (1991) Los Alamos National Laboratory
[7] Yoshida T., Tachibana T., Storrer F., Oyamatsu K., Katakura J.: *J. Nucl. Sci. Technol.*, **36**, 135 (1999)
[8] Algora A., Tain J.L., Private communication, (2002)
[9] Greenwood R.C., Helmer R.G., Putnam M.H., Watts K.D.: *Nucl. Instr. and Meth.* **A390** (1997) 95.
[10] JEF-2.2 Radioactive decay Data, JEF Report 13 (1994) OECD Nuclear Energy Agency
[11] Akiyama, M., An,S.: *Proc. Int. Conf. on Nuclear Data for Science and Technology*, Antwerp, p.237 (1982) and references therein.
[12] Dickens J.K., Love T.A., McConnell J.W., Peelle R.W.: *Nucl. Sci. Eng.*, **78**, 126 (1981)
[13] Nguyen H.V.: *Proc. Int. Conf. on Nuclear Data for Science and Technology*, Trieste, p.835 (1997)
[14] Sonzogni A.A.: *Nuclear Data Sheets*, **93**, 599 (2001)

JP0450502

JAERI－Conf 2004－005

3.12 The Search for Isomers of ^{156}Pm through the β-decay of ^{156}Nd

Osamu SUEMATSU[1], Michihiro SHIBATA[2], Yasuaki KOJIMA[3],
Akihiro TANIGUCHI[4], Kiyoshi KAWADE[1] and Yoichi KAWASE[4]
[1]*Department of Energy Engineering and Science, Nagoya University*
[2]*Radioisotope Research Center, Nagoya University*
[3]*Quantum Energy Applications, Hiroshima University*
[4]*Research Reactor Institute, Kyoto University*
e-mail:o-suematu@ees.nagoya-u.ac.jp

The search for isomers of ^{156}Pm has been performed through the β-decay of ^{156}Nd. The sources of the ^{156}Nd were obtained from mass-separated fission products of ^{235}U at the Kyoto University Reactor (KUR). Plastic scintillators, two HPGe detectors, and a Si(Li) detector were used. In the present experiment, more than 30 γ-rays from the β-decay of the ^{156}Nd were newly observed. The 150.8 keV isomeric transition (I.T.) from ^{156m}Pm was successfully measured. This transition was assigned to the M3 multipolarity, from the result of the conversion electron measurement. A spin and a parity of 1^- were reasonable for the isomeric state based on the M3 multipolarity of the I.T. and the 4^- β-decaying state of the ^{156}Pm.

1. Introduction

Nuclear data of neutron-rich isotopes are required for estimation of a decay heat of nuclear reactors and studies for a utilization of radioactive waste. For odd-odd nuclei, nuclear data are insufficient compared to neighboring even-even or odd-A nuclei, whose data are preferentially acquired from the viewpoint of nuclear physics. For substantial nuclear data, odd-odd nuclei must be studied as well as the other nuclei. Neutron-rich odd-odd nuclei with the mass number around A=150 have a characteristic that many of them have isomeric states. In this region, an isomer search is significant for substantial nuclear data.

We can expect isomers of ^{156}Pm, because isomers have been reported at the mass number of A=152, 154 in neutron-rich Pm isotopes[1, 2]. Concerning excited levels of ^{156}Pm, some authors have been reported in refs.[3-5]. But level structure of the ^{156}Pm is not made clear and isomers are not reported. In this work, we aimed at searching isomers of the ^{156}Pm through

the β-decay of the ^{156}Nd by means of a decay spectroscopy.

2. Experiment

The sources of the ^{156}Nd were obtained from fission products of ^{235}U using the on-line mass separator installed at the T-1 through tube of the Kyoto University Reactor (KUR-ISOL). The amount of 50 mg of UF_4 target was irradiated by thermal neutrons with a flux of 3×10^{12} n/cm^2·s. Fission products were transported to a thermal ion source by the He-N_2 gas-jet system[6]. They were ionized and mass separated by an analyzing magnet, whose resolution was ΔM/M~1/600. The mass separated fission products were collected on an alminium-coated Mylar tape and moved to a measuring position after a predetermined time interval of 12.5 s. This interval was estimated from the reported half-life of 5.47(11) s of the ^{156}Nd[3].

In measuring conversion electrons, three detectors were used; a Si(Li) detector (500 mm^2×6 mm^t) for conversion electrons, a 31 % GMX detector for γ-rays and plastic scintillator (80 mm×90 mm×1 mm^t) for β-rays. In measuring γ-rays, the Si(Li) detector was replaced by a LOAX detector (52 mm$^\phi$×20 mm^t) for low energy γ-rays. The plastic scintillator was placed at the distance of near zero from the Mylar tape for covering large solid angle. The small vacuum chamber for the Si(Li) detector was separated from the ISOL chamber by a 0.5 μm^t polyester film to protect the cooled surface of the Si(Li) detector against residual vapors.

Measurements on A=156 nuclei were performed during about 55 hours for both conversion electrons and γ-rays. Singles and β-gated singles spectra for conversion electrons, γ-rays, γ-γ and e-γ coincidence data were taken. Singles spectra were measured in the Spectrum Multi Scaling mode to determine the half-life of the ^{156}Nd.

To search isomers, we compared the β-gated spectra with the singles spectra[7]. The I.T. from the long-lived isomer is expected that it is scarcely observed in the β-gated spectrum. This expectation was backed up by the measurement of the 168.5 keV I.T. from mass-separated ^{93m}Y. Thus, the present measurement system of the Si(Li) detector can distinguish I.T.s from the other transitions. The efficiency and the energy calibrations for the HPGe detectors were made by the standard sources of ^{133}Ba, ^{152}Eu and ^{137}Cs. These calibration of the Si(Li) detector were made by the mass-separated sources of ^{93m}Y, ^{93}Rb, ^{140}Cs and ^{146}La. The Monte Carlo calculations (EGS4) were also used to estimate a peak efficiency of the Si(Li) detector. The efficiency of the Si(Li) detector was constant in the energy range from 70 keV to 1000 keV.

3. Results

Gamma-ray singles spectrum for A=156 nuclei measured by the GMX detector is shown in Fig.1. In the present experiment, we observed about 40 γ-rays associated with the β-decay

of the ^{156}Nd from coincidences with Pm X-rays. More than 30 γ-rays were newly observed. The 150.8 keV γ-ray was the most intense among measured γ-rays. The γ-ray intensities agreed with those of K. Okano *et al.*[4]. Using the 144.8-, 169.2- and 190.2 keV γ-rays, we determined the β-decay half-life of the ^{156}Nd. Decay curves of these γ-rays are presented in Fig.2. We tentatively obtained the half-life of 5.2(1) s as a weighted mean value of half-lives of three γ-rays. This half-life is somewhat shorter compared to the result reported by Greenwood *et al.*[3].

A portion of electron singles spectrum around 100 keV is shown in Fig.3 together with the β-gated spectrum. The 105.6-, 143.4- and 149.1 keV electron peaks were corresponded to the K-, L- and M-conversion electron peaks of the 150.8 keV I.T. from ^{156m}Pm. The following results confirmed that these electron peaks were originated from the I.T.; (1) no coincidences with β-rays, (2) coincidences with X-rays from the Pm, (3) approximately the same half-life as the γ-rays from the β-decay of the ^{156}Nd. In Fig.3, the K-, L- and M-electron peaks of the 150.8 keV transition were scarcely observed in the β-gated spectrum. From the e-γ coincidence data, the 105.6 keV K-electron peak was coincident with K_α and K_β X-rays of Pm. It means that the electrons were emitted from an excited level of the ^{156}Pm. The decay curve of the 105.6 keV K-electron peak is also presented in Fig.2. The half-life of the electron peak was 5.13(2) s. This value agrees with the half-life of 5.2(1) s of γ-rays from the β-decay of the ^{156}Nd. If the radiative equilibrium is approved between the ^{156}Nd and the ^{156m}Pm, the half-life of 5.13(2) s of the electron peak leads to conclusion that the electrons are emitted from the excited level of the daughter nucleus of the ^{156}Nd, that is, the ^{156m}Pm. This assumption is correct from the multipolarity of the 150.8 keV transition described later. From foregoing results, the 150.8 keV transition is the I.T. from the ^{156m}Pm.

Experimental K- and L-internal conversion coefficients (I.C.C.s) of the 150.8 keV I.T. are presented in Fig.4 together with the theoretical values[8]. Experimental values were obtained from the electron and the γ-ray singles spectra. We found the ratio of the interested I.C.C. to the well evaluated one and determined the value of the interested I.C.C.s. The normalization of the conversion coefficients was made using the 267.8 keV known E2 transition following the β-decay of the ^{156}Pm. Errors are estimated from the upper and the lower value of the I.C.C.s, which are obtained from the different normalizations and at two measuring positions of the GMX detector (8 mm and 46 mm). From the Fig.4, the 150.8 keV I.T. was assigned to be the M3 multipolarity. Using Moszkowski formula, the half-life of the isomer is estimated to be 253 ms. The radiative equilibrium is considered to be approved between the ^{156}Nd and the ^{156m}Pm because the half-life of the ^{156m}Pm is much shorter than the one of the ^{156}Nd.

4. Discussion

A spin and a parity of the isomer were estimated based on a placement of the 150.8 keV I.T. in the decay scheme, M3 multipolarity of the I.T. and the 4^- β-decaying state of the ^{156}Pm[5]. From the e-γ coincidence data, the 105.6 keV K-electron peak was only coincident with K_α and K_β X-rays of Pm and not coincident with the other γ-rays. Then, the I.T. directly populates the 4^- state of the ^{156}Pm. In consideration for the M3 multipolarity of the I.T., the isomer is likely to be 1^- state.

We tentatively propose a proton-neutron configuration for the 1^- isomeric state from systematics of ground states in neighboring odd-A nuclei. In odd-A isotones with the neutron number of N=95, the ν3/2[521] was reported for the ground states of ^{157}Sm and ^{159}Gd. In odd-A isotopes with the proton number of Z=61, the π5/2[532] for ^{153,155,157}Pm and the π5/2[413] for ^{151}Pm were reported as a configuration of the ground state. From these configurations, $\{\pi 5/2[413]\text{-}\nu 3/2[521]\}_{1^-}$ is the only probable configuration for the 1^- isomeric state. If the 4^- state is the ground state, the configuration of the 1^- state may be an example of a violation of Gallagher-Moszkowski rules[9]. Concerning energy level ordering of the 1^- and the 4^- states, detailed analyses are now in progress.

5. Conclusion

The search for isomers of the ^{156}Pm has been performed through the β-decay of the ^{156}Nd. In the present experiment, we observed about 40 γ-rays associated with the β-decay of the ^{156}Nd. More than 30 γ-rays were newly observed. The β-decay half-life of the ^{156}Nd was estimated to be 5.2(1) s. The 150.8 keV I.T. from the ^{156m}Pm was successfully observed and assigned to be the M3 multipolarity. This transition directly populates the 4^- β-decaying state of the ^{156}Pm. Based on these results, the spin and the parity of the new isomeric state is likely to be 1^-. The proton-neutron configuration of $\{\pi 5/2[413]\text{-}\nu 3/2[521]\}_{1^-}$ for the 1^- isomeric state was tentatively proposed from the systematics in neighboring odd-A nuclei.

Reference

1) W. R. Daniels and D. C. Hoffman, *Phys. Rev.*, **C4**, 919 (1971).
2) O. Tannila and J. Kantele, *Z. Phys.*, **251**, 87 (1972).
3) R. C. Greenwood, R. A. Anderl, J. D. Cole, *et al.*, *Phys. Rev.*, **C35**, 1965 (1987).
4) K. Okano and Y. Kawase, NEANDC(J)-140/U, (1989).
5) M. Hellström, B. Fogelberg, L. Spanier, *et al.*, *Phys. Rev.*, **C41**, 2325 (1990).
6) A. Taniguchi, K. Okano, T. Sharshar, *et al.*, *Nucl. Instrum. Methods*, **A351**, 378 (1994).
7) Y. Kojima, A. Taniguchi, M. Shibata, *et al.*, *Eur. Phys. J.* (in press)
8) F. Rösel, H. M. Fries, K. Alder, *et al.*, *At. Data. Nucl. Data Tables*, **21**, 91 (1978).
9) C. J. Gallagher and S. A. Moszkowski, *Phys. Rev.*, **111**, 1282 (1958).

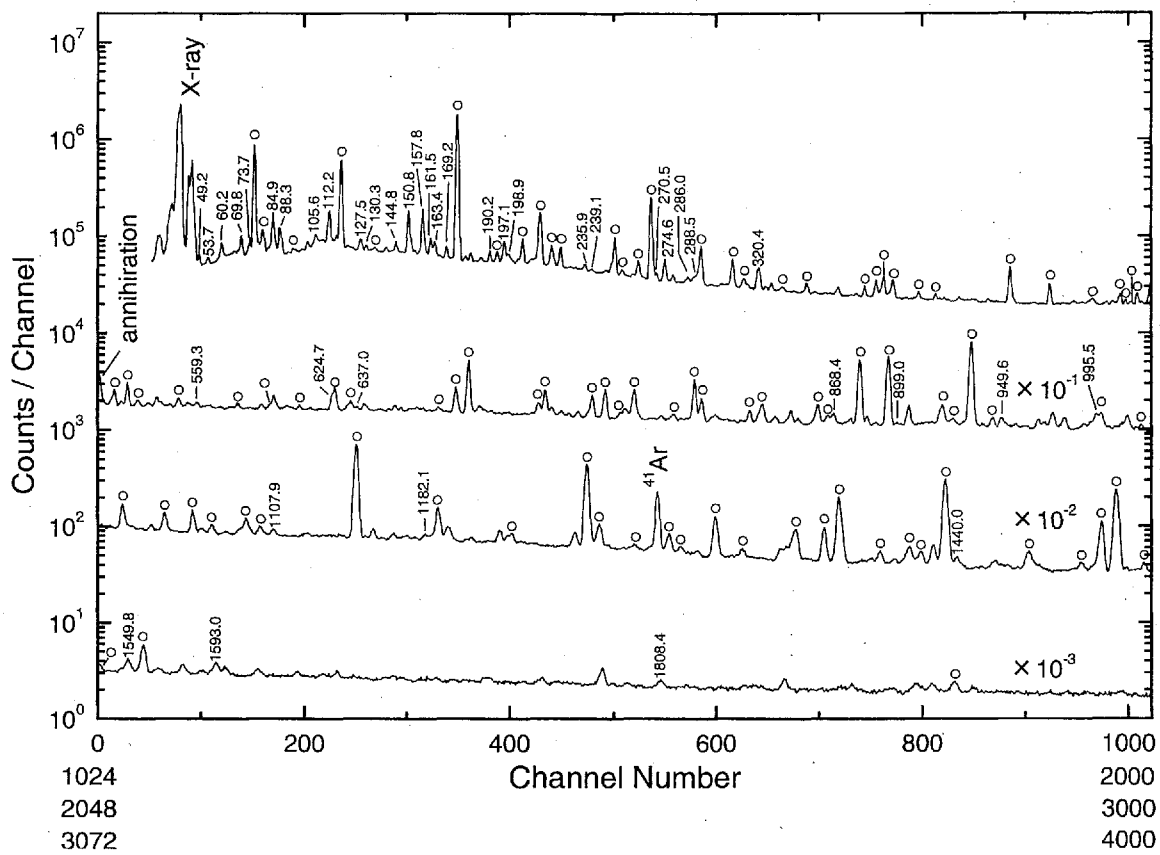

Fig.1 A γ-ray singles spectrum in the decay of the ^{156}Nd measured by the GMX detector. Energies are given in keV. Gamma-ray peaks marked by opened circles represent γ-rays from the decay of the ^{156}Pm.

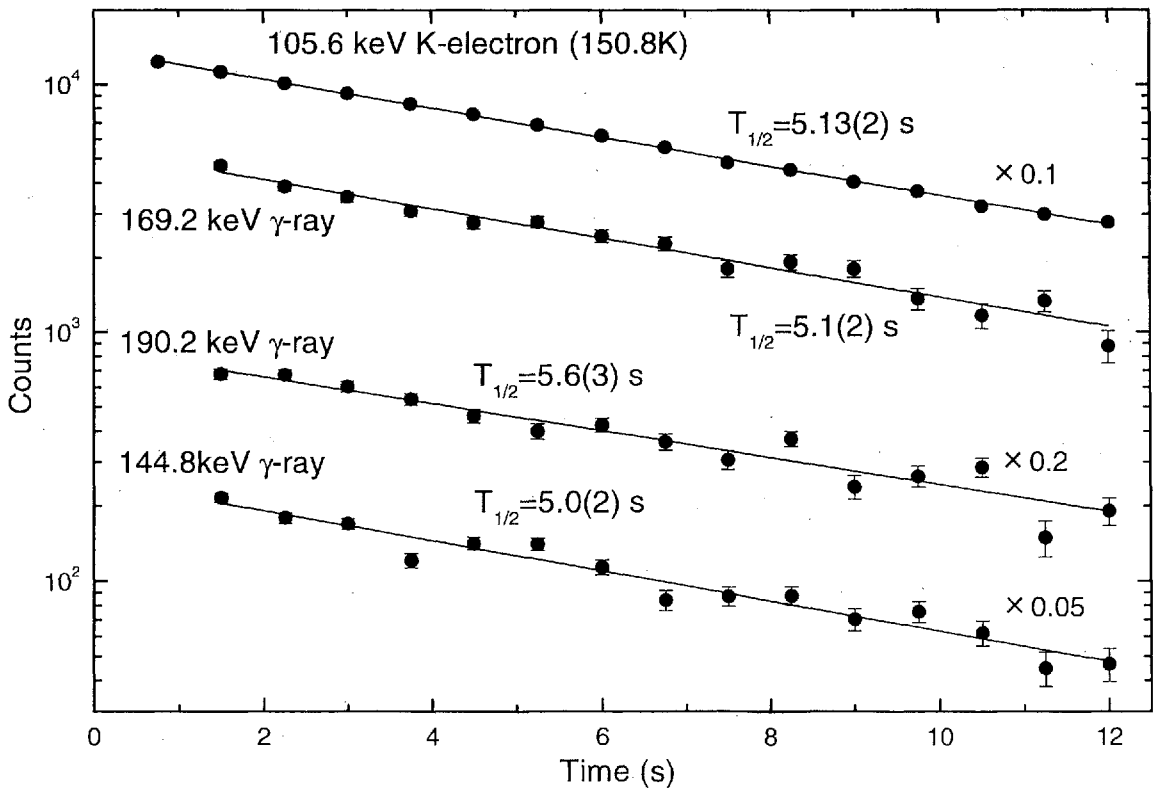

Fig.2 Decay curves of the 144.8-, 169.2-, 190.2 keV γ-ray and the 105.6 keV K-electron of 150.8 keV isomeric transition (150.8K).

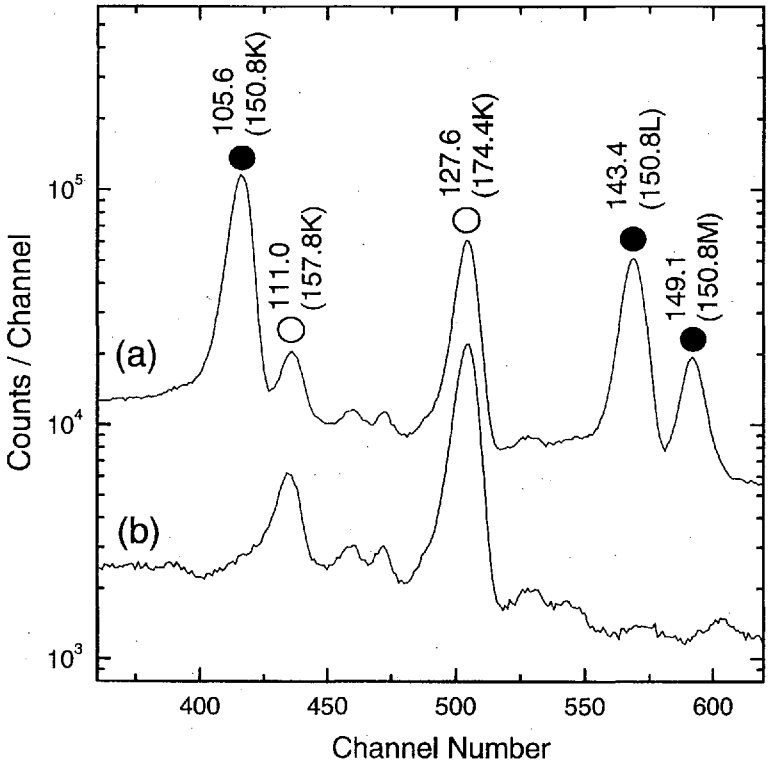

Fig.3 A portion of (a) the electron singles and (b) the β-gated electron singles spectra for A=156 nuclei. Energies are given in keV. Closed and opened circles represent electrons from the decay of the ^{156}Nd and the ^{156}Pm, respectively.

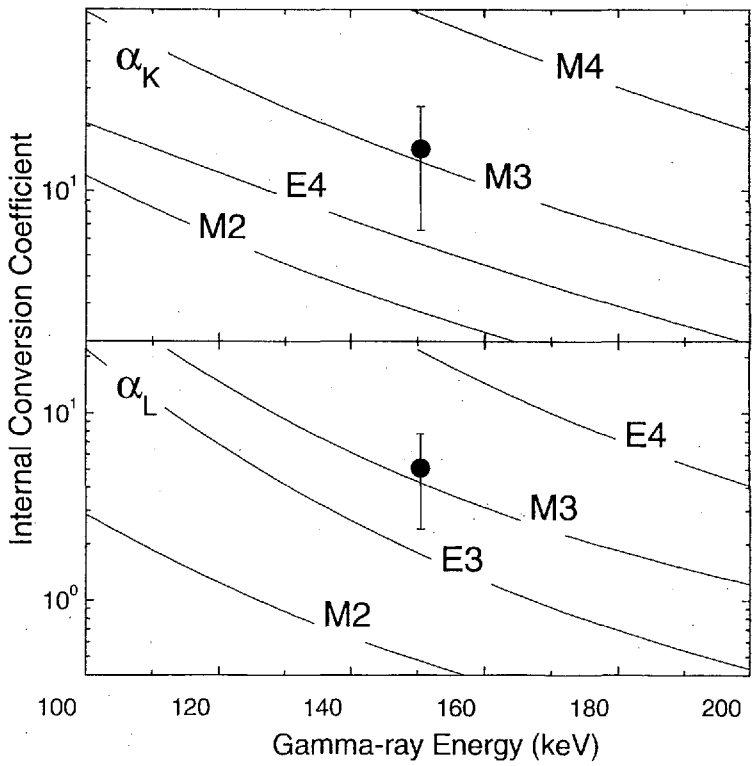

Fig.4 Experimental K- and L-internal conversion coefficients for the 150.8 keV I.T.. Solid lines mean theoretical values taken from ref.[8].

3.13 Saturation of Asymmetric Nuclear Matter

K. Oyamatsu[1,2,3] and K. Iida[2]
[1]*Department of Media Theories and Production, Aichi Shukutoku University*
Nagakute, Nagakute-cho, Aichi-gun, Aichi 480-1197, Japan
[2]*The Institute of Physical and Chemical Research (RIKEN)*
Hirosawa, Wako, Saitama 351-0198, Japan
[3]*Department of Physics, Nagoya University*
Furo-cho, Chigusa-ku, Nagoya, Aichi 464-8602, Japan
email: oyak@asu.aasa.ac.jp

Abstract

We examine relations among the parameters characterizing the phenomenological equation of state (EOS) of nearly symmetric, uniform nuclear matter near the saturation density by comparing macroscopic calculations of radii and masses of stable nuclei with the experimental data. The EOS parameters of interest here are the symmetry energy S_0, the density symmetry coefficient L, and the incompressibility K_0 of symmetric nuclear matter at the normal nuclear density. In this study, we also examine the incompressibility of asymmetric matter, which was fixed in a certain functional form in our previous study. This parameter could be important in the description of neutron-rich nuclei and neutron-star matter. In the present study, we treat the incompressibility of the asymmetric matter as a free parameter in fitting the masses and radii, obtain essentially the same EOS parameter values as those in the previous study, and confirm the two important features for symmetry energy; a strong correlation between S_0 and L, and the upper bound of L which is an increasing function of K_0. The present results strongly support the the prediction of the previous study that the matter radii of neutron-rich nuclei depend strongly on L while being almost independent of K_0. This is a feature that will help to determine the L value via systematic measurements of nuclear size.

1 Introduction

The equation of state (EOS) of nuclear matter is the key nuclear property that determines macroscopic nuclear properties such as nuclear masses and radii. The saturation density and energy of symmetric nuclear matter, which consists of equal numbers of neutrons and protons, are determined rather precisely from masses and radii of stable nuclei, in which numbers of neutrons and protons are not very different. In near future, a radioactive ion beam will enable us to measure nuclear masses and radii of heavy nuclei with large neutron excess. In order to make full use of the future experiment for the empirical determination of asymmetric matter EOS, it is important to clarify what kind of EOS properties can be determined from stable nuclei, and what kind of EOS properties can not be determined from stable nuclei but from neutron rich nuclei. In this paper, we focus on the empirical saturation properties of the EOS to be obtained from stable nuclei.

The energy per nucleon near the saturation point of symmetric nuclear matter is generally expressed as [1]

$$w = w_0 + \frac{K_0}{18n_0^2}(n-n_0)^2 + \left[S_0 + \frac{L}{3n_0}(n-n_0) + \frac{K_{asym}}{18n_0^2}(n-n_0)^2\right]\alpha^2. \tag{1}$$

Here w_0, n_0 and K_0 are the saturation energy, the saturation density and the incompressibility of symmetric nuclear matter. The neutron excess is defined as $\alpha = 1 - 2x$ using proton fraction x. The parameters S_0 (the symmetry energy), L (the density symmetry coefficient) and K_{asym} characterize the density dependent symmetry energy $S(n)$ at $n \approx n_0$;

$$S_0 = S(n_0), \tag{2}$$

$$L = 3n_0(dS/dn)_{n=n_0}, \tag{3}$$

$$K_{asym} = 9n_0^2(d^2S/dn^2)_{n=n_0}. \tag{4}$$

From Eq. (1), the saturation density n_s and energy w_s of asymmetric nuclear matter with fixed proton fraction are given, up to the second order of α, by

$$n_s = n_0 - \frac{3n_0L}{K_0}\alpha^2, \tag{5}$$

$$w_s = w_0 + S_0\alpha^2. \tag{6}$$

One useful empirical parameter to characterize the saturation of asymmetric nuclear matter is the slope, y, of the saturation line near $\alpha = 0$ ($x = 1/2$) [1]. It is expressed as

$$y = -\frac{K_0S_0}{3n_0L}. \tag{7}$$

In this paper, we systematically examine empirical relations among the six EOS parameters in Eq. (1). Specifically, we use a parametrized EOS, which is simple but flexible enough to fit non-relativistic and relativistic phenomenological EOS's at $n < 2n_0$. The parameter values are chosen to fit masses and radii of stable nuclei in the Thomas-Fermi approximation.

2 Macroscopic description of nuclei

In constructing a macroscopic nuclear model, we begin with a simple expression for the bulk energy per nucleon [5],

$$w = \frac{3\hbar^2(3\pi^2)^{2/3}}{10m_nn}(n_n^{5/3} + n_p^{5/3}) + (1-\alpha^2)v_s(n)/n + \alpha^2v_n(n)/n, \tag{8}$$

where

$$v_s = a_1n^2 + \frac{a_2n^3}{1+a_3n} \tag{9}$$

and

$$v_n = b_1n^2 + \frac{b_2n^3}{1+b_3n} \tag{10}$$

are the potential energy densities for symmetric nuclear matter and pure neutron matter, and m_n is the neutron mass. Here, replacement of the proton mass m_p by m_n in the proton kinetic energy makes only a negligible difference. Equation (8) can well reproduce the microscopic calculations of symmetric nuclear matter and pure neutron matter by Friedman and Pandharipande [3] and of asymmetric nuclear matter by Lagaris and Pandharipande [4]. Furthermore the expression can also reproduce phenomenological Skyrme Hartree-Fock and relativistic mean field EOS's.

We determine the parameters included in Eqs. (9) and (10) in such a way that they reproduce data on radii and masses of *stable* nuclei. In the limit of $n \to n_0$ and $\alpha \to 0$ ($x \to 1/2$), expression (8) reduces to the usual form (1) [2].

We describe a spherical nucleus of proton number Z and mass number A within the framework of a simplified version of the extended Thomas-Fermi theory [5]. We first write the total energy of a nucleus as a function of the density distributions $n_n(\mathbf{r})$ and $n_p(\mathbf{r})$ according to

$$E = \int d^3r n(\mathbf{r}) w\left(n_n(\mathbf{r}), n_p(\mathbf{r})\right) + F_0 \int d^3r |\nabla n(\mathbf{r})|^2 + \frac{e^2}{2} \int d^3r \int d^3r' \frac{n_p(\mathbf{r}) n_p(\mathbf{r}')}{|\mathbf{r}-\mathbf{r}'|} + N m_n + Z m_p, \tag{11}$$

where the first, second and third terms on the right hand side are the bulk energy, the gradient energy with an adjustable constant F_0, and the Coulomb energy, respectively. The symbol $N = A - Z$ denotes the neutron number. Here we ignore shell and pairing effects. We also neglect the contribution to the gradient energy from $|\nabla(n_n(\mathbf{r}) - n_p(\mathbf{r}))|^2$; this contribution makes only a little difference even in the description of extremely neutron-rich nuclei, as clarified in the context of neutron star matter [5].

For the present purpose of examining the macroscopic properties of nuclei such as masses and radii, it is sufficient to characterize the neutron and proton distributions for each nucleus by the central densities, radii and surface diffuseness different between neutrons and protons, as in Ref. [5]. We thus assume the nucleon distributions $n_i(r)$ $(i = n, p)$, where r is the distance from the center of the nucleus, as

$$n_i(r) = \begin{cases} n_i^{\rm in} \left[1 - \left(\dfrac{r}{R_i}\right)^{t_i}\right]^3, & r < R_i, \\ 0\ , & r \geq R_i. \end{cases} \tag{12}$$

Here R_i roughly represents the nucleon radius, t_i the relative surface diffuseness, and $n_i^{\rm in}$ the central number density. The proton distribution of the form (12) can fairly well reproduce the experimental data for stable nuclei such as ^{90}Zr and ^{208}Pb [5].

3 Optimization using smoothed nuclear data

The EOS parameters a_1–b_3 and F_0 are determined from masses and radii of stable nuclei in the same way as in Refs. [2, 5] using the empirical values for nine nuclei on the smoothed β-stability line ranging $25 \leq A \leq 245$ (see Table A.1 in Ref. [5], which is based on Refs. [6, 7]). In contrast to Refs. [2, 5] in which the b_3 value was fixed, the b_3 value is also varied in the present study to have a feeling about K_{asym} dependence. For fixed slope y and incompressibility K_0, such a comparison is made by a usual least squares fitting, which gives rise to an optimal set of the parameters a_1–b_3 and F_0. Here, we set y and K_0 as -1800 MeV fm^3 $\leq y \leq -200$ MeV fm^3 and 180 MeV $\leq K_0 \leq$ 360 MeV; the numerical results for n_0, w_0, S_0, L and F_0 are obtained for about 200 combinations of y and K_0. All of them reproduce the input nuclear data almost equally.

The b_3 value, which is optimized in the present study, is found rather close to the value in the previous study ($b_3 = 1.58632$ fm^3) [2] as shown in Fig. 1. The optimum relations among the EOS parameters obtained in the present study is quite similar to those in the previous study because the EOS parameters at $n = n_0$ are not sensitive to b_3. The parameter b_3 only softens the asymmetric matter EOS at high densities.

As shown in Fig. 2 the present study confirms the empirical correlation between S_0 and L obtained in the previous study [2],

$$S_0 \approx B + CL, \tag{13}$$

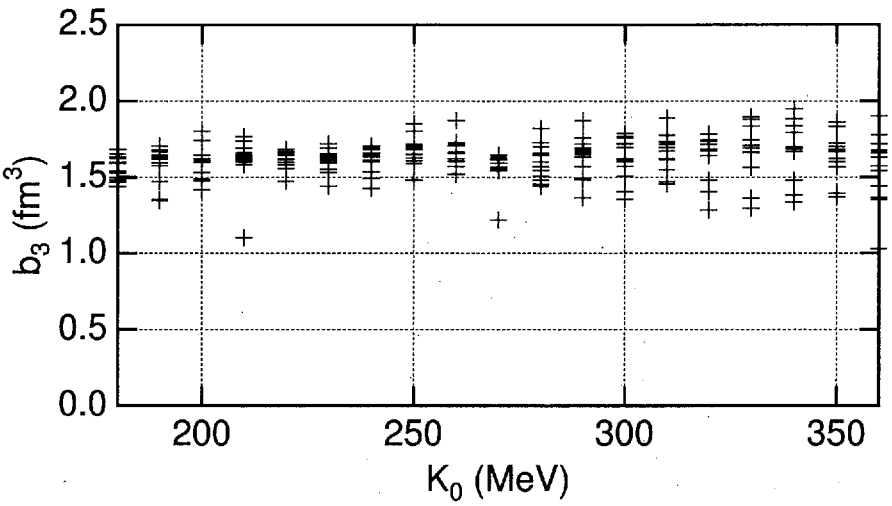

Figure 1: The b_3 value in Eq. (10). This value was fixed in the previous study [2].

with the same values of the coefficients ($B \approx 28$ MeV and $C \approx 0.075$). A similar result, $B = 29$ MeV and $C = 0.1$, was obtained from various Hartree-Fock models with finite-range forces by Farine et al. [8]. As for the saturation of asymmetric nuclear matter, the above correlation is the only information that can be obtained from stable nuclei. This is the reason why there is significant difference among empirical asymmetric matter EOS's although they reproduce properties of stable nuclei.

The saturation energy of symmetric nuclear matter, w_0, always takes a value of -16.1 ± 0.2 MeV. As shown in Fig. 3, the present study obtains the same weak correlation between n_0 and K_0 as the previous study [2]. This is a feature found among non-relativistic phenomenological Skyrme Hartree-Fock EOS's (see Fig. 4 of Ref. [9]).

In Fig. 4, the uncertainties in L and K_0 is represented as a band, which reflects the constraint on (y, K_0). In this band, L increases with increasing y for fixed K_0. The upper bound ($y = -200$ MeV fm^3) reaches a large value of L, which increases with increase in K_0.

4 Summary

About 200 sets of the EOS parameters are systematically obtained from fitting to masses and radii of stable nuclei using a simplified Thomas-Fermi model paying attention to large uncertainties in K_0 and L values.

As for symmetric nuclear matter, the saturation density density n_0 has a weak K_0 dependence while the saturation energy is w_0 is essentially constant.

There is a strong correlation between S_0 and L : $S_0 \approx 28 + 0.075L$ (MeV). However, the L value can not be singled out from stable nuclei although the upper bound of L can be estimated as an increasing function of K_0 from the empirical constraint on the slope of the saturation line. This is all we obtain from stable nuclei about asymmetric nuclear matter. As a consequence, empirical EOS's for asymmetric matter can vary significantly in spite that they reproduce properties of stable nuclei almost equally.

From the present study allowing a wider EOS parameter space, it is found that an artificial

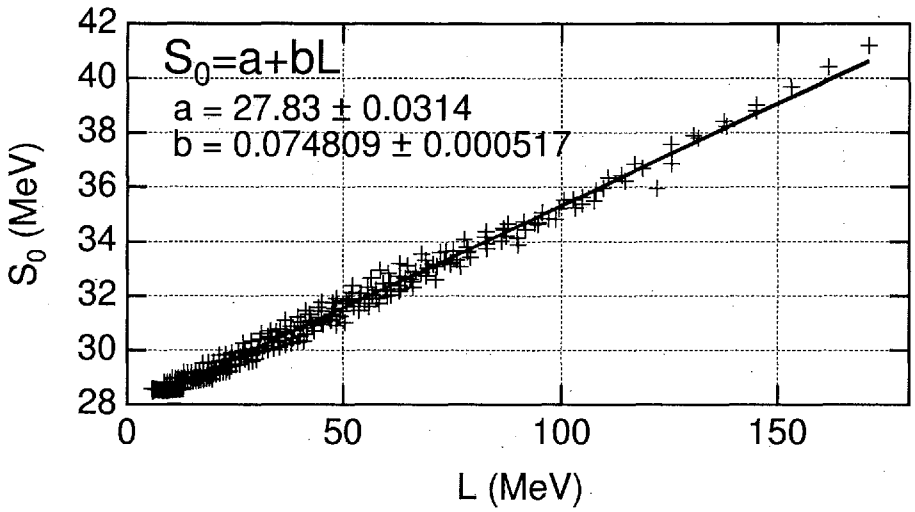

Figure 2: The empirical correlation between S_0 and L obtained in the present study.

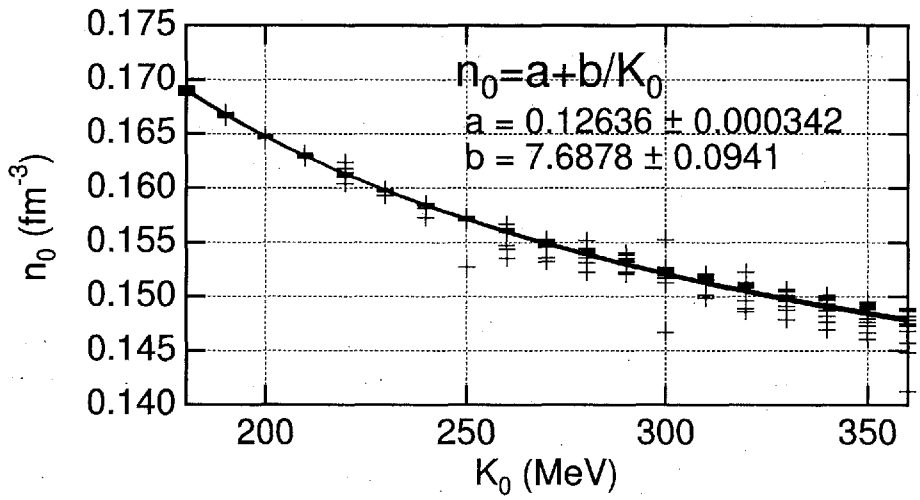

Figure 3: The empirical correlation between n_0 and K_0 obtained in the present study.

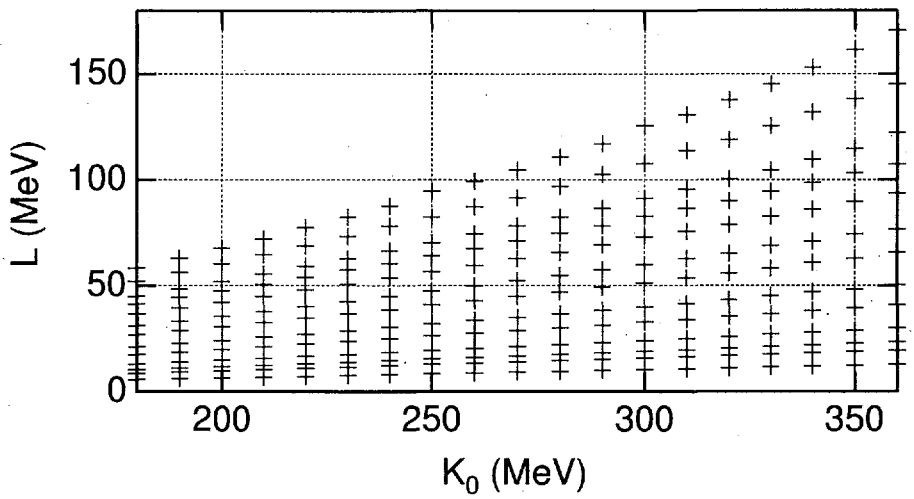

Figure 4: The optimum (L, K_0) values.

constraint in the previous study ($b_3 = 1.586$ fm^3) makes little difference in determining the EOS. Hence, the present results supports the following scenario of our previous study; the L value can not be determined from stable nuclei, but could be determined from neutron-rich nuclei. From these results, we conclude that future systematic measurements of the matter radii of neutron-rich nuclei could help deduce the L value, which in turn could give useful information about the presence of pasta nuclei in neutron star crusts.

References

[1] K. Oyamatsu, I. Tanihata, Y. Sugahara, K. Sumiyoshi, H. Toki, Nucl. Phys. A 634 (1998) 3.

[2] K. Oyamatsu and K. Iida, Prog. Theor. Phys. 109 (2003) 631.

[3] B. Friedman, V.R. Pandharipande, Nucl. Phys. A 361 (1981) 502.

[4] I.E. Lagaris, V.R. Pandharipande, Nucl. Phys. A 369 (1981) 470.

[5] K. Oyamatsu, Nucl. Phys. A 561 (1993) 431.

[6] M. Yamada, Prog. Theor. Phys. 32 (1964) 512.

[7] H. de Vries, C.W. de Jager, C. de Vries, At. Data Nucl. Data Tables 36 (1987) 495.

[8] M. Farine, J.M. Pearson, B. Rouben, Nucl. Phys. A 304 (1978) 317.

[9] J.P. Blaizot, Phys. Rep. **64**, 171 (1980).

JP0450504

JAERI－Conf 2004－005

3.14 Time Periodic Behaviors of the Compound Nucleus Coherent with the Incident Neutron Wave at Resonances

Makio OHKUBO
N.Resonance Lab, 1663-39,Senba-cyo, Mito-shi, Ibaraki-ken 310-0851 Japan

Abstract

For an isolated resonance, time periodic behavior or recurrence of the compound nucleus is required by S-matrix theory, and the energies of the normal modes, which compose the state, are restricted to be commensurable (integer ratios) with each other. Then the excitation energies E_x are written as a sum of inverse integers: $E_x = G\sum\frac{1}{n}$, where n=integers, and G=34.5MeV. The time periods of the normal modes are integer multiples of $\tau_0 = 2\pi\hbar/G = 1.20\times10^{-22}s$. Integer ratios in E_x/S_n are found for many of ^{16}O+n resonances, the probability of appearance of which is proved to be $\sim 10^{-2}$ if the levels are distributed randomly. This will be an evidence of time coherency between the recurrence of the compound nucleus and the incident neutron wave. Resonance reaction mechanism is discussed.

1. Introduction

In slow neutron nucleus reactions, many resonances are observed with an average level density $\sim 10^2 \sim 10^6$/MeV for light to heavy nuclei [1]. These resonances correspond to quasi-stable states of the compound nucleus(CN) above the neutron separation energy S_n ~8MeV, where many degrees of freedom will be excited and mixed to form very complicated structures. Therefore, neutron resonances are surmised to form a quantum chaos. In fact, statistical properties of the observed neutron resonance data are in good agreement with the predictions of Random Matrix Theory(RMT): Wigner(GOE) distribution for nearest neighbor level spacings, Porter-Thomas distribution for strengths, and Δ_3 statistics for long range correlations.

However, several properties are observed which contradict the predictions of RMT. One of them is the crystalline-like structure of resonance dispositions. Using a Fourier-like analysis and D_{ij} (spacings between two arbitrary levels) distributions, several level spacings can be found (hereafter called dominant spacings) which appear more frequently than expected from GOE in the energy region considered. These position/spacing correlations are widely found in neutron resonances of many nuclei in a wide mass region, with large deviations from GOE distributions of levels [2-8]. Examples of dominant spacings are 4.4eV(^{177}Hf), 5.5eV(^{123}Sb), 14.6eV(^{238}U), 17.6eV(^{168}Er), 142eV(^{75}As), 213eV(^{240}Pu),....

Moreover, it is very interesting to observed that the ratio of dominant spacings of different nuclei are simple integer ratios: in the above cases 5.5eV(^{123}Sb)/ 4.4eV(^{177}Hf) = 5/4, 14.6eV(^{238}U)/17.6eV (^{168}Er) =5/6, 142eV(^{75}As)/ 213eV(^{240}Pu)= 2/3, etc. For resonances of light nuclei in keV to MeV region, similar dominant spacings and integer ratios are widely found [8]. For the neutron resonances of light and magic e-e nuclei up to several hundred keV, many of the dominant spacings are expressed as G/n ,(G=34.5MeV, n: integer) [9,10]. These features are completely different from the ordinary understanding of neutron resonances as quantum chaos.

These facts provided the motivation to reconsider the mechanism of neutron resonance reactions, and we previously developed the "Recurrence model" of the compound nucleus for neutron resonance reactions[11], in which time behaviors of M normal modes ($M \leq 10$) excited in the compound nucleus are treated in a semi-classical way.

In this article, time periodic behaviors of the CN are discussed, which are deduced from S-matrix theory, coherent with the incident neutron wave at resonances. Simple integer ratios are found between E_x and S_n for many of ^{16}O+n resonances, the probability of appearance of which is calculated to be very small assuming random dispositions of resonance levels. This will be an evidence of the time coherency between the CN and the incident neutron wave.

2. S-matrix, response function and normal modes

For a sharp resonance of medium and heavy nuclei, resonance width is of the order of $\Gamma \sim 1eV$, which means dumping or friction in CN is very small, and an almost closed system. Its excitation energy $E_x \sim 8MeV$ is conserved during life time $\sim \hbar/\Gamma \sim 10^{-14}s$, extremely long compared to the transit time of neutron in nuclear potential($\sim 10^{-21}s$). Wave packet length of incident neutron is very long compared to the nuclear size. For the lowest resonance of ^{238}U at 6.7 eV with Γ=0.025eV, wave packet length L $\sim$ hv/Γ is estimated by uncertainty principle to be 10^{-8}m, where v is velocity of the neutron and h is Plank's constant. This value is in good agreement with the coherent length of neutron $\sim$10nm (10^{-8}m) measured by neutron interferometer for thermal neutron.

As describe below, S-matrix theory provides time periodic behaviors of the compound nucleus which is coherent with the incident neutron wave at resonance.
An S-matrix $S(E)$ is defined for the neutron-nucleus reaction from which the cross section $\sigma_s(E) = (\pi/k^2)(2l+1) \mid 1-S(E) \mid^2$, etc. is determined. A relation between $S(E)$ and the response function is discussed after Sitenko [12]. For an s-wave resonance, the incident wave $\psi^-(r,t)$ and outgoing wave $\psi^+(r,t)$ around the interaction region of radius R are,

$$\psi^-(r,t) = \int_0^\infty dE' a(E')(1/r)exp(-ik'r - (i/\hbar)E't), \qquad \text{..... (1)}$$

$$\psi^+(r,t) = \int_0^\infty dE' a(E')S(E')(1/r)exp(ik'r - (i/\hbar)E't). \qquad \text{..... (2)}$$

The response function $F(\tau)$ is defined by the causality principle, as,

$$\psi^+(r,t) = \int_0^\infty d\tau F(\tau)\psi^-(r,t-\tau). \qquad \text{..... (3)}$$

Mulitping Eqs.(1),(2),(3) by $exp(-iEt/\hbar)$ and integrating over t from -∞ to ∞, $S(E)$ can be expressed as a Fourier transform of the response function $F(\tau)$,

$$S(E)e^{2ikR} = \int_0^\infty d\tau F(\tau)e^{i\frac{E\tau}{\hbar}}, \qquad \text{..... (4)}$$

where τ is the time for the response to come back.

Eq.(4) is a basic relation on which the following discussions stand. In the continuum region, $S(E)$ has no peak, and $F(\tau)$ is expected to be a non-periodic or stochastic function of infinitely long time period. In contrast for an isolated resonance at E_0, $S(E)$ has a peak at E_0, then $F(\tau)$ must be a periodic function with a period $\tau_{rec} = 2\pi\hbar/E_0$ during a life time $\sim h/\Gamma$, where Γ is the total width of the resonance. That is, the scattered wave $\psi^+(r,t)$ is significant if $F(\tau)$ and the incident wave are time-coherent with each other.

Because of time periodic boundary condition for an isolated resonance, the response function $F(\tau)$ can be expressed by a Fourier series with higher harmonics of periods τ_j=τ_{rec}/k_j and frequencies $\omega_j = 2\pi/\tau_j$, where k_j are integers, $(j = 1,2,..M)$. For multiple components ($M \geq$2), the ratios τ_i/τ_j must form integer ratios k_i/k_j, $(i,j = 1,2,...M)$. That is, frequency ratios as well as time periods of the components are commensurable(forming integer ratios)with each other. Therefore, a unit time τ_0 exist, and τ_j is written as $n_j\tau_0$, where n_j is an integer. The recurrence time τ_{rec} is the least common multiple(LCM) for the ensemble $(n_j; j = 1,2,...,M)$ multiplied by τ_0. The frequency component ω_j is propotional to the inverse integers ω_j=$(2\pi/\tau_0)/n_j$.
An example of recurrence for multiple waves is shown in Fig.1.

The responce function $F(\tau)$ for an isolated resonance is considered to be under the influence of an ensemble of normal modes excited on the compound nucleus, the total excitation energy of which is

$$E_x = \hbar(\omega_1 + \omega_2 + .. + \omega_M) = \frac{2\pi\hbar}{\tau_0}\sum_{j=1}^{M}\frac{1}{n_j} = G\sum_{j=1}^{M}\frac{1}{n_j} \qquad (n_j : \text{integer}). \qquad \text{..... (5)}$$

Though G and τ_0 are not necessarily constant for all resonances, there are many cases where G and τ_0 seem constant. In this case, level spacings D take the form,

$$D = G(\sum\frac{1}{m} - \sum\frac{1}{n}) = G\frac{i}{k} \qquad (\text{i,k : integers}). \qquad \text{..... (6)}$$

The normal modes, simultaneously excited in the compound nucleus at resonances, will formally correspond to M eigen functions for M hamiltonians ($M \leq 10$). The total Hamiltonian is , $H = H_1 + H_2 + ... + H_M$, and the compound nuclear states $\Phi(x,t)$ are described as a direct product as, $\Phi(x,t) = \Phi_1(x_1,t) \otimes \Phi_2(x_2,t) \otimes \ ... \ \Phi_M(x_M,t)$. Though the detailed structure of $\Phi_j(x_j,t)$ is not clear, the requirement of time periodicity must be fulfilled; $\Phi_j(x,t+\tau_j) = \Phi_j(x,t)$ $(j = 1,2,...M)$, where τ_j =$\tau_0 \times n_j$. The total system recurs with a time period τ_{rec} as,

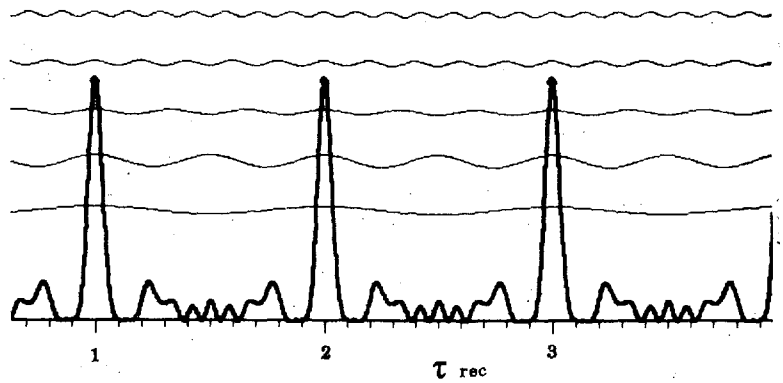

Figure 1: An example of 5 wave recurrence as function of time. Bold line : $(\sum_{j=1}^{5} a_j cos(\omega_j t))^2$, where $\omega_j = (2\pi/\tau_{rec})$ times 1,2,3, 5, and 7, with amplitudes a_j propotional to 3,5,2,2, and 2. Fine lines: each component $a_j cos(\omega_j t)$. At every time interval τ_{rec}, the system recurs to the initial phase.

$$\Phi(x, t + \tau_{rec}) = \Phi(x, t), \qquad \text{.....} \quad (7)$$

where

$$\tau_{rec} = \tau_0 \times \mathrm{LCM}(n_1, n_2, ..., n_M). \qquad \text{.....} \quad (8)$$

The unit time τ_0 is related to G (= 34.5MeV) as,

$$\tau_0 = \frac{2\pi\hbar}{G} = 1.20 \times 10^{-22}\mathrm{s} = 36(fm/C). \qquad \text{.....} \quad (9)$$

Time periods of all the normal modes are integer multiples of τ_0, which will be the minimum response time required to maintain the identity of quasi-stable states in the nuclear system. Furthermore, τ_0 is similar to the nuclear reaction time or evaporation time measured in heavy ion collisions at high energy.
G is nearly equal to the Fermi energy, above which no "fine structure resonance" is observed even for light nuclei, and continuum or chaotic features are predominant.
Furthermore, G seems to be related to the energies of ordinary excited states[13].

3 Resonance Reaction Mechanism

The total excitation energy $E_x = S_n + E_n$ is devided into M normal modes, the average number of which is estimated by the "Recurrence model"[11] to be,

$$M = 1 + \frac{ln(E_x/D)}{ln(2\pi)}, \qquad \text{.....} (10)$$

where D is the average level spacing.
M values are in good agreement with the exciton numbers from the exciton model of a Fermi gas. These normal modes will be fast deformations or particles in orbit with definite frequencies. At every recurrence time, the phase of the compound nucleus recurs almost to its initial value. For a simple case, $F(\tau)$ behaves like a pulse array with a pulse separation τ_{rec}, like an intermittent pulse as shown in Fig.1. At the instance of recurrence, nuclear potential deformation becomes maximum so that the neutron wave penetrates easily through the nuclear surface, and the interference takes place between the pass-by component and the trapped component of the incident wave. This behavior is similar to a time slit which opens periodically at τ_{rec}.
Assuming a constant G and several steps of integral furcation, we can expect integer ratios among dominant spacings of different nuclei down to the eV region, as described in [2-8]. For a large M the average recurrence time is extreemly extended by the LCM factor. It is observed that the recurrence is time-coherent with the de Broglie wave frequency of the incident neutron wave :

$$\tau_{rec} = Q \times \frac{2\pi\hbar}{E_n}, \qquad \text{.....} \quad (11)$$

where E_n is the recoil corrected neutron energy, and Q is a simple integer ratio $Q = m/n(m, n$: small integer). By varying the incident neutron energy E_n for a fixed target nucleus, sets of normal modes will be excited as resonance reactions if τ_{rec} fulfils Eq.(11), under selection rules not

discussed here.

In the observed resonances of ^{16}O +n up to 6 MeV neutron energy[14], we found that 15 resonances out of 37 fulfil Eq.(11) with high accuracy [15]. In the region 1.0$\leq E_n \leq$ 3.6 MeV or 5.0$\leq E_x \leq$7.5 MeV, 11 resonances out of 13 situate on integer ratios, where the probability are calculted to be 0.6×10^{-2} if the resonance levels are disposed randomly. Though the probability 0.6% is not very small, we think that the appearance of the integer ratios in many resonances is not by chance, but by physical reason. This will be an evidence which indicates time periodic behaviors of ^{17}O compound nucleus coherent with the incident neutron wave. Details of probability calculation are described in Apendix. Similar integer ratios are found in the resonances of light nuclei.

For resonances in the keV and eV region, the Eq.(11) will be fulfilled for each resonance with long recurrence time τ_{rec}, which reflects many normal modes possible to be excited simultaneously. According to the recurrence model[11], average recurrence time can be estimated as

$$(2\pi)^{M-1} \times \frac{2\pi\hbar}{E_x}, \quad \ldots\ldots\ldots\ldots\ldots \quad (12),$$

where M is number of normal modes coupled. As an example of possible furcations, the initial energy E_x can be decomposed into sets of two elements $G(1/\mathrm{m} + 1/\mathrm{n})$, three elements $G(1/\mathrm{i} + 1/\mathrm{j} + 1/\mathrm{k})$, four elements, ... These decompositions will continue to a large number of elements $M \leq 10$. Each element corresponds to the normal mode that can be excited in the compound nucleus. But the total number of elements will be limited. For each set $(n_1, n_2, ..., n_M)$, the LCM and recurrence time τ_{rec} are defined. However, to be measured as resonances, multiple recurrences will be needed during the passage of a wave packet of finite coherent length $\sim 10^{-8}m$. Therefore sets of very large LCM will be physically unimportant, or not observed. In contrast, observed resonances will have relatively small LCM, therefore simple integer ratios may exist in energy/spacing among them. This will be the reason of integer ratios among different nuclei described in section 1.

The discussions above are based on the properties of a semi-classical wave. In classical physics and in laser physics, amplitude summation of many waves of different frequencies is a familiar feature. In contrast, this a much less common way to formulate the recurrence of many waves on the compound nucleus in the framework of ordinary quantum mechanics. However, the time behavior of the phase of matter wave is experimentally observed in ultra-cold atoms in Bose-Einstein condensates. In order to understand the precise mechanism of neutron resonances including strengths, selection rules and level clusters in a wide energy region, a more sophisticated approach will be needed including non-linear properties of matter wave.

Appendix.
Probability for the Appearance of Integer Ratios in E_x/S_n in ^{16}O+n Resonances

It is interesting that simple integer ratios are found between E_x and S_n and E_n^* for many of ^{16}O+n resonances, where S_n = 4143.36keV. For examples, E_x/S_n = (11/10)×0.9987 for the 1st resonace at E_x = 4551.9keV, (13/16)×0.9970 for 2nd resonances at 5084.2keV, (10/13)×0.9979for third resonance at 5375.1keV,etc.. , as shown in Table 1. Original parameters of 37 resonances in $E_x \leq$ 10MeV are by Sayer et al.[14].

In Fig.2, resonance energies in E_x/S_n, rational points m/n for n=2,3,4,..,13 are plotted. When E_x/S_n is close to an integer ratio m/n, relative error Δ is defined as,

$$\Delta = (E_x/S_n)/(\mathrm{m/n}) - 1 \quad \ldots\ldots\ldots \quad (A1).$$

For most of the resonances, Δ gather around 0 within a width of 0.0052, as shown in Fig.3.

We have calculated the probability of appearance of integer ratios x=m/n (n$\leq$13) for these resonances assuming random distribution of excitation energies $E_x = S_n + E_n*$ in the region.

To minimize end effect, the region near S_n and $2S_n$ are excluded. The probability calculation is made in 5.0 $\leq E_x \leq$ 7.5MeV, in which 14 resonances are observed. We regard two resonances with very small energy difference (at E_x=7378.2 and 7380.8 keV) as one resonance for the probability calculation. Integer ratios (E_x/S_n=m/n, n$\leq$13) are found in 11 resonances out of 13, with Δ= 0.0052 , as shown in Table 1 and Fig.2 and 3. In the region there are 36 rational ponts with average width 32.5keV. For random sampling in this region, probability p to be on a rational point is estimated as,

$$\mathrm{p} = 36 \times 0.0325/(7.5\text{-}5.0) = 0.468 \quad \ldots\ldots\ldots\ldots\ldots (A2)$$

Average value of appearance is 13×0.468=6.1. Probability of 11 times apppearance in 13 trials is given by the binomial distribution $B(11; 13, p)$ as,

$$B(11; 13, p) = {}_{13}C_{11} p^{11} (1-p)^2 = 0.51 \times 10^{-2} \quad \ldots\ldots\ldots\ldots \quad (A3)$$

and $$\sum_{k=11}^{13} B(k;13,p) = 0.6 \times 10^{-2}. \qquad \text{..... (A4)}$$

Though the sample number is small, random hypothethis on level dispositions can be rejected with a level of 1% test. As an alternative hypothesis, integer ratio in E_x/S_n or E_x/E_n^* must be accepted. That is, time behaviors of the ^{16}O+n compound nucleus are time coherent with the incident neutron wave at resonances.

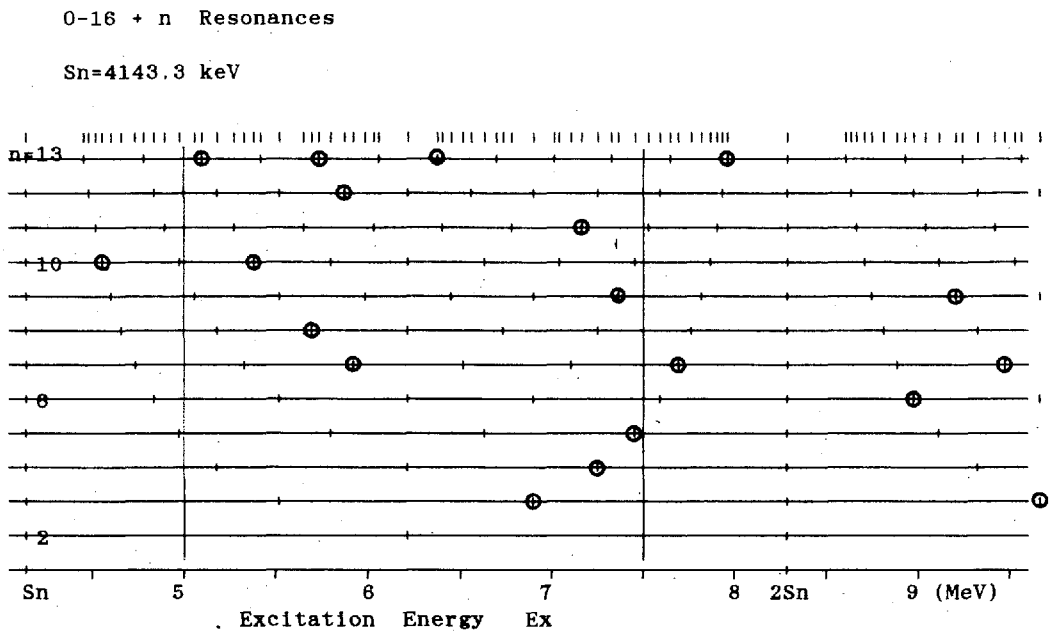

Figure 2: Distribution of excitation energies for ^{16}O+n resonances showing integer ratios E_x/S_n=m/n, classified by denominator n. In the region $5.0 \leq E_x \leq 7.5MeV$, 11 resonances out of 13 are at integer ratios E_x/S_n = m/n ;(n ≤13), as shown in appendix and Table 1. Small deviations from the integer ratios are shown in Fig.3.

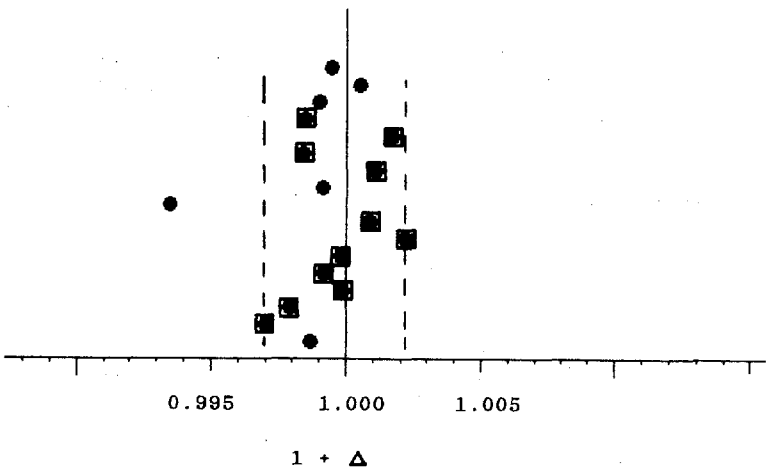

Figure 3: Distribution of 1+Δ (=(E_x/S_n)/(m/n)) around 1.000 for the resonances in Table 1. The squares correspond to the resonances of "A" in the Table. Dash lines show the boundary of errors with a width 0.0052.

Table 1 Integer Ratios E_x/S_n for resonances of ^{16}O+n up to $E_x \leq$8MeV

j	$J\ \pi$	E_x (keV)	E_n (keV)	E_n^* (keV)	E_x/S_n	$1+\Delta$	
1	3/2-	[a]4551.9	434.3	408.5	11/10	0.9987	
2	3/2+	5084.2	1000.2	940.8	16/13	0.9970	A
3	3/2-	5375.1	1309.4	1231.7	13/10	0.9979	A
4	7/2-	5696.7	1651.4	1553.4	11/8	0.9999	A
5	5/2-	5732.3	1689.1	1588.8	18/13	0.9992	A
6	3/2+	5868.7	1834.1	1725.2	17/12	0.9998	A
7	1/2-	5932.0	1901.4	1788.5	10/7	1.0022	A
8	1/2+	6380.2	2377.9	2236.7	20/13	1.0009	A
9	5/2+	[b]6860.7	2888.7	2717.2	5/3	0.9935	
10	7/2-	6971.9	3006.9	2828.4	32/19	0.9991	
11	5/2-	7164.6	3211.8	3021.1	19/11	1.0011	A
12	3/2+	7239.1	3291.0	3095.6	7/4	0.9984	A
13	5/2+	7378.2	3438.8	3234.7	16/9	1.0017	A
14	5/2-	[c]7380.8	3441.5	3237.3			
15	3/2-	7446.9	3511.9	3303.5	9/5	0.9985	A
16	7/2-	[a]7686.9	3767.0	3543.4	13/7	0.9990	
17	1/2-	[a]7896.3	3989.6	3752.8	40/21	1.0005	
18	1/2+	[a]7963.3	4060.8	3819.8	25/13	0.9994	

E_x, E_n are from [14]. S_n=4143.3keV a)excluded to minimize end effect in probability calculation. b)excluded because of large deviation in S_n/E_x from 1.0. c)excluded because of too small difference in E_x to the neighbor. The resonances marked "A" fulfil the criteria: 5.0$\leq E_x \leq$7.5MeV, (E_x/S_n=m/n , n$\leq$13) and Δ in a width of 0.0052.

References

[1] *Landolt-Börnstein New Series Vol 16/B*, "Neutron Resonance Parameters", Springer(1998)

[2] S.Sukhoruchkin: *Proc.Conf.Nucl.Data for Reactors, Paris,1966*,Vol 1, p159, Vienna,1967 ; S.Sukhoruchkin: *Proc. Int. Conf. on Statistical Properties of Nuclei* (Plenum, New York 1972) p.215

[3] K.Ideno, M.Ohkubo: "Nonrandom distributions of neutron resonance levels" *J.Phys.Soc.Jap.* 30,620(1971);

[4] C.Coceva, F.C.Corvi, P.Giacobbe, and M.Stefanon; *Proc. Int. Conf. on Statistical Properties of Nuclei* (Plenum, New York 1972) p.447

[5] K.Ideno: "Nonstatistical behaviours of the level spacing distributions in neutron resonances" *J.Phys.Soc.Jap* 37,581(1974)

[6] F.N.Belyaev,S.P.Borovlev: "Non-statistical effects in the distribution of distances between neutron levels", *Yad.Fiz.*27.289(1978), transl.*Sov.J.Nucl.Phys.*27(2),157(1978)

[7] G.Rohr: "The dynamics of nucleon in a nucleus studied with neutron resonances"; *Low energy nuclear dynamics*,(World Scientic,1995),p130

[8] S.Sukhoruchkin: "Tuning effect in nuclear data.II" E3-2000-192,ISINN-8,Dubna 2000, "COMNRF-Combined Nuclear Reaction File", ISINN-7,E3-98-212,Dubna 1999, Shell stabilization of excitations in odd odd nuclei"ISINN-4, E3-96-336 Dubna 1996,

[9] M.Ohkubo: "Regular level structures in s-wave neutron resonances in light or magic e-e nuclei up to several hundred keV" *INDC(JPN)* -185/U ,JAERI-Conf 2000-005, p325,

[10] M.Ohkubo: "Quantum recurrence in neutron resonances and a unit time in nuclei" *INDC(JPN)* -188/U, JAERI-Conf 2001-006, p300

[11] M.Ohkubo: "Recurrence of the compound nucleus in neutron resonance reactions" *Phys.Rev.C*, 53,1325(1996)

[12] A.G. Sitenko: *Lecture in Scattering Theory*(Pergamon, New York 1971)

[13] M.Ohkubo;" Non-statistical level disposition analysis in neutron resonances"*J.Nucl.Sci.Technol. Supplement 2, Proc. Int.Conf. Nuclear Data for Science and Technology,Oct.2001,Tsukuba,Japan* p508 (2002).

[14] R.O.Sayer,L.C.Leal,L.M.Larson,R.R.Spencer,and R.Q.Wright: "R-Matrix Evaluation of ^{16}O Neutron Cross Sections up to 6.3 MeV" *J.Nucl.Sci.Technol. Supplement 2, Proc. Int.Conf. ND2001* p88, (2002).

[15] M.Ohkubo:"Recurrence of the excited states of nuclei and time coherency of the de Broglie wave in ^{16}O+n resonances" *INDC(JPN)*-191/U, JAERI-Conf 2003-006, p259

JP0450505

JAERI－Conf 2004－005

3.15 Evaluation of Neutron Reaction Cross Sections for Astrophysics

T. Kawano[1], S. Chiba[2], T. Maruyama[2], Y. Utsuno[2], H. Koura[3], and A. Seki[4,2]
[1] *Los Alamos National Laboratory*
Los Alamos, NM 87545, USA
[2] *Japan Atomic Energy Research Institute*
Tokai-mura, Ibaraki 319-1195, Japan
[3] *RIKEN, Waseda University*
Wako, Saitama 351-0198, Japan
[4] *Ibaraki University*
Mito, Ibaraki 310-8512, Japan
e-mail: kawano@lanl.gov

We have developed a code system to evaluate nuclear reaction cross sections for the nucleosynthesis. The system includes an interface to Reference Input Parameter Library (RIPL), as well as some systematics to extrapolate the parameters into unstable regions. We are focusing on neutron capture processes important for s- and r-processes. The structure of the system is reviewed, and calculated capture cross sections in the fission product mass region are compared with experimental data available.

1. Introduction

The Hauser-Feshbach statistical model with width fluctuation correction has been widely used for neutron nuclear data evaluations, and the input parameters have been improved extensively. In many cases this model calculation gives a satisfactory fitting to experimental data, and this is regarded as one of the standard technique to evaluate nuclear data nowadays. This model calculation is also applicable to calculate nuclear cross sections which are needed for nucleosynthesis. One of the different aspect of the HF calculations for astrophysics is that many of the target nuclei are unstable, and a quality of calculation strongly depends on the model parameters. We have developed a code system to evaluate nuclear reaction cross sections for nucleosynthesis. The system includes an interface to Reference Input Parameter Library (RIPL)[1], as well as some systematics to extrapolate the parameters into unstable regions. In this paper the structure of the system is reviewed, and calculated capture cross sections are compared with experimental data available.

2. HFM Code System

2.1 Program CoH

The code system to calculate reaction cross sections consists of the Hauser-Feshbach-Moldauer code CoH and some databases. Since global parameterization is adequate for cross section calculation of unstable nuclides, the code has built-in global optical potentials — Koning-Delaroche Global Potential[2] for n and p, and Lemos' Potential[3] for α-particle. For γ-ray emission, an E_1 transition is taken into account.

2.2 Database for Input Parameters

Nuclear masses and reaction Q-values are calculated with the KUTY mass formula[5] if the data is not found in the Audi-Wapstra mass table[4]. The KUTY mass formula is also used to calculate level density parameters. Groud-state J^{π} values for many unstable nuclei are also unknown quantities. Those values are estimated by the Nilsson-Strutinsky method.

Reference Input Parameter Library (RIPL)[1] was compiled at IAEA, which is a library containing nuclear model parameters mainly for the statistical Hauser-Feshbach model calculation. Nuclear masses, excited levels, optical potential parameters, level densities, GDR parameters, fission barriers are stored in RIPL. The calculation system retrieves the excited level data, level density parameters, γ-ray strength function, and GDR parameters from RIPL-2. This retrieval is automated by some small utility programs. The procedure of cross section calculation is schematically shown in Fig. 1.

We employ a generalized Lorentzian-form for the γ-ray strength function given by

$$f_{\mathrm{E1}}(E_\gamma) = C\sigma_0\Gamma_0 \left\{ \frac{E_\gamma \Gamma(E_\gamma, T)}{(E_\gamma^2 - E_0^2)^2 + E_\gamma^2 \Gamma^2(E_\gamma, T)} + 0.7 \frac{\Gamma(E_\gamma = 0, T)}{E_0^3} \right\}, \tag{1}$$

where the constant C can be obtained by an experimental $2\pi\langle\Gamma_\gamma\rangle/D_0$ value taken from RIPL if available, otherwise $C = 8.68 \times 10^{-8}$ mb^{-1} MeV^{-2}, the GDR parameters σ_0, Γ_0, and E_γ are calculated with the systematics given in RIPL-2.

We adopt the Ignatyuk type level density parameters which includes shell effects,

$$a = a^* \left\{ 1 + \frac{\delta W}{U} \left(1 - e^{-\gamma U} \right) \right\}, \tag{2}$$

where a^* is the asymptotic level density parameter, U is the excitation energy, δW is the shell correction energy, and γ is the damping factor. The asymptotic level density parameters a^* was estimated based on the Gilbert-Cameron type level density parameters in RIPL-2 and the shell correction and pairing energies taken from the KUTY mass formula. The systematics of a^* parameter can be expressed by a smooth function of the mass number A, as shown in Fig. 2. The dashed and dot-dashed lines are similar systematics but they used different shell and pairing energies. We obtained $a^* = 0.140A + 2.65 \times 10^{-5}A^2$, which is shown by the solid line.

3. Calculated Capture Cross Section

Capture cross sections of Gd isotopes were calculated with this system. The model parameters used were "default" to show a quality of evaluation with our input parameters. The calculated capture cross sections σ_γ are compared with experimental data of Wisshak *et al.*[6] in Fig. 3. Evaluated cross sections in ENDF/B-VI and JENDL-3.3 are also shown in this figure. The evaluated cross sections fall down to zero at certain energies because unresolved resonance parameters are given below there. The comparison shown here is, of course, in the case of stable nuclides, and those agreements with the experimental data do not necessarily ensure that the system gives us reasonable cross sections for unstable nuclides. However, if we anchor the cross section calculations to the experimental data available, extrapolation of the parameter systematics to the unstable region becomes more reliable.

Figure 4 shows a comparison of calculated capture cross sections, σ_γ, with those in JENDL-3.3 in the fission-product (FP) mass range — from ^{69}Ga to ^{204}Hg. We have calculated the capture cross section (at 1 MeV) of 195 nuclides without any adjustment, and these cross sections are expressed by ratios to the JENDL-3.3 data. Many of calculated σ_γ 's were from

0.1×(JENDL) to 2×(JENDL), but the CoH calculation tends to underestimate. One of the possible reasons is level densities. When we have a few discrete level data, the calculation becomes more sensitive to the level density parameters, because the level density representation is used for the compound excited states even the excitation energy is low. We need to improve the level density systematics for unstable targets to obtain a reasonable agreement with the evaluated cross sections.

4. Conclusion

Our goal is to generate cross sections of more than 3000 nuclides for astrophysics applications. We have developed an automated cross section calculation system which consists of the optical model and the Hauser-Feshbach-Moldauer theory. The system links to modern theories of nuclear mass and ground state J^{π} value estimation, and links to RIPL level density parameters, discrete level data, and photo reaction data. We have shown some examples; capture cross sections for Gd isotopes, and comparison with JENDL-3.3 FP data. Our HFM calculation still tends to underestimate capture cross section for some cases. We need to improve the level density systematics for unstable targets.

References

[1] "Handbook for Calculations of Nuclear Reaction Data — Reference Input Parameter Library —," IAEA-TECDOC-1034, International Atomic Energy Agency (1998); RIPL-2 Handbook, International Atomic Energy Agency [to be published].

[2] A.J. Koning, J.-P. Delaroche, *Nucl. Phys. A,* **713**, 231 (2003).

[3] O.F. Lemos, Orsay Report, Series A, No.136 (1972).

[4] G. Audi, A. H. Wapstra, *Nucl. Phys. A,* **595**, 409 (1995).

[5] H. Koura, M. Uno, T. Tachibana, M. Yamada, *Nucl. Phys. A,* **674**, 47 (2000).

[6] K. Wisshak, F. Voss, F. Kaeppeler, K. Guber, L. Kazakov, N. Kornilov, G. Reffo, *Pyhs. Rev. C,* **52**, 2762 (1995).

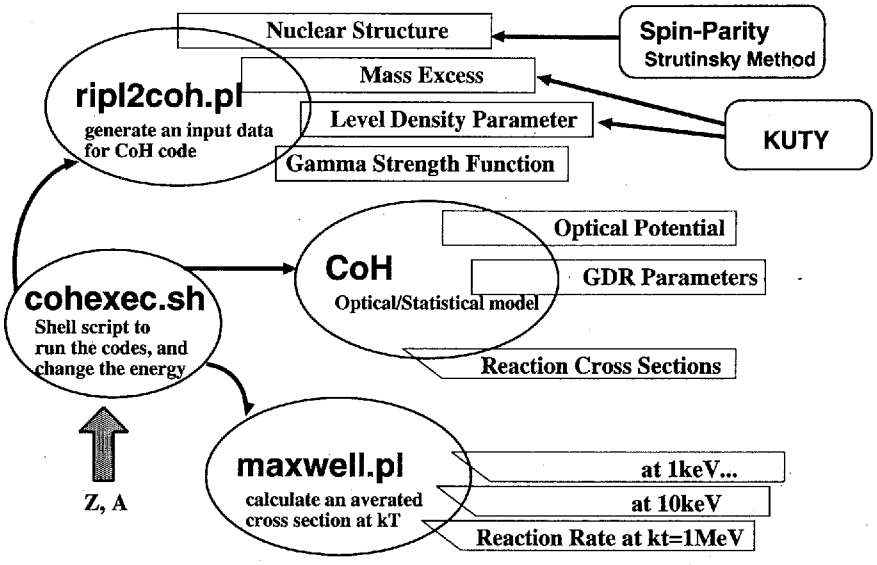

Fig. 1: Nuclear reaction cross section calculation system.

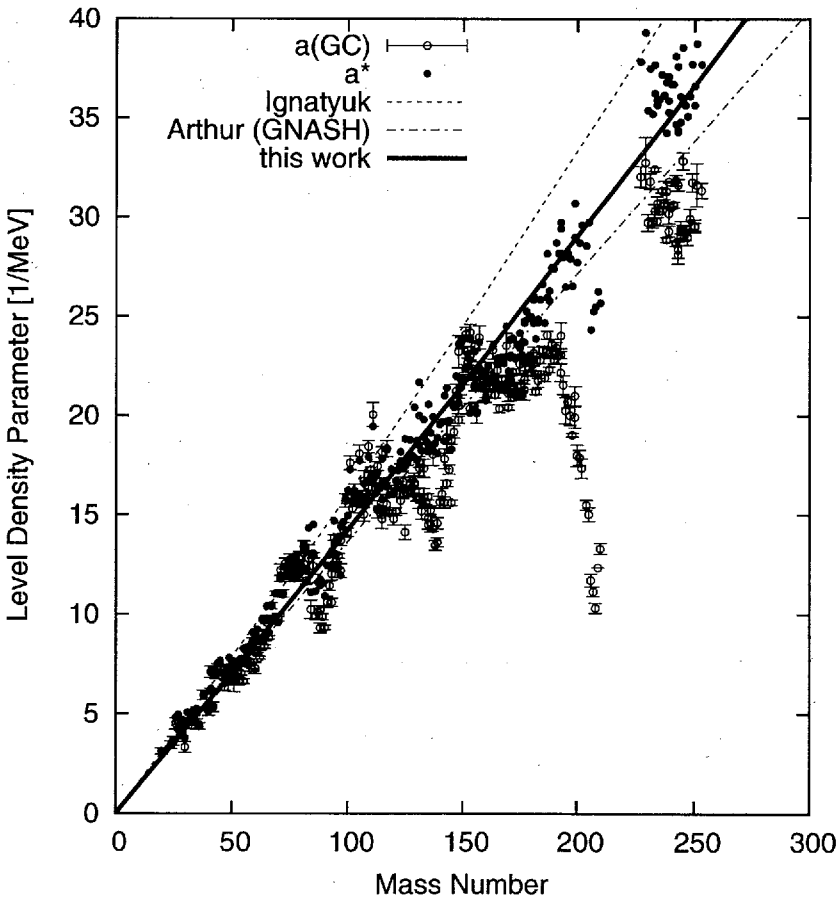

Fig. 2: Level density parameters a and a^* as a function of A.

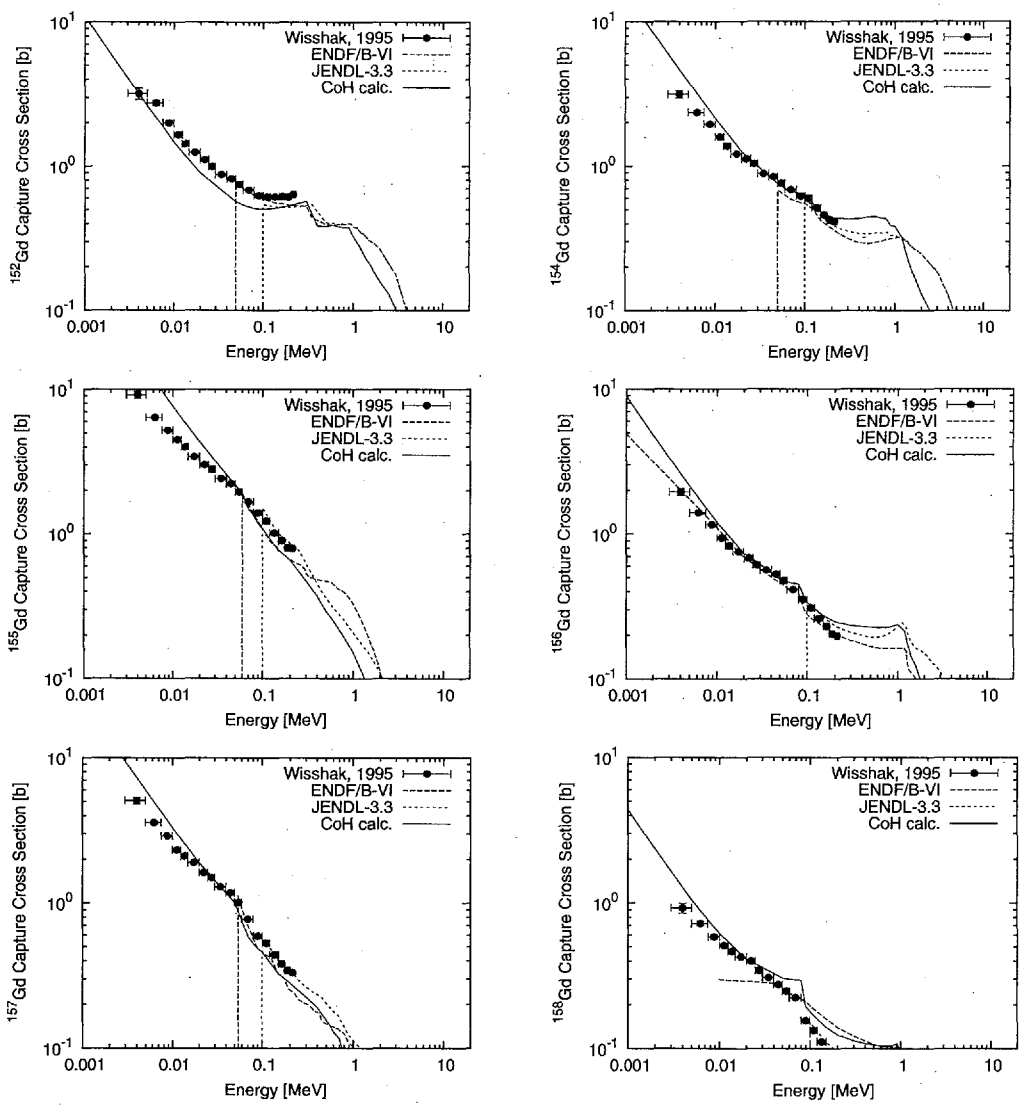

Fig. 3: Comparison of calculated capture cross sections for Gd isotopes with experimental data.

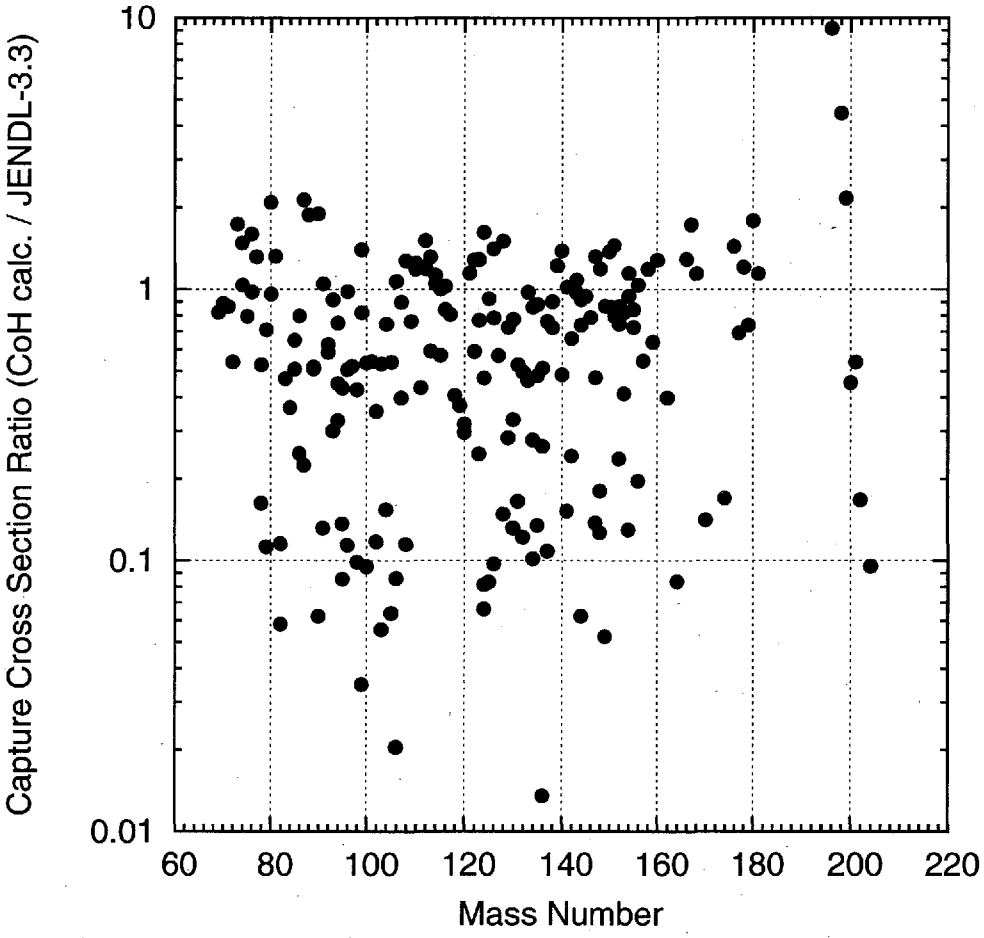

Fig. 4: Calculated capture cross section ratio to JENDL-3.3. The neutron incident energy is 1 MeV, and no adjustments of model parameters were made.

3.16 A design study of the Ge crystal for a pair-spectrometer system by using the EGS-4 code

Hitoshi SAKANE, Kazuyoshi FURUTAKA, Oleg SHCHERBAKOV, Hideo HARADA,
Toshiyuki FUJII* and Hajimu YAMANA*
Japan Nuclear Cycle Development Institute, Tokai works, Tokai-mura,
Naka-gun Ibaraki-ken 319-1194
*Research Reactor Institute, Kyoto University, Kumatori-cho,
Sennann-gun, Osaka 590-0494
e-mail: sakane.hitoshi@jnc.go.jp

A Ge crystal dimension of a pair-spectrometer system was optimized to improve its performance for the prompt gamma ray spectroscopy. To demonstrate the performance of the pair-spectrometer system, it was applied to the measurement of prompt gamma rays which are emitted from ^{15}N produced in thermal neutron capture reaction, in the energy range up to 10.8 MeV.

1 Introduction

For the transmutation study of radioactive wastes, it is important to obtain precise thermal neutron capture cross section of long-lived fission products and minor actinides. However, the capture cross sections for some nuclides have not yet been obtained or are poor in accuracy, because they can not be measured by conventional activation methods. Therefore, we have started the development of a measurement method of the thermal neutron capture cross section by prompt gamma ray spectroscopy.

The cross sections are determined on the basis of energy equivalence between Q-value and an energy sum of cascading gamma rays per a neutron capture reaction. However, prompt gamma ray spectra of isotopes in the medium and heavy mass region, even though measured with a Ge detector, tend to be so complicated that each peak of gamma rays can not be resolved. To deduce the sum of gamma ray energy from raw spectrum of gamma rays, unfolding is needed which enables to extract the full energy deposition from continuum component of spectra. To minimize the error in the unfolding process, the pair-spectrometer system is developed since it was expected that double escape peaks (DEP) were clearly enhanced and then high DSP to total ratio obtained especially for high energy prompt gamma rays.

In this work, a coaxial Ge crystal dimension of the pair-spectrometer system was optimized to improve its performance for the prompt gamma ray spectroscopy. To demonstrate the performance of the pair-spectrometer system, it was applied to the measurement of prompt gamma rays emitted from ^{15}N

produced in thermal neutron capture reaction using a Ge detector with a similar shape as the optimized one.

2 Optimization of crystal shape using EGS-4 code

A pair-spectrometer consists of a Ge detector and multisected BGO annulus surrounded by the Ge detector. When an energy of incident gamma ray exceeds pair creation threshold, an electron-positron pair within the central Ge detector can be created. The two 511-keV gamma rays from annihilation of the positron are emitted in opposite directions. When these gamma rays are detected simultaneously in each of opposite BGO detectors, the event in a Ge detector is recorded. By using this method, peak(DEP)-to-total ratio is improved dramatically which strongly affects the accuracy of spectrum unfolding method. Peak-to-total ratios were calculated by using the EGS-4 code [1] in the case of a pair-spectrometer using a bisected BGO annulus, 17 cm in length, 11 cm in inner diameter and 21cm in outer diameters. A schematic view of the pair-spectrometer is shown in Fig. 1.

The dimension of the Ge crystal affects on the peak-to-total ratio strongly. In case of pair-spectrometer mode, peak-to-total ratio is defined as ratio of DEP counts to total counts. The calculated peak-to-total ratios are shown in Fig.2 as a function of the length of Ge crystal for three operation mode: pair-spectrometer mode, Compton suppression mode and singles mode. A diameter of Ge crystal was fixed at 5 cm and an energy of incident gamma ray was fixed at 10 MeV. As its length increases, the ratio increases. The ratio in the pair-spectrometer mode is about 10 times higher than that in singles mode, about 5 times higher than that in Compton suppression mode. The correlation of peak-to-total ratio relative to diameter of Ge crystal is shown in Fig. 3. In this calculation, a length of Ge crystal was fixed at 12 cm and an energy of incident gamma ray was fixed at 10 MeV. The ratio reaches its maximum at a diameter of 5 cm. The dependence of an energy of incident gamma ray on peak-to-total ratios are shown in Fig. 4. When irradiated with 10 MeV gamma rays, in the case of 5-cm diameter and 12-cm length, peak-to-total ratio of about 80 % is achieved in the pair-spectrometer mode. The ratios in the singles mode and in the Compton suppression mode are 7% and 14% for the same crystal size.

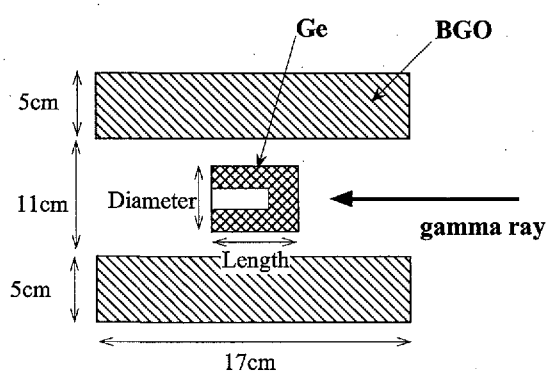

Fig. 1 The schematic view of pair spectrometer.

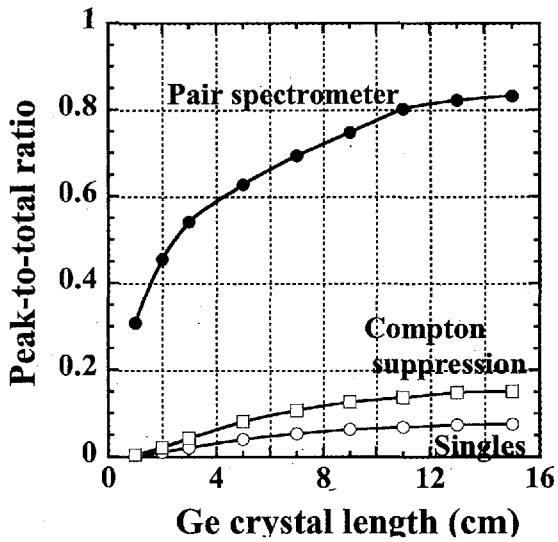

Fig. 2 The correlation peak-to-total ratio relative to Ge crystal length.

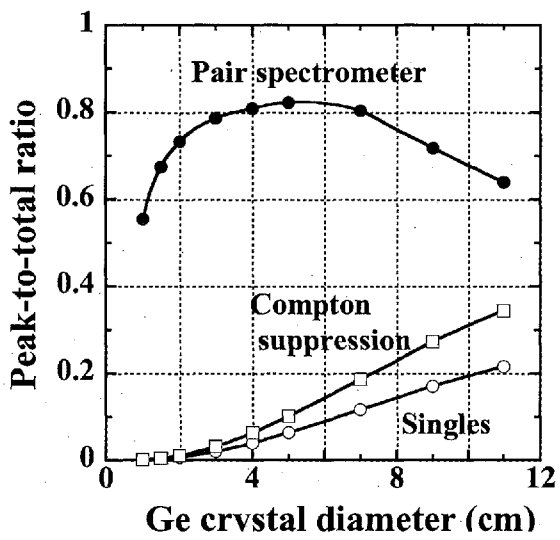

Fig. 3 The correlation of peak-to-total ratio relative to Ge crystal diameter.

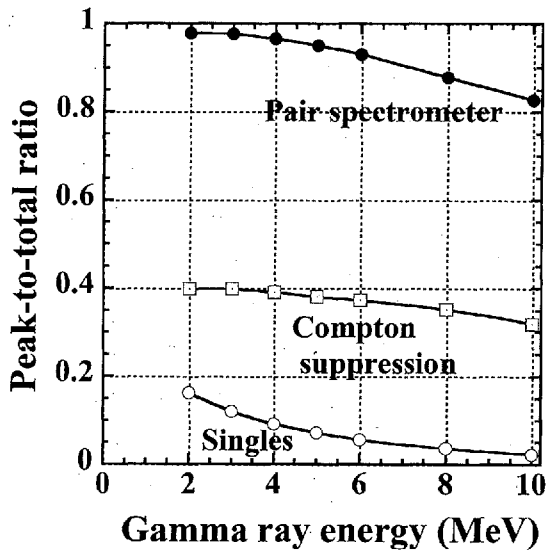

Fig. 4 The correlation of peak-to-total ratio relative to energy of gamma ray

3 Experiment

To demonstrate the performance of the optimized pair-spectrometer system, it was applied to the measurement of prompt gamma rays emitted from ^{15}N produced in thermal neutron capture reaction using a Ge detector with a approximately dimension as the optimized one. The irradiation by thermal neutron was carried out using the B4 neutron guide tube facility in the Kyoto University Research Reactor Institute. The neutron flux at the irradiation position was about 2×10^{7} n · cm^{-2} · s^{-1}. The irradiated sample was D-substituted melamine ($C_3D_6N_6$) [2] to reduce the strong background gamma-ray from the $^{1}H(n,\gamma)$ reaction. The setup of the experiment was shown in Fig. 5. The pair-spectrometer system consists of an n-type Ge detector and the BGO detector described in chapter 2. Relative detection efficiency of the Ge detector is 90% of that of 3 inch×3 inch NaI. The neutron flux at the sample position was measured by detecting a decay gamma ray emitted form ^{28}Al produced in the $^{27}Al(n,\gamma)$ reaction. To subtract the contribution of background gamma rays originated from scattering neutrons, gamma rays generated by irradiate Carbon foils were measured.

The prompt gamma ray spectra were obtained in singles mode, Compton suppression mode and pair-spectrometer mode, simultaneously. These spectra were shown in Fig. 6. Closed circles show the position of full-energy peaks. The peak-to-total ratio for 10.8 MeV gamma ray was about 4% in pair-spectrometer mode, 0.1% in singles mode and 0.2% in Compton suppression mode. The pair-spectrometer system was demonstrated to have the high ability to measure high-energy gamma rays with high peak-to-total ratio.

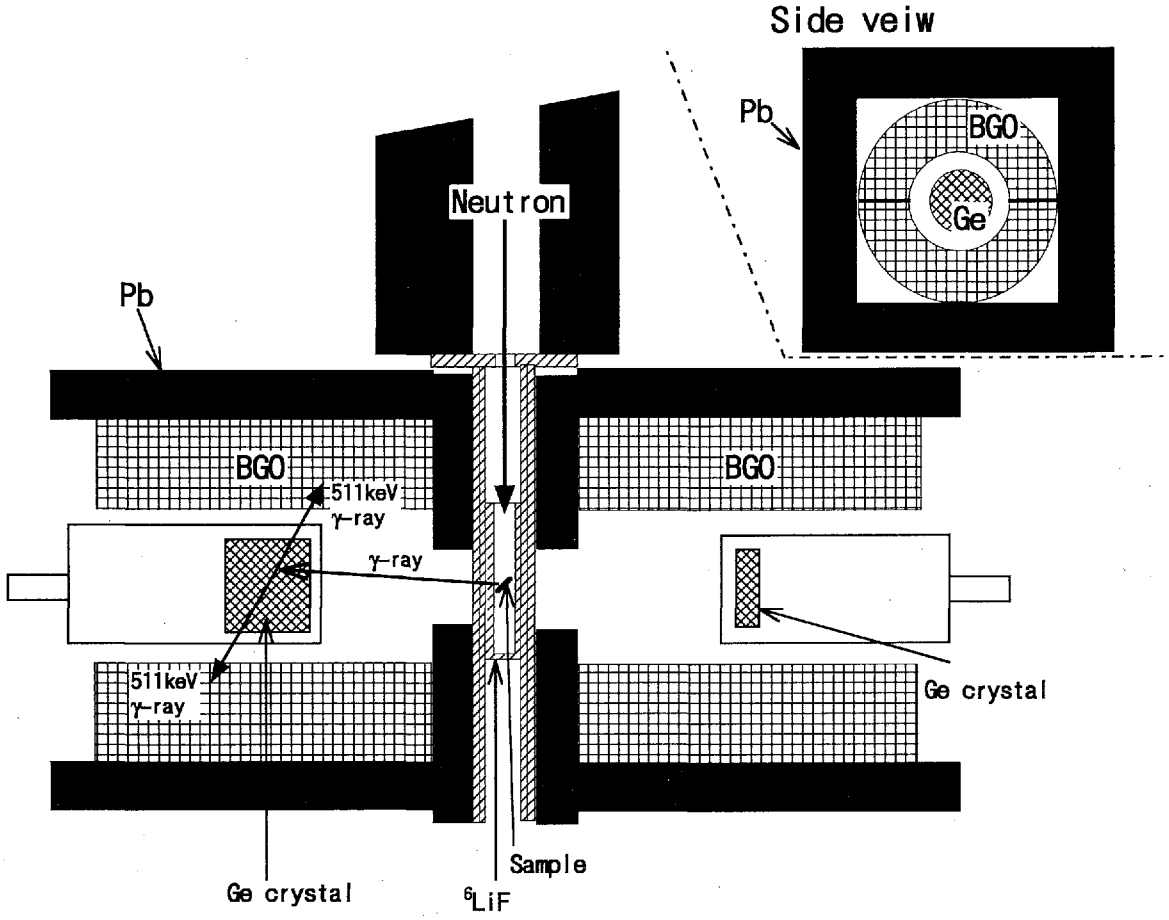

Fig. 5 The setup of the experiment.

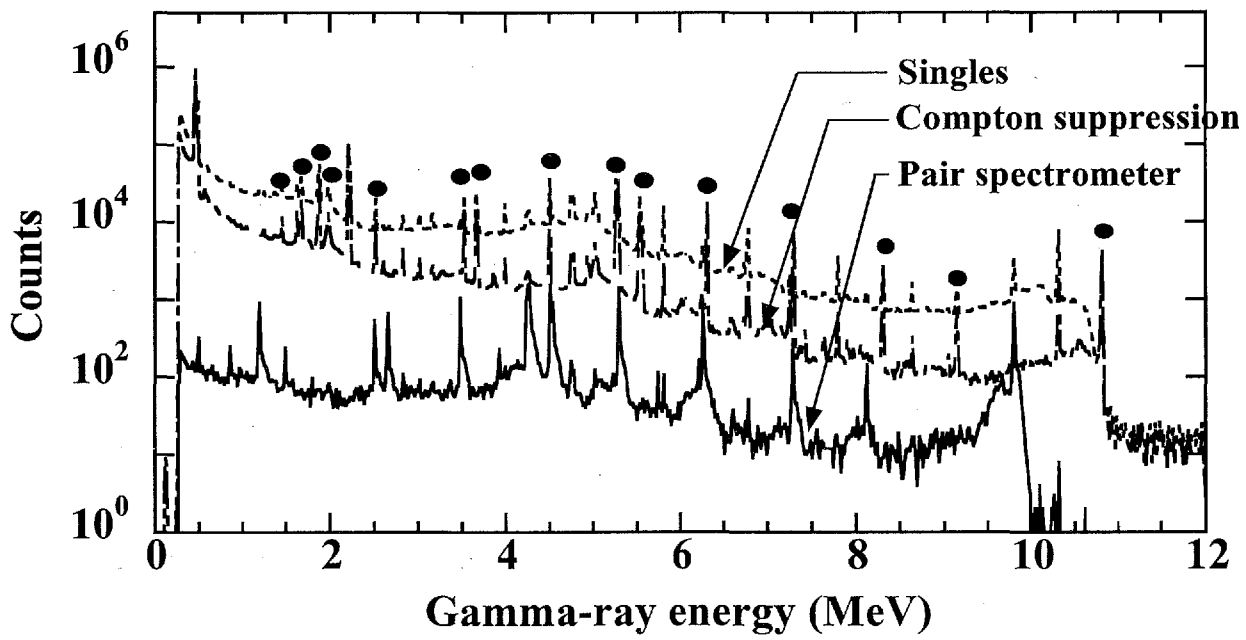

Fig. 6 The spectrum of prompt gamma ray emitted from ^{15}N. Closed circles show the position of full energy peaks.

4 Response of the pair-spectrometer

The response of the pair-spectrometer was studied by comparing the calculated spectra with experimental one. The comparison between calculation and experiment in pair-spectrometer mode is shown in Fig. 7. Solid and dashed lines in the figure represent the calculated spectra and experimental one, respectively. The calculated spectrum agrees with the experimental one above 7 MeV, however, the calculation is lower than the experimental one below 7 MeV. Further study of the response function is required.

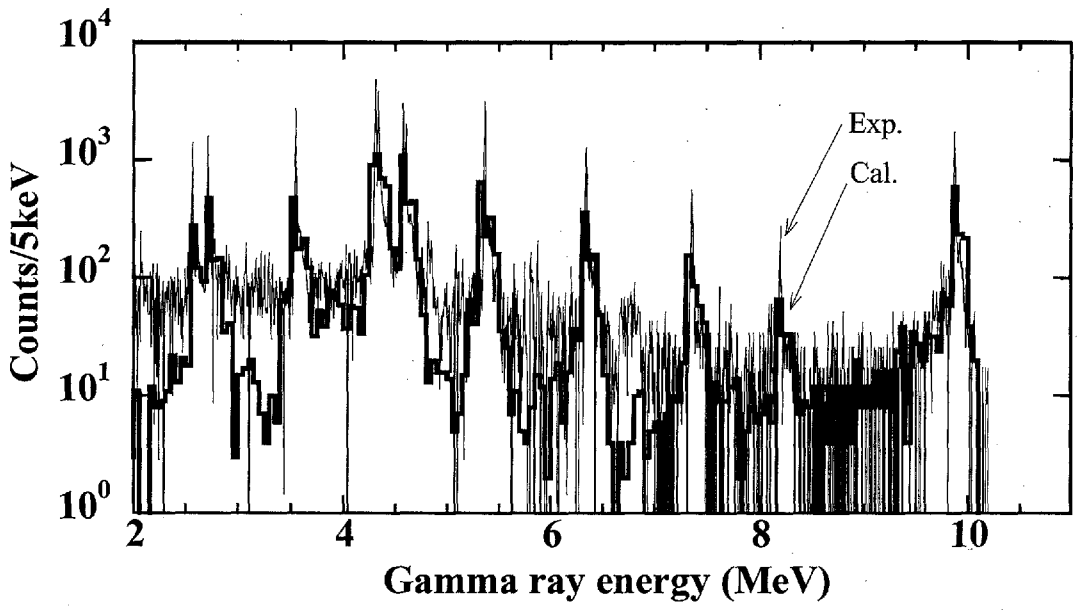

Fig. 7 Comparison between calculation spectrum and experiment ones.

5 Conclusion

In the course of the development of a method of thermal-neutron capture cross section measurement by unfolding prompt gamma ray spectra, a coaxial Ge crystal dimension of the pair-spectrometer system was optimized to improve the pair-spectrometer's performance for the prompt gamma ray spectroscopy. The pair-spectrometer system was demonstrated to have the high ability to measure high-energy gamma rays with high peak-to-total ratio.

References

[1] W.R. Nelson, H. Hirayama and W.O. Rogers: The EGS4 Code System SLAC-265 (December 1985) .

[2] S. Nakamura, H. Harada, H. Takayama, K. Kawade: The development of melamine-D for the precise measurement of detection efficiencies of high energy γ-rays, JAERI-Conf 2003-006 (2003) pp.237.

3.17 Q_β Measurement Using a Well-type HPGe Detector

H. Hayashi[1], O. Suematsu[2], M. Shibata[3], Y. Kojima[4], A. Taniguchi[5] and K. Kawade[2]
[1]Department of Nuclear Engineering, Nagoya University
[2]Department of Energy Engineering and Science, Nagoya University
[3]Radioisotope Research Center, Nagoya University
[4]Quantum Energy Applications, Hiroshima University
[5]Research Reactor Institute, Kyoto University
e-mail: h032414m@mbox.nagoya-u.ac.jp

We demonstrated that Q_β-values were measured by using a well-type HPGe detector with a BGO detector based on the total absorption method. Four β-sources (^{142}Pr, ^{90}Y, ^{42}K, ^{38}Cl) were measured. In the analysis, following four process were discussed; random pile-up, electron response functions, γ-ray response functions and a folding method. We consider that our detector may decide the Q_β-values within accuracy of 10 keV, even if there is no information about decay schemes.

1. Introduction

Mass data of nuclei far from β stability are one of the most important nuclear data. One of the ways to determine atomic masses is to measure β endpoint energies (Q_β). The β-γ coincidence method was mainly used. The method needs precise information about decay scheme and intense sources. The total absorption method isn't under these restrictions (Fig.1). The BGO total absorption detector, which had a high efficiency, was used by Shibata *et al.* [1] and determine the Q_β within an accuracy about 200 keV. In this work, we aimed at demonstrating a HPGe total absorption detector, has a good resolution in addition to a high efficiency, and achieving precise Q_β measurement about 10 keV.

2. Experiments

Our detector consisted of a well-type HPGe detector (85 mm$^{\phi}$×89 mm^{l}) and a BGO scintillator (25 mm^{t}×150 mm^{l}) for Compton suppression. Four nuclides (^{142}Pr, ^{90}Y, ^{42}K, ^{38}Cl), which had a simple decay scheme, were prepared by a thermal neutron irradiation at the Kyoto University Reactor. By controlling total counting rate, less than 1k CPS, random pile up was inhibited as low as possible. Singles spectra of the HPGe, the BGO detector and their coincidence data were taken.

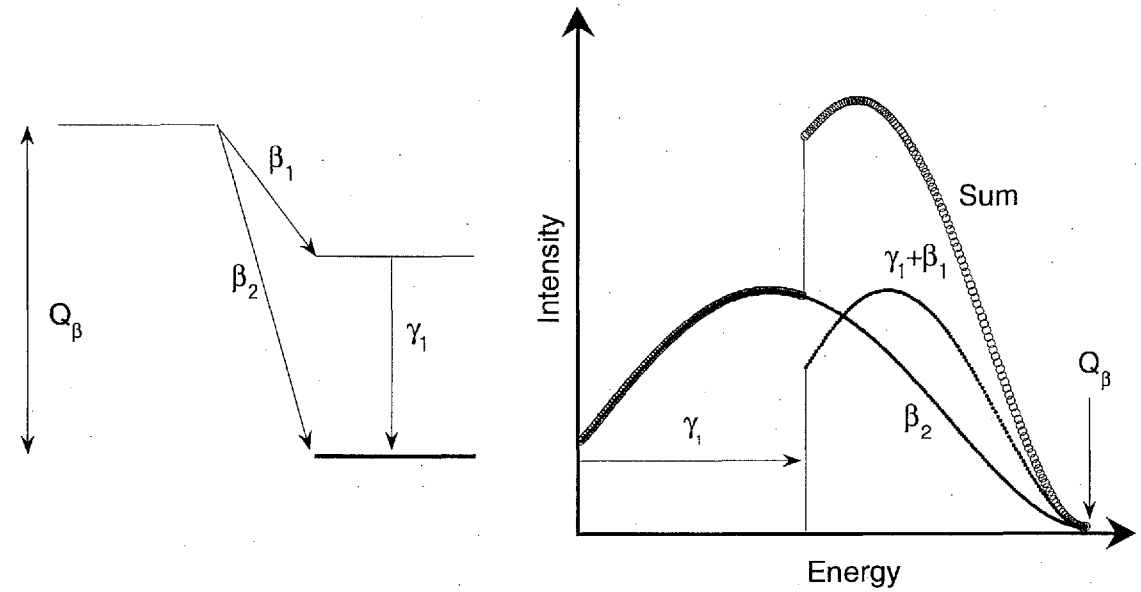

Fig.1 Concept of total absorption method. All β-rays and following γ-rays are completely absorbed by one detector. End-point energies of each β-component gives the same Q_β. Q_β is determined without knowledge of the decay scheme, and good statistics around Q_β is obtained.

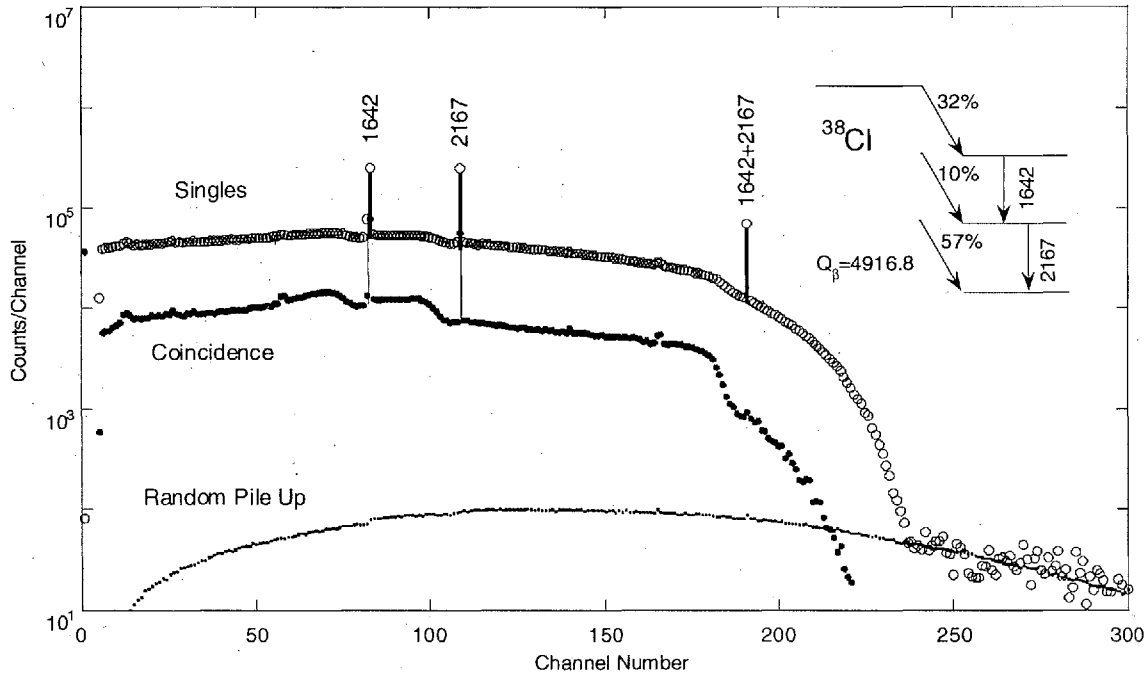

Fig.2 Spectrum of ^{38}Cl. A random pile up spectrum was generated by Monte Carlo simulation.

3. Analysis methodology

In the ideal case, full energy of β-rays and γ-rays were completely absorbed. For a real detector, there are some distortions caused by energy losses, energy struggling, scatterings, escapes etc. Response functions enabled us to analyze experimental spectra.

Experimental data, subtracted background, were analyzed following four steps.

(1)Subtraction of random pile-up

Random pile-up spectra were generated by the Monte Carlo calculations. Random pile-up spectra were made by using spectra, which didn't contain the pile-up, and amplified to fit intensity. Then they were subtracted from experimental spectra (Fig.2).

(2)Calculation of electron response function

Response functions for electrons were calculated by the Monte Carlo simulation code (EGS4), at the energy region 1-8MeV. These response functions were divided into three elements; peak, escape and scattering (Fig.3). However, they did not exactly fit single β-component spectrum such as ^{90}Y, we modified a ratio of these elements to agree with experimental spectrum.

The β-rays were detected after passing an Al window (0.4 mm^{t}) and a dead layer of Ge detector. Energy losses from these effects were described later.

(3)Subtraction of distortions caused by γ-ray response functions

Because of not considering the information about the decay schemes, we could not use the information such as I_γ, I_β, E_γ etc. Following approach shows that we didn't need γ-ray response functions. In γ-ray response functions, Compton scattering parts contributed to distort sum spectra. Some events including the scattering were distinguished; they were just coincidence spectra. Sum spectra subtracted coincidence spectrum didn't include the distortions.

The BGO detector covered only side of the HPGe detector. If we amplified the coincidence spectrum by 1.4, incomplete BGO detector can be regard as ideal BGO detector covering Ge with solid angle of 4π (Fig.4). The value of 1.4 was lead by simulation involved various γ-ray cascades.

(4)Folding-Method

The folding method was used. If folding spectrum agrees with experimental spectrum, a slope of a "ratio of experiment to the folding" equaled zero (Fig.5).

We also simulated that even if there were no information about β-transitions, the folding spectrum gave a nearly true Q_β within 10keV.

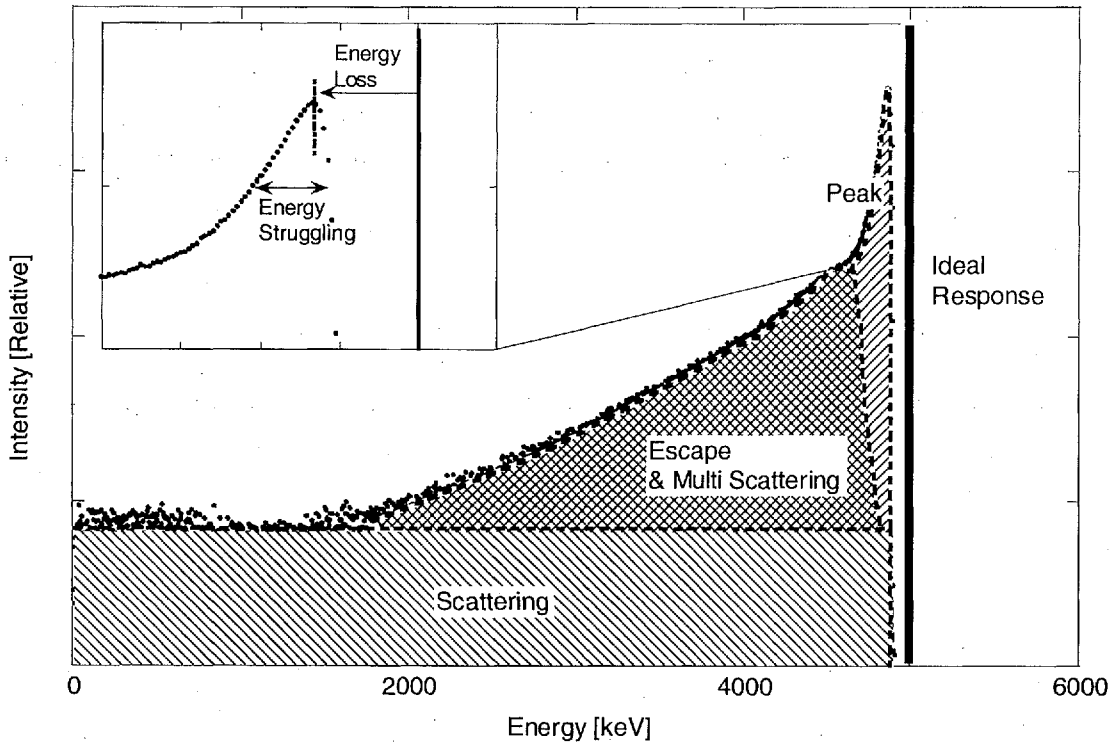

Fig.3 Response function for 5MeV electron. The response function is divided by three parts.

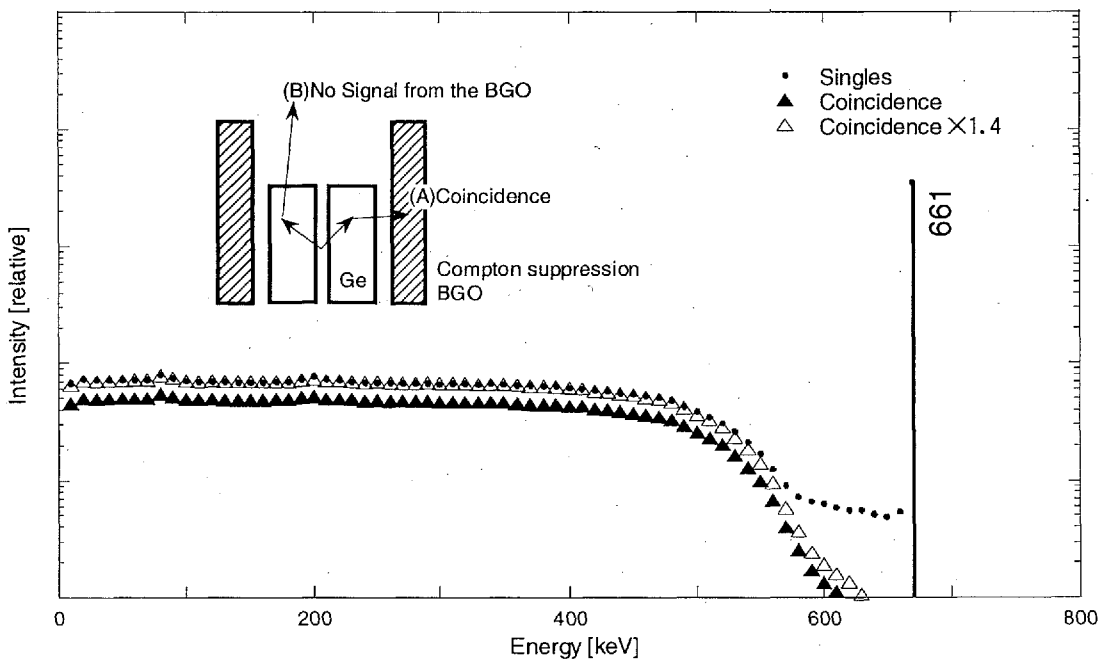

Fig.4 Gamma-ray response function. Because top and bottom of the HPGe are not covered by the BGO, there are some photons that escape through the region (B). Lost photons are compensated by 1.4 timed coincidence spectrum.

4. Results

A comparison of experimental values with evaluated vales was shown in fig.6. Line for the β-ray measurement was uniformly shifted from the gamma one within fluctuation of 5 keV for the region 2-5 MeV. A difference between two lines indicated energy losses for electrons. 5 keV uncertainty was satisfied the demand (10keV). An energy loss of 164 keV is consistent with the thickness of Al window (0.4mm^t) and the dead layer (15μm^t).

5. Conclusion and Future Plans

We can demonstrate the Q_β measurement using a well-type HPGe detector based on the total absorption method. We consider that our detector may decide the Q_β-values within accuracy of 5 keV for the nuclides, which have precise information about decay schemes. Even if there is no information about decay schemes, from simulation, our detector may decide Q_β-values within accuracy of 10 keV.

For the precise estimation of energy losses and check of the analysis way against nuclides, which have more complex decay schemes, we must measure many nuclides. Then we will determine the Q_β of neutron-rich isotopes far from β stability, using the isotope separator on-line.

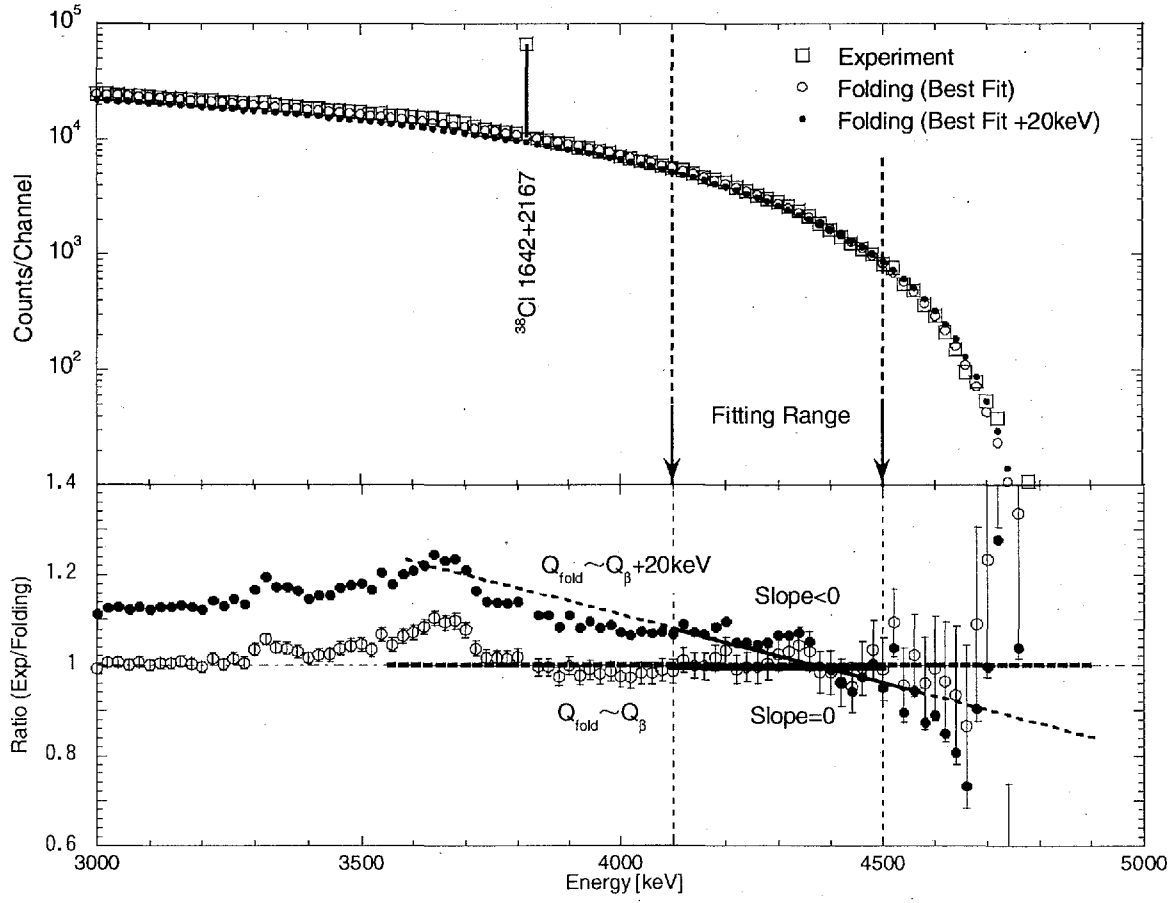

Fig.5 Experimental and folding spectrum for ^{38}Cl. If a Q_{fold}, which is obtained by folding method, nearly equals Q_β, a slope of the ratio becomes zero.

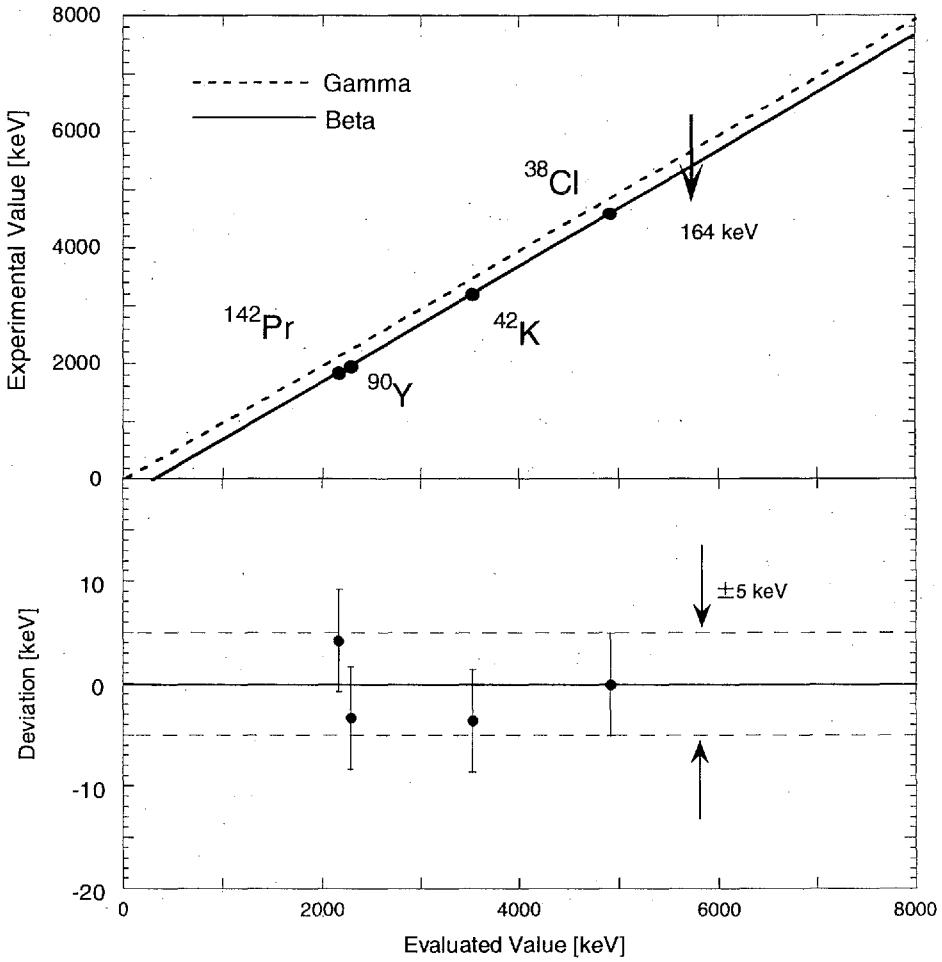

Fig.6 A comparison of experimental values with evaluated values. The broken line and the solid line are obtained from γ-rays and β-rays, respectively. Difference between these lines is caused by energy losses for electrons.

Reference

[1] M. Shibata, Y. Kojima, H. Uno, K. Kawade, A. Taniguchi, Y. Kawase, S. Ichikawa, F. Maekawa, Y. Ikeda, "Application of a total absorption detector to Q_β determination without the knowledge of the decay scheme," Nucl. Instr. and Meth. **A 459** (2001) 581-585

3.18 REACTOR PHYSICS TESTS FOR THE JOYO MK-III START-UP CORE

Takashi SEKINE, Shigetaka MAEDA, Kenji YOKOYAMA, Gou CHIBA and Takafumi AOYAMA
Experimental Reactor Division, Irradiation Center, O-arai Engineering Center
Japan Nuclear Cycle Development Institute
4002 Narita, O-arai, Ibaraki 311-1393 JAPAN
e-mail: sekine@oec.jnc.go.jp

The performance test of the JOYO MK-III core was conducted to fully characterize the upgraded core. The measured data of reactor physics tests were accumulated and compared with the calculation results. These data will be used as the benchmark data for validating nuclear data library and testing reactor calculations.

1. INTRODUCTION

JOYO had been operated from 1983 to 2000 as the MK-II fast neutron irradiation facility. In order to meet various requirements for irradiation tests, JOYO was recently upgraded to the MK-III design. The four main components of the MK-III upgrade[1] are 1) increase in fast neutron flux and enlargement of irradiation space, 2) improved irradiation test subassemblies, 3) modified heat transfer system for the 40% power increase, and 4) improved plant availability. MK-III performance tests began in July 2003 to fully characterize the upgraded core and heat transfer system. Results of the tests, which focus on the neutronics characteristics, are presented here.

2. CHANGES IN THE SUBASSEMBLY LOADING FOR THE MK-III UPGRADE

Figure 1 and **Table 1** show the core configurations and main parameters of the MK-II and MK-III cores. The fuel region is divided into two radial enrichment zones in the MK-III core to flatten the neutron flux distribution. The maximum number of driver fuel subassemblies was increased from 67 to 85. The equivalent diameter of the initial MK-III core is approximately 80 cm. This increases the fraction of the core volume where test irradiations can be done in a high neutron flux. The core height was decreased from 55 cm to 50 cm to obtain a higher neutron flux with smaller power peaking. With these core modifications, the maximum fast neutron flux ($E \geq 0.1$ MeV) increased from 3.2×10^{15} n/cm^2·s to 4.0×10^{15} n/cm^2·s and the reactor power increased from 100 MWt to 140 MWt.

Two of six control rods were shifted from the third row to the fifth row to provide high-fast-neutron-flux loading positions for instrumented-type irradiation subassemblies. The outer two rows of radial stainless steel reflectors were replaced by the shielding subassemblies, which contain 45 % enriched boron carbide. This reduces the total neutron flux at the in-vessel spent fuel storage rack to about 30 % of the MK-II core value.

3. APPROACH TO CRITICALITY AND EXCESS REACTIVITY

3.1 Measurements

Because of the many reactor loading changes, the approach to criticality was carried out cautiously. Biases based on calculations of the last MK-II operational cycle were used along with the calculated predictions of excess reactivity and control rod worths to predict the critical rod bank position of the initial MK-III core. At each rod withdrawal step, counts of source-range monitors were measured and compared to check for reasonable agreement. Inverse count rate was plotted versus the calculated reactivity insertion, as shown in **Fig. 2**.

The isothermal core temperature during the excess reactivity measurement was about 250 °C. Based on the measured critical rod bank position and the measured rod worths as described below, the zero power excess reactivity was estimated to be 2.99 ± 0.09 %Δk/kk'. The measured excess reactivity was within a safety requirement limit.

3.2 Calculation

Excess reactivity was predicted by five methods in preparation for the initial MK-III approach to criticality.

- The "MAGI" method was the standard method used for MK-II analyses.[2] The base MAGI calculation uses finite-difference diffusion theory with one mesh per subassembly and 5 cm mesh intervals axially. It

uses 7-group homogeneous neutron cross sections based on JENDL-3.2. A difference between the measured and calculated excess reactivity for the last MK-II operational cycle is +0.69 %Δk/kk' which is applied to the base-calculation prediction for the MK-III core as the bias correction factor.

• The "HESTIA" method was adopted as the standard method for MK-III core management analyses. Consequently, it was used for the approach to criticality. It features finer detail in space (24 triangles/subassembly and 2.5 cm axial mesh in the fuel) and energy (18 groups for neutron and 7 groups for gamma-ray) to improve calculation accuracy. The bias correction factor for the excess reactivity is +1.89 %Δk/kk'. In other respects, the approach is the same as MAGI.

• The "JUPITER" method applies mesh, transport, heterogeneity and three other corrections to a 6 triangle per subassembly diffusion theory calculation. The bias correction factor is +0.67 %Δk/kk'.

• The MCNP code was used to model the reactor components pin by pin, with continuous energy JENDL-3.2 cross sections. The bias correction factor is +0.25 %Δk/kk'.

• The "JUPITER Adjusted" method is the same as the "JUPITER" method except the ADJ2000R adjusted cross section set [3] is used instead of the bias correction for the base calculation.

A comparison of the excess reactivity results, measured and predicted by each of the calculation methods, is shown in **Fig. 3**. The range of calculated values brackets the measured value. The approach described in Ref. [4] was used to derive the uncertainties in the calculated values using the covariance and sensitivity coefficient. All of the calculated values are within two standard deviations from the measured value.

4. CONTROL ROD CALIBRATIONS

All the six control rods have the same poison-type design. The poison section contains B_4C enriched to 90 % in ^{10}B. The poison section is 650 mm long, which is also the axial distance the rod can move. As noted above, two of the rods, No. 2 and 5, are in the fifth row in the MK-III design. Each of these rods is worth about 40 % as much as any of the four rods in the third row.

4.1 Period Method

4.1.1 Measurement

Reference calibrations use a period-like method with uniform rod bank positions. The measured rod is moved from 0 mm to 650 mm in steps about 9 ¢ each. An example of a differential rod worth profile from the reference calibrations is shown in **Fig. 4**. It can be seen that the random error at each calibration step can be significant. However, the effect on the full-travel rod worth is very small.

4.1.2 Calculation

The base calculation uses transport theory, 7 group cross sections and an XYZ geometry representation of the core in the TRITAC code [5] considering the actual rod bank positions at the measurement. The bias factors are based on the period measurements in the last MK-II operational cycle.

Experimental and calculated control rod worths of the reference calibrations are compared in **Table 2**. The rod worth uncertainty has an estimated random component of 0.3 % and an estimated systematic component of 1.0 %, which add in quadrature to 1.0 %. Converting reactivity unit from cent to Δk/kk', adds the 3 % uncertainty in k_{eff}, for a total uncertainty of 3.2 %. The biased calculated worths are smaller than the measured ones by 3 % to 4 % for rods in the third row but are 1 % for rods in the fifth row.

4.2 Juggling Method

Juggling calibrations are more dynamic measurements, in which exactly critical condition is not required once the calibration begins. This is the routine calibration approach at JOYO for calibrating control rods in the third row. At the beginning, two rods are at 295 mm (poison inserted to 30 mm below the fuel center) and other two rods are at 650 mm (fully withdrawn). These four rods are calibrated over the 295 mm to 650 mm range by alternately moving one rod up and another rod down in steps. The reactivity and power traces during several steps of such a calibration are shown in **Fig. 5**.

The reference and juggling calibration measurement results are compared in **Table 3**. In order to make this comparison, the effect of the different rod shadowing in the two approaches was removed by calculation verified with measurement data described in 4.3. Both measurement results agree within 0.9 %. As the juggling method is performed in a short time, it is practical as a routine control rod calibration procedure and can be used as the alternative for the period method.

4.3 Shadowing Measurement

Shadowing measurements were performed to test the ability of calculations to account for shadowing effects. Accordingly, one of the shadowing experiments consisted of calibrating Rod No. 1 two times, once

with Rod No. 4 half inserted (325 mm) and once with Rod No. 4 fully withdrawn (650 mm) as illustrated in **Fig. 6.** The results from all four shadowing experiments are shown in **Table 4**. For example, in the first case of the table, Rod No. 1 was calibrated first with Rod No. 4 half down and then with Rod No. 4 up. According to the measurement, the worth of Rod No. 1 increases by 6 % when Rod No. 4 is down, while the calculation estimates 4 % increase. Thus, it is confirmed that calculated adjustments that account for shadowing are accurate.

5. ISOTHERMAL TEMPERATURE COEFFICIENT

5.1 Measurement

To begin the isothermal temperature coefficient measurement, a uniform temperature of approximately 250 °C was established throughout the primary system (isothermal), and the excess reactivity was determined. Next the reactor power was increased in 20 °C steps, measuring excess reactivity at each step, until the primary system reached approximately 350 °C. The next day, the reactor temperature was brought back to 250 °C by cooling the coolant sodium by the natural air circulation in the dump heat exchangers with the temperature decreasing in 20 °C steps. The ascending and descending measurements were repeated, providing four measurements of the temperature coefficient.

The measurements results are shown in **Table 5**. There is a clear difference between coefficients measured with the temperature increasing and decreasing. This difference is considered to be related with a time lag of control rod drive shaft expansion during the measurements.

5.2 Calculation

The calculated isothermal temperature coefficient has two main components, Doppler broadening of neutron cross section resonances, and thermal expansion of the fuel and core. The values of these components are -0.00053 and -0.00315 %Δk/kk'/°C, respectively. A ultra fine group correction [6] was used in the computation of Doppler broadened cross sections. The items contributing to the thermal expansion include the coolant density reduction, the core radial expansion and the fuel axial expansion. The ratios of the calculated coefficient to the experimental ones are shown in **Table 5**. The average C/E is 0.994 for the ascending temperature measurements, 0.954 for the descending temperature measurements.

6. POWER COEFFICIENT

During the MK-III performance test, the reactor power was repeatedly increased and decreased, and the burn-up and power dependence of the power coefficient was measured with the same reactor inlet temperature condition. The measurement results are shown in **Fig. 7**. The measured power coefficients were negative in all the power range. The absolute value of the power coefficients were decreased, when reactor power reached 120 MWt for the first time. This is considered to be caused by the restructuring of the fuel pellet. Further investigation will be performed to understand the change of the power coefficient.

After that, power coefficient was measured 7 times. The measured results of November 4th and 8th are shown in Fig. 7. These values became about a half of the ones measured at the low burn-up of the MK-III performance core mostly considering fresh fuels, and were same in the MK-II equilibrium core.

7. CONCLUSIONS

The core performance of the upgraded JOYO MK-III was successfully evaluated by a series of reactor physics tests. The MK-III design predictions are consistent with the performance test results obtained to date. Most of the C/Es are within 5% of unity. The measurements provided benchmark data for nuclear data library and testing reactor calculations. The JOYO MK-III will be ready to serve as a powerful irradiation test facility for the fast reactor development needs of JAPAN and the world.

REFERENCES

[1] T. Sekine, et al., "Upgrade of Irradiation Test Capability of the Experimental Fast Reactor JOYO," Proc. of 11th International Symposium on Reactor Dosimetry, Brussels, Belgium, August 18-23, 2002, p.447-454 (2002).
[2] Y. Ohkawachi, et al., "JOYO MK-II Core Characteristics Database -Update to JENDL-3.2-," Proc. of the 2002 Sympo. on Nuclear Data, Tokai, Japan, November 21-22, 2002, JAERI-Conf 2003-006, p.294-299 (2003).
[3] M. Ishikawa, et al., "Development of a Unified Cross-Section Set ADJ2000 Based on Adjustment Technique for Fast Reactor Analysis," Journal of Nuclear Science and Technology, Supplement 2, p.1073-1076 (2002).
[4] T. Takeda, et al., "Prediction Uncertainty Evaluation Methods of Core Performance Parameters in Large Liquid-Metal Fast Breeder Reactors," Nuclear Science and Engineering, 103, p.157-165 (1989).

[5] M. Bando et al., "Three-Dimensional Transport Calculation Method for Eigenvalue Problems Using Diffusion Synthetic Acceleration," Journal of Nuclear Science and Technology, **22** (10), p.841-850 (1985).
[6] K. Sugino, "JUPITER Experimental Analyses Using a New Constant Set Based on JENDL-3.2" Journal of Nuclear Science and Technology, Supplement 2, p.1002-1005(2002).

Table 1. Main Core Parameters of JOYO MK-II and MK-III

Specification			MK-III Core	MK-II Core
Reactor Thermal Power		(MWt)	140	100
Max. Number of Driver Fuel*			85	67
Equivalent Core Diameter		(cm)	80	73
Core Height		(cm)	50	55
^{235}UEnrichment		(wt%)	18	18
Pu Content: Pu/(Pu+U)		(wt%)	23/30**	30
Fissile Pu Content: (^{239}Pu+^{241}Pu)/(Pu+U)		(wt%)	16/21**	21
Max. Linear Heat Rate of Fuel Pin		(W/cm)	420	400
Max. Burn-up of Fuel(Pin Average)		(GWd/t)	90	75
Total Neutron Flux		(n/cm^2・s)	5.7x10^{15}	4.5x10^{15}
Fast Neutron Flux		(n/cm^2・s)	4.0x10^{15}	3.2x10^{15}
Number of Control Rod	In the 3rd Row		4	6
	In the 5th Row		2	0
Reflector/Shielding			SUS/B_4C	SUS/SUS
Flow Rate of Primary Sodium		(t/h)	2,700	2,200
Primary Coolant Temperture (Inlet/Outlet)		(℃)	350/500	370/500
Operation Period per Cycle		(day)	60	70

*Includeing "Number of Irradiation Test Fuel"
**Inner Core / Outer Core

Table 2. Period Method Results of the Total Worth

Rod	Exp. Worth (%Δk/kk')	Base Calc. (%Δk/kk')	Bias Factor	Biased Calc. (%Δk/kk')	C/E
1	2.09 ±0.07	2.01	1.00	2.01	0.96
2	0.80 ±0.03	0.80	0.98	0.79	0.98
3	2.03 ±0.07	1.97	1.00	1.99	0.97
4	2.08 ±0.07	2.01	1.00	2.01	0.97
5	0.78 ±0.03	0.80	0.98	0.79	1.00
6	2.06 ±0.07	1.97	1.00	1.97	0.96

Table 3. Rod Worths (295-650mm) Measurements from Two Approaches

Rod	Period Method (%Δk/kk')	Juggling (%Δk/kk')
1	1.13	1.14
3	1.11	1.12
4	1.13	1.14
6	1.14	1.15

Table 4. Shadowing Experiment Results

Measured Rod No.	Shadow Rod No.	Change in Rod Worth	
		Exp.	Cal.
1	4	+6%	+4%
1	6	-7%	-7%
5	3	+6%	+6%
5	6	-14%	-14%

Table 5. Isothermal Temperature Coefficient

	Temperature Direction	Isothermal Temp. Coef. (%Δk/kk'/ °C)		C/E
		Exp.	Cal.	
1	ascending	-0.00370	-0.00368	0.995
2	ascending	-0.00375		0.981
3	descending	-0.00386		0.952
4	descending	-0.00385		0.955

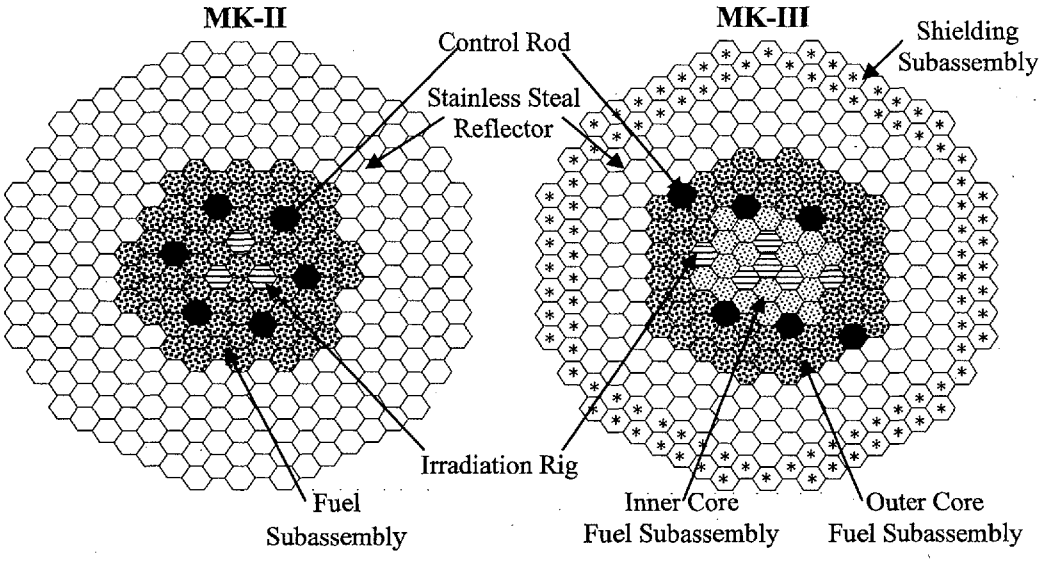

Fig. 1. Comparison of JOYO MK-II and MK-III cores

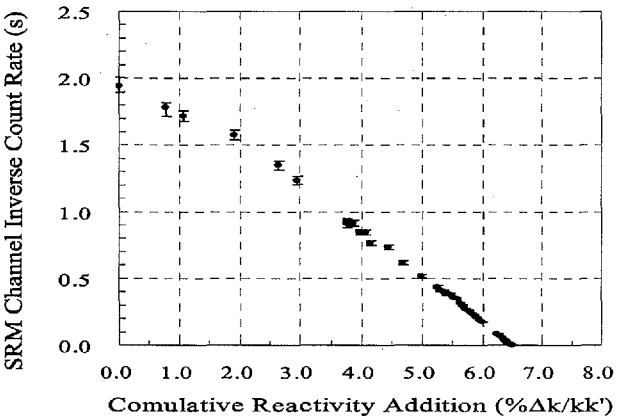

Fig. 2. MK-III Initial Approach to Criticality

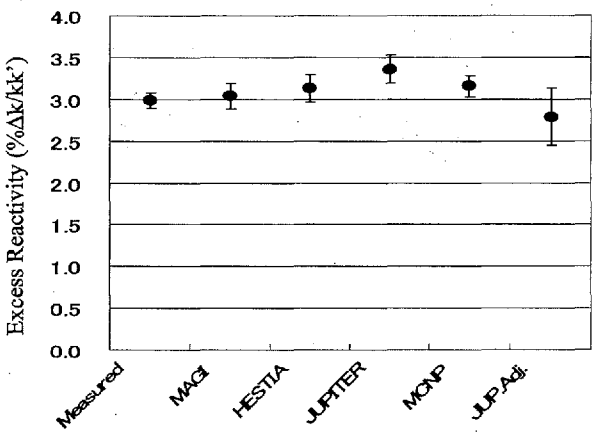

Fig. 3. Measured and Calculated Excess Reactivity

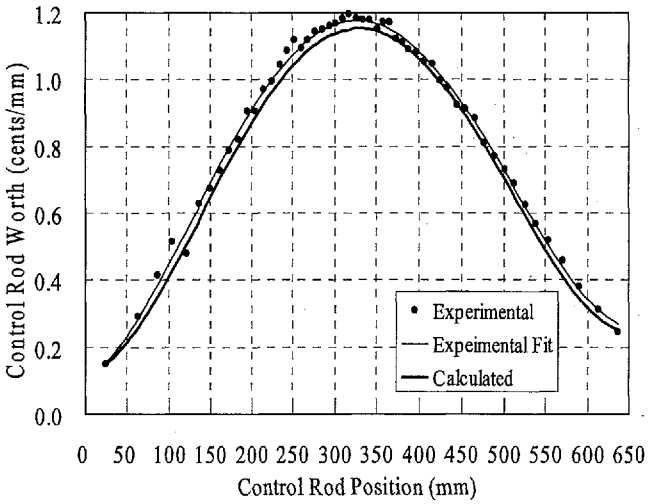

Fig. 4. Comparison of Calculated and Measured Axial Rod Worth Profile

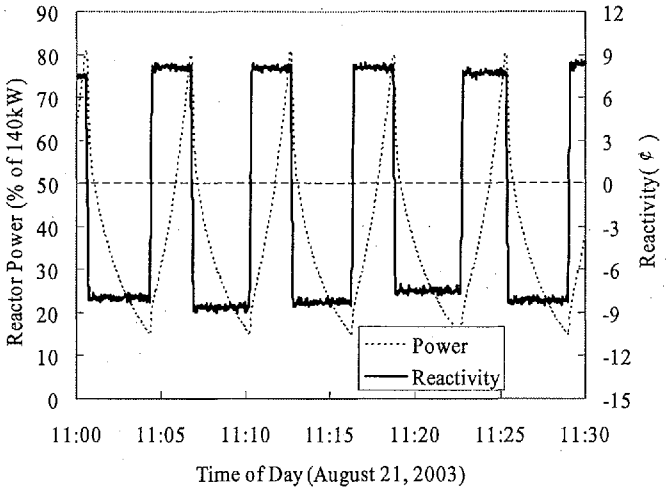

Fig. 5. Reactivity and Power Traces from a Juggling-Type Rod Calibration

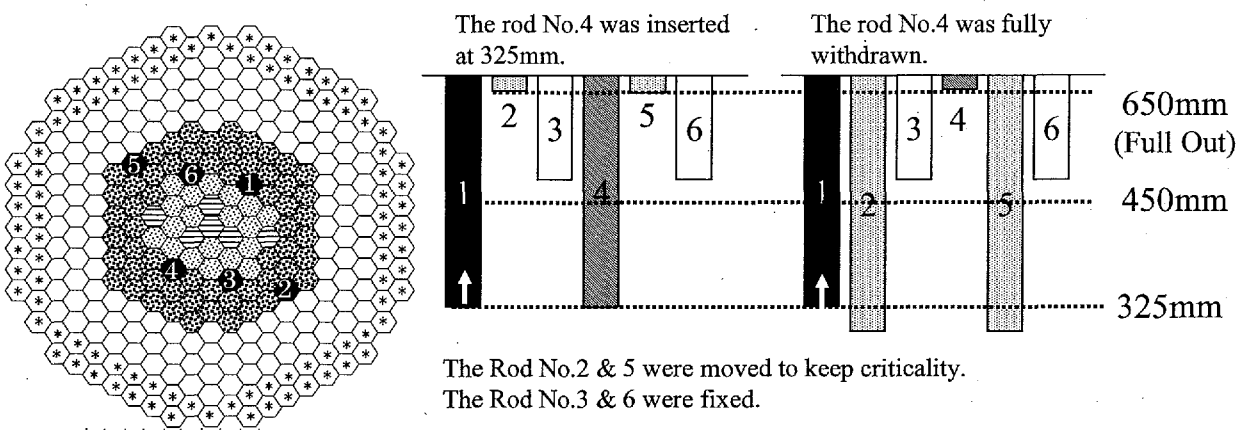

Fig. 6. Control Rod Pattern of Shadowing Effect Measurements

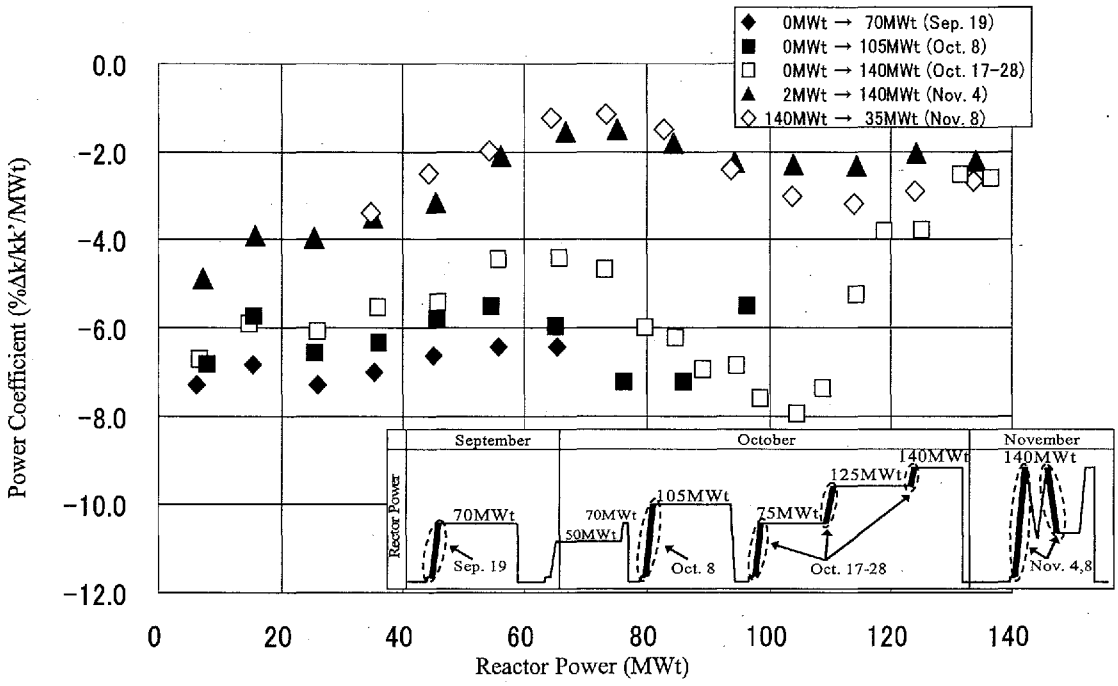

Fig. 7. Power Coefficient Measurements Results

JP0450509

JAERI－Conf 2004－005

3.19 Effect of Neutron Anisotropic Scattering in Fast Reactor Analysis

Gou Chiba

O-arai Engineering Center, Japan Nuclear Cycle Development Institute
4002 Narita, O-arai, Ibaraki, 311-1393, Japan
e-mail:go_chiba@oec.jnc.go.jp

Numerical tests were performed about an effect of a neutron anisotropic scattering on criticality in the Sn transport calculation. The simplest approximation, the consistent P approximation and the extended transport approximation were compared with each other in one-dimensional slab fast reactor models. JAERI fast set which has been used for fast reactor analyses is inadequate to evaluate the effect because it doesn't include the scattering matrices and the self-shielding factors to calculate the group-averaged cross sections weighted by the higher-order moment of angular flux. In the present study, the sub-group method was used to evaluate the group-averaged cross sections. Results showed that the simplest approximaton is inadequate and the transport approximation is effective for evaluating the anisotropic scattering.

I Introduction

A neutron transport equation in a whole core has been usually solved by the discrete ordinate method (Sn method) in the fast reactor analyses in Japan. In the Sn method, a neutron anisotropic scattering has been considered by the transport approximation, in which the total cross sections are replaced by the transport cross sections. The transport approximation makes it possible to evaluate the P_1 effect of an anisotropic scattering without an increase of computational burden in comparison to a calculation with an isotropic scattering. When higher-order anisotropic scattering is necessary to be considered, the simplest approximation, in which angular flux is assumed to be separable into the energy-dependent and the angle-dependent functions, is used. It has not been shown clearly that the these appoximations are adequate for the evaluation of the neutron anisotropic scattering.

In the present paper, we reviewed the method to evaluate the neutron anisotropic scattering with some papers(1, 2) and extracted a problem caused by a limitation of the JAERI Fast Set which has been used in fast reactor analyses in Japan. After that, we showed another approach to evaluate the anisotropic scattering and carried out numerical tests in simple fast reactor models.

II Review of Theory

For simplicity, a one-dimensional slab system is considered. A static neutron transport equation is described as below.

$$\mu\frac{d\phi(x,\mu,E)}{dx} + \Sigma_t(x,E)\phi(x,\mu,E) = \int d\mu' \int dE' \phi(x,\mu',E')\Sigma_s(x,\mu'\to\mu,E'\to E) + Q(x,\mu,E) \tag{1}$$

Scattering cross section can be shown as

$$\Sigma_s(x,\mu'\to\mu,E'\to E) = \Sigma_s(x,\mu_0,E'\to E) \tag{2}$$

where μ_0 means the cosine of the scattering angle. After scattering cross sections and angular flux are extended by the Legendre polynomials, Eq.(1) is transformed to

$$\mu\frac{d\phi(x,\mu,E)}{dx}+\Sigma_t(x,E)\phi(x,\mu,E)= \sum_{l=0}^{\infty}\frac{2l+1}{4\pi}P_l(\mu)\int dE'\phi_l(x,E')\Sigma_{s,l}(x,E'\to E)+Q(x,\mu,E). \tag{3}$$

When Eq.(3) is averaged within an energy group, total cross section is defined as

$$\Sigma_{t,g}(x,\mu)=\frac{\int_{E\in g}\Sigma_t(x,E)\phi(x,\mu,E)dE}{\int_{E\in g}\phi(x,\mu,E)dE}. \tag{4}$$

This means that the group-averaged total cross section should be dependent on the angle. Since it is difficult to apply the angular-dependent total cross section to reactor calculations, several methods have been described in Ref.(1) and (2).

In the first method, it is assumed that the angular flux can be separated into the energy-dependent and the angular-dependent functions. Then group-averaged total cross sections can be calculated by using neutron flux as a weighting function and the cross sections become independent on the angle. Under the assumption, Eq.(3) can be rewritten as

$$\mu\frac{d\phi_g(x,\mu)}{dx}+\Sigma^0_{t,g}(x)\phi_g(x,\mu)=\sum_{l=0}^{\infty}\frac{2l+1}{4\pi}P_l(\mu)\sum_{g'=1}^{G}\phi_{l,g'}(x)\Sigma^l_{s,l,g'\to g}(x)+Q_g(x,\mu) \tag{5}$$

where $\Sigma^0_{t,g}(x)$ means the group-averaged total cross section calculated by using the 0-th moment of angular flux as a weight and $\Sigma^l_{s,l,g'\to g}$ means the l-th order of scattering cross section calculated by using the l-th moment of angular flux. In the present paper, this method is refered as "the simplest approximation".

The second method is to extend angular flux in left hand side of Eq.(3) by the Legendre polynomials. After the extension, Eq.(3) can be rewritten as

$$\mu\frac{d\phi_g(x,\mu)}{dx}=\sum_{l=0}^{\infty}\frac{2l+1}{4\pi}P_l(\mu)\sum_{g'=1}^{G}\phi_{l,g'}(x)\left[\Sigma^l_{s,l,g'\to g}(x)-\Sigma^l_{t,g}(x)\delta_{gg'}\right]+Q_g(x,\mu). \tag{6}$$

After adding $\Sigma_g(x)\phi_g(x,\mu)$ to both sides of this equation, Eq.(6) can be rewritten as

$$\mu\frac{d\phi_g(x,\mu)}{dx}+\Sigma_g(x)\phi_g(x,\mu)=\sum_{l=0}^{\infty}\frac{2l+1}{4\pi}P_l(\mu)\sum_{g'=1}^{G}\phi_{l,g'}(x) \times\left[\Sigma^l_{s,l,g'\to g}(x)+(\Sigma_g(x)-\Sigma^l_{t,g}(x))\delta_{gg'}\right]+Q_g(x,\mu). \tag{7}$$

When $\Sigma_g(x)$ is defined as $\Sigma^0_{t,g}(x)$, it is called as "the consistent P approximation". If $\Sigma^0_{t,g}(x)$ is assumed to be equal to $\Sigma^l_{t,g}$, Eq.(7) is coincident with Eq.(5).

If we consider the anisotropic scattering up to the P_L order in Eq.(7), an ignorance of the higher-order than P_{L+1} causes an error. The term of P_{L+1} is

$$\frac{1}{4\pi}(2L+3)P_{L+1}(\mu)\sum_{g'=1}^{G}\phi_{L+1,g'}\left[\Sigma^{L+1}_{s,L+1,g'\to g}(x)+((\Sigma_g(x)-\Sigma^{L+1}_{t,g}(x))\delta_{gg'}\right]. \tag{8}$$

To minimize the term, an approximation is used.

$$\sum_{g'}^{G}\phi_{L+1,g'}\Sigma^{L+1}_{s,L+1,g'\to g}(x)\approx\sum_{g'}^{G}\phi_{L+1,g}\Sigma^{L+1}_{s,L+1,g\to g'}(x) \tag{9}$$

The cross section $\Sigma_g(x)$ can be defined to minimize the error as below.

$$\Sigma_g(x) = \Sigma_{t,g}^{L+1}(x) - \sum_{g'=1}^{G} \Sigma_{s,L+1,g\to g'}^{L+1}(x) \tag{10}$$

This is the third method, called as "the extended transport approximation".

In the present paper, these described methods, the simplest approximation, the consistent P approximation and the extended transport approximation, were used to evaluate the anisotropic scattering in Sn calculations.

III Application

Usually, JAERI Fast Set(JFS) has been used for fast reactor analyses in Japan. JFS includes the infinite-dilution cross sections, the scattering matrices of the P_0 component and the self-shielding factors. The self-shielding factors are implemented to calculate the flux-weighted group-averaged cross sections. In addition, the current-weighted group-averaged cross section can be calculated for only the total reaction because it is necessary to define the transport cross section in the transport approximation. When we evaluate the anisotropic scattering with the described methods, it is necessary to evaluate the group-averaged cross section weighted by the higher-order moment of angular flux. The scattering matrices of the higer order components were given in the new type of the JFS library under a development in JNC. Therefore, we have to add "the higher order moment-weighted" self-shielding factors to the new JFS. But it needs much works to calculate the self-shielding factors and to reconstract the format of the new JFS.

This problem can be overcome easily by introducing the sub-group method(3). In the sub-group method, a descritization is carried out with not energy but total cross section. The n-th order moment of angular flux $\phi_n(E)$ can be expressed as below in the large homogeneous medium by the B_N method.

$$\phi_n(E) \propto \frac{1}{[\Sigma_t(E)]^{n+1}} \tag{11}$$

Group-averaged cross section weighted by the n-th order moment, $\sigma_{x,g}^n$, is calculated as

$$\sigma_{x,g}^n = \frac{\int_{E\in g} dE\sigma_x(E)\phi_n(E)}{\int_{E\in g} dE\phi_n(E)} = \frac{\int_{E\in g} dE\sigma_x(E)\frac{1}{[\Sigma_t(E)]^{n+1}}}{\int_{E\in g} dE\frac{1}{[\Sigma_t(E)]^{n+1}}} = \frac{\int_{E\in g} dE\sigma_x(E)\frac{1}{[\sigma_t(E)+\sigma_0]^{n+1}}}{\int_{E\in g} dE\frac{1}{[\sigma_t(E)+\sigma_0]^{n+1}}} \tag{12}$$

σ_0 means the background cross section. A descritization of Eq.(12) is carried out with the sub-group method as below.

$$\sigma_{x,g}^n = \frac{\sum_{b=1}^{B} \sigma_{x,b}\frac{P_b}{(\sigma_{t,b}+\sigma_0)^{n+1}}}{\sum_{b=1}^{B} \frac{P_b}{(\sigma_{t,b}+\sigma_0)^{n+1}}} \tag{13}$$

The sub-group parameters, P_b, $\sigma_{x,b}$ and $\Sigma_{t,b}$, can be prepared by the MOMENTOF code(4) developed by Japan Nuclear Cycle Development Institute. The parameters are defined to preserve the cross section moment(5) in the code. In unresolved resonance energy region, TIMS-1 code(6) is utilized to make a "ladder" of resonance.

IV Numerical tests and results

To evaluate the effect of the anisotropic scattering, one-dimensional slab fast reactor models were constructed. We prepared three homogeneous mediums, fuel, blanket and reflector, whose number densities are shown in Table 1 and constructed three models using these mediums as shown in Table 2. Model 1 is a conventional fast reactor, model 2 is a plutnium burning reactor and model 3 is a heterogeneously blanket-loaded reactor.

Sub-group parameters were prapared with the MOMENTOF code from JENDL-3.2 and $\sigma^n_{x,g}$ was evaluated. An energy group structure was defined the same as JFS. Scattering matrices implemented in JFS were used. One-dimensional trasport calculations were performed by the ANISN code(7). One mesh per 2.5 cm was given and the Sn order was set to be 16.

At first, we evaluated a sensitivity of a weighting function used for calculations of group-averaged scattering cross sections to k_{eff}. We used different methods for the calculations. The "correct" functions described in Eq.(11) were used in one method and the neutron flux was used commonly in the other method. Results obtained with the simplest approximation and the consistent P approximation are shown in Table 3. The sensitivity is the largest in a result of model 2 with the consistent P approximation and a difference between two weight funtions is 100pcm. These results mean that it is adequate to use a neutron flux as a weighting function approximately for calculation of the higher-order scattering cross sections.

Next, comparisons between the simplest approximation and the consistent P approximation were carried out. Results are shown in Table 4. Differences are 300pcm in model 1, 130pcm in model 3 and 1000pcm in model2. These were caused by the approximation to separate angular flux into energy-dependent and angular-dependent functions and the results showed that the error should not be ignored. The effects to consider the higher-order anisotropic scattering, a difference between the results of P_1 and P_3 calculations, were observed about 50pcm in model 2 and it was not so large.

Comparisons between the consistent P approximation and the extended transport approximation were also carried out. Results are shown in Table 5. Convergences of k_{eff}s were observed in both the approximations as an increase of considered P_L order and the converged values agreed with each other. Differences between k_{eff} obtained by the transport approximation and the converged one are 40pcm in model 1, 60pcm in model 2 and 20pcm in model 3. This results show that the transport approximation is adequate to evaluate the anisotropic scattering in the analyse of these simple models.

V Conclusion

Several papers were reviewd and numerical tests were performed about a neutron anisotropic scattering. The simplest approximation, the consistent P approximation and the extended transport approximation were compared with each other in one-dimensional slab reactor models. The results showed that the transport approximation, which has been used for fast reactor analyses in Japan, is adequate for considering the anisotropic scattering. In the present study, the evaluations were performed in the simple reactor models. Therefore it is necessary to evaluate the effect in the more realistic model and we are going to perform it.

If the higher-order anisotropic scattering must be considered, the higher-order moment-weighted group-averaged cross sections are necessary. In the present paper, it is shown to be adequate to use a neutron flux as a weighting function approximately for calculations of the higher order scattering cross sections. However, higher-order moment-weighted total cross

sections are necessary because the simplest approximation should not be used. Therefore "the higher-order moment-weighted" self-shielding factors for the total reaction should be added to JFS library. Another candidate to overcome the problem is an introduction of the sub-group method. The sub-group method is very useful because of the flexibility in an evaluation of an in-group flux.

References

[1] G.I.Bell, *al el.*,"Multitable Treatments of Anisotropic Scattering in Sn Multigroup Transport Calculations," *Nucl. Sci. Eng.*, **28**,376 (1967).

[2] G.I.Bell, S. Glasstone,*Nuclear Reactor Theory*, Van Nostrand Reinhold Company (1970).

[3] Y.Ronen,*Handbook of Nuclear Reactors Calculations* , CRC Press, Boca Raton, Florida,(1986).

[4] G.Chiba,"Development of the sub-group parameter preparing code, MOMENTOF," JNC TN9400 2003-053 (2003).

[5] P.Ribon, J.M.Maillard, "Probability tables and gauss quadrature; Application to neutron cross-sections in the unresolved energy range," Topical Meeting on Advences in Reactor Physics and Safety, Saratoga Springs, (1986).

[6] H.Takano, *et al.*, *TIMS-1: A Processing Code for Production of Group Constants of Heavy Resonant Nuclei,* JAERI 1267, Japan Atomic Energy Reserch Institute, (1994).

[7] D.K.Parsons,*ANISN/PC manual*, EGG-2500, (1987).

Table 1: Number densities of homogeneous mediums (Unit:$10^{24} atoms/cm^3$)

	Fuel	Blanket	Reflector
U-238	8.4×10^{-3}	1.4×10^{-2}	
Pu-239	9.6×10^{-4}		
Fe-Nat.	1.1×10^{-2}	6.2×10^{-3}	5.3×10^{-2}
Cr-Nat.	1.9×10^{-3}	1.7×10^{-3}	1.5×10^{-2}
Ni-Nat.			6.7×10^{-3}
C	1.1×10^{-3}		
O	1.6×10^{-2}	2.3×10^{-3}	
Na	9.5×10^{-3}	4.7×10^{-3}	

Table 2: Model configuration (Unit:cm)

	Model 1	Model 2	Model 3
Reflective boundary	0	0	0
Fuel region	0-42.5	0-35	0-22, 27.5-50, 55-77.5
Blanket region	42.5-57.5	35-65	22.5-27.5, 50-55, 77.5-92.5
Reflector region	57.5-72.5	-	92.5-107.5
Vacuum boundary	75.2	65	107.5

Table 3: Sensitivity of weighting function of scattering cross section on k_{eff}

	Model 1		Model 2		Model 3	
	ϕ_0	ϕ_l	ϕ_0	ϕ_l	ϕ_0	ϕ_l
Simplest P0	1.02321		1.01773		1.01263	
Simplest P1	1.00488	1.00502	0.99904	0.99981	1.00341	1.00346
Simplest P3	1.00514	1.00528	0.99941	1.00017	1.00356	1.00362
Simplest P5	1.00514	1.00528	0.99941	1.00017	1.00356	1.00362
Consistent P1	1.00188	1.00204	0.98899	0.98996	1.00209	1.00215
Consistent P3	1.00217	1.00233	0.98944	0.99040	1.00225	1.00231

Table 4: k_{eff}s obtained by the simplest and the consistent P approximation

	Model 1		Model 2		Model 3	
	Simplest	Consistent	Simplest	Consistent	Simplest	Consistent
P0	1.02321		1.01773		1.01263	
P1	1.00502	1.00204	0.99981	0.98996	1.00346	1.00215
P2	1.00528	1.00234	1.00020	0.99041	1.00364	1.00233
P3	1.00528	1.00233	1.00017	0.99040	1.00362	1.00231
P3-P1 (pcm)	26	29	36	44	16	16

Table 5: k_{eff}s obtained by the consisntent P and extended transport approximation

	Model 1		Model 2		Model 3	
	Consistent	Ext. Trans.	Consistent	Ext. Trans.	Consistent	Ext. Trans.
P0	1.02321	1.00275	1.01773	0.99101	1.01263	1.00251
P1	1.00204	1.00224	0.98996	0.99036	1.00215	1.00224
P2	1.00234	1.00233	0.99041	0.99037	1.00233	1.00231
P3	1.00233	1.00233	0.99040	0.99037	1.00231	1.00231

JP0450510

JAERI－Conf 2004－005

3.20 Validation of JENDL-3.3 for the HTTR Criticality

Minoru GOTO, Naoki NOJIRI and Satoshi SHIMAKAWA
Department of HTTR Project, Japan Atomic Energy Research Institute
3607 Oarai-machi, Higashi-ibaraki-gun, Ibaraki-ken 311-1394
e-mail: mgotoh@oarai.jaeri.go.jp

Validation of JENDL-3.3 has been performed for the HTTR criticality using the MVP code with a "lattice-cell" of infinite models and a "whole-core" of finite models. It was found that the *keff* values calculated with JENDL-3.3 was decreased about 0.2-0.4%Δk from one with JENDL-3.2. The criticality prediction was closed to the experimental data in the critical approach situation of the HTTR.

1. Introduction

Benchmark calculations for several water-moderated reactors had been performed with JENDL-3.3 which is the latest version of the Japan Evaluated Nuclear Data Library (JENDL) and the *keff* values are obtained good agreements with the experimental data rather than JENDL-3.2 which is the previous version of JENDL[1].

Concerning to high temperature gas-cooled reactors, obtaining good calculation results with JENDL-3.3 are expected as mentioned above, too. To improve the HTTR core calculations with high accuracy, the JENDL-3.3 has been attempted in this study.

This report describes the applicability of JENDL-3.3 to the HTTR criticality and the comparisons between the calculation results with JENDL-3.2 and the experimental data.

2. General descriptions of the HTTR

2.1 Core structure

The HTTR is a graphite-moderated, helium-cooled thermal reactor which has 30MW of thermal power and 950℃ of outlet coolant-gas temperature. Radial and axial views of the HTTR are shown in Fig.1. The center of the core is constructed with fuel assembly blocks with different 12 kinds of enrichment (3.4-9.9wt-%U), control rod guide blocks, reflector blocks and irradiation blocks, and is surrounded by the permanent reflector. There are two types of the fuel assembly blocks with 33 and 31 fuel rods which composed 14 fuel compacts. Each fuel compact composes about 13,000 coated fuel particles of 0.92mm diameter.

2.2 Critical approach

The critical approach of the HTTR was carried out by the fuel addition method at room temperature. In this situation, the dummy graphite blocks were replaced to the flesh fuel blocks from outer core region and then the annular core was made with 18 fuel columns. Each fuel column consists of five fuel blocks. The initial critical state was achieved with 19 fuel columns and the full core with 30 fuel columns, i.e. 150 fuel brocks, was successfully constructed.

3. Calculation methods

Calculations for the HTTR criticality were performed by the continuous energy Monte Carlo code MVP[2] with the neutron cross section sets based on JENDL-3.3 and JENDL-3.2. In the calculations, there were two different geometrical models which were "whole-core" and "lattice-cell" for following issues.

(1) the discrepancy between the calculated *keff* value and the experimental data of the critical approach

(2) the contribution of each nuclide data on the *keff* discrepancy between JENDL-3.3 and JENDL-3.2

(3) the major cause of the *kinf* discrepancy on temperature dependency

The calculation conditions are shown in Table1. The first two issues were performed with the "whole-core" model, and the last issue was performed with the "lattice-cell" model. The standard deviations of the calculation results with the "whole-core" model and the "lattice-cell" model were less than 0.03% and 0.01%, respectively. The history numbers of the each calculation were 8,000,000.

4. Calculation results and discussions

4.1 Critical approach

Calculated *keff* values for the critical approach are shown in Fig.2 and the initial critical state would be achieved by 18 fuel columns loaded. In the experiment that was achieved by 19 fuel columns loaded. The *keff* line with JENDL-3.3 is under the one with JENDL-3.2 and its discrepancy is 0.2-0.4%Δk, therefore JENDL-3.3 gives slightly better *keff* value rather than JENDL-3.2. However, an overestimation to the experimental data about 0.8%Δk is remained.

4.2 Nuclide contributions to the critical calculations

The *keff* discrepancy caused by the difference of JENDL's version and the contributions of the differences of each nuclide data to the discrepancies were shown in Fig.3. For 18 and 30 fuel columns loaded cores, JENDL-3.3 gives 0.30 and 0.40%Δk smaller *keff* value than JENDL-3.2, respectively. Here, the U-235 data of JENDL-3.3 gives 0.35 and 0.45%Δk smaller *keff* value than one of JENDL-3.2. The *keff* discrepancy caused by the difference of another nuclide data was less than 0.10%Δk. As the results, the discrepancy caused by the difference of JENDL's version is dominated by the difference of the U-235 data.

In order to treat S(α,β) data, the MVP neutron cross section sets based on JENDL-3.3 and JENDL-3.2 were taken it form ENDF/B-VI and ENDF/B-III, respectively. With the improvement from ENDF/B-III to ENDF/B-VI, upper energy limitation of the S(α,β) data of Graphite was extended. However, it was confirmed that the influence of this difference on the *kinf* values is negligible.

4.3 *kinf* and *keff* values with JENDL-3.3

The ratios of the *kinf* or the *keff* values with JENDL-3.3 to JENDL-3.2 for the HTTR at high and room temperature conditions and the water-moderated reactors at room temperature were plotted by uranium enrichment in Fig.4[1]. There is a difference between the distribution pattern of the ratios for all reactors at room temperature and the HTTR at high temperature.

To reveal the reason of the difference in the distribution pattern mentioned above, the temperature dependencies of the ratio of the HTTR *kinf* values were examined. As shown in Fig.5,

the ratios decreased according with the rise of temperature.

Furthermore, to examine the temperature dependency of the *kinf* values in detail, the analysis was performed by using the four-factor formula. Each of the factors is defined following equations and each of their right hand factors which means reaction rate can be obtained directly from the MVP calculations[3].

$$\varepsilon = \frac{[\nu \cdot \Sigma_f \cdot \phi \cdot V]_{fast}^{fuel} + [\nu \cdot \Sigma_f \cdot \phi \cdot V]_{thermal}^{fuel}}{[\nu \cdot \Sigma_f \cdot \phi \cdot V]_{fast}^{fuel}} \quad (1)$$

$$p = \frac{[\Sigma_a \cdot \phi \cdot V]_{thermal}^{whole}}{[\Sigma_a \cdot \phi \cdot V]_{fast}^{whole} + [\Sigma_a \cdot \phi \cdot V]_{thermal}^{whole}} \quad (2)$$

$$f = \frac{[\Sigma_a \cdot \phi \cdot V]_{thermal}^{fuel}}{[\Sigma_a \cdot \phi \cdot V]_{termal}^{whole}} \quad (3)$$

$$\eta = \frac{[\nu \cdot \Sigma_f \cdot \phi \cdot V]_{thermal}^{fuel}}{[\Sigma_a \cdot \phi \cdot V]_{thermal}^{fuel}} \quad (4)$$

where,

ε: first fission factor, p: resonance escape probability,
f: thermal utilization, η: thermal regeneration rate,
ν: number of neutrons per fission, Σ: macroscopic cross section,
ϕ: flux and V: volume.

In the equations, the neutron energy range was divided into the thermal and the fast range with a boundary value 4.5eV. From Fig.6, the discrepancy between the *kinf* values with JENDL-3.3 and JENDL-3.2 at room temperature was dominated by discrepancy of the p and η values. The temperature dependency of the *kinf* values was dominated only by the η values discrepancy. By considering the nuclide contributions to each reaction rate in the equation (2) and (4), it was found that the discrepancies of the p and η values mentioned above were caused mainly by the difference of the U-235 fission data.

The ratios of the η values with JENDL-3.3 to JENDL-3.2 and the neutron spectra at 300K and 1200K are plotted by neutron energy in Fig.7. In the equation (4), the ν value is approximately constant and $\Sigma_a^{U235} >> \Sigma_a^{U238}$, therefore the η values are in proportion to the ratio of microscopic fission cross section data of U-235 to microscopic absorption cross section data of U-235. Figure7 suggests that the neutron spectrum is shifted to the right by the rise of temperature and this shift causes decreasing the η values ratio. This effect makes the discrepancy of the *kinf* values increase. This will be an important for the calculations of the temperature coefficients at high temperature.

5. Summary

For the HTTR criticality analysis, the calculations by the MVP code with JENDL-3.3 provides some improvements as follows,

For room temperature conditions;

(1) JENDL-3.3 gives 0.4%Δk better *keff* value than JENDL-3.2 and 0.8%Δk overestimation to the experimental data, however, is remained.

(2) Discrepancies between the *keff* values with JENDL-3.3 and JENDL-3.2 are

caused mainly by the difference of the p and η values of the U-235 data.

For high temperature conditions;

(3) Discrepancies between the *kinf* values with JENDL-3.3 and JENDL-3.2 become large according with the rise of temperature.

(4) This is because that the magnitude of the temperature dependency of the *kinf* values with JENDL-3.3 is grater than one with JENDL-3.2 and

(5) it is caused by the difference between the η values with JENDL-3.3 and JENDL-3.2 in thermal energy range.

The calculations with JENDL-3.3 will be employed successfully in the future works.

References

[1] K. Okumura and T. Mori: JAERI-Review 2003-023, p.59

[2] T. Mori and M. Nakagawa: JAERI-Data/Code 94-007

[3] K. Okumura: Private communications

Table 1 Calculation conditions

System temperature	Calculation model	Critical index	Comparative data	History number	Standard deviation (1σ)
300, 600, 900 and 1200K	lattice-cell with STG**	*kinf*	Calc. with J32***	8,000,000	< 0.01%
300K, ~1200K*	whole-core with STG	*keff*	Calc. with J32 and Exp. data (300K)	8,000,000	< 0.03%

* at FULL power condition
** statistical geometry
*** JENDL-3.2

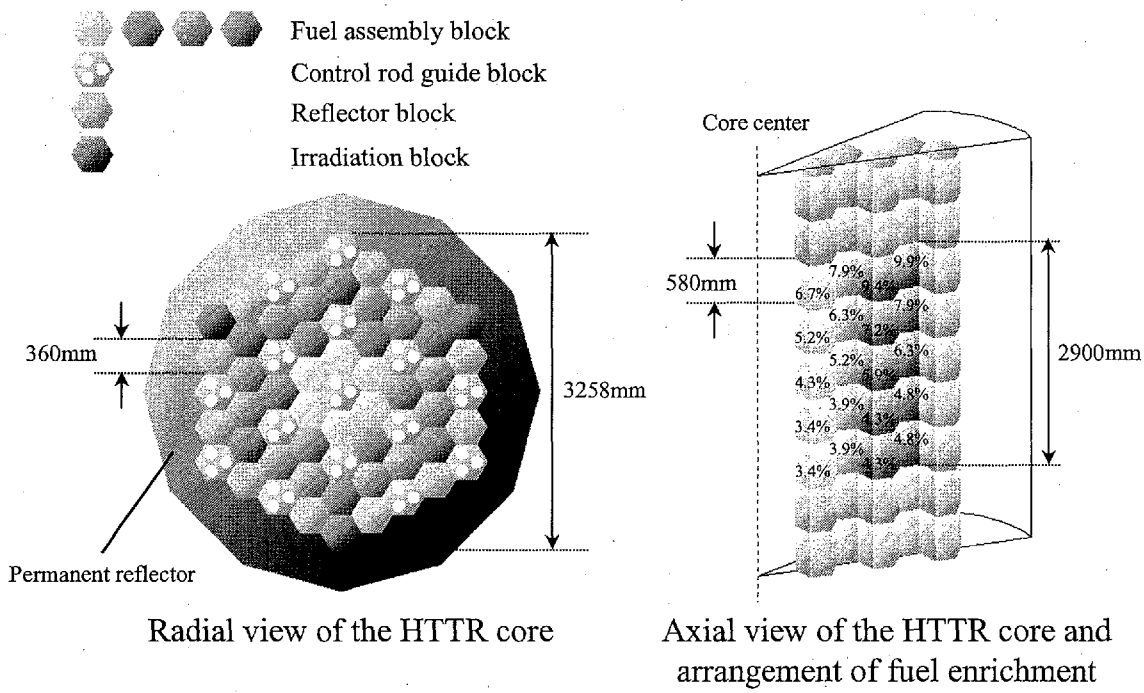

Fig.1 Radial and axial view of the HTTR core and arrangement of fuel enrichment

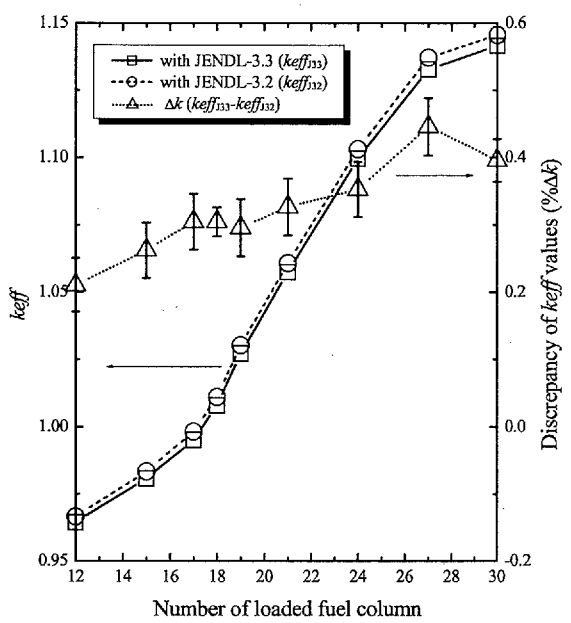

Fig.2 Calculated *keff* values for the critical approach

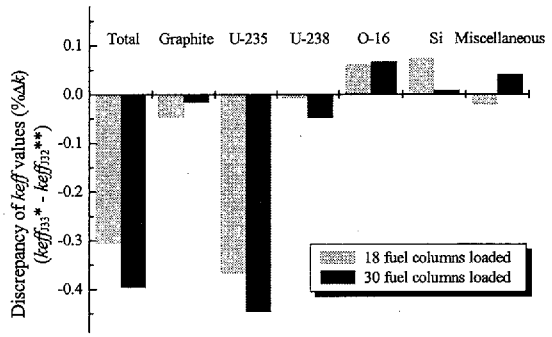

Fig.3 Contributions of the nuclide data to the *keff* values

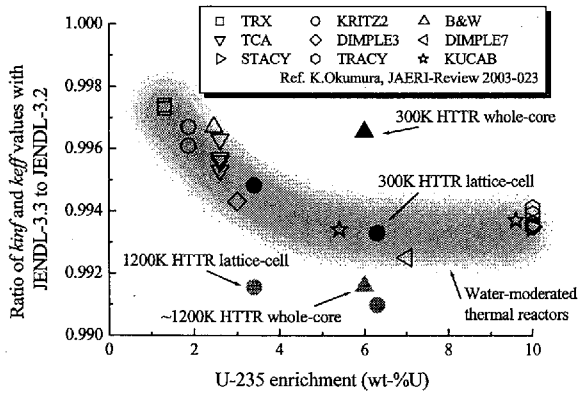

Fig.4 Distributions of the ratios of the *kinf* and *keff* values

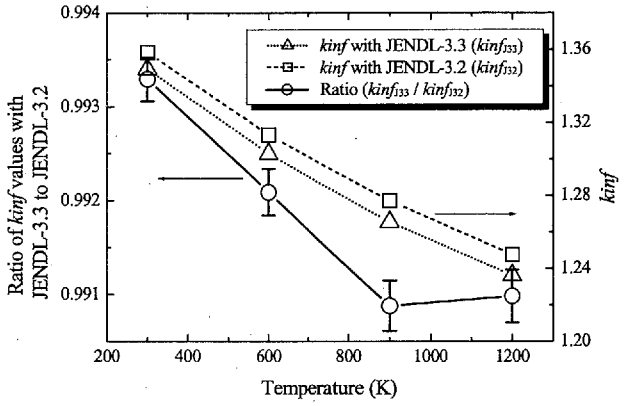

Fig.5 Temperature dependency of the ratios of the *kinf* values

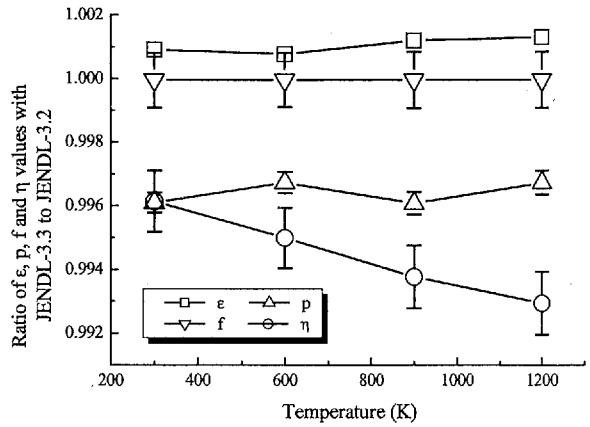

Fig.6 Temperature dependency of the ratio of the four factors

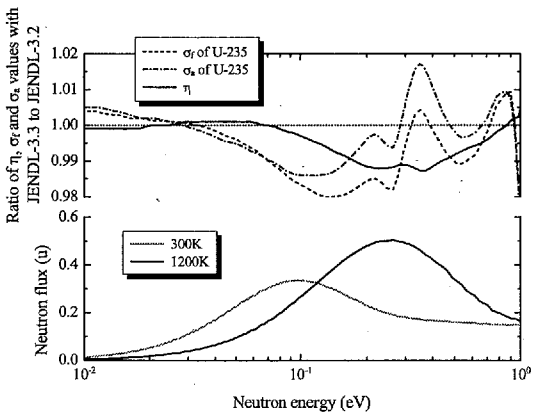

Fig.7 Ratios of the η values and the neutron spectra at 300 and 1200K

3.21 Some Comments to JSSTDL-300

Chikara KONNO
Center for Proton Accelerator Facilities, Japan Atomic Energy Research Institute
Tokai-mura, Naka-gun, Ibaraki-ken 319-1195 JAPAN
e-mail : konno@cens.tokai.jaeri.go.jp

The effects of the problems (weighting function independent on Legendre order and f-table) of JSSTDL-300 for self-shielding correction were examined through a simple benchmark test. The following results were obtained;

1) The effect of inappropriate transport approximation originating from weighting function independent on Legendre order is large if the self-shielding correction is large.
2) The effect of incomplete f-table is dependent on each nucleus. Particularly it is very large for copper.

1. Introduction

The self-shielding correction in multigroup libraries is essential in order to obtain appropriate results in Sn calculations. The Bondarenko method [1] by using f-table is often used as the self-shielding correction and gives good results. Recently it is pointed out that the transport approximation with a weighting function (WF) dependent on Legendre order is important for appropriate self-shielding correction.[2]

JSSTDL-300 [3], a common multigroup library of neutron 300 groups and gamma 104 groups for shielding applications produced from JENDL-3.2 [4] with the PROF-GROUCH-G/B [5] code by Japanese Nuclear Data Committee, is widely applied in Japan. However, the self-shielding correction in JSSTDL-300 is probably inadequate due to the following two reasons.

1) The weighting function independent on Legendre order is adopted.
2) The f-table of elastic scattering is used as that of scattering matrix for elastic scattering.

Effects of the above problems are examined through a simple benchmark test in this paper.

2. Review of Transport Approximation

The transport approximation (consistent-P approximation) [6] for a group g with the Bondarenko method is the following approximation;

$$\sigma_{l\ g\leftarrow g}^{SN} = \sigma_{l\ g\leftarrow g}^{PN} - (\sigma_{ltg}^{PN} - \sigma_{0tg}^{PN}), \tag{1}$$

$$\sigma_{g}^{SN} = \sigma_{0tg}^{PN}, \tag{2}$$

$$\sigma_{ltg}^{PN} = \frac{\int_g \sigma_t(E) W_l(E) dE}{\int_g W_l(E) dE}, \tag{3}$$

$$\sigma_{l\ g\leftarrow g}^{PN} = \frac{\int_g dE' \int_g dE \sigma_l(E' \rightarrow E) W_l(E')}{\int_g dE' W_l(E')}, \tag{4}$$

$$W_l(E) = \frac{C(E)}{[\sigma_0 + \sigma_t(E)]^{l+1}}, \tag{5}$$

where *PN* means PN cross sections, *SN* means SN cross sections, l is Legendre order, $\sigma_t(E)$ is the energy-dependent total cross section, $\sigma_l(E' \rightarrow E)$ is the energy-dependent scattering cross section, $W_l(E)$ is a weighting function, $C(E)$ is a smooth function of neutron energy E, and s_0 is the background cross section. It should be noted that the denominator of the weighting function in Eq. (5) is not $(\sigma_0+\sigma_t(E))$, but $(\sigma_0+\sigma_t(E))^{l+1}$, i.e. dependent on Legendre order. Thus the term in parentheses in the right side of Eq. (1) is not always zero, though it is zero if the weighting function is independent on Legendre order. The NJOY [7] and TRANSX [6] code system adopts the following weighting function,

$$W_0(E) = \frac{C(E)}{[\sigma_0 + \sigma_t(E)]}, \tag{6}$$

$$W_{l\geq 1}(E) = \frac{C(E)}{[\sigma_0 + \sigma_t(E)]^2}. \tag{7}$$

Reference 2 shows that the transport approximation with this weighting function gives appropriate self-shielding correction, though the weighting function is different from Eq. (5) for Legendre order of ≥ 2.

The weighting function of Eq. (6) is used independently on Legendre order in JSSTDL-300. Hence the term in parentheses in the right side of Eq. (1) is automatically zero. As described later, this is not appropriate.

If the self-shielding effect is small, the term in parentheses in the right side of Eq. (1) is very small, which lead to no problem, since $W_l(E)$ is a smooth function of neutron energy E and σ_{ltg}^{PN} is almost the same as σ_{0tg}^{PN}.

3. Simple Benchmark Test

A simple benchmark test was carried out in order to examine whether the self-shielding correction in JSSTDL-300 is appropriate or not. The calculation model of this benchmark test consisted of a natural aluminum, iron, nickel or copper sphere of 1 m in radius with a 20 MeV neutron source in the center. Neutron spectra and integrated neutron fluxes in the sphere were calculated with the Sn code ANISN [8]. The following multigroup libraries of neutron 175 groups (VITAMIN-J [9]) with self-shielding correction were adopted for ANISN,

1) multigroup library generated from JSSTDL-300 (abbreviation : JSSTDL),
2) multigroup library with the weighting function of Eq. (6) independent on Legendre order generated from JENDL-3.2 by using the NJOY99.67 and TRANSX codes (abbreviation : NJOY, $WF_{L\geq 1}=WF_{L=0}$),
3) multigroup library with the weighting function of Eqs. (6) and (7) dependent on Legendre order and no transport approximation (the term in parentheses in the right side of Eq. (1) is neglected) generated from JENDL-3.2 by using the NJOY99.67 and TRANSX codes (abbreviation : NJOY, $WF_{L\geq 1}\neq WF_{L=0}$, No transport approximation)],
4) multigroup library with the weighting function of Eqs. (6) and (7) dependent on Legendre order and transport approximation [Consistent-P] generated from JENDL-3.2 by using NJOY99.67 and TRANSX (abbreviation : NJOY, $WF_{L\geq 1}\neq WF_{L=0}$, Transport approximation [consistent-P]).

The difference between ANISN calculations with the fist and second libraries indicates the effect due to incomplete f-table in JSSTDL-300. That between ANISN calculations with the second and third libraries corresponds to the effect due to weighting function only except for transport approximation. That between ANISN calculations with the third and fourth libraries reflects the effect due to transport approximation. These calculated results were compared with those obtained with MCNP4C [10] and FSXLIB-J3R2 [11] generated from JENDL-3.2.

Figure 1 shows calculated neutron spectra at 10 cm from the center in aluminum, iron, nickel and copper spheres. Since the self-shielding effect is small in aluminum, all the ANISN calculations for the aluminum sphere show almost the same results, which agree with the MCNP calculation well. On the contrary, the ANISN calculations are different each other for the iron, nickel and copper spheres.

In order to investigate the difference among the ANISN calculations in details along the distance from the center of the sphere, ratios of integrated neutron fluxes calculated with ANISN to those with MCNP are plotted in Figs. 2 ~ 5 for aluminum, iron, nickel and copper spheres, respectively. All the ANISN calculations for the aluminum sphere show almost the same results up to 90 cm from the center, which agree with the MCNP calculation within 30 %. The effect of the inadequate f-table in JSSTDL is small in iron, while it is large for integrated neutron flux from 10 to 100 keV in the nickel sphere and neutron fluxes below 1 MeV in the copper sphere. The effect of the weighting function not including transport approximation is small. The effect of the transport approximation is large in the iron, nickel and copper spheres. The ANISN calculations with the fourth multigroup library, which adopted appropriate transport approximation, agree with the MCNP calculations best. However, the agreement between the ANISN calculation with the fourth multigroup library and the MCNP calculation is not so good in the copper sphere. The reason of this disagreement is probably due to group structure as described in Ref. 12.

The P_1 coefficients of in-group scattering matrix of the four multigroup libraries are plotted in Fig. 6 for natural aluminum, iron, nickel and copper. It is demonstrated that they are very different between JSSTDL and the fourth multigroup library, which leads to the difference of neutron fluxes in Figs. 2 ~ 5.

4. Summary

The effects of the below problems of JSSTDL-300 for self-shielding correction were examined through a simple benchmark test.

1) The weighting function independent on Legendre order is adopted.
2) The f-table of elastic scattering is used as that of scattering matrix for elastic scattering.

The following results were obtained.

1) The effect of inappropriate transport approximation originating from a weighting function independent on Legendre order is large if the self-shielding correction is large.
2) The effect of incomplete f-table depends on each nucleus. Particularly it is very large for copper.

The JSSTDL-300 library should be modified for the weighting function (appropriate transport approximation) and f-table.

Acknowledgments

This work was supported in part by Research Committee on Adequacy of Radiation Shielding in Atomic Energy Society of Japan.

References

[1] Bondarenko I.I. (Ed.) : Group Constants for Nuclear Reactor Calculations, Consultants Bureau, New York, (1964).
[2] Konno C. and Ikeda Y. : JAERI-Conf 2003-06 p. 213 (2003).
[3] Hasegawa A. and Yamano N. : J. Nuc. Sci. Technol., Supplement 1, 723, (2000).
[4] Nakagawa T., et al. : J. Nucl. Sci. Technol., 32, 1259 (1995).
[5] Hasegawa A. : private communications.
[6] MacFarlane R.E. : LA-12312-MS (1993).
[7] MacFarlane R.E. and Muir D.W. : LA-12740-M (1994).
[8] DOORS3.2 : One, Two- and Three-Dimensional Discrete Ordinates Neutron/Photon Transport Code System, RSICC CODE PACKAGE CCC-650 (1998).
[9] Vontobel P. and Pelloni S. : EIR-Bericht Nr. 636 (1987).
[10] Briesmeister J.F.(Ed.) : LA-13709-M (2000).
[11] Kosako K., et al.: JAERI-Data/Code 94-020 (1994).
[12] Konno C., et al. : JAERI-Conf 98-003 p. 198 (1998).

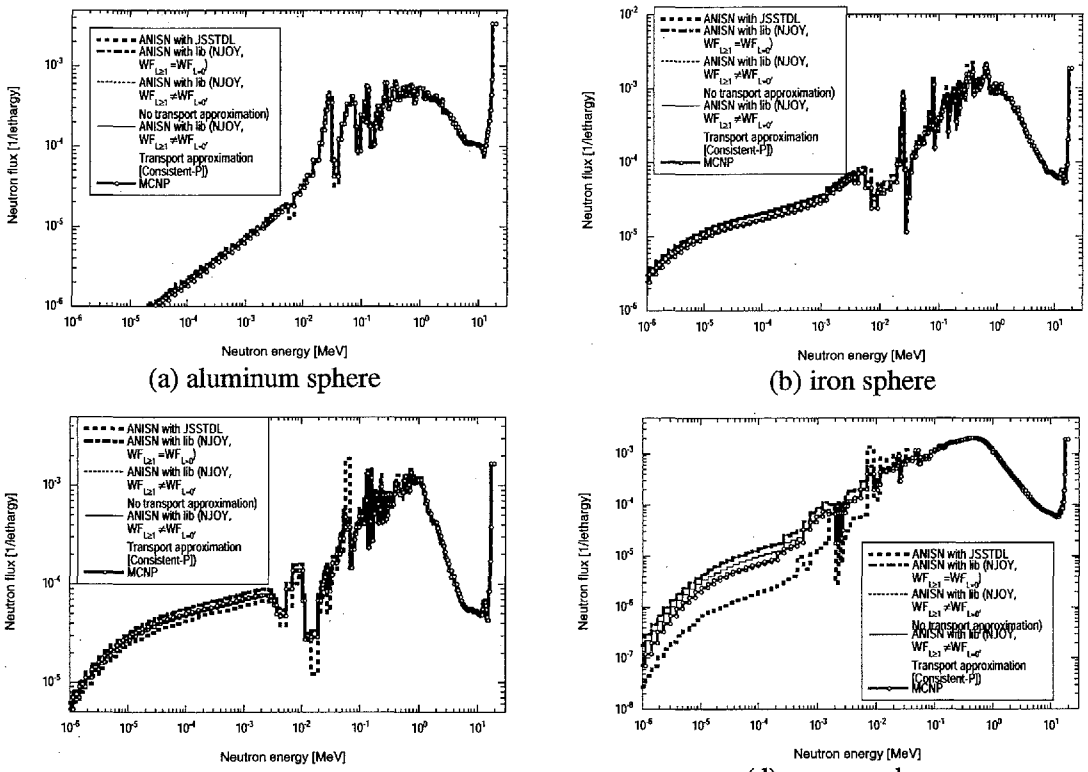

(a) aluminum sphere (b) iron sphere

(c) nickel sphere (d) copper sphere

Fig. 1 Calculated neutron spectra at 10 cm from the center.

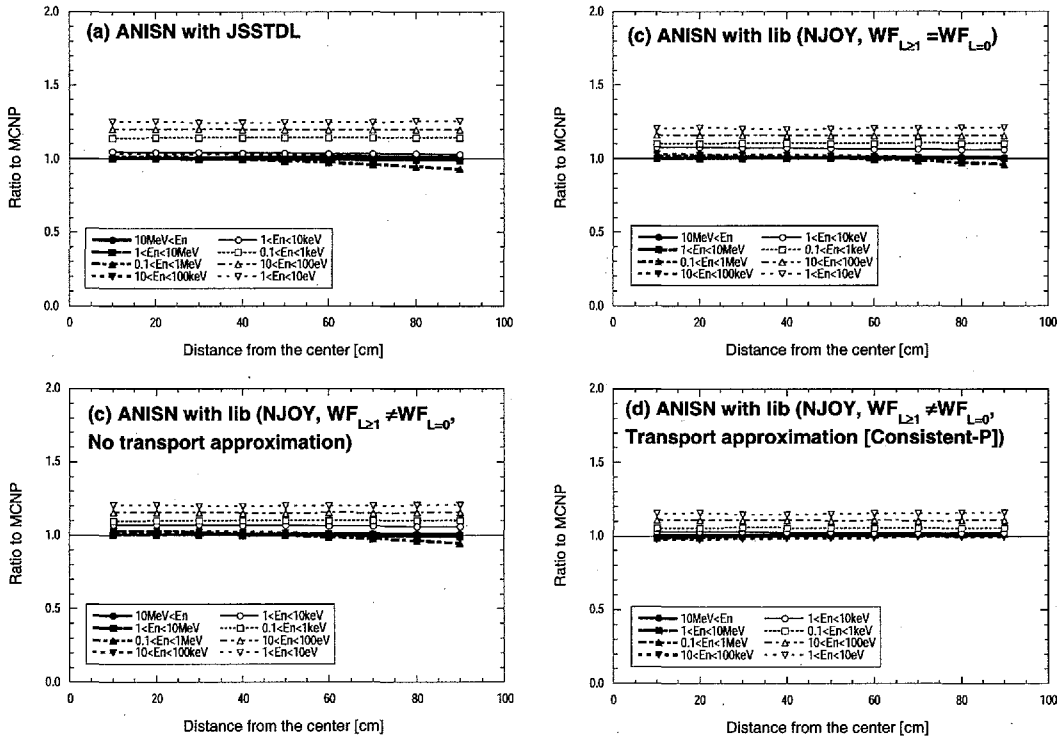

Fig. 2 Ratio of integrated neutron fluxes calculated with ANISN to those with MCNP in aluminum sphere.

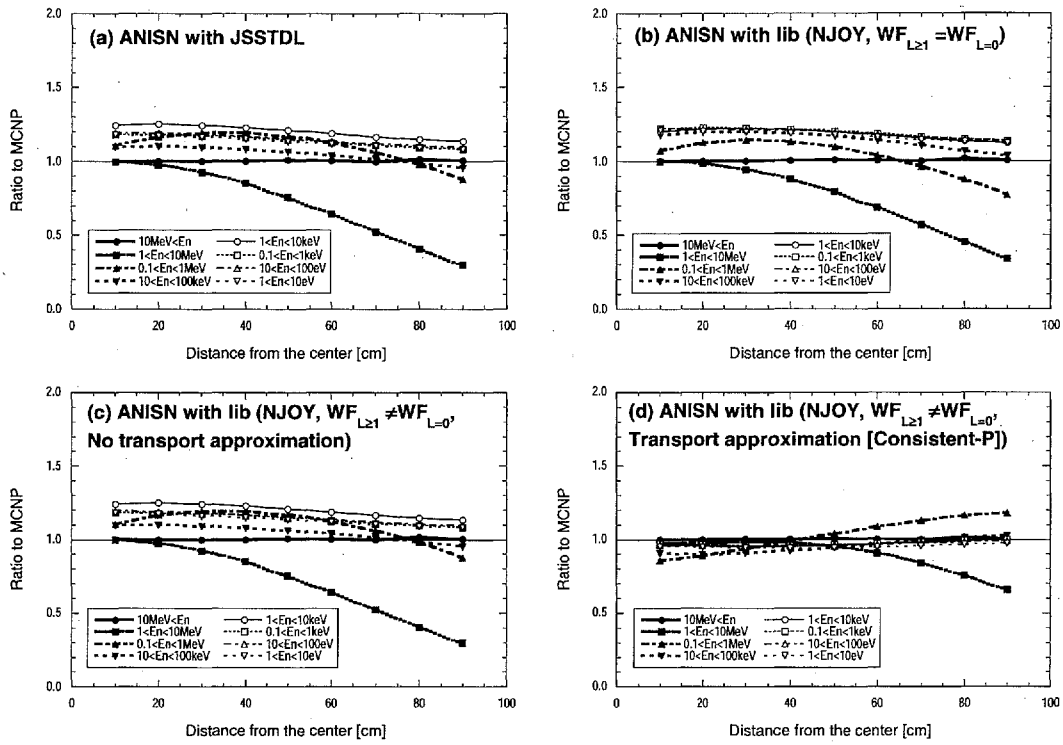

Fig. 3 Ratio of integrated neutron fluxes calculated with ANISN to those with MCNP in iron sphere.

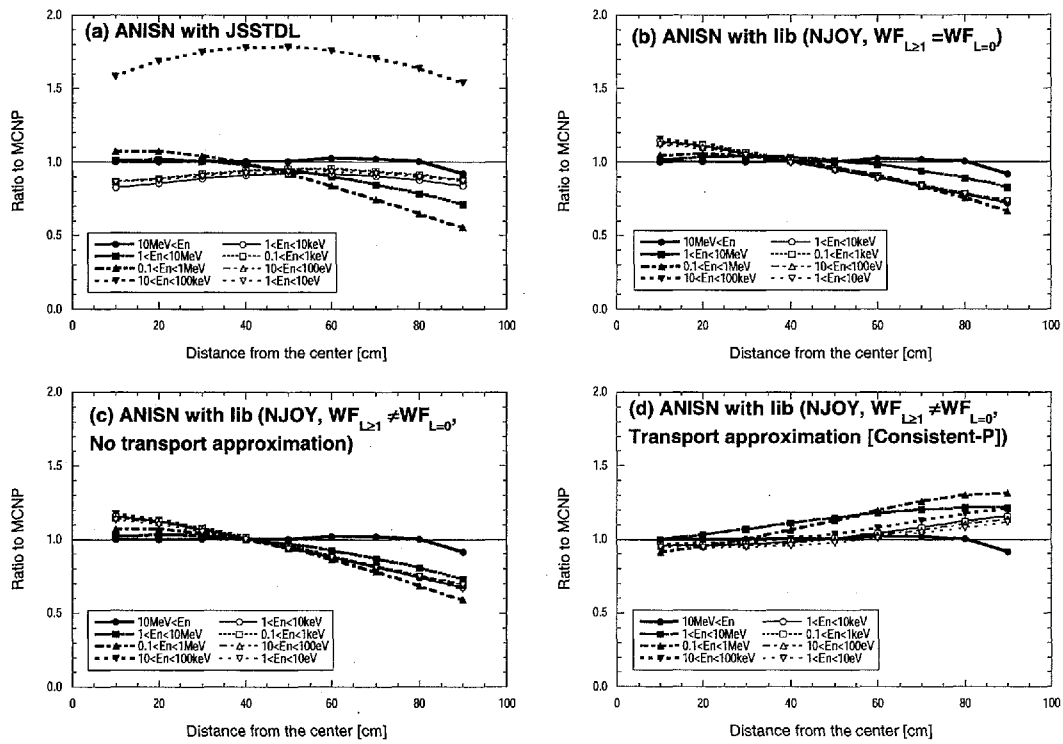

Fig. 4 Ratio of integrated neutron fluxes calculated with ANISN to those with MCNP in nickel sphere.

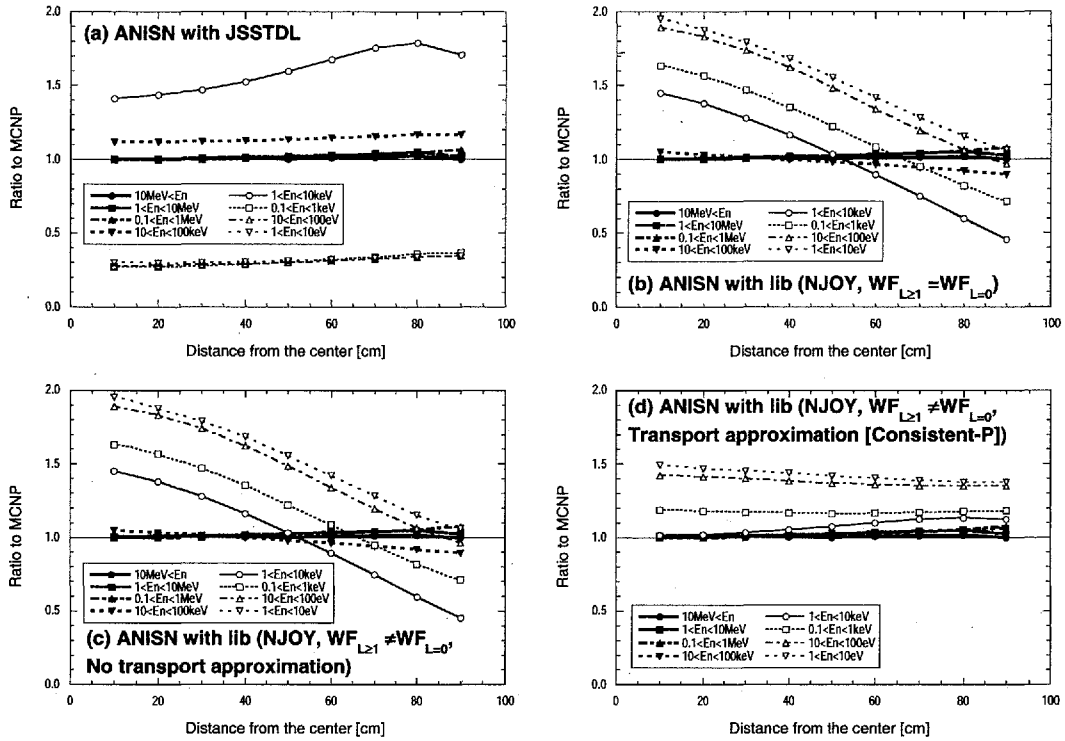

Fig. 5 Ratio of integrated neutron fluxes calculated with ANISN to those with MCNP in copper sphere.

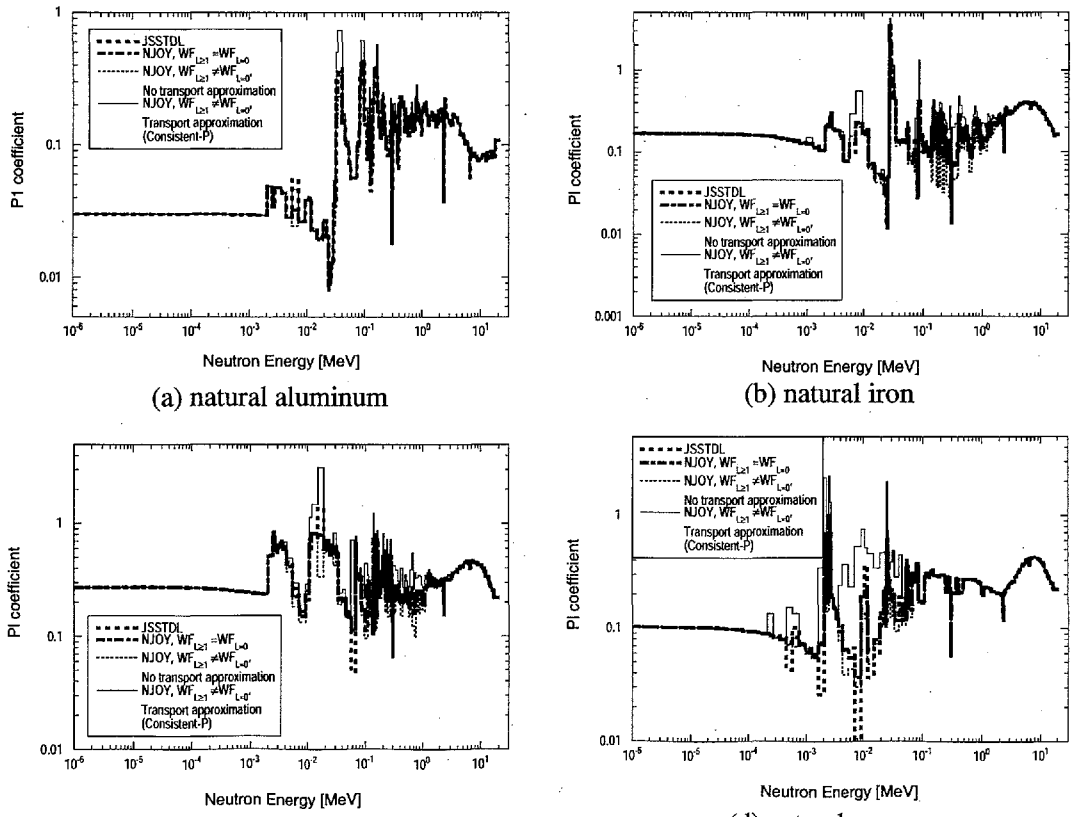

(a) natural aluminum (b) natural iron

(c) natural nickel (d) natural copper

Fig. 6 P_1 coefficients of in-group scattering matrix of the four multigroup libraries.

3.22 Comment to Unresolved Resonance Data in JENDL-3.3

Chikara KONNO
Center for Proton Accelerator Facilities, Japan Atomic Energy Research Institute
Tokai-mura, Naka-gun, Ibaraki-ken 319-1195 JAPAN
e-mail : konno@cens.tokai.jaeri.go.jp

It is found out that the self-shielding correction for the unresolved resonances of many nuclei in JENDL-3.3 is too large around the upper energy of the unresolved resonance region. Probably the average reduced neutron widths or the upper energy of the unresolved resonance region in many nuclei in JENDL-3.3 are not appropriate. All the unresolved resonance data in JENDL-3.3 should be rechecked and revised by considering self-shielding correction in the next version.

1. Introduction

JENDL (JENDL-3.1 ~ JENDL-3.3) tends to use unresolved resonance data more than other evaluated nuclear data libraries. Not only heavy nuclei such as uranium, but also fission products such as niobium in JENDL include unresolved resonance data. However, these unresolved resonance data were not often used in neutronics calculations since the previous MCNP code Could not deal with unresolved resonance data so far.

At ND2001, the international conference on nuclear data for science and technology in 2001, it was pointed out that the leakage neutron spectrum from a niobium sphere of 0.5 m in radius with a 20 MeV neutron in the center, which was calculated with ANISN [1], MCNP4C [2] (this version can treat unresolved resonance data) and JENDL-3.3 [3], had a large strange bump around 100 keV as shown in Fig. 1, which originated from self-shielding correction for the unresolved resonance data.[4] It is considered that the unresolved resonance data of ^{93}Nb in JENDL-3.3 have some problems. Causes of this phenomenon are examined in this paper.

2. Self-shielding correction for unresolved resonance region of ^{93}Nb in JENDL-3.3

In order to check cross section data of ^{93}Nb in JENDL-3.3, the following multigroup libraries of pure ^{93}Nb in JENDL-3.3 were produced with self-shielding correction of the resolved resonance region;

1) multigroup library with self-shielding correction of the unresolved resonance region,
2) multigroup library without self-shielding correction of the unresolved resonance region.

The first multigroup library was generated with the TRANSX code [5] from MATXSLIB-J33 [6]. The second multigroup library were made with the TRANSX code from a MATXS file which was produced from JENDL-3.3 with the NJOY99.67 code [7] modified for JENDL-3.3 [6] in the same condition as MATXSLIB-J33 except for skipping self-shielding correction for unresolved resonance data. These multigroup libraries include response data such as elastic scattering cross section and (n,γ) reaction cross section. Since the unresolved resonance data are given for elastic scattering and (n,γ) reaction, self-shielding correction for the elastic scattering and (n,γ) cross section data was investigated in the unresolved resonance region. Figures 2 and 3 show the elastic scattering and (n,γ) cross section data deduced from the above multigroup libraries, respectively. It is found out that the elastic scattering cross sections of ^{93}Nb with self-shielding correction have a large ramp at the upper energy of the unresolved resonance region. The self-shielding correction of elastic scattering in the unresolved resonance region is too large

around the upper energy [100 keV] of the unresolved resonance region, while that for (n,γ) reaction is small. It is considered that this large self-shielding correction around the upper energy [100 keV] of the unresolved resonance region for elastic scattering causes the large bump around 100 keV in Fig. 1.

3. Unresolved resonance data of ^{93}Nb in JENDL-3.3

Then why is the self-shielding correction too large around the upper energy of the unresolved region of ^{93}Nb in JENDL-3.3? Next the unresolved resonance data, particularly average reduced neutron widths, of ^{93}Nb in JENDL-3.3 were checked. The average reduced neutron widths of ^{93}Nb in JENDL-3.3 are the following,

$\overline{\Gamma}^{0}_{n,l=0,j=4}$ = 0.0085323 eV at 7 ~ 100 keV,
$\overline{\Gamma}^{0}_{n,l=0,j=5}$ = 0.006981 eV at 7 ~ 100 keV,
$\overline{\Gamma}^{0}_{n,l=0,j=4}$ = 0.1832 eV at 7 ~ 100 keV,
$\overline{\Gamma}^{0}_{n,l=0,j=4}$ = 0.14249 eV at 7 ~ 100 keV,
$\overline{\Gamma}^{0}_{n,l=0,j=4}$ = 0.11658 eV at 7 ~ 100 keV,
$\overline{\Gamma}^{0}_{n,l=0,j=4}$ = 0.098646 eV at 7 ~ 100 keV.

The average reduced neutron widths are the same at both the lower energy [7 keV] and upper energy [100 keV] of the unresolved energy region. Probably the average reduced neutron widths are too large around the upper energy of the unresolved energy region. The larger average reduced neutron widths are required to reproduce average elastic scattering cross sections in the unresolved resonance region, but they case larger self-shielding correction.

Another view is also considered. The upper energy of the unresolved resonance region for all fission products is impartially set to 100 keV in JENDL. The upper energy [100 keV] of the unresolved resonance region may be too small.

The average reduced neutron widths and/or the upper energy of the unresolved resonance region of ^{93}Nb in JENDL-3.3 should be revised.

4. Other nuclei with unresolved resonance data in JENDL-3.3

Do other nuclei with unresolved resonance data in JENDL-3.3 have the same problem as ^{93}Nb? The elastic scattering cross sections with self-shielding correction for each nuclei [100 % abundance] with unresolved resonance data in JENDL-3.3 were deduced with TRANSX from MATXSLIB-J33 and plotted. As a result, it is found that elastic scattering cross sections in many nuclei have a similar strange ramp at the upper energy of the unresolved resonance region as shown in Figs. 4 and 5. Table 1 summarizes all the nuclei with unresolved resonance data in JENDL-3.3 and the nuclei which have the same problem as ^{93}Nb.

5. Summary

Causes for a strange bump around 100 keV appeared in calculated leakage neutron spectra from a niobium sphere of 0.5 m in radius with a 20 MeV neutron in the center were examined. As a result, it is found out that the self-shielding correction for the unresolved resonances is too large around the upper energy of the unresolved resonance region in ^{93}Nb of JENDL-3.3 . The following reasons for this problem are pointed out.

1) The average reduced neutron widths are larger around the upper energy of the unresolved resonance region.

and/or

2) The upper energy of the unresolved resonance region are smaller.

The above problem appears for many nuclei with unresolved resonance data in JENDL-3.3. All the unresolved resonance data in JENDL-3.3 should be rechecked and revised by considering self-shielding correction in the next version.

This time I focused on JENDL-3.3, but probably other nuclear data libraries such as ENDF/B-VI also have the same problem for unresolved resonance data as JENDL-3.3. In the near future unresolved resonance data of other nuclear data libraries will be investigated.

Acknowledgments

The author gratefully acknowledges helpful discussions with Dr. T. Nakagawa and Dr. K. Okumura, Japan Atomic Energy Research Institute. He also thanks to members of the Shielding Integral Test Working Group in Japanese Nuclear Data Committee. This work was supported in part by Research Committee on Adequacy of Radiation Shielding in Atomic Energy Society of Japan.

References

[1] DOORS3.2 : One, Two- and Three-Dimensional Discrete Ordinates Neutron/Photon Transport Code System, RSICC CODE PACKAGE CCC-650 (1998).
[2] Briesmeister J.F.(Ed.) : LA-13709-M (2000).
[3] Shibata K., et al. : J. Nucl. Sci. Tech. 39, 1125 (2002).
[4] Konno C., et al. : J. Nuc. Sci. Tech, Supplement 2, 1037 (2002).
[5] MacFarlane R.E. : LA-12312-MS (1993).
[6] Kosako K., et al. : JAERI-Data/Code 2003-011 (2003).
[7] MacFarlane R.E. and Muir D.W. : LA-12740-M (1994).

Table 1 Nuclei with unresolved resonance data in JENDL-3.3.

As-75, Se-74, -76, -77, -78, -79, **-80, -82,** Br-79, **-81, Kr-78, -80, -82, -83, -84, -85, Rb-85, -87, Sr-86, -87, -89, -90, Y-89, -91, Zr-91, -92, -93, -94, -95, Nb-93, -94, -95, Mo-92, -94, -95,-96, -97, -98, -100,** Tc-99, **Ru-96, -98, -99, -100, -101, -102, -103, -104, -106,** Rh-103, -105, **Pd-102, -104, -105, -106,** -107, **-108, -110,** Ag-107, -109, **Cd-106, -108, -110, -111, -112,** -113, **-114,-116,** In-113, -115, **Sn-112, -114, -115, -116, -117, -118, -119, -120, -122, -123, -124, -126, Sb-121, -123,** -124, **-125, Te-120, -122,** -123, **-124,** -125, **-126, -128, -130,** I-127, **-129, -131,** Xe-124, **-126, -128,** -129, **-130,** -131, **-132,-133, -134, -135,** Cs-133, -134, **-135, -136, -137,Ba-130,** -132, **-134,** -135, **-136,** -137, **-140,** La-138, **-139,** Ce-141, **-142, -144, Pr-141, -143, Nd-142, -143, -144, -145, -146,** -147, **-148, -150, Pm-147,** -148, **-149, Sm-144, -147, -148,** -149, **-150,** -151, **-152,** -153, **-154,** Eu-151, -152, -153, -154, -155, **-156, Gd-152, -154,** -155, **-156,** -157, **-158, -160,** Tb-159, Er-167, Hf-174, -176, -177, **-178,** -179, **-180,** Ta-181, Pa-231,-233, U-233, -234, -235, -236, -237, -238, Np-237, Pu-236, -238, -239, -240, -241, **-242,** Am-241, -242, -243, **Cm-240,** -241, **-242,** -243, **-244,** -245, **-246,** -247, **-248, -249, -250,** Bk-249, -250, Cf-249, **-250, -252**

Bold : Strange ramp appears in the elastic scattering cross section.

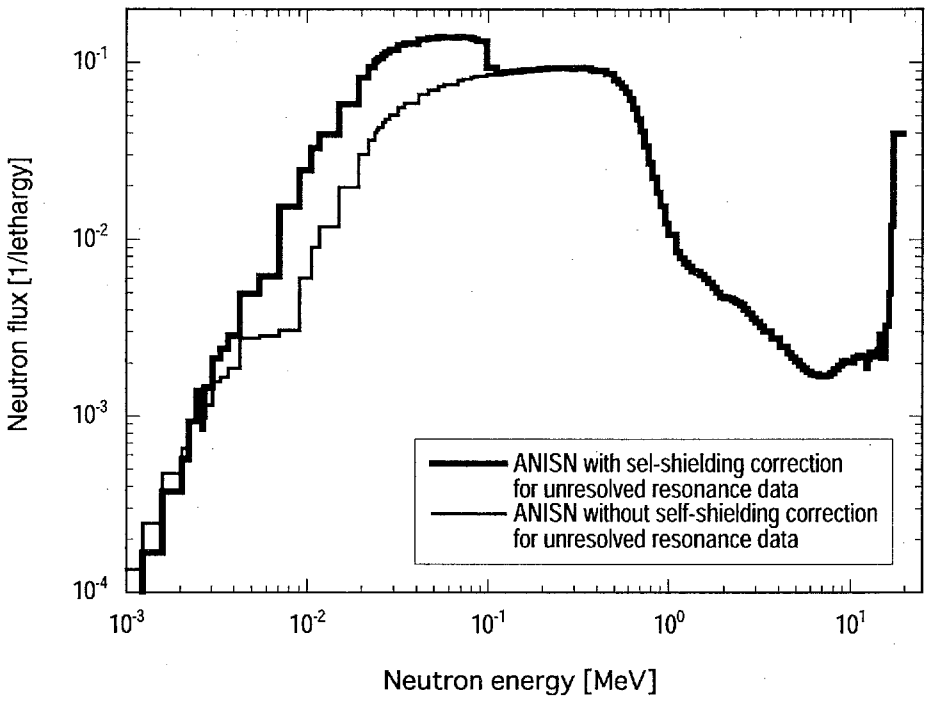

(a) ANISN calculation

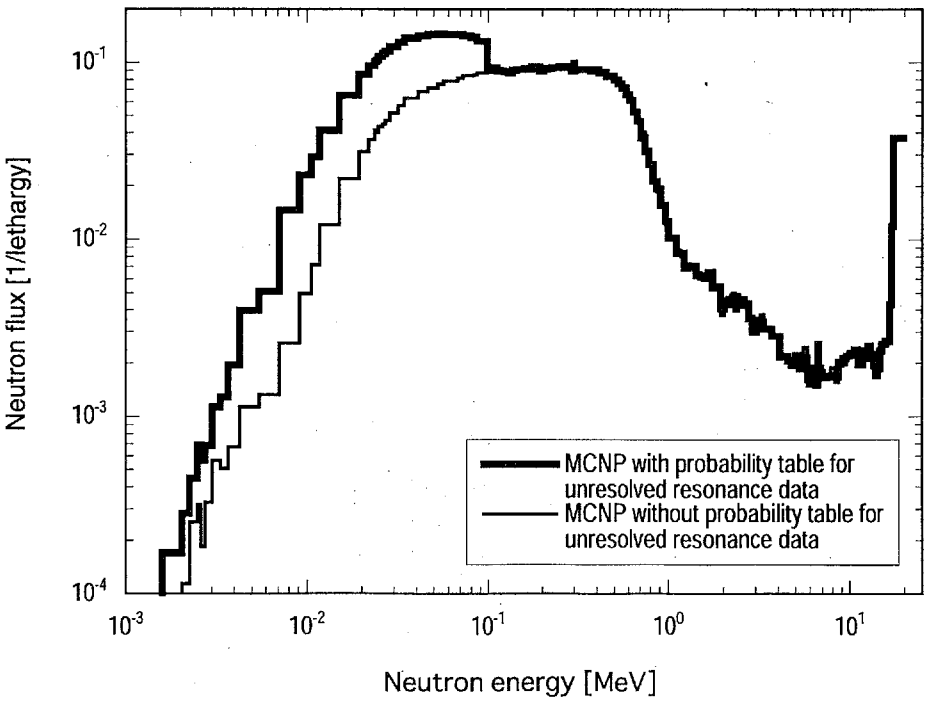

(b) MCNP calculation

Fig. 1 Calculated leakage neutron spectra from a niobium sphere of 0.5 m in radius with a 20 MeV neutron in the center.

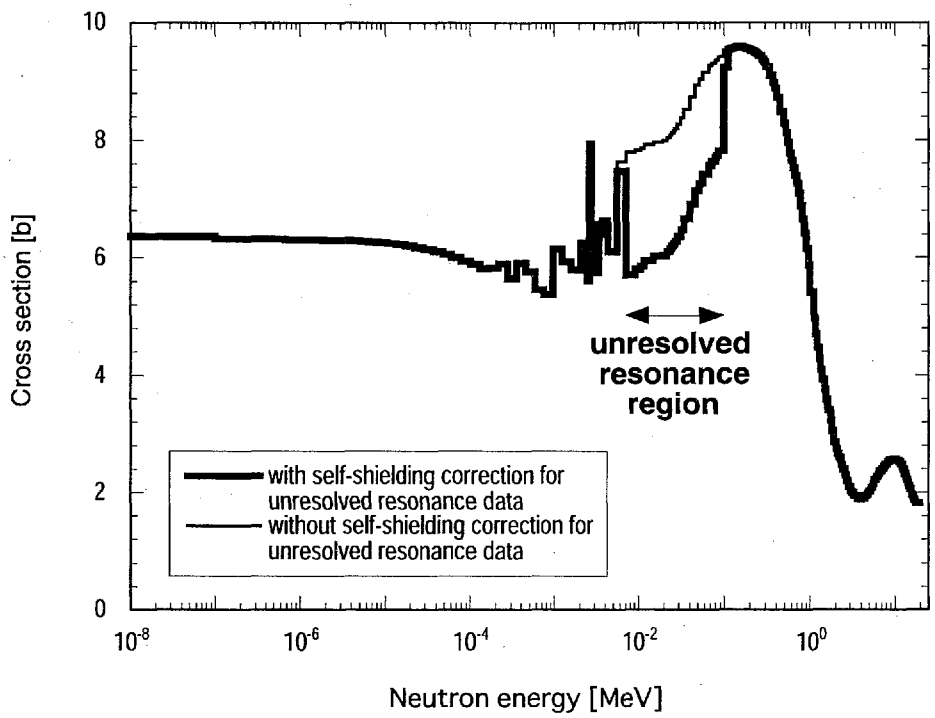

Fig. 2 Self-shielding corrected elastic scattering cross section of ^{93}Nb in JENDL-3.3.

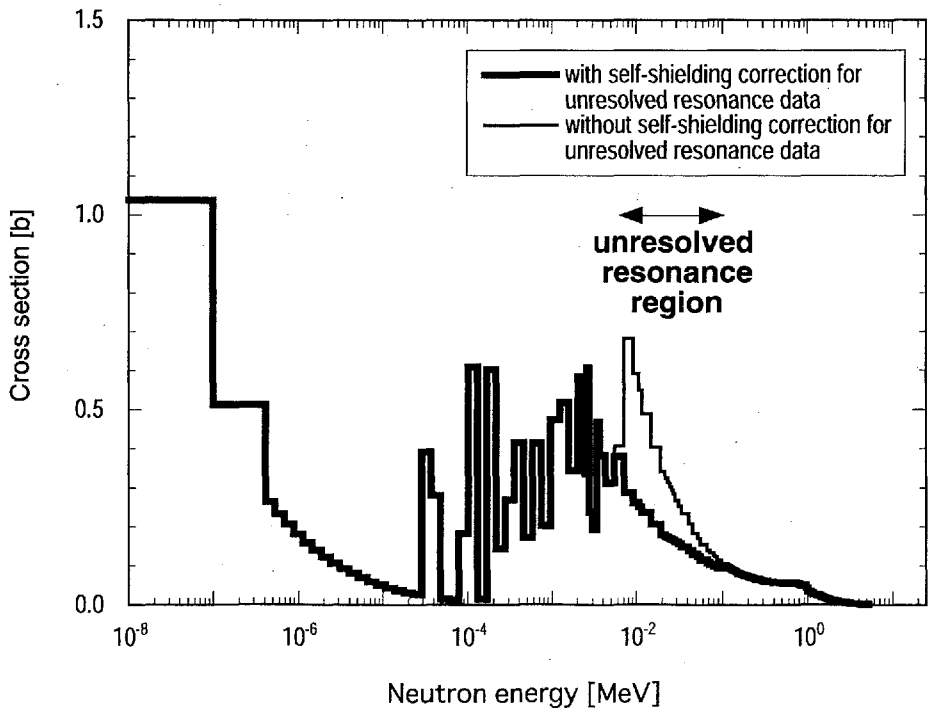

Fig. 3 Self-shielding corrected (n,γ) cross section of ^{93}Nb in JENDL-3.3.

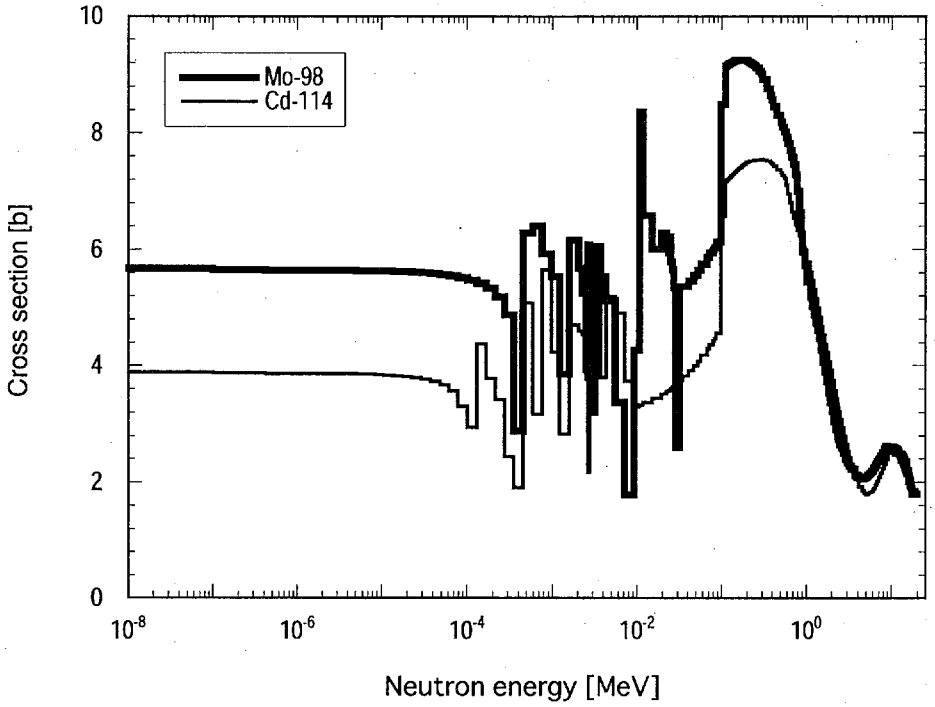

Fig. 4 Self-shielding corrected elastic scattering cross section of ^{98}Mo and ^{114}Cd in JENDL-3.3.

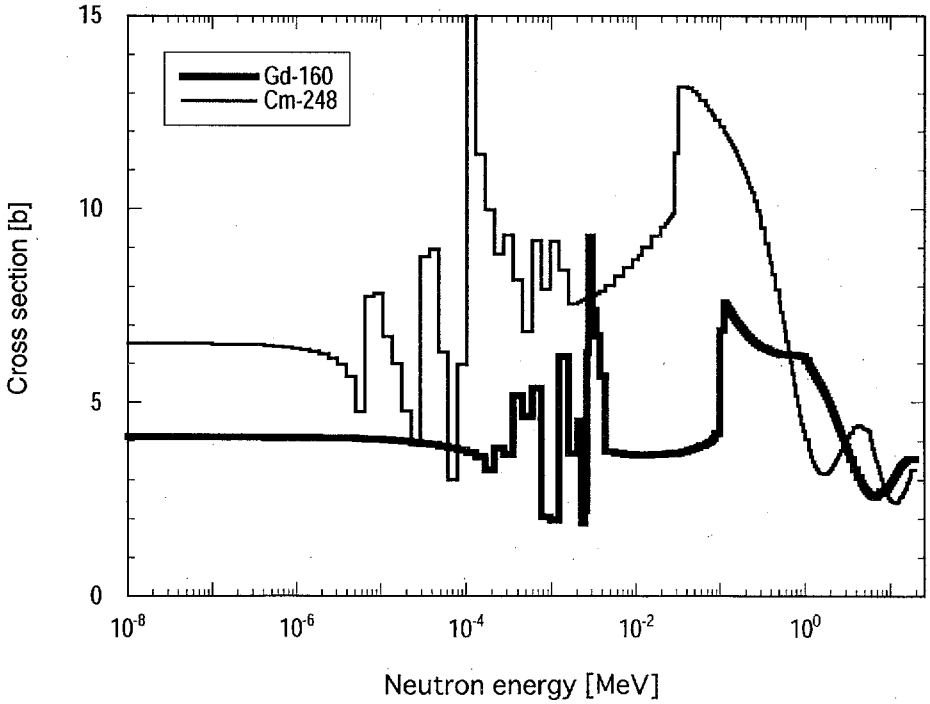

Fig. 5 Self-shielding corrected elastic scattering cross section of ^{160}Gd and ^{248}Cm in JENDL-3.3.

JP0450513

JAERI－Conf 2004－005

3.23 Cross Section Model and Scattering Law of Liquid Water for Design of a Cold Neutron Source

Yoshinobu EDURA[1], Seiji TASAKI and Nobuhiro MORISHIMA

Department of Nuclear Engineering, Kyoto University, Yoshida, Sakyo-ku, Kyoto 606-8501, Japan
E-mail: edura@nucleng.kyoto-u.ac.jp

Abstract: A cross section model for cold neutron scattering in light water is developed, which describes various molecular motions inherent to hydrogen-bonded water molecules especially in terms of jump- and rotational-diffusion processes. Inter- and intra-molecular vibrations are also included. A systematic analysis is performed of a velocity autocorrelation function, a generalized frequency distribution and double-differential and total cross sections. Good agreement with the results of computer molecular dynamics and neutron scattering experiments is found. A wide range of cross section evaluation for neutron energies from 0.1 μeV to 10 eV and liquid temperatures between the melting and boiling points is performed. This permits us to generate such low-energy neutron cross section libraries as group constants set and scattering law for ultra-cold, very-cold, cold and thermal neutrons. Together with the libraries for liquid ^{4}He, H_2, D_2 and solid and liquid CH_4, a powerful tool for design of an advanced low-energy neutron source is now ready for use.
Keywords: Light water, Molecular dynamics, Cross section, Scattering law, Cold neutron, Thermal neutron, Neutron source.

1 Introduction

Cold (~ 1 meV) and thermal (~ 25 meV) neutrons are expected to be useful in studying microscopic structures and molecular dynamics of various materials such as soft condensed matters, bio-molecules, super-conductors and industrial products. To utilize these neutrons actually, a spallation neutron source is being constructed in Japan, USA and Europe. High-energy (~MeV) neutrons generated from a spallation target must be moderated to thermal and cold neutrons with an optimized hydrogenous material like light water (H_2O), liquid H_2 and solid CH_4. Hence neutronic properties of such moderators need to be studied especially in terms of scattering and slowing-down processes. The present paper is devoted in this direction. A cross section model for neutron scattering in liquid water is devolped, which is applicable to a wide range of incident neutron energy from 0.1 μeV (ultra-cold) to 10 eV (epi-thermal) and all practical temperatures between melting and boiling points.

Another purpose of the present paper is to describe water-molecule dynamics in terms of hydrogen-bonding properties and related various relaxation processes on the molecular translations and rotations

[1] Corresponding author.

in a wide time scale from ~0.001 to ~100 ps. A set of characterizing functions such as a velocity auto-correlation function, an intermediate scattering function and a dynamical scattering law is systematically calculated. These are necessary for a physical and unified interpretation of neutron-scattering and molecular-dynamics results.

In Sec. 2, a brief description is given of the double-differential cross section model of light water. Sec. 3 discusses many cross-section results, both double-differential and total, by comparison with available experimental results at various practical temperatures. Sec. 4 is devoted to the generation of group-constants set and scattering law. Some concluding remarks are given in Sec. 5.

2 Cross Section Model

The physical properties of liquid water are especially anomalous at low temperatures, for instance, as is the case with H_2O showing the maximum density at 4 °C, the minimum isothermal compressibility at 46 °C, non-Arrhenius behavior of the self-diffusion coefficient, and so on. For this complexity of water, a theoretical model of water dynamics remains to be developed. On the other hand, recent scattering experiments with light, X-ray and neutron are being characterizing the structure and dynamics of water at the microscopic level. In particular, neutron scattering is applied to study the translational and rotational motions of water molecules in the hydrogen-bond network with a finite lifetime. More recently, computer molecular-dynamics simulations have served for the interpretation of experimental results in terms of effective potentials of water molecule and various transport properties of liquid water.

The present paper aims at developing an accurate model of water based on the newly available experimental data and computer simulation results. The main object is twofold, i.e. to interpret systematically the data in an energy-momentum domain and the results in a space-time domain, and to generate a cross-section library for design of a low-energy neutron source. This requires the model to be capable of quantitative treatment in a wide range of the above-mentioned domain. At present, attention is paid to light water (H_2O) as an incoherent scatter showing individual motions of water molecule. The following features for molecule dynamics are taken into account:

- A water molecule is hindered in translational motion by a hydrogen-bond network formed intermittently with an average residence time having strong temperature dependence.
- Translational diffusion and vibration are repeated as a jump diffusion process [1]. The former is characterized with the self-diffusion constant at given temperature, while the latter vibration is due to an intermolecular motion with bending and stretching modes.
- Rotational motions of molecule are consisting of two parts, i.e. a rotational diffusion process with a large relaxation (reorientational) time having an Arrhenius behavior [2], and a hindered rotation with the librational band centered around 65 meV on account of intermolecular coupling with surrounding molecules.
- Intramolecular vibrations with bending, stretching and asymmetric stretching modes are also included.
- These motions tend to behave as free gases of H and O at a very-short time scale of, say, 0.001 ps, which is required to reproduce a free-atom cross section for an epithermal neutron.

All these dynamics are described in an explicit form by a velocity auto-correlation function $\phi(t)$ and, equivalently, a generalized frequency distribution function $D(\omega)$. Their changes in liquid temperature are involved with translational and rotational diffusion coefficients, a residence time, a reorientational time and so on. Once $\phi(t)$ or $D(\omega)$ has been constructed, a space-time density correlation function $G_s(r,t)$ for individual motions can be obtained readily by the Gaussian approximation. Also the analytical Fourier transform of $G_s(r,t)$ with respect to r yields an intermediate scattering function

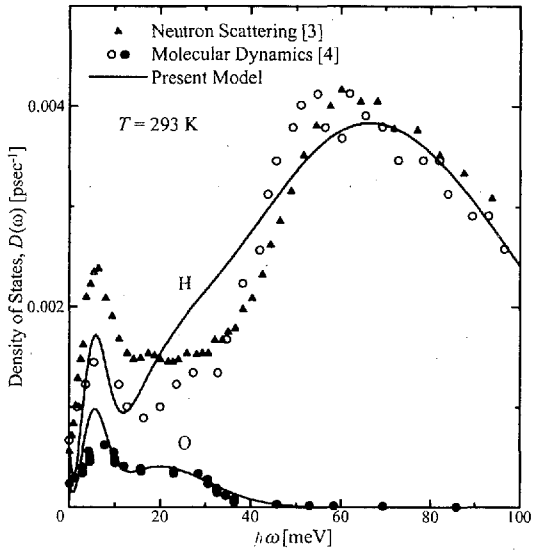

Fig. 1: Behavior of $D(\omega)$ for water at 293 K.

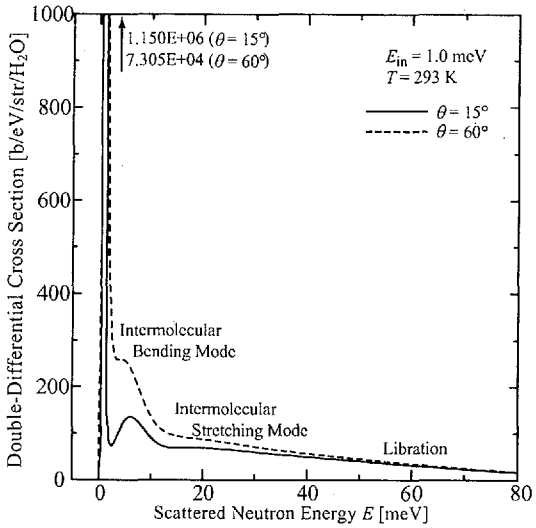

Fig. 2. Behavior of $d^2\sigma_s/d\varepsilon dQ$ for water at 293 K with E_0 = 1.0 meV and θ = 15° and 60°.

$F_s(Q,t) = \exp[-Q^2W(t)/2]$ where Q is the momentum transfer as $Q\hbar$ and $W(t)$ is the width function as a mean squared displacement of molecule during t. By the numerical Fourier transform of $F_s(Q,t)$ with respect of t ranging from ~0.001 to ~100 ps, various scattering cross sections can be determined: a scattering law

$$S_s(Q,\omega) = \frac{1}{2\pi}\int F_s(Q,t)\exp(-i\omega t)\,dt \tag{1}$$

$$= 2S_{H,s}(Q,\omega) + \left(\frac{b^2_{O,inc} + b^2_{O,coh}}{b^2_{H,inc} + b^2_{H,coh}}\right)S_{O,s}(Q,\omega), \tag{2}$$

a double-differential cross section

$$\frac{d^2\sigma_s}{d\varepsilon dQ} = \frac{1}{\hbar}\left(b^2_{H,inc} + b^2_{H,coh}\right)\frac{k}{k_0}S_s(Q,\omega), \tag{3}$$

by the incoherent approximation, an angular distribution $f(\theta)$ and a total cross section $\sigma_t(E_0)$ where $\varepsilon = \omega\hbar$ is the energy transfer and θ is the scattering angle, E_0 is the neutron incident energy, k_0 and k are the wavenumbers of incident and scattered neutrons, respectively.

3 Molecular Dynamics and Scattering Results

Fig. 1 shows $D(\omega)$ as a function of ε, together with the those by experiment [3] and molecular dynamics [4]. The one for H has a dominant component around 60 meV by the hindered rotation of molecule and a lower-energy component consisting of the translational diffusion near 0 meV and the translational stretching and bending vibrations around 6 and 20 meV. The one for O, however, indicates mainly the motions of center-of-mass in terms of translational stretching and bending vibrations. Intramolecular vibrations with the characteristic energies of 200 and 463 meV are beyond the energy range shown. It is also to be noted that $\phi(t)$ and $F_s(Q,t)$ are found to be consistent with the recent molecular-dynamics results [5] at many different temperatures.

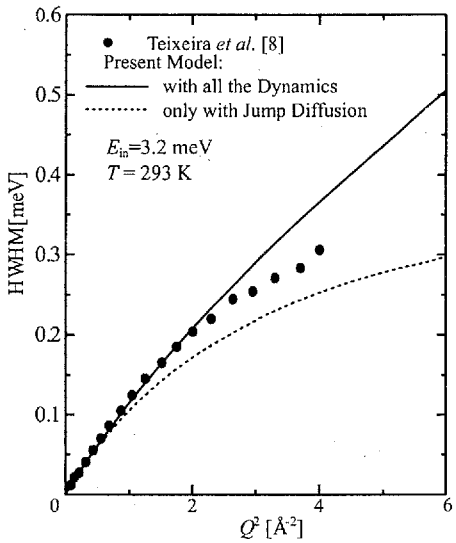

Fig. 3. The half-width at half maximum for the quasi-elastic scattering in water at 293 K with E_0 =3.2 meV.

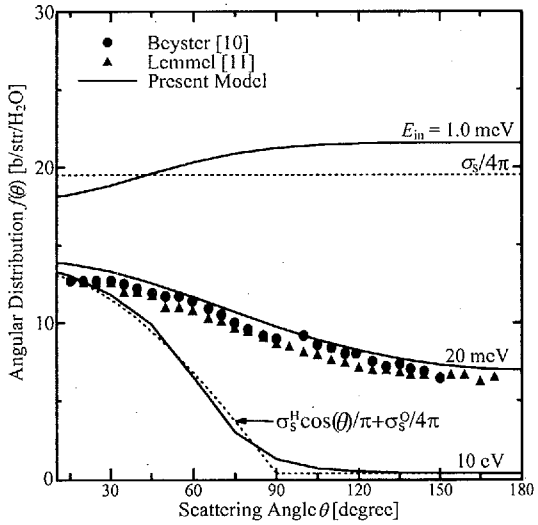

Fig. 4. Behavior of $f(\theta)$ for water at 293 K with E_0 = 1 meV, 20 meV and 10eV.

Fig. 2 shows $d^2\sigma_s/d\varepsilon dQ$ of light water at 293 K for θ = 15° and 60° with E_0 = 1 meV. They are composed of two components: a very high and sharp peak by quasi-elastic scattering due to the jump and rotational diffusion processes and a relatively broad peak by inelastic up-scattering arising from the de-excitation of intermolecular vibrations and hindered rotations. With an increase in θ, the quasi-elastic peak becomes broad and small to overlap the inelastic peak. Comparison with the experimental results [6, 7] for water at 299 K with E_0 = 5, 151 and 304 meV is satisfactorily made.

Fig. 3 shows the half-width at half-maximum for the quasi-elastic peak of water at 293 K as a function of Q^2. Also shown is the experimentally-estimated results for the quasi-elastic component extracted from the data [8]. The solid line includes all the dynamics modes while the broken line with only the jump diffusion process. Consequently, the latter is relatively similar in saturation behavior with the experiment. Such an analysis is performed successfully in comparison with those on neutron scattering at many different temperatures [6, 9].

Fig. 4 shows $f(\theta)$ for the three different E_0, compared with the experimental results [10, 11]. For a 10-eV neutron, forward scattering in a free H is significant. On the contrary, a 1-meV neutron scatters nearly isotropically though a backward up-scattering is slightly seen by the de-excitation of intermolecular vibrations and librations. The result of a thermal neutron indicates a mid-behavior between the above extremes.

4 Group Constant and Scattering Law

As a powerful tool for the design assessment of practical cold neutron sources, a set of group constants for liquid water is generated. Light water at 5, 27, 52 and 77 °C is evaluated by using the cross section model. The energy range from 0.1 μeV to 10 eV is divided at equal logarithmic (lethargy) intervals into 80 groups. The angular distribution of scattering cross section is represented by the Legendre expansion up to a maximum order 3 which is almost adequate for reproduction of forward scattering in free atoms, H and O, by an epithermal neutron. The weighting flux is a Maxwellian plus $1/E$ spectrum with the same temperature as water.

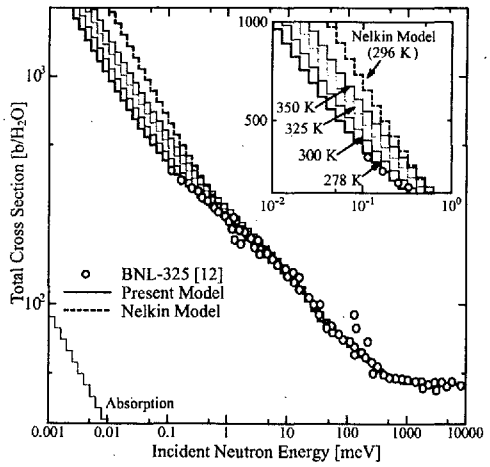

Fig. 5. Behavior of σ_t and σ_a for water at 278, 300, 325 and 350 K.

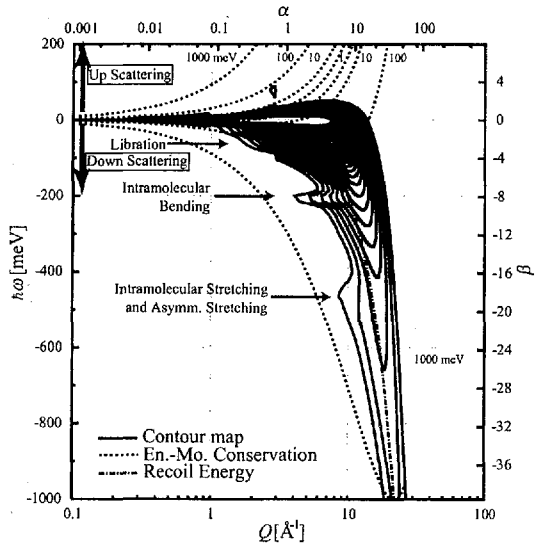

Fig. 6. Contour map of $S_{H,s}(Q,\omega)$ for water at 293 K.

Fig. 5 shows the group-constant results of σ_t and total absorption cross section σ_a for water at four different temperatures. Also shown are the experimental results from BNL-325 [12] and the ones by the Nelkin model at 296 K [13]. With an increase in T, up-scattering at lower energies below about 1 meV becomes significant, while σ_t approaches a free atom cross section of 44.6 b/H_2O at energies above about 1 eV. It can be seen from Fig. 5 that there are good agreement with the experiment at ordinary temperature and essential difference in σ_t between liquid water and molecular gas. It may be also noted that the calculated average cosine of θ indicates a gradual transition from forward scattering to uniform one with decreasing E, which agrees well with the experimental result [10].

Along with the group constant generation, a data file of $S_s(Q,\omega)$ is created in the ENDF/B-VI format. A wide range of momentum and energy transfer is covered: $Q = 0.11$ to 35 Å^{-1} and $\hbar\omega = -10$ eV (down scattering) to 100 meV (up scattering), which correspond to α ($= \hbar^2Q^2/2m/kT$) from 0.001 to 100 and β ($= \hbar\omega/kT$) from -400 to 4, respectively, where m is the neutron mass and $kT = 25.24$ meV at 293 K. Fig. 6 shows a typical result of $S_{H,s}(Q,\omega)$ for water at 293 K. At smaller Q, the intermolecular dynamics inherent to liquid water are significant while, at larger Q, the intramolecular motions and the recoil scattering in free H atom become effective.

5 Concluding Remarks

(a) The physical properties of hydrogen-bonded liquid water have still remained unsettled especially from a microscopic viewpoint. Hence a neutron scattering study is planned to determine directly $F_s(Q,t)$ by means of a neutron spin echo (NSE) technique [14]. Temperature dependences of intermolecular modes and diffusion processes will probably be observed both for light and heavy water. Among many variations of NSE spectrometers, the Mieze type would be most suitable for this experiment, since high experimental efficiency is attainable by very short distance between water sample and neutron detector: the NSE does not need an energy analyser after the sample and instead uses the Larmor precession as an internal measure of neutron energy. At present, such inelastic and quasi-elastic scattering is now being planned using a new Mieze spectrometer to be developed at the C3-1-2-2 beam port of the JRR-3M reactor.

(b) The present cross section model makes possible the systematic interpretation of neutron-scattering and molecular-dynamics results on $\phi(t)$, $D(\omega)$, $W(t)$, $G_s(r,t)$, $F_s(Q,t)$, $S_s(Q,\omega)$, $d^2\sigma_s/d\varepsilon dQ$, $f(\theta)$ and $\sigma_t(E_0)$. A wide range of usefulness is found for neutron energies from ultra-cold (0.1 μeV) to epithermal (10 eV) neutron areas and liquid temperatures between melting and boiling points. Furthermore, a set of group constants for light water at all practical temperatures is generated. Those for heavy water will soon be ready for use [15]. By the combined use of the already-generated group constants on liquid ^{4}He, H_2, D_2 and CH_4 and also solid CH_4 [16], we may proceed to the preliminary study of an advanced low-energy neutron source on ultra-cold, very cold and cold neutrons.

Acknowledgement

The authors sincerely thank Dr. Takamasa Mori of JAERI-Tokai for his valuable information on the thermal neutron scattering library.

References

[1] K. S. Singwi, A. Sjölander, *Phys. Rev.*, **119**, 863(1960).

[2] V. F. Sears, *Can. J. Phys.*, **44**, 1999(1966) .

[3] M. -C. Bellissent-Funel *et al.*, *Phys. Rev. E*, **51**, 4558(1995).

[4] G. C. Lie, E. Clementi, *Phys. Rev. A*, **33**, 2679(1986).

[5] D. Di. Cola *et al.*, *J. Chem. Phys.*, **104**, 4223(1996).

[6] M. Sakamoto *et al.*, *J. Phy. Soc. Japan, Sup. B-II*, **17**, 370(1962).

[7] O. K. Harling, *J. Chem. Phys.*, **50**, 5279(1969).

[8] J. Teixeira *et al.*, *Phys. Rev. A*, **31**, 1913(1985).

[9] F. Cavatorta *et al.*, *J. Phys.: Condensed Matter*, **6**, A113(1994).

[10] J. R. Beyster, *Nucl. Sci. Eng.*, **31**, 254(1968).

[11] H. D. Lemmel, *Nukleonik*, **7**, 265(1965).

[12] D. I. Garber, R. R. Kinsey, *BNL-325 Vol. II*, (1976).

[13] M. Nelkin, *Phys. Rev.*, **119**, 741(1960).

[14] S. Tasaki *et al.*, *Physica B*, **335**, 234(2003); S. Tasaki *et al.*, *Physica B*, **311**, 02(2002) .

[15] N. Morishima, Y. Aoki, *Ann. Nucl. Energy*, **22**, 147(1995).

[16] Y. Abe, N. Morishima, *Nucl. Instrum. Method A*, **481**, 414(2002); N. Morishima, Y. Matsuo, *Nucl. Instrum. Method A*, **490**, 308(2002); Y. Matsuo, N. Morishima, Y. Nagaya, *Nucl. Instrum. Method A*, **496**, 446(2003); Y. Sakurai, T. Mitsuyasu, N. Morishima, *Nucl. Instrum. Method A*, **506**, 199(2003).

3.24 Nuclear data relevant to single-event upsets (SEU) in microelectronics and their application to SEU simulation

Yukinobu Watanabe, Yasuyuki Tukamoto, Akihiro Kodama, and Hideki Nakashima
Department of Advanced Energy Engineering Science, Kyushu University, Kasuga, Fukuoka 816-8580, Japan
Corresponding email: watanabe@aees.kyushu-u.ac.jp

A cross-section database for neutron-induced reactions on ^{28}Si was developed in the energy range between 2 MeV and 3 GeV in order to analyze single-event upsets (SEUs) phenomena induced by cosmic-ray neutrons in microelectronic devices. A simplified spherical device model was proposed for simulation of the initial process of SEUs. The model was applied to SEU cross-section calculations for semiconductor memory devices. The calculated results were compared with measured SEU cross-sections and the other simulation result. The dependence of SEU cross-sections on incident neutron energy and secondary ions having the most important effects on SEUs are discussed.

1. Introduction

In recent years, the radiation effects known as single-event upsets (SEUs) in microelectronics have been recognized as a key reliability concern for many current and future silicon-based integrated circuit technologies [1]. Cosmic-ray neutrons ranging from MeV to GeV are regarded as one of the major sources of the SEUs in devices used on the ground or in airplanes. A microscopic picture of the cosmic-ray induced SEUs is given as follows. Energetic neutrons interact with materials used in the devices, and light charged particles and heavy ions can be generated via a nuclear reaction with a silicon nucleus. They can give rise to local charge burst in a sub micron-size volume, which results in upsets of the memory cell information quantum. Therefore, nuclear reaction data to describe the interaction of neutrons with the nuclides contained in the devices are highly requested as a fundamental physical quantity necessary for SEU simulations. Thus, we have recently developed a cross section database for silicon, using evaluated nuclear data files (JENDL-3.3 and LA150) and QMD calculations for energies ranging from 2 MeV to 3 GeV [1]. So far, it has been applied successfully to several SEU simulations [2][3].

In the present work, we propose a simplified model of calculating SEU cross sections based on the Monte Carlo method as the first stage to apply our developed nuclear reaction database to the SEU simulation, instead of our previous BGR model [2]. Using the present model, we analyze systematic experimental data [4] for SRAM in the energy range up to 160 MeV and a simulation result [3] for DRAM up to 1GeV. In the analyses, the dependence of SEU cross sections on incident neutron energy is investigated, and the secondary ions having the most significant effect on SEUs are specified. In addition, the effect of critical charge and sensitive volume on SEU cross sections is discussed.

2. Cross section database for n+^{28}Si reaction

The JENDL-3.3 library [5] was used to obtain the double-differential cross sections (DDXs) for light charged particles (p and α) and all recoils(^{24,25}Mg, ^{27,28}Al, and ^{27,28}Si) in the

n+ ^{28}Si reaction at neutron energies between 2 and 20 MeV. The data for energies between 20 to 150 MeV were taken from the LA150 library [6] in which the DDXs of all recoils are included. We have calculated the cross sections for energies above 150 MeV using the QMD [7] plus statistical decay model (GEM [8]) calculation.

3. A simple Monte Carlo model for charge generation and collection

We consider SEU events in a simplified spherical device as shown in Fig.1. The interaction and sensitive volumes are concentric spheres with radii R_i and R_s, respectively. A nuclear reaction with Si takes place in the interaction volume, and secondary ions are generated and move in the device while slowing down. The energy deposited by a secondary ion into the sensitive volume is obtained by using SRIM code [9]. It is assumed that the whole charge (Q) generated by the ions into the sensitive volume is collected into the capacitor, and if Q is greater than the critical charge, Q_c, and then the SEU happens eventually. In this model, the initial processes of the SEU event, namely, nuclear reactions with the Si nucleus and the following charge deposition by the secondary ions, are taken into account properly, while the transport calculation of the generated charge by drift and diffusion processes is neglected and the size of the sensitive volume is introduced as a model parameter, R_s.

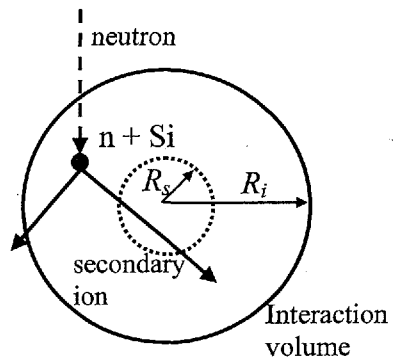

Fig.1 Schematic illustration of simplified spherical device model

Within this simplified model, the SEU cross section for incident neutron energy, E_n, is given by

$$\sigma_{SEU}(E_n) = \sum_j \sigma^j_{SEU}(E_n) = N_{Si} \sum_j \int_{r \le R_i} d\vec{r} \left[\iint_{Q>Q_c} \left(\frac{d^2\sigma_j}{dE_j d\Omega_j} \right) dE_j d\Omega_j \right], \quad (1)$$

where j denotes the kind of generated secondary ion, N_{Si} is the number density of the Si nucleus, and $(d^2\sigma_j/dE_j d\Omega_j)$ is the double-differential production cross section of the secondary ion j. In practical calculations, isotropic angular distribution is assumed for emission of the secondary ion for simplicity, therefore $(d^2\sigma_j/dE_j d\Omega_j)$ is replaced by $(d\sigma_j/dE_j)/4\pi$ in Eq.(1). This assumption represents approximately a situation where neutrons are incident into the device uniformly from any directions. The three-fold integration over the interaction volume and the energy and angle of secondary ion in Eq.(1) is made using a Monte Carlo method under a condition $Q > Q_c$. The size of the interaction volume, R_i, is determined by a condition where the calculation converges.

Using the neutron flux, $\phi(E_n)$, the cosmic-ray induced SEU rate is finally obtained by

$$\text{SEU rate} = \int \sigma_{SEU}(E_n)\phi(E_n)dE_n , \quad (2)$$

where the IBM model [10] is used for the cosmic ray flux in the present calculation.

4. Results and discussion

Figure 2 shows a comparison of the calculation with measured data [4] for SRAMs with 256Kb or 1Mb. The measured data are normalized to the data of Cypress. One can notice that the energy dependence of the measured $\sigma_{SEU}(E_n)$ is nearly similar and the magnitude alone depends strongly upon the devices. Accordingly, two parameters, Q_c and R_s, were determined

so that the energy dependence of the measured data is reproduced well and the magnitude was finally normalized to the data of Cypress. The resultant best-fit values are Q_c=53 fC and R_s=1.0 μm. The calculation with these values shows satisfactory agreement with the measured data over the whole neutron energy range. The results with different Q_c and R_c are also shown in **Fig.3** to see the sensitivities of these parameters to the calculation results. All the calculations are normalized at 40 MeV for comparisons.

In **Fig.4**, the ratio of each secondary ion to the calculated SEU cross-sections is plotted as a function of the incident neutron energy. It is found that heavy ions such as Na, Mg, and Al have a large contribution to SEU and light reaction products such as O and N become significant with increasing energy. One notices that Mg has the most significant contribution at energies below 20 MeV. This can be explained by the energy spectra of secondary ions at an incident energy of 20 MeV shown in **Fig.5**. The critical charge Q_c=53 fC corresponds to the energy deposit, E_{dep}=1.2 MeV. The energy spectra of Mg isotopes are distributed over wider energy range beyond 1.2 MeV compared with the other isotopes, and thus the cross sections of Mg integrated over the energy range become largest. This is the reason why Mg plays the most significant role below 20 MeV in SEUs for the device with Q_c=53 fC. In addition, it is found that the contribution from Si is reduced with decrease in neutron energy. This trend can be explained by the fact that the elastic and inelastic cross sections become small and their angular distributions become more forward-peaked as the neutron energy increases. It should be noted that the present results obtained by these analyses of SRAM are similar to our previous results by the BGR model [2].

Our calculation based on the present simplified model is compared with a more realistic SEU simulation [3] for DRAM with Q_c=30 fC in **Fig.6**. Both results are normalized at 40 MeV for comparison. Our nuclear reaction database was also used in the latter simulation. Both calculations show good agreement below 150 MeV, while our calculation is about 20 % smaller than the latter one above 150 MeV. This may indicate that it is enough possible to investigate the energy dependence of SEU cross sections within the framework of this simplified model, although it is limited to predict the magnitude correctly.

Figure 7 illustrates how lighter reaction products such as C, N and O have the most significant contribution at the highest incident energy of 1 GeV, while heavier reaction products such as Na, Mg, and Al are dominant at 50 MeV. To see the range effect of these secondary ions, the radial distributions of SEUs are plotted for O and Mg as a function of the distance from the center of the device at E_n=50 MeV and 1 GeV in **Fig.8**. The contribution from the outer region far from the sensitive region becomes important for light reaction products such as O. This trend is appreciable as the incident energy increases. Thus, it is found that the generation of light reaction products having the long range affects SEUs predominantly in the high incident energy range.

Finally, the cosmic-ray induced SEU rates were calculated using Eq.(2) as functions of R_s and Q_c. The result is presented in **Fig.9**. The SEU rate is reduced as R_s decreases. In the case of Q_c =0, the SEU rate is proportional to R_s^2, which corresponds to the geometrical cross section of the sensitive volume having the spherical shape. As R_s becomes smaller, the dependence of the SEU rate upon Q_c becomes strong and the SEU rate is reduced remarkably as Q_c becomes large. On the other hand, there is such a correlation that reduction of the sensitive volume size leads to that of Q_c in realistic devices. Therefore, it is expected that the slope of reduction of SEU rate against R_s does not become so steep. More realistic simulation will be necessary to discuss the device scaling effect on SEUs in details.

5. Summary and conclusions

The nuclear reaction database suitable for the neutron-induced SEU simulation was developed for incident energies ranging from 2 MeV to 3 GeV by using the evaluated nuclear data files (JENDL-3.3 and LA150) and the QMD calculation. A simplified spherical device model was proposed to simulate the initial processes, i.e., nuclear reactions and the following charge deposit by secondary ions, in the SEU phenomena. The SEU cross sections were calculated using the Monte Carlo method, by introducing the assumption that SEU occurs if the initial charge deposited by secondary ions in a sensitive volume exceeds the critical charge. The calculated results reproduced well the energy dependence of the measured SEU cross sections for energies and the other simulation result. From the analyses, it was found that heavy reaction products (Na, Mg, Al, etc.) have crucial contributions at low-incident energies but light reaction products (C, N, O, etc.) become dominant as the incident energy increases. This can be explained by the differences in the range and linear energy transfer of ions.

Nuclear reaction data for the elements except Si included in the devices (e.g., B, N, O, Al, P, Ti, Cu, As, Ta, etc.) will be also required for more detailed SEU simulations. To meet the requirement, one of our future tasks related to SEUs is an extension of the present nuclear reaction database. It is expected that this task will be accomplished in the JENDL high-energy file project [11] that is now in progress.

Acknowledgements

The authors are grateful to Mr. Y. Kawakami and Dr. M. Hane for valuable discussions about SER simulations.

References

[1] For instance, J.F. Ziegler et al., IBM J. Res. Develop. **40**, No.1 (1996); H. Ibe et al., Applied Physics, **70**, No.11, 1308 (2001) [in Japanese].
[2] T. Ikeuchi et al., J. of Nucl. Sci. and Technol., Suppl. **2**, 1380 (2002); Y. Tukamoto, Y. Watanabe, and H. Nakashima, Proc. of the 2002 Symp. on Nuclear Data, Nov. 21-22, 2002, JAERI, Tokai, Japan, JAERI-Conf. 2003-006 (2003), p. 265.
[3] Y. Kawakami et al., NEC Research & Development, **43**(2), 146 (2002).
[4] K. Johansson et al., IEEE Trans. Nucl. Sci., **45**, 2519 (1998); ibid., **46**, 1427 (1999).
[5] K. Shibata et al., J. of Nucl. Sci. and Technol. **39**, 1125 (2002).
[6] M.B. Chadwick et al., Nucl. Sci. Eng. **131**, 293 (1998).
[7] K. Niita et al., JQMD code, JAERI-Data/Code 99-042 (1999).
[8] S. Furihata, Nucl. Inst. Method in Phys. Res. B **171**, 251 (2000); S. Furihata and T. Nakamura, J. Nucl. Sci. and Technol. Suppl. **2**, 758 (2002).
[9] J.F. Ziegler, SRIM code (1999).
[10] J.F. Zieger et al., IBM J. Res. Develop. **40**, 19 (1996).
[11] T. Fukahori et al., J. of Nucl. Sci. and Technol., Suppl. **2**, 1380 (2002).

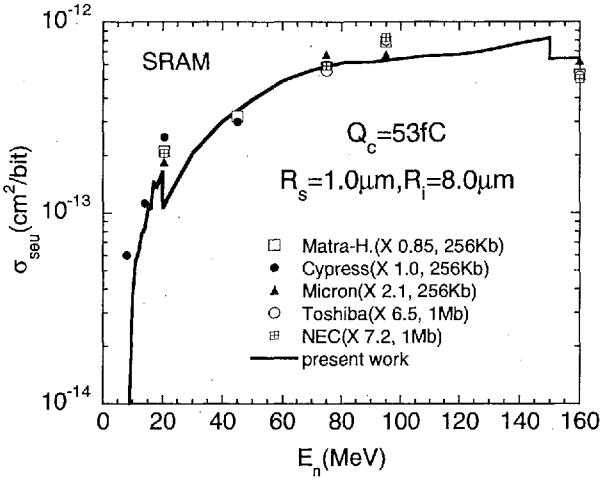

Fig.2 Comparison of calculated SEU cross sections with measured ones [4] for SRAMs. The measured data are normalized to the data of Cypress.

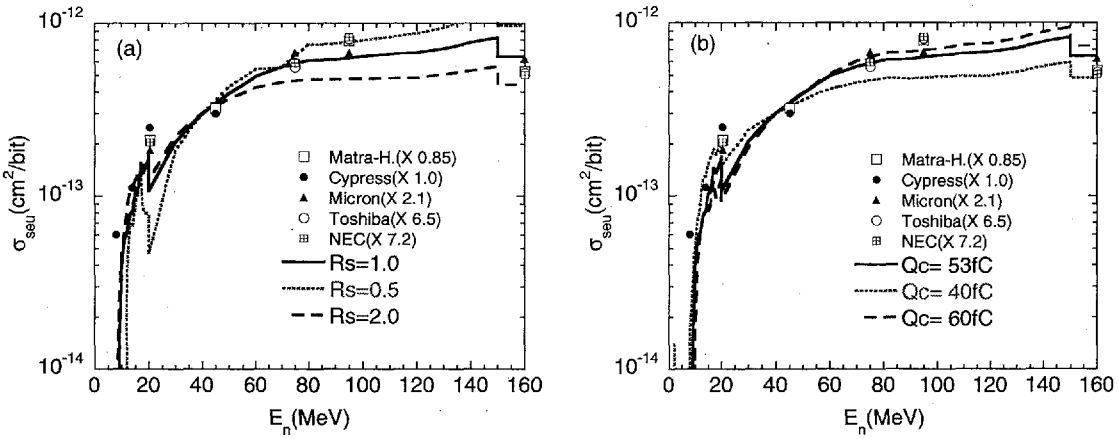

Fig.3 Same as in Fig.2, but the sensitivities of (a) R_s and (b) Q_c to the calculated results are shown.

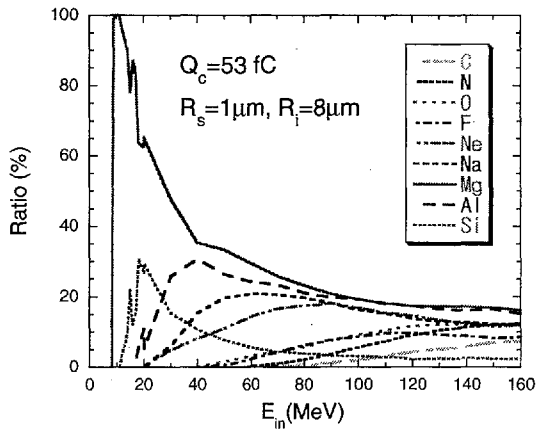

Fig.4 Ratio of each secondary ion to total SEU cross sections as a function of incident neutron energy.

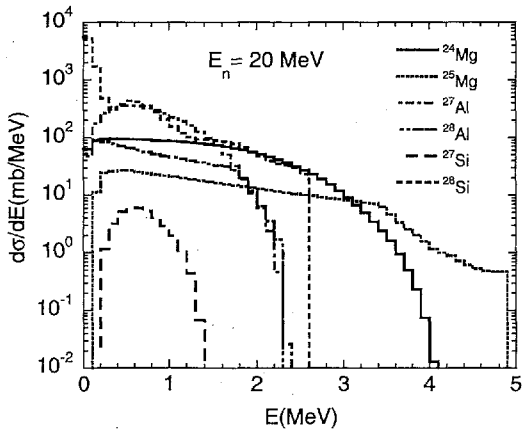

Fig.5 Energy spectra of all secondary ions for an incident energy of 20 MeV.

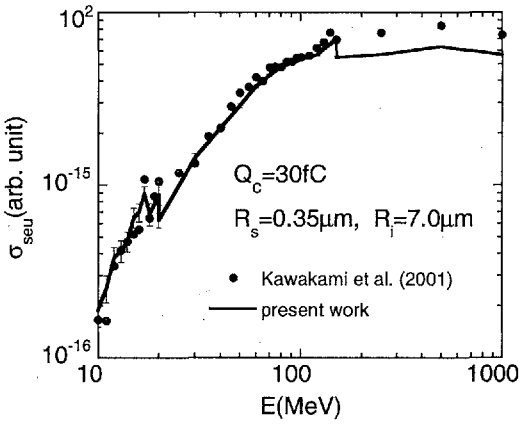

Fig.6 Comparison of calculated SEU cross sections with other simulation result [3] for a DRAM device with Q_c=30 fC. Both results are normalized at 40 MeV.

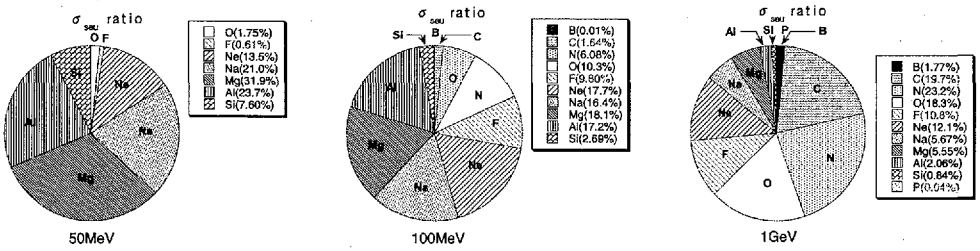

Fig.7 Ratio of each secondary ion to total SEU cross sections at E_n= 50 MeV, 100 MeV and 1 GeV for the device with Q_c=30 fC shown in Fig.6.

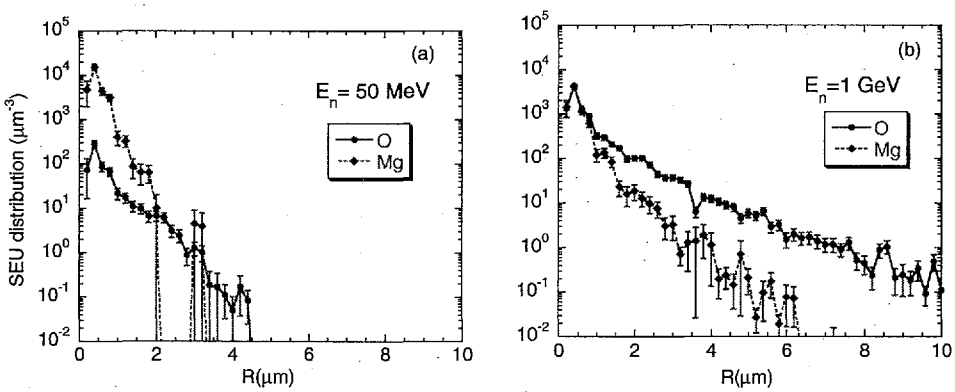

Fig.8 Radial distribution of SEUs at E_n= 50 MeV and 1 GeV for a device with Q_c=30fC and R_s=0.35μm. The error bar indicates the statistical error included in the Monte Carlo calculation.

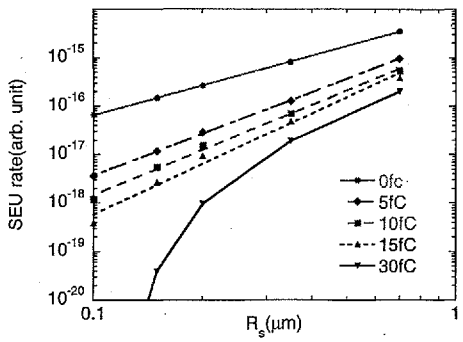

Fig.9 Sensitivities of Q_c and R_s to SEU rate

3.25 Neutron-induced semiconductor soft error simulation using the PHITS Monte Carlo simulator

Takanobu Handa[1] Koji Niita[2] Hidenori Sawamura[1]

1. *Computer Software Development Co., Ltd. (CSD)*
Konan 2-16-5-6F Minato-ku Tokyo 108-0075 Japan E-mail:handa@csd.co.jp
2. *Research Organization for Information Science & Technology (RIST)*
2-4,Shirakata,Tokai-mura,Naka-gun,Ibaraki-ken 319-1106,Japan E-mail:niita@hadron02.tokai.jaeri.go.jp

Abstract

We have performed a neutron-induced soft error simulation using the PHITS Monte Carlo simulator. We validated our technique by comparing the MBGR (Modified Burst Generation Rate) values estimated by our simulation and a well known MBGR table by Fujitsu Laboratories, Ltd. We also evaluated a neutron-induced soft error rate of a SRAM cell as a function of the critical charge as well as a representation using a generally used unit, FIT rate [error/10^9 hour/device].

1 Soft error

A charge deposition in a semiconductor memory cell by a cosmic-ray radiation causes a temporary bit information upset. This phenomenon is known as a soft error or also called as a single event upset. Cosmic-ray neutron is one of the most important source of the soft error on the ground. A neutron-nucleus interaction generates ions, protons and other particles. These ions and protons induce electron-hole pairs in a memory cell. Soft error occurs when the charge is greater than a critical charge. Figure 1 shows an image view of a soft error process. By the evolution of semiconductor manufacturing processes, soft error problem is expected to be more serious in future because of the required charge decrease for storing a bit information.

2 Cosmic rays

Protons are the main source of cosmic-rays outside of the earth. Cosmic-ray neutrons are generated by interactions between cosmic-ray protons and atmosphere. The neutron flux on the earth has been measured by IBM [1]. The measured neutron flux in Tokyo is around 12 n/cm^2/hour. Figure 2 shows the theoretical calculation of the energy distribution of cosmic-rays in New York. The best fit of the measured neutron flux distribution by IBM is shown in the equation (1) and (2) [2]. These equations are used for the neutron energy distribution input of our simulation. The flux is normalized to the neutron flux in Tokyo.

$$Flux(E) = 1.5 \times \exp(F(ln(E))) \tag{1}$$

$$F(X) = -5.2752 - 2.6043X + 0.5985X^2 - 0.08915X^3 + 0.003694X^4 \tag{2}$$

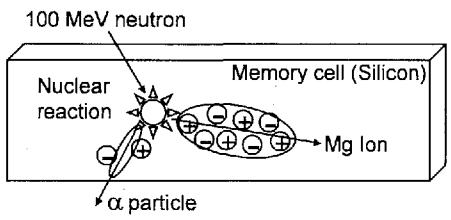

Figure 1: An image view of a neutron-induced soft error process.

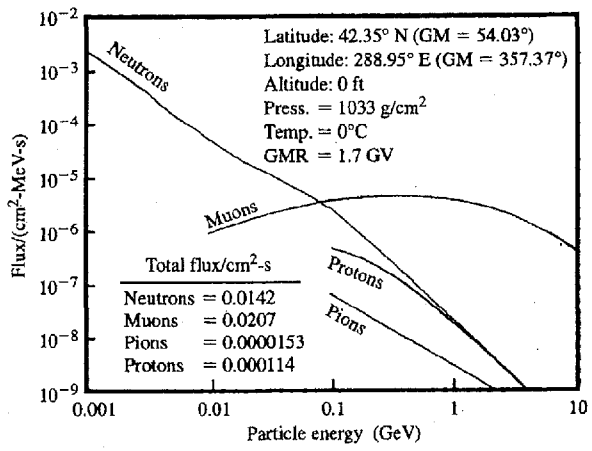

Figure 2: Theoretical energy distribution of cosmic-rays in New York city.

3 Simulation method by the PHITS Monte Carlo simulator

The soft error simulation requires high energy neutron transport up to at least 1000 MeV, neutron-nucleus reaction models, and transportation of generated heavy ions by the spallation. The PHITS Monte Carlo simulator [3] has all those functions. Especially, the implementation of a QMD (Quantum Molecular Dynamics) model is a great advantage.

PHITS is the first general purpose heavy ion transport Monte Carlo code over the incident energies from several MeV/nucleon to several GeV/nucleon. For the heavy ion transport calculation, Shen's formula, the SPAR code, and the JQMD [4] code are included. We show a concept view of the soft error simulation flow chart by the PHITS simulator in Figure 3. Neutron flux, the energy distribution, the direction, and the geometry information are the principal inputs of the PHITS simulator. PHITS outputs deposit energy distribution in the specified sensitive region. Deposit energy distributions caused by a specific particle type are also available. The induced charge is transformed from the deposit energy using the average required energy to produce an electron-hole pair, 3.6 eV/(e-h pair) [5]. For example, if the critical charge is 10 fC, corresponding deposit energy is 0.225 MeV.

4 Validation

As a validation of the PHITS simulation, we compared the MBGR (Modified Burst Generation Rate) values calculated by the PHITS and the well known MBGR table by the NISES simulator (Fujitsu) [6]. The MBGR value is an error rate of the unit volume of a sensitive layer in a memory cell as a function of the sensitive layer depth, d, and the critical charge, Q_C. The Q_C dependence of the soft error rate, SER, of the memory cell with depth d is derived as follows[6],

$$SER(d, Q_C) = MBGR(d, Q_C) \cdot N \cdot V_s \cdot C \tag{3}$$

where $MBGR(d, Q_C)$ is the burst generation rate, N is the neutron flux, V_s is the sensitive volume, and C is the collection efficiency which must usually be determined by experiment. We list the

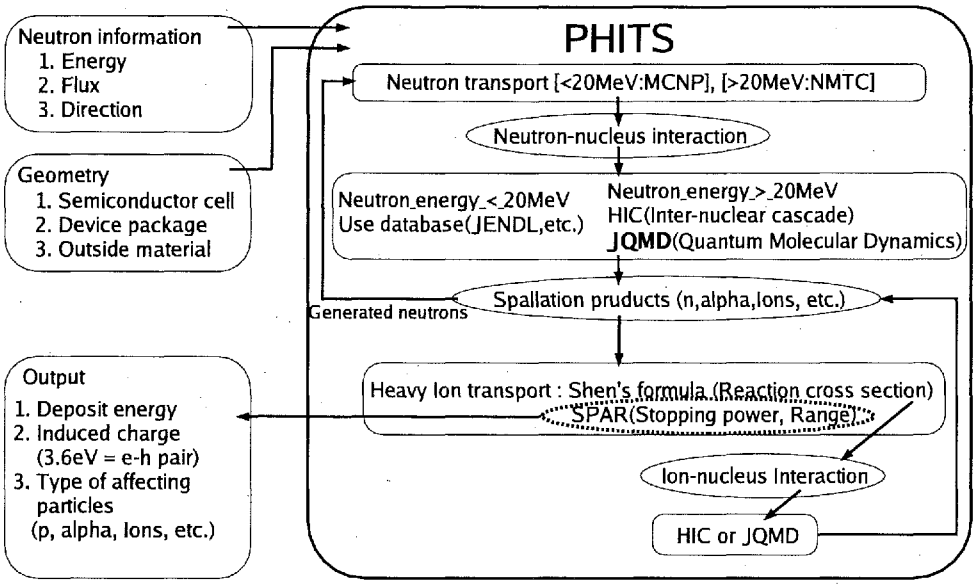

Figure 3: The concept flow chart of the soft error simulation by PHITS.

input geometry below and the schematic view is shown in Figure 4.

Geometry	:	Silicon bulk 1 mm×1 mm×30 μm
Neutron direction	:	Incident vertically in random place.
Neutron energy	:	Random following the IBM model. (10 MeV - 1000 MeV)
Sensitive layer	:	1 mm× 1 mm× (0.35 μm, 0.7 μm, 1.4 μm, 2.8 μm, 5.6 μm).
Number of incident neutrons	:	0.5 billions (5.6 μm thick) to 40 billions (0.35 μm thick)

The PHITS outputs deposit energy distribution in the sensitive region. We convert the deposit energy into the induced charge and calculate probability of events where the induced charge is greater than a critical charge. The MBGR value is derived by normalizing the error probability in a unit volume of the sensitive region. Figure 5 shows the critical charge dependence of MBGR values in every depth of the sensitive volume. Results by PHITS simulation and the MBGR table by NISES simulator are shown in the same plot. Two results by different simulators agree well and the difference is as much as only about a factor of two. Currently, publicly available MBGR value by NISES simulation is limited within the critical charge between 10 fC and 150 fC. However, in the state of the art semiconductor processes, the critical charge reaches a few fC mark. We extend the lower limit of the critical charge to 1 fC.

In Figure 5, a crossing point is seen in the MBGR plots by PHITS simulation. Plots of thicker sensitive layer and plots of thinner sensitive layer cross around the critical charge of 20 fC. This is because the major contributing particles are different depending on the deposit energy.

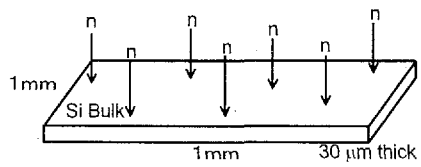

Figure 4: Schematic view of the MBGR calculation.

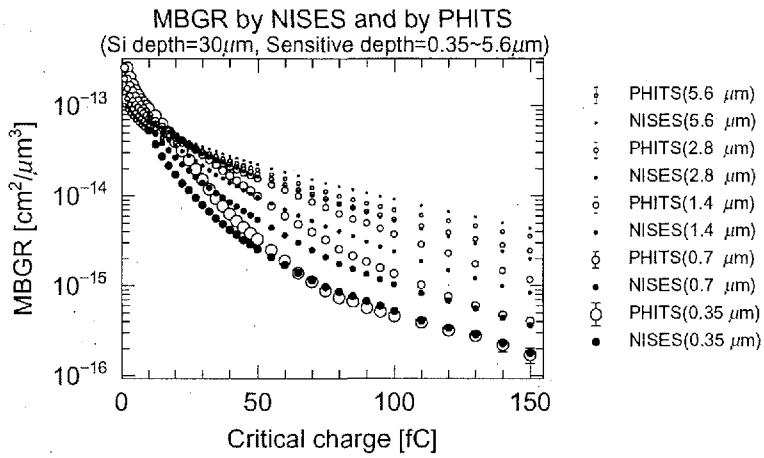

Figure 5: BGR comparison between two methods: by PHITS(CSD) and by NISES(Fujitsu).

If the critical charge is large, only heavy ions with large LET contribute energy deposit and the heavy ions stop close to the place of the nuclear interaction. The MBGR value is bigger if the sensitive layer is thicker, because 1: the probability of a nuclear interaction in the unit volume does not depend on the sensitive layer depth, and 2: the mean trajectory of heavy ions in the sensitive region is longer when the sensitive layer is thicker.

If the critical charge is small, protons are the main source of the energy deposition. The range of a proton is much longer than that of ions. For instance, the range of a 2 MeV proton is about 40 μm in the silicon. This means that the protons traveling from interactions away from the sensitive layer also contribute to the error rate. After normalizing in the unit volume, since the probability that a proton penetrates the sensitive layer does not much depend on the sensitive layer depth, the MBGR values with thinner sensitive layer is bigger when the critical charge is small. The detail of the contributing particles are shown in the next section.

5 SRAM simulation

We performed a more realistic soft error simulation by assuming a simplified SRAM cell. The geometry and the simulation conditions are as follows. The schematic view of this geometry is shown in Figure 6.

Geometry	:	Silicon bulk 40 μm × 40 μm ×40 μm
Neutron direction	:	Incident vertically in random place.
Neutron energy	:	Random following the IBM model.(10 MeV - 1000 MeV)
Neutron flux	:	12 n/cm^2/hour
Sensitive region	:	1.72 μm × 1.72 μm × 1.42 μm
Number of incident neutrons	:	40 billions.

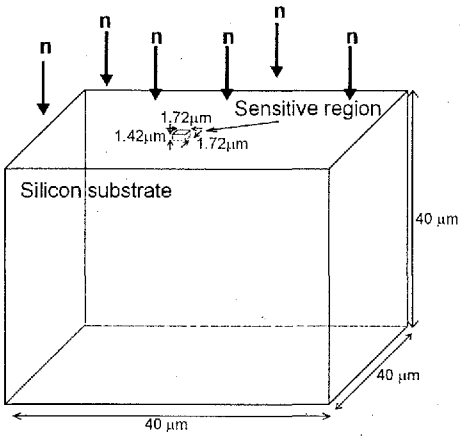

Figure 6: Schematic view of the soft error simulation of a SRAM cell.

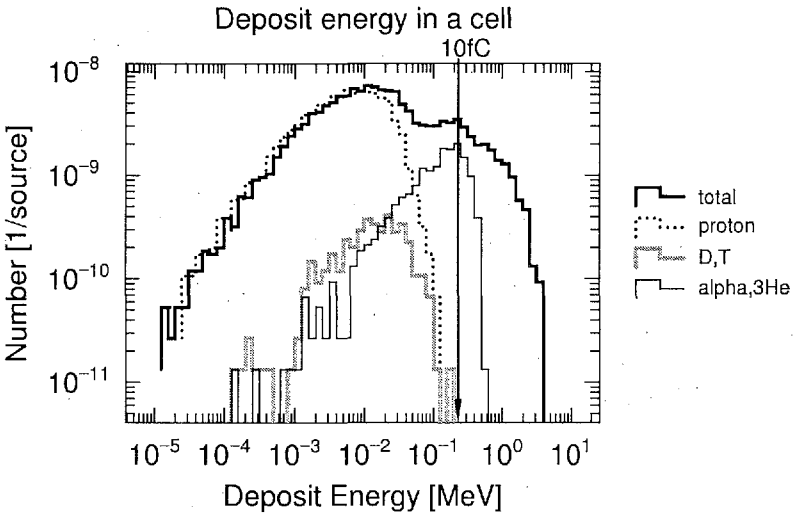

Figure 7: Deposit energy distribution in the sensitive region of a SRAM cell.

As a result of the simulation for a SRAM device, Figure 7 shows deposit energy distributions caused by some typical types of Ions as well as the distribution by all particles including heavy ions. Heavy ions dominate above the deposit energy greater than 0.6 MeV(~30 fC). Helium ions dominate around the deposit energy of 0.2 MeV(~10 fC). Below 0.1 MeV(~5 fC), hydrogen nuclei are more important, especially, protons are the critical source because of the longer range. This effect is also shown in Figure 8, an inflection point is seen at the critical charge is around 10 fC to 20 fC. In future, estimating proton behavior would be much more important for devices with smaller critical charge. Taking into account further materials around the cell will also be important because of the longer proton range.

We evaluated the error rate of a SRAM cell using similar method as MBGR calculation. In this simulation, the probability is not normalized in a unit volume. Figure 8 shows the critical charge dependence of the error rate of a cell. The unit of left axis is the error rate of a cell. The unit of right axis is the FIT rate [error/10^9 h/device] of a device with 1 M cells. For example, in case of a device with 1 M cells, if the critical charge of the device is 10 fC, the device has an error rate of 3300 FIT. If we assume that eight cells are used for storing one byte information, the result shows that a personal computer with 256M bytes memory encounters a soft error every 5 months.

In the same plot, error rate of a cell evaluated simply from MBGR values are also shown. We used equation 3 and MBGR values of the 1.4 μm depth calculated by the PHITS. The collection efficiency is assumed to be one. These two plots agree well around the critical charge is smaller than about 10 fC. Above 10 fC, the difference extends as the critical charge increases. This can be explained as follows. In the MBGR calculation, there is no boundary of the sensitive region in the direction parallel to the silicon surface. If the direction of the trajectory of a generated ion is parallel to the silicon surface, the output of the deposit energy is large. Therefore, the MBGR method tends to overestimate the probability of large deposit energy.

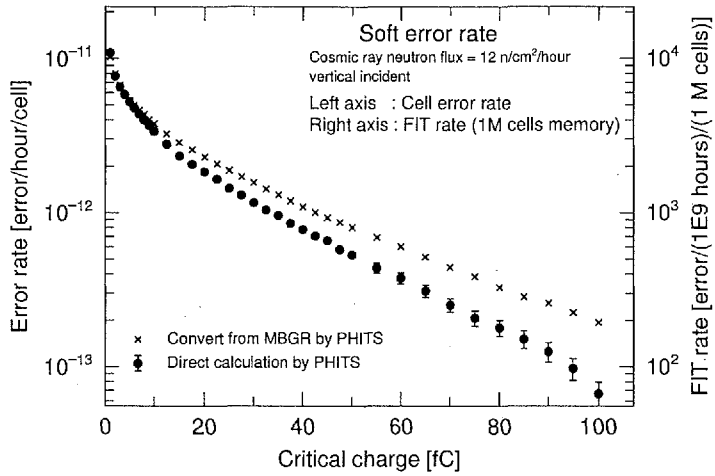

Figure 8: Soft error rate as a function of the critical charge. The unit of left axis is the error rate of a memory cell. The unit of right axis is the FIT rate [error/10^9 h/device] of a device with 1 M cells.

6 Summary

We successfully performed a soft error simulation using the PHITS Monte Carlo simulator. As a result of the validation, our MBGR calculation result agrees with a famous MBGR table by Fujitsu NISES simulator. The soft error rate simulation for a SRAM device shows a critical charge dependence of the error rate. The result shows that the soft error rate increases sharply as the critical charge decreases. We understand that the proton influence increases dramatically below 0.1 MeV deposit energy which corresponds to the critical charge of about 5 fC. Since the soft error critical charges of cutting edge technology devices are already below 5 fC, estimating effects of neutron-induced soft error would be very important for future devices.

References

[1] J.F. Ziegler "Terrestrial cosmic rays" IBM J. Res. Develop. Vol.40, No.1 January, 1996

[2] J.F. Ziegler "Terrestrial cosmic ray intensities" IBM J. Res. Develop. Vol.42, No.1 January, 1998

[3] H.Iwase, K.Niita T.Nakamura "Development of General-Purpose Particle and Heavy Ion Transport Monte Carlo Code " Journal of Nuclear Science and Technology, Vol.39, No.11, P.1142-1151 (Nov.2002)

[4] Koji Niita et. al. "Analysis of the (N,xN') reactions by quantum molecular dynamics plus statistical decay model" Phys.Rev.C52:2620-2635,1995

[5] Particle Data Group, Phys.Rev.D 66, 2002

[6] Y.Tosaka et.al. "Simulation Technologies for Cosmic Ray Neutron-Induced Soft Errors : Models and Simulation Systems." IEEE Trans. Nucl. Sci., NS-46, pp.774-780 (1999)

This is a blank page.

Appendix: Participant List

AKINO Fujiyoshi	JAERI
ANDO Yoshihira	Toshiba Co.
ANDOH Masaki	JAERI
Artisyuk, Vladimir	Tokyo Inst. of Tech.
ARUGA Takeo	JAERI
ASAI Masato	JAERI
ASAKURA Yohei	Nagoya Univ.
BABA Mamoru	Tohoku Univ.
CHATANI Hiroshi	Kyoto Univ.
Chen Wenge	CAS
CHIBA Gou	JNC
EDURA Yoshinobu	Kyoto Univ.
FUJIMOTO N.	JAERI
FUKAHORI Tokio	JAERI
FUKUSHIMA Masahiro	JAERI
FUMIZAWA Motoo	JAERI
FURUTAKA Kazuyoshi	JNC
GOKO Shinji	Konan Univ.
GOTO Jun	JAERI
GOTO Minoru	JAERI
HAGIWARA Masayuki	Tohoku Univ.
HANDA Takanobu	CSD
HANDA Yuichi	Musashi Inst. of Tech.
HARA Kaoru-Yamasaki	Konan Univ.
HARADA Masahide	JAERI
HASEGAWA Akira	JAERI
HAYASHI Hiroaki	Nagoya Univ.
HORI Jun-ichi	Kyoto Univ.
HORIGUCHI Takayoshi	Hiroshima Int. Univ.
ICHIHARA Akira	JAERI
ICHIKAWA Takatoshi	JAERI
IGASHIRA Masayuki	Tokyo Inst. of Tech.
IKEZOE Hiroshi	JAERI
ISHIKAWA Makoto	JNC
ITOGA Toshiro	Tohoku Univ.
IWAMOTO Osamu	JAERI
IWANAGA K.	JAERI
KATAKURA Jun-ichi	JAERI
KAWABE Katsuya	JCAC
KAWADE Kiyoshi	Nagoya Univ.
KAWAI Masayoshi	KEK
KAWAKAMI Yukiya	NEC
KAWASAKI Hiromitsu	CRC
KAWASAKI Kenji	JAERI
KIM Guinyun	KNU
KIMURA Atsushi	JAERI
KIMURA Itsuro	INSS
KOBAYASHI Katsuhei	Kyoto Univ.
KOBAYASHI Katsutoshi	JAERI
KOJIMA Kensuke	JAERI
KONNO Chikara	JAERI
KOSAKO Kazuaki	SAE
KUGO Teruhiko	JAERI
KUNIEDA Satosi	Kyushu Univ.
LEE Young-Ouk	KAERI
MAEDA Shigetaka	JNC
MAKI Koichi	Hitachi Ltd.
MATSUMOTO Hideki	MHI
MEIGO Shin-ichiro	JAERI
MIYAZAKI Itaru	Nagoya Univ.
MIZUMOTO Motoharu	JAERI
MORI Takamasa	JAERI
MURATA Isao	Osaka Univ.
MURATA Toru	AITEL
NAGAI Yasuki	Osaka Univ.
NAGAYA Yasunobu	JAERI
NAKAGAWA Tsuneo	JAERI
NAKAJIMA Ken	Kyoto Univ.
NAKAO Makoto	JAERI
NIITA Koji	RIST
NISHINAKA Ichiro	JAERI
NISHIO Katsuhisa	JAERI
NOJIRI Naoki	JAERI
OHKI Shigeo	JNC
OHKUBO Makio	N. Resonance Lab.
OHSAKI Toshiro	Tokyo Inst. of Tech.
OHSAWA Takaaki	Kinki Univ.
OIGAWA Hiroyuki	JAERI

OKAJIMA Shigeaki	JAERI
OKUMURA Keisuke	JAERI
OKUNO Hiroshi	JAERI
OSA Akihiko	JAERI
OTSUKA Naohiko	JAERI
OYAMATSU Kazuhiro	Aichi Shukutoku Univ.
SAKANE Hitoshi	JNC
SAKURAI Kiyoshi	JAERI
SAKURAI Takeshi	JAERI
SASA Toshinobu	JAERI
SATO Tatsuhiko	JAERI
SATOH Daiki	JAERI
SEKINE Takashi	JNC
SHIBATA Keiichi	JAERI
SHIBATA Michihiro	Nagoya Univ.
SHIMAKAWA Satoshi	JAERI
SHIMIZU Toshiaki	Nagoya Univ.
SHINDO Ryuichi	JAERI
SHONO Akira	JNC
SUEMATSU Osamu	Nagoya Univ.
SUGITA Takeshi	SSL
Sultana, Sadia Afroze	Kyushu Univ.
SUYAMA Kenya	JAERI
TACHIBANA Takahiro	Waseda U. Senior High School
TAHARA Yoshihisa	MHI
TAKAMURA Atsusi	SSL
TAKANO Hideki	JAERI
TOH Yosuke	JAERI
TSUDA Shuichi	JAERI
TSUJI Masatoshi	TEC
Uddin, Md. Shuza	Tohoku Univ.
UTSUNOMIYA Hiroaki	Konan Univ.
WATANABE Yukinobu	Kyushu Univ.
YAMAMOTO Kazuki	JAERI
YAMANE Tsuyoshi	JAERI
YAMANO Naoki	SAE
YOKAYAMA Kenji	JNC
YOKOMIZO Hideaki	JAERI
YONAI Shunsuke	Tohoku Univ.
YOSHIDA Tadashi	Musashi Inst. of Tech.
YOSHIDA Yoshitaka	INSS
Yu Weixiang	CIAE
ZUKERAN Atsushi	Hitachi Ltd.

国際単位系 (SI) と換算表

表 1　SI 基本単位および補助単位

量	名　称	記　号
長　さ	メートル	m
質　量	キログラム	kg
時　間	秒	s
電　流	アンペア	A
熱力学温度	ケルビン	K
物質量	モル	mol
光　度	カンデラ	cd
平面角	ラジアン	rad
立体角	ステラジアン	sr

表 2　SI と併用される単位

名　称	記　号
分，時，日	min，h，d
度，分，秒	°，′，″
リットル	l，L
トン	t
電子ボルト	eV
原子質量単位	u

1 eV = 1.60218 × 10^{-19} J

1 u = 1.66054 × 10^{-27} kg

表 3　固有の名称をもつ SI 組立単位

量	名　称	記号	他の SI 単位による表現
周波数	ヘルツ	Hz	s^{-1}
力	ニュートン	N	$m \cdot kg/s^2$
圧力，応力	パスカル	Pa	N/m^2
エネルギー，仕事，熱量	ジュール	J	N·m
工率，放射束	ワット	W	J/s
電気量，電荷	クーロン	C	A·s
電位，電圧，起電力	ボルト	V	W/A
静電容量	ファラド	F	C/V
電気抵抗	オーム	Ω	V/A
コンダクタンス	ジーメンス	S	A/V
磁束	ウェーバ	Wb	V·s
磁束密度	テスラ	T	Wb/m^2
インダクタンス	ヘンリー	H	Wb/A
セルシウス温度	セルシウス度	℃	
光束	ルーメン	lm	cd·sr
照度	ルクス	lx	lm/m^2
放射能	ベクレル	Bq	s^{-1}
吸収線量	グレイ	Gy	J/kg
線量当量	シーベルト	Sv	J/kg

表 4　SI と共に暫定的に維持される単位

名　称	記　号
オングストローム	Å
バーン	b
バール	bar
ガル	Gal
キュリー	Ci
レントゲン	R
ラド	rad
レム	rem

1 Å = 0.1 nm = 10^{-10} m

1 b = 100 fm^2 = 10^{-28} m^2

1 bar = 0.1 MPa = 10^5 Pa

1 Gal = 1 cm/s^2 = 10^{-2} m/s^2

1 Ci = 3.7 × 10^{10} Bq

1 R = 2.58 × 10^{-4} C/kg

1 rad = 1 cGy = 10^{-2} Gy

1 rem = 1 cSv = 10^{-2} Sv

表 5　SI 接頭語

倍数	接頭語	記　号
10^{18}	エクサ	E
10^{15}	ペタ	P
10^{12}	テラ	T
10^{9}	ギガ	G
10^{6}	メガ	M
10^{3}	キロ	k
10^{2}	ヘクト	h
10^{1}	デカ	da
10^{-1}	デシ	d
10^{-2}	センチ	c
10^{-3}	ミリ	m
10^{-6}	マイクロ	μ
10^{-9}	ナノ	n
10^{-12}	ピコ	p
10^{-15}	フェムト	f
10^{-18}	アト	a

（注）

1. 表 1 − 5 は「国際単位系」第 5 版，国際度量衡局 1985 年刊行による。ただし，1 eV および 1 u の値は CODATA の 1986 年推奨値によった。
2. 表 4 には海里，ノット，アール，ヘクタールも含まれているが日常の単位なのでここでは省略した。
3. bar は，JIS では流体の圧力を表わす場合に限り表 2 のカテゴリーに分類されている。
4. EC 閣僚理事会指令では bar，barn および「血圧の単位」mmHg を表 2 のカテゴリーに入れている。

換　算　表

力	N(=10^5dyn)	kgf	lbf
	1	0.101972	0.224809
	9.80665	1	2.20462
	4.44822	0.453592	1

粘　度　1 Pa·s(N·s/m^2) = 10 P(ポアズ)(g/(cm·s))

動粘度　1 m^2/s = 10^4 St(ストークス)(cm^2/s)

圧力	MPa(=10 bar)	kgf/cm^2	atm	mmHg(Torr)	lbf/in^2(psi)
	1	10.1972	9.86923	7.50062 × 10^3	145.038
	0.0980665	1	0.967841	735.559	14.2233
	0.101325	1.03323	1	760	14.6959
	1.33322 × 10^{-4}	1.35951 × 10^{-3}	1.31579 × 10^{-3}	1	1.93368 × 10^{-2}
	6.89476 × 10^{-3}	7.03070 × 10^{-2}	6.80460 × 10^{-2}	51.7149	1

エネルギー・仕事・熱量	J(=10^7 erg)	kgf·m	kW·h	cal(計量法)	Btu	ft·lbf	eV
	1	0.101972	2.77778 × 10^{-7}	0.238889	9.47813 × 10^{-4}	0.737562	6.24150 × 10^{18}
	9.80665	1	2.72407 × 10^{-6}	2.34270	9.29487 × 10^{-3}	7.23301	6.12082 × 10^{19}
	3.6 × 10^6	3.67098 × 10^5	1	8.59999 × 10^5	3412.13	2.65522 × 10^6	2.24694 × 10^{25}
	4.18605	0.426858	1.16279 × 10^{-6}	1	3.96759 × 10^{-3}	3.08747	2.61272 × 10^{19}
	1055.06	107.586	2.93072 × 10^{-4}	252.042	1	778.172	6.58515 × 10^{21}
	1.35582	0.138255	3.76616 × 10^{-7}	0.323890	1.28506 × 10^{-3}	1	8.46233 × 10^{18}
	1.60218 × 10^{-19}	1.63377 × 10^{-20}	4.45050 × 10^{-26}	3.82743 × 10^{-20}	1.51857 × 10^{-22}	1.18171 × 10^{-19}	1

1 cal = 4.18605 J (計量法)

= 4.184 J　(熱化学)

= 4.1855 J　(15 °C)

= 4.1868 J (国際蒸気表)

仕事率　1 PS (仏馬力)

= 75 kgf·m/s

= 735.499 W

放射能	Bq	Ci
	1	2.70270 × 10^{-11}
	3.7 × 10^{10}	1

吸収線量	Gy	rad
	1	100
	0.01	1

照射線量	C/kg	R
	1	3876
	2.58 × 10^{-4}	1

線量当量	Sv	rem
	1	100
	0.01	1

(86 年 12 月 26 日現在)

Proceedings of the 2003 Symposium on Nuclear Data, November 27-28, 2003, JAERI, Tokai, Japan